Surender Kumar Sharma *Editor*

Complex Magnetic Nanostructures

Synthesis, Assembly and Applications

Springer

Complex Magnetic Nanostructures

Surender Kumar Sharma
Editor

Complex Magnetic Nanostructures

Synthesis, Assembly and Applications

Springer

Editor
Surender Kumar Sharma
Department of Physics
Federal University of Maranhão
São Luis, MA, Brazil

Department of Physics
H. P. University
Shimla, India

ISBN 978-3-319-52086-5 ISBN 978-3-319-52087-2 (eBook)
DOI 10.1007/978-3-319-52087-2

Library of Congress Control Number: 2017935571

© Springer International Publishing AG 2017
This work is subject to copyright. All rights are reserved by the Publisher, whether the whole or part of the material is concerned, specifically the rights of translation, reprinting, reuse of illustrations, recitation, broadcasting, reproduction on microfilms or in any other physical way, and transmission or information storage and retrieval, electronic adaptation, computer software, or by similar or dissimilar methodology now known or hereafter developed.
The use of general descriptive names, registered names, trademarks, service marks, etc. in this publication does not imply, even in the absence of a specific statement, that such names are exempt from the relevant protective laws and regulations and therefore free for general use.
The publisher, the authors and the editors are safe to assume that the advice and information in this book are believed to be true and accurate at the date of publication. Neither the publisher nor the authors or the editors give a warranty, express or implied, with respect to the material contained herein or for any errors or omissions that may have been made. The publisher remains neutral with regard to jurisdictional claims in published maps and institutional affiliations.

Printed on acid-free paper

This Springer imprint is published by Springer Nature
The registered company is Springer International Publishing AG
The registered company address is: Gewerbestrasse 11, 6330 Cham, Switzerland

Preface

The magnetic properties of nanoparticles have long been an object of study, but there remains an irritating diversity of phenomena that await full comprehension. The main implication of magnetic nanoparticles is the uniformity in the magnetic properties of individual particles in real dispersion systems, which makes it possible to directly correlate the magnetic properties of a whole material with those of each individual particle.

One of the main aims in preparing this book was to highlight the complex magnetic behavior of magnetic nanosystems composed of a core-shell, heterodimer, dumbbell geometries, and so on and their utility for application purposes. This book does not provide a comprehensive review of the many studies concerned with complex magnetic nanoparticles; instead, we concentrate our attention on presenting an expansive synopsis, furnishing key examples, and trying to motivate a deeper than usual examination of cutting-edge fundamental developments in the field. This will likely distinguish the book from other works in the literature.

The book will provide a forum for critical evaluations of many aspects of complex magnetism that are at the forefront of nanoscience today. The chapters do not cover the entire range of issues associated with nanomagnetism, which would be infinite, but rather present highlights, especially in the domains of interest to the authors and editor, while keeping an eye on the most up-to-date research in the field. I hope that the book, which will probably emerge as the primary text dealing with the general aspects of complex magnetic nanoparticles, will prove useful for all the various people interested in nanomagnetism: from beginning- and graduate-level students up to advanced specialists in both academic and industrial settings. The first few chapters allow the book to be used as a first text on research in this area and therefore will benefit readers coming to the subject from diverse perspectives.

São Luis, Brazil
November 2016

Dr. Surender Kumar Sharma

Contents

Contributors

Khuram Ali Nano-Optoelectronics Research Laboratory, Department of Physics, University of Agriculture Faisalabad, Faisalabad, Pakistan

Hafeez Anwar Department of Physics, University of Agriculture Faisalabad, Faisalabad, Pakistan

Tanuja Bisht Department of Chemistry, Government Post Graduate College, Champawat, Uttarakhand, India

Keya Chaudhuri Molecular Genetics Division, CSIR-Indian Institute of Chemical Biology, Kolkata, India

Trupti R. Das Functional Nanomaterials Research Laboratory, Department of Applied Physics, Indian Institute of Technology (Indian School of Mines), Dhanbad, Jharkhand, India

Suryakanti Debata Functional Nanomaterials Research Laboratory, Department of Applied Physics, Indian Institute of Technology (Indian School of Mines), Dhanbad, Jharkhand, India

P.B.A. Fechine Departamento de Química Analítica e Físico-Química, Group of Chemistry of Advanced Materials (GQMAT), Universidade Federal do Ceará—UFC, Fortaleza, Brazil

Adriana I. Figueroa Magnetic Spectroscopy Group, Diamond Light Source, Didcot, UK

Rafael M. Freire Departamento de Química Analítica e Físico-Química, Group of Chemistry of Advanced Materials (GQMAT), Universidade Federal do Ceará—UFC, Fortaleza, Brazil

Tiago M. Freire Departamento de Química Analítica e Físico-Química, Group of Chemistry of Advanced Materials (GQMAT), Universidade Federal do Ceará—UFC, Fortaleza, Brazil

Wesley S. Galvão Departamento de Química Analítica e Físico-Química, Group of Chemistry of Advanced Materials (GQMAT), Universidade Federal do Ceará—UFC, Fortaleza, Brazil

Bhaskar Garg Department of Chemistry, Indian Institute of Technology Roorkee, Roorkee, Uttarakhand, India

Yasir Jamil Nano-Optoelectronics Research Laboratory, Department of Physics, University of Agriculture Faisalabad, Faisalabad, Pakistan

Yasir Javed Nano-Optoelectronics Research Laboratory, Department of Physics, University of Agriculture Faisalabad, Faisalabad, Pakistan

Paramita Karfa Department of Applied Chemistry, Indian Institute of Technology (Indian School of Mines), Dhanbad, Jharkhand, India

Latif U. Khan Brazilian Nanotechnology National Laboratory (LNNano), Brazilian Center for Research in Energy and Materials (CNPEM), Rua Giuseppe Máximo Scolfaro, Campinas, São Paulo, Brazil

Zahid U. Khan Departamento de Imunologia, Instituto de Ciências Biomédicas-IV, Universidade de São Paulo, São Paulo, SP, Brazil

Chi-Hung Lee Department of Physics, National Central University, Jhongli, Taiwan

Wen-Hsien Li Department of Physics, National Central University, Jhongli, Taiwan

Oscar Moscoso Londoño LMBT, Instituto de Física "Gleb Wataghin", Universidade Estadual de Campinas, Campinas, SP, Brazil

Universidad Autónoma de Manizales, Antigua Estación del Ferrocarril, Manizales, Colombia

Rashmi Madhuri Department of Applied Chemistry, Indian Institute of Technology (Indian School of Mines), Dhanbad, Jharkhand, India

Samir Mandal Molecular Genetics Division, CSIR-Indian Institute of Chemical Biology, Kolkata, India

Santanu Patra Department of Applied Chemistry, Indian Institute of Technology (Indian School of Mines), Dhanbad, Jharkhand, India

Ekta Roy Department of Applied Chemistry, Indian Institute of Technology (Indian School of Mines), Dhanbad, Jharkhand, India

Sarveena Department of Physics, H. P. University, Shimla, India

Prashant K. Sharma Functional Nanomaterials Research Laboratory, Department of Applied Physics, Indian Institute of Technology (Indian School of Mines), Dhanbad, Jharkhand, India

Surender Kumar Sharma Department of Physics, Federal University of Maranhão, São Luis, MA, Brazil

Department of Physics, H. P. University, Shimla, India

Navadeep Shrivastava Department of Physics, Federal University of Maranhão, São Luis, MA, Brazil

Institute of Chemistry, University of São Paulo, São Paulo, SP, Brazil

M. Singh Department of Physics, H. P. University, Shimla, India

Leandro M. Socolovsky LSA, INTECIN, Facultad de Ingeniería, Universidad de Buenos Aires-CONICET, Buenos Aires, Argentina

K.R. Justin Thomas Department of Chemistry, Indian Institute of Technology Roorkee, Roorkee, Uttarakhand, India

Chapter 1
Consequences of Magnetic Interaction Phenomena in Granular Systems

Leandro M. Socolovsky and Oscar Moscoso Londoño

1.1 Introduction

Magnetic granular materials are composites in which a matrix is filled with magnetic particles that have sizes in the nanometer range. Examples of such materials are those prepared by sputtering, where two or more elements that do not easily form compounds are deposited onto a substrate; an incomplete multilayer deposition; a heterogeneous alloy; nanoparticles incorporated into a matrix by physical methods; or even agglomerations of nanoparticles covered with another substance. Figure 1.1 shows two such granular materials. For several decades nanostructures have been produced by physical and chemical methods. Enhanced techniques for the manipulation of matter at the nanoscale have enabled the preparation of better controlled nanostructures. Such magnetic granular materials have interesting physical and chemical properties that are also of technological interest. Some of those physical properties are related to magnetism, like superparamagnetism, or, in connection with magnetotransport, giant magnetoresistance (GMR), tunneling magnetoresistance (TMR), and the giant Hall effect (GHE). Some of these are currently being exploited in computer hard disks, perpendicular recording of magnetic bits, and in biomedical applications such as drug delivery and magnetohyperthermia, among others. The read heads of modern hard disks, which use the GMR effect, represent the first

L.M. Socolovsky (✉)
LSA, INTECIN, Facultad de Ingeniería, Universidad de Buenos Aires-CONICET, Av. Paseo Colón 850, C1063ACV, Buenos Aires, Argentina
e-mail: lsocolovsky@fi.uba.ar

O. Moscoso Londoño
LMBT, Instituto de Física "Gleb Wataghin", Universidade Estadual de Campinas, Campinas, SP, Brazil

Universidad Autónoma de Manizales, Antigua Estación del Ferrocarril, Manizales, Colombia
e-mail: omoscoso@ifi.unicamp.br; oscar.moscosol@autonoma.edu.co

© Springer International Publishing AG 2017

S.K. Sharma (ed.), *Complex Magnetic Nanostructures*,
DOI 10.1007/978-3-319-52087-2_1

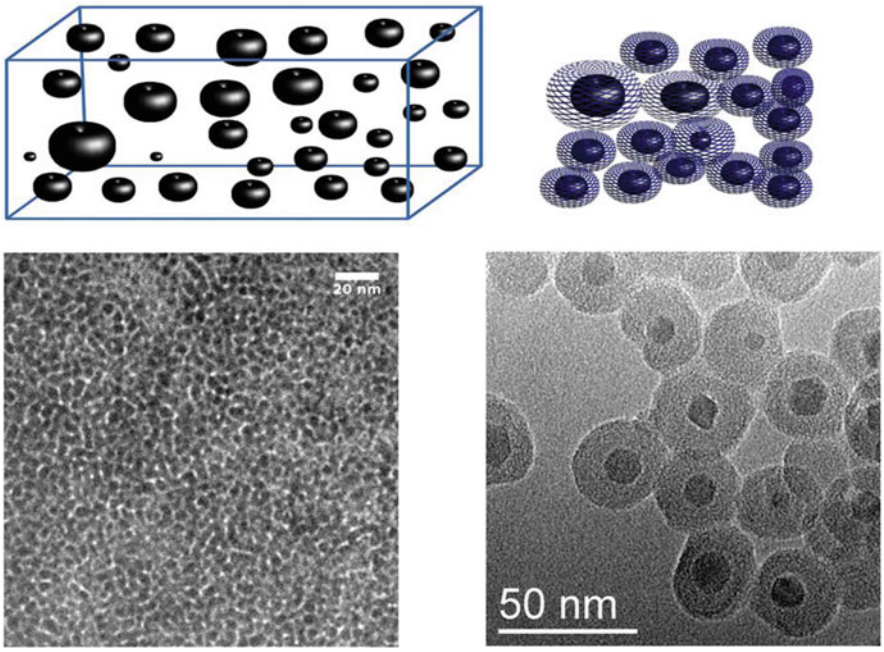

Fig. 1.1 *Above*: A granular material can be formed by the dispersion of nanoparticles in a matrix (*left*) or by the clustering of grafted nanoparticles (*right*). *Below*: (*left*) cobalt nanoparticles in a silica matrix; (*right*) magnetite nanoparticles grafted with silica (Image courtesy Dr. D. Muraca)

practical realization of spintronics [1]. Spintronics is considered a new technology that differs from electronics in that it can be used to control the spins of electron instead of their electrical charge, opening up new possibilities for devices that will cause them to run faster and with less thermal energy losses.

Our focus in this chapter is on phenomena that occur in magnetic granular materials, considering the broad spectrum of interest they have attracted in very disparate areas of research, for example, chemistry, physics, biology, medicine, and various branches of engineering. For most workers in these fields, we believe, an article that presents a first approach to experimental results found using the most common measurement techniques would be of great practical value. We expressly omit any discussions of in-depth theory and less common measurement techniques. Our purpose is to review briefly some important concepts, recent results, and discussions and to highlight the connections between magnetic and magnetotransport phenomena, stressing experimental results and the best known analyses. We present results obtained from various experiments performed in the course of our research.

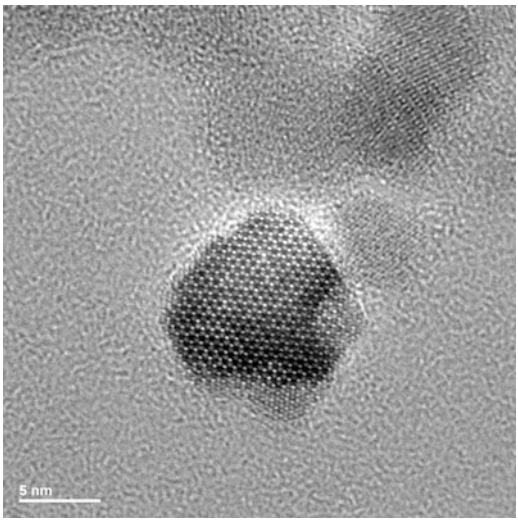

Fig. 1.2 Transmission electron microscopy image of a magnetite nanoparticle. Atoms are seen as *dots*, and the crystalline arrangement is evident. Surface atoms are a significant fraction

1.1.1 Superparamagnetism

A single magnetic nanoparticle of a few nanometers (Fig. 1.2) can be composed of a magnetic material like iron, cobalt, nickel, gadolinium, or their alloys, and some oxides of iron, cobalt, and manganese have a magnetic order of their own given by interchange or super-interchange interactions, depending on the material [2, 3]. Magnetic materials tend to minimize energy by breaking down their magnetic order into domains, which are regions that are magnetized in different orientations. Frontiers between domains are called domain walls, which require the creation of extra energy. If a magnetic material is small enough, that extra energy is costly compared with that needed to remain a unique magnetic domain. In that case, to keep energy in a minimum, the magnetic order inside a nanoparticle will not break down into domains, so it will remain a magnetic monodomain. In a first approximation, all atoms in the nanoparticle will add their magnetic moments to form a supermoment, which represents nanoparticle magnetization as a whole. In other magnetic materials that are antiferromagnetic (AFM) or ferrimagnetic (FiM), the net magnetic moment of the atomic arrangement will represent the nanoparticle's whole magnetization. This supermoment also indicates that all atomic magnetic moments will behave in unison in response to external magnetic fields [4].

Considering that competition over the energy needed to create a domain wall and to minimize energy use, all magnetic materials will have a critical size for a tiny magnetic particle to become a monodomain. Theoretically, for a uniaxial spherical crystal with a large anisotropy constant K, the critical radius r_c is

$$r_c \approx 9\frac{(AK)^{1/2}}{\mu_0 M_s^2}, \tag{1.1}$$

where A is the exchange constant, μ_0 is the constant of magnetic permeability, and M_s is the saturation magnetization. Using the preceding expression, r_c is 3 nm for Fe and 4–8 nm for Co [3, 5]. This critical size must be taken as a rough first approximation owing to the simplifications performed in that calculation. More accurate models give larger critical radii [3]. Critical sizes are below 100 nm for most magnetic materials [5, 6]. Most experiments conducted with magnetic nanoparticles use magnetite, maghemite, or cobalt ferrite, which have approximate critical sizes of 64, 45, and 50 nm [5], respectively.

Because of the crystalline order in nanoparticles, supermoments tend to align with some specific crystallographic orientations. Those orientations are known as *easy axes*. Thermal energy causes supermoments to flip among easy axes. At a high enough temperature and for a given period of observation time (measurement time), this flipping causes the average magnetic moment of nanoparticle supermoments to be zero. In other words, a magnetic material, if small enough, will appear as a nonmagnetic material at, for example, room temperature. We can measure a nonzero magnetization if our measurement device is fast enough at a given temperature. As a consequence, depending on the technique used for measuring, we can "see" the magnetic moment of a nanoparticle if our instrument is fast enough to measure some supermoment at a given orientation. If the device takes measurements too slowly, the supermoment will flip back and forth between easy axis orientations, so the measured average moment will be zero. This property is called *superparamagnetism* (SPM), and it is considered a type of magnetic order in materials [2, 6–10]. For details on this mechanism and its formulation, see Knobel et al. [4]. Early formulations of superparamagnetic theory started by considering a set of noninteracting magnetic nanoparticles. The magnetization, M, of these kinds of magnetic systems can be described by a Langevin function L:

$$\frac{M}{M_S} = \coth\left(\frac{\mu H}{k_B T}\right) - \frac{k_B T}{\mu H} = L\left(\frac{\mu H}{k_B T}\right), \tag{1.2}$$

where M_S is the saturation magnetization, H the magnetic field, T the absolute temperature, μ the magnetic moment (supermoment), and k_B the Boltzmann constant.

In these schemes, all atoms behave in similar way, regardless of whether they are in the core of the nanoparticle or on the surface. It is also assumed that there is only one easy axis. These descriptions apply in the study of granular systems in first approximations. Of course, these are naïve descriptions that do not take into account surface effects, more than one easy axis, close nanoparticles, or distributed properties such as size, moment, or blocking temperature distributions, for example [4].

1.1.2 Anisotropies

The energies of interactions are manifested through a quantity called anisotropy, K. Anisotropy derives from two basic origins: spin-orbit and magnetostatic interactions. We briefly enumerate those that are usually found in nanoparticles: magnetocrystalline, surface, shape, and strain anisotropies.

1. **Magnetocrystalline anisotropy**: this is a manifestation of the internal energy's dependence on the direction of spontaneous magnetization. It forces a magnetic moment to stay in certain preferred orientations that coincide with crystallographic axes because electron orbits are linked to them. Although magnetocrystalline anisotropy changes with temperature, in most analyses in SPM experimental studies, this is not considered explicitly [3, 9]. It is important to stress that it is this anisotropy that orients the magnetization of a nanoparticle.
2. **Surface anisotropy**: atoms located at surfaces experience a break in symmetry in their interactions because the near-neighbor population is different from those atoms located at the core. In nanoparticles, the surface-to-volume ratio is large because of the small dimensions, so this effect can be important [11]. As is made clear in Fig. 1.2, which shows a 7 nm nanoparticle, several atoms are located on or close to the surface. The smaller the particle, the more relevant this anisotropy becomes, eventually surpassing the effects of magnetocrystalline anisotropies. The roughness of the interface is also another source of the anisotropy.
3. **Shape anisotropy**: this type of anisotropy depends on the differences in the shape of the magnetic specimen, which gives rise to different demagnetization factors in different orientations. If it is spherical, there is no such contribution.
4. **Strain anisotropy**: this comes from mechanical stresses induced by the deformation of the crystalline structure.

Detailed discussions on anisotropies can be found in the excellent and enjoyable book of Aharoni and in the very useful reviews of Bedanta [5, 9, 10] and Majetich [12].

Magnetostriction plays an important role in interactions with temperature by shrinking or expanding nanocrystals, which can change their shape and size. Also, dependences with temperature of magnetocrystalline anisotropy factors contribution to modifications of the energy barrier [9]. In real systems all those anisotropies are considered, through their effects on the measured magnetization, as an effective value, K_{ef}. This effective value is calculated using

$$\tau = \tau_0 \mathrm{e}^{\frac{E_\mathrm{B}}{k_\mathrm{B} T}}, \tag{1.3}$$

in which $E_\mathrm{B} = K_{\mathrm{ef}}\, V$, where τ is the relaxation time, which is spent by the supermoment to jump between easy axes. The constant τ_0 is the attempt time, in which the magnetization vector "tries" to jump between easy axis directions. It is accepted that τ_0 has values in a range of 10^{-9}–10^{-11} s. The reciprocal of this parameter has dimensions of frequency and is denoted by f_0 [4, 5, 9–12].

A systematic study on well-prepared cobalt ferrite nanoparticles showed a consistency with this usage of an effective anisotropy with an explicit dependence on temperature and a phenomenological model that works with that material [13, 14]. In brief, it is through anisotropies that specific characteristics of nanoparticles and granular materials will be reflected in magnetic properties.

1.2 Interactions Among Nanoparticles

In real systems, nanoparticles are not very far from each other, so in principle, the magnetism of one nanoparticle should affect others. Principally, two long-range interactions, known as dipolar and RKKY, must be considered in granular materials. A dipolar interaction is described by

$$E = \frac{\mu_0}{4\pi r^3}\left[\left(\vec{m_1}\cdot\vec{m_2} - \frac{3}{r^2}\left(\vec{m_1}\cdot\vec{r} + \vec{m_2}\cdot\vec{r}\right)\right)\right], \tag{1.4}$$

where m_1 and m_2 are the magnetization vectors of entities like nanoparticles, separated by a distance r [6]. Since a nanoparticle can have hundreds or thousands of atoms, a typical value of m can be on the order of 10^3–10^5 Bohr magnetons. At close distances, this energy term can be relevant. In any case, the dipolar energy calculated using this expression should be taken as an upper limit.

As can be seen, dipolar energy depends on nanoparticles' magnetic moment separation and their mutual alignment [5–7]. Because real nanoparticle systems contain between at least 10^{10} and 10^{20} nanoparticles/cm^3, use of the preceding equation makes it rather difficult to quantify the dipolar effects in a nanostructured system. In this situation, Hansen and Mørup show that for a set of randomly distributed magnetic nanoparticles, the dipolar energy can be calculated using

$$E_\mathrm{d} \approx \frac{\mu_0}{4\pi}\frac{m^2}{r^3}. \tag{1.5}$$

In this formulation, m and r are assumed to be the averages of the magnetic moment and the nanoparticle separation, respectively [14].

In a granular material, another important type of long-range interaction is the well-known RKKY interaction. Such interactions, formulated by Ruderman, Kittel, Kasuya, and Yoshida in the mid-1950s, appears in materials with itinerant electrons. In the particular case of nanoparticles supported in a metallic matrix, the RKKY interaction does not involve a direct coupling between magnetic nanoparticle moments but is mediated by itinerant electrons, which are subject to a localized magnetic moment that polarizes them [8], that is, the mediated electrons are affected by a spin-dependent local potential. This interaction is present in granular materials where the matrix is metallic. RKKY interactions are oscillatory and fall with the

cubic power of distance. At large distances the term that regulates the strength of this interaction, the exchange parameter J, is

$$J = J_0 \left[\frac{\cos\left(2k_F r + \varphi\right)}{\left(2k_F r\right)^3} \right], \tag{1.6}$$

where J_0 is a constant, k_F is the Fermi momentum, and φ is a phase that depends on the matrix and the magnetic entity. The parameter J can have positive or negative values, depending on the distance. Details on this expression are not important for our study and can be found in [8, 9, 15, 16].

Besides when magnetic nanoparticles are close enough or in contact, a direct exchange, or a Dzyaloshinskii–Moriya or superexchange, interaction is established among surface magnetic ions with spins $\boldsymbol{S_i}$ and $\boldsymbol{S_j}$, which belong to different nanoparticles:

$$H_{DM} = \overrightarrow{d_{ij}} \cdot \left(\overrightarrow{S_i} \times \overrightarrow{S_j} \right). \tag{1.7}$$

When nanoparticles are very close to each other, or even in contact, a dipolar interaction is not the predominant one. Direct interaction between magnetic ions located on different nanoparticles can be common, so a new magnetic state emerges. This state is usually called *superspin glass* (SSG) [5]. This name might no seem appropriate at first sight because the origin of the new state does not lie in the competing RKKY interaction, as is the case for spin glasses [17]. When percolation is established, then we have a state called *superferromagnetism* (SFM) [5, 18]. In the authors' opinion, more appropriate names could be used, such as *interacting superparamagnetism* (I-SPM) instead of SSG or *percolated superparamagnetism* (P-SPM) instead of SFM. A qualitative magnetic phase diagram is shown in Fig. 1.3.

We can think of these magnetic behaviors in granular systems as balls of the same size that fill a large glass box (Fig. 1.4). Let us imagine black balls as magnetic nanoparticles and the white matter that surrounds them as a nonmagnetic matrix. We begin by considering the box filled exclusively by white matter: our system is nonmagnetic. If we randomly add more balls, which may be far apart, we will have a canonical superparamagnetic system. With the addition of more balls, the system more closely resembles a real superparamagnet. We can easily see that as our magnetic nanoparticle concentration increases (with the addition of more balls), some of the balls will come into close contact with each other, sometimes with more than two balls, and we see SSG or I-SPM states. If we continue to fill the receptacle, we will see more and more chains of balls, until we see a pathway spanning the whole box. This point is called the *percolation limit*, and its magnetic manifestation is the SFM or P-SPM state. When this percolated state is reached, there will still be isolated balls, so we must expect a complex magnetic behavior that will show both SPM and ferromagnetic features. By adding more balls, we finally obtain a fully ferromagnetic state.

Percolation is a geometrical concept [19]. The situation presented here just shows contacting particles. Because we are talking about magnetism, which is force that

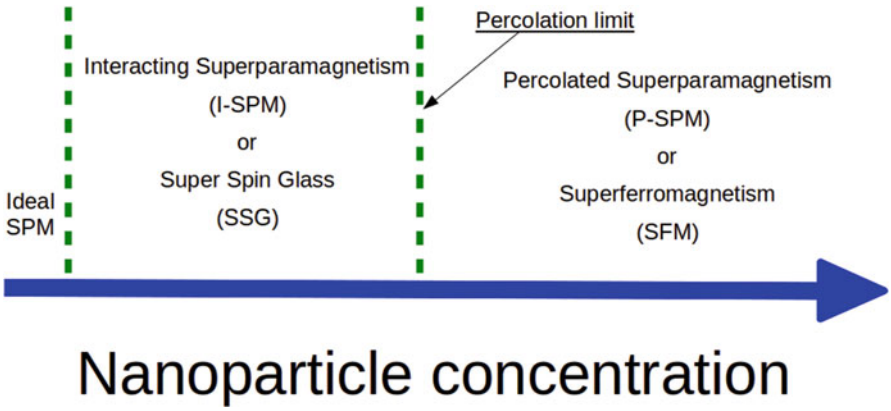

Fig. 1.3 Changing nanoparticle concentration, in three phases. Less-concentrated granular materials behave as predicted by theory. The intermediate range (I-SPM or SSG) can be described, at lower concentrations, by Dormann–Bessais–Fiorani, Mørup, or T^* models [4]. At higher concentrations, only a T^* model can describe magnetic behavior. Close to the percolation limit all models fail. At that percolation limit, a long-range magnetic order, based on direct interchange between atoms, starts to become established until a full ferromagnetic-like (e.g., FM or AFM) order sets in

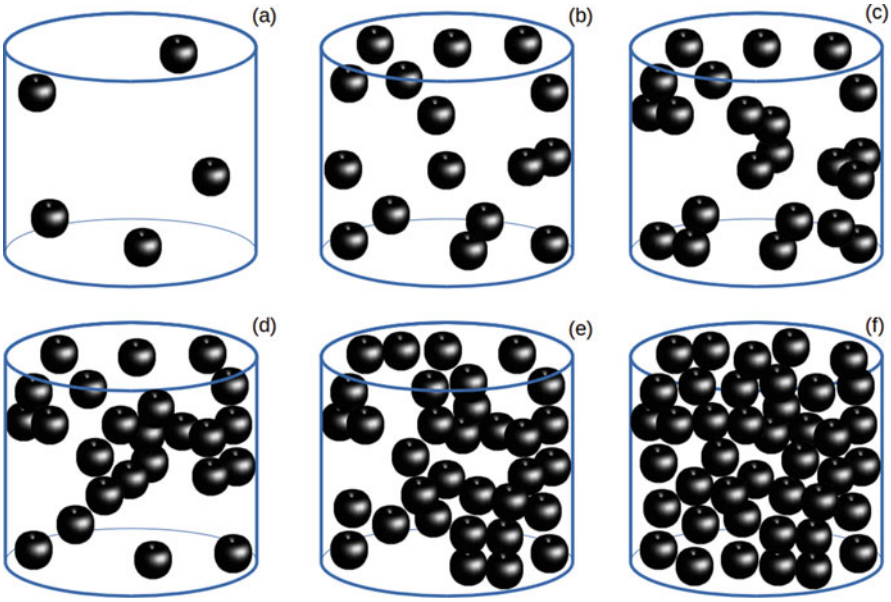

Fig. 1.4 *Black balls* represent magnetic nanoparticles. As the receptacle is filled with magnetic nanoparticles, the system evolves from a noninteracting system to a fully percolated one. Pictures (**a**–**c**) represents granular materials above percolation threshold, and (**d**–**f**) represent percolated systems

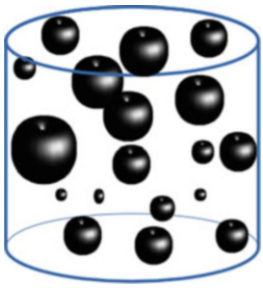

Fig. 1.5 In real samples there are larger and smaller nanoparticles, each with a magnetic moment of different magnitude

acts at a distance, it is not strictly necessary that the nanoparticles be touching each other. Direct exchange can be sizable at distances of up to a few nanometers, so a coupled magnetic ordering can be established, even without direct contact between nanoparticles [20]. A question arises: when can a granular material be considered to be diluted or noninteracting? As we saw from the earlier equations, the strength of forces among nanoparticles depends not only on distances but also on the supermoment and size [21]. As a rule of thumb, a dispersion of 0.01 vol.% or less can be considered as being close to a noninteracting system [22].

Also, to depict a real system, we must consider the size distribution, so in our imaginary experiment, we must use larger and smaller balls (Fig. 1.5). Clearly, the supermoments of larger nanoparticles exert a stronger influence on their neighborhoods compared to smaller nanoparticles, as was pointed in the work of Allia et al. [23].

Initially, we considered a nonmagnetic matrix. This matrix can, in principle, be a conductive, semiconductive, or dielectric material. It can also have a different magnetic order, like an antiferromagnet, that can lead to the emergence of very interesting properties, like the shift of the blocked regime of the superparamagnetic state to higher temperatures. Such a granular system can enable denser recording on hard disk drives. In a disk, a bit is recorded by orienting a magnetic sector on the surface in one direction or another, representing a 1 or a 0, the basis for binary code. Because this recording sector must be small, to allow for dense recording, its size approaches the superparamagnetic limit. If that size is small enough to be in the superparamagnetic state at room temperature or slightly higher, it is not possible to keep the magnetization as at the original level. To avoid that superparamagnetic limit, it was demonstrated that it is possible to produce a granular material with the desired effect [24, 25]. A granular structure like that described in the cited articles is composed of superparamagnetic cobalt nanoparticles in an antiferromagnetic matrix. The matrix, made up of cobalt oxide, helps to retain the magnetization by shifting the blocking temperature to higher temperatures than that of the original nanoparticle, as would be the case in a nanosized sector alone. This architecture makes it possible to overcome the size limitation, thereby enabling dense recording.

1.2.1 Footprints of a Granular System

When we need to know whether a material is composed of superparamagnetic particles and how they are dispersed in the matrix, we can use magnetic measurements. Two easy ones are magnetization M versus temperature T (M vs. T) and magnetization versus the applied magnetic field H (M vs. H).

1.2.1.1 Magnetization vs. Temperature Measurements

Magnetization temperature dependence is commonly used to investigate the magnetic behavior of nanoparticle systems. This is usually done in two modes, first by freezing the sample without an applied field up to a low enough temperature (usually a few Kelvin), then applying a very small magnetic field, followed by measuring the magnetization at various increasing temperatures. This mode is called zero field cooling (ZFC). Using the same procedure but this time cooling the sample in the same applied field will give a slightly different curve, called field cooling (FC). The reason for using such modes can be understood if we consider that when our sample is cooled without a magnetic field (ZFC), nanoparticle's supermoments are frozen in random orientations. When a sample reaches the desired temperature, a magnetic field of a few oersted is set. This magnetic field establishes an orientation for those supermoments to follow. Because all supermoments are frozen in fixed positions, the measured magnetization will be almost zero. Raising the temperature will add thermal energy to our sample, so supermoments will have more freedom to move, to follow the magnetic field orientation. In this way, the measured magnetization will increase as more and more supermoments become unfrozen in a process known as unblocking. This will occur until a majority of the supermoments become unblocked. The temperature at which this happens is called the *blocking temperature*, T_B. Thermal energy introduces disorder because the supermoments gain energy to flip between easy axes. The disordering of more and more supermoments takes place when the temperature is raised, so the measured magnetization decreases, following a Curie-type law. Although this type of magnetism type is referred to as superparamagnetic, it is common to use the term *blocked state* when the system is at temperatures below T_B and to call it a *superparamagnetic state* when it is at temperatures above T_B. The functional form for a system consisting of noninteracting nanoparticles is

$$M_{ZFC}(T) = \frac{M_S^2 H}{3K_{ef}}\left[\ln\left(\frac{\tau_m}{\tau}\right)\frac{1}{T}\int_0^T T_B f\left(T_B\right) dT_B + \int_T^\infty f\left(T_B\right) dT_B\right]. \tag{1.8}$$

Note that in the preceding function, $M_{ZFC}\,(T)$ is dependent on the magnetization saturation M_S, applied magnetic field H, effective anisotropy K_{ef}, the measurement time τ_m, and the attempt time τ_0, which is assumed to be on the order of

10^{-9}–10^{-10} s, as mentioned earlier. Also, such a dependence was weighted using a blocking temperature distribution, which of course is directly related to the size distribution.

All real systems contain relatively larger and smaller particles, regardless of the method used to fabricate them. This distribution of sizes usually follows a lognormal or Gaussian function. This means that the exponential term in Eq. 1.3 is different, not only because of the volume but because of the anisotropy. Most nanoparticle systems have a lognormal size distribution. Because they are nonsymmetric, the mean value is different from the median and mode values. Knobel et al. present an interesting discussion on this point [4].

On the other hand, a large number of magnetic nanostructured systems have been reported as superparamagnetic and studied in the framework of this theory. Nevertheless, a lack of agreement between experimental data and standard superparamagnetic theory, as well as the obtained spurious parameters, is commonly observed. Anisotropy constant K is generally calculated using the approximate equation

$$K_{\mathrm{ef}} = 25 k_{\mathrm{B}} T_{\mathrm{B}} / V, \tag{1.9}$$

which derives from Eq. 1.3, in which are applied logarithms evaluated at the blocking temperature T_{B}. It is considered that a characteristic measurement time for DC magnetometry lies around 100 s [4]. The first challenge, which involves the use of Eq. 1.9, is to correctly determine the blocking temperature, for which there is no established protocol, meaning some research groups use the maximum of the ZFC curve, whereas others, knowing that the sample has distributed properties (e.g., distribution of sizes, blocking temperatures, anisotropies), first determine the blocking temperature distribution, generally through

$$f\left(T_{\mathrm{B}}\right) = \frac{d}{dT}\left(M_{\mathrm{ZFC}} - M_{\mathrm{FC}}\right), \tag{1.10}$$

from which the mean blocking temperature $\langle T_{\mathrm{B}} \rangle$ can be extracted [26]. According to the Ref. [27], the derivative method is the best for obtaining the blocking temperature distribution [25].

We depict this process to illustrate the following remarks. Figure 1.6 shows six different types of ZFC curves commonly seen in real granular materials. Each curve corresponds to the physical situation described in Fig. 1.4. Here, *a*, *b*, and *c* correspond to nonpercolated systems. The first one, *a*, is typical of a noninteracting system. Characteristic features we can observe in such curves include (1) a concavity at low temperatures, (2) a rounded peak, and, at $T \geq T_{\mathrm{peak}}$, (3) a decrease in the magnetization with temperature, approximately following a $1/T$ dependence.

For other interacting systems, the peak shifts to higher temperatures and the high-temperature side of the curve departs from a Curie-type law at temperatures close to that of the maximum, as seen in *b*. The third one, *c*, corresponds to a

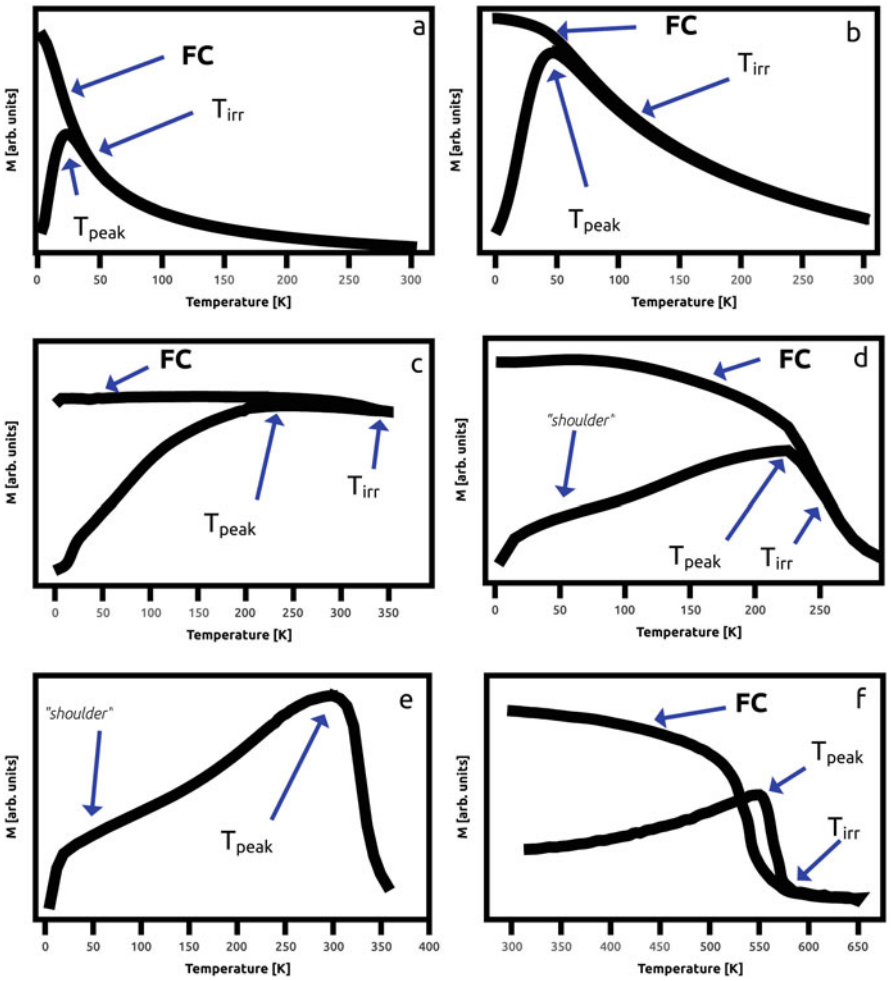

Fig. 1.6 The maximum of a ZFC is called the *peak temperature*, T_{peak}. The irreversibility temperature, T_{irr}, is also marked. (**a**) Magnetite nanoparticles dispersed in paraffin at very low concentration. (**b**) Magnetite nanoparticles grafted with SiO_2; dipolar interaction plays a role. (**c**) Magnetite nanoparticles grafted with acetic acid, compressed in pellets. (**d**) Fe–Cu alloy, with iron concentration slightly *above* the percolation limit. (**e**) Fe–Cu alloy, percolated; its blocking temperature is above 300 K. FC was not recorded. (**f**) Fully percolated Fe–Cu alloy. A T_{B} above 550 K is evident. The FC curve seems to show that a structural change could happen at those high temperatures. Each panel can be viewed as corresponding to the situations in Fig. 1.4. Measurements were done in a field of 20 Oe

strongly interacting system, but still nonpercolated. It consists of a broad, almost rounded peak, with its maximum close to room temperature. Here the *d*, *e*, and *f* plots correspond to increasingly percolated systems. Three features are seen on these curves: (1) a concavity or an almost straight increase in the magnetization

until a plateau is reached, yielding to a characteristic "shoulder", (2) an acute peak at higher temperatures, and (3) a fall in magnetization at higher temperatures that do not closely follow a Curie law. The shoulder actually does not have a straightforward interpretation. Other examples of these situations can be seen in Fig. 1.8 of this chapter or in Fig. 1.3 of Ref. [28].

An FC measurement is the complementary curve of a ZFC one. When we measure in FC mode, because we freeze our sample with an applied field, a nanoparticle's supermoments tend to align with the lines of the external magnetic field, which is easier when the interaction strength is weak. Thus, when we start measuring at low temperatures, a nonzero magnetization is measured. It is observed that when interactions are relatively stronger, the low temperature part of the FC curve has magnetization values closer to that of the maximum in the ZFC curve. For noninteracting systems the functional form for FC curves is

$$M_{\mathrm{FC}}(T) = \frac{M_{\mathrm{S}}^2 H}{3K_{\mathrm{ef}}} \ln\left(\frac{\tau_{\mathrm{m}}}{\tau_0}\right)\left[\frac{1}{T}\int_0^T T_{\mathrm{B}} f\left(T_{\mathrm{B}}\right) dT_{\mathrm{B}} + \int_T^{\infty} f\left(T_{\mathrm{B}}\right) dT_{\mathrm{B}}\right]. \tag{1.11}$$

For systems close to or at percolation there are no mathematical expressions to depict magnetic vs. temperature curves. Some attempts have been made, but no mathematical models have been developed for such systems. Two studies published by Tournus et al. demonstrate the impact of the size distribution and sweeping rate of temperatures on ZFC FC curves and attempt to obtain a better description, despite the curious crossover of the FC curve below ZFC, close to T_{B}, which had not been seen in prior experiments [29, 30].

Moreover, because of the size distribution, FC and ZFC curves diverge at temperatures above T_{B}, called the *irreversibility temperature* T_{irr}, if the size distribution is very small, blocking temperature T_{B} is almost equal to irreversibility temperature T_{irr}, as was observed in a carefully prepared and measured system [31].

Magnetization is usually measured using coils, as in vibrating sample magnetometers, which use the movement of a magnetic sample to induce an electromotive force (emf) on the detecting coils. These devices are able to measure with confidence up to 10^{-5} emu. A useful, but expensive, device is a SQUID magnetometer, which uses a Josephson junction to measure magnetization at the highest sensitivity. In practice, it is possible to accurately measure magnetizations of 10^{-7} emu or even less [32].

1.2.1.2 Curie-Type Behavior

At temperatures above T_{B}, in which the magnetic moments are in the superparamagnetic regime, magnetization falls with increasing temperature. In a noninteracting system, the magnetization follows a Curie law:

$$M\left(H,T\right) = \frac{N\mu^2 H}{3k_{\mathrm{B}}T} = \frac{M_{\mathrm{s}}^2 VH}{3k_{\mathrm{B}}T} = C\frac{H}{T}, \tag{1.12}$$

where H is the applied magnetic field, $N = 1/V$ is the density of nanoparticles per volume unit, $\mu = M_s V$ is the sample magnetic moment, M_s is the saturation magnetization, k_B is the Boltzmann constant, and T is the temperature [4]. Dividing M by H, we obtain the magnetic susceptibility χ. Because it is calculated from a measured magnetization in a fixed field, it is called DC or static susceptibility (χ_{DC}). Equation 1.12 can be rewritten as

$$\chi_{DC} = \frac{M}{H} = \frac{C}{T}. \tag{1.13}$$

We can use Eqs. 1.12 and 1.13 to calculate the mean magnetic moment of each particle, if we have their volume, by plotting the magnetization vs. the inverse temperature. Alternatively, we can plot $1/M$ or $1/\chi$ vs. T to obtain a more viewable graph (Fig. 1.7). In this case, the slope of the high-temperature straight part is

$$\frac{1}{C} = \frac{3k_B}{M_s^2 V}. \tag{1.14}$$

For interacting systems, we can consider using a Curie–Weiss law,

$$\chi_{DC} = \frac{M}{H} = \frac{C}{T - \theta}, \tag{1.15}$$

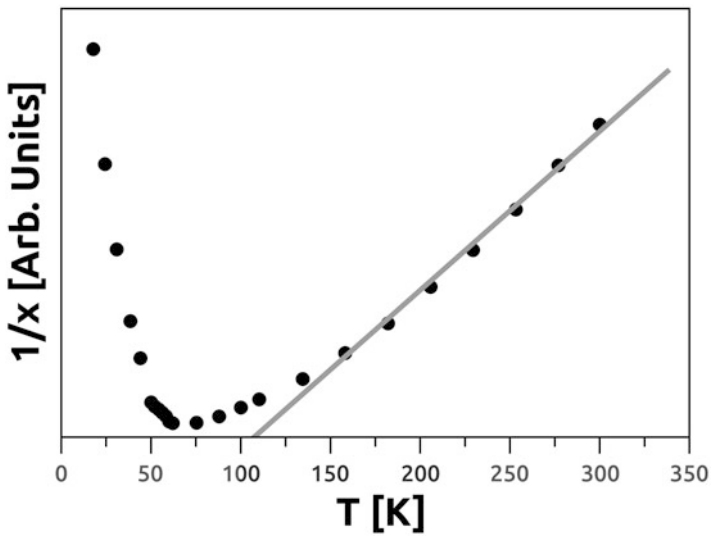

Fig. 1.7 Plot of inverse susceptibility vs. temperature of iron nanoparticles dispersed in paraffin; the high-temperature part can be fitted to a Curie-type law

where θ is a phenomenological parameter that takes into account the interaction strength. In this case, θ cannot be associated with the interpretation given for canonical ferromagnets or antiferromagnets [32].

It is seen that a curve like that in Fig. 1.7 departs from a straight line near the blocking temperature, that is, from a Curie behavior ("paramagnetic"). Such a departure is more pronounced when interactions are stronger or there is a considerable size distribution.

An alternative way to visualize these behaviors is to plot $M\,T/H$ as a function of temperature:

$$MT/H \approx C\,(1 + T_{\mathrm{CF}}/T)\,. \tag{1.16}$$

Magnetic behavior at high temperatures must be a constant (if $T_{\mathrm{CF}} = 0$) or a monotonically decreasing function of T (if $T_{\mathrm{CF}} \neq 0$). Here, C is the aforementioned Curie constant and T_{CF} is the ordering temperature of the ferromagnetic phase.

Such measurements must be taken using very small applied fields, lower than the anisotropy field, to obtain the details of the curve [4]. Usually, researchers use a magnetic field of 20 Oe. In higher applied fields, the peaks become wider and the details are lost. Recall M vs. H curves. Our analysis is valid if we are in the straight part of the initial curve, where it has a linear dependence on the applied field.

1.2.1.3 Susceptometry

A useful alternative to characterize magnetic granular materials is through a susceptometer device. It makes it possible to measure the first derivative of magnetization with respect to the applied magnetic field dM/dH. This quantity is the so-called magnetic susceptibility, χ, also known as dynamical or AC susceptibility (χ_{AC}). In such a measurement, in-phase (χ') and out-of-phase (χ'') susceptibilities are measured by applying an oscillating magnetic field H of frequency ω and recording an induced voltage in pick-up coils proportional to χ through a lock-in technique, together with the dephasing angle φ.[1] This is a measure of the ability of the system magnetization to follow the oscillating magnetic field H. A larger χ' means that the magnetization can respond to H. At the highest frequencies it becomes difficult for the system to follow H. The dragging effect is reflected by χ''.

The functional forms of these recorded quantities are as follows:

$$\begin{aligned} \chi' &= \chi \cos\varphi, \\ \chi'' &= \chi \sin\varphi. \end{aligned} \tag{1.17}$$

In a susceptibility vs. temperature measurement of a magnetic granular system, χ' has a shape closely resembling that of a ZFC curve, so our earlier depiction of the

[1] A more advanced version of this technique is used in modern SQUID devices.

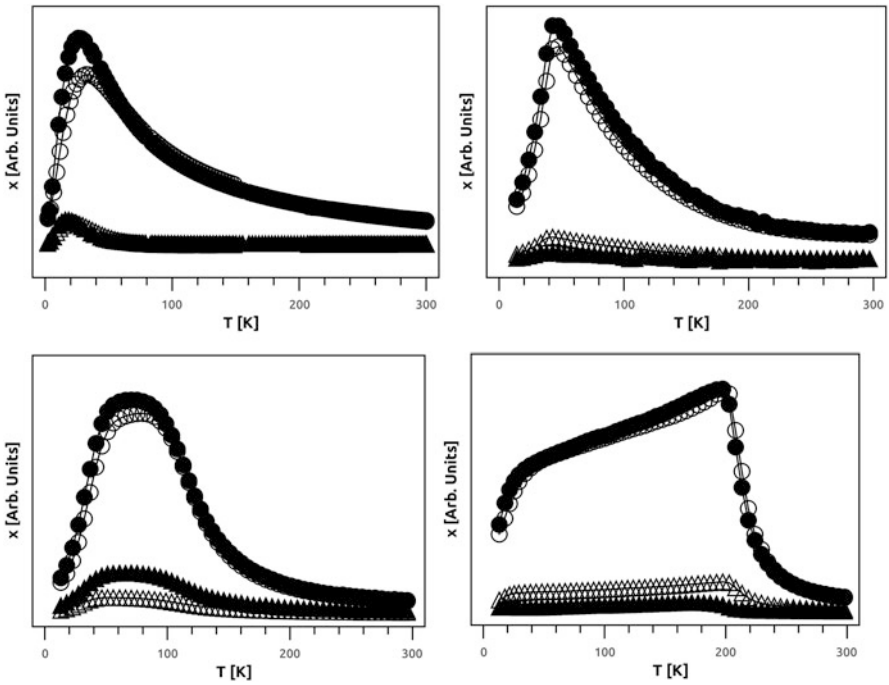

Fig. 1.8 In-phase χ' (*dots*) and out-of-phase χ'' (*triangles*) AC susceptibilities of a lightly interacting system composed of packed silica-covered Fe_3O_4 nanoparticles (*upper left*), a strongly interacting system composed of $Fe_{14}Cu_{86}$ (*upper right*), an almost percolating interacting system composed of $Fe_{17}Cu_{83}$ (*lower left*), and a percolated system composed of $Fe_{30}Au_{70}$ (*lower right*). High-frequency measurements are indicated by *open symbols*, low-frequency by *black symbols*

shapes of the curves can also be used (Fig. 1.8). The χ'' curve shows an interesting feature. Because this phase is representative of the energy dissipation in the system, it gives an additional view on it. The maximum in χ' or χ'' can be used as the blocking temperature, but the blocking temperature is best represented by the peak of χ'' [33]. This peak of the χ'' curve usually occurs at lower temperatures than the peak of the χ' measurement. In a normal susceptometer, χ'' is small compared with χ'. In adapted SQUID devices, this χ'' signal is bigger. Based on the relationships of both susceptibilities Cole–Cole plots, information about the frequency attempt τ_0 and energy barrier distribution can be obtained. A useful article on the underlying physics is that of García Palacios [34]. A measurement of χ'' vs. temperature in strongly interacting systems, even percolated ones, displays a peak that more or less still corresponds to the effect of individual nanoparticles.

1.2.1.4 Néel–Arrhenius and Vogel–Fulcher Laws

Using Eq. 1.3 we show how energy barriers affect relaxation times. This equation is known as the Néel–Arrhenius (N–A) law [35]. The relaxation time τ for a system of noninteracting superparamagnetic particles follows that law, which we repeat here to compare with the Vogel–Fulcher (V–F) law in this section:

$$\tau = \tau_0 \exp\left(\frac{K_{\text{ef}} V}{k_{\text{B}} T}\right). \tag{1.18}$$

As explained earlier, K_{ef} is the effective anisotropy constant, V is the volume of the nanoparticle, and τ_0 must take values between 10^{-9} s and 10^{-11} s for superparamagnetic systems. However, only in a few systems, which are closest to the ideal, the N–A model works in an appropriate way, for example, systems reported by Torres et al. [13]. In this report, the authors present the validity of the N–A model for highly anisotropic $Co_xFe_{3-x}O_4$ nanoparticles, from which are obtained realistic values for the response time. Nevertheless, in most published papers, when the N–A law is applied on a nanoparticle system, nonphysical values of τ_0 are obtained. This behavior is commonly attributed to nanoparticle interaction effects. One of the first works to address this challenge was that of Shtrikmann and Wohlfarth [35], who used a mean field approximation to propose a V–F law. Such model establishes that the magnetization processes are perturbed by a dipole field emerged from the interactions among particles. This perturbation is immersed in a fictitious temperature T_0 and expressed as

$$\tau = \tau_0 \exp\left(\frac{K_{\text{ef}} V}{k_{\text{B}} (T - T_0)}\right) \tag{1.19}$$

Despite the fact that the V–F model does not take into account the surface effects or polydisperse properties present in all real nanoparticle systems, the use of this model provides a more physically relevant result. Table 1.1 presents the values of τ_0 obtained for some systems composed of magnetic nanoparticles by means of N–A and V–F laws.

As can be seen in Table 1.1 and in most cases where nanoparticle interactions are relevant, the response time takes nonphysical values when the N–A law is used. Despite the fact that these values are physically incorrect, it is interesting to observe that in interacting or weakly interacting nanoparticle systems, there is a clear tendency to underestimate these parameters. However, such values can be corrected by adopting the Vogel–Fulcher expression from which values ranging between 10^{-9} and 10^{-11} s are obtained.

Table 1.1 Values of τ_0 obtained by applying both Néel–Arrhenius and Vogel–Fulcher models on granular materials composed of monodomain magnetic nanoparticles

Sample	Mean NP size (nm)	τ_0 using N–A law (s)	τ_0 using V–F law (s)	Reference
γ-F_2O_3	4.9	–	2.5×10^{-11}	[36]
Fe_3O_4	3.8	4.9×10^{-36}	4.7×10^{-10}	[37]
	4.5	1.6×10^{-16}	3.2×10^{-10}	
Fe_3O_4	5.5	$\sim 10^{-32}$	10^{-13}	[38]
γ-F_2O_3 (powder)	4	3×10^{-18}	5.2×10^{-7}	[39]
γ-F_2O_3 (compacted)	1.6×10^{-42}	9.7×10^{-8}		
Ni (1.9 wt%)-SiO_2	4.3	3.4×10^{-10}	1.7×10^{-9}	[40]
Ni (2.7 wt%)-SiO_2	5	2.9×10^{-11}	2.1×10^{-10}	
Ni (4 wt%)-SiO_2	4.9	4.2×10^{-11}	1.4×10^{-10}	
Ni (7.9 wt%)-SiO_2	5.3	1.3×10^{-12}	1.2×10^{-10}	
Ni (12.8 wt%)-SiO_2	5.5	5.8×10^{-15}	6.3×10^{-10}	
Fe_3O_4	4.9	–	6×10^{-6}	[41]
CoO-Pt core-shell	4	6×10^{-19}	2.4×10^{-11}	[42]
Fe_3O_4	7.5	9.5×10^{-10}	9.8×10^{-10}	[43]
Au-Fe_3O_4 dimer	11	1.8×10^{-16}	1.4×10^{-9}	
Au-Fe_3O_4 core-shell	15	5.9×10^{-14}	8.9×10^{-9}	
$CoFe_2O_4$	4.5	6.8×10^{-27}	–	[44]
	6.3	1.5×10^{-32}	–	

1.2.1.5 Nonlinear Susceptibility

A special analysis of nonlinear susceptibilities sheds light on systems that can be considered to be of the spin-glass type. To do that, AC susceptibility must be measured at different driving fields. Each measurement must be fitted with a polynomial expression to extract linear and nonlinear terms. In this case, magnetization is written

$$M = M_0 + \chi_1 H + \chi_2 H^2 + \chi_3 H^3. \tag{1.20}$$

In this kind of study, higher-order terms of susceptibility are analyzed. The peak in χ_3 corresponds to a blocking temperature or spin-glass transition temperature [12, 32].

Another alternative that allows for a different way to study magnetization in a sample is provided by Mössbauer spectroscopy, which is based on the resonant absorption on certain isotopes. The effect is quite remarkable on iron, so for many magnetic materials it is a very useful technique. One feature that a Mössbauer experiment can measure is the hyperfine magnetic field, B_{hf}, which is a measure of the internal fields sensed at the nuclear level. B_{hf} is seen as a sextet of peaks in an absorption vs. energy graph. It has been observed in granular systems that such a sextet collapses to a singlet or doublet when the temperature is raised. Because the dominant frequency corresponds to a Larmor precession, which in this case corresponds to that of the nuclear magnetic moment with the surrounding magnetic field, we can make a distinct measure of a sample's magnetization. By measuring

changes in absorption at an energy corresponding to one of those peaks, we see the transition from blocked to superparamagnetic states as a function of temperature. Because the Larmor frequency for the iron isotope used in this spectroscopy, Fe^{57}, is $\nu \approx 10^{10}$ Hz, an additional frequency is available to study the dependence of the blocking temperature, as used in a pioneer work by Dormann et al. [45]. This technique is called Mössbauer thermal scanning (MTS) [46, 47]. Without appropriate equipment, this measurement can be made simply by taking Mössbauer spectra at different temperatures. An extended criterion says that when half of the sextet area turns into a singlet or doublet, this is the blocking temperature [48, 49]. Studies on blocking temperatures can be used to plot a magnetic phase diagram, which can help to understand magnetic alloys [49, 50].

1.2.1.6 Magnetization vs. Magnetic Field Measurements

Magnetization M vs. applied magnetic field H is a customary measurement for characterizing magnetic materials. In granular systems, this measurement shows a characteristic S-shaped curve. Depending on the temperature at which this measurement is taken, it either displays hysteresis (at $T < T_B$) or it does not (at $T > T_B$). For noninteracting systems, M vs. H curves will collapse into a single curve if the magnetization is plotted against H/T [4, 51]. Conversely, if they do not collapse into the same curve, the system has nonnegligible interactions. On a real granular system, we must take into account the magnetic response of the matrix. High field values follow an asymptotic curve if the magnetic response of the matrix is not important. The nonsaturation effect is due to uncompensated spins on the surfaces of nanoparticles [11, 52]. If the magnetic response of the matrix is important, if it is paramagnetic or diamagnetic, the effect on the M vs. H curve is evident at high fields, so to analyze separately the contributions of nanoparticles, we must subtract a straight line using the extreme parts of the curve at the highest fields. A positive slope that changes with temperature indicates a paramagnetic matrix. A negative slope, which does not change with temperature, indicates a diamagnetic matrix. We must also take into account that some matrices can be composed of mixtures of magnetic materials, so mixed behaviors should be expected. In addition, recall that all materials have a magnetic response (Fig. 1.9) [2, 3, 7, 53].

1.2.2 Models Commonly Used to Describe Interactions in Sets of Nanoparticles

There are commonly two schools of thought when it comes to analyzing magnetic interactions in systems of nanoparticles. One of those schools is based on the Dormann–Bessais–Fiorani [54] model, which uses energy barriers to describe the effect on a nanoparticle of a full ensemble; the other school uses the Mørup

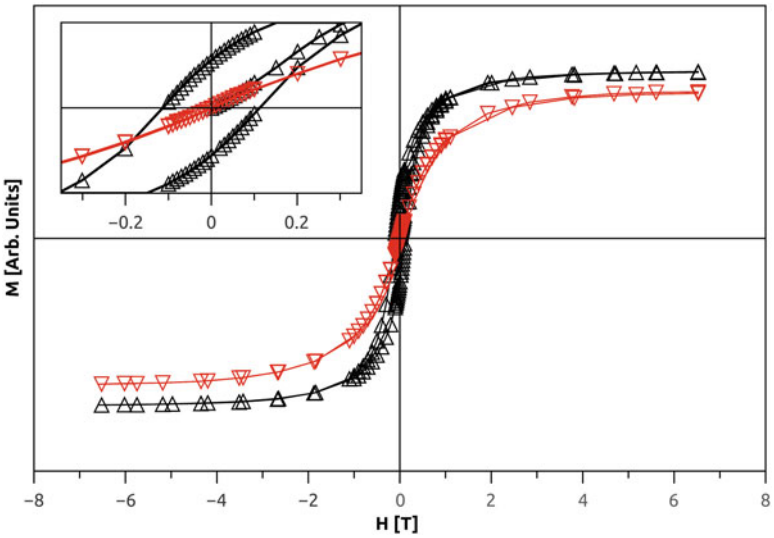

Fig. 1.9 M vs. H curves measured at 5 and 350 K of a sample composed of iron nanoparticles in a SiO_2 matrix. Both measurements (which are S-shaped) were taken at temperatures far from the blocking temperature ($T_B \approx 35$ K). The 5 K curve (*up black triangle*), which is in the blocked state, shows an important coercive field, while at 350 K (*down red triangle*), which is in the superparamagnetic state, it shows little coercivity. Saturation magnetization is lower in the high-temperature measurement, as it should be

model [55], in which a mean field approximation is proposed. Both models are based on approximations commonly used in physics and are discussed in detail in Ref. [56]. The first one seems to represent experimental results better than the second. But in more interacting systems, a third approach, developed by Allia et al., the so-called T^* model, has shown better depictions of real systems [23, 57].

This model, sometimes called the T-star model or interacting superparamagnetic model (ISP), was proposed as a phenomenological approach that treats nanoparticle magnetic moments as interacting through dipolar-type long-range fields, and the overall effect can be modeled by a fictitious temperature, T^*, which should be added to the real temperature in the denominator of the Langevin function argument. The new temperature, called the *apparent temperature*, has the effect of slowing the approach to saturation and can be written $T_A = T + T^*$, where T^* is related to the dipolar interaction energy through $\varepsilon_D = k_B\, T^*$. Then the modified Langevin function has the form

$$M(H,T) = n_{CO}\int_0^{\infty} \mu_{CO} L\left(\frac{\mu_{CO} H}{k_B\,(T+T^*)}\right) f(\mu_{CO})\, d\mu_{CO}, \tag{1.21}$$

where the suffix $_{CO}$ refers to corrected values. To solve the modified Langevin equation, it is necessary first to determine T^*, which can be accomplished by starting with the low-field inverse susceptibility, given by

$$\frac{\rho}{\chi} = 3k_B N_{CO}\left[\frac{T}{(\delta M_s)^2}\right] + \beta, \tag{1.22}$$

where N_{CO} is the *corrected* number of magnetic moments of superparamagnetic particles per unit volume, which is related to the number of magnetic moments of superparamagnetic particles per mass unit through $N_{RE} = n_{RE}\,\delta$, with δ being the bulk density of the magnetic nanoparticle. ρ is a parameter introduced to consider the nanoparticle size distribution, which can be determined from the relationship among average values:

$$\rho = \frac{\langle \mu_{CO}^2 \rangle}{\langle \mu_{CO} \rangle^2} = \frac{\langle \mu_{AP}^2 \rangle}{\langle \mu_{AP} \rangle^2}, \tag{1.23}$$

where μ_{AP} is the magnetic moment magnitude obtained from the standard Langevin equation, called *apparent* because its values are screened by the nanoparticle interaction effects. The susceptibility χ is obtained from the low-field region of M vs. H curves, and ρ is estimated from the lognormal distribution obtained from the parameters σ and $\langle \mu_{AP} \rangle$. By plotting ρ/χ vs. $T/(\delta M_s)^2$ and following the relationship between apparent and real values shown in Ref. [23], one obtains β and, therefore, T^* [23].

But even this model fails when systems are close to the percolation limit [57, 58]. As discussed earlier, in almost and fully percolating systems, magnetic behavior is complex. Particularly since the publication of the aforementioned works of Dormann–Bessais–Fiorani and Mørup, many experiments have been conducted and theoretical developments made on mildly interacting systems, but few advances have been made in theoretical models that can accurately describe systems that are close to percolation or fully percolating.

1.2.3 Experiments on Granular Materials with Controlled Interactions

1.2.3.1 Dispersions of Nanoparticles in Polymers

These are a class of magnetic granular systems made of magnetic nanostructures, such as nanoparticles, embedded in a nonmagnetic and viscous matrix. Given that in this kind of nanomaterial it is relatively simple to adjust the nanoparticle concentration, and therefore interactions between them, these materials are excellent candidates for experimentally studying some fundamental aspects of magnetism at the nanoscale.

1.2.3.2 Experimental Evidence of Dipolar Interaction Influence on ZFC-FC Curves

In this section, we discuss how the strengthening of dipolar interactions among magnetic nanoparticles significantly affects the shape, and therefore the obtained parameters, of ZFC-FC curves. To this end, we have prepared two sets of magnetic nanocomposites based on citric acid–coated magnetite (Fe_3O_4) nanoparticles, which are distributed on a nonmagnetic matrix of polyvinyl alcohol (PVA). For the first system (labeled A), we used nanoparticles with 7 nm mean diameter, while in the second one we used nanoparticles of 10 nm (labeled B). For the details on nanoparticle synthesis, please see Refs. [59, 60]. In both systems, the PVA was loaded with 0.5 wt.%, 3 wt.%, 15 wt.%, and 30 wt.% of citric acid–coated magnetite nanoparticles (magnetic nanocomposite preparation details are available in Ref. [60, 61]).

As explained earlier and shown in the examples of Fig. 1.6, we see a similar behavior in this experiment (Fig. 1.8). It is possible to observe that by increasing the concentration of magnetic nanoparticles, and thereby strengthening the dipolar interactions among magnetic nanoparticles, the blocking temperature shifts to higher temperatures. Often this type of shift is used to compare the magnetic properties of nanostructured systems composed of nanoparticles of different sizes or phases, and the observed differences, such as the aforementioned blocking temperature displacements or broadening of the ZFC curve, are associated with the intrinsic nanoparticle size distribution, surface effects, or anisotropies of diverse origins, to mention just a few. However, in nanostructured systems based on the same magnetic constituent (the same magnetic nanoparticles in our experiment), the experimental dissimilarities must be based on other phenomena, like dipolar interactions or clustering effects. It is important to mention that proximity effects can alter the anisotropy of individual nanoparticles or even form smaller regions of different anisotropies [61] (Fig. 1.10).

We used a derivative method to obtain the blocking temperature distributions of each sample to get a mean value of T_B. We found that for both systems, each synthesized using the same batch of magnetic nanoparticles, different mean blocking temperature values were obtained (Fig. 1.11).

Using Eq. 1.9, allows us to obtain the effective anisotropy constant K. Then, using 7 and 10 nm as mean diameters to find the nanoparticle volume and using the mean blocking temperature $\langle T_B \rangle$, different values of K are obtained for each sample (Table 1.2). For example, we find for system A, $K = 9.03 \times 10^4$ J/m^3 for a 0.5 wt.% sample or $K = 2.6 \times 10^5$ J/m^3 for 30 wt.% sample, while for system B, loaded with 10 nm-Fe_3O_4 nanoparticles, values of $K = 3.22 \times 10^4$ J/m^3 for a 0.5 wt.% sample or $K = 5.6 \times 10^4$ J/m^3. Differences between the anisotropy values of a particular system should not exist because anisotropy is an intrinsic property that must remain unaltered for a non-interacting nanoparticulated system. However, as can be noted for the PVA loaded with 7 nm Fe_3O_4, differences in almost one order of magnitude are observed. Regardless of whether the ZFC maximum is used as the blocking temperature, the dissimilarities among the obtained K values are larger (Table 1.2).

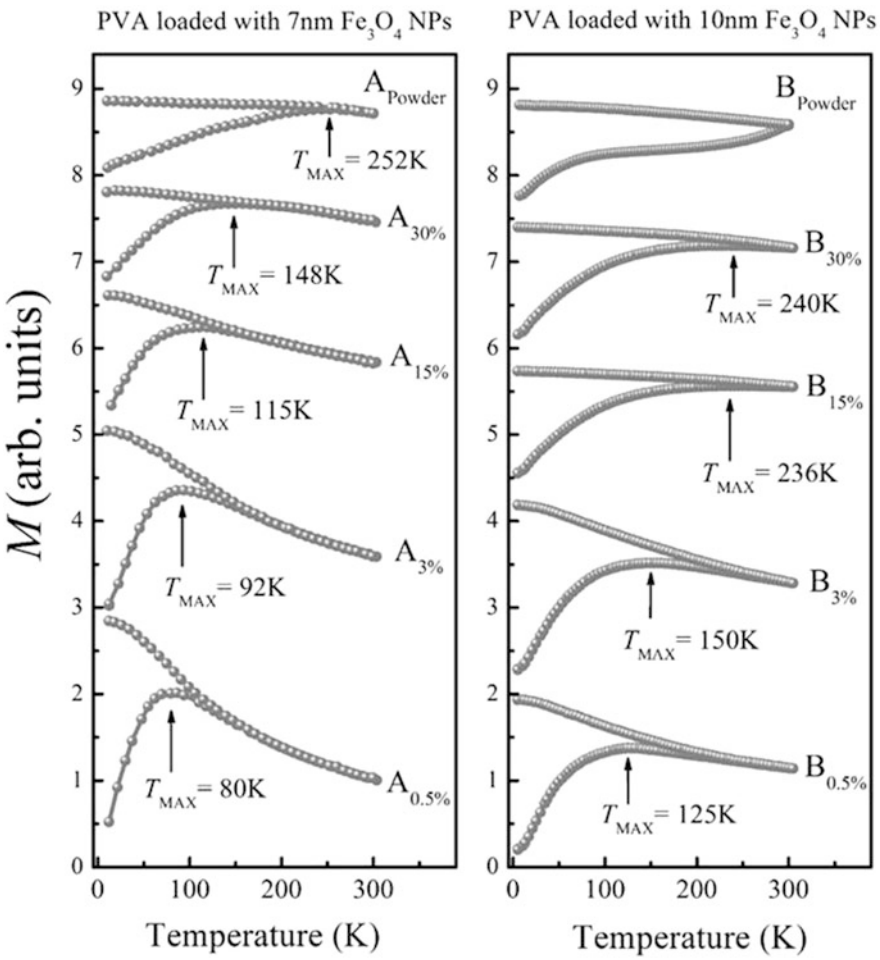

Fig. 1.10 Zero field cooling and FC curves obtained for both PVA loaded with (*left*) 7 nm and (*right*) 10 nm magnetite nanoparticles. The effect of interactions can be seen as the nanoparticle concentration increases. Powder samples are composed of single nanoparticles in close contact, with only the coating of citric acid separating them

Now, the question arises as to what the correct anisotropy value is, and what is its real dependence with magnetic strenght. We have magnetite nanoparticles in which the effective anisotropy's largest contribution comes from the magnetocrystalline anisotropy (due to the spin–orbit interaction). In addition, recall that in the presented systems the magnetic nanoparticles are not percolated. We believe that the value that is closest to that of a nanoparticle alone should come from a system in which the magnetite nanoparticles are in the lower interacting state. This means that interactions modify the anisotropy constant, as was observed by Ferrari et al. [62].

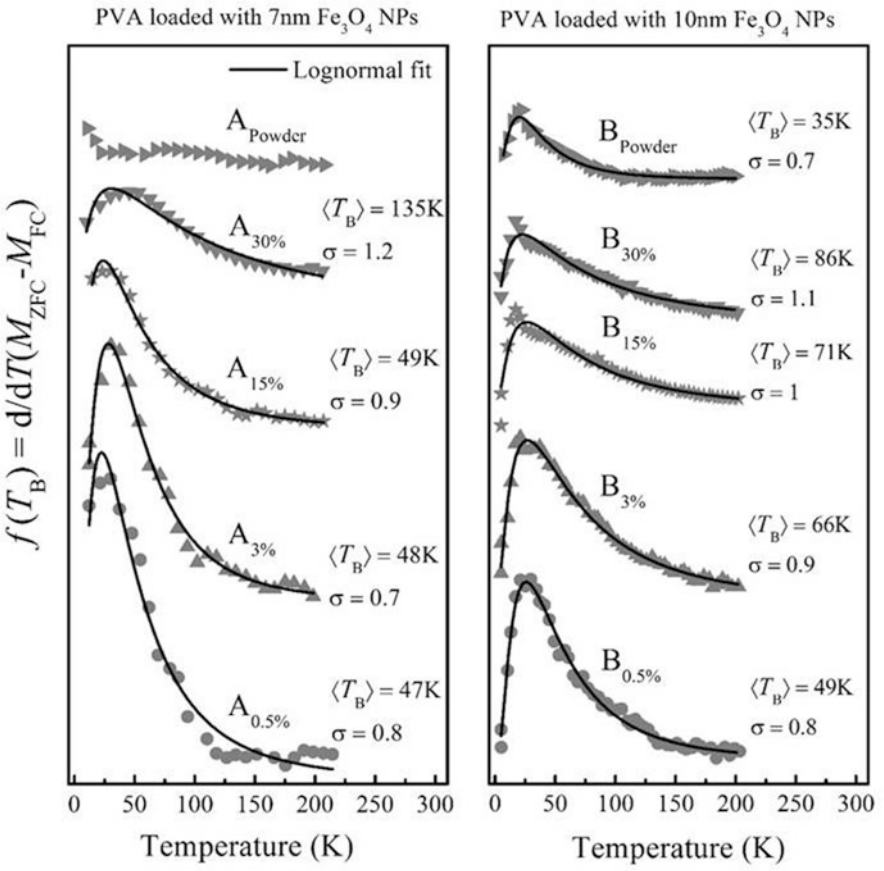

Fig. 1.11 Blocking temperature distribution obtained for both PVA loaded with (*left*) 7 nm and (*right*) 10 nm magnetite nanoparticles. *Symbols*: obtained from derivative method. *Straight line*: lognormal fit from where the mean blocking temperature T_B and the lognormal standard σ deviation were determined

Note that when anisotropy constants are studied or compared, careful attention should be paid specifically to the dilution conditions, besides the size and grafting of the nanoparticle.

1.2.4 Comment on Spin-Glass Systems

A different way of building systems similar to those we have reviewed so far is by using a spin-glass system. A spin glass is formed when magnetic ions are randomly dispersed in a nonmagnetic matrix. At very low concentrations of magnetic ions

Table 1.2 Anisotropy values obtained for both systems using $\langle T_B \rangle$ through the derivative method, $K_{\langle TB \rangle}$ (column 4), maximum of ZFC curve, $K_{T\text{-}ZFC}$ (last column)

NP mean size	wt. % of NP	$\langle T_B \rangle$ (K)	$K_{\langle TB \rangle}$ (10^4 J/m^3)	T_{ZFC} (K)	$K_{T\text{-}ZFC}$ (10^4 J/m^3)
7 nm (system A)	0.5	47	9.03	80	15.3
	3	48	9.22	92	17.6
	15	49	9.41	115	22.1
	30	135	26.0	148	28.4
10 nm (system B)	0.5	49	3.22	125	8.24
	3	66	4.35	150	9.88
	15	71	4.68	236	15.5
	30	86	5.66	240	15.8

(less than 1 at.%) some features appear that resemble those of superparamagnetic systems, like a cusp in a magnetization or susceptibility vs. temperature measurement, or irreversibilities in a ZFC-FC curve. The origin of that magnetic order is frustration because of the competing interactions among magnetic ions, like RKKY and others mentioned earlier, which makes it different from the thermally activated process that is SPM [8, 16, 63]. When the concentration of magnetic atoms is increased, some ions will be close enough to establish direct interactions like direct interchange, super interchange, or Dzyalonskii–Moriya interchange. Those interactions are stronger than RKKY, so the magnetic landscape becomes more complicated. If we look at the conformation of the sample, at a concentration of atomic ions of a few atomic percent, we see that those that are in close contact can be regarded as nanoparticles, despite their origin. Those regions in close contact have interactions like direct interchange or super interchange, as in a regular nanoparticle. This is called *cluster glass* (CG) [64, 65]. For face-centered-cubic (fcc) arrangements, percolation takes place at concentrations of approximately 17 at.% for ferromagnetic ordering and 45 at.% for antiferromagnetic ordering. Chains of interconnected magnetic ions are distinguishable, which produces regions of ferromagnetic (or antiferromagnetic) order. This state is called *quasi-ferromagnetism* (QFM). They used to be called *mictomagnetic* (mixed magnetism) because it was believed that they were mixtures of antiferro and ferromagnetic interactions [64, 65]. In addition, the term *reentrant magnetism* is also used. Earlier, discussions took place about the physical situation for this state, but now the state is interpreted as a transverse component freezing of the magnetization vector [66].

Because in some systems it can be difficult to adequately characterize an unknown material and determine whether it is a spin-glass or superparamagnetic system, we can use a criterion that takes into account blocking (or glassy) temperatures and frequencies, obtained in susceptibility vs. temperature measurements [16]. Such a criterion is known as the Mydosh parameter Φ [16] and can be calculated from the maximum of the imaginary part of AC susceptibility (T_M), according to the equation

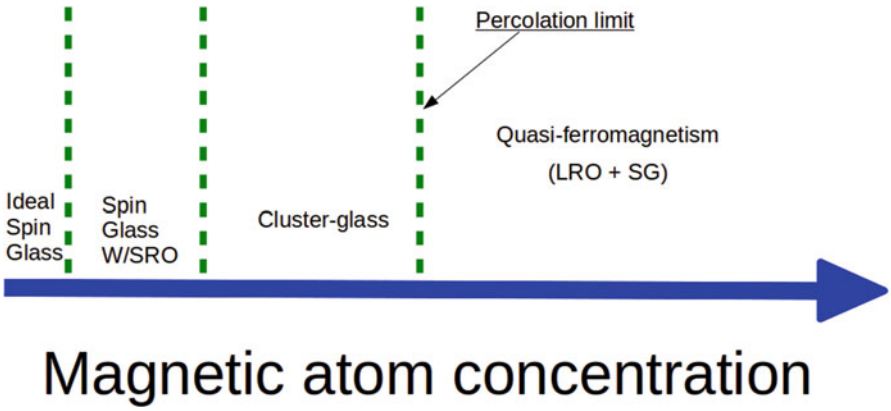

Fig. 1.12 Magnetic phases when magnetic atom concentration is increased. At very low concentrations of less than 1 at.%, we have canonical spin glasses. Increasing the concentration produces a phase where spin-glass structures coexist with short-range magnetic order (SRO), such as direct interchanges between neighboring magnetic atoms. Above 10 at.%, bigger SRO regions appear, forming clusters that can be viewed as nanoparticles. Crossing the percolation limit, we encounter a long-range magnetic order (LRO) that causes ferromagnetic features in the magnetic behavior

$$\Phi = \frac{\Delta T_{\mathrm{M}}}{T_{\mathrm{M}}\, \Delta \log(\omega)}, \tag{1.24}$$

where ΔT_{M} is the frequency shift for the temperature of that maximum, and ω is the frequency of the measurement [16]. Values of $\Phi < 0.018$ are found for canonical spin glasses. Higher values, on the order of 10^{-1}, are typical of superparamagnetic systems. In almost and fully percolated systems, Φ values are small, independently of whether the system is a spin glass or SPM in origin (Fig. 1.12).

These systems have been studied systematically since the 1960s. Interestingly, one of the most studied systems is Au: Fe, both of whose elements are metallic. Since they do not form alloys, they are prone to segregation, so a tendency to form aggregates of pure iron is expected. The enthalpy of formation is positive [67]. At room temperature and concentrations above 1 at % it is not difficult to imagine that nanoparticles of iron can form from the migration of isolated atoms. Experiments on such a system started as early as the 1930s, but the term *spin glass* was coined only in the early 1970s. The subject attracted the attention of theoreticians who developed models to describe these systems [12].

An interesting experiment on a special type of nanoparticle was performed by Nunes et al. [68]. They prepared by chemical synthesis nickel nanoparticles with an almost amorphous internal atomic structure. Those nanoparticles have an approximate diameter of 12 nm, but inside, the atoms are highly disordered, forming small clusters of just a few atoms. This leads to a magnetic behavior that is closer to a cluster-glass system, despite the fact that it is formed by very well-defined nanoparticles. In this experiment, ZFC-FC measurements showed a maximum close

to 20 K that did not change if higher fields were used, at least up to 1000 Oe, a characteristic of spin glasses. AC susceptibility measurements showed, by applying the Mydosh criterion, that the system could be treated as a spin-glass one ($\phi = 0.01$), so it must be regarded as a cluster glass. The same researchers also investigated smaller Ni nanoparticles, approximately 5 nm, prepared using a similar synthesis route [69]. They found that SPM order no longer existed to give rise to a mixture of paramagnetic and ferromagnetic orders, again despite the existence of very well-defined nanoparticles. An important increase in surface anisotropy was also registered.

1.3 "Giant" Magnetotransport Properties

Magnetic granular materials display interesting magnetotransport properties: giant magnetoresistance (GMR), tunneling magnetoresistance (TMR), and the giant Hall effect. All three effects arise as a consequence of the interaction between electrons and a nanoparticle's magnetic moment.

1.3.1 Giant Magnetoresistance

Magnetoresistance is the effect of changing electrical resistance when a magnetic field is applied. Electrical resistance has different origins. One of them is the scattering of electrons due to magnetism. It is an effect with wide technological applications, from magnetic wires (used in black boxes as a rough way to record crew conversations) and flexible ribbons (such as those used in cassette tapes) to hard disk heads. When produced by spin-dependent scattering on nanostructured magnetic entities, like coupled multiple layers of nanometric thicknesses or nanoparticles in a matrix, the change is negative and it is called GMR. A negative change means that the electrical resistance falls when a magnetic field is applied.

In experiments, this change is usually calculated through

$$\mathrm{GMR} = -\frac{[R\,(H_{\max}) - R(0)]}{R(0)}, \tag{1.25}$$

where $R(H_{\max})$ and $R(0)$ are the electrical resistances measured at the maximum magnetic field $H_{\max}$ and at the zero field.

Alternatively, we can use $R(H_c)$ instead of $R(0)$ if the coercive field is well marked or if it is large, as is the case for multilayered materials. The minus sign means only that the change is negative, and sometimes it is calculated without it, as shown in Fig. 1.13.

Giant magnetoresistance is produced by differential spin-dependent scattering due to the relative orientation of moments of magnetic entities, as in sandwiched

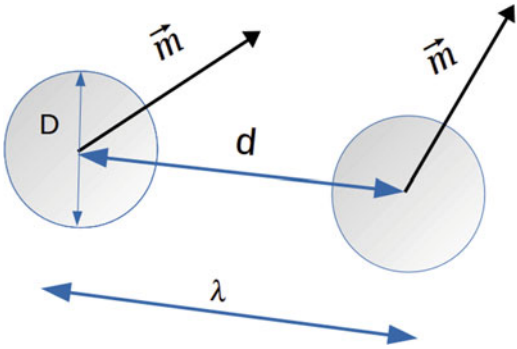

Fig. 1.13 Nanoparticles with a size of D, at a distance d. This distance must be equal to or less than the electron correlation length, λ

multiple layers [70] or granular materials [71]. In granular materials it is isotropic, and in multiple layers it depends on the relative orientation of the sandwiched layers to the electrical current. An electrical current can be considered as being divided into two subbands, each corresponding to a spin orientation, parallel or antiparallel to the local magnetization of the entity (magnetic nanoparticle or layer). If two entities that are close enough to allow electrons to retain their coherence (spin orientation) have their moments aligned in an antiparallel orientation, the subband of electrons with spins in the same orientation of the magnetization of the first entity ("spin-up") will not experience magnetic scattering when passing through the first one. When a current that does not lose its spin coherence encounters a second entity, it will experience magnetic scattering because their moments are not parallel. For another subband composed of electrons with spins in an antiparallel orientation ("spin-down"), the situation will be the opposite: it will suffer magnetic scattering when passing through the first entity, but not the second one, which is parallel to it. If we apply an external magnetic field, the entities will tend to align, increasingly so if the strength of the field is raised. With this magnetic landscape, a spin-up current will not suffer scattering in the first or second entity. A spin-down current will experience scattering of magnetic origin in both entities. We can see that the first configuration (parallel–antiparallel entities) has a higher resistance than the second case (parallel–parallel) and intermediate resistances with partially oriented entities. Usually, both situations are compared by solving a simple circuit by Kirchhoff laws. The effect on the measurement is depicted in Fig. 1.12.

The GMR effect was first identified and explained in multiple layers, so the theory differentiated two geometrical situations, current in plane (CIP) and current parallel to the plane (CPP), depending on the relative orientations of the current and the plane of the layers. In granular materials there is no such geometrical situation. GMR in granular materials was modeled theoretically in Ref. [72]. The basic condition for GMR is that the electron correlation length, λ, should be at least equal to or larger than the interparticle distance, d. Polarization of the spin current is kept through jumps, as explained earlier. This condition of $\lambda \approx d$ or larger says that the effect will be observable in enough concentrated granular materials. More in-depth models were discussed in the 1990s.

GMR was observed and interpreted first in multiple Fe-Cr layers in two contemporary experiments done almost simultaneously by the groups of Albert Fert and Peter Grünberg [73, 74]. Fert had already studied theoretically and developed a two-subband model for the resistivity in ferromagnetic metals [75]. Experimental realization of those sandwiches with thicknesses of just a few nanometers was only possible when MBE machines were available, in the late 1980s. GMR in granular materials was first reported by Chien in 1992 [76], but it had been previously observed by other researchers, as noted even in that article. Systems that are regarded as canonical spin glasses, like Au-Fe, show negative magnetoresistance. Nigam and Majumdar, in an article published in 1983, analyzed magnetoresistance measured in several samples of canonical spin glasses, in concentrations of magnetic solute that reached approximately 10 at.%, which cannot be considered a diluted magnetic sample (see our earlier discussion on the magnetism of spin glasses) [77]. Some results on magnetoresistance on diluted alloys that form spin glasses were collected in Refs. [78, 79], and in Ref. [80]. The first report on a so-called negative magnetoresistance on a spin glass–like system, at least from what we investigated, was reported by Nakhimovich in 1941, in a Soviet physics journal [81].

In granular systems, GMR depends on the relative orientation of nanoparticles' supermoments (Figs. 1.13 and 1.14). When a magnetic field is applied, supermoments align. The greater the field strength, the greater the alignment of supermoments and, hence, the lower the electrical resistance [72, 82]. An interesting theory of GMR in granular materials was presented in an article by Ferrari et al., where spin-dependent scattering was taken into account within nanoparticles and their boundaries (Fig. 1.15) [83].

At low nanoparticle concentrations, GMR scales with the square of magnetization. In concentrated systems, as an effect of increased magnetic interaction, this relationship no longer exists. In such systems it is seen, in low fields, that magnetoresistance vs. magnetization parabola flattens [84]. This is clearly seen in the article of Liu et al., where 8–9 nm magnetite nanoparticles were compressed into pellets, to show the GMR. This effect does not scale with M^2, as is clearly seen in Fig. 1.15. It is also seen in Refs. [84–85].

The effect is greater when NP concentration is close to the percolation limit. When this limit is crossed, mixed effects take place. A lower GMR effect can be recorded, owing to the remaining nanoparticles that are still relatively free to orientate with the field and the chains of nanoparticles that have ferromagnetic interactions among them [86].

1.3.2 Tunneling Magnetoresistance

TMR is a cousin effect of GMR. It also undergoes a negative change in electrical resistance when a magnetic field is applied. In granular materials it appears when the matrix is a dielectric, preventing electron transfer between nanoparticles, so no exchange forces are present. There are only magnetostatic forces between

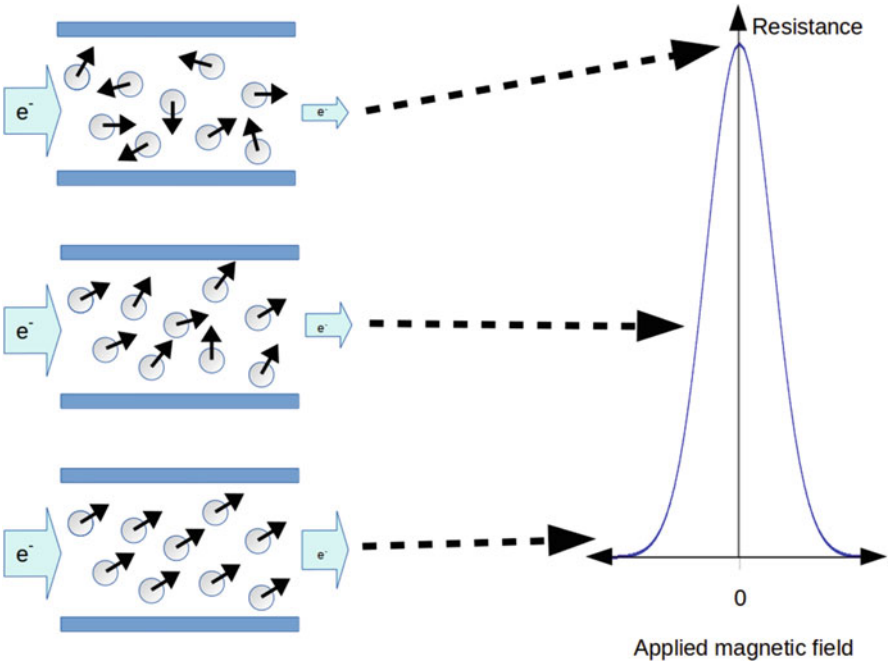

Fig. 1.14 Alignment of a nanoparticle's supermoment with an external magnetic field causes electrical resistance to drop

nanoparticles that act at distance. Instead of an electrical current formed by freely moving electrons, the formation of current depends on the electrons' tunneling between adjacent magnetic entities (again, sandwiched layers or nanoparticles), which changes the relative orientation of their magnetic moments by the application of an external magnetic field. The population of subbands at the Fermi level of each magnetic entity changes.

Jullière discovered this effect in multiple Fe-Ge layers in 1975, years before GMR was discovered [87]. The electrical properties of granular materials with dielectric matrices were extensively studied by Abeles et al. and reported in a seminal article in 1975 [88]. Interesting theoretical analyses have been reported since the development of granular materials with nonmagnetic matrices [89, 90].

TMR is usually calculated as

$$\mathrm{TMR} = -\frac{[R(H_s) - R(H_c)]}{R(H_c)}, \tag{1.26}$$

where $R(H_s)$ and $R(H_c)$ are respectively the resistances measured at the magnetic saturation H_s and coercive field H_c. Alternatively, we can use $R(0)$ instead of $R(H_c)$

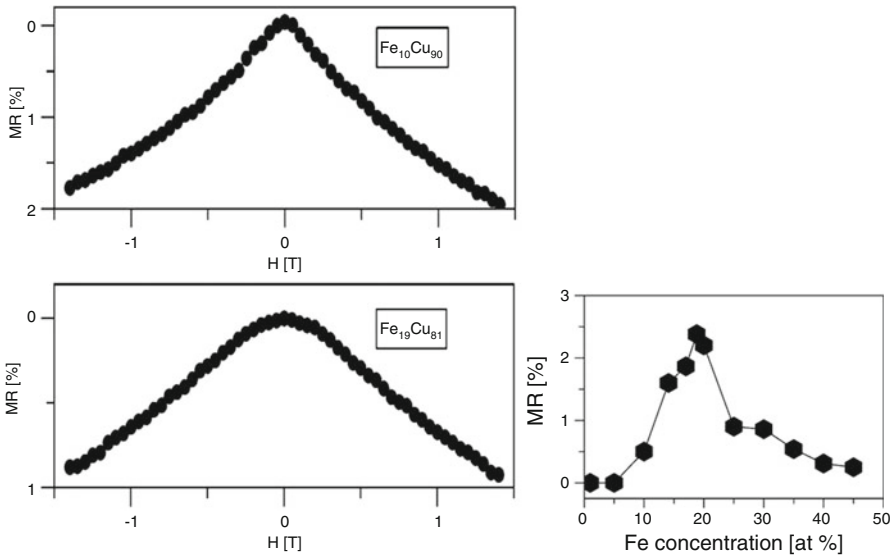

Fig. 1.15 Magnetoresistance of a Fe-Cu alloy prepared by mechanical alloying, measured at 77 K. (*Left*, *upper panel*): $Fe_{10}Cu_{90}$; (*left*, *lower panel*): $Fe_{19}Cu_{81}$, note the rounded curve at low fields. *Right panel*: GMR increases with increasing concentration of the magnetic material, up to the percolation limit, around 20 at.% in this case [51]

if the coercive field is not well defined or is small, and both cases are common in granular materials at room temperature or with a wide size distribution, as is the case with GMR presented earlier.

In Jullière's model, TMR is related to the polarization, P, of spins of the tunneling electrons by

$$\text{TMR} = \frac{P^2}{\left(1+P^2\right)}. \tag{1.27}$$

Similarly to what happened with GMR, TMR was measured first in multilayered systems, followed by granular materials. Impressive values have been recorded, sometimes greater than their multilayered counterparts [91]. Some groups have measured large TMRs at room temperature in granular samples of Fe_3O_4 in polymeric matrices [92, 93].

Magnetoresistance has been found in nanoparticles grafted with oleic acid, a system that can also be considered granular. Those experiments were based on the fact that grafting prevents direct contact between nanoparticles and retains a distance of around 2–4 nm. By thermal annealing or chemical treatment, the distance between nanoparticles can be reduced to less than 1 nm [94–97]. Unfortunately, in those functionalized nanoparticles grafting seems to be different if nanoparticles are close enough, so in concentrated samples nanoparticles have a tendency to form chains, as was observed experimentally [98].

1.3.3 Giant Hall Effect

In 1995 Pakhomov et al. discovered a large extraordinary Hall effect in granular materials [99]. A Hall effect is measured using the common Hall setup. It is recorded by measuring the voltage perpendicular to the direction (Hall voltage) of an injected electrical current, with an applied magnetic field H perpendicular to the plane defined by both quantities. The initial curve resembles that of a hysteresis. Hall resistivity ρ_{H} is related to H (through magnetic induction B) and sample magnetization M through the empirical expression

$$\rho_{\mathrm{H}} = R_0 B + R_{\mathrm{EHE}} \mu_0 M, \tag{1.28}$$

where R_0 is the ordinary Hall coefficient, and R_{EHE} is the extraordinary one [100]. The first term is the usual effect that appears as a consequence of the Lorentz force that is exerted by the external magnetic field on charge carriers. The second term is the extraordinary part, which is due to the scattering of the polarized conduction d electrons and in granular systems can be very large (Fig. 1.16).

The sources of this effect are not clear. The effect is associated with spin-dependent scattering at nanoparticle surfaces. This breaks the spatial symmetry on the trajectories of charge carriers and produces two effects, skew scattering and a side jump [101]. Skew scattering is a constant deviation of the trajectories of charge carriers [102]. It is usually described by

$$R_{\mathrm{EHE}} = A\rho + B\rho^2. \tag{1.29}$$

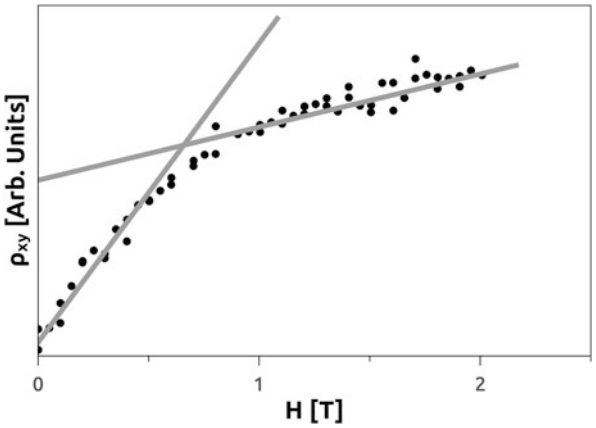

Fig. 1.16 A typical Hall resistivity curve. The low-field part is almost straight, in which the contribution of the first term in Eq. 1.28, which is the ordinary part, contributes slightly to the Hall resistivity. Thus, the slope of this part is almost the extraordinary contribution, and R_{EHE} can be extracted from this value. The high-field part, where magnetization is reversible, is almost straight, so a second slope can be calculated. From that, the ordinary Hall resistivity can be calculated

Frequently the second term is dropped, so it is accepted that R_{EHE} has a linear dependence on ρ. At low temperatures or in metals, where resistivity is small, skew scattering is usually considered the main mechanism for this extraordinary Hall resistivity [101].

The second mechanism is the side jump, a lateral quantum displacement of charges, which results in a quadratic dependence on ρ of R_{EHE} [101, 103]. This mechanism is usually considered in concentrated granular materials, and it is important at high temperatures.

Thus, it is considered that a measurement of the extraordinary Hall resistivity should scale with ordinary resistance to a power of 1 or 2, depending on the mechanism. A shorter expression is used:

$$R_{\mathrm{EHE}} = \alpha \rho^{n}. \tag{1.30}$$

For several systems is measured an intermediate power law, which is indicative of a mixed mechanism. But in other systems, a power law with $n > 2$ arises, indicating that a third mechanism for the extraordinary Hall resistance is possible [101]. The GHE seems to depend also on solitary atoms that might exist between nanoparticles or nanoparticle surface roughnesses [101, 104, 105].

By annealing granular samples of metallic nanoparticles embedded in a silica matrix, detectable changes in the extraordinary Hall resistivity have been measured. It was observed that the GHE diminishes for annealed samples, which leads to a connection of this effect with structural characteristics in which, because of thermal treatment, surface roughness smoothes and possible isolated atoms have enough energy to migrate. In this way, possible sources for the large values of this parameter have been considered, such as metallic atoms forming chains or roughness in nanoparticle surfaces [104, 105]. In granular materials close to percolation there are regions or large chains of nanoparticles that short-circuit the passage of charges, and they do not contribute to spin-dependent scattering [106].

The GHE has been reported in granular materials produced by magnetron sputtering [105–107]. It is also seen in magnetoresistance measurements as an imbalance between negative and positive magnetic fields' semi-axis.

All these so-called giant effects are stronger when the granular system is close to the percolation limit. After this point, because of increasingly ferromagnetic-like interactions among nanoparticles, those effects diminish [28, 86, 106–108].

1.4 Conclusions

Granular materials show features that are interesting for both academic studies and technological applications. A basic set of characterizations can be made using equipment available in several laboratories. Zero field cooling and field cooling magnetization vs. temperature measurements provide important information, in addition to unambiguously showing the existence of nanoparticles and an approx-

imate idea of their sizes. In particular, susceptibility measurements are highly valuable for studying granular materials. It should be clear that to determine the properties of individual nanoparticles, they must be measured in dilutions. Spin-glass systems in medium and high concentrations share characteristics with granular materials. We propose the use of the term i*nteracting superparamagnetism* (I-SPM) instead of SSG and *percolated superparamagnetism* (P-SPM) instead of SFM. There exists an intimate relationship between the superparamagnetic characteristics of granular materials with so-called giant magnetotransport properties, known as giant magnetoresistance, tunneling magnetoresistance, and the giant Hall effect.

Actual knowledge of the magnetic and magnetotransport properties points to the need for updated experiments with much better controlled structures. Studies on magnetic granular systems must be conducted with an eye toward their structural properties owing to their effect on magnetic and magnetotransport properties.

Acknowledgements LMS wants to acknowledge ANPCyT and CONICET (Argentina), CNPq, and FAPESP (Brazil). OML acknowledges FAPESP Grant 2014/26672-8 and COLCIENCIAS for the fellowship awarded from 2010 to 2014. LNNano-CNPEM (Campinas, Brazil) is acknowledged for the transmission electron microscopy images taken there with a JEOL 3010 URP and a 2100 MSC TEM microscopes.

References

1. Fert A (2008) The present and the future of spintronics. Thin Solids Films 517(1):2–5
2. Martin DH (1967) Magnetism in solids. Iliffe Books Ltd, Londres
3. O'Handley RC (2000) Modern magnetic materials: principles and application. Wiley, New York
4. Knobel M, Nunes WC, Socolovsky LM, De Biasi E, Vargas JM, Denardin JC (2008) Superparamagnetism and other magnetic features in granular materials: a review on ideal and real systems. J Nanosci Nanotech 8:2836
5. Bedanta S, Petracic O, Kleemann W (2015) Supermagnetism. In: Buschow KHJ (ed) Handbook of magnetic materials. Elsevier B.V., Amsterdam
6. Guimarães AP (2009) Principles of nanomagnetism. Springer, Berlin
7. Blundell S (2001) Magnetism in Condensed Matter. Oxford University Press, London
8. Hurd CM (1982) Varieties of magnetic order in solids. Contemp Phys 23(5):469
9. Aharoni A (1996) Introduction to the theory of ferromagnetism. Clarendon Press, Oxford
10. Bedanta S, Kleemann W (2009) Supermagnetism. J Phys D: Appl Phys 42:013001
11. Battle X, Labarta A (2002) Finite-size effects in fine particles: magnetic and transport properties. J Phys D: Appl Phys 35:R15–R42
12. Majetich SA, Sachan M (2006) Magnetostatic interactions in magnetic nanoparticle assemblies: energy, time and length scales. J Phys D: Appl Phys 39:R407–R422
13. Zener C (1954) Classical theory of the temperature dependence of magnetic anisotropy energy. Phys Rev 96(5):1335
14. Torres TE, Lima E Jr, Mayoral A, Ibarra A, Marquina C, Ibarra MR, Goya GF (2015) Validity of the Néel-Arrhenius model for highly anisotropic $Co_xFe_{3-x}O_4$ nanoparticles. J Appl Phys 118:183902
15. Skomski R (1999) RKKY interactions between nanomagnets of arbitrary shape. Europhys Lett 48(4):455–460
16. Mydosh JA (1993) Spin Glasses. Taylor & Francis, Washington, DC

17. Skomski R (2001) Are there superspin glasses? J Appl Phys 109:07E149
18. Mørup S (1994) Superferromagnetic nanostructures. Hyp Int 9:171–185
19. Essam JW (1980) Percolation theory. Reports on Progress in Physics 43(7):833–912
20. Bakuzis AP, Morais PC (2004) Dilution effect upon the superferromagnetic ordering of two-dimensional magnetic nanodots. Phys. Stat. Sol. (C) 1(12):3332–3335
21. Yang HT, Liu HL, Song NN, Du HF, Zhang XQ, Cheng ZH, Shen J, Li LF (2011) Determination of the critical interspacing for the noninteracting magnetic nanoparticle system. Appl Phys Lett 98:153112
22. Vargas JM, Nunes WC, Socolovsky LM, Knobel M, Zanchet D (2005) Phys Rev B 72:184428
23. Allia P, Coisson M, Tiberto P, Vinai F, Knobel M, Novak MA, Nunes WC (2001) Granular Cu-Co alloys as interacting superparamagnets. Phys Rev B 64:144420
24. Skumryev V, Stoyanov S, Zhang Y, Hadjipanayis G, Givord D, Nogués J (2003) Beating the superparamagnetic limit with exchange bias. Nature 423:850–853
25. Gamino M, Michea S, Denardin JC, Schelp LF, Dorneles LS. Exchange-biased extraordinary Hall effect in SiO_2/Co/CoO multilayers (unpublished results)
26. Luis F, Petroff F, Torres JM, García LM, Bartolomé J, Carrey J, Vaurès A (2002) Magnetic relaxation of interacting Co clusters: crossover from two- to three-dimensional lattices. Phys Rev Lett 88:217205
27. Bruvera IJ, Zélis PM, Calatayud MP, Goya GF, Sánchez FH (2016) Determination of the blocking temperature of magnetic nanoparticles: the good, the bad, and the ugly. J Appl Phys 118(18):184304
28. Socolovsky LM, Denardin JC, Brandl AL, Knobel M (2003) Magnetotransport, magnetic, and structural properties of TM–SiO_2 (TM=Fe, Co, Ni) granular alloys. Mat Char 50:117–121
29. Tournus F, Bonet E (2011) J Mag Magn Mat. 323:1109
30. Tournus F, Tamion A (2011) J Mag Magn Mat 323:1118
31. Knobel M, Nunes WC, Winnischofer H, Rocha TCR, Socolovsky LM, Mayorga CL, Zanchet D (2007) Effects of magnetic interparticle coupling on the blocking temperature of ferromagnetic nanoparticle arrays. M. Journal of Non-Crystalline Solids 353:743–747
32. Socolovsky LM, Sánchez FH, Shingu PH (2002) Physica B: Phys Cond Matter 3201-4:149–152
33. Fernández van Raap MB, Sánchez FH, Rodríguez Torres CE, Casas LI, Roig A, Molins E (2005) J Phys: Cond Matter 17:6519
34. García-Palacios JL (2000) On the statics and dynamics of magneto-anisotropic nanoparticles. Adv Chem Phys 112:1–210
35. Shtrikmann S, Wohlfarth EP (1981) The theory of the Vogel-Fulcher law of spin glasses. Phys Lett A 85:467
36. Bittova B, Poltierova-Vejpravova J, Roca AG, Morales MP, Tyrpekl V (2010) Relaxation phenomena in ensembles of $CoFe_2O_4$ nanoparticles. J Phys: Conference Series 200:072012
37. Fang M, Strom V, Olsson RT, Belova L, Rao KV (2012) Particle size and magnetic properties dependence on growth temperature for rapid mixed co-precipitated magnetite nanoparticles. Nanotechnology 23:145601
38. Barbeta VB, Jardim RF, Kiyohara PK, Effenberger FB, Rossi LM (2010) Magnetic properties of Fe_3O_4 nanoparticles coated with oleic and dodecanoic acids. J Appl Phys 107:073913
39. Nadeem K, Krenn H, Traussnig T, Wurschum R, Szabo DV, Letofsky-Papst I (2011) Effect of dipolar and exchange interactions on magnetic blocking of maghemite nanoparticles. J Mag Magn Mat 323:1998–2004
40. Masunaga SH, Jardim RF, Fichtner PFP, Rivas J (2009) Role of dipolar interactions in a system of Ni nanoparticles studied by magnetic susceptibility measurements. Phys Rev B 80:184428
41. Parekh K, Upadhyay RV, Aswal VK (2009) Monodispersed superparamagnetic Fe_3O_4 nanoparticles: synthesis and characterization. J Nanosci Nanotech 9:2104–2110
42. Zelenaková A, Zelenak V, Michalík S, Kovác J, Meisel MW (2014) Structural and magnetic properties of CoO-Pt core-shell nanoparticles. Phys Rev B 89:104417

43. Umut E, Pineider F, Arosio P, Sangregorio C, Corti M, Tabak F, Lascialfari A, Ghigna P (2012) Magnetic, optical and relaxometric properties of organically coated gold–magnetite (Au–Fe_3O_4) hybrid nanoparticles for potential use in biomedical applications. J Mag Magn Mat 324:2373–2379
44. Vázquez-Vázquez C, López-Quintela MA, Buján-Núñez MC, Rivas J (2011) Finite size and surface effects on the magnetic properties of cobalt ferrite nanoparticles. J Nanopart Res 13:1663–1676
45. Dormann JL, D'Orazio F, Lucari F, Tronc E, Prené P, Jolivet JP, Fiorani D, Cherkaoui R, Noguès M (1996) Thermal variation of the relaxation time of the magnetic moment of g-Fe_2O_3 nanoparticles with interparticle interactions of various strengths. Phys Rev B 53:14291
46. Socolovsky LM, Sánchez FH (2003) Thermal scanning studies of percolated Fe–Cu granular alloys. Mat Char 50:123–125
47. Mendoza Zelis P, Pasquevich G, Sanchez FH, Martinez N, Veiga A (2002) Phys Lett A 298:55–59
48. Mørup S, Dumesic JA, Topsoe H (1980) In: Cohen RL (ed) Applications of Mössbauer spectroscopy, vol 2. Academic Press, New York, p 1
49. Chien CL, Liou SH, Kofalt D, Yu W, Egami T, Watson TJ, McGuire TR (1986) Magnetic properties of Fe_xCu_{100-x} solid solutions. Phys Rev B 33:3247
50. Socolovsky LM, Sánchez FH, Shingu PH (2001) Magnetic structure of Fe_xCu_{100-x} magnetoresistive alloys produced by mechanical alloying. Hyp Interact 133:47–52
51. Bean CP, Livingston JD (1959) Superparamagnetism. J Appl Phys 30:120
52. Kodama H, Berkovitz AE, Mc Niff EJ Jr, Foner S (1996) Surface spin disorder in $NiFe_2O_4$ nanoparticles. Phys Rev Lett 77:394
53. Cullity BD (1972) Introduction to magnetic materials. Addison-Wesley, Reading
54. Dormann JL, Bessais L, Fiorani D (1997) A dynamic study of small interacting particles: superparamagnetic model and spin-glass laws. Adv Chem Phys 98:283
55. Mørup S, Tronc E (1994) Superparamagnetic relaxation of weakly interacting particles. Phys Rev Lett 72:3278
56. Dormann JL, Fiorani D, Tronc E (1999) On the models for interparticle interactions in nanoparticle assemblies: comparison with experimental results. J Mag Magn Mater 202:251
57. Brandl AL, Socolovsky LM, Denardin JC, Knobel M (2005) Effects of dipolar interactions on magnetic properties of granular solids. J Mag Magn Mater 294:127–132
58. Knobel M, Nunes WC, Brandl AL, Vargas JM, Socolovsky LM, Zanchet D (2004) Interaction effects in magnetic granular systems. Phys B: Phys Cond Matt 354(1–4):80–87
59. Kang YS, Risbud S, Rabolt JF, Stroeve P (1996) Synthesis and characterization of nanometer-size Fe_3O_4 and γ-Fe_2O_3 particles. Chem Mater 8:2209–2211
60. Moscoso-Londoño O, Gonzalez JS, Muraca D, Hoppe CE, Alvarez VA, López-Quintela A, Socolovsky LM, Pirota KR (2013) Structural and magnetic behavior of ferrogels obtained by freezing thawing of polyvinyl alcohol/poly(acrylic acid) (PAA)-coated iron oxide nanoparticles. Eur Polym J 49:279
61. Moscoso-Londoño O, Muraca D, Oliveira LAS, Pirota KR, Socolovsky LM (2013) The effect of coated-Fe_3O_4 nanoparticles on magnetic properties of ferrogels produced by diffusion route. IEEE Transactions on Magnetics 49(8):4551–4554
62. Ferrari EF, Brandl AL, Piccin R, Denardin JC, Socolovsky LM, Knobel M. Reduction in the magnetic anisotropy energy of exchange coupled nanometric particles (unpublished results)
63. Mydosh JA (2015) Rep Prog Phys 78:052501
64. Coles BR, Sarkissian BVB, Taylor RH (1978) The role of finite magnetic clusters in Au-Fe alloys near the percolation concentration. Phil Mag B 37:489–498
65. Sarkissian BVB (1981) The appearance of critical behaviour at the onset of ferromagnetism in AuFe alloys. J Phys F Metal Phys 11:2191–2208
66. Campbell IA, Senoussi S (1992) Phil Mag B 65(6):1267
67. Topor L, Kleppa OJ (1984) Thermochemistry of binary liquid gold alloys: the systems Au-Ni, Au-Co, Au-Fe, and Au-Mn. Metall Trans B 15B:673

68. Nunes WC, De Biasi E, Meneses CT, Knobel M, Winnischofer H, Rocha TCR, Zanchet D (2008) Appl Phys Lett 92(18):183113
69. De Biasi E, León-Vanegas A, Nunes WC, Sharma SK, Haddad P, Rocha TCR, Santos Duque JG, Zanchet D, Knobel M (2008) Eur Phys J B 66(4):503–508
70. Levy PM (1994) Solid State Physics 47:367
71. Chien CL, Xiao JQ, Jiang JS (1993) Giant negative magnetoresistance in granular ferromagnetic systems. J Appl Phys 73(10):5309
72. Camblong HE, Levy PM, Zhang S (1995) Phys Rev B 51:2216052
73. Baibich MN, Broto JM, Fert A, Van Dau FN, Petroff F, Etienne P, Creuzet G, Friederich A, Chazelas J (1988) Giant magnetoresistance of (001) Fe/(001) Cr magnetic superlattices. Phys Rev Lett 61:2472
74. Binasch G, Grünberg P, Saurenbach F, Zinn W (1989) Enhanced magnetoresistance in layered magnetic structures with antiferromagnetic interlayer exchange. Phys Rev B 39(7):4828(R)
75. Fert A (1969) Two-current conduction in ferromagnetic metals and spin wave-electron collisions. J Phys C 2(2):1784
76. Xiao JQ, Jiang JS, Chien CL (1992) Giant magnetoresistance in nonmultilayer magnetic systems. Phys Rev Lett 68(25):3749
77. Nigam AK, Majumdar AK (1979) Anomalous magnetoresistance in AuFe alloys. J App Phys 50:1712
78. Gerritsen AK (1953) The magnetoresistances of alloys of a noble metal and a transition metal at low temperatures. Physica 19(1–12):61–73
79. Gerritsen AK (1957) Resistance and magneto-resistance of dilute alloys of gold with iron at low temperatures. Physica 23(6–10):1087–1099
80. Rohrer H (1968) Magnetoresistance of dilute alloys. Phys Rev B 174(2):583
81. Nakhimovich NM (1941) Dependence of the electrical resistance of gold and several of its alloys on a magnetic field al low temperatures. J Phys V 2–3:141
82. Maekawa S, Inoue J, Itoh C (1996) J Appl Phys 79:8
83. Ferrari EF, da Silva FCS, Knobel M (1999) Phys Rev B 59(13):8412
84. Allia P, Knobel M, Tiberto P, Vinai F (1995) Magnetic properties and giant magnetoresistance of melt-spun granular $Cu_{100-x}-Co_x$ alloys. Phys Rev B 52:15398–11541
85. Liu K, Zhao L, Klavins P, Osterloh FE, Hiramatsu H (2003) Extrinsic magnetoresistance in magnetite nanoparticles. J App Phys 93:7951
86. Kechkrakos D, Trohidou KN (2002) Physica B 318:360
87. Julliere M (1975) Phys Lett A 54(3):225
88. Abeles R, Sheng P, Coutts MD, Arie Y(1975) Structural and electrical properties of granular metal films. Adv Phys 24–3:407–461
89. Kechkrakos D, Trohidou KN (2005) Phys. Rev. B 71:054416
90. Inoue J, Maekawa S (1996) Theory of tunneling magnetoresistance in granular magnetic films. Phys. Rev. B 53(18):11927–11929
91. Denardin JC, Knobel M, Dorneles LS, Schelp LF (2004) Structural and magnetotransport properties of discontinuous Co/SiO_2 multilayers. Mat Sci Eng B 112(2–3):120–122
92. Varfolomeev AV, Zavyalov AS, Volkov AV, Volkov IA, Moskvina MA, Polyakov SN, Malashko AP, Bayburtskiy FS, Baldokhin YV, Stepanov GV (2006) Preparation and investigation of magnetic composite materials properties on the basis of magnetite and polyvinyl alcohol. Oxidation Comm 29(3):693–697
93. Wang W, Yu M, Chen Y, Tang J (2006) Large room-temperature spin-dependent tunneling magnetoresistance in a Fe_3O_4-polymer composite system. Phys Rev B 73:134412
94. Black CT, Murray CB, Sandstrom RL, Sun S (2000) Spin-dependent tunneling in self-assembled cobalt-nanocrystal superlattices. Science 290:1131–1134
95. Taub N, Tsukernik A, Markovich G (2009) J Mag Magn Mater 321:1933
96. Poddar P, Fried T, Markovich G (2002) First-order metal-insulator transition and spin-polarized tunneling in Fe_3O_4 nanocrystals. Phys Rev B 65:172405
97. Markovich G (2013) Magneto-transport and magnetization dynamics in magnetic nanoparticle assemblies. Mat Today 38:939

98. Bonini M, Fratini E, Baglioni P (2007) SAXS study of chain-like structures formed by magnetic nanoparticles. Mat Sci Eng C 27:1377–1381
99. Pakhomov AB, Yan X, Zhao B (1995) Appl Phys Lett 67:3497
100. Hurd M (1972) The Hall effect in metals and alloys. Plenum Press, New York
101. Gerber A, Milner A, Finkler A, Karpovski M, Goldsmith L, Tuaillon-Combes J, Boisron O, Mélinon P, Perez A (2004) Correlation between the extraordinary Hall effect and resistivity. Phys Rev B 69:224403
102. Karplus R, Luttinger M (1954) Hall effect in ferromagnetics. Phys Rev 95:1154
103. Berger L (1970) Side-jump mechanism for the Hall effect on ferromagnets. Phys Rev B2:4559
104. Jing XN, Wang N, Pakhomov AB, Fung KK, Yan X (1996) Effect of annealing on the giant Hall effect. Phys Rev B 53:14032
105. Socolovsky LM, Oliveira CLP, Denardin JC, Knobel M, Torriani IL (2005) Nanostructure of granular Co-SiO_2 thin films modified by thermal treatment and its relationship with giant Hall effect. Phys Rev B 72:184423
106. Denardin JC, Pakhomov AB, Brandl AL, Socolovsky LM, Knobel M, Zhang XX (2003) Appl Phys Lett 82(5):763–765
107. Socolovsky LM, Oliveira CLP, Denardin JC, Knobel M, Torriani IL (2006) Nanostructure and giant Hall effect in $TM_x(SiO_2)_{1-x}$ (TM = Co, Fe, Ni) granular system. J Appl Phys 99:08C511
108. Socolovsky LM, Sánchez FH, Shingu PH (2001) Giant magnetoresistive properties of Fe_xAu_{100-x} alloys produced by mechanical alloying. J Mag Magn Mat 226–230:736

Chapter 2
Size and Shape Control Synthesis of Iron Oxide–Based Nanoparticles: Current Status and Future Possibility

Khuram Ali, Yasir Javed, and Yasir Jamil

2.1 Introduction

Magnetic phenomena at the atomic scale were discovered in the early twentieth century, whereas the discovery of the first known magnetic material (Fe_3O_4) revolutionized the field of magnetism. The magnetic properties of a material depend on temperature, the applied magnetic field, and pressure. A change in these variables will result in the existence of two or more forms of magnetism. Ferro- and ferrimagnetic materials like Fe_3O_4 and some of their alloys have particles whose shape is asymmetrical when they are obtained by the grinding of bulk materials, whereas they can possess a spherical shape only when manufactured through plasma atomization or wet chemistry or when in aerosol and gas phases. Depending on the procedure used to form particles, they can be crystalline or amorphous spherical in shape. To a large extent, the synthesis process determines the degree of impurities in a particle, as well as the presence of structural defects, and, hence, the division of these defects inside the particle structure can be used to discover its magnetic properties [1, 2].

Magnetization depends on the number of unpaired valence electrons present in the atoms of solids and on the relative orientations of the neighboring magnetic moments [3]. Two types of motion of electrons in atoms are responsible for magnetism. One is the spin of electrons around the atom's axis, and the other is the motion of electrons in an orbit around the nucleus. Iron (Fe), nickel (Ni), manganese (Mn), and cobalt (Co) are magnetic materials that have a net magnetic moment. In transition metal atoms, the magnetic moment is due to electron spin [4].

K. Ali (✉) • Y. Javed • Y. Jamil
Nano-Optoelectronics Research Laboratory, Department of Physics, University of Agriculture Faisalabad, Faisalabad 38040, Pakistan
e-mail: khuram_uaf@yahoo.com; myasi60@gmail.com; yasirjamil@yahoo.com

© Springer International Publishing AG 2017

S.K. Sharma (ed.), *Complex Magnetic Nanostructures*,
DOI 10.1007/978-3-319-52087-2_2

2.1.1 Classification of Magnetic Materials

In solids, materials may be categorized by their response to an externally applied magnetic field. There are five basic types of magnetism, paramagnetism, diamagnetism, ferromagnetism, ferrimagnetism, and antiferromagnetism. The magnetic properties of a material are governed by the electronic structure of the atoms within the material. They vary from weakly magnetic (diamagnetic) to permanently magnetic (ferromagnetic).

The most important property of a magnetic material is the magnetic susceptibility (χ), defined by

$$\chi = \frac{M}{H}, \tag{2.1}$$

where M is the magnetization and H the magnetic field, both of which are measured in units of A/m. In general, the magnetic susceptibility is different for each material, temperature dependent (except in diamagnetic materials), and of the form

$$\chi = \frac{C}{T \pm \theta}. \tag{2.2}$$

2.1.1.1 Diamagnetism

Diamagnetism is a basic property of all matter, but it is an extremely weak property. The susceptibility (χ) is negative and on the order of approximately 10^{-5}. The other characteristic behavior of diamagnetic materials is that their susceptibility is independent of temperature. The origin of diamagnetism is due to the noncooperative behavior of orbiting electrons when exposed to an applied external magnetic field. Diamagnetic materials are composed of atoms having no net magnetic moments (i.e., all the orbital shells are filled and there are no unpaired electrons). When a small field is applied, a small negative magnetization is generated that is proportional to the applied field strength (Fig. 2.1a).

2.1.1.2 Paramagnetism

Because of the magnetic field generated by unpaired electrons, atoms may behave like magnets under the influence of an external magnetic field. However, when the applied magnetic field is removed, the thermal fluctuations would cause the magnetic moment of paramagnetic atoms to move randomly. In the presence of a relatively low magnetic field, this effect can be described by Curie's law,

$$\chi_{\text{para}} = \frac{M}{H} = \frac{C}{T}, \tag{2.3}$$

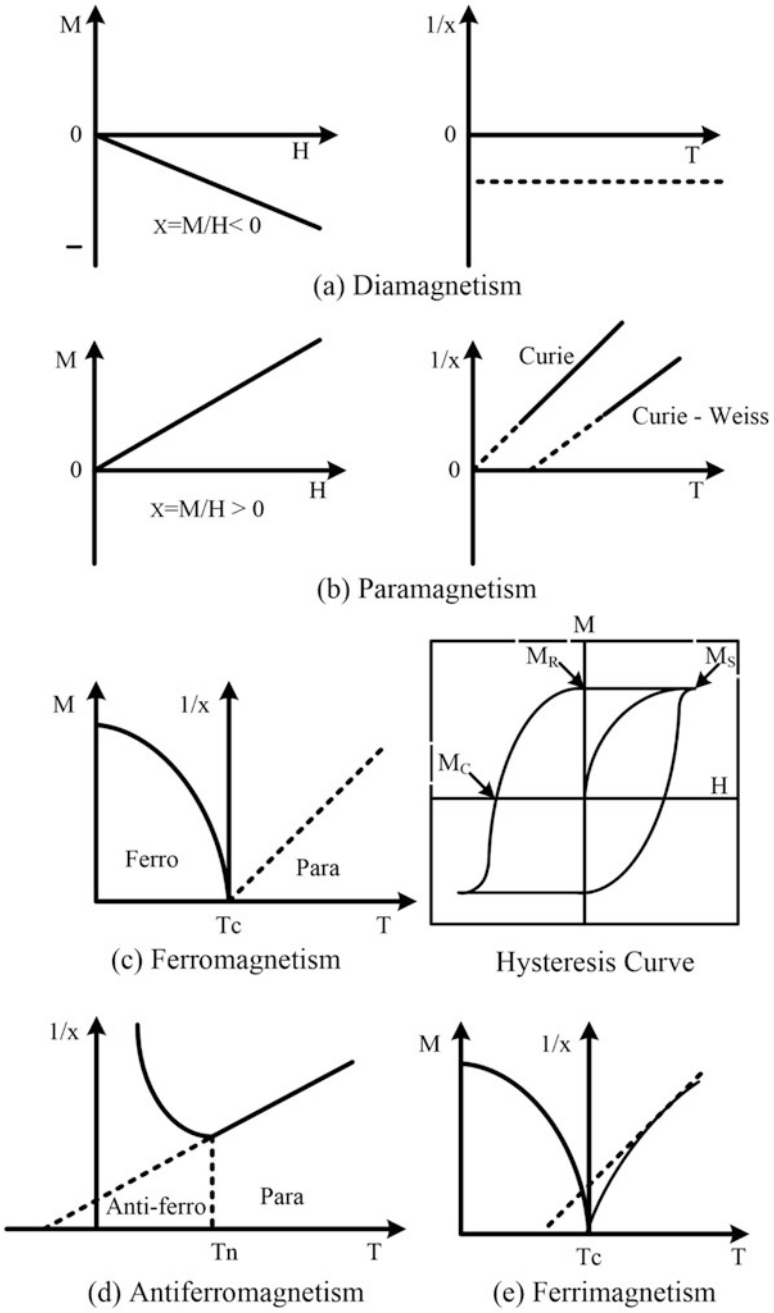

Fig. 2.1 (**a**–**e**) Different kinds of magnetism and their main behavior

where C is the Curie constant. The expected behaviors of paramagnetic materials with an applied external magnetic field and with temperature are shown in Fig. 2.1b. In general, the response of a material to a magnetic field, that is, the magnetic susceptibility (χ), is on the order of 10^{-3}–10^{-5}.

2.1.1.3 Ferromagnetism

Ferromagnetic materials exhibit parallel alignment of magnetic moments to one another, resulting in a large net magnetization, even in zero magnetic fields, known as spontaneous magnetization. The atomic dipole moments in these materials are characterized by very strong positive interactions produced by electronic exchange forces, which results in a parallel alignment of atomic moments. The two distinct features of ferromagnetic materials are a magnetic ordering temperature and spontaneous magnetization.

Ferromagnetism is strongly temperature dependent, and the magnetization of a ferromagnetic material is inversely proportional to temperature by the Curie–Weiss law:

$$\chi = \frac{C}{T - \theta}. \tag{2.4}$$

The Curie temperature is the temperature above which exchange forces cease to be present, that is, above that temperature a ferromagnetic material randomizes owing to the thermal energy, as in paramagnetic systems (Fig. 2.1c). They have relatively large susceptibilities, and in general, magnetic saturation is achieved through fields lower than for paramagnetic systems by a factor of 10^4.

2.1.1.4 Antiferromagnetism

Antiferromagnetic materials are characterized by a weak magnetic susceptibility of the order of paramagnetic materials. In a simple antiferromagnetic material, the atoms can be divided into two sublattices, where magnetic dipole moments are aligned antiparallel, which causes a small magnetic susceptibility in these materials. The temperature above which antiferromagnetic order ceases to exist is called the Neel (T_N) temperature (Fig. 2.1d). Above T_N, antiferromagnetic materials have a slight positive susceptibility comparable to that of paramagnetic materials. Below T_N, however, antiferromagnetic materials have a spontaneous magnetization in the absence of an external field that causes the magnetic dipole moments of sublattices to align antiparallel to each other.

2.1.1.5 Ferrimagnetism

Ferrimagnetic materials, like ferromagnetic materials, have a spontaneous magnetization below a critical temperature called the Curie temperature (T_C). The magnitude of the magnetic susceptibility (χ) of ferro-/ferrimagnetic materials is identical, while the alignment of magnetic dipole moments is drastically different (Fig. 2.1e). The magnetic dipole moments in a ferrimagnetic material are divided into two sublattices and classified as a subset of antiferromagnetic materials. Each sublattice can be treated as a ferromagnetic material, and the difference between the magnetic dipole moments for the sublattices results in a net magnetization for ferrimagnetic materials. The major difference between ferrimagnetic and antiferromagnetic materials is that either the magnitude or the number of moments of sublattices is different.

The most important crystalline ferrimagnetic substances are double oxides of iron, as in $MO.Fe_2O_3$, where M is a divalent metal. These are based on the spinel structure; the protypical example is magnetite, Fe_3O_4. As the temperature rises, the alignment of the spins is disturbed by thermal energy and the magnetization decreases. At a certain temperature, called the Curie temperature T_C, this alignment becomes completely disordered and the magnetization vanishes.

2.1.1.6 Superparamagnetism

Superparamagnetic materials are a special class of magnetic materials. They are single-domain particles that behave like ordinary ferromagnetic materials below T_C because they have rather large magnetic susceptibilities, are saturated in moderate magnetic fields, and display coercivity and remanence. Above T_C, however, superparamagnetic materials behave like ordinary paramagnetic materials in that they display no hysteresis (i.e., no coercivity or remanence).

The idea of superparamagnetism was first developed and proposed by Neel [5, 6] to describe the possibility of thermal fluctuations in single-domain ferromagnetic clusters. In general, the magnetic anisotropy energy of a particle is proportional to its volume. In a given crystal of volume V, the magnetic anisotropy energy is given by

$$E_A = KV\sin^2\theta, \tag{2.5}$$

where K is the anisotropy energy constant and θ the angle between the magnetization vector and easy axis of nanoparticles [7]. When the volume of a single-domain cluster is small enough, the magnetic anisotropy energy of the cluster approaches its thermal energy, causing the magnetization to flip between easy axes through an anisotropy barrier in the same way as in a classical paramagnetic system [8] but, with a giant magnetic moment, that of a single atom, hence the term *superparamagnetism*.

2.1.2 Ferrites

Ferrites are considered a very important class of oxides with significant magnetic properties. Ferrites have been widely studied and applied over the past several decades. To say that ferrites have magnetic properties means they will attract magnets of opposite polarity and iron-based alloys and repel magnets of similar polarity. Ferrites also possess dielectric properties, which mean that they do not conduct electricity when electromagnetic waves pass through them. In various applications, this gives them an advantage over Ni, Fe, and transition metals that possess magnetic properties ("ferromagnetic") because these metals conduct electricity when electromagnetic waves pass through them [9]. The phenomenon of *ferromagnetic* ferrites is the converse of *ferromagnetic* metals. In ferrimagnetism, there is not just one arrangement but distinct alignments of perpendicular and parallel magnetic moments. It is these alignments that give them their remarkable properties. This property can be attained through various crystal structures [10].

2.1.2.1 Applications of Ferrites

Ferrites have applications in such devices as antenna cores, transformers and tuned inductors, compasses, injection pumps, starter motors, loudspeakers, antilock braking systems, microphones, eddy current brakes, telephone rings, switches, alternators, stepping motors, drills, clocks, printers, washing machines, computers, sensors, dampers, energy meter discs, electrochemical transducers, nuclear magnetic resonance spectrometers, DC motors for magnetic devices, magnetic bearings, robotics, clutches and brakes, coupling, orthodontics, instrumentation, lifting apparatus, cancer cell separators, wound closures, magnetic resonance imaging (MRI) body scanners, and ferromagnetic probes. Ferrites are mainly used as inductive components in electronic circuits like impedance matching networks, filters, and low-noise amplifiers. Ferrites have various power applications, such as video and TV systems, computers, and both medium-sized and small gadgets [11, 12].

2.1.2.2 Types of Ferrites

Ferrites are mainly categorized into two major groups, hard ferrites and soft ferrites. In 1945, the first so-called soft ferrite was produced by J. L. Snoek in the Netherlands for commercial purposes [13]. Ferrites are produced in specific sizes and shapes and used for antenna applications, and soft ferrites have multiplied in number and in terms of shapes and sizes. Ferrites have wide applications in electronics, and ferrite devices are the best choice for both modern and conventional applications because of their low cost and because of the continuous improvements being made in their material properties [14].

The magnetic field strength of soft ferrites decreases with time, so their magnetization is temporary. Soft ferrites have numerous applications, such as in inductors, radio frequency interference filters, and transformers [15]. Soft ferrites are a type of black and gray ceramic material and are brittle, inert, and hard. Soft ferrites possess a spinel structure. The usual composition of ferrites is $MeFe_2O_4$, where Me denotes one or more divalent metals like Mg, Mn, Cu, Ni, Fe, and Zn. Soft magnets can become magnetized when drawn toward another magnet, that is, they possess an obvious magnetism only when they are in a magnetic field. They are not permanently magnetized and are used in applications such as cores of distribution power transformers, rotor and stator materials for generators, and motors and electronic transformers [16].

Magnetite (Fe_2O_3) is a weak hard ferrite. Hard ferrites have a basically permanent magnetism. Over time, artificial hard ferrites with fine characteristics were acquired but in the laboratory, with an analogous soft magnetic material being fabricated. A hard magnet attracts other magnetized materials to itself. It retains this obvious magnetism, more or less permanently.

Hard ferrites are mostly used as permanent magnets in brushless and synchronous motors, loudspeakers, and telephone receivers. Hard magnets or hard ferrites also behave as permanent magnets. Hard ferrites are magnetic materials that retain their magnetism after being magnetized. Generally such materials have a very high coercivity (>10 kA/m) [17].

Currently, the most significant use of ferrites is as a medium for the transmission of microwaves. At very high frequencies (above approximately 500 MHz, and in the range of 1–30 GHz), some ferrites show a nonreciprocal effect. This means that electromagnetic waves passing through ferrites behave differently and travel in different directions. This phenomenon is used to construct one-way transmission lines, junctions to control microwave "traffic," and other microwave-controlled appliances. Today, the latest telecommunications systems would not be possible without ferrites. Ferrites are studied extensively, for example, because of their applications at high frequencies and in low eddy current losses, their usefulness at microwave frequencies and mechanical stiffness, and the high coercivity of selected ferrites; in addition, ferrites are used as insulators with magnetic properties, and some ferrites have square hysteresis loops. On the basis of their crystalline structure, ferrites are categorized into four main classes: cubic or spinel ferrites, hexaferrites, orthoferrites, and garnets [18].

2.2 Structural and Magnetic Properties of Nanomaterials

This section aims to provide an understanding of the structural properties of nanomaterials since their technologically relevant properties depend on their structure at the nanoscale.

2.2.1 Crystal Structures

For iron, there are 16 different forms of oxide. In 13 compounds, iron is in its trivalent form, while in the three remaining compounds, −FeO, $-Fe(OH)_2$, and Fe_3O_4, it is in divalent form. All oxides, hydroxides, and oxide hydroxides (or oxyhydroxides) of iron have a crystalline structure. Iron oxides are usually arranged in close packed lattices in hexagonal (hcp) or cubic (ccp) arrangements, where interstitial sites are partially filled by Fe^{2+} or Fe^{3+}, mostly in octahedral sites, and in a few cases in a tetrahedral geometry. The iron oxide structures are described here.

2.2.1.1 Magnetite (Fe_3O_4)

Magnetite occurs in nature as magnetic ore, known as lodestone. Magnetite differs from the majority of other iron oxides in that it contains both trivalent and divalent iron ions. Both magnetite and maghemite have an inverse spinel structure, and differentiating between the two structures in diffraction patterns remains a challenge [19]. Magnetite has a face-centered cubic (fcc) structure on 30 O^{2-} ions arranged in a cubic close-packed arrangement in accordance with [20] in a regular pattern. The lattice parameter of the unit cell is $a = 0.839$ nm. There are eight crystal motifs per unit cell [21]. Its chemical formula can be described as $A[AB]O_4$, where $A = Fe^{3+}$, $B = Fe^{2+}$, and brackets indicate octahedral sites. In an inverse spinel structure, all the Fe^{2+} and half of the Fe^{3+} cations occupy octahedral sites and the remaining half of the trivalent iron occupy tetrahedral sites [22, 23]. The distribution of Fe^{3+} cations at the tetrahedral sites suggests the degree of disorder λ in the spinel structure, and the value of λ for an inverse spinel is $\lambda = 1/2$. Figure 2.2 shows the order of the Fe and O layers along the (001) direction.

The Fe^{2+} cations can be substituted with other metal cations, which produce different types of metal ferrites, such as $CoFe_2O_4$, $MnFe_2O_4$, $ZnFe_2O_4$, and $NiFe_2O_4$. The substituting ions are adjusted by the expansion or contraction of the oxygen framework to compensate the size difference from Fe^{2+} [25–28].

2.2.1.2 Maghemite γ-Fe_2O_3

Maghemite nanoparticles are broadly applicable in biomedicine owing to their excellent magnetic properties. At the same time, they can be made biocompatible and produce low toxicity [29, 30]. Maghemite occurs in nature as a weathering product of structurally related magnetite. The iron oxide γ-Fe_2O_3 is typically described both in a cubic system (space group $P4_3$ 32) with disordered Fe vacancy or in a tetragonal system (space group $P4_12_12$) with full site ordering and $c/a \approx 3$. Magnetite and maghemite have a similar spinel crystalline structure and, hence, identical electron diffraction patterns. Nevertheless, the latter have both Fe^{3+} and Fe^{2+}

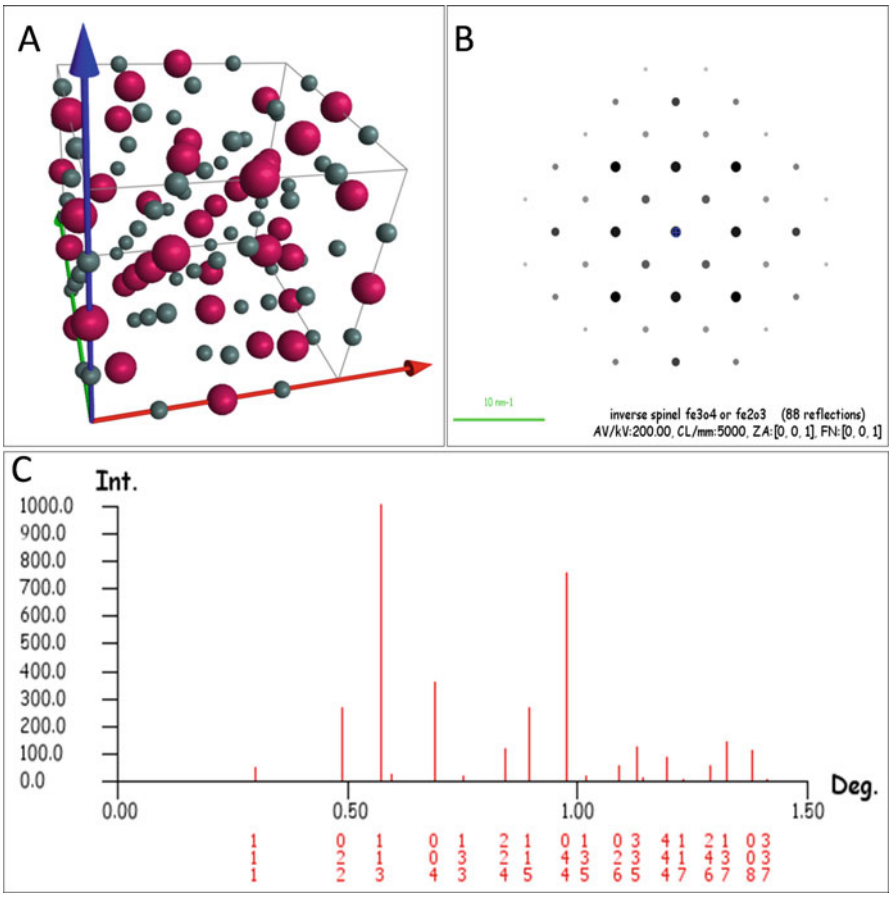

Fig. 2.2 Atomic structure and diffraction of inverse spinel magnetite simulated with JEM software [24]: (**a**) 3-D crystal structure along [001] zone axis (*gray spheres* oxygen atoms, *purple spheres* iron atoms). (**b**) Diffraction pattern oriented along [001] zone axis. (**c**) Powder electron diffraction pattern of inverse spinel magnetite or maghemite (angle described in powder electron diffraction is 2θ). The indexes of the diffraction peaks are given in *red*. (Note that chemically disordered maghemite would exhibit the same diffraction patterns as **b** and **c**; see next section). Space group: Fd3m. Atomic positions: Fe_1: 0.125, 0.125, 0.125; Fe_2: 0.5, 0.5, 0.5; O: 0.254, 0.254, 0.254. Lattice parameters: $a = 0.839$ nm

cations, whereas in maghemite, all the iron ions are in the trivalent state. The charge neutrality of the unit cell is compensated by the existence of cation vacancies. The cubic form of maghemite has a lattice parameter, $a = 0.834$ nm. Each unit cell of maghemite contains 32 oxygen ions, 21 1/3 ferric ions, and 2 1/3 vacancies. Eight Fe ions are located in the tetrahedral sites, and the remaining is randomly distributed over the octahedral sites, whereas vacancies occupy only the octahedral sites. Thus,

maghemite's chemical formula can be changed to A [AΔ] O_3, where A = Fe^{3+}, Δ = vacancies, and brackets indicate octahedral sites [31]. This structure can also be described using the Fd3m cubic space group.

The character and extent of arranging iron vacancies in octahedral sites have been studied by researchers for many years. Vacancy ordering depends on the nature of the precursor, the size of the crystallite, and the amount of iron ions in the structure. The space group Fd3m suggests a random distribution of cation vacancies over octahedral sites like magnetite, but vacancy ordering with 2 2/3 vacancies per unit cell is not permissible owing to the fractional number of vacancies. Thus, it is necessary to extend the cell three times along *c*, which ends in a tetragonal space group ($P4_12_12$), giving a formula of $Fe^{3+}{}_{24}$ [$Fe^{3+}{}_4O_8$] O_{96}. The lattice parameters are $a = 0.833$ nm and $c = 2.501$ nm. Usually, the tetragonal maghemite is associated with an ordered form and the cubic with a disordered form, but cubic phases with vacancy ordering still exist [32]. Figure 2.3 shows the chemically ordered maghemite crystalline structure and diffraction pattern simulated by JEMS software. By comparing the simulated diffractions of Figs. 2.2 and 2.3, we can observe additional superstructure reflections in the diffraction of the chemically ordered maghemite structure (Fig. 2.3). This chemical order allows us to differentiate between maghemite and magnetite using electron diffraction on HRTEM.

In brief, maghemite contains cation vacancies, which may be ordered (tetragonal superstructure), partially ordered (cubic structure), or totally disordered with a high possibility of the vacancies being aggregated [33].

2.2.1.3 Hematite α-Fe_2O_3

Hematite has remarkable applications in the field of gas sensors, magnetic storage media, solar cells, water splitting, and environmental treatment due to its nontoxicity, biodegradability, low corrosion, and low processing expenses [34–38]. It also serves as a starting material for synthesizing maghemite and magnetite [39].

Hematite can be described in a hexagonal (rhombohedral) $R\bar{3}c$ space group. In hexagonal unit cells, the lattice parameters are $a = 0.5034$ nm and $c = 1.375$ nm. The number of crystal motifs per unit cell is six. For hexagonal symmetry, the Miller index is (hkil), where it is usually equal to $-(h+k)$.

The crystallographic structure of hematite is similar to α-Al_2O_3, corundum. The anions form a hexagonal close-packed structure differentiated by the regular successive change in two layers; the atoms in both layers occupy the vertices of a sequence of equilateral triangles, and the atoms in one layer are located directly over the centers of the triangles in the neighboring layers. The cations occupy two-thirds of the octahedral sites [21]. In other words, the oxygen ions occupy hexagonal sites and the Fe cations are located only in the adjacent octahedral sites, though the six adjacent neighboring oxygen ions of an iron ion are slightly misaligned. Moreover, the four iron ions around each oxygen ion are not arranged in a regular

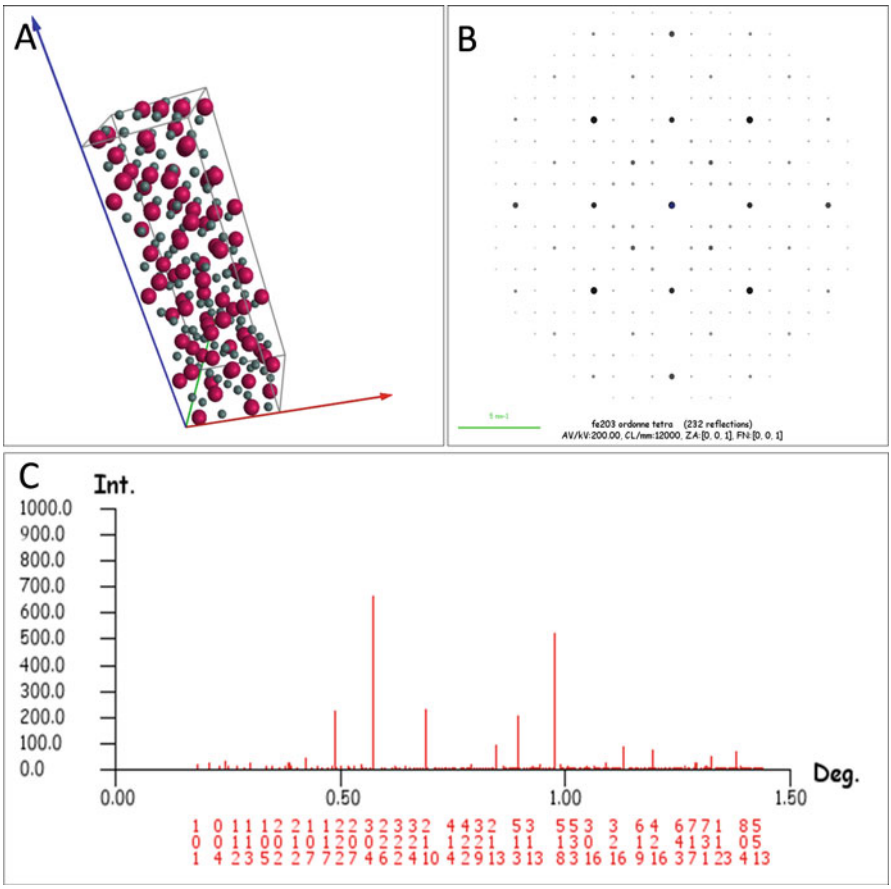

Fig. 2.3 Atomic structure and diffraction of chemically ordered maghemite simulated with JEMS for chemically ordered maghemite [24]: (**a**) 3-D crystalline structure along [001] zone axis (*gray spheres* oxygen atoms, *purple spheres* iron atoms). (**b**) Diffraction pattern oriented along [001] zone axis. (**c**) Powder electron diffraction pattern of chemically ordered maghemite (angle described in powder electron diffraction is 2θ). The indexes of the diffraction peaks are given in *red*. Space group: $P4_12_12$. Atomic positions: **Fe**: (0.742, 0.992, 0.039), (0.2579, 0.0079, 0.2057), (0.492, 0.7579, 0.1224), (0.615, 0.615, 0), (0.385, 0.385, 0.166), (0.375, 0.135, 0.08), (0.865, 0.625, 0.0867), (0.875, 0.365, 0.003), (0.125, 0.125, 0) and **O**: (0.611, 0.861, −0.0047), (0.361, 0.889, 0.0787), (0.389, 0.139, 0.162), (0.122, 0.377, 0.0003), (0.877, 0.378, 0.0837), (0.878, 0.623, 0.166), (0.374, 0.628, 0.0007), (0.128, 0.126, 0.084), (0.626, 0.372, 0.1673), (0.373, 0.376, 0.0843), (0.624, 0.627, 0.0843), (0.124, 0.873, 0.001). Lattice parameters: $a = 0.83$ nm, $c = 2.501$ nm

tetrahedron [40]. Figure 2.4 shows a 3-D view of the structure of hematite consisting of hcp arrays of oxygen ions placed along the [001] direction; Fe^{3+} occupy two-thirds of the sites, arranged in a regular pattern, with two filled sites accompanied by one unoccupied site in the (001) plane.

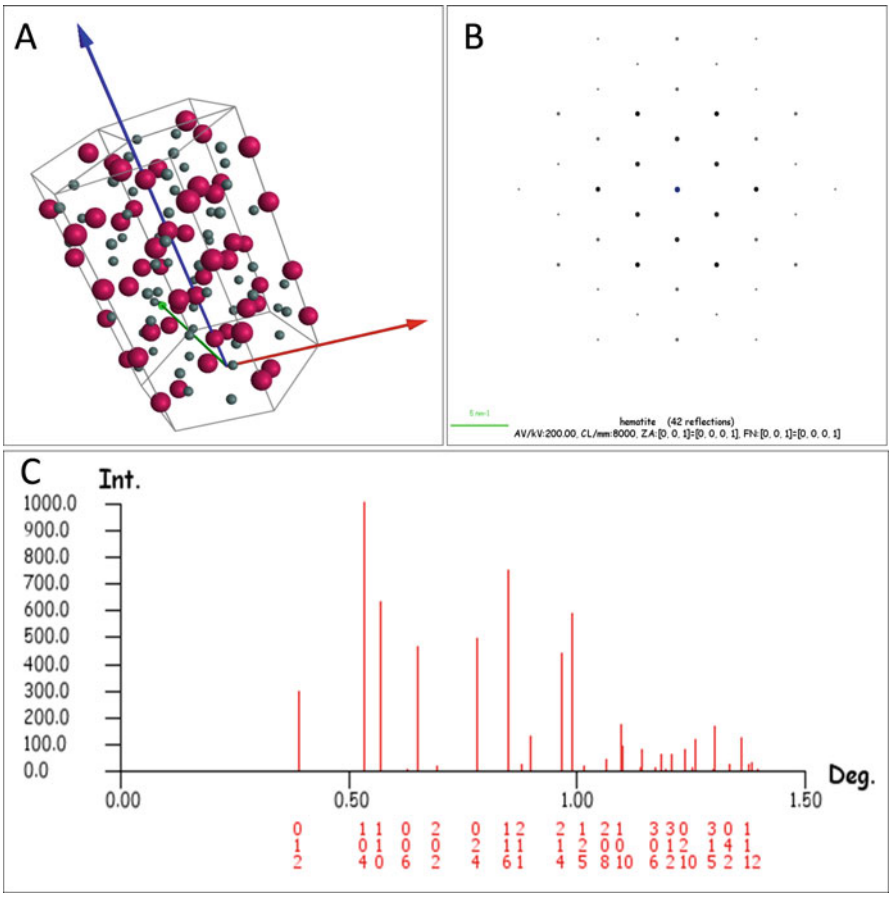

Fig. 2.4 Atomic structure and diffraction of hematite simulated with JEMS [24]: (**a**) 3-D crystalline structure along [001] zone axis (*gray spheres* oxygen atoms, *purple spheres* iron atoms). (**b**) Diffraction pattern oriented along [001] zone axis. (**c**) Powder electron diffraction pattern of hematite (angle described in the powder electron diffraction is 2θ). The indexes of the diffraction peaks are given in *red*. Space group: $R\bar{3}c$. Atomic positions: Fe: 0, 0, 0.3553 and O: 0.3059, 0, 0.25. Lattice parameters: $a = 0.503$ nm, $c = 1.375$ nm

2.2.1.4 Ferrihydrite

Ferrihydrite (Fh) is an extensive hydrous ferric oxyhydroxide mineral present on the Earth's surface [41, 42]. It has been reported that ferrihydrite also occurs in the core of the ferritin protein in living entities and serves to store excess iron [43]. Although we have not observed ferrihydrite in ferritins of ex vivo mice samples, we discuss the structure of ferrihydrite here. Ferrihydrite is a poorly crystalline iron oxyhydroxide. It has an estimated composition of $5Fe_2O_3.9H_2O$, although the actual formula for ferrihydrite is still not established owing to a lack of accurate knowledge of its water

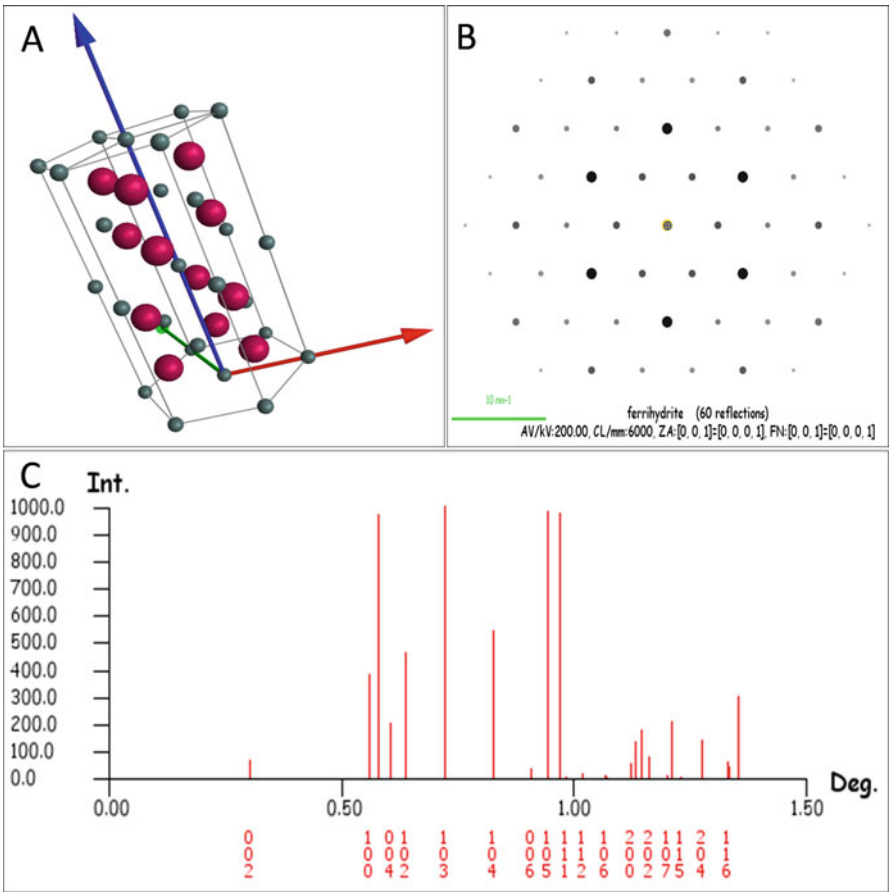

Fig. 2.5 Atomic structure and diffraction of ferrihydrite simulated with JEMS [24]: (**a**) 3-D crystalline structure along [001] zone axis (*gray spheres* oxygen atoms, *purple spheres* iron atoms). (**b**) Diffraction pattern oriented along [001] zone axis. (**c**) Powder electron diffraction pattern of ferrihydrite (angle described in the powder electron diffraction is 2θ). The indexes of the diffraction peaks are given in *red*. Space group: P31c. Atomic positions: Fe: 0.333, 0.666, 0.136, O (OH): 0, 0, 0, and O (OH): 0.666, 0.333, 0.25. Lattice parameters: $a = 0.295$ nm, $c = 0.937$ nm

content. The degree of crystallinity of ferrihydrite is classified as two-line, four-line, and six-line ferrihydrite because it is well known that the number and width of X-ray diffraction (XRD) peaks are directly linked to crystallinity. Figure 2.5a shows the 3-D arrangement of atoms in ferrihydrite that has a hexagonal structure with unit cell parameters of $a = 0.296$ nm and $c = 0.949$ nm. The space group of this structure is P31c [21]. Figure 2.5b, c shows the diffraction pattern along the [001] direction and powder electron diffraction pattern obtained by JEM software [37], respectively.

2.2.1.5 Cobalt Ferrite (Cobalt Ferrite Nanoparticles)

Cobalt ferrites belong to the so-called hard ferrites and have many applications in the fields of medicine, permanent magnets, catalysts, microwave devices, and high-density information storage [44–47]. They are crystallized in an inverse spinel structure just like magnetite, except that divalent iron ions are replaced by cobalt ions [48]. As the ionic radii of divalent Fe and Co are the same, there is no change in the lattice parameter (i.e., $a = 0.839$ nm) of the unit cell.

2.3 Nucleation, Growth, and Arrested Growth

2.3.1 Introduction

The isolation of solid states from liquid phases is an ancient method, but currently it plays a key role in various industrial procedures. To attain the quality of fine products, for economic reasons and environmental effects, the optimization of this phase is necessary [49].

To attain this goal, various theoretical and experimental principles or procedures have been developed. In physical chemistry the following procedures are studied: solubility product, crystal growth, supersaturation, common ion effect, filtration, crystallization, heterogeneous and homogeneous nucleation, precipitation, and coprecipitation. In addition to the effects of pressure, temperature, and additives, the kinetic, thermodynamic, and statistical features of nucleation, precipitation, and crystallization are verified. Some significant methods, such as crystal growth and nucleation, are mostly used in different environments like alloys, vapor phases, interfaces, and glass matrices. The most common approach for the analysis of these methods is to develop a specific treatment. In the liquid phase, the main conditions for the appropriate precipitation procedure are purity and the recovery of the majority of the final product [9].

2.3.1.1 Thermodynamic Considerations

The thermodynamic stability of a substance A in a solution with respect to the pure crystalline solid phase depends on the difference ($\Delta\mu$) between the chemical potential (μA) of A in both phases:

$$\Delta\mu = \mu_{\mathrm{A,solid}} - \mu_{\mathrm{A,solution}} = RT \ln \frac{a_{\mathrm{A,sat.solution}}}{a_{\mathrm{A,solution}}}. \tag{2.6}$$

If Dμ < 0, then some portion of species A will develop a solid phase moving from the solution to the solid phase until Dμ = 0 and a dynamic equilibrium is established between A in both the solid and liquid phases. On the other hand,

if $D\mu > 0$, in saturated solution ($a_{A,sat\ solution}$), if the activity of A in the state of equilibrium with pure A is more than that in the actual solution ($a_{A,solution}$), the material will remain completely molecularly isolated in the liquid phase. Also, the system will be thermodynamically stable and have a single phase. Because of these main properties, $D\mu$ is also known as the driving force behind crystallization.

For sparingly soluble solutes, the driving force ($D\mu$) is associated with entropy (ΔS) and enthalpy (ΔH):

$$\Delta\mu = \Delta H - T\Delta S. \tag{2.7}$$

The preceding equation highlights the relationship between entropic and energetic terms used to control the factors of the crystallization method. Various thermodynamic equations are used to predict the pressure and temperature dependency of the driving force ($D\mu$) [50]. Also, when the activity coefficients in the liquid and solid phases are known, thermodynamics establishes the relationship between the driving force ($D\mu$) and the solubility of nonionic and ionic solutes [51].

2.3.1.2 Kinetic Considerations

Usually, above the solubility limit, crystallization or precipitation occurs rapidly in the presence of a solid phase established due to different substances (heterogeneous nucleation) or the same substance (secondary nucleation). The existence of a solid phase that interacts with the solution offers a surface on which molecules of species A could grow as well as nucleate [52, 53]. In this situation, the factors that control the rate of the entire procedure are (1) the nature and area of the solid phase exposed to the solution; (2) the appearance of the species on the surface of the solid phase and vice versa by mechanical agitation, thermal diffusion, or convection currents; and (3) the incorporation rate of the precursors to the crystal lattice [54, 55]. The incorporation phase contains the partial release of solvating species, the adsorption of a precursor, and a useful setup in the lattice. Usually, anisotropic morphologies are examined when fewer or more molecules are trapped in specific crystal faces.

In homogeneous nucleation, the creation of a solid phase cannot take place owing to the absence of a preexisting solid phase, and the liquid system will be stable kinetically [56–58]. The creation of a crystalline phase is not a single-step process; it is a multistep process that requires the strengthening of molecular groups of cumulative size according to the scheme

$$A_{N-1} + A \rightleftarrows A_N \tag{2.8}$$

or, in agglomeration processes,

$$A_i + A_j \rightleftarrows A_{i+j}. \tag{2.9}$$

At the molecular level, Brownian diffusion of species is a driving force behind these methods that allows their random occurrence. For this purpose, a thermodynamics property must be considered to know whether the solid phase will be established or not from ionic or molecular precursors. The free energy of formation of a nucleus comprised of N molecules, DG_f, given by

$$\Delta G_f = N\Delta_\mu + \Delta G_s. \tag{2.10}$$

The preceding equation is comprised of the term $N\Delta_\mu = \mathrm{NkT}\ \ln \frac{a_{\mathrm{A,sat.solution}}}{a_{\mathrm{A,solution}}}$, which includes the thermodynamic driving force for the growth of aggregate, and the other term ΔG_S is a result of the formation of a boundary between the surroundings and the aggregate. The last term of the preceding equation is given by

$$\Delta G_s = A_{N\gamma_s}, \tag{2.11}$$

where A_N represents the aggregate surface ($A_N = \mathrm{K_N N^{2/3}}$) and γ_s is the interfacial energy per unit surface.

According to the molecular approach, the interfacial energy ΔG_s determines the difference in the energetic state between the species situated in the interior and at the particle surface. This should be positive because at the surface, the energetic state of a species must be greater than that in bulk; then the boundary would be enhanced indefinitely [51].

If the molecules are at the surface or in a bulk, the time average of all the forces acting on them is zero. The strength and number of chemical bonds formed at the surface is smaller than that of bulk species. Embryos are thermodynamically unstable against abnormal growth.

Here, two states, such as bulk and surface species, have been considered. But it must be taken into account that when two phases interact with each other, an imprecise and interfacial domain is produced [54]. In a particle, this indicates the presence of more than two states of A. The first term for the supersaturated solutions ($\mathrm{a_{A,solution}} > \mathrm{a_{A,sat.solution}}$) will be negative, but the second term will always be positive. In these conditions, the dependency of such contributions and of ΔG_f on N is shown in Fig. 2.6.

The value of N^* corresponding to the maximum ΔG_f is known as the critical aggregation number. Aggregates with $N > N^*$ are known as nuclei; they grow naturally because a decrease in free energy increases their size. Aggregates with $N < N^*$ are known as embryos; they decompose because a decrease in the system free energy decreases N.

2.3.2 Growth Mechanism and Size Control

According to kinetic and thermodynamics properties, above the supersaturation threshold, the boundless growth of a nanoparticle is a natural process, and the growth rate can be managed by changing some factors such as temperature,

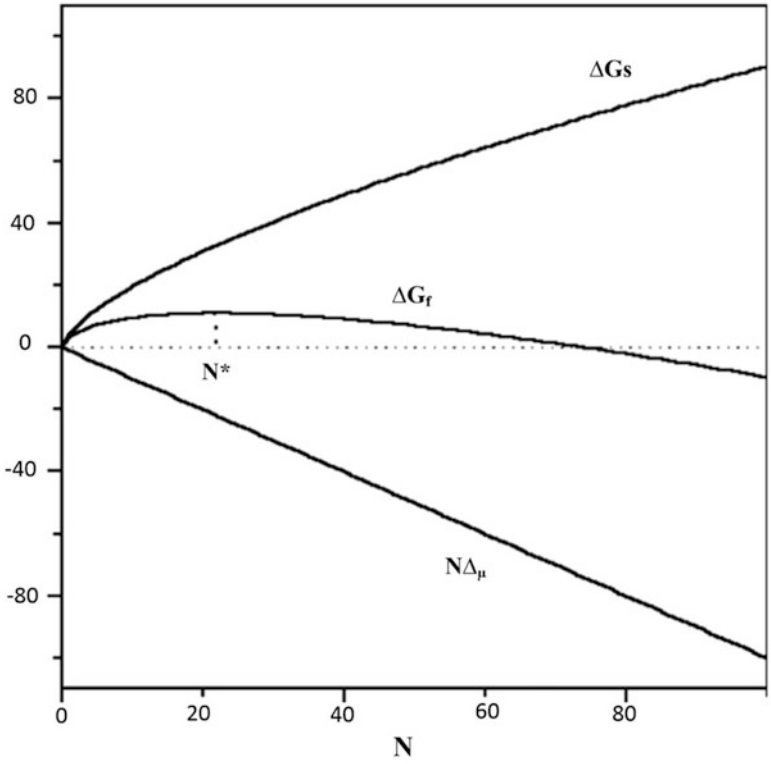

Fig. 2.6 N dependence of free energy of formation of a nucleus (ΔG_f), bulk crystal ($N\Delta_\mu$), and interface (ΔG_S). Figure reprinted/adapted with permission from [51]

supersaturation degree, and additive presence. To place a constraint on this process, other phenomena must play a role. The proper use of these parameters can lead to thermodynamic or kinetic refined nanoparticles of a controlled size [59]. The important types will be further discussed in the following subsections.

2.3.2.1 Nanoparticle Size Dependence on Time

In supersaturated solutions, the possibility of critical aggregate formation is very important in homogeneous conditions. There are three different methods that describe crystal growth, competitive and normal growth and nucleation. Moreover, other processes occur, such as aggregation, crystal growth, agglomeration, recrystallization, nucleation, time aging, induction time, solid-phase transitions, and amount of solid phase. Overlapping zones occur because not all phases are well isolated in time [60–62].

When the concentration of precursor becomes negligibly small, competitive growth controls the whole process. During this step, a movement of mass from minute particles to bigger particles takes place, and the following equation describes the time dependency of a cluster size:

$$\bar{r} \propto t^{0.33}. \tag{2.12}$$

It must be pointed out that the preceding equation represents the tendency toward an indefinite growth of crystal size. Mostly, when the size of a particle attains a system-acquired value as a result of the association of smaller aggregates or a growing process, it manages to isolate from the liquid state under the influence of the gravitational force that arises owing to Brownian movements.

In these conditions, a lower or upper solid phase depending on the bulk medium and the density of particles is developed. From homogeneous solutions, the precipitation of scarcely soluble materials results in an extensive particle size distribution owing to the random growth of a crystal [63]. After precipitation, various secondary processes can take place, such as aging, recrystallization, and aggregation. These processes involve additional changes in the structure, size, effectivity, and shape of crystals [64].

2.3.2.2 MNP Growth Inhibition and Size Control

In some situations, the growth of a particle is due to the existence of some other phenomenon. Various physicochemical methods allow one to control the size of nanoparticles:

- Passivation of nanoparticle surface by adsorption of suitable species,
- Charging of nanoparticles,
- Compartmentalization of nanoparticles in different zones.

Every mechanism has its own uniqueness and drawbacks that must be considered when selecting a synthesis process [65]. The stability of particles is due to the presence of a net charge and the establishment of an electric double layer surrounding the particle. In polar solvents, this is a very common phenomenon because the particle can adsorb ionic species of the solution, or species placed on the particle surface can separate, emitting ions to the adjacent medium. A double layer that surrounds the particle is generated by these methods along with an electrostatic effect on other neighboring ionic species. Owing to electrostatic forces, particles having similar charges or bounded by an electrical double layer repel each other. In such circumstances, when the particle–particle repulsive force overcomes attractive forces, such as hydrogen bonding and van der Waals forces, a stable scattering takes place. Electrostatic stabilization is powerfully reactive in the presence of electrolyte solution, to their charge and concentration, and at relatively low concentrations of nanoparticles, stable scattering can occur [66]. In particular, two contradictory results can be observed: ions resulting from electrolyte

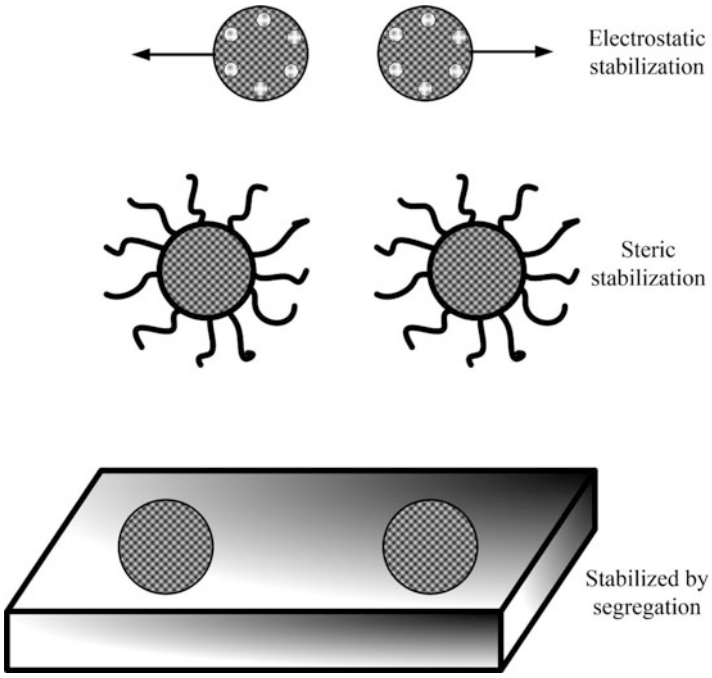

Fig. 2.7 Mechanisms allowing nanoparticle size stabilization. Figure reprinted/adapted with permission from [68]

dissociation can be selectively adsorbed, creating a charge on the surface of a nanoparticle or neutralizing preexisting charges. It must be taken into account that when two particles come into contact with each other, the charge distribution around each particle is changed as a result of the charge mobility on the particle surface, electrostatic forces, or the charged double layer coating the particles (Fig. 2.7). The subsequent charge distribution involves a reduction in the repulsive forces, so the particles will be able to approach each other and other distance dependent interactions can play their role. In addition, other attractive forces, for example, capillary forces and chemical bonds, can become effective at small distances [67]. For instance, it has been observed that negatively charged silica particles are easily deposited in the presence of negatively charged polymer latexes [68].

The double layer electrostatic repulsion and the presence of a net charge on the surface can regulate the stability of particle diffusion in polar and aqueous media [69, 70]. Some particular mechanisms, like proton exchange between surrounding medium and particle surface, are used to sustain surface charges in solvents with small dielectric constants [71]. Particles can also be stabilized by the deliberate use of suitable capping agents. From a molecular approach, molecules that show a chemical or physical affinity for species located at the surface of nanoparticles and form a shielding layer that makes the nanoparticle surface unreactive against

precursor incorporation and agglomeration are known as capping agents. The action of capping agents depends on their particular structure. In particular, they have an unreactive moiety attracted toward the environment and another type of molecular moiety exhibiting an affinity for the surface of nanoparticles. In the presence of unreactive additives or electrolytes, stabilization achieved through surface capping is usually not responsive. For nanoparticles, capping with chemically bonded species may serve as a catalyst.

In different domains, particles can be stabilized against abnormal growth by compartmentalization or segregation. This approach depends on the material exchange method and the inhibition of nanoparticle encounters. This strategy can be attained by scattering particles in a solid matrix or chemically attaching them to the surface of an appropriate substrate. In these situations, particle growth can be avoided by suspending diffusive methods. In various applications (catalysis or optical), this strategy has been extensively used in the preparation of nanoparticles.

Owing to the synthesis of nanoparticles in microheterogeneous systems, a stable-sized nanoparticle can be attained. Compared to the aforementioned mechanisms, this approach has unique characteristics. The formation of nanoparticles takes place in two steps: (1) slow growth of nuclei and (2) fast growth. At high concentrations, separation is obvious [72, 73].

In microheterogeneous systems, specific stabilization mechanisms are observed. Such microheterogeneous systems are used to stabilize nanoparticles. The nanoscopic domains of microhetrogeneous systems serve as a physical border that prevents nanoparticles and precursor diffusion, agglomeration, and encounters. In homogeneous media, the rate of formation of nanoparticles is generally faster than in microheterogeneous systems. This is similar to what is observed in biological systems, such as liposomes or biological membranes.

When a collection of molecules is restricted in a nano-sized area, some additional factors that play a role in the stability of the system could originate from the following sources:

1. Owing to the adsorption on the aggregate surface of a monolayer of surfactant molecules, the particle interfacial energy changes. It must be determined whether the aggregate surface is lipophilic or hydrophilic, as this feature controls the alignment of micellar aggregate or surfactant on the particle surface. If a nanoparticle is isolated in water, a subsequent layer of surfactant molecules is usually created, coating the primary layer and creating a bilayer surrounding the particle, and the surface is known as hydrophilic [74].
2. The encounter frequency decreases owing to the screening effect of the surfactant layer on internanoparticle attractive interactions and to the diffusion of micelles in the solvent medium.
3. A significant reduction in the particle growing process owing to the drastic decrease of the diffusion rate provides sufficient time for various other processes, for example, particle coating with a special type of molecule allowing for stabilization and regulation of small-sized particles.

4. Inhibition of heterogeneous nucleation occurs owing to the coating effect of a monolayer of surfactant molecules on particles or possible solid surfaces in the system.
5. An adjustment takes place in the microscopic processes that make it possible to control the growth and formation of nanoparticles.
6. Thermodynamic and kinetic factors vary in confined spaces.

2.3.3 Novel Synthesis Methods for Size-Controlled MNPs

Spinel ferrites have remarkable magnetic and electrical properties. The sintering and synthesis of ferrites is considered a powerful technique in current ceramic research, and spinel ferrites have notable applications. Because of their low coercivity and high resistance, spinel ferrites have been extensively used in transformers and microwave appliances. The spinel structure is based on a fcc arrangement of oxygen atoms with the stuffing of cations in either octahedral or tetrahedral spaces within this arrangement; in a unit cell 8 out of 64 tetrahedral sites and 16 out of 32 octahedral sites are occupied. These kinds of compounds have both inverse and normal spinel structures. For a normal spinel structure, the octahedral holes are filled by Fe^{3+} ions and the tetrahedral holes are occupied by transition metal ions [75]. In an inverse spinel structure, half the Fe ions pack all the tetrahedral sites and the transition metal ions and the other half of the Fe ions fill all the octahedral sites.

Various chemical methods applied to synthesize magnetic nanoparticles (MNPs) have been presented [76], including the polyol method [77], flow injection synthesis [78], and electrochemical techniques [79, 80]. Because of the colloidal nature of superparamagnetic nanoparticles, it is difficult to synthesize them [60]. Comprehensive studies on the synthesis of small MNPs with well-defined shapes have been conducted by many researchers [21, 81].

2.3.3.1 Classical Synthesis by Coprecipitation

In chemical routes of preparation of nanoparticles with preferred physical properties, the structural and chemical properties of the elements also play an important role. Fine chemical homogeneity can be attained by mixing constituents at the molecular level. Moreover, this makes it possible to control the shape and size distribution during synthesis. Chemical methods of preparation have emerged as an important technique and are used for the synthesis of spinel ferrite nanoparticles [82].

The coprecipitation process is the most proficient technique used for the synthesis of MNPs. This technique involves mixing ferrous and ferric ions in a molar ratio of 1:2 in a solution at room temperature or higher. The formation of ferric oxide can be achieved under the following chemical reaction:

$$Fe^{2+} + 2Fe^{3+} + 8OH^- \rightleftarrows Fe(OH)_2 + 2Fe(OH)_3 \rightarrow Fe_3O_4 + 4H_2O. \quad (2.13)$$

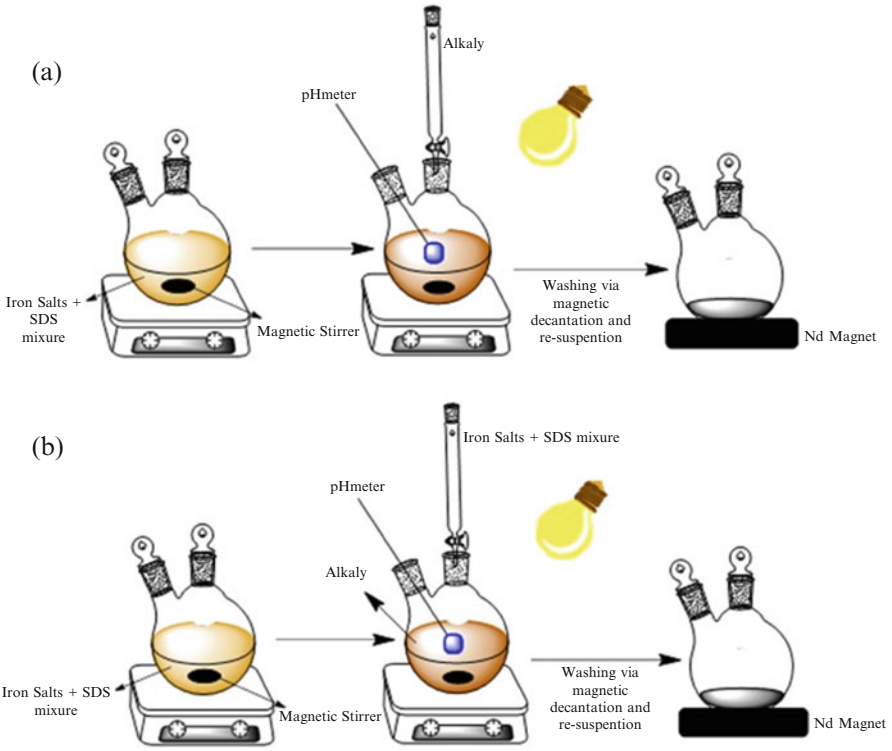

Fig. 2.8 Coprecipitation method. (**a**) Traditional synthesis. (**b**) Inverted synthesis. MNPs synthesized by coprecipitation and modified with sodium dodecyl sulfate (SDS) in a postsynthesis step. Inverted coprecipitation was carried out by adding the Fe^{2+}/Fe^{3+} aqueous solution containing the proper amount of SDS to the alkali solution. Figure reprinted/adapted with permission from [86]

The reaction is controlled by changing the solution pH. The growth of a ferric oxide nucleus is comparatively simple when the pH of the solution is greater than 11, while the nucleation of a ferric oxide nucleus is comparatively simple when the solution pH is less than 11 [83]. Coprecipitation has been examined mostly in the preparation of ferric oxide nanoparticles because of its ease of use in gram-scale fabrication (Fig. 2.8) [84]. Many researchers have reported the extensive coprecipitation synthesis of ferric oxide nanoparticles, where their magnetic properties and morphology at various different temperatures were examined [85]. Various modified coprecipitation processes have been developed. Many researchers have reviewed the advancements and developments in this field over the last decade [83]. In the presence of oxygen, magnetite (Fe_3O_4) oxidizes and converts to maghemite:

$$Fe_3O_4 + 2H^+ \rightarrow \gamma\text{-}Fe_2O_3 + Fe^{2+} + H_2O. \tag{2.14}$$

This equation shows that iron ions are desorbed from the Fe_3O_4 surface, producing cationic holes and forming γ-Fe_2O_3. Hence, the oxidation of Fe_3O_4 involves the oxidation–reduction of the surface of magnetite (Fe_3O_4). Maghemite and magnetite differ from each other in terms of the distribution of iron ions in the tetrahedral and octahedral sites of the spinel structure [79].

In an octahedral site, maghemite (γ-Fe_2O_3) has cationic holes. The ordering of vacancies is related to the synthesis process, which results in symmetry lowering and perhaps superstructures. The vacancies may be partially or completely random or absolutely well arranged. According to the results of XRD and Fourier transform infrared (FTIR) spectroscopy, vacancy ordering occurs only for particles greater than 5 nm in size [87].

The coprecipitation method is used for the fabrication of nanoparticles on a large scale. However, kinetic factors control only the crystal growth while the particle size distribution cannot be definitively measured. The mechanism of this process can be described by the two phases [88, 89]; First, when the concentration of reactant approaches critical supersaturation, an initial short nucleation occurs. Second, due to the dispersion of solutes to the crystal's surface, regular growth of nuclei takes place. Several parameters are used to control the surface and magnetic properties, shape, and size of iron oxide nanoparticles (IONPs). By varying the temperature, pH, Fe^{2+}/Fe^{3+} ratio, and ionic strength, the shape and size of IONPs can be modified [79].

Many researchers have examined the effect of the main parameters on the production of IONPs using the coprecipitation technique. For instance, in [90] the effect of the Fe^{2+}/Fe^{3+} ratio on the magnetic properties, size, and morphology of coprecipitated nanoparticles is discussed.

The effect of iron concentration and iron media have been examined [91]. The Fe^{2+}/Fe^{3+} ratio is the main parameter used to attain the desirable yield and size of IONPs during synthesis. Increasing the Fe^{2+}/Fe^{3+} ratio reduces the preparation yield and enhances the mean particle size.

Moreover, the ionic strength and acidity of the precipitation agent are the main factors on which the mean size of magnetic nanoparticles depends [92]. Narrow particle size distribution and small particle size can be attained under elevated ionic strength [93].

Biocompatibility and aggregation are major hindrances in biomedical applications of IONPs. In the coprecipitation process, various biomolecules and surfactants are directly inserted. The coprecipitation technique is one of the most established and effective techniques used in the synthesis of IONPs with high saturation magnetization, and to overcome the limitations of this technique more attention should be devoted, for instance, to the use of a strong base in reactions and a wide particle size distribution [83].

2.3.3.2 Synthesis by Hydrothermal Method

The hydrothermal method is one of the well-known techniques that have attracted scientific community for nanomaterial synthesis. This is due to its simple and easy synthesis mechanisms. This technique is economical and highly efficient and has potential for large-scale production. In general, the hydrothermal method uses an aqueous medium in a reaction reactor under high temperature and pressure. The size and shape of the particles can be accurately controlled by adjusting the synthesis parameters such as temperature, pressure, reaction time, concentrations and ratio of reactants, type of solvent, and reaction path. In the hydrothermal method, the size of the particle is usually controlled by the crystal growth and rate of nucleation [94]. Generally, nanomaterials synthesized by the hydrothermal method do not need further calcination at high temperatures, which minimizes the risk of nanomaterial reclustering. The hydrothermal method can be used to synthesize a wide range of nanostructured materials [95, 96]. A generalized hydrothermal method for various types of nanomaterial synthesis can be explained as shown in Fig. 2.9.

Magnetic nanoparticles have also been synthesized using the hydrothermal technique. In this regard, octahedral $NiFe_2O_4$ ferrites were synthesized by hydrothermal reaction under mild conditions. FTIR spectroscopy and XRD were employed for constitution measurements and composition of these ferrites. Morphological measurements were done by scanning electron microscopy and these were found octahedral in morphology having mean particle size of ca 40 nm. Crystallite size from XRD analysis was obtained as 39 nm, which is in good agreement with

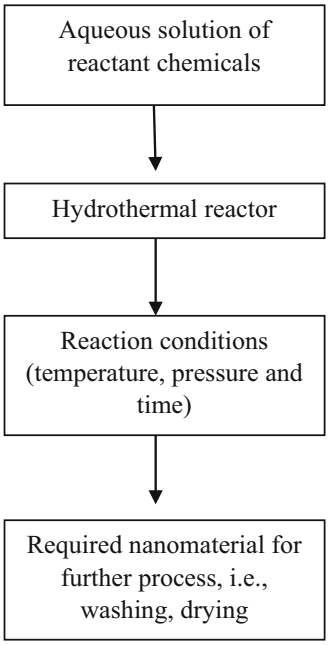

Fig. 2.9 Generalized hydrothermal method for various types of nanomaterial synthesis. Reproduced with permission from [96]

scanning electron microscopy (SEM) results. Electron diffraction and consequent transmission electron microscopy studies confirmed the single crystalline nature and morphology of the octahedral nanoparticles. Magnetic behavior was also investigated, and it was shown that $NiFe_2O_4$ octahedrons had the same coercivity because of the lower morphological anisotropy [97]. TEM investigations revealed that cobalt oxide nanorods have a nanoporous structure, involving the aggregations of nanorods. Magnetic properties indicate that cobalt oxide nanorods have a lower Ne transition temperature, around 35 K. The optical properties of cobalt oxide nanorods were investigated by ultraviolet-visible and Raman spectroscopy [98].

Various properties of cobalt ferrite ($CoFe_2O_4$) nanoparticles have been examined. The hydrothermal technique via a polyethylene glycol (PEG) was used for the synthesis of cobalt ferrite nanoparticles. TEM and XRD analysis were used to investigate the morphological, structural properties of the prepared nanoparticles, and a vibrating sample magnetometer (VSM) was used to examine the magnetic properties. The formation of a pure spinel phase was verified by XRD analysis and the crystallite size was in the range of 10.0–32.0 nm. An increase in the average size of the cobalt ferrite ($CoFe_2O_4$) nanoparticles was also reported as the hydrothermal temperature increased. The size and morphology of the nanoparticles were affected by the hydrothermal temperature, and the morphology of the cobalt ferrite ($CoFe_2O_4$) nanoparticles transformed into an octahedral from a spherical shape as the hydrothermal temperature increased. The characterization of the magnetic properties showed that the coercivities and saturation magnetization of the synthesized cobalt ferrite ($CoFe_2O_4$) nanoparticles become enhanced as the mean size of the cobalt ferrite ($CoFe_2O_4$) nanoparticles increases [99].

Nanoparticles of magnetite (Fe_3O_4) were synthesized using the hydrothermal technique. A contrast agent was used in these nanoparticles to study their applications in MRI. Ferric chloride ($FeCl_3$) and ferrous chloride tetrahydrate ($FeCl_2.4H_2O$) were used as precursors, with sodium hydroxide as reducing agent to start the precipitation of magnetite (Fe_3O_4). Then a layer of chitosan (CHIT) was deposited on the surface of the magnetite's (Fe_3O_4) nanoparticles to increase its biocompatibility and stability. TEM was used to investigate the size distribution of the prepared magnetite (Fe_3O_4) nanoparticles. XRD analysis confirmed the formation of a cubic inverse spinel structure of magnetite (Fe_3O_4) nanoparticles. The FTIR spectrum showed the presence of CHIT on the surface of the synthesized magnetite. The magnetic properties of the magnetite nanoparticles were characterized using a VSM at room temperature. A customized phantom study of MRI proved that the Fe_3O_4 nanoparticles showed better results as contrast agent [100].

The cause of the inhibition of the surfactant was studied for $NiFeO_4$ nanoparticles prepared by the hydrothermal method. The sample was prepared in the presence of sodium dodecyl sulfate and glycerol. XRD, inductively coupled plasma atomic emission spectrometer (ICP-AES), transmission electron microscopy (TEM), and vibrating sample magnetometer (VSM) techniques were employed to investigate the specimens. The crystallinity was increased by increasing the temperature.

In the presence of surfactants, the crystallinity of the $NiFe_2O_4$ nanoparticles was decreased. Furthermore, all of the ferrite nanoparticles were highly paramagnetic at room temperature [101].

2.3.3.3 Polyol Method

Currently, the polyol method has become a preferred technique in the preparation of uniform MNPs. The polyol technique is widely used at high levels of biomedical applications as a tool of investigation; for example, MRI is a polyol technique [102]. Polyols [e.g., ethylene glycol (EG), diethylene glycol (DEG)] are used to reduce metal salts to small-sized metal particles [103]. This process has been used for the production of inorganic compounds [104]. The polyol method was first used for the preparation of noble metals (Pt, Ru, and Au) and other metals like cobalt (Co), copper (Cu), and nickel (Ni) [105, 106]. Nowadays, this synthesis method is being used to synthesize several metals, such as iron-based alloys [107], that can be used in various applications such as in biomedicine.

The polyol method [108] is similar to a sol-gel process. In a sol-gel process, an oxidation reaction is involved, but in the polyol method, a reduction reaction is involved [60], and such a reduction reaction is useful for the synthesis of both microparticles and nanoparticles with well-described shapes and a narrow range of sizes [109]. Polyols such as PEG possess some remarkable properties. They serve as solvents owing to their relatively high dielectric constant and their high boiling point (BP), they occur in a wide temperature range (25 °C to BP) for the preparation of inorganic mixtures [110].

Polyols do not just act as solvents and reducing agents but also serve as stabilizers to manage particle sizes and are used to prevent particle accumulation. In the polyol synthesis method, a metal precursor mixture is suspended in a liquid polyol. First, the suspension is stirred and then heated to a relatively high temperature; this temperature should be as high as the BP of polyols [60, 111]. The narrow size and well-defined shape of nonagglomerated metal nanoparticles can be attained by controlling the kinetics of precipitation [102]. By raising the temperature of reaction or inducing heterogeneous nucleation, some particles, like those of submicrometer-size, can be synthesized. Iron nanoparticles can also be obtained by disproportionation of $Fe(OH)_2$ in organic medium [108].

Recently, Cai and Wan [104] presented a simple process by modifying the polyol process to directly attain nonaggregated MNPs. [104]. The four major kinds of polyols are ethylene glycol (EG), diethylene glycol, triethylene glycol, and tetraethylene glycol [104, 111]. Cuboid iron-manganese oxide nanoparticles with unprecedented dimensions as large as 33 ± 5 nm (average body-centered diagonal) were obtained in monodisperse form by varying the ester content. The shape and size of these unusually large MNPs can be controlled simply by varying the surfactant composition, leading to increased control over the dimensions of the nanoparticles (Fig. 2.10).

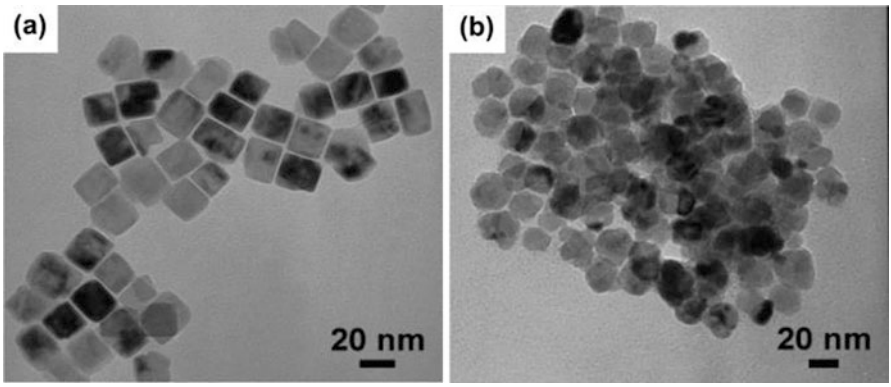

Fig. 2.10 Shape variation of iron-manganese oxide nanoparticles. Figure reprinted/adapted with permission from [20]

Only the reaction with triethylene glycol produced nonagglomerated MNPs of small size and uniform shape (Fig. 2.9). This result shows that the polyol solvent performs a vital role in determining the colloidal stability and morphology of the obtained particles [104]. The occurrence of polyol ligands on the surface of MNPs can be confirmed by FTIR spectroscopy analysis [60]. When sodium hydroxide (NaOH) and Fe (II) chloride reacts with EG, precipitation arises at a low temperature of 80–100 °C [102].

2.3.3.4 Electrochemical Method

The electrochemical process has been used extensively to prepare different phases of iron oxide nanoparticles like Fe_3O_4 or γ-Fe_2O_3 [58]. In this process, a current is passed through a cathode and anode placed in an electrolyte. In an electrolyte, the anode can be oxidized into a metal ion and the cathode can then be reduced to a metal in the presence of stabilizers. At the electrode–electrolyte boundary, synthesis occurs. The electrosynthesis process has various specific characteristics. The electrochemical process occurs near the electrode with a relatively high potential gradient (105 Vcm^{-1}) [79]. Under these conditions, the reactions form products that cannot be obtained using other techniques. The product formed in this reaction is deposited on an electrode, known as a thin film. If a properly shaped electrode is immersed in an electrolyte, a uniform polarization is acquired. The temperature should be moderate and not be as high as the BP of the electrode [79]. The electrochemical process relies on both oxidation and reduction reactions; by changing and regulating the cell potential, the power of both oxidization and reduction can be selected and regularly altered. This unique characteristic cannot be achieved by other synthesis methods. The structure of the thin film or coating can be measured by altering the bath composition [79]. However, this technique

has some limitations, for example, all reactions take place at room temperature, and the electrosynthesis process forms rough products. X-ray characterization of synthesized products formed in this process reveals amorphous impurities [79].

The electrochemical synthesis of maghemite nanoparticles was carried out in an organic medium. Using this method, 3–8 nm γ-Fe_2O_3 particles were prepared from an Fe electrode in a liquid medium of a cationic surfactant [58, 112]. The size of maghemite (γ-Fe_2O_3) nanoparticles can be adjusted by the current density [102]. Under oxidizing conditions, electrochemical deposition has been used for the production of Fe_2O_3 and Fe_3O_4 nanoparticles [113].

In this method, the particle size can be managed by changing the current density or potential. Moreover, it is possible to avoid the aggregation of magnetic nanoparticles if the synthesis is carried out in the presence of surfactants [80]. Some work has been done in this field. Using a conventional process, a size of 20 or 30 nm of Fe_3O_4 nanoparticle is difficult to obtain. The electrochemical synthesis of magnetite (Fe_3O_4) is carried out in an aqueous solution [80]. The particles generated in this process are hydrophobic, and the surface of these particles can easily be changed by an exchange reaction with specific biomolecules. Various techniques, such as TEM, IR spectroscopy, and XRD, have been used mostly for the characterization of generated nanoparticles [80].

2.3.3.5 Flow Injection Technique

The flow injection synthesis (FIS) technique is an adapted form of the coprecipitation process [83]. In various "matrices" like emulsion, the reaction zone confinement is mostly utilized to obtain small nanoparticles. Moreover, a particular pattern of a device can serve as a substitute for the "matrix" confinement [60, 114]. The synthesis of MNPs depends on the flow injection synthesis method. This method is comprised of segmented or continuous mixing of substances in a capillary vessel. In the reaction, various precursors can be inserted by injecting an adjustable amount of flow. Flow injection synthesis has some advantages, for example, high mixing homogeneity and reproducibility. Alvarez studied the impact of chemical factors on the characteristics of various materials [115]. MNPs with a size of 2–7 nm can be obtained in this process [60, 116].

2.4 Strategies to Control the Size and Shape

The morphology and size control of nanoparticles is an important topic for researchers and represents a challenge [117–119]. This topic has further specified applications that might be used more proficiently in different areas. For example, different in vivo properties have been detected using needle or spherically shaped MNPs [120]. Likewise at the cellular level, it seems essential to know MNPs' surface charge for interpreting their uptake capability [121].

Using expensive, complex, and energy-intensive procedures like the acetyl acetanoate of Fe, a polyol, the preparation of identical and nearly individual MNPs can be achieved; however, coprecipitation is proposed when a low-cost, non-time-consuming, and simple method is desired. This popular method includes aqueous salt solutions of iron (Fe^{2+}/Fe^{3+}) and a base used as precipitant medium. In inert atmosphere, this process is normally carried out at comparatively very high temperatures, 70–90 °C [122]. The particles formed as a result of the process normally possess an arbitrary size and morphology. An additional constraint is connected to the accumulation trend in the coprecipitation agents. Particles of iron oxide can form large clusters owing to the anisotropic dipolar attraction, thereby displaying the particular properties connected to single-domain magnetic nanostructures [123].

Comparable studies are also found in other fields; for example, Roth et al. have investigated the impact of numerous experimental variables (e.g., reaction temperature, salt concentration, ratio of Fe^{3+}/Fe^{2+}, and ratio of hydroxide ions to iron ions). They focused largely on the influence of those variables on the size and the magnetization. In this respect, it was found that by adjusting the Fe^{2+}/Fe^{3+} ratio and raising the concentration of iron salts, the saturation magnetization can be improved. The concentration of iron salt and the ratio of hydroxide ions to iron ions affected the particle size [124].

Fang et al. estimated that by using the coprecipitation process, the MNP size was affected by the temperature and the base addition rate [125]. Quick mixing significantly affected the size of particles. It was also found that temperature further affected the size of particles. The influence of the variety of the base was observed by Mascolo et al. These writers tested three different types of base, $(C_2H_5)_4NOH$, NaOH, and KOH, carrying out coprecipitation at room temperature. They revealed a connection between the pH established in coprecipitation media and the tendency of magnetic nanoparticles to agglomerate. That pH is strongly influenced by the alkali nature [126].

The existence of additives, for instance surfactants, was an additional variable that has been widely studied. In this work, MNPs were manufactured by the process of coprecipitation and was improved using SDS in the postsynthesis step. Nanoparticles were consumed for the recovery and removal of nickel, zinc, and copper from industrial wastewater. This research showed that high adsorption capabilities might be obtained in less time thanks to the high surface area and also short diffusion route of SDS-coated Fe_3O_4 MNPs [127].

The current work was applied to perform a control of three significant properties of MNPs: surface change, shape, and size. The aim was to attain monodomain MNPs that were tunable by varying only the experimental conditions related to the methodology of preparation. Progress in nanotechnology is linked with nanoscale accuracy. MNPs are being used in an increasing number of commercial applications. The present work has the ability to control the crystallinity, shape, and size of MNPs and the development of new production methods [60, 128] by accurately adjusting the array magnitudes together with the crystallization of MNPs. The position and properties of MNPs on surfaces can be controlled using

biomineralization proteins. Naturally, complex synthetic functions are performed by proteins. Biomineralization proteins yield an inorganic mineral structure within biological organisms. Biomineralization proteins have been produced for millions of years to regulate the variety of ore below slightly aqueous states [7]. Numerous other biomineralizing biomolecules have been found or improved to prepare desirable materials in vitro and to shape the creation of abiotic materials (including silver, CoPt, and FePt [129–132].

Magnetotactic bacteria can develop extremely uniform MNPs constituted of magnetite, that is, magnetic iron oxide, Fe_3O_4, within the distinctive lipid organelles called magnetosomes. The crystallization of magnetite MNPs is controlled by the biomineralization proteins that remain inside the magnetosome membrane. Numerous proteins were discovered firmly bound to MNPs of the magnetite in the magnetotactic bacterium *Magnetospirillum magneticum* AMB-1 by Arakaki et al. [133]. One protein in particular, Mms6, comprises a hydrophobic N-terminal region for incorporation into the magnetosome membrane and an acidic C-terminal region that can powerfully fix iron ions; it is supposed to nucleate and regulate the development of magnetite in vivo [134]. It has also been revealed that refined Mms6 is able to regulate the development of MNPs of magnetite in vitro (Fig. 2.11) [135].

The method of synthesis of nanomaterials shows some very important measures that will regulate the particular size, size distribution, shape, the surface chemistry of particles, and, thus, their magnetic properties. The nanoparticles of iron oxide have been synthesized by a coprecipitation reaction between ferric and ferrous salts having inorganic bases, very strong bases, NaOH, and somewhat mild bases like NH_4OH. All these schemes indicate that magnetic behavior is similar to that of superparamagnetic materials. Using the aforementioned method, MNPs have been produced that are very small, 1–2 nm, and that have a precise uniform size; the standard deviation is less than 10%. A very uniform coating of silica (1 nm thin) is

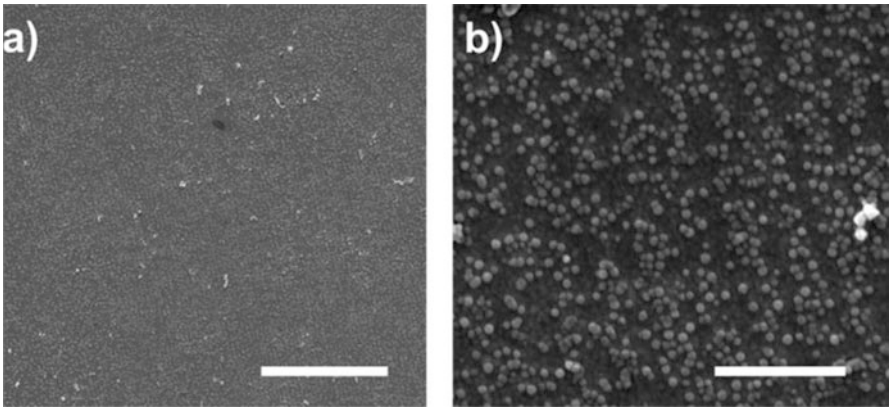

Fig. 2.11 SEM pictures of gold surfaces covered with whole layer of cysteine-tagged Mms6 protein patterned by interferometric lithography (IL) at a disclosure dose of 100 J cm^{-2}. Figure reprinted/adapted with permission from [136]

made using base-catalyzed hydrolysis and the reaction of polymerization of TEOS in microemulsion. It is very important to mention that the insignificant particle size of composites makes it a less acceptable candidate for in vivo applications [9].

2.5 Safety and Surface Stability of Magnetic Nanoparticles

The frequent use of nanomaterials in industrial and medical fields raises questions about their safe use and requires a comprehensive understanding of their life cycle in the body after exposure. Scientists claim that biodegradable nanoparticles are more suitable for biomedical applications because of their efficient metabolization. However, at the nanoscale, properties depend on the particles' size or shape (owing to a large surface-to-volume ratio) and as a result of physical and chemical transformations, the technologically relevant properties of nanoparticles can be changed drastically [137]. Therefore, it is important to provide an extensive understanding about the interactions of nanoparticles with biological environments. Additionally, the evaluation of degraded products is still very challenging owing to the complex phenomena in vivo [138]. For example, the dissolution of crystals can liberate toxic soluble ions, such as Fe^{2+} and Zn^{2+}. On the other hand, other factors, such as a coating polymer, can reduce crystal dissolution and increase the circulation time and persistence of nanoparticles. Recently various research groups have focused on these important issues to understand the life cycle of nanoparticles in vivo [139].

MNPs have less liberty for rotation and translation owing to dipole–dipole magnetic interactions at the cellular level. This reduces magnetic susceptibility and increases the blocking temperature. Consequently, the specific absorption rate of nanoparticles might fall after internalization if an AC magnetic field is applied. It is observed that degradation is a step-by-step dissolution process controlled by surface reaction processes. The physical transformations of nanoparticles indicate the loss of magnetic properties over time. Functionalization or coating of nanoparticles is one of the important factors used to control degradation mechanisms. Organic polymers or inorganic shells can be used as coating [140]. Organic polymers have been used to make nanoparticles biocompatible. This kind of polymer can also serve as a first barrier to control degradation. However, the nature and distribution of the polymer plays an important role in the dissolution of a crystal. An inorganic shell is also a potential candidate to control degradation mechanisms. For inorganic coatings, a complete shell is necessary to control the loss of the core part, in other words, a better cover rate of the core is an important factor. Additionally, an inorganic shell, for example gold, can lend its plasmon properties to nanoparticles. As a result, thermotherapy and plasmon therapy can be used simultaneously from a single nanoparticle. In conclusion, we need degradable nanoparticles, but the process of biodegradation should be delayed so that nanoparticles can be employed for the required application for a specified time [141].

2.6 Applications

2.6.1 Industrial Applications

Magnetic iron oxides (MIOs) are mostly used in porcelain, ceramics, and paints as synthetic pigments. They have attracted much attention in industry and other fields. These materials are attractive and useful in materials science and have vast applications in different fields [142, 143]. Both hematite and magnetite are used as catalysts for various reactions, for instance, in high-temperature water–gas shift reactions and in the preparation of ammonia. The synthesis of butadiene, the oxidation of alcohols, and Fishere–Tropsch synthesis for hydrocarbons are other reactions [144, 145].

2.6.2 Environmental Applications

For in situ applications, IONPs exhibit great flexibility. Supported and catalyzed NPs have been synthesized to increase their efficacy and speed of remediation [146]. Due to some unresolved ambiguities related to the use of IONPs, these substances are recognized as very useful tools in the rectification of various kinds of pollutants in air, soil, and water at both field and experimental levels [31]. Currently, various MNPs have been examined for the removal of both inorganic and organic contaminants.

2.6.3 Organic Pollutants

MNPs are used for the removal of excessive concentrations of organic mixtures [147, 148]. Dyes usually exist in wastewater flows in various branches of industry, for example, in the paint industry, tanneries, and textiles. Hence, MNPs could be suitable for the handling of textile waste.

2.6.4 Inorganic Pollutants

The main feature in metal toxin removal is the formation of functionalized sorbents for affinity or selective removal of harmful metal ions from complex matrices. For the removal of metal ions, MNPs are mostly used as sorbents. Because of the high surface area, MNPs exhibit high [149, 150] efficacy and ability in the removal of various metal ions. These results could be utilized to plan a suitable adsorption treatment for the recovery and removal of metal ions from wastewater.

2.6.5 Analytical Applications

1. *Fluorescence techniques*. Magnetic luminescent nanoparticles present a higher surface area-to-volume ratio owing to their small size than recently employed microbeads that result in faster reaction kinetics and an effective reaction homogeneity. Thus, the formation of magnetic fluorescent particles, such as silica nanoparticles embedded with quantum dots (QDs) and iron oxide, and Fe_2O_3 particles coated with dye-doped silica shells, shells of QDs or polystyrene magnetic beads with entrapped organic dyes or quantum dots [151], is quite simple. But, the application of MNPs is restricted generally to biological applications, for instance cellular imaging.
2. *Encapsulation of MNPs in polymeric matrixes*. The encapsulation of inorganic particles in organic polymers provides the particles with significant properties that bare, uncoated particles lack [152]. A polymer coating on these particles decreases their susceptibility to leaching, increases their compatibility with other organic constituents, and shields the surfaces of particles from oxidation.

   Encapsulation of MNPs in inorganic matrixes. Magnetic properties can be controlled by a simple heating method, and silica has been described to be an efficient approach to controlling magnetic properties [153]. A surface enriched in silica is indicative of surface silanol groups that can simply react with silane coupling agents and alcohols to produce dispersions [154].

2.6.6 Biomedical Applications

There are various biological and clinical applications of MNPs such as in vitro and in vivo applications. For in vivo applications, MNPs are used for diagnostic applications such as MRI as well as in therapies such as drug targeting and hyperthermia, while for in vitro applications, MNPs are mostly used in diagnostic selection, separation, and magnetorelaxometry [155, 156].

2.6.7 In Vivo Applications

For in vivo applications, two main factors, the surface and size functionality of MNPs, play a vital role. Even without affecting surface ligands, superparamagnetic iron oxide (SPIO) nanoparticle diameters greatly affect in vivo biodistribution. Ultrasmall SPIOs and particles with diameters 10–40 nm play a vital role for the prolonged circulation of blood [76].

1. *Therapeutic applications*. Hyperthermia: Employing SPIOs in varying-current magnetic fields arbitrarily reverses the direction of magnetization between both parallel and antiparallel directions. In the form of heat it allows for the transfer

of magnetic energy to particles. For in vivo applications, a property that can be used to enhance the temperature of malignant cells is known as hyperthermia. Cancerous cells are very responsive to an elevated temperature than healthy cells [157]. Also, the use of nanometer-sized magnetic particles is preferred instead of micron-sized magnetic particles because at reasonable AC magnetic fields, nanoparticles absorb much more power [158, 159], which is largely dependent on particle shape and size, and allows for the use of precise synthetic methods for fabricating uniform particles.

2. *Drug delivery*. For drug delivery, drug targeting is a very recent development. Over the last decade, the applications of IONPs in drug targeting have taken on great importance [160]. Magnetic NPs in combination with an external magnetic field allow for the delivery of particles to the required target locations, fix them at the local site while the medication is released, and act locally (magnetic drug targeting) [161]. The transport of drugs to a specific location can reduce side effects and diminish the required dose.

2.6.8 In Vitro Applications

1. *Diagnostic applications*

   a. *Separation and selection*. Currently solid-phase extraction has attracted a lot of attention. Solid phase extraction (SPE) is a technique to isolate and preconcentrate required constituents from a sample matrix. SPE is used for the determination of trace pollutants in ecological samples. Nowadays, nanoparticles have undergone significant advancements and have a considerable effect on sample extraction. This technique is considered the best substitute for the usual sample concentration processes [162–164].

   b. *Magnetorelaxometry*. Two relaxation procedures are Neel relaxation and Brownian relaxation. In Neel relaxation, the internal magnetization vector of the nanoparticles decreases in the direction of the axis inside the core [165]. In Brownian relaxation, particles achieve rotational diffusion in a carrier liquid. Brownian and Neel relaxation can be determined by their distinct relaxation times [166]. Moreover, Neel relaxation does not depend on the dispersal of nanoparticles, whereas Brownian relaxation occurs only in liquids, magnetorelaxometry is based on the hydrodynamic size and core size [167]. For magnetorelaxometry application, the advantage of decreasing the size of particles to the nanometer size is virtually identical to those explained for selection and separation applications.

   c. *MRI*. At the interface between medical diagnostics and nanomaterials, SPIO nanoparticles are treated as a group of new probes mostly suitable for both in vivo and in vitro molecular imaging as well as cellular imaging. In MRI, superparamagnetic contrast agents produce an increase in proton relaxation compared to paramagnetic contrast agents. Therefore, a smaller quantity of

SPIO agent is required to medicate the human body than a paramagnetic contrast agent. To relate the magnetic fluids to MRI contrast agents, the SPIO should be separated into biodegradable and biocompatible carriers.

d. *Bioseparation*. In biomedical research, for analysis it is required to separate the particular biological objects such as cells, DNAs, and proteins from their natural environment. In bioseparation applications, MNPs possess various excellent features owing to their high surface area and small size. In bioprocesses, SPIO nanoparticles have been mostly used for the purification and separation of biomolecules and cells [168–170].

2. *Catalysis applications*. Recently, catalysts supported by MNPs have been mostly used to compensate for the shortcomings of heterogeneous catalysis. Magnetic separation of catalysts in liquid-phase reactions is more reliable than centrifugation and cross-flow filtration, particularly when the catalysts are of submicrometer size. These small and magnetically divisible catalysts can combine high dispersal and reactivity with a simple separation process. The different kinds of transition metal–catalyzed reactions employing MNPs involve hydroformylation [171], carbon–carbon cross-coupling reactions, polymerization [172] reactions, and hydrogenation.

2.7 Future Prospects

Many reviews have been presented research related to the applications of SPIO nanoparticles as a contrast agent. MRI is not suitable for in situ monitoring. Thus, for in situ monitoring of nanoparticles in living cells a simple and precise approach is required. The use of nanometer-sized fluorescence probes is preferred over usual organic fluorescence probes in many application because they could produce good results by yielding strong fluorescence. The fluorescent signal can simply be affected by the background distortions produced by the matrix, and cells are the major issue in cell imaging employing fluorescent nanoprobes.

It is not easy to attain a high signal-to-noise ratio. Furthermore, it is still challenging to control the dynamics of MNPs and owing to these limitations precision is required. Specifically, it is important to have stepwise control over the synthesis process and understand the dynamics of MNPs and their behavior at each step.

The examples and techniques described in this section should be encouraging. In a pure way, various effective synthetic processes can be developed from these examples and techniques. These processes can be performed in a cost-effective way. The controlled synthesis of the nanostructure of nanomaterials can be attained using a simple method of perceiving theoretical principles and the molecular depiction of the retained systems. By easily varying the nature of the reacting species, the synthesis of MNPs by the various examples used in this section can be focused on the MNPs of all materials. Synthetic procedures have great potential in common applications.

In industry, more effort must be made to understand the structure of MNPs and to control the spatial distribution of nanomaterials. Further, novel and attractive nanomaterials could be synthesized by applying the latest microscopic techniques with new mixtures.

References

1. Grossman H, Myers W, Vreeland V, Bruehl R, Alper M, Bertozzi C, Clarke J (2004) Detection of bacteria in suspension by using a superconducting quantum interference device. Proc Natl Acad Sci 101:129–134
2. Chung S, Hoffmann A, Bader S, Liu C, Kay B, Makowski L, Chen L (2004) Biological sensors based on Brownian relaxation of magnetic nanoparticles. Appl Phys Lett 85:2971–2973
3. Duan F, Guojun J (2005) Introduction to condensed matter physics. World Scientific, Singapore
4. Ehrenreich H, Spaepen F (2001) Solid state physics. Academic Press
5. Néel L (1949) Effects of thermal fluctuations on the magnetization of small particles. CR Acad Sci Paris 228:1953
6. Néel L (1949) Theory of magnetic viscosity of fine grained ferromagnetics with application to baked clays. Ann Geophys 5:41
7. Leslie-Pelecky DL, Rieke RD (1996) Magnetic properties of nanostructured materials. Chem Mater 8:1770–1783
8. Morrish AH (2001) In: Morrish AH (ed) The physical principles of magnetism. Wiley-VCH, p 696. isbn:ISBN 0-7803-6029-X
9. Akbarzadeh A, Samiei M, Davaran S (2012) Magnetic nanoparticles: preparation, physical properties, and applications in biomedicine. Nanoscale Res Lett 7:1
10. Rümenapp C, Gleich B, Haase A (2012) Magnetic nanoparticles in magnetic resonance imaging and diagnostics. Pharm Res 29:1165–1179
11. Tang SC, Lo IM (2013) Magnetic nanoparticles: essential factors for sustainable environmental applications. Water Res 47:2613–2632
12. Colombo M, Carregal-Romero S, Casula MF, Gutierrez L, Morales MP, Boehm IB, Heverhagen JT, Prosperi D, Parak WJ (2012) Biological applications of magnetic nanoparticles. Chem Soc Rev 41:4306–4334
13. Sugimoto M (1999) The past, present, and future of ferrites. J Am Ceram Soc 82:269–280
14. Smit J, Wijn H (1954) Physical properties of ferrites. Adv Elect Electron Phys 6:69–136
15. Van Der Zaag P (1999) New views on the dissipation in soft magnetic ferrites. J Magn Magn Mater 196:315–319
16. Polking MJ, Alivisatos AP, Ramesh R (2015) Synthesis, physics, and applications of ferroelectric nanomaterials. MRS Commun 5:27–44
17. Hausner HH (2015) Modern materials: advances in development and applications. Elsevier, Amsterdam, Netherlands
18. Reddy DHK, Yun Y-S (2016) Spinel ferrite magnetic adsorbents: alternative future materials for water purification? Coord Chem Rev 315:90–111
19. Hill RJ, Craig JR, Gibbs G (1979) Systematics of the spinel structure type. Phys Chem Miner 4:317–339
20. Leem G, Sarangi S, Zhang S, Rusakova I, Brazdeikis A, Litvinov D, Lee TR (2009) Surfactant-controlled size and shape evolution of magnetic nanoparticles. Cryst Growth Des 9:32–34
21. Cornell RM, Schwertmann U (2003) The iron oxides: structure, properties, reactions, occurrences and uses. John Wiley & Sons, Hoboken, NJ

22. Gossuin Y, Gillis P, Hocq A, Vuong QL, Roch A (2009) Magnetic resonance relaxation properties of superparamagnetic particles. Wiley Interdiscip Rev Nanomed Nanobiotechnol 1:299–310
23. Rohrer GS (2001) Structure and bonding in crystalline materials. Cambridge University Press, Delhi
24. Stadelmann P (1987) EMS-a software package for electron diffraction analysis and HREM image simulation in materials science. Ultramicroscopy 21:131–145
25. Jang JT, Nah H, Lee JH, Moon SH, Kim MG, Cheon J (2009) Critical enhancements of MRI contrast and hyperthermic effects by dopant-controlled magnetic nanoparticles. Angew Chem 121:1260–1264
26. Kang E, Park J, Hwang Y, Kang M, Park J-G, Hyeon T (2004) Direct synthesis of highly crystalline and monodisperse manganese ferrite nanocrystals. J Phys Chem B 108:13932–13935
27. Song Q, Zhang ZJ (2004) Shape control and associated magnetic properties of spinel cobalt ferrite nanocrystals. J Am Chem Soc 126:6164–6168
28. Tromsdorf UI, Bigall NC, Kaul MG, Bruns OT, Nikolic MS, Mollwitz B, Sperling RA, Reimer R, Hohenberg H, Parak WJ (2007) Size and surface effects on the MRI relaxivity of manganese ferrite nanoparticle contrast agents. Nano Lett 7:2422–2427
29. Dronskowski R (2001) The little maghemite story: a classic functional material. Adv Funct Mater 11:27–29
30. Lévy M, Wilhelm C, Siaugue J-M, Horner O, Bacri J-C, Gazeau F (2008) Magnetically induced hyperthermia: size-dependent heating power of γ-Fe_2O_3 nanoparticles. J Phys Condens Matter 20:204133
31. Waychunas GA (1991) Crystal chemistry of oxides and oxyhydroxides. Rev Mineral Geochem 25:11–68
32. Chen T, Xu H, Ji J, Chen J, Chen Y (2003) Formation mechanism of ferromagnetic minerals in loess of China: TEM investigation. Chin Sci Bull 48:2260–2267
33. Matijevic E, Good RJ (2012) Surface and colloid science. Springer, Berlin
34. Klahr BM, Martinson AB, Hamann TW (2010) Photoelectrochemical investigation of ultrathin film iron oxide solar cells prepared by atomic layer deposition. Langmuir 27:461–468
35. Saremi-Yarahmadi S, Wijayantha KGU, Tahir AA, Vaidhyanathan B (2009) Nanostructured α-Fe2O3 electrodes for solar driven water splitting: effect of doping agents on preparation and performance. J Phys Chem C 113:4768–4778
36. Wu C, Yin P, Zhu X, Ouyang C, Xie Y (2006) Synthesis of hematite (α-Fe2O3) nanorods: diameter-size and shape effects on their applications in magnetism, lithium ion battery, and gas sensors. J Phys Chem B 110:17806–17812
37. Zeng S, Tang K, Li T, Liang Z, Wang D, Wang Y, Zhou W (2007) Hematite hollow spindles and microspheres: selective synthesis, growth mechanisms, and application in lithium ion battery and water treatment. J Phys Chem C 111:10217–10225
38. Zhang G, Gao Y, Zhang Y, Guo Y (2010) Fe_2O_3-pillared rectorite as an efficient and stable Fenton-like heterogeneous catalyst for photodegradation of organic contaminants. Environ Sci Technol 44:6384–6389
39. Cheng C-J, Lin C-C, Chiang R-K, Lin C-R, Lyubutin IS, Alkaev EA, Lai H-Y (2008) Synthesis of monodisperse magnetic iron oxide nanoparticles from submicrometer hematite powders. Crystal Growth Design 8:877–883
40. Morrish AH (1994) Canted antiferromagnetism: hematite. World Scientific, Singapore
41. Cameron AG (1973) Abundances of the elements in the solar system. Space Sci Rev 15:121–146
42. Suess HE, Urey HC (1956) Abundances of the elements. Rev Mod Phys 28:53
43. Fleischer RL, Price PB, Walker RM (1975) Nuclear tracks in solids: principles and applications. University of California Press, Berkeley, CA
44. Ngo A, Pileni M (2001) Assemblies of ferrite nanocrystals: partial orientation of the easy magnetic axes. J Phys Chem B 105:53–58

45. Raj K, Moskowitz B, Casciari R (1995) Advances in ferrofluid technology. J Magn Magn Mater 149:174–180
46. Singhal S, Singh J, Barthwal S, Chandra K (2005) Preparation and characterization of nanosize nickel-substituted cobalt ferrites (Co 1− xNixFe_2O_4). J Solid State Chem 178:3183–3189
47. Sousa MH, Tourinho FA, Depeyrot J, Da Silva GJ, Lara MCF (2001) New electric double-layered magnetic fluids based on copper, nickel, and zinc ferrite nanostructures. J Phys Chem B 105:1168–1175
48. Rooksby H, Willis B (1953) Crystal structure and magnetic properties of cobalt ferrite at low temperatures.
49. Thanh NT, Maclean N, Mahiddine S (2014) Mechanisms of nucleation and growth of nanoparticles in solution. Chem Rev 114:7610–7630
50. Fanun M (2016) Colloids in drug delivery. CRC Press, Boca Raton, FL
51. Liveri VT (2006) Nucleation, growth, and arrested growth in confined space. In: Controlled synthesis of nanoparticles in microheterogeneous systems. Springer, New York, pp 75–90
52. Marchal P, David R, Klein J, Villermaux J (1988) Crystallization and precipitation engineering—I. An efficient method for solving population balance in crystallization with agglomeration. Chem Eng Sci 43:59–67
53. Mersmann A (1999) Crystallization and precipitation. Chem Eng Process Process Intensif 38:345–353
54. Dirksen J, Ring T (1991) Fundamentals of crystallization: kinetic effects on particle size distributions and morphology. Chem Eng Sci 46:2389–2427
55. Franke J, Mersmann A (1995) The influence of the operational conditions on the precipitation process. Chem Eng Sci 50:1737–1753
56. Costa CBB, Maciel MRW, Maciel Filho R (2007) Considerations on the crystallization modeling: population balance solution. Comput Chem Eng 31:206–218
57. Banfield JF, Zhang H (2001) Nanoparticles in the environment. Rev Mineral Geochem 44:1–58
58. Pascal C, Pascal J, Favier F, Elidrissi Moubtassim M, Payen C (1999) Electrochemical synthesis for the control of γ-Fe2O3 nanoparticle size. Morphology, microstructure, and magnetic behavior. Chem Mater 11:141–147
59. Cote LJ, Teja AS, Wilkinson AP, Zhang ZJ (2002) Continuous hydrothermal synthesis and crystallization of magnetic oxide nanoparticles. J Mater Res 17:2410–2416
60. Laurent S, Forge D, Port M, Roch A, Robic C, Vander Elst L, Muller RN (2008) Magnetic iron oxide nanoparticles: synthesis, stabilization, vectorization, physicochemical characterizations, and biological applications. Chem Rev 108:2064–2110
61. Hua CC, Zakaria S, Farahiyan R, Khong LT (2008) Size-controlled synthesis and characterization of Fe. Sains Malaysiana 37:389–394
62. Mehnert W, Mäder K (2001) Solid lipid nanoparticles: production, characterization and applications. Adv Drug Deliv Rev 47:165–196
63. Sun L, Huang C, Gong T, Zhou S (2010) A biocompatible approach to surface modification: biodegradable polymer functionalized super-paramagnetic iron oxide nanoparticles. Mater Sci Eng C 30:583–589
64. Marciano V, Minore A, Liveri VT (2000) A simple method to prepare solid nanoparticles of water-soluble salts using water-in-oil microemulsions. Colloid Polym Sci 278:250–252
65. Chen D, Tang X, Wu J, Zhang W, Liu Q, Jiang Y (2011) Effect of grain size on the magnetic properties of superparamagnetic Ni 0.5 Zn 0.5 Fe_2O_4 nanoparticles by co-precipitation process. J Magn Magn Mater 323:1717–1721
66. Wilson K, Harris L, Goff J, Riffle J, Dailey J (2002) A generalized method for magnetite nanoparticle steric stabilization utilizing block copolymers containing carboxylic acids. Eur Cell Mater 3:206–209
67. Levy L, Hochepied J, Pileni M (1996) Control of the size and composition of three dimensionally diluted magnetic semiconductor clusters. J Phys Chem 100:18322–18326

68. Wang W, Efrima S, Regev O (1999) Directing silver nanoparticles into colloid-surfactant lyotropic lamellar systems. J Phys Chem B 103:5613–5621
69. Qi L, Gao Y, Ma J (1999) Synthesis of ribbons of silver nanoparticles in lamellar liquid crystals. Colloids Surf A Physicochem Eng Asp 157:285–294
70. Andersson M, Alfredsson V, Kjellin P, Palmqvist AE (2002) Macroscopic alignment of silver nanoparticles in reverse hexagonal liquid crystalline templates. Nano Lett 2:1403–1407
71. Liveri VT (2006) Controlled synthesis of nanoparticles in microheterogeneous systems. Springer, Berlin
72. Wu S-H, Chen D-H (2004) Synthesis of high-concentration Cu nanoparticles in aqueous CTAB solutions. J Colloid Interface Sci 273:165–169
73. Rabatic BM, Pralle MU, Tew GN, Stupp SI (2003) Nanostructured semiconductors templated by cholesteryl-oligo (ethylene oxide) amphiphiles. Chem Mater 15:1249–1255
74. Yang H, Guo R, Wang H (2001) Lubrication of the mixed system of Triton X-100/n-C 10 H 21 OH/H_2O lamellar liquid crystal and ZnS nanoparticles. Colloids Surf A Physicochem Eng Asp 180:243–251
75. Padhi A, Nanjundaswamy K, Masquelier C, Okada S, Goodenough J (1997) Effect of structure on the Fe^{3+}/Fe^{2+} redox couple in iron phosphates. J Electrochem Soc 144:1609–1613
76. Lu AH, Salabas EEL, Schüth F (2007) Magnetic nanoparticles: synthesis, protection, functionalization, and application. Angew Chem Int Ed 46:1222–1244
77. Park BK, Jeong S, Kim D, Moon J, Lim S, Kim JS (2007) Synthesis and size control of monodisperse copper nanoparticles by polyol method. J Colloid Interface Sci 311:417–424
78. Faraji M, Yamini Y, Saleh A, Rezaee M, Ghambarian M, Hassani R (2010) A nanoparticle-based solid-phase extraction procedure followed by flow injection inductively coupled plasma-optical emission spectrometry to determine some heavy metal ions in water samples. Anal Chim Acta 659:172–177
79. Ramimoghadam D, Bagheri S, Hamid SBA (2014) Progress in electrochemical synthesis of magnetic iron oxide nanoparticles. J Magn Magn Mater 368:207–229
80. Cabrera L, Gutierrez S, Menendez N, Morales M, Herrasti P (2008) Magnetite nanoparticles: electrochemical synthesis and characterization. Electrochim Acta 53:3436–3441
81. Teja AS, Koh P-Y (2009) Synthesis, properties, and applications of magnetic iron oxide nanoparticles. Prog Cryst Growth Charact Mater 55:22–45
82. Suwalka O, Sharma RK, Sebastian V, Lakshmi N, Venugopalan K (2007) A study of nanosized Ni substituted Co–Zn ferrite prepared by coprecipitation. J Magn Magn Mater 313:198–203
83. Wu W, Wu Z, Yu T, Jiang C, Kim W-S (2016) Recent progress on magnetic iron oxide nanoparticles: synthesis, surface functional strategies and biomedical applications. Sci Technol Adv Mater 16(2):023501
84. Massart R (1981) Preparation of aqueous magnetic liquids in alkaline and acidic media. IEEE Trans Magn 17:1247–1248
85. Wei W, Quanguo H, Rong H, Jingke H, Hong C (2007) Preparation and characterization of magnetite Fe3O4 nanopowders. Rare Metal Mater Eng 36:238–243
86. Azcona P, Zysler R, Lassalle V (2016) Simple and novel strategies to achieve shape and size control of magnetite nanoparticles intended for biomedical applications. Colloids Surf A Physicochem Eng Asp 504:320–330
87. Morales MDP, Veintemillas-Verdaguer S, Montero M, Serna C, Roig A, Casas L, Martinez B, Sandiumenge F (1999) Surface and internal spin canting in γ-Fe_2O_3 nanoparticles. Chem Mater 11:3058–3064
88. Sugimoto T (1987) Preparation of monodispersed colloidal particles. Adv Colloid Interf Sci 28:65–108
89. Boistelle R, Astier J (1988) Crystallization mechanisms in solution. J Cryst Growth 90:14–30
90. Jolivet J, Henry M, Livage J (2000) Metal oxide chemistry and synthesis: from solution to oxide. Wiley, New York

91. Babes L, Denizot BT, Tanguy G, Le Jeune JJ, Jallet P (1999) Synthesis of iron oxide nanoparticles used as MRI contrast agents: a parametric study. J Colloid Interface Sci 212:474–482
92. Jiang W, Yang H-C, Yang S-Y, Horng H-E, Hung J, Chen Y, Hong C-Y (2004) Preparation and properties of superparamagnetic nanoparticles with narrow size distribution and biocompatible. J Magn Magn Mater 283:210–214
93. Tartaj P, González-Carreño T, Serna CJ (2004) From hollow to dense spheres: control of dipolar interactions by tailoring the architecture in colloidal aggregates of superparamagnetic iron oxide nanocrystals. Adv Mater 16:529–533
94. Wang X, Zhuang J, Peng Q, Li Y (2005) A general strategy for nanocrystal synthesis. Nature 437:121–124
95. Anderson SA, Rader RK, Westlin WF, Null C, Jackson D, Lanza GM, Wickline SA, Kotyk JJ (2000) Magnetic resonance contrast enhancement of neovasculature with αvβ3-targeted nanoparticles. Magn Reson Med 44:433–439
96. Khollam Y, Dhage S, Potdar H, Deshpande S, Bakare P, Kulkarni S, Date S (2002) Microwave hydrothermal preparation of submicron-sized spherical magnetite (Fe_3O_4) powders. Mater Lett 56:571–577
97. Kasapoğlu N, Baykal A, Toprak MS, Köseoğlu Y, Bayrakdar H (2007) Synthesis and characterization of $NiFe_2O_4$ nano-octahedrons by EDTA-assisted hydrothermal method. Turk J Chem 31:659–666
98. Wang G, Shen X, Horvat J, Wang B, Liu H, Wexler D, Yao J (2009) Hydrothermal synthesis and optical, magnetic, and supercapacitance properties of nanoporous cobalt oxide nanorods. J Phys Chem C 113:4357–4361
99. Kadier W, Sadeh B, Duamet B, Aman M (2014) Hydrothermal synthesis and properties of CoFe2O4 magnetic nanoparticles 31.
100. Haw CY, Mohamed F, Chia CH, Radiman S, Zakaria S, Huang NM, Lim HN (2010) Hydrothermal synthesis of magnetite nanoparticles as MRI contrast agents. Ceram Int 36:1417–1422
101. Nejati K, Zabihi R (2012) Preparation and magnetic properties of nano size nickel ferrite particles using hydrothermal method. Chem Cent J 6:1
102. Tartaj P, Del Puerto MM, Veintemillas-Verdaguer S, González-Carreño T, Serna CJ (2003) The preparation of magnetic nanoparticles for applications in biomedicine. J Phys D Appl Phys 36:R182
103. Sugimoto T (2000) Fine particles: synthesis, characterization, and mechanisms of growth. CRC Press, Boca Raton, FL
104. Cai W, Wan J (2007) Facile synthesis of superparamagnetic magnetite nanoparticles in liquid polyols. J Colloid Interface Sci 305:366–370
105. Viau G, Ravel F, Acher O, Fiévet-Vincent F, Fiévet F (1994) Preparation and microwave characterization of spherical and monodisperse Co20Ni80 particles. J Appl Phys 76:6570–6572
106. Majidi S, Zeinali Sehrig F, Farkhani SM, Soleymani Goloujeh M, Akbarzadeh A (2016) Current methods for synthesis of magnetic nanoparticles. Artificial Cells Nanomed Biotechnol 44:722–734
107. Viau G, Fievet-Vincent F, Fievet F (1996) Monodisperse iron-based particles: precipitation in liquid polyols. J Mater Chem 6:1047–1053
108. Fievet F, Lagier J, Blin B, Beaudoin B, Figlarz M (1989) Homogeneous and heterogeneous nucleations in the polyol process for the preparation of micron and submicron size metal particles. Solid State Ionics 32:198–205
109. Tzitzios V, Petridis D, Zafiropoulou I, Hadjipanayis G, Niarchos D (2005) Synthesis and characterization of L1 0 FePt nanoparticles from Pt–Fe_3O_4 core-shell nanoparticles. J Magn Magn Mater 294:e95–e98
110. Jezequel D, Guenot J, Jouini N, Fievet F (1995) Submicrometer zinc oxide particles: elaboration in polyol medium and morphological characteristics. J Mater Res 10:77–83

111. Liu J, Qiao SZ, Hu QH (2011) Magnetic nanocomposites with mesoporous structures: synthesis and applications. Small 7:425–443
112. Reetz MT, Helbig W, Quaiser SA (1996) Electrochemical methods in the synthesis of nanostructured transition metal clusters. Active Metals Prep Charact Appl:279–297
113. Khan H, Petrikowski K (2000) Anisotropic structural and magnetic properties of arrays of Fe 26 Ni 74 nanowires electrodeposited in the pores of anodic alumina. J Magn Magn Mater 215:526–528
114. Pankhurst Q, Thanh N, Jones S, Dobson J (2009) Progress in applications of magnetic nanoparticles in biomedicine. J Phys D Appl Phys 42:224001
115. Salazar-Alvarez G, Muhammed M, Zagorodni AA (2006) Novel flow injection synthesis of iron oxide nanoparticles with narrow size distribution. Chem Eng Sci 61:4625–4633
116. Pankhurst QA, Connolly J, Jones SK, Dobson J (2003) Applications of magnetic nanoparticles in biomedicine. J Phys D Appl Phys 36:R167
117. Rodríguez-López A, Cruz-Rivera J, Elías-Alfaro C, Betancourt I, Ruiz-Silva H, Antaño-López R (2015) Fine tuning of magnetite nanoparticle size distribution using dissymmetric potential pulses in the presence of biocompatible surfactants and the electrochemical characterization of the nanoparticles. Mater Sci Eng C 46:538–547
118. Chatterjee K, Sarkar S, Rao KJ, Paria S (2014) Core/shell nanoparticles in biomedical applications. Adv Colloid Interf Sci 209:8–39
119. Herea D, Chiriac H, Lupu N, Grigoras M, Stoian G, Stoica B, Petreus T (2015) Study on iron oxide nanoparticles coated with glucose-derived polymers for biomedical applications. Appl Surf Sci 352:117–125
120. Khoee S, Shagholani H, Abedini N (2015) Synthesis of quasi-spherical and square shaped oligoamino-ester graft-from magnetite nanoparticles: effect of morphology and chemical structure on protein interactions. Polymer 56:207–217
121. Calatayud MP, Sanz B, Raffa V, Riggio C, Ibarra MR, Goya GF (2014) The effect of surface charge of functionalized Fe 3 O 4 nanoparticles on protein adsorption and cell uptake. Biomaterials 35:6389–6399
122. Šutka A, Lagzdina S, Käämbre T, Pärna R, Kisand V, Kleperis J, Maiorov M, Kikas A, Kuusik I, Jakovlevs D (2015) Study of the structural phase transformation of iron oxide nanoparticles from an Fe2+ ion source by precipitation under various synthesis parameters and temperatures. Mater Chem Phys 149–150:473–479
123. Lassalle V, Avena M, Ferreira M (2009) A review of the methods of magnetic nanocomposites synthesis and their applications as drug delivery systems and immobilization supports for lipases. Current Trends Polymer Sci 13:37–67
124. Roth H-C, Schwaminger SP, Schindler M, Wagner FE, Berensmeier S (2015) Influencing factors in the c-precipitation process of superparamagnetic iron oxide nano particles: a model based study. J Magn Magn Mater 377:81–89
125. Fang M, Ström V, Olsson RT, Belova L, Rao KV (2012) Particle size and magnetic properties dependence on growth temperature for rapid mixed co-precipitated magnetite nanoparticles. Nanotechnology 23:145601
126. Mascolo MC, Pei Y, Ring TA (2013) Room temperature co-precipitation synthesis of magnetite nanoparticles in a large pH window with different bases. Materials 6:5549–5567
127. Adeli M, Yamini Y, Faraji M (2012) Removal of copper, nickel and zinc by sodium dodecyl sulphate coated magnetite nanoparticles from water and wastewater samples. Arab J Chem. doi:10.1016/j.arabjc.2012.10.012
128. Reddy LH, Arias JL, Nicolas J, Couvreur P (2012) Magnetic nanoparticles: design and characterization, toxicity and biocompatibility, pharmaceutical and biomedical applications. Chem Rev 112:5818–5878
129. Wang B, Chen K, Jiang S, Reincke F, Tong W, Wang D, Gao C (2006) Chitosan-mediated synthesis of gold nanoparticles on patterned poly (dimethylsiloxane) surfaces. Biomacromolecules 7:1203–1209
130. Naik RR, Stringer SJ, Agarwal G, Jones SE, Stone MO (2002) Biomimetic synthesis and patterning of silver nanoparticles. Nat Mater 1:169–172

131. Reiss BD, Mao C, Solis DJ, Ryan KS, Thomson T, Belcher AM (2004) Biological routes to metal alloy ferromagnetic nanostructures. Nano Lett 4:1127–1132
132. Galloway JM, Bird SM, Bramble JP, Critchley K, Staniland SS (2013) Biotemplating magnetic nanoparticles on patterned surfaces for potential use in data storage. In: MRS Proceedings. Cambridge University Press, Delhi, pp 231–237
133. Arakaki A, Webb J, Matsunaga T (2003) A novel protein tightly bound to bacterial magnetic particles in Magnetospirillum magneticum strain AMB-1. J Biol Chem 278:8745–8750
134. Galloway JM, Arakaki A, Masuda F, Tanaka T, Matsunaga T, Staniland SS (2011) Magnetic bacterial protein Mms6 controls morphology, crystallinity and magnetism of cobalt-doped magnetite nanoparticles in vitro. J Mater Chem 21:15244–15254
135. Wang L, Prozorov T, Palo PE, Liu X, Vaknin D, Prozorov R, Mallapragada S, Nilsen-Hamilton M (2011) Self-assembly and biphasic iron-binding characteristics of Mms6, a bacterial protein that promotes the formation of superparamagnetic magnetite nanoparticles of uniform size and shape. Biomacromolecules 13:98–105
136. Bird SM, El-Zubir O, Rawlings AE, Leggett GJ, Staniland SS (2016) A novel design strategy for nanoparticles on nanopatterns: interferometric lithographic patterning of Mms6 biotemplated magnetic nanoparticles. J Mater Chem C 4:3948–3955
137. Kolosnjaj-Tabi J, Lartigue L, Javed Y, Luciani N, Pellegrino T, Wilhelm C, Alloyeau D, Gazeau F (2016) Biotransformations of magnetic nanoparticles in the body. Nano Today 11(3):280–284
138. Lartigue L, Alloyeau D, Kolosnjaj-Tabi J, Javed Y, Guardia P, Riedinger A, Péchoux C, Pellegrino T, Wilhelm C, Gazeau F (2013) Biodegradation of iron oxide nanocubes: high-resolution in situ monitoring. ACS Nano 7:3939–3952
139. Javed Y, Lartigue L, Hugounenq P, Vuong QL, Gossuin Y, Bazzi R, Wilhelm C, Ricolleau C, Gazeau F, Alloyeau D (2014) Biodegradation mechanisms of iron oxide monocrystalline nanoflowers and tunable shield effect of gold coating. Small 10:3325–3337
140. Mazuel F, Espinosa A, Luciani N, Reffay M, Le Borgne R, Motte L, Desboeufs K, Michel A, Pellegrino T, Lalatonne Y (2016) Massive intracellular biodegradation of iron oxide nanoparticles evidenced magnetically at single endosome and tissue levels. ACS Nano 10(8):7627–7638
141. Kolosnjaj-Tabi J, Javed Y, Lartigue L, Volatron J, Elgrabli D, Marangon I, Pugliese G, Caron B, Figuerola A, Luciani N (2015) The one year fate of iron oxide coated gold nanoparticles in mice. ACS Nano 9:7925–7939
142. Jun YW, Choi JS, Cheon J (2006) Shape control of semiconductor and metal oxide nanocrystals through nonhydrolytic colloidal routes. Angew Chem Int Ed 45:3414–3439
143. Nunez NO, Tartaj P, Morales MP, Pozas R, Ocana M, Serna CJ (2003) Preparation, characterization, and magnetic properties of Fe-based alloy particles with elongated morphology. Chem Mater 15:3558–3563
144. Park S-J, Kim S, Lee S, Khim ZG, Char K, Hyeon T (2000) Synthesis and magnetic studies of uniform iron nanorods and nanospheres. J Am Chem Soc 122:8581–8582
145. Dumestre F, Chaudret B, Amiens C, Renaud P, Fejes P (2004) Superlattices of iron nanocubes synthesized from Fe [N (SiMe3) 2] 2. Science 303:821–823
146. Wang L, Luo J, Fan Q, Suzuki M, Suzuki IS, Engelhard MH, Lin Y, Kim N, Wang JQ (2005) Monodispersed core-shell Fe3O4@ Au nanoparticles. J Phys Chem B 109:21593–21601
147. Caruntu D, Cushing BL, Caruntu G, O'connor CJ (2005) Attachment of gold nanograins onto colloidal magnetite nanocrystals. Chem Mater 17:3398–3402
148. Lyon JL, Fleming DA, Stone MB, Schiffer P, Williams ME (2004) Synthesis of Fe oxide core/Au shell nanoparticles by iterative hydroxylamine seeding. Nano Lett 4:719–723
149. Zambaux M, Bonneaux F, Gref R, Dellacherie E, Vigneron C (1999) Preparation and characterization of protein C-loaded PLA nanoparticles. J Control Release 60:179–188
150. Stolnik S, Illum L, Davis S (1995) Long circulating microparticulate drug carriers. Adv Drug Deliv Rev 16:195–214

151. Savva M, Duda E, Huang L (1999) A genetically modified recombinant tumor necrosis factor-α conjugated to the distal terminals of liposomal surface grafted polyethyleneglycol chains. Int J Pharm 184:45–51
152. Peracchia MT, Vauthier C, Passirani C, Couvreur P, Labarre D (1997) Complement consumption by poly (ethylene glycol) in different conformations chemically coupled to poly (isobutyl 2-cyanoacrylate) nanoparticles. Life Sci 61:749–761
153. Sah H (1999) Stabilization of proteins against methylene chloride/water interface-induced denaturation and aggregation. J Control Release 58:143–151
154. Velge-Roussel F, Breton P, Guillon X, Lescure F, Bru N, Bout D, Hoebeke J (1996) Immunochemical characterization of antibody-coated nanoparticles. Experientia 52:803–806
155. Piao Y, Kim J, Na HB, Kim D, Baek JS, Ko MK, Lee JH, Shokouhimehr M, Hyeon T (2008) Wrap–bake–peel process for nanostructural transformation from β-FeOOH nanorods to biocompatible iron oxide nanocapsules. Nat Mater 7:242–247
156. Liu C, Wu X, Klemmer T, Shukla N, Weller D, Roy AG, Tanase M, Laughlin D (2005) Reduction of sintering during annealing of FePt nanoparticles coated with iron oxide. Chem Mater 17:620–625
157. Mikhaylova M, Kim DK, Bobrysheva N, Osmolowsky M, Semenov V, Tsakalakos T, Muhammed M (2004) Superparamagnetism of magnetite nanoparticles: dependence on surface modification. Langmuir 20:2472–2477
158. Jeong U, Teng X, Wang Y, Yang H, Xia Y (2007) Superparamagnetic colloids: controlled synthesis and niche applications. Adv Mater 19:33–60
159. Hyeon T (2003) Chemical synthesis of magnetic nanoparticles. Chem Commun:927–934
160. Casula MF, Jun Y-W, Zaziski DJ, Chan EM, Corrias A, Alivisatos AP (2006) The concept of delayed nucleation in nanocrystal growth demonstrated for the case of iron oxide nanodisks. J Am Chem Soc 128:1675–1682
161. Kwon SG, Piao Y, Park J, Angappane S, Jo Y, Hwang N-M, Park J-G, Hyeon T (2007) Kinetics of monodisperse iron oxide nanocrystal formation by "heating-up" process. J Am Chem Soc 129:12571–12584
162. Dubertret B, Skourides P, Norris DJ, Noireaux V, Brivanlou AH, Libchaber A (2002) In vivo imaging of quantum dots encapsulated in phospholipid micelles. Science 298:1759–1762
163. Gao X, Cui Y, Levenson RM, Chung LW, Nie S (2004) In vivo cancer targeting and imaging with semiconductor quantum dots. Nat Biotechnol 22:969–976
164. Pellegrino T, Manna L, Kudera S, Liedl T, Koktysh D, Rogach AL, Keller S, Rädler J, Natile G, Parak WJ (2004) Hydrophobic nanocrystals coated with an amphiphilic polymer shell: a general route to water soluble nanocrystals. Nano Lett 4:703–707
165. White MA, Johnson JA, Koberstein JT, Turro NJ (2006) Toward the syntheses of universal ligands for metal oxide surfaces: controlling surface functionality through click chemistry. J Am Chem Soc 128:11356–11357
166. Caruso F (2001) Nanoengineering of particle surfaces. Adv Mater 13:11–22
167. Stöber W, Fink A, Bohn E (1968) Controlled growth of monodisperse silica spheres in the micron size range. J Colloid Interface Sci 26:62–69
168. Yi DK, Selvan ST, Lee SS, Papaefthymiou GC, Kundaliya D, Ying JY (2005) Silica-coated nanocomposites of magnetic nanoparticles and quantum dots. J Am Chem Soc 127:4990–4991
169. Yi DK, Lee SS, Papaefthymiou GC, Ying JY (2006) Nanoparticle architectures templated by SiO2/Fe2O3 nanocomposites. Chem Mater 18:614–619
170. Kim J, Lee JE, Lee J, Yu JH, Kim BC, An K, Hwang Y, Shin C-H, Park J-G, Kim J (2006) Magnetic fluorescent delivery vehicle using uniform mesoporous silica spheres embedded with monodisperse magnetic and semiconductor nanocrystals. J Am Chem Soc 128:688–689
171. Yoon TJ, Yu KN, Kim E, Kim JS, Kim BG, Yun SH, Sohn BH, Cho MH, Lee JK, Park SB (2006) Specific targeting, cell sorting, and bioimaging with smart magnetic silica core–shell nanomaterials. Small 2:209–215
172. Yoon T-J, Kim JS, Kim BG, Yu KN, Cho M-H, Lee J-K (2005) Multifunctional nanoparticles possessing a "magnetic motor effect" for drug or gene delivery. Angew Chem Int Ed 44:1068–1071

Chapter 3
Bimagnetic Core/Shell Nanoparticles: Current Status and Future Possibilities

Tiago M. Freire, Wesley S. Galvão, Rafael M. Freire, and P.B.A. Fechine

3.1 Introduction

Bimagnetic materials have been known since 1956, when Meiklejohn and Bean [1] reported a shifted hysteresis loop along the magnetic field axis in a thin film system containing a ferromagnetic (FM) core and antiferromagnetic (AFM) interface. Since then, bimagnetic structures have been studied widely and new phenomena were discovered (i.e., exchange-coupled magnet and exchange bias). In general, research on bimagnetic systems of thin films has been driven by (1) the possibility of an increased number of FM/AFM combinations in thin films; (2) the easy synthesis of the FM/AFM microstructure; and (3) the fundamental role of exchange bias, spin valve, and tunneling devices [2]. However, a lack of control in the growth of the AFM layer leads to a poor crystallinity and high structural disorder in the system, which results in inferior magnetic properties [3]. Therefore, the development of new bimagnetic materials with different morphologies is of interest. In this perspective, systems with a core/shell arrangement are promising since the different magnetic phases may be combined to maximize the contact interface. However, less attention has been paid to this issue owing to difficulties in the synthesization of such structures [4].

Demand for magnetic materials and advances in synthetic chemistry have motivated the fabrication of nanoparticles (NPs) with tuned and improved properties with the development of novel and promising technologies [5]. These materials have often been used in modern societies in areas such as electronics [2], optical

T.M. Freire • W.S. Galvão • R.M. Freire • P.B.A. Fechine (✉)
Departamento de Química Analítica e Físico-Química, Group of Chemistry of Advanced Materials (GQMAT), Universidade Federal do Ceará—UFC, Campus do Pic, CP 12100, Fortaleza, 60451-970, Brazil
e-mail: tiagomfreire.ufc@gmail.com; wesleygalvao28@hotmail.com; rafael.m.freire@gmail.com; pbafechine@gmail.com; fechine@ufc.br

© Springer International Publishing AG 2017

S.K. Sharma (ed.), *Complex Magnetic Nanostructures*,
DOI 10.1007/978-3-319-52087-2_3

engineering [6], catalysis [7], and biomedical engineering [8]. Recent advances in the fabrication of magnetic NPs, in particular bimagnetic core/shell NPs, have attracted considerable attention owing to the possibility of combining materials with different magnetic properties [2]. Such combinations give rise to interface interactions such as exchange coupling, exchange bias, and proximity effects [9]. Furthermore, exchange interactions between core and shell provide an extra degree of freedom to tune and improve magnetic properties [4].

The synthesis of bimagnetic materials has been performed using both chemical and physical approaches. However, in the majority of the works devoted to core/shell bimagnetic NPs, syntheses are rather focused on the use of chemical methods due to the greater control of crystallinity, phase composition, size, or shapes [5, 10]. The most common methods are coprecipitation [11], thermal decomposition [8], metal reduction [12], and partial surface oxidation [13]. Nevertheless, these methods do not allow the formation of a core/shell structure with separate control over core and shell. Recently, approaches based on seeded growth have been widely studied since it allows the formation of complex structures such as $FePt@ZnFe_2O_4$ [14], $Fe@Fe_xO_y$ (where the Fe of the shell can have different oxidation states) [15] and $CoFe_2O_4@MnFe_2O_4$ [16]. These methods enable independent control of core and shell thickness during the synthesis. As a result, considerable control over the core diameter and shell thickness is obtained with excellent crystallinity.

The synergistic combination of material characteristics has led to the formation of multifunctional NPs with original and appealing properties, which depends on the structural and morphological features [17–19]. Thus, many efforts are being made to improve the understanding of the magnetic properties of bimagnetic systems. Song et al. [16] showed that bimagnetic materials exhibited different magnetic properties compared to the chemical or physical mixture of the individual phases. Recently, Juhin et al. [20] combined different techniques to elucidate the composition, morphology, and magnetic properties of an Fe-oxide/Mn-oxide system. They observed the existence of an interdiffused intermediated layer formed by Fe diffusion to the shell and Mn diffusion to the core, creating a system of the type core@shell@shell. Furthermore, they suggested that the layer thickness of the inner shell modified the magnetic properties of the material. In 2013, Estrader et al. [21] demonstrated for the first time the existence of an interfacial AFM coupling in high-quality FM soft/hard core/shell NPs based on iron and manganese oxides; such coupling will likely lead to new results in exchange interactions as a positive exchange bias. Therefore, recent advances in core/shell bimagnetic NPs make these materials interesting for research since the Monte Carlo simulation has demonstrated the possibility of novel effects such as compensation points or proximity effects [22].

Bimagnetic materials have received much attention, mainly owing to the phenomena of exchange coupling and exchange bias that typically occur when FM or ferrimagnetic (FiM) materials are in physical contact with an AFM material and the composite is below the Curie temperature (T_C) and above the Néel temperature (T_N). Hence, when $T_N < T < T_C$, the spin interface in AFM materials tends to couple to the spins in the FM materials. Most studies on core/shell bimagnetic

NPs have applied a synthesis system composed of a transition metal into the FM core and the corresponding passivation shell, for instance, Co/CoO [1], Ni/NiO [3], and Fe/Fe_xO_y [15], or with different oxidation states, as in CrO_2/Cr_2O_3 [23] and MnO_A/MnO_B (where A and B represent the oxidation state of the Mn of the core and shell) [24]. However, this approach has some drawbacks: (1) the shell is always derived from the core, limiting control of the layer growth; (2) since the shell is formed from the surface treatment of the core materials, choices for the core/shell phases are limited; and (3) the shell forms with lower crystallinity [4].

Some researchers have also suggested bimagnetic materials mainly for biomedicine, permanent magnets, and recording media [25]. In this last case, however, there are no reports on the practical applications of bimagnetic core/shell NPs [4]. A few years ago, some basic properties, such as superparamagnetic blocking temperature (T_B), switching field (H_S), and structured self-assembled arrays of core/shell NPs or possible graded anisotropy in core/shell NPs, had already been experimentally enhanced.

The use of bimagnetic NPs as permanent magnets has emerged as an alternative to the use of materials based on rare earth elements [26]. The energy product $(BH)_{max}$ is defined as the maximum amount of magnetic energy stored in a magnet and is directly proportional to the remanence magnetization (M_r). Thus, the exchange-coupled effect can be used to adjust the M_r of a bimagnetic material, improving their magnetic properties. Leite et al. investigated a $CoFe_2O_4/CoFe_2$ system and observed that the exchange coupling between the magnetic hard and soft phases increased by approximately 115% the energy product compared with the isolated phase of $CoFe_2O_4$ [27]. Nandwana et al. studied $FePt/Fe_3O_4$ core/shell NPs in optimized conditions and found an energy product of 17.8 MGOe, which is 36% higher than the theoretical value for isotropic single-phase FePt [28]. Despite progress, the energy product of the core/shell bimagnetic system of free rare earths is still smaller than similar system contained in rare earths [4].

The use of a core/shell bimagnetic system in biomedical applications is still limited, but some researchers have already demonstrated the potential use of these materials in magnetic resonance imaging (MRI) [29] and hyperthermia [8]. Yoon et al. [14] synthesized $Fe@MFe_2O_4$ (M = Mn, Fe and Co) core/shell NPs and demonstrated that a bimagnetic system exhibited better transverse relaxivity (r_2) values than their single phases.

3.2 Magnetic and Structural Properties

The huge interest in the miniaturization of devices has motivated the development of new materials in nanometric dimensions. This has led to new opportunities in the field of nanomagnetism, exploring new magnetic properties such as exchange bias, exchange coupling, and proximity effects. The understanding of these properties is extremely important for further progress in various technological applications such as high-density magnetic storage media, permanent magnets, and read heads.

In this context, bimagnetic materials have been widely studied. Here we present an overview of the main magnetic phenomena along with the main structure of bimagnetic materials.

3.2.1 Proximity Effect

The proximity effect generally occurs when two or more systems having different functionalities and long-range orderings are in atomic contact with each other. It is quite natural to imagine that in the interface of this system a novel magnetic arrangement will appear that will give rise to new phenomena and properties [30]. The terminology of the proximity effect emerged in the 1960s [31]. However, it is important to highlight a theoretical study published by Zuckermann in 1953 [32]. He demonstrated the possibility of FM material to induce magnetization in paramagnetic (PM) materials owing to the proximity effect. Moreover, this study predicted that the magnetic ordering temperature of the PM component would rise by increasing the thickness of the FM layer. In fact, Zuckermann et al. demonstrated that the component with a higher ordering temperature could enhance the magnetic ordering temperature of the other component [33]. The proximity effect has also been observed in systems with different interfaces, such as FM/FM, PM/AFM, FiM/FM, and FM/DMS (diluted magnetic semiconductor) [9].

The proximity effect can also be analyzed in different systems from the observation of different effects such as (1) the enhancement in T_N of AFM materials, (2) variation of the coercivity of an FM/AFM system far above the T_N of the AFM phases, (3) changes in the T_C for FM materials in an AFM/FM system, (4) the displacement of the T_B, and (5) the reorientation of the transition temperature in FM/AFM systems [33, 34]. In systems containing three layers, modifications in their magnetic properties owing to the proximity effect are also observed. Among these modifications can be mentioned an enhancement of the perpendicular magnetic anisotropy of FM/AFM bilayer systems by incorporation of an ultrathin FM underlayer and by the existence of the exchange bias effect in FM/PM/AFM through a relativity thick PM layer [35, 36]. Hence, there exists a wide range of combinations of magnetic materials that present the proximity effect, and research in this area is promising in terms of technological innovation. This will occurs mainly in media recording, biomedical, and spintronic areas owing to the appearance of effects such as exchange coupling and exchange bias.

3.2.2 Exchange Coupling

The magnetic properties of FM or FiM materials can be understood from key parameters such as the coercive field (H_C), saturation magnetization (M_S), and M_r, which are obtained from the magnetization loop (Fig. 3.1). Materials that saturate

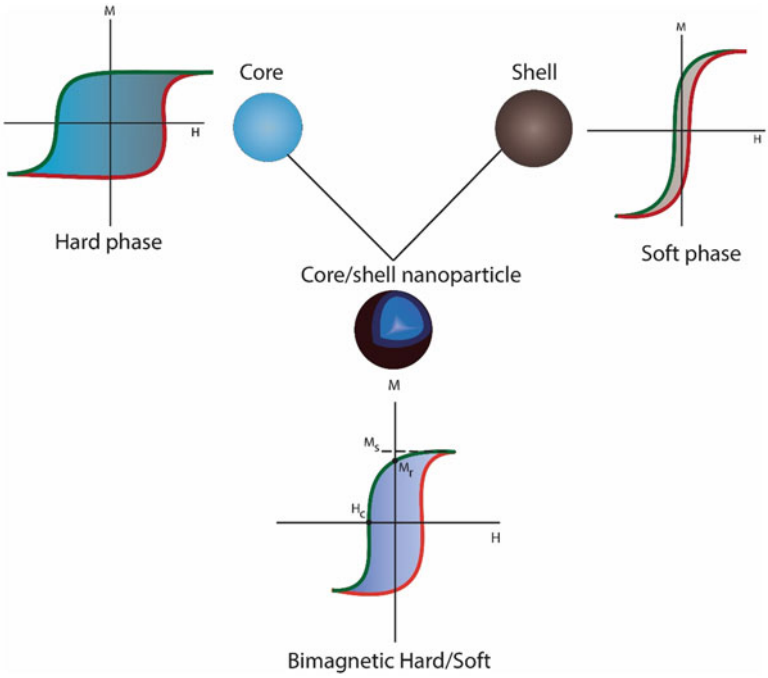

Fig. 3.1 Exchange coupling between soft and hard magnetic phases

by application of a weak magnetic field have a narrow hysteresis loop with a small H_C. These materials are classified as soft magnets. By contrast, hard magnets are saturated in a strong magnetic field and have a wide hysteresis loop with large H_C. The exchange coupling effect between hard and soft phases can be considered as being a synergistic effect that rushes between the two phases. This effect may improve some magnetic properties such as H_C and M_S. Figure 3.1 shows an example of an exchange-coupled hard-soft phase.

The exchange coupling effect has been widely demonstrated in core/shell NPs by various research groups [21, 26, 37]. However, most studied were carried out on thin films [38]. The use of advanced approaches, such as ΔM plots, has demonstrated that an increase in the hard–soft contact area from the heterodimer morphology to the core/shell structure significantly increases the influence of the hard–soft exchange-coupled effect about the magnetic properties of the systems [28]. Xu et al. reported that the key parameter in achieving effective exchange coupling is to control the size of the hard and soft phases at the nanoscale [37]. This occurs because the size control of the phases makes it possible that the magnetization direction in both rotate coherently [39]. Hence, recent advances in chemical synthesis have produced materials with strong exchange coupling from the control of the core size and thickness [40]. Additionally, exchange coupling has been proposed as an efficient tool to tune the magnetic properties of nanosystems for various applications [39].

3.2.3 Exchange Bias

The exchange bias effect was first studied by Meiklejonh and Bean in 1956 [1]. They described this effect as a magnetic coupling phenomenon that occurs in the interphase between the FM and AFM phases. This description was related to the Co/CoO system. The main indications of the exchange bias effect in the system are (1) a shifted hysteresis loop with positive or negative H_C values, along the field axis after being field cooled (FC) from above the T_N; (2) a gradual decrease in the exchange bias field (H_{ex}) with increases in the number of loop cycles in a cyclic hysteresis loop study; and (3) an increase in the coercivity in a FC hysteresis compared to the corresponding zero field cooled (ZFC) hysteresis curve. Moreover, other features of exchange bias are the presence of unidirectional anisotropies, asymmetric reversal of a hysteresis loop, and a vertical shift of the FC hysteresis loop along the magnetization axis [9]. Figure 3.2 describes some evidence for the exchange bias effect.

The exchange bias phenomenon is generally observed in systems with FM/AFM interfaces. This phenomenon may also be visualized in other types of interface, such as FM/spin glass [41], FM/FiM [42], FiM/AFM [24], AFM/DMS [43]. Systems containing FM/AFM interfaces have been widely studied starting with the paradigm established by Meiklejonh and Bean [44]. Because exchange bias is a function of the system interface, a satisfactory quantitative and qualitative understanding is difficult owing to the low volume of the interface [45]. However, various theoretical models, such as those by Stoner-Wohlfarth, Meiklejonh and Bean, and Mauri, random fields have been proposed to explain exchange bias effects [46]. All these models consider a thin film structure composed of FM/AFM interfaces. Iglesias et al. in 2008 proposed a model to explain the exchange bias effect for NPs having a core/shell structure and comprising FM/AFM interfaces [47]. This model considered a spin inside a sphere of radius R, localized in the lattice nodes. Inside the sphere are different regions, the FM core, AFM shell, and core/shell interfaces formed by core spin nearest to the shell and shell spin nearest to the core. This model takes into account microscopic parameters such as anisotropy and exchange effects based in the Heisenberg classical spin model $\overrightarrow{S_i}$, interacting according to the following microscopic Hamiltonian (Eq. 3.1):

$$\frac{H}{K_B} = -J_C \sum_{(i,j)\in C} \overrightarrow{S_i} \bullet \overrightarrow{S_j} - J_S \sum_{(i,j)\in Sh} \overrightarrow{S_i} \bullet \overrightarrow{S_j} - J_{int} \sum_{(i\in C, j\in Sh)} \overrightarrow{S_i} \bullet \overrightarrow{S_j}$$

$$- K_C \sum_{(i\in C)\in Sh} \left(S_i^z\right)^2 - K_S \sum_{(i\in Sh)} \left(S_i^z\right)^2 - \sum_{i=1}^{N} \overrightarrow{h} \bullet \overrightarrow{S_i} \tag{3.1}$$

In this equation, the first three terms describe the exchange interaction in different regions of the core/shell interface of the particle. The fourth and fifth terms correspond to the on-site uniaxial anisotropy from the core and shell. The last term

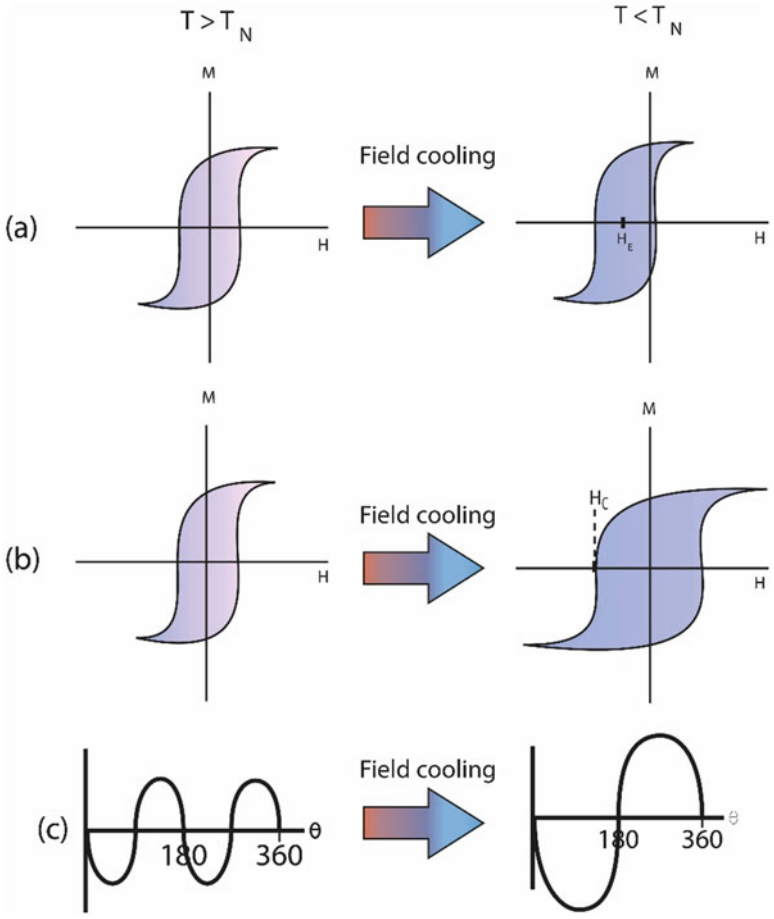

Fig. 3.2 Main indications of the existence of an exchange bias effect in FM/AFM system: (**a**) loop shift, (**b**) coercivity enhancement, (**c**) unidirectional anisotropy

is the Zeeman energy coupling to an external magnetic field. Thus, from this model, which takes into account a spherical particle with core@shell structure, being composed by core FM, shell AFM and a FM-AFM interface, Fig. 3.3 illustrates the origin of the hysteresis loop in an offset core/shell NP phenomenon.

Initially, it was considered that the core/shell structure had an interface shared between the FM and AFM phases and the T_C of the FM was greater than the T_N of the AFM phase ($T_C > T_N$). Then, first the magnetization loop was built from the application of an external magnetic field at temperature T such that $T_C > T > T_N$. In this condition, after the magnetic saturation of the material, the spins from the FM phase would be aligned along the magnetic field direction, while the spins from the AFM phase, which are in the paramagnetic state, will remain random (Fig. 3.3a). At this point, without reversing the direction of the magnetic field, the FM/AFM

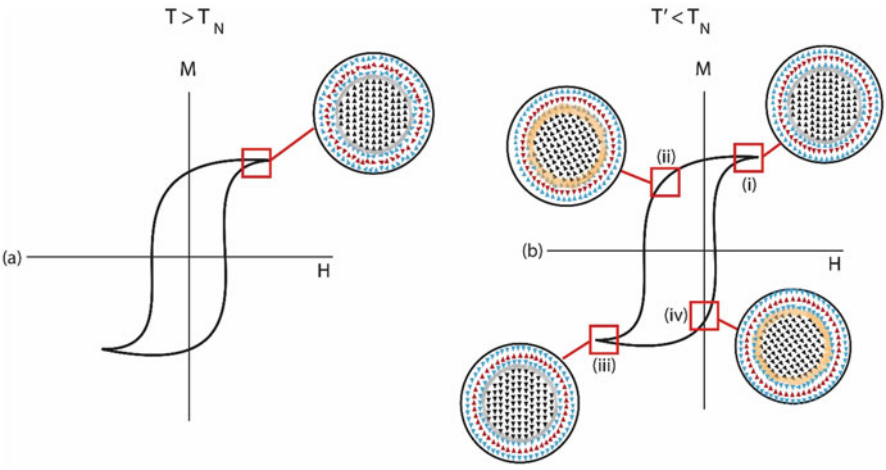

Fig. 3.3 Schematic drawing showing spin configuration of FM/AFM system: (**a**) with T above T_N of AFM shell; (**b**) when system is cooled, temperature T' such that $T' < T_N$ of AFM shell

system is cooled to T' such that $T' < T_N$. After field cooling, the shell changes from the paramagnetic to the antiferromagnetic state. Moreover, the first layer of the AFM phase will align parallel or antiparallel to the FM spins owing to an interaction that occurs at the interface (Fig. 3.3bi). Reverting the direction of the magnetic field will cause the FM spins try to align in the direction of the field. However, if the AFM anisotropy is large enough, the spins in the AFM phase will remain fixed (Fig. 3.3bii). Consequently, owing to the interface coupling, more Zeeman energy would be required to rotate the FM spins, resulting in an increase in the H_C (left side in the magnetization loop). When all FM spins are reversed, a negative M_S is expected (Fig. 3.3biii). When the magnetic field reverts back to positive values, the FM spins require less Zeeman energy to return to their initial configuration (Fig. 3.3biv). Stages (ii) and (iv) may be summarized by saying that in stage (iii) the shell exerts a torque on the FM spins in an unfavorable direction of the applied magnetic field, while in stage (iv), the torque is favorable to the field. Because of this effect, a shift is observed in the FC hysteresis loop along the magnetic field axis.

3.3 Chemically Modified Surfaces

Surface modification is one of the most common methods for the synthesis of bimagnetic NPs [2, 4]. It is known that many transition metals in their oxidized stage are AFM, such as FeO, NiO, and CoO, while the same metals in their metallic or nonoxidized form are FM (e.g., Fe, Ni, and Co) [2]. In this sense, chemical surface modification consists in promoting the formation of core/shell

phases from the oxidation of a transition metal, forming combinations, such as Fe/Fe_3O_4, Ni/NiO, Co/CoO, and so on. Two metals in different oxidation states can also form bimagnetic NPs, like Fe_3O_4/FeO or $FeAl/FeAl_2O_4$ [2]. Despite the simplicity of this method, there are some drawbacks, as it is not possible to form core/shell structures with different metal combinations, because of the fact that the shell is obtained from the oxidation of the core. In this way, there are no large combinations of FM/AFM materials. In addition, it is not simple to control the shell thickness and obtain a core/shell with precise structures [2]. There are few studies about the effect of changing the parameters in chemical surface treatments. However, many authors have reported on the relation between the core sizes and the obtained values of H_{ex} and H_C. Lavorato et al. [5] showed that the core in core/shell NPs occupies approximately 12% of the total NP volume. Thus, the system presents magnetic properties with strong dependence on the magnetic nature of the core. The core/shell properties are very different compared to single-phase particles of similar volume in AFM/FiM systems [5]. However, when the core diameter is very large (more than the critical single-domain radius), the changes in the loop shift become roughly independent of the core. Marianna Vasilakaki et al. studied the behavior of exchange bias in doubly inverted AFM core/hard FiM shell NPs in different core sizes [48]. The results showed that H_C and H_{ex} depend on core sizes in different ways. In very small cores, H_{ex} is a contribution from the uncompensated spin surface. In moderate core sizes, the uncompensated spins of the core and shell also contribute to H_{ex}. For large core sizes, the value of H_{ex} increases with increases in the core and shell thickness.

Core/shell NPs can be divided roughly into two categories: organic and inorganic. In this section, we will focus on the synthesis of inorganic materials belonging to a subclass of metal-based materials. The broad class of metal-based core/shell NPs can, in turn, be subdivided into three different parts: metallic NPs, metal salts, and metal oxides. In general, the first class (metallic NPs) can be synthesized from a reduction reaction of their metal salts using reducing agents (e.g., $NaBH_4$, hydrazines) or via transmetallation using the intrinsic redox properties of the metal precursors. The second class (metal salts) uses the precipitation reactions of metal salt precursors and counterions in the presence of stabilizer/capping agents.

Metal oxide NPs have been synthesized by sol-gel, coprecipitation, or thermal decomposition methods [49]. Lastly, metal oxides are generally obtained by the sol-gel method. This section will present some established methodologies for the synthesis of core/shell nanocomposites with a focus on the metal salt class.

3.3.1 Thermal Decomposition

Thermal decomposition is probably the most common method used to grow a shell [4]. This method involves the thermal decomposition of organometallic compounds such as M(acetylacetonate), M(oleate), or M(carbonyl), where M is a metal element in the presence of surfactants and organic solvents having high

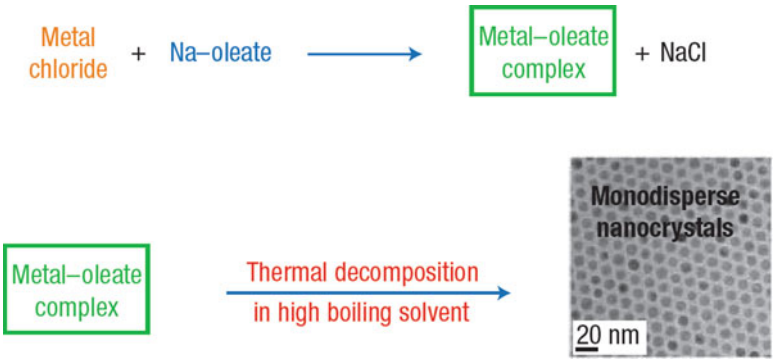

Fig. 3.4 Overall scheme for ultra-large-scale synthesis of monodisperse nanocrystals [53]. Reproduced with permission from [53] . Copyright 2004 Nature Publishing Group

boiling points [50–53] (Fig. 3.4). The main advantage of using an organic complex is the lower temperature required for decomposition (250 °C) compared to a carbonyl complex (500 °C) [54].

The control of the nucleation process and crystal growth are crucial to control the size and shape. These parameters exert a significant influence on the magnetic properties of core/shell structures [54]. In this sense, thermal decomposition is an excellent alternative to control the size and shape from the suitable choice of temperature and metal precursors [51].

Thermal decomposition is generally used for the synthesis of transition metal oxides from a chemical treatment of the core surface. The presence of a vacant d-orbital in the valence orbital of a metal allows for the formation of metal complexes through the formation of a secondary bond between the metal and electron-donating ligands. In general, the methodology consists in the stabilization of metal salts with surfactant solutions. Afterwards, the solution is mixed with an organic compound to form an organometallic complex. Lastly, the organometallic complex is decomposed to form a metal or metal oxides depending on the type of vapor used in the procedures [54]. After removal of stabilizing agent from the core, the surface atoms are oxidized into the corresponding metal oxide by atmospheric oxidation and storage in organic solvent to avoid oxidation. As an example, cobalt from a dicobalt octacarbonyl complex, ($Co_2(CO)_8$), is decomposed into Co metal at 500 °C in an argon atmosphere. Then the surface layers of the cobalt are oxidized to form a cobalt oxide Co/CoO core/shell [55].

Many research groups have studied inverted AFM/FiM core/shell systems, and FeO/Fe_3O_4 has been the most thoroughly investigated [26, 56, 57]. Błażej Leszczyński et al. studied the influence of the oxidation process on FeO/Fe_3O_4 core/shell NPs over a few weeks. The NPs synthesized were stored at atmospheric conditions, and the paramagnetic FeO was oxidized into FiM Fe_3O_4. The synthesis procedure was carried out as described by Park et al. [53], according to a general scheme (Fig. 3.4). In summary, sodium oleate was added on vigorous stirring to a

solution of hexane, ethanol, and water to complete solubilization. Then iron salts were added to form an iron oleate complex. Finally, the iron oleate was added to a three-neck flask containing trioctylamine (TOA) and 1 mL oleic acid (OA) solutions. The solution was gently stirred and initially heated to 200 °C (2 °C/min). Thereafter, it was heated to 310 °C (3 °C/min) for 30 min and quickly cooled. The precipitate formed was washed, sonicated, centrifuged, and stored for further use. The magnetic loops, combined with transmission electron microscopy (TEM) and X-ray diffraction (XRD), showed the presence of paramagnetic FeO as core and ferromagnetic Fe_3O_4 as shell. The authors concluded that the oxidation of FeO caused disordering of the AFM phase and the appearance of additional defects.

In general, the $Fe_xO|Fe_3O_4$ system has been presented as an alternative for storage devices. However, the low magnetic anisotropy of the ferromagnetic layer has presented a difficulty for the use of this system as a permanent magnet [26]. This limitation can be overcome by the doping of spinel ferrite by cobalt ions. In this connection, E. Lottini et al. [26] investigated the exchange bias properties in a family of $Co_xFe_{1-x}O|Co_xFe_{3-x}O_4$ AFM/FiM core|shell NPs by one-pot thermal decomposition of $(Co^{2+}Fe^{3+})$-oleate, following a procedure slightly modified from Park et al. [53]. In the synthesis procedure, salts of iron and cobalt were dissolved in ethanol and hexane solution and heated in refluxing condition for 4 h. Subsequently, metal-complex ($(Co^{2+}Fe^{3+})$-oleate) and oleic acid were dissolved in 1-octadecene and docosane in a three-neck round-bottom flask. The mixture was heated until it reached the decomposition temperature at a rate of 3 °C/min. To control the particle size, four different decomposition temperatures were chosen (300, 315, 335, and 350 °C) and progressively larger average sizes were obtained. The core/shell architecture was formed from the oxidized core leading to the formation of highly monodisperse, single inverted AFM/FiM core/shell NPs with variable AFM-core and constant FiM-shell thickness. Strong magnetic exchange-coupled core-shell magnets were obtained by a doping process, and the observed results are of interest for the realization of novel rare earth–free permanent magnets.

3.3.2 Seed-Mediated Growth

Methods promoting chemical surface modification by oxidation of the core are limited in relation to the possible combination of core/shell structures, as described previously. Recently, bimagnetic NPs consisting of two different metal combinations of core and shell were synthesized by a seed growth methodology. This technique consists in promoting thermal decomposition at high temperatures of the metal complex on previously prepared particles (seeds). Walid Baaziz et al. synthesized $Fe_{3-\delta}O_4$@CoO core/shell NPs in a two-step process [58]. In typical thermal decomposition synthesis, a two-neck round-bottom flask was charged with $Fe(stearate)_2$, oleic acid, and octyl ether, used as solvent. The mixture was sonicated and stirred at 120 °C to the formation of a clean solution. Then the solution was heated at a rate of 5 °C/min at approximately 287 °C for 120 min. The solution

containing Fe_3O_4 (seeds) was cooled at 100 °°C. The second step consisted of growing a layer of CoO on the Fe_3O_4 ferrite. The amount of Co (stearate)$_2$ dissolved in octadecene was added to the previous solution and heated again to reflux for 3 h under argon (heating rate of 1 °C/min). After cooling to room temperature, the Fe_3O_4@CoO precipitates were washed, centrifuged, and suspended in chloroform. The high quality of the core/shell interface resulted in a large exchange bias between the FiM and AFM components. In addition, the prepared core/shell structure showed an enhancement of the magnetocrystalline anisotropy and an increase in the blocking temperature in comparison to the bare single-phase sample.

Thermal decomposition is a very useful technique for synthesizing core/shell NPs and has great versatility in terms of possible combinations. However, the method is expensive and has other disadvantages, such as its use of toxic organic solvents as carbonyls, as well as its complexity.

3.3.3 Coprecipitation

Coprecipitation is one of the oldest methods of synthesizing magnetic NPs [59]. The method promotes the formation of the material owing to the reaction of precipitation of the salts in aqueous solution using a base as precipitant agent and can be used to form a new layer on the NPs [50]. This technique has been mainly used in the synthesis of bimagnetic (core/shell) NPs from the treatment of NP surfaces. Yelenich et al. [60] synthesized $Fe_{3-x}O_4/CoFe_2O_4$ core/shell by coprecipitation. In that work, previously prepared Fe_3O_4 was used as the core upon which precipitation will occur. Initially, $Co(NO_3)_2{\cdot}6H_2O$ and $FeCl_3{\cdot}9H_2O$ were dissolved in diethylene glycol (DEG), and the solution was stirred for 10–20 min to homogenization. Argon atmosphere was used to avoid iron oxidation. Then the alkaline solution of NaOH was added to the mixture to form hydroxide species (M-OH). After 2 h of stirring, $Fe_{3-x}O_4$ NPs in DEG were added to the reaction medium and the system was heated to 200–220 °C (90 min). Unlike magnetite (Fe_3O_4), the cobalt ferrite phase does not crystallize at room temperature, requiring an increase in temperature to that at which M-OH converts into oxides (M-O) through the replacement of hydroxide bridge oxygen linkages. In this way, the increase in temperature will cause the precipitation of cobalt NP on the Fe_3O_4 surface to form an $Fe_{3-x}O_4/CoFe_2O_4$ core/shell. It is important to mention that this method can be used to increase the number of shells owing to the new precipitation on the previous shell.

Guangdong Zhou et al. [61] synthesized core/shell Fe_2O_3/Ni_2O_3 at room temperature by co-precipitation. The core/shell NPs presented an excellently typical bipolar resistance switching memory effects. The core/shell structures were embedded in a high-k HfSiO matrix for device fabrication with a metal–insulator–metal (MIM) structure. Initially, three different solutions were prepared: I–HCl (12 mol/L, 4 L) in $Ni(NO_2)_2$ (0.1 mol/L, 10 mL); II–30 mL of 1 mol/L $FeCl_3$; and III–400 mL of 0.7 mol/L NaOH. Then solutions II and III were poured into solution I, forming a mixture that was then heated to boil for 10 min. The brown precipitate formed from

the reaction was washed with deionized water to obtain $FeOOH/Ni(OH)_2$. Finally, the γ-Fe_2O_3/Ni_2O_3 was fabricated from heating $FeOOH/Ni(OH)_2$ in 0.1 mol/L $FeCl_2$ solution for 30 min.

Many recent studies have shown a series of experimental conditions that might influence morphologic and magnetic properties during the coprecipitation [50, 62–64]. In this sense, the particle size and morphology of NPs may by tailored through the control of the synthesis parameter, such as concentration of precipitant agent, salt concentration, and pH [62]. It was demonstrated that base concentration may act in the nucleation process, causing an increase in particle size and M_S and have a large effect on the purity of the obtained product [63]. In addition, the types of base have a significant effect on synthesis. It is observed that no magnetic species are formed when strong alkalis, such as KOH and NaOH, are used [50]. By contrast, other authors have demonstrated the use of ammonium hydroxide in a pH range of 8.8 to 10 does not form nonmagnetic species [64]. The effect of temperature is one of the most common reaction parameters used to control the kinetics of NP formation. In general, the working temperature range depends on the reaction mechanisms of core/shell formations. In this regard, a low temperature is preferred for coprecipitations, while high temperatures are needed during thermal decomposition to promote the calcination of precursors [54]. Coprecipitation is an easy and inexpensive technique, but the major drawback is that the particle size must be controlled, so it has the tendency to form polydisperse products [50]. In addition, a wide particle size distribution results in a wide range of T_B, making it unsuitable for many magnetic applications.

3.3.4 Hydrothermal and Solvothermal

Hydrothermal and solvothermal methods may be a good choice to synthesize transition-metal oxide or ferrite NPs. The differences between the two methods depend on the type of solvent. In the hydrothermal method, water is used as solvent, while in the solvothermal method, an organic solvent, for example, methanol, ethanol, ethylene glycol, or glycerol, is used [65]. In both methodologies, the reagents are dissolved in a suitable solvent and the mixture is exposed in a reactor to heat (Fig. 3.5). Sattar et al. synthesized $CoFe_2O_4/NiFe_2O_4$ core/shell NPs with good thermal stability using the hydrothermal method [66]. In this work, a previously synthesized $CoFe_2O_4$ surface was modified using sodium citrate. Then the surface-modified $CoFe_2O_4$ was redispersed in a mixture of $Ni(NO_3)_2$ and $Fe(NO_3)_2$ to form a $NiFe_2O_4$ layer on the core surface. The mixture remained under vigorous stirring while the pH was adjusted to 12. The solution was mixed together in a flask and stirred for 1 h. Finally, the obtained product was filtered and washed with water several times until the pH of the solution reached 7. It was observed that the thermal stability of the magnetic properties of the single phase was enhanced using a shell of $NiFe_2O_4$ as a shell. Further, the different thickness of the $NiFe_2O_4$ shell may be of interest for adjusting the magnetic parameter for the desired applications.

Fig. 3.5 Hydro-/solvothermal synthesis reactor. (**a**) Teflon-lined stainless steel cap; (**b**) closed reactor

3.3.5 Sputtering Gas Condensations

The sputtering technique consists in the bombardment of a target by particles (gas ions or atoms) with high kinetic energy [67]. The objective is to promote the erosion of the material during plasma bombardment. The erosion occurs when the energy of the particles in the plasma is higher than the surface binding energy of the material [67]. This process is known as sputtering. Many magnetic core/shell nanostructures formed by FiM cores surrounded by an AFM shell have attracted much attention owing to their potential use in several applications, such as ultra-high-density recording and biomedical applications [54]. Skumryev et al. synthesized cobalt NPs by gas condensation of sputtered atoms in a so-called cluster gun [68] incorporated inside a conventional sputtering apparatus [25]. In this work, the authors promoted the incorporation of cobalt NPs either in a matrix (C or Al_2O_3) or in an AFM matrix (CoO). The oxygen was incorporated inside the sputtering chamber to promote the oxidation of the particles, resulting in a Co@CoO core/shell structure. The continuous deposition of a layer of material of thickness 15–20 nm followed by a layer of NPs for ten repetitions resulted in the growth of the particle size. Kołtunowicz et al. produced $CoFeZr@Al_2O_3$ core/shell granular films with thicknesses of 1 μm^3 by sputtering. The authors applied a comparative analysis of the composite and the core. This type of nanocomposite has been widely studied due to its frequent application in inductors, generators, sensors, and transformers. Figure 3.6 presents a TEM image of the nanocomposite.

It has been established that g-factor extracted from the FMR spectra of films with core/shell NPs decreases with x below a value of $g = 2.0023$ for free electrons that is atypical for metallic NPs. This effect is associated with the formation of an interface between the FM core and AFM (FiM) oxide shell of NPs. According to the authors, the results obtained from the experiments demonstrate the reduction of the g-factor showing the formation of a core/shell interface.

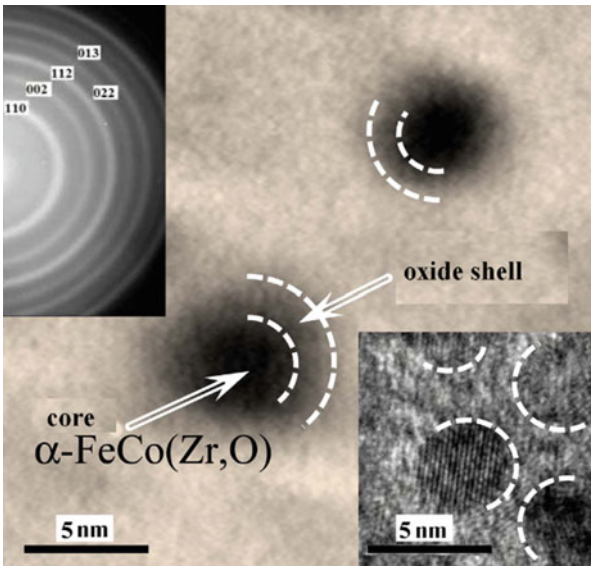

Fig. 3.6 Bright-field TEM image taken from $(FeCoZr)_{36}(Al_2O_3)_{64}$ film illustrating a core/shell structure of NPs. The *insets* show a selected area of electron diffraction (*top*) and a high-resolution TEM image (*bottom*) of the film. Reproduced with permission from [69]. Copyright 2017, with permission from Elsevier

3.4 Characterization

The core/shell architecture is probably a difficult type of nanoscale structure to build up. In this sense, characterizations must be performed to display the structural, morphologic, and magnetic properties of the core and shell. In general the most important experimental tools used to characterize core/shell NPs are dynamic light scattering (DLS), scanning electron microscopy (SEM), TEM, thermal gravimetric analysis (TGA), X-ray photoelectron spectroscopy (XPS), photoluminescence (PL), and UV-vis spectroscopy [70]. For bimagnetic NPs, the same techniques can be utilized, but magnetic measurements must be performed. Furthermore, XRD needs to be performed to elucidate the crystalline structure of the core and shell. Obviously, the requirements of the characterization techniques used relate to the desired application. For instance, biomedical applications require a surface functionalization. Consequently, XPS or infrared (IR) spectroscopy must be used to investigate functional groups on the surface of the shell. Therefore, one must carefully choose the characterization technique to obtain the most complete information about the structure, morphology, and magnetic properties of synthesized core/shell NPs.

3.4.1 X-Ray Diffraction

XRD is one of the most important characterization tools to determine the crystalline structure of inorganic NPs. This technique is frequently used to perform the identification of the crystalline phase structures such as ferrites [71], for example,

by utilizing the International Center for Diffraction Data (ICDD) catalog. Beyond this, some structural parameters, such as crystallite size, can also be obtained. In this regard, it is important to mention that one should carefully proceed to calculate these parameters. For instance, the average crystallite size (L) is given by the well-known Scherrer equation (Eq. 3.2) [72]:

$$L = \frac{K\lambda}{\beta \cos\theta} \tag{3.2}$$

where K is the shape coefficient for the reciprocal lattice point, λ the wavelength of the incident radiation, β the full width at half-maximum of the peak, and θ the Bragg angle. K is a coefficient normally taken as 0.9 [73, 74] and L the first approximation to estimate NP size. However, it is important to highlight that the β value in Eq. 3.2 needs to be corrected since this parameter can be affected by instrumental and microstrain (ε) contributions [75, 76]. If this correction is not performed, the β value will be found to be higher than the actual value and, consequently, the L value will display a negative error, i.e., the NP size will be found to be smaller than the real one. Therefore, the correction can provide a more accurate L value and the correlation with other characterization techniques may be used to estimate more accurately the particle size. Given this, a correction is often performed using the Rietveld method [77]. Moreover, one can also find other structural parameters, for example, density and the lattice parameter. It is well known that the Rietveld procedure is precise in evaluating the crystalline structure, although the ε contribution for β cannot be removed using this method. In this situation, another way to calculate L taking into account ε is through the Williamson–Hall equation, which can be written as follows:

$$\frac{\beta}{\lambda}\cos\theta = \frac{K}{L} + \frac{4\varepsilon}{\lambda}\sin\theta \tag{3.3}$$

Using Eq. 3.3, the L value will be much more accurate. In addition, the construction of a Williamson–Hall plot ($\frac{\beta}{\lambda}\cos\theta$ versus $\sin\theta$) allows for the identification of lattice expansion or compression. More information to calculate the NPs size can be found in a very helpful tutorial letter published by Gonçalves et al. [72].

For bimagnetic core/shell NPs, mainly XRD has been used to identify crystalline phases. Troitiño et al. [78] have studied the exchange bias effect in hybrid CoO@Fe_3O_4 core/shell octahedron-shaped NPs. They used XRD measurements to identify the CoO phase before and after the Fe_3O_4 coating. The XRD pattern before the coating presented in Fig. 3.7 clearly displayed diffraction peak characteristics of the face-centered cubic lattice related to the CoO phase. After the coating process, the XRD pattern remained almost the same, except for small angles, where a low-intensity peak related to the Fe_3O_4 was observed. Therefore, no significant difference could be seen between core and shell, which may be explained by the thin layer on the surface of the core and a slight mismatch between the CoO and Fe_3O_4 phases. In another study, Juhin et al. [20] present direct evidence for an interdiffused

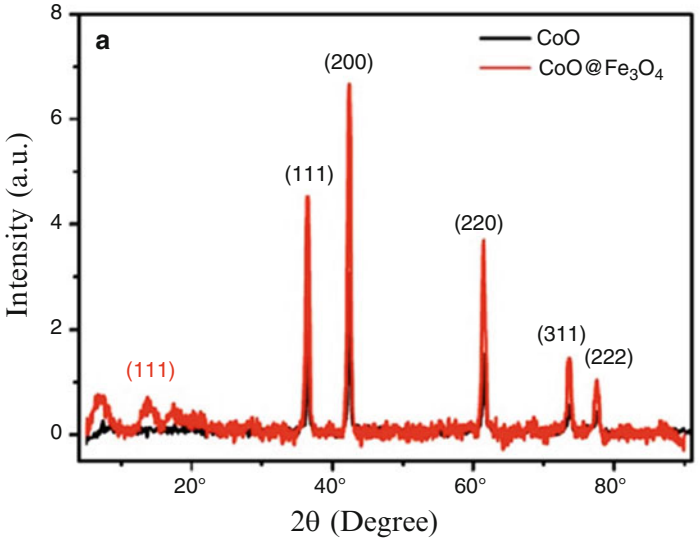

Fig. 3.7 XRD patterns of CoO core before (*black*) and after (*red*) coating with Fe_3O_4. Reproduced with permission from [78]. Copyright 2014 American Chemical Society

intermediate layer in bimagnetic core/shell NPs. They studied a multilayer γ-Fe_2O_3 (5.0 nm)/$(Fe,Mn)_3O_4$ (1.1 nm)/Mn_3O_4 (0.3 nm) structure. The XRD pattern of this onionlike structure displayed diffraction peaks related to the cubic spinel phase, which could be attributed to the γ-Fe_2O_3 or Fe_3O_4. Once these two crystals have the same structure, only XRD cannot be used to differentiate between them. Therefore, additional techniques, such as Raman spectroscopy, must be used. The phase Mn_3O_4 was also observed in the XRD pattern. Unlike the study performed by Troitiño et al. [78], Juhin et al. were able to differentiate between core and shell by [20].

The Rietveld method based on the XRD data was also used to characterize the bimagnetic core/shell NPs. The use of this powerful tool to extract structural parameters can be observed in the work published by Lavorato et al. [79]. In this work, the size effect in bimagnetic CoO/CoFe2O4 core/shell NPs was studied. First, the crystalline phases were identified. Thus, diffraction peaks attributed to the CoO and $CoFe_2O_4$ were clearly observed. However, the XRD pattern was dominated by diffraction peaks from the CoO core phase. Then the authors carried out Rietveld refinements [80] to obtain the NPs' size. They found the CoO core to be in the range 2–6 nm, while the $CoFe_2O_4$ shell was observed to range from 4.5 to 45 nm for all the synthesized samples. A TEM study was also performed in their work. The NP size found through XRD was larger than the values achieved using TEM images. To understand this mismatch, it is important to mention the XRD results were used to estimate the crystallite volume of the core/shell NPs, while the TEM, a more powerful technique, can be used to obtain information about the shell thickness.

In addition, the TEM images also showed that the $CoFe_2O_4$ crystallites increased in size with a preferential orientation over the CoO phase. Therefore, this could also account for the larger values of the NP size obtained through XRD.

3.4.2 TEM

TEM is a powerful tool to observe the morphology, shape, and size of core/shell NPs. Furthermore, owing to the difference in electron scattering from the core and shell, this technique can also be useful in distinguishing between them and to determine the size of the core as well as thickness of the shell. Thus, in recent decades, the TEM technique has been largely applied in the determination of bimagnetic core/shell structures [4, 20, 21, 66, 81–84]. For example, Zeng et al. investigated the modification of the dimension of the core/shell structure of $FePt@Fe_3O_4$ systems by controlling the $Fe(acac)_3$/FePt ratio. In this work, TEM images were used to distinguish the core and shell and to determine the NP size and shell thickness. However, this differentiation of the core from the shell is only possible where there is a large difference in the atomic composition between core and shell. For core/shell NPs where there is no large difference in the atomic composition of core and shell, TEM use is limited.

To fully exploit the TEM technique, other modalities of imaging were developed as HRTEM, bright-field TEM (BFTEM), dark-field TEM (DFTEM), scanning TEM (STEM), and energy-filtrated TEM (EFTEM). From the images obtained with these modalities, it is possible to distinguish core from shell even in samples with low contrast [85]. HRTEM and BFTEM images make it possible to observe the lattice interlayer spacing of the samples. This allows for correlating this technique with XRD. DFTEM modalities, such as high-angle annular dark field (HAADF), are especially of interest for discerning core from shell since the image is predominantly obtained using Rutherford scattered electrons, which is most susceptible to the difference in atomic number, Z [86]. Moreover, STEM can use both to create dark-field images with contrast ratios proportional to the Z and, hence, may provide detailed information on the composition of the nanoparticles, from the use of energy dispersive spectroscopy (EDS) and electron energy loss spectroscopy (EELS), to better visualize the extent of the shell [86]. Thus, TEM can be considered one of the most important techniques of in NP core/shell characterization since it makes it possible to obtain a huge volume of information about the structure of core/shell NPs [86]. This technique is widely applied in academic research and in industry. Figure 3.8 shows several TEM micrographs obtained from different modalities.

Actually, the correlation of TEM with other characterization techniques has shown evidence of the existence of a layer between the core and the shell [83]. Recently, Estrader et al. managed to resolve the core/shell structure of γ-$Fe_2O_3@Mn_3O_4$ using different TEM images and EELS [21]. They observed the formation of NPs, irregular in shape, that is often assigned to a discontinuous growth of the shell. Subsequently, Juhin et al. studied the same system as Estrader et al. and

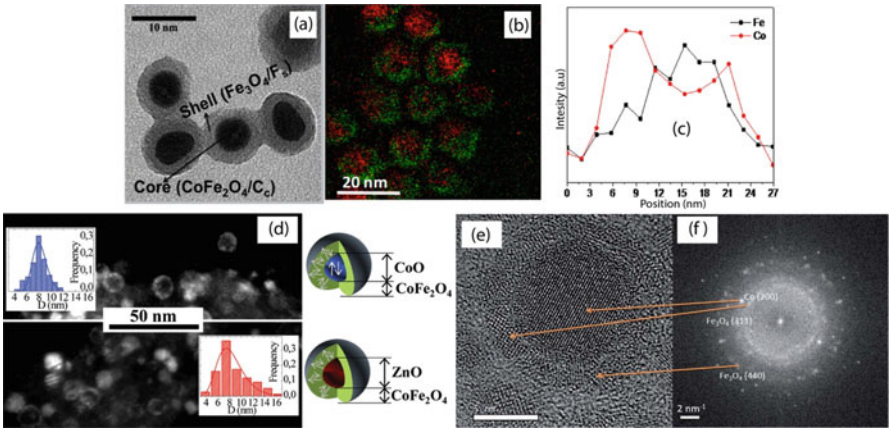

Fig. 3.8 TEM micrographics obtained from different modalities: (**a**) TEM image core/shell with spherical morphology [87] (Reprinted with permission from [87]. Copyright 2016 with permission from Elsevier); (**b**, **c**) EFTEM image showing distribution of Fe (*red*) and Co (*green*) along NP $Fe_{3-\delta}O_4$@CoO [84] (Reprinted with permission from [84]. Copyright (2015) American Chemical Society); (**d**) DFTEM micrographs of two different systems CoO/$CoFe_2O_4$ (*upper panel*) and ZnO/$CoFe_2O_4$ (*bottom panel*) [5] [Reprinted with permission from [5]. Copyright (2015) American Chemical Society]; (**e**, **f**) HRTEM and BFTEM image obtained from core and shell, respectively [86]. [Reprinted with permission from [86]. Copyright (2013) Royal Society of Chemistry]

observed the existence of an intermediate layer between core and shell [20]. This result was obtained using different TEM images and EELS. However, it is important to highlight the correlation between TEM results and other characterization techniques such as FC/ZFC magnetization versus temperature curves, first-order reversal curve (FORC) diagrams and RIXD–MCD for a better understanding of the interface phenomenon. Thus, it is important to correlate the results obtained by TEM with those of the other techniques. Specifically, for bimagnetic core/shell NPs, the correlation between TEM images and magnetic measurements can provide information essential for understanding the magnetic properties.

3.4.3 Magnetic Measurements

Magnetic hysteresis curves in FC mode are generally used to characterize exchange coupling between core/shell magnetic phases. This can be performed using commercial magnetometers such as a vibrating sample magnetometer or superconducting quantum interference device (SQUID). In this technique, the sample is placed under sinusoidal motion that occurs between suitably sensing coils [88]. In the presence of an external magnetic field, the spins of electrons from the samples aligned themselves to create their own magnetic field that is opposed to the external

magnetic applied. The resulting magnetic flux change induces a voltage in the sensing coils that is proportional to the magnetic moment of the sample. As the external magnetic field increases, the intensity also increases the number of electrons aligned until reaching the maximum value, denoted M_S.

Based on the obtained hysteresis curves, it is possible to classify magnetic material into two classes: soft or hard. Soft materials can be readily saturated in a weak magnetic field and are classified by their large permeability and lower H_C (>1 Oe). On the other hand, hard materials require a large H_C (<10 Oe) to bring the net magnetization back to zero [39]. Recently, a mixture between soft/hard magnetic structures was found from the synthesis of bimagnetic core/shell NPs. In this case, the hysteresis loop can also provide information about the exchange interaction at the interface between FM and AFM core/shell phases. Sattar et al. obtained the magnetic curves of bimagnetic $CoFe_2O_4/NiFe_2O_4$ core/shell NPs as a mixture of isolated characteristics of both compounds. This coupling between interfaces provides a hysteresis loop that behaves as a single magnetic compound without the kind of unusual drops, kinks, or shoulders that often form from the simple superposed loops of soft and hard phases.

The exchange coupling between the core/shell transition phases can also be visualized by low-temperature experiments. In this case, the coupling is observed as the shift in the hysteresis curve after the cooling of the sample in a region above T_N of the AFM phase and below the T_C (in the case of the FM phase) in materials composed of FM–AFM interfaces [89]. This procedure refers to the conventional exchange bias, when T_N is much lower than T_C. This occurs, when the size of the soft phase (D) is reduced to approximately twice the domain wall width of the hard phase, according to Eq. 3.4:

$$D \leq 2\delta = 2\pi \sqrt{\frac{A}{K_H}}, \tag{3.4}$$

where δ is the domain wall width of the hard phase [39]. In this case, the decrease of the limit size of the soft phase for exchange coupling occurs at a certain temperature when the constant of anisotropy (K_H) is large enough to give 2δ, which is smaller than the size of the soft phase, leading to a two-step magnetization reversal behavior [39].

Magnetic interactions between phases can also be described using the δM method (Henkel plot). In this methodology, the behavior of the interaction is defined as $\delta M = M_d - (1 - 2M_r)$, where M_d is the reduced direct current demagnetization remanence and M_r the reduced isothermal remanence magnetization. Initially, a field is applied to promote the complete inversion of spins and then turn off. Then a minimum field is applied and turned off to obtain the M_r of the sample. The process is repeated many times, obtaining a series of values of M_r while slightly increasing the reverse magnetic field to obtain M_s in the reverse direction. Positive values of δM found in this procedure indicate the presence of exchange coupling between bimagnetic phases [90].

In recent years, many studies have been conducted for exchange-coupled nanomagnets containing high uniaxial magnetocrystalline anisotropy (K) materials, with

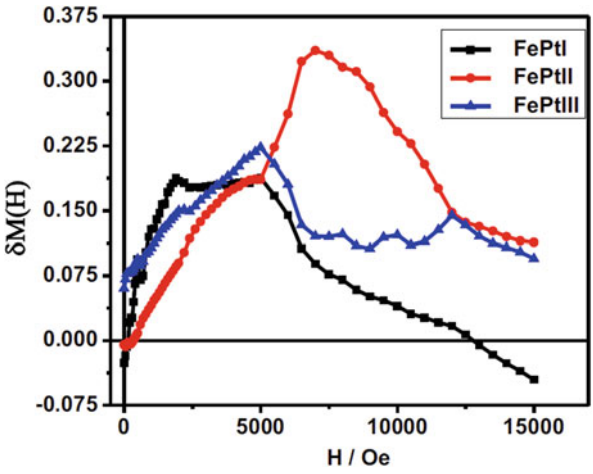

Fig. 3.9 Henkel plots of (**a**) FePtI, (**b**) FePtII, and (**c**) FePtIII . Reprinted with permission from [90]. Copyright 2016 with permission from Elsevier

ordered phase (face-centered tetragonal, $L1_0$). Alloys of $L1_0$-FePt are chemically ordered and show high values of K and H_C and can be used in high-density magnetic memory applications. Sachchidanand et al. synthesized $L1_0$-FePt/f_{cc}-FePt exchange-coupled nanomagnets and used Henkel plots to confirm the exchange coupling between ordered and disordered phases of three samples of FePt (Fig. 3.9) [90].

In this work, Pt–Fe_3O_4 was converted into $L1_0$-FePt/f_{cc}-FePt exchange-coupled nanocomposites by solid-state reductive annealing using 4% H_2 at 700 °C for 2 h (FePtI), 4 h (FePtII), and 6 h (FePtIII), respectively, with positive values for δM. The positive values of δM indicate a dominant exchange interaction between hard–hard and hard–soft phases. In addition, the lowest percentage of $L1_0$ phases and negative values found for FePtI indicates a range of independent magnetization reversal among hard phases that is a result of weak intergranular exchange coupling among hard grains. Thus, the positive values for δM indicate a strong interaction between hard–hard and hard–soft phases in the core/shell structure and cooperative switching between magnetic spins, which results in the highest strength of exchange coupling. The data obtained from the Rietveld refinement of XRD shows a volume fraction of 0.89 for the FePtII hard phase.

The formation of FM/AFM interfaces can also provide an extra source of anisotropy in very small NPs to increase the so-called superparamagnetic limit (SL) [91, 92]. By decreasing the NP size, the total K energy of the particle becomes comparable with the thermal energy [92]. In this case, the thermal fluctuations promote random flipping of the magnetic moment with time, and the NPs become superparamagnetic (nonmagnetic) [91, 92]. The SL has been challenged by the storage industry, which seeks to miniaturize hard drives. With the decrease in the size of devices, the magnetic "bits" become thermally unstable [92]. The exchange coupling between core/shell phases can delay or extend this SL. The FM/AFM interactions between phases promote so-called exchange bias (Fig. 3.10).

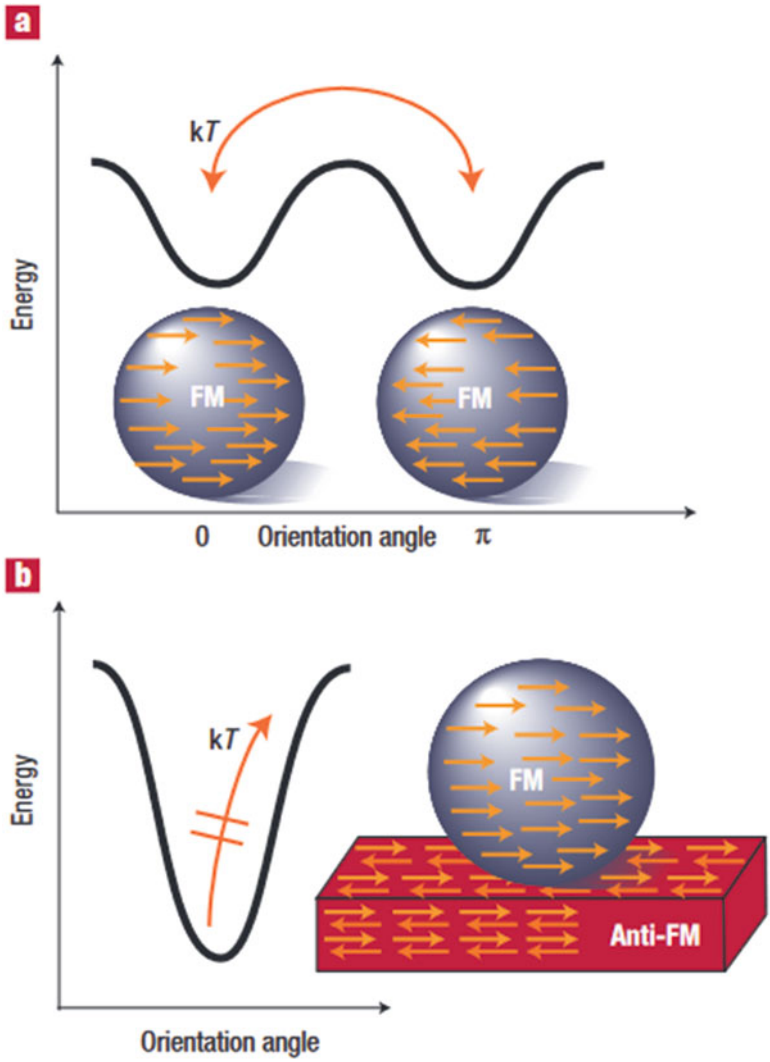

Fig. 3.10 Exchange bias in small magnetic structures [53]. Reproduced with permission from [53]. Copyright 2003 Nature Publishing Group

In the case of exchange bias, the hysteresis loop is shifted and is no longer focused at the zero field. As a result, H_C increases. In other words, the increase in the external field is necessary to exchange electron spins, promoting an additional magnetic anisotropy to align the FM moments in a certain direction (Fig. 3.10b) [92]. Skumryev et al. synthesized Co@CoO FM–AFM structures and promoted the incorporation of cobalt NPs in a matrix (C or Al_2O_3) via sputtering gas condensation [25]. They found the T_B to be around 10 K to the cobalt inserted in an Al_2O_3 matrix.

On the other hand, the Co@CoO FM–AFM reached a T_B of approximately 290 K. According to the authors, this enhancement of stability was due to the contribution of the AFM phase of CoO. The ZFC–FC curves and the shift in the hysteresis loops showed that an extra anisotropy was induced, and thus, the NPs remained magnetically stable, increasing the SL for the sample.

The characterization of core/shell structures is critical because it is necessary to combine both techniques to characterize both the core and the shell. Thus, depending on the characteristics of the bilayer system, a unique technique may not be sufficient. The major techniques for the characterization of the core/shell structures are those that help in the measurement of size, shell thickness, elemental and surface analysis, and thermal stability, among others. In this sense, TEM, XRD, and magnetic measurements represent principal techniques for core/shell characterization.

3.5 Applications

Magnetic NPs are among the most important classes of nanoscale structures to be used in many technological applications in fields like biomedicine [93, 94] and magnetic energy storage [95]. In addition, advances in synthetic chemistry allowing for control of the self-assembly of nanostructures became a formidable tool for building new nanostructures. In this regard, it is important to highlight bimagnetic core/shell NPs since interactions between magnetic nanostructures utilized as building blocks may give rise to coupling properties such as exchange bias [1, 96] or proximity effect [9]. The bimagnetic core/shell architecture has been used for over five decades. This magnetic nanoscale model emerged as early as 1961, when Falk and Hooper published a research paper on elongated iron-cobalt: ferrite particles to develop permanent magnets [97]. Since then, advancements have occurred and the applicability of this bimagnetic core/shell system has grown exponentially. For instance, permanent magnets [98], microwave absorption [12], and hyperthermia [39] are among the applications where improvements have been observed in recent years.

3.5.1 Hyperthermia

Inorganic NPs are widely known as a great tool in biomedicine [99]. The nanoscale holds great advantage over the traditional treatment of diseases, considering that the size of particles in the 10^{-9} m range improve selectivity by targeting specific locations in the body. As a consequence, the concentration of drugs used to heal patients can decrease, which makes diminishes the side effects [100]. If NPs have magnetic properties, selectivity can be improved thanks to the effect of the external magnetic field. It is possible to control NPs inside the body through external

manipulation. Therefore, all improvements mentioned earlier can be enhanced using nanoscale systems [101]. Besides all these improvements in the biomedical field provided by the nanoscale and magnetism, bimagnetic core/shell systems can retain all those properties, bringing out new properties provided by the exchange interaction between two magnetically ordered phases. According to the literature [102], core/shell NPs can contribute to improving magnetic hyperthermia compared to single-phase magnetic NPs when exposed to an oscillating magnetic field. This is explained by the great capacity to generate heat. However, to understand this, the reader first needs to understand the heat generation mechanism using magnetic NPs. In this sense, the first process involves hysteresis losses. Thermal energy can be measured by integrating the area of hysteresis loops when magnetic NPs have been exposed to an external oscillating magnetic field. As a result, heat is generated during the magnetization reversal cycle. This mechanism is primarily important for multidomain NPs. On the other hand, Néel and Brown relaxation processes are essential for single-domain NPs. Once these kinds of NPs have no hystereses in their magnetization reversal cycles, hysteresis losses cannot be treated as a mechanism to generate heat. For Néel relaxation, a quick directional change in the spins in a crystal lattice is observed, while the NPs do not rotate. Mathematically, the time of this relaxation process (τ_N) in this case can be calculated using Eq. 3.5 [103]:

$$\tau_N = \tau_0 e^{KV/K_B T}, \tag{3.5}$$

where τ_0 is approximately 10^{-9} s [104], K the anisotrophy constant, V the volume of the NPs, K_B the Boltzmann constant, and T the temperature. Unlike the relaxation process described, Brownian relaxation is related to NPs physical movements, while the spins remain stopped in the crystal lattice. The Brownian relaxation time (τ_B) can be described by Eq. 3.6 [105]:

$$\tau_B = \frac{3V_{hyd}}{K_B T}\eta, \tag{3.6}$$

where V_{hyd} is the hydrodynamic NP size and η is the viscosity. It is important to mention that Eqs. 3.5 and 3.6 are used to describe and classify pure Néel or Brownian relaxation times in a zero field, respectively. In these relaxation processes, heat generation is related to the reorientation of the spins and entire NPs, respectively. Frequently, both relaxation times may contribute to the generation of heat in single-domain NPs. In this case, an effective relaxation time (τ_{eff}), a combination of Néel and Brownian relaxation times, needs to be calculated. In this connection, τ_{eff} is given by Eq. 3.7:

$$\tau_{eff} = \frac{\tau_B \tau_N}{\tau_B + \tau_N}. \tag{3.7}$$

Finally, the third way to generate heat is the viscous losses. At first glance, the reader may think of this mechanism as being a consequence of Brownian relaxation. However, the literature has demonstrated viscous losses by exposing large magnetic NPs to a rotating external magnetic field [106]. Given all the mechanisms mentioned earlier, the literature reports a general formula to quantify induced heat (P) in multidomain NPs using Eq. 3.8 [107]:

$$P = \mu_0 \pi \chi'' f H_{\text{apply}}^2, \tag{3.8}$$

where μ_0 is the vacuum permeability, χ" the AC magnetic susceptibility (imaginary part), and f and H_{apply} the frequency and strength of the applied AC magnetic field, respectively. Specifically, for single-domain NPs, the most frequently NPs used in biomedical applications, the literature also reports an equation to describe heat generation considering only Néel and Brownian relaxation times. In this case, P can be calculated through the following relationship (Eq. 3.9) [108]:

$$P = \frac{(mH\omega\tau_{\text{eff}})^2}{\left[2\tau_{\text{eff}} K_{\text{B}} T \rho V \left(1 + \omega^2 \tau_{\text{eff}}^2\right)\right]}, \tag{3.9}$$

where m is the magnet moment of NPs, ω is the field angular frequency, and ρ is the density. From the preceding equations, it is clear that in experiments, characteristics of magnetic NPs, such as size, must be controlled in order to adjust the heat generation. Additionally, the literature reports the specific absorption rate (SAR), which is also known as specific loss power (SLP), as a parameter used to evaluate magnetic NPs for hyperthermia treatment [109]. In this sense, higher values are desired because the amount of magnetic materials used in heat generation can be reduced. The SAR can be estimated in terms of heat capacity (C), NP mass (m_{NPs}), time (t), and T using Eq. 3.10:

$$\text{SAR} = \frac{\Delta T}{\Delta t} \cdot \frac{C}{m_{\text{NPs}}}. \tag{3.10}$$

It is important to mention that the SAR calculated using Eq. 3.10 is limited since heat generation will change for the same magnetic fluid containing NPs by changing f and H_{apply}. This is very clear looking at Eq. 3.9, where P can be estimated. Therefore, it is plausible to assume that the SARis of an extrinsic nature (equipment-dependent), and its value does not express the full potential of magnetic NPs [110].

Regarding bimagnetic core/shell NPs, some researchers have already evaluated the use of iron-cobalt/ferrite core/shell NPs for cancer thermotherapy [111]. In this research, Habib et al. demonstrated that heating generation power could be improved by tuning the magnetic anisotropy through composition or shape variations. Moreover, the authors predicted an SLP value of 450 W/g for Fe-Co/$CoFe_2O_4$ core/shell NPs, which demonstrated their feasibility for use in biomedical applications. Recently, Lee et al. [8] attracted a lot of attention with their recent work. The authors synthesized 15 nm $CoFe_2O_4$@$MnFe_2O_4$ NPs and performed

an investigation into its ability to generate heat. By taking advantage of the exchange-coupling interaction between two magnetically ordered phases, they were able to control the magnitude of effective magnetic anisotropy and maximize the specific loss power. To perform a comparison with $CoFe_2O_4$@$MnFe_2O_4$ NPs, 9 nm $CoFe_2O_4$, 15 nm $MnFe_2O_4$, and 9, 12, and 15 nm Fe_3O_4 were synthesized and their heat generation powers were investigated. The SLP values found for these single-phase magnetic NPs were in a range from 100 to 450 W/g. On the other hand, 15 nm $CoFe_2O_4$@$MnFe_2O_4$ NPs presented an SLP value of 1710 W/g, which is approximately four times higher than the largest value (414 W/g) for $CoFe_2O_4$. It is important to highlight all these SLP values. They were obtained using f and H_{apply} of 500 kHz and 37.3 kA/m, respectively. Clearly, this demonstrates the advantageous use of core/shell NPs to adjust heat generation power. To check the performance of hard–soft core/shell obtained NPs, an antitumor study was conducted on mice (Fig. 3.11). It was found that the tumor was eliminated after 18 days for a group of mice receiving hyperthermia treatment. In vivo experiments with Feridex and doxorubicin were also performed, but the bimagnetic core/shell structure was found to be more efficient. A few patents for hyperthermia can also be found in the literature [112, 113]. In these patents, the inventors synthesized bimagnetic core/shell structures and compared the heat generation to conventional magnetic NPs such as the cited commercial product named Feridex [112] and Fe_3O_4 [113]. In both cases, the studies demonstrated the advantageous utilization of a nanoscale structure for hyperthermia treatment.

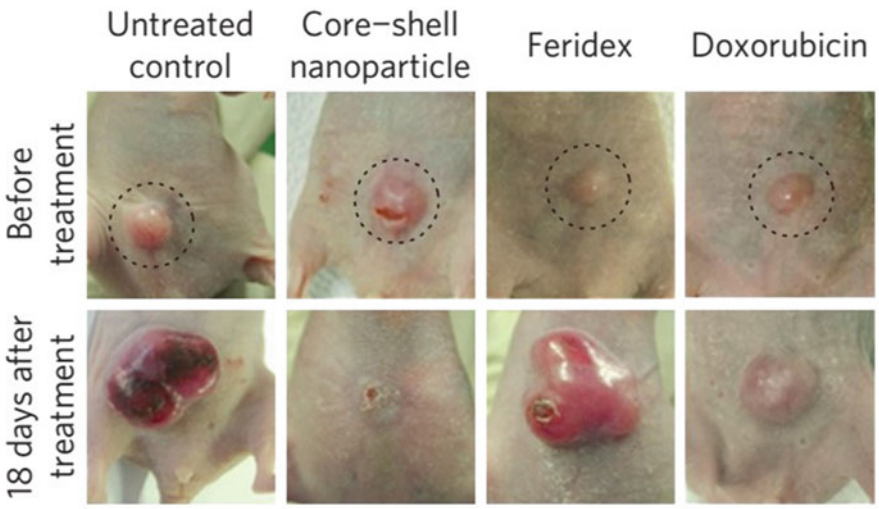

Fig. 3.11 In vivo results. U87MG cancer cells in nude mice before treatment (*upper row*, *dotted circle*) and 18 days after treatment. For comparison, untreated control, $CoFe_2O_4$@$MnFe_2O_4$ hyperthermia, Feridex hyperthermia, and doxorubicin were used. The same amounts (75 mg) of NPs and doxorubicin were injected into the tumor. Reproduced with permission from [8]. Copyright 2011 Nature Publishing Group

The most research involving bimagnetic core/shell NPs for biomedical applications are done in connection with hyperthermia. This may be explained by the recent interest of the scientific community in these kinds of nanoscale structures [4]. Major advances have been made in hyperthermia treatment, but the real potential of the core/shell architecture in the biomedical field remains unknown. Since their applicability in MRI and drug delivery was demonstrated, for example, they have not been fully exploited.

3.5.2 Permanent Magnets

In recent years, permanent magnets have been used in a broad range of technological devices, including motors, separators, speakers, cell phones, and household appliances [114]. Because of their observed versatility, demand for magnetic materials, in particular in connection with their ability to deliver a magnetic flux to air gaps with no energy cost, surged over the course of the twentieth century. This has led to a search for new materials, as well as improvements in known materials [98]. Traditionally, research on permanent magnets has focused on rare earth–based materials owing to their large anisotropy values [115, 116]. However, the price of such materials rose because of the growing demand for permanent magnets in conditions of limited supplies of rare-earth elements [117]. Therefore, researchers have focused on discovering alternative materials instead of developing high-performance rare earth–based permanent magnets. Here, it is important to highlight bimagnetic core/shell NPs since self-assembly between hard and soft magnetically ordered phases seems very promising (compared to conventional single-phase materials) owing to the combination of permanent magnetic field and magnetization [118, 119]. These materials can be rare earth–free, which reduces the cost of the final product. The procedure to synthesize bimagnetic core/shell NPs is fast and provides great control over the crystalline phase used as the building block of self-assembly systems. Taken together, these factors are more than enough to make these systems more attractive. However, this will be true only if the H_C and BH_{max} are found to have values comparable to those found in rare earth element–based magnets [120]. To evaluate this situation, H_C can be given by Eq. 3.11:

$$H_C = \frac{2K}{\mu_0 M_S}\alpha, \tag{3.11}$$

where K and α are both constants related to the uniaxial anisotropy (as mentioned) and microstructure, respectively [119]. Similarly, BH_{max} can be estimated using Eq. 3.12 or 3.13:

$$BH_{max} = \frac{1}{4}\mu_0 M_S^2 \tag{3.12}$$

or

$$BH_{\max} = \frac{1}{2}\mu_0 M_S H_C. \tag{3.13}$$

Equation 3.12 is valid for$H_C > \frac{1}{2}M_S$, while Eq. 3.13 can be used for $H_C < \frac{1}{2}M_S$. Interestingly, M_S is important for both equations, but for rare earth–free permanent magnets Eq. 3.13 should be used to calculate $BH_{\max}$. Therefore, it is easy to understand why research in permanent magnets has focused on rare earth–based materials in recent decades. Once rare earth elements have higher H_C values, the $BH_{\max}$ will also be large. However, it is important to highlight that large M_S values tend to suppress H_C. In this sense, research must show how to play with these parameters to design a great rare earth–free permanent magnet with $BH_{\max}$ as high as possible. To control this, the exchange bias needs to be controlled. In this sense, the modulation of this parameter was demonstrated by Sun et al. [121] in core/shell FeO/Fe_3O_4 NPs. For the first time, the exchange bias parameter was investigated as a function of the dimension of the AFM core and FiM shell. In this research, monodisperse 35 nm FeO NPs were initially synthesized via reductive decomposition at 300 °C. The different 6.5, 8.5, and 9.4 nm Fe_3O_4 shell thicknesses were obtained through a controlled oxidation process using dry air at 25, 60, and 100 °C. The authors controlled the exchange bias values as well as the magnitude of the coercive field as long as the size of these building block changed. Both these parameters were found to be smaller with oxidation. This can be explained by the reduction in the AFM/FiM interface area and AFM core anisotropy energy. Studying the same nanoscale structure, Khurshid et al. [57] successfully synthesized quasi-octopod-shaped core/shell FeO/Fe_3O_4 NPs. A strong exchange bias effect was observed. This parameter was calculated using Eq. 3.14:

$$H_{ex} = \frac{\left|H_C^+ + H_C^-\right|}{2}, \tag{3.14}$$

where H^+ and H^- denote the coercive field of the ascending and descending curves in the magnetization reversal cycle, respectively. H_{ex} denotes the exchange bias parameter, and the value found for the quasi-octopod-shaped core/shell FeO/Fe_3O_4 NPs was approximately 1900 Oe. When this parameter is H_C-dependent and H_C is controlled, this work can provide a better understanding of how to precisely adjust H_C to obtain a good value for $BH_{\max}$. Moreover, a classical Meiklejonh–Bean model was used to explain the results. As far as the authors know, the frozen spins located at the core/shell interface seemed to play a key role in the exchange bias effect. Besides the size of the core/shell architecture or frozen spins, another way to control the exchange bias is by using the cooling and resonance field. This was successfully demonstrated by Estrader et al. [21]. Interestingly, they presented for the first time an AFM coupling in a core/shell structure compound by FiM phases (Fe_3O_4–Mn_3O_4). This novel coupling was found to be independent of the core/shell size or morphology, which is totally different behavior than that observed

by Khurshid et al. [57]. The control of the exchange bias found by Estrader et al. [21] was easily made based on the cooling and resonance field. For instance, H_{ex} values were found to change sign for large cooling fields, which means the loops shift to the opposite direction. On the other hand, H_C values were weakly affected by the cooling field. Thus, this parameter is mainly governed by the intrinsic properties of the counterparts rather than the AFM character of the coupling. The easy control over the observed coupling properties can be a powerful tool in developing a rare earth–free permanent magnet.

Cobalt-based NPs have been frequently used in bimagnetic core/shell NPs for permanent magnet development purposes [4, 39]. Recently, López-Ortega et al. [122] have emphasized $Co_xFe_{3-x}O_4$ materials as being among the most promising building blocks to develop rare earth–free permanent magnets. The authors mention some reasons for this, such as their large H_C values, high stability, and easy/cheap synthesis. These characteristics make $Co_xFe_{3-x}O_4$ materials very attractive. In this regard, Lottini et al. [26] prepared a cobalt ferrite–based structure with high magnetic anisotropy. They synthesized bimagnetic core/shell NPs of composition $Co_{0.3}Fe_{0.7}O|Co_{0.6}Fe_{2.4}O_4$ and investigated their magnetic properties as well as their capability to store energy. In their research, the phases used to build up the core/shell NPs gave rise to an H_{ex} value of 8.6 kOe for 9 nm synthesized core/shell NPs. This result was attributed to the high crystallinity of the phases as well as the high K values of the AFM counterpart. Moreover, it was also plausible to assume a high quality of the interface with the FiM shell. Furthermore, the large observed H_{ex} value further suggests an enhanced H_C, which can be easily inferred from Eqs. 3.11 and 3.14. According to the authors, 8.6 kOe is the largest H_{ex} value ever reported for a core/shell architecture. Therefore, the results found in this research suggested an improvement in energy storage capability, which demonstrated that the core/shell structure synthesized could serve as an efficient rare earth–free permanent magnet. Because the interest in the rare earth–free permanent magnets is recent, advances obtained using a core/shell architecture must be considered with respect to the development of rare earth–free permanent magnet alternatives.

3.5.3 Other Applications

The use of magnetic NPs has been investigated over decades by researchers worldwide [123]. For example, their applicability in the biomedical field is well known [124–128]. However, the same cannot be observed of bimagnetic core/shell architecture. Besides the applications already mentioned, this complex nanoscale structure may serve as a powerful platform for drug delivery and MRI, for example. In this regard, Liu et al. [29] prepared a PEGylated $FePt@Fe_2O_3$ core/shell NPs and investigated their potential use for MRI and drug delivery. To selectively target and kill cancerous cells, folic acid and doxorubicin (DOX) were used to modify

the bimagnetic core/shell system, respectively. The authors discovered that the nanoscale system obtained had great potential as a multifunctional drug carrier. The folate-modified nanoscale system could effectively target cancerous cells. A great tumor contrast was observed in an animal study, for example. A patent involving bimagnetic core/shell NPs for MRI images [129] was recently filed. In this study, the authors used a hard ($CoFe_2O_4$)–soft ($ZnFe_2O_4$ or $MnFe_2O_4$) core/shell architecture to improve the contrast image based on the T_2 relaxation time. In the biomedical field, cell manipulation is also an application to be considered since magnetic control over cells could be used for tissue engineering [130], for example. A patent in this application was also recently filed [131]. Unlike the patent mentioned for MRI, this case involves the use of soft–hard core shell NPs. By doing a proper surface modification, the nanoscale system could specifically attach different cells. Therefore, the use of an external magnetic field provided an easy and cheap way to control the cells.

Another interesting application for bimagnetic core/shell NPs is in magnetic recording data. In this connection, it is important to mention that the use of these complex systems for magnetic recording purposes is not new. As early as 1966 Falk [132] had already studied a magnetic tape containing γ-Fe_2O_3 and $CoFe_2O_4$ in a soft/hard structure as a potential material for conventional recording media. As a consequence, surprising advances have been seen in in storage data, along with cost reductions, in recent decades [133], although this evolutionary trend will not last forever given that definite physical limits exist. The literature mentions the trilemma of magnetic recording [134], which involves problems with thermal decay, writeability, and signal-to-noise ratio (SNR) (Fig. 3.12). The first problem is directly related to the barrier energy, which is given by KV. Once the NP size decreases, the value for barrier energy also decreases, becoming comparable to K_BT (thermal energy). If $KV < K_BT$, the spin can change from one equilibrium direction to another. This would cause the loss of data being magnetically recorded. The most likely way to resolve the thermal decay issue would be to work with high K value–based materials like $CoFe_2O_4$, for example. However, the K value cannot be too high because the writeability should decrease since the magnetic fields required to perform a magnetic recording would far exceed the capabilities of current write heads [4]. This relates to the second problem of the trilemma. Finally, the third

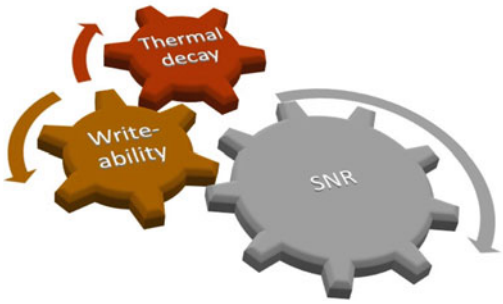

Fig. 3.12 The trilemma of magnetic recording field: thermal decay, write ability, and SNR

problem is usually related to an insufficient SNR. It is well known that high values for this parameter can be obtained when the recording medium has small particles approaching superparamagnetism [135–137], although this is somewhat related to the first and second problems. Therefore, researchers must know how to play with NP characteristics to obtain a great balance among the trilemma problems. In this light, Victora et al. [138] proposed an exchange-coupled medium compound by soft and hard regions for a 1 Tb/in^2 perpendicular magnetic recording. When the magnetically ordered soft phase achieves small K values, the writeability is expected to be higher. By contrast, the magnetically ordered hard phase should provide the desired thermal stability. Therefore, the combination of these two different natures can be a powerful strategy for improving even more the magnetic storage capability and makes hard–soft core/shell NPs great candidates. As a consequence, some patents involving these complex nanoscale structures for recording media can be found in the literature [139–141].

The core/shell architecture has also been used in microwave absorption. In this application, it is important to mention that humans are exposed to considerable electromagnetic "pollution" caused by the rapid growth of electronic equipment. This so-called pollution can be called electromagnetic interference, and it can affect both the functioning of electronic equipment and human health [142, 143]. To solve this pollution-related problem, the design of materials that have a strong absorption in a broad frequency range and are lightweight antioxidants has been studied. Traditionally, the materials used to construct microwave absorbers are found to be ferrites [144, 145], ferroelectric materials [146], and polymers [147], among others. However, these materials do not meet all the requirements mentioned earlier. For instance, ferrites have strong absorption, but the thickness required is too large [148]. Thus, the development of materials for microwave absorption is highly desirble. In this regard, the bimagnetic core/shell structure is worth highlighting since the dissimilar magnetic properties of the core and shell can improve the performance of microwave devices. This was clearly demonstrated by Kim et al. [149], Hennig et al. [150], and Imaoka et al. [151] in their patents.

Finally, applications of bimagnetic core/shell NPs are expected in other fields over time. For instance, Sayan et al. [152] have already studied the magnetocaloric effect of core/shell Fe/γ-Fe_2O_3. Change in the magnetic entropy was found to be an excellent parameter for the study of temperature and field-dependent magnetic freezing. This should be useful for magnetic refrigeration, for example. In this connection, it is worth mentioning that the full potential of bimagnetic core/shell NPs remains unknown, and more applications are expected in the near future.

Acknowledgments This work was partly sponsored by CAPES, CNPq, and Funcap (Brazilian agencies).

References

1. Meiklejohn WH, Bean CP (1956) New magnetic anisotropy. Phys Rev 102(5):1413–1414
2. Nogués J et al (2005) Exchange bias in nanostructures. Phys Rep 422(3):65–117
3. Rinaldi-Montes N et al (2016) Bridging exchange bias effect in NiO and Ni(core)@NiO(shell) nanoparticles. J Magn Magn Mater 400:236–241
4. López-Ortega A et al (2015) Applications of exchange coupled bi-magnetic hard/soft and soft/hard magnetic core/shell nanoparticles. Phys Rep 553:1–32
5. Lavorato GC et al (2015) Magnetic interactions and energy barrier enhancement in core/shell bimagnetic nanoparticles. J Phys Chem C 119(27):15755–15762
6. Qian H-S et al (2010) ZnO/ZnFe2O4 magnetic fluorescent bifunctional hollow nanospheres: synthesis, characterization, and their optical/magnetic properties. J Phys Chem C 114(41):17455–17459
7. Lee J et al (2009) Metal-organic framework materials as catalysts. Chem Soc Rev 38(5):1450–1459
8. Lee J-H et al (2011) Exchange-coupled magnetic nanoparticles for efficient heat induction. Nat Nanotechnol 6(7):418–422
9. Manna PK, Yusuf SM (2014) Two interface effects: exchange bias and magnetic proximity. Phys Rep 535(2):61–99
10. Hu X-W et al (2015) Starfish-shaped Co3O4/ZnFe2O4 hollow nanocomposite: synthesis, supercapacity, and magnetic properties. ACS Appl Mater Interfaces 7(18):9972–9981
11. Gomes JDA et al (2008) Synthesis of core−shell ferrite nanoparticles for ferrofluids: chemical and magnetic analysis. J Phys Chem C 112(16):6220–6227
12. Li X et al (2011) The enhanced microwave absorption property of CoFe2O4 nanoparticles coated with a Co3Fe7–Co nanoshell by thermal reduction. Nanotechnology 22(4):045707
13. Mourdikoudis S et al (2007) Effect of air xexposure on structural and magnetic features of FeCo nanoparticles. Mod Phys Lett B 21(18):1161–1168
14. Yoon T-J et al (2011) Highly magnetic core–shell nanoparticles with a unique magnetization mechanism. Angew Chem Int Ed 50(20):4663–4666
15. Somaskandan K et al (2008) Surface protected and modified iron based core-shell nanoparticles for biological applications. New J Chem 32(2):201–209
16. Song Q, Zhang ZJ (2012) Controlled synthesis and magnetic properties of bimagnetic spinel ferrite CoFe2O4 and MnFe2O4 nanocrystals with core–shell architecture. J Am Chem Soc 134(24):10182–10190
17. Casavola M et al (2009) Exchange-coupled bimagnetic cobalt/iron oxide branched nanocrystal heterostructures. Nano Lett 9(1):366–376
18. Chaubey GS et al (2008) Synthesis and characterization of bimagnetic bricklike nanoparticles. Chem Mater 20(2):475–478
19. Lima E et al (2012) Bimagnetic CoO core/CoFe2O4 shell nanoparticles: synthesis and magnetic properties. Chem Mater 24(3):512–516
20. Juhin A et al (2014) Direct evidence for an interdiffused intermediate layer in bi-magnetic core-shell nanoparticles. Nanoscale 6(20):11911–11920
21. Estrader M et al (2013) Robust antiferromagnetic coupling in hard-soft bi-magnetic core/shell nanoparticles. Nat Commun 4:2960
22. Zaim A, Kerouad M, El Amraoui Y (2009) Magnetic properties of a ferrimagnetic core/shell nanocube Ising model: a Monte Carlo simulation study. J Magn Magn Mater 321(8):1077–1083
23. Yu MH et al (2003) Towards a magnetic core–shell nanostructure: a novel composite made by a citrate–nitrate auto-ignition process. Mater Sci Eng: B 103(3):262–270
24. Salazar-Alvarez G et al (2007) Synthesis and size-dependent exchange bias in inverted core−shell MnO|Mn3O4 nanoparticles. J Am Chem Soc 129(29):9102–9108
25. Skumryev V et al (2003) Beating the superparamagnetic limit with exchange bias. Nature 423(6942):850–853

26. Lottini E et al (2016) Strongly exchange coupled core|shell nanoparticles with high magnetic anisotropy: a strategy towards rare earth-free permanent magnets. Chem Mater 28(12):4214–4222
27. Leite GCP et al (2012) Exchange coupling behavior in bimagnetic CoFe2O4/CoFe2 nanocomposite. J Magn Magn Mater 324(18):2711–2716
28. Nandwana V et al (2009) Bimagnetic nanoparticles with enhanced exchange coupling and energy products. J Appl Phys 105(1):014303
29. Liu Y et al (2013) PEGylated FePt@Fe2O3 core-shell magnetic nanoparticles: potential theranostic applications and in vivo toxicity studies. Nanomed Nanotechnol Biol Med 9(7):1077–1088
30. Manna PK et al (2011) The magnetic proximity effect in a ferrimagnetic Fe3O4 core/ferrimagnetic γ-Mn2O3 shell nanoparticle system. J Phys Condens Matter 23(50):506004
31. Hauser J, Theuerer H, Werthamer N (1966) Proximity effects between superconducting and magnetic films. Phys Rev 142(1):118
32. Zuckermann M (1973) The proximity effect for weak itinerant ferromagnets. Solid State Commun 12(7):745–747
33. Lenz K, Zander S, Kuch W (2007) Magnetic proximity effects in antiferromagnet/ferromagnet bilayers: the impact on the Néel temperature. Phys Rev Lett 98(23):237201
34. Won C et al (2005) Studies of FeMn/Co/Cu(001) films using photoemission electron microscopy and surface magneto-optic Kerr effect. Phys Rev B 71(2):024406
35. Wang B-Y et al (2013) Enhanced perpendicular magnetic anisotropy in Fe/Mn bilayers by incorporating ultrathin ferromagnetic underlayer through magnetic proximity effect. Appl Phys Lett 103(4):042407
36. Valev VK et al (2006) Direct observation of exchange bias related uncompensated spins at the CoO/Cu interface. Phys Rev Lett 96(6):067206
37. Xu X et al (2015) Exchange coupled SrFe12O19/Fe-Co core/shell particles with different shell thickness. Electron Mater Lett 11(6):1021–1027
38. Heinrich B (2008) Exchange coupling in magnetic multilayers. In: Zabel H, Bader SD (eds) Magnetic heterostructures: advances and perspectives in spinstructures and spintransport. Springer, Berlin, pp 185–250
39. Liu F, Hou Y, Gao S (2014) Exchange-coupled nanocomposites: chemical synthesis, characterization and applications. Chem Soc Rev 43(23):8098–8113
40. Lopez-Ortega A et al (2012) Strongly exchange coupled inverse ferrimagnetic soft/hard, MnxFe3-xO4/FexMn3-xO4, core/shell heterostructured nanoparticles. Nanoscale 4(16):5138–5147
41. Ali M et al (2007) Exchange bias using a spin glass. Nat Mater 6(1):70–75
42. Khurshid H et al (2014) Tuning exchange bias in Fe/γ-Fe2O3 core-shell nanoparticles: impacts of interface and surface spins. Appl Phys Lett 104(7):072407
43. Huang P-H, Huang H-H, Lai C-H (2007) Coexistence of exchange-bias fields and vertical magnetization shifts in ZnCoO/NiO system. Appl Phys Lett 90(6):062509
44. Inderhees SE et al (2008) Manipulating the magnetic structure of Co core/CoO shell nanoparticles: implications for controlling the exchange bias. Phys Rev Lett 101(11):117202
45. Radu F, Zabel H (2008) Exchange bias effect of ferro-/antiferromagnetic heterostructures. In: Radu F, Zabel H (eds) Magnetic heterostructures. Springer, Berlin, pp 97–184
46. Radu F, Zabel H (2008) Exchange bias effect of ferro-/antiferromagnetic heterostructures. In: Zabel H, Bader SD (eds) Magnetic heterostructures: advances and perspectives in spinstructures and spintransport. Springer, Berlin, pp 97–184
47. Iglesias O, Labarta A, Batlle X (2008) Exchange bias phenomenology and models of core/shell nanoparticles. J Nanosci Nanotechnol 8(6):2761–2780
48. Vasilakaki M, Trohidou KN, Nogués J (2015) Enhanced magnetic properties in antiferromagnetic-core/ferrimagnetic-shell nanoparticles. Sci Rep 5
49. Gawande MB et al (2015) Core–shell nanoparticles: synthesis and applications in catalysis and electrocatalysis. Chem Soc Rev 44(21):7540–7590

50. Galvão WS et al (2016) Super-paramagnetic nanoparticles with spinel structure: a review of synthesis and biomedical applications. Solid State Phenom 241:139–176
51. Singamaneni S et al (2011) Magnetic nanoparticles: recent advances in synthesis, self-assembly and applications. J Mater Chem 21(42):16819–16845
52. Leszczyński B et al (2016) The influence of oxidation process on exchange bias in egg-shaped FeO/Fe3O4 core/shell nanoparticles. J Magn Magn Mater 416:269–274
53. Park J et al (2004) Ultra-large-scale syntheses of monodisperse nanocrystals. Nat Mater 3(12):891–895
54. Ghosh Chaudhuri R, Paria S (2011) Core/shell nanoparticles: classes, properties, synthesis mechanisms, characterization, and applications. Chem Rev 112(4):2373–2433
55. Lee W-R et al (2005) Redox-transmetalation process as a generalized synthetic strategy for core-shell magnetic nanoparticles. J Am Chem Soc 127(46):16090–16097
56. Sun X et al (2011) Tuning exchange bias in core/shell FeO/Fe3O4 nanoparticles. Nano Lett 12(1):246–251
57. Khurshid H et al (2013) Synthesis and magnetic properties of core/shell FeO/Fe3O4 nano-octopods. J Appl Phys 113(17):17B508
58. Baaziz W et al (2013) High exchange bias in Fe3−δO4@ CoO core shell nanoparticles synthesized by a one-pot seed-mediated growth method. J Phys Chem C 117(21):11436–11443
59. Kooti M, Matturi L (2011) Microwave-assisted fabrication of γ-Fe2O3 nanoparticles from tris (acetylacetonato) iron (III). Int NanoLett 1:38–42
60. Yelenich O et al (2015) Synthesis and properties MFe2O4 (M=Fe, Co) nanoparticles and core–shell structures. Solid State Sci 46:19–26
61. Zhou G et al (2016) synthesized core–shell Fe2O3/Ni2O3 at room temperature by co-precipitation. The core/shell NPs presented an excellently typical bipolar resistance switching memory effects. J Alloys Compd 678:31–35
62. Kikuchi T et al (2011) Preparation of magnetite aqueous dispersion for magnetic fluid hyperthermia. J Magn Magn Mater 323(10):1216–1222
63. Baumgartner J et al (2013) Nucleation and growth of magnetite from solution. Nat Mater 12(4):310–314
64. Castro VF, de Queiroz AA (2011) Pontos quânticos magneto ativos: uma nova fronteira para a medicina terapêutica e diagnóstica. Rev Bras Fís Méd 4(3):15–18
65. Freire R et al (2013) MZnFe2O4 (M= Ni, Mn) cubic superparamagnetic nanoparticles obtained by hydrothermal synthesis. J Nanopart Res 15(5):1–12
66. Sattar A, El-Sayed H, ALsuqia I (2015) Structural and magnetic properties of CoFe2O4/NiFe2O4 core/shell nanocomposite prepared by the hydrothermal method. J Magn Magn Mater 395:89–96
67. Kruis FE, Fissan H, Peled A (1998) Synthesis of nanoparticles in the gas phase for electronic, optical and magnetic applications—a review. J Aerosol Sci 29(5):511–535
68. Haberland H et al (1993) Thin film growth by energetic cluster impact (ECI): comparison between experiment and molecular dynamics simulations. Mater Sci Eng: B 19(1):31–36
69. Kołtunowicz TN et al (2017) Ferromagnetic resonance spectroscopy of CoFeZr-Al2O3 granular films containing "FeCo core–oxide shell" nanoparticles. J Magn Magn Mater 421:98–102
70. Ghosh Chaudhuri R, Paria S (2012) Core/shell nanoparticles: classes, properties, synthesis mechanisms, characterization, and applications. Chem Rev 112(4):2373–2433
71. Freire RM et al (2013) $MZnFe_2O_4$ (M = Ni, Mn) cubic superparamagnetic nanoparticles obtained by hydrothermal synthesis. J Nanopart Res 15(5):1616
72. Gonçalves NS et al (2012) Size–strain study of NiO nanoparticles by X-ray powder diffraction line broadening. Mater Lett 72:36–38
73. Monshi A, Foroughi MR, Monshi MR (2012) Modified Scherrer equation to estimate more accurately nano-crystallite size using XRD. World J Nano Sci Eng 2:154–160
74. Holzwarth U, Gibson N (2011) The Scherrer equation versus the 'Debye-Scherrer equation'. Nat Nanotechnol 6(9):534

75. Ji W et al (2014) Mechanical alloying synthesis and spark plasma sintering consolidation of CoCrFeNiAl high-entropy alloy. J Alloys Compd 589:61–66
76. Weibel A et al (2005) The big problem of small particles: a comparison of methods for determination of particle size in nanocrystalline anatase powders. Chem Mater 17(9):2378–2385
77. Rietveld H (1967) Line profiles of neutron powder-diffraction peaks for structure refinement. Acta Crystallogr 22(1):151–152
78. Fontaíña Troitiño N et al (2014) Exchange bias effect in CoO@Fe3O4 core–shell octahedron-shaped nanoparticles. Chem Mater 26(19):5566–5575
79. Gabriel CL et al (2014) Size effects in bimagnetic CoO/CoFe2O4 core/shell nanoparticles. Nanotechnology 25(35):355704
80. Rodríguez-Carvajal J (1993) Recent advances in magnetic structure determination by neutron powder diffraction. Phys B: Condens Matter 192(1):55–69
81. Estradé S et al (2012) Distinguishing the core from the shell in MnOx/MnOy and FeOx/MnOx core/shell nanoparticles through quantitative electron energy loss spectroscopy (EELS) analysis. Micron 43(1):30–36
82. Nellist PD, Pennycook SJ (2000) The principles and interpretation of annular dark-field Z-contrast imaging. In: Peter WH (ed) Advances in imaging and electron physics. Elsevier, San Diego, pp 147–203
83. Krycka KL et al (2013) Resolving material-specific structures within Fe3O4|γ-Mn2O3 core|shell nanoparticles using anomalous small-angle X-ray scattering. ACS Nano 7(2):921–931
84. Liu X et al (2015) Systematic study of exchange coupling in core–shell Fe3−δO4@CoO nanoparticles. Chem Mater 27(11):4073–4081
85. Sathya A et al (2016) CoxFe3–xO4 nanocubes for theranostic applications: effect of cobalt content and particle size. Chem Mater 28(6):1769–1780
86. Knappett BR et al (2013) Characterisation of Co@Fe3O4 core@shell nanoparticles using advanced electron microscopy. Nanoscale 5(13):5765–5772
87. Khan U et al (2016) Response of iron oxide on hetero-nanostructures of soft and hard ferrites. Superlattices Microstruct 92:374–379
88. Dodrill B (1999) Magnetic media measurements with a VSM. Lake Shore Cryotronics, Westerville, p 575
89. Gao Y et al (2016) Exchange bias effect in CuCr2O4/Cr2O3 nanogranular systems. J Alloys Compd 673:126–130
90. Srivastava S, Gajbhiye NS (2016) Exchange coupled L1 0-FePt/fcc-FePt nanomagnets: synthesis, characterization and magnetic properties. J Magn Magn Mater 401:969–976
91. Chikazumi S (1997) Physics of ferromagnetism. Oxford University Press, New York, pp 482–498
92. Eisenmenger J, Schuller IK (2003) Magnetic nanostructures: overcoming thermal fluctuations. Nat Mater 2(7):437–438
93. Pankhurst QA et al (2003) Applications of magnetic nanoparticles in biomedicine. J Phys D Appl Phys 36(13):R167
94. Bao Y et al (2016) Magnetic nanoparticles: material engineering and emerging applications in lithography and biomedicine. J Mater Sci 51(1):513–553
95. Frey NA et al (2009) Magnetic nanoparticles: synthesis, functionalization, and applications in bioimaging and magnetic energy storage. Chem Soc Rev 38(9):2532–2542
96. Nogués J, Schuller IK (1999) Exchange bias. J Magn Magn Mater 192(2):203–232
97. Falk RB, Hooper GD (1961) Elongated iron-cobalt: ferrite, a new, lightweight, permanent magnet material. J Appl Phys 32(3):S190–S191
98. Balamurugan B et al (2012) Prospects for nanoparticle-based permanent magnets. Scr Mater 67(6):542–547
99. Giner-Casares JJ et al (2016) Inorganic nanoparticles for biomedicine: where materials scientists meet medical research. Mater Today 19(1):19–28
100. Arruebo M et al (2007) Magnetic nanoparticles for drug delivery. Nano Today 2(3):22–32

101. Chomoucka J et al (2010) Magnetic nanoparticles and targeted drug delivering. Pharmacol Res 62(2):144–149
102. Mamiya H (2013) Recent advances in understanding magnetic nanoparticles in AC magnetic fields and optimal design for targeted hyperthermia. J Nanomater 2013:17
103. Sharifi I, Shokrollahi H, Amiri S (2012) Ferrite-based magnetic nanofluids used in hyperthermia applications. J Magn Magn Mater 324(6):903–915
104. Knobel M et al (2008) Superparamagnetism and other magnetic features in granular materials: a review on ideal and real systems. J Nanosci Nanotechnol 8(6):2836–2857
105. Suto M et al (2009) Heat dissipation mechanism of magnetite nanoparticles in magnetic fluid hyperthermia. J Magn Magn Mater 321(10):1493–1496
106. Hergt R, Andrä W (2007) Magnetic hyperthermia and thermoablation. In: Magnetism in medicine, Wiley, New York, pp 550–570
107. Rosensweig RE (2002) Heating magnetic fluid with alternating magnetic field. J Magn Magn Mater 252:370–374
108. Kim D-H, Nikles DE, Brazel CS (2010) Synthesis and characterization of multifunctional chitosan-MnFe2O4 nanoparticles for magnetic hyperthermia and drug delivery. Materials 3(7):4051–4065
109. Wang X, Gu H, Yang Z (2005) The heating effect of magnetic fluids in an alternating magnetic field. J Magn Magn Mater 293(1):334–340
110. Kallumadil M et al (2009) Suitability of commercial colloids for magnetic hyperthermia. J Magn Magn Mater 321(10):1509–1513
111. Habib AH et al (2008) Evaluation of iron-cobalt/ferrite core-shell nanoparticles for cancer thermotherapy. J Appl Phys 103(7):07A307
112. Cheon JW, Jang JT (2011) Heat generating nanomaterials. Google patents
113. Ivkov R et al (2014) A process for making iron oxide nanoparticle preparations for cancer hyperthermia. Google patents
114. Coey JMD (2002) Permanent magnet applications. J Magn Magn Mater 248(3):441–456
115. Hirotoshi F, Hiroshi I (1992) Effect of intergrain exchange interaction on magnetic properties in isotropic Nd-Fe-B magnets. Jpn J Appl Phys 31(5R):1347
116. Kronmüller H et al (1996) Micromagnetism and microstructure of hard magnetic materials. J Phys D Appl Phys 29(9):2274
117. Shen J et al (2015) Synthesis and characterization of rare-earth-free magnetic manganese bismuth nanocrystals. RSC Adv 5(8):5567–5570
118. Zeng H et al (2002) Exchange-coupled nanocomposite magnets by nanoparticle self-assembly. Nature 420(6914):395–398
119. Skomski R, Coey JMD (1993) Giant energy product in nanostructured two-phase magnets. Phys Rev B 48(21):15812–15816
120. Imran K, Jisang H (2014) Potential rare earth free permanent magnet: interstitial boron doped FeCo. J Phys D Appl Phys 47(41):415002
121. Sun X et al (2012) Tuning exchange bias in core/shell FeO/Fe3O4 nanoparticles. Nano Lett 12(1):246–251
122. López-Ortega A et al (2015) Exploring the magnetic properties of cobalt-ferrite nanoparticles for the development of a rare-earth-free permanent magnet. Chem Mater 27(11):4048–4056
123. Bedanta S et al (2013) Magnetic nanoparticles: a subject for both fundamental research and applications. J Nanomater 2013:22
124. Pedro T et al (2003) The preparation of magnetic nanoparticles for applications in biomedicine. J Phys D Appl Phys 36(13):R182
125. Pankhurst QA et al (2009) Progress in applications of magnetic nanoparticles in biomedicine. J Phys D Appl Phys 42(22):224001
126. Hao R et al (2010) Synthesis, functionalization, and biomedical applications of multifunctional magnetic nanoparticles. Adv Mater 22(25):2729–2742
127. Tran N, Webster TJ (2010) Magnetic nanoparticles: biomedical applications and challenges. J Mater Chem 20(40):8760–8767

128. Weissleder R et al (1989) Superparamagnetic iron oxide: pharmacokinetics and toxicity. Am J Roentgenol 152(1):167–173
129. Yang SP et al (2013) Method for preparing core-shell structure ferrite magnetic nanocomposite used in NMR imaging contrast agent
130. Robert D et al (2010) Magnetic micro-manipulations to probe the local physical properties of porous scaffolds and to confine stem cells. Biomaterials 31(7):1586–1595
131. Weissleder R, Lee H, Yoon TJ (2013) Magnetic nanoparticles
132. Falk RB (1966) Magnetic recording tape with magnetic layer of oxide coated iron-cobalt alloy particles in a binder. US
133. Terry WM (2005) Ultimate limits to thermally assisted magnetic recording. J Phys Condens Matter 17(7):R315
134. Richter HJ (2007) The transition from longitudinal to perpendicular recording. J Phys D Appl Phys 40(9):R149
135. Hans Jürgen R (1999) Recent advances in the recording physics of thin-film media. J Phys D Appl Phys 32(21):R147
136. Mallinson J (1969) Maximum signal-to-noise ratio of a tape recorder. IEEE Trans Magn 5(3):182–186
137. Mallinson JC (1991) A new theory of recording media noise. IEEE Trans Magn 27(4):3519–3531
138. Victora RH, Shen X (2008) Exchange coupled composite media. In: Proceedings of the IEEE, vol 96(11), pp 1799–1809
139. Misra DK (2011) FeRh-FePt core shell nanostructure for ultra-high density storage media: US
140. Hattori Y (2011) Magnetic particle and method of preparing the same, and magnetic recording medium: US
141. Shukla N et al (2013) Method of producing self-assembled cubic FePt nanoparticles and apparatus using same: US
142. Luo J et al (2016) Synthesis, characterization, and microwave absorption properties of reduced graphene oxide/strontium ferrite/polyaniline nanocomposites. Nanoscale Res Lett 11(1):1–14
143. Cheng Y et al (2010) Preparation, magnetic and microwave absorption properties of La0.5Sr0.5MnO3/La(OH)3 composites. Mater Res Bull 45(6):663–667
144. Gairola SP et al (2010) Enhanced microwave absorption properties in polyaniline and nanoferrite composites in X-band. Synth Met 160:2315–2318
145. Li Y et al (2015) Nd doping of bismuth ferrite to tune electromagnetic properties and increase microwave absorption by magnetic-dielectric synergy. J Mater Chem C 3(36):9276–9282
146. Chang H-Y, Cheng S-Y, Sheu C-I (2008) Microwave sintering of ferroelectric PZT thick films. Mater Lett 62(21–22):3620–3622
147. Fan M, He ZF, Pang H (2013) Microwave absorption enhancement of CIP/PANI composites. Synth Met 166:1–6
148. Zhu C-L et al (2010) Fe3O4/TiO2 core/shell nanotubes: synthesis and magnetic and electromagnetic wave absorption characteristics. J Phys Chem C 114(39):16229–16235
149. Kim SW, Park JH, Kim YB (2010) Magnetic composite powders, preparing method thereof and electromagnetic noise suppressing films comprising same: US
150. Hennig I et al (2013) Microwave absorbing composition: US
151. Imaoka N et al (2008) Magnetic material for high frequency wave, and method for production thereof
152. Sayan C et al (2013) Magnetic entropy change in core/shell and hollow nanoparticles. J Phys Condens Matter 25(42):426003

Chapter 4
Bifunctional Nanomaterials: Magnetism, Luminescence and Multimodal Biomedical Applications

Latif U. Khan and Zahid U. Khan

Abbreviations

AA	Acrylic acid
AC	Alternating current
Acac	Acetylacetone
B.M.	Bohr magneton
Calix	Calixarene
CNT	Carbon nanotube
CPE	Carbon-paste electrode
CS	Chitosan
CT	Computed tomography
CTAB	Cetyltrimethyl-ammonium bromide
Cup	*N*-nitrosophenylhydroxylamine
DNA	Deoxyribonucleic acid
DTAB	Dodecyltrimethylammonium bromide
FI	Fluorescent imaging
FITC	Fluorescein isothiocyanate
GO	Graphene oxide
IgG	Immunoglobulin G

L.U. Khan (✉)
Brazilian Nanotechnology National Laboratory (LNNano), Brazilian Center for Research in Energy and Materials (CNPEM), Rua Giuseppe Máximo Scolfaro, 10.000 Polo II de Alta Tecnologia de Campinas - CEP 13083-970, Campinas, São Paulo, Brazil.
e-mail: latif.khan@lnnano.cnpem.br

Z.U. Khan
Departamento de Imunologia, Instituto de Ciências Biomédicas-IV, Universidade de São Paulo, Av. Lineu Prestes, 1730, 05508-000, São Paulo, SP, Brazil
e-mail: zahidkhan@usp.br

© Springer International Publishing AG 2017

S.K. Sharma (ed.), *Complex Magnetic Nanostructures*,
DOI 10.1007/978-3-319-52087-2_4

IUPAC	International Union of Pure and Applied Chemistry
IVCT	Intervalence charge transfer
LBL	Layer-by-layer
mcDNA	Minicircle DNA
MNPs	Magnetic nanoparticles
MRI	Magnetic resonance imaging
MRT	Magnetic resonance tomography
MTT	Microculture tetrazolium assay
MWCNT	Multiwalled carbon nanotube
NADH	Nicotinamide adenine dinucleotide
NIR	Near-infrared
NIPAM	*N*-isopropylacrylamide
OA	Oleic acid
o/w	Oil dispersed in water
PAH	Poly(allylamine hydrochloride)
PCEM	Point charge electrostatic model
PCL	Poly(ε-caprolactone)
PEG	Polyethylene glycol
PET	Positron emission tomography
Phen	1,10-phenanthroline
PLGA	Poly(lactic-*co*-glycolic acid)
PMAA	Poly(methacrylic acid)
PMI	*N*-(2,6-diisopropylphenyl)-perylene-3,4-dicarbonacidimide
PS	Polystyrene
PSS	Poly(styrenesulfonate)
PVP	Poly(vinylpyrrolidone)
QD	Quantum dot
rGO	Reduced graphene oxide
SAR	Specific absorption rate
siRNA	Small interfering RNA
SLPC	Specific losses per cycle
SPECT	Single-photon emission computed tomography
St	Styrene
TEOS	Tetraethyl orthosilicate
UCNPs	Upconversion luminescent nanoparticles
w/o	Water dispersed in oil

4.1 Introduction

Bifunctional nanosized materials, coassembling magnetic and photonic features into single-entity nanostructures [1, 2], have demonstrated great potential in wide range of multimodal biomedical applications, for example, as drug delivery carriers [3], in the photothermal destruction of tumor cells [4], as multimodal MRI contrast agents [5], in quantitative DNA analyses [6], and in magnetic hyperthermia for cancer

therapies [7–9]. Several reports have focused on the preparation, characterization, and biological applications of bifunctional optical and magnetic nanomaterials. Generally, these nanoscale materials can be obtained by coating or layer-by-layer (LBL) deposition of rare-earth phosphors [3, 10] quantum dots (QDs) [11] on magnetic core nanoparticles, polymer-assisted encapsulation or coassembly of magnetic nanoparticles and luminophores in single nanostructures [12], and functionalization of Fe_3O_4 with fluorescent dyes [13] or luminescent metal complexes [14].

Magnetite crystallizes in inverse spinel structures with Fe^{2+} and Fe^{3+} ion distribution, represented by the structural formula $(Fe^{3+})[Fe^{3+}Fe^{2+}]O_4$, where the parentheses denote tetrahedral (*A*) sites and the square brackets denote octahedral [*B*] sites [15]. Fe_3O_4 can be modified by the introduction of d transition-metal cations into its structure, such as Co^{2+}, Ni^{2+}, Cu^{2+}, Mn^{2+}, and Zn^{2+}. These modified ferrospinels are commonly known as ferrites, an important class of iron oxides with the general formula MFe_2O_4 [16–18]. Ferrites show a spinel-type structure in which oxygen (O^{2-}) ions form a face-centered cubic (fcc) close packing and the M^{2+} and Fe^{3+} ions occupy either tetrahedral (*A*) or octahedral (*B*) interstitial sites.

The intriguing structural feature has been obtained in ferrites by changing the scale of the particle size. When the materials are prepared in the microscopic range, they present an inverse spinel structure $(Fe)[MFe]O_4$, where () and [] mean *A* and *B* sites, respectively [19, 20]. However, in the nanometric range, they present a mixed-spinel structure $(Fe_{1-x}M_x)[Fe_{1+x}M_{1-x}]O_4$ $(0 < x < 1)$, where x is the so-called inversion degree [19], which indicates the cation distribution in the spinel structure.

The electronic structure of magnetic MFe_2O_4 ferrites shows only 3d energy states of metal ions near the Fermi level [21], so that optical absorption due to electric dipole–induced transitions is not expected at optical frequencies (parity forbidden) [22]. However, the diagonal components of the dielectric tensors of these compounds obtained by optical measurements show strong absorption bands in the visible range. They are attributable to d–d intervalence charge transfer (IVCT) transitions in which a d electron of an M^{2+} ion is transferred to a neighboring Fe^{3+} ion, residing at octahedral sites, through optical excitation [21, 22]. This charge transfer cannot occur between cations at octahedral and tetrahedral sites because the change in geometry between the two sites is too great. A similar cation-to-cation charge transfer is responsible for the color of the black mineral magnetite or lodestone [23].

In addition, like ferric oxide (hematite, α-Fe_2O_3) and various Fe^{3+} ions containing iron oxide, hydroxides give many soils and rocks a ruddy color. At the simplest level, the color derives from O^{2-} or $^{-}OH \rightarrow Fe^{3+}$ charge transfer because Fe^{3+} (d^5) ions readily accept extra electrons in their half-filled shells to become Fe^{2+} (d^6) ions [23]. Therefore, iron oxides are usually strong luminescence quenchers [24]. This phenomenon occurs via an energy transfer process when a luminescent center (e.g., RE^{3+} ion) is in direct contact with or is in proximity to a magnetic metal oxide surface (e.g., Fe_3O_4). To overcome this difficulty, an intermediate layer or spacer is usually added to separate iron oxide nanoparticles and luminophores [1, 12]. Therefore, magnetic ferrite nanoparticles are coated with, for example, organic

macrocycles, polymers, or silica before the introduction of a luminophore (e.g., rare-earth phosphor) to prepare the luminescent and magnetic nanomaterials.

Interest in luminescent materials containing RE^{3+} ions has grown considerably owing to their unique ability to exhibit well-defined narrow emission bands in different spectral ranges from visible to near-infrared (NIR) with relatively long lifetimes and high quantum yields [25, 26]. These characters make RE^{3+} materials efficient candidates for multidisciplinary photonic applications [27], recently extended from laser physics to, for example, materials sciences, optical markers, agriculture, and medical diagnostics.

The photoluminescence properties of RE^{3+} ions are mainly due to the 4f energy level structures [28], which are only slightly affected by the chemical environment owing to the effective shielding of 4f electrons by external filled 5s and 5p subshells [25]. Therefore, the absorption and emission spectra of the 4f intraconfigurational transitions of RE^{3+} ions retain more or less their atomic character and show similar absorption and emission lines irrespective of the host matrix or organic ligand [1, 29]. Rare-earth complexes have become valuable candidates for light conversion molecular devices (LCMDs) since the introduction of intramolecular energy transfer from organic ligands to RE^{3+} ions (*antenna effect*) [30] and after the issue of very low molar absorption coefficients (1.0 M^{-1} cm^{-1}) [29] of 4f–4f transitions was overcome. Therefore, the designs of efficient luminescent RE^{3+} complexes have become an important research subject [31] and are being investigated extensively using different organic ligands as sensitizers [32].

RE^{3+} ions are paramagnetic owing to the presence of unpaired electrons, with the exception of La^{3+}, Lu^{3+}, and Y^{3+}. Their magnetic properties are determined entirely by the ground state (except for Sm^{3+} and Eu^{3+} ions) because the excited states are so well separated from the ground state owing to the spin–orbit coupling and are thermally inaccessible [33]. The magnetic moment of RE^{3+} ions is essentially independent of the chemical environment, and one cannot distinguish between different coordination geometries. However, the magnetic moments of rare-earth ions [1] also contribute to the total magnetization of luminescent and magnetic nanomaterials. This chapter presents a concise overview of the key concepts of various strategies to fabricate bifunctional nanomaterials and their magnetism and photoluminescence behaviors, as well as their multimodal biomedical applications.

4.2 Strategies for Designing Bifunctional Nanomaterials

Luminescent and magnetic nanomaterials are usually fabricated by integrating magnetic nanoparticles with luminophores (e.g., RE^{3+} ion–doped compounds) by various synthetic methods. These materials are commonly achieved as hybrid conjugates of magnetic and luminescent entities or core-shell nanostructures, which are obtained by coating or LBL deposition of rare-earth phosphors and QDs on magnetic core nanoparticles. The other interesting way is the functionalization of magnetic iron oxide nanoparticles with fluorescent dyes and luminescent

complexes. For the sake of understanding, the strategies of preparation of bifunctional nanomaterials are divided into two parts, the synthesis of magnetic core nanoparticles and synthesis of bifunctional luminescent and magnetic nanomaterials.

4.2.1 Synthesis of Magnetic Core Nanoparticles

Magnetic nanoparticles (MNPs) are of various chemical compositions, crystalline structures, and phases, for example, iron oxides: Fe_3O_4, γ-Fe_2O_3, and α-Fe_2O_3 [34–38]; spinel-type ferrites: MFe_2O_4 (M^{2+}: Co, Mg, Mn, and Zn) [15–18, 21, 22]; pure metals: Fe and Co [39–41]; and alloys: $CoPt_3$ and FePt [42, 43]. Remarkable advances in chemical methods of synthesis have allowed for the preparation of MNPs with relatively narrow size distributions, good chemical stabilities, and a broad range of compositions, specific shapes, and morphologies. Several popular methods, including coprecipitation, thermal decomposition, hydrothermal synthesis, microemulsion, sol-gel synthesis, sonochemical reaction, flow injection synthesis, electrospray synthesis, and laser pyrolysis techniques, are used to synthesize high-quality MNPs [15, 44–46]. However, the most common methods for the preparation of MNPs are chemical coprecipitation, thermal decomposition, microemulsion, and hydrothermal synthesis. In this connection, we explain typical and representative examples of each synthetic process with the corresponding formation mechanism.

4.2.1.1 Coprecipitation

Generally, coprecipitation can be defined as "the simultaneous precipitation of more than one substance from a homogeneous solution," which results in the formation of a crystalline structure of a single phase (e.g., Fe_3O_4). Coprecipitation is probably the most convenient and efficient chemical pathway to synthesize MNPs. Iron oxides (either Fe_3O_4 or γ-Fe_2O_3) are usually prepared from a stoichiometric mixture of aqueous Fe^{2+}/Fe^{3+} salt solutions by the addition of a base, such as $NH_3{\cdot}H_2O$ or NaOH, under an inert atmosphere at room or elevated temperatures. The chemical reaction of Fe_3O_4 formation may be represented by Eq. 4.1:

$$Fe^{2+} + 2Fe^{3+} + 8OH^- \rightarrow Fe_3O_4 + 4H_2O \tag{4.1}$$

Thermodynamically, the complete coprecipitation of Fe_3O_4 is expected at a pH between 8 and 14 in inert atmosphere [15, 47]. However, owing to its sensitivity to oxidation, magnetite (Fe_3O_4) is usually transformed into maghemite (γ-Fe_2O_3) in the presence of oxygen:

$$Fe_3O_4 + 2H^+ \rightarrow \gamma\text{-}Fe_2O_3 + Fe^{2+} + H_2O. \quad (4.2)$$

Oxidation in air is not the only way to change magnetite (Fe_3O_4) into maghemite (γ-Fe_2O_3). However, the pH of the suspension is also affected by Fe_3O_4, as shown by Eq. 4.2, under acidic and anaerobic conditions, and surface Fe^{2+} ions are desorbed as hexaaqua complexes in solution [15, 47]. Therefore, acidic solutions usually cause the dissolution of magnetite.

Coprecipitation is a very convenient and favorable way to prepare a broad range of nanomaterials of various chemical compositions owing to the relatively mild reaction conditions, low cost of required equipment, simple protocols, and short reaction time. Therefore, this method is not only a preferred way to synthesize magnetic iron oxide nanoparticles but is also commonly used to prepare a wide range of rare-earth ion (RE^{3+})–doped luminescent nanomaterials, such as rare earth ion (RE^{3+})–doped alkaline-earth tungstates: MWO_4:RE^{3+} (M^{2+}: Ca, Sr, and Ba) [48], rare-earth fluorides: $NaYF_4$:RE^{3+} [49], LaF_3:RE^{3+} [50], and others. The great advantage of the coprecipitation method is that it yields a large amount of nanoparticles. However, polydisperse and large size distribution particles are usually obtained with this method owing to the kinetic factors that control the growth of crystals. Generally, two processes are involved in the growth and formation of particles [15, 45, 51, 52]: a rapid nucleation (aggregation of nanometric building blocks such as prenucleation clusters), which occurs when the concentration of species reaches critical supersaturation, and the slow growth of nuclei by the diffusion of solutes to crystal surfaces. Therefore, to produce monodisperse iron oxide nanoparticles, control of these processes is important. In a supersaturated solution when nuclei form at the same time, the subsequent growth of these nuclei results in the formation of particles with a very narrow size distribution [15].

Magnetic properties, such as saturation magnetization, coercive field, and blocking temperature, also depend on particle size, and a large particle size distribution results in a wide range of blocking temperatures [53]. The variety of factors should be adjusted to control the size, shape, magnetic characteristics, and other features of iron oxide nanoparticles. The control of the size, shape, and composition of MNPs depends on the type of iron salts used (e.g., chlorides, sulfates, nitrates, perchlorates), Fe^{2+}/Fe^{3+} ratio [15, 45], air or inert atmosphere, reaction rate, and temperature [54]. Kim and coworkers [55] reported that the synthesis of magnetite under continuous nitrogen gas flow not only protects critical oxidation but also reduces the particle size when compared with coprecipitation methods that do not involve the removal of oxygen. In this regard, the particle size is reduced from 8.0 nm (air atmosphere) to 6.0 nm (nitrogen atmosphere). The particle size also depends on the pH and ionic strength of the precipitation medium. It has been reported that by controlling the pH and ionic strength imposed by noncomplexing salt (e.g., $NaNO_3$) in the medium, the particle size decreases with increasing pH and

ionic strength. Above a critical pH value, which depends on the ionic strength and temperature, secondary particle growth by Ostwald ripening no longer takes place [15, 56]. The stabilization of nanoparticles seems to result from thermodynamics rather than kinetics. Recently, significant advances have been made in the use of organic additives such as chelating organic acids (citric, gluconic, and oleic acids) and polymer surface complexing agents (e.g., dextran, carboxydextran, starch, polyvinyl alcohol, calixarenes) in coprecipitaion syntheses of iron oxide nanoparticles [45]. These organic additives stabilize nanoparticles in situ during growth and control their size.

4.2.1.2 Thermal Decomposition

The thermal decomposition method can be simply described as the decomposition of organometallic compounds (e.g., iron acetylacetonate) at high refluxing temperatures in high-boiling-point organic solvents (e.g., diphenyl ether) containing stabilizing surfactants (e.g., oleic acid and oleylamine). The most commonly used organometallic compounds are metal acetylacetonates [$M(acac)_n$], where M: Fe, Mn, Co, Ni, Cr, and $n = 2$ or 3 [57], cupferronates (M_xCup_x), where cup: *N*-nitrosophenylhydroxylamine ($C_6H_5N(NO)O^-$) [58], carbonyls, for example, iron pentacarbonyl [$Fe(CO)_5$], and others. [41]. Fatty acids, oleic acid, oleylamine, and hexadecylamine are more often used as surfactants. In addition, diphenyl ether, diethylene glycol, octylamine, octyl ether, hexadecanediol, octadecene, 1-hexadecene, and 1-octadecene are high-boiling-point organic solvents that are usually used in this method [15, 45, 57, 59]. It is noteworthy that the ratios of the starting materials, such as organometallic precursors, surfactants, and solvents, are the important parameters for controlling the size and morphology of MNPs. In addition, the reaction temperature, reaction time, and aging period may also be crucial for the efficient control of size and morphology [45].

The apparatus used for the preparation of nanoparticles by thermal decomposition can be easily designed synthetically in a laboratory (Fig. 4.1). It consists of a three-necked, round-bottom flask mounted on a heating/stirring plate and equipped with a glass water condenser. The temperature can be also monitored with a thermometer immersed in silicon oil's beaker, which is mounted on the heating/stirring plate. The inert atmosphere in the reaction medium can be maintained by the continuous flow of nitrogen or argon gas during the entire period of reaction.

Thermal decomposition is an efficient chemical method that is usually used to synthesize monodisperse MNPs with high crystallinity, controlled shape, and a narrow size distribution. A wide variety of MNPs can be prepared by this method, including magnetic metal oxides (e.g., Cr_2O_3, MnO, Co_3O_4, NiO, iron

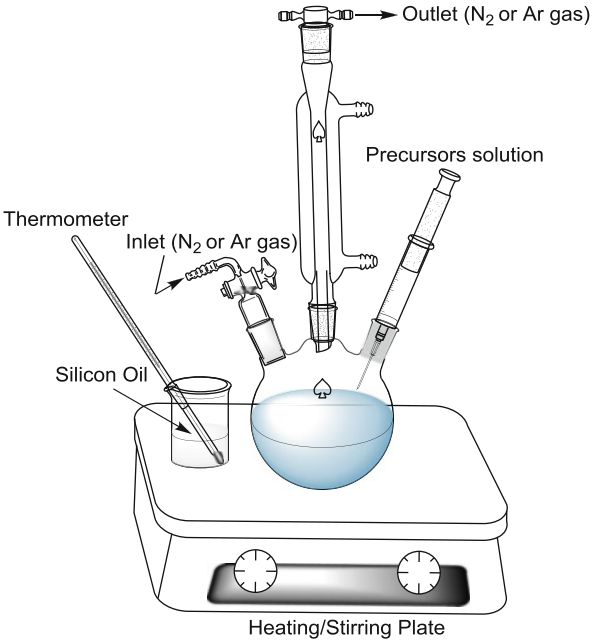

Fig. 4.1 Schematic illustration of apparatus used in synthesis of nanoparticles by thermal decomposition method (designed by author)

oxides ferrites), metallic nanoparticles (Fe, Ni, Co), and alloys ($CoPt_3$, FePt) [15, 39–41, 43, 45, 57, 58]. In addition, this chemical method has been used very commonly to prepare high-quality, various narrow-size-distribution rare earth ion–doped luminescent nanoparticles [60] such as $LiYF_4:RE^{3+}$ [61], $NaYF_4:RE^{3+}$ [62], $NaGdF_4:RE^{3+}$ [63], $NaLuF_4:RE^{3+}$ [64], $BaYF_5:RE^{3+}$ [65], $KY_3F_{10}:RE^{3+}$ [65], $BaGdF_5:RE^{3+}$ [66], $YOF:RE^{3+}$ [67], LaOF, and LuOF [68].

The advantage of metallic nanoparticles is their larger magnetization compared to metal oxides. Therefore, they are interesting candidates for data-storage devices. The precursors, which contain a zero-valence metal, such as metal carbonyls, usually undergo thermal decomposition and initially produce metal particles, but subsequent oxidation can lead to the formation of oxide nanoparticles as well. For instance, iron pentacarbonyl has been reported to decompose in a mixture of octyl ether and oleic acid at 100 °C, but subsequent addition of trimethylamine oxide $(CH_3)_3NO$ as a mild oxidant at high temperature results in the formation of monodisperse γ-Fe_2O_3 nanocrystals. Metallic iron nanoparticles have also been synthesized by thermal decomposition of $[Fe(CO)_5]$ at high temperature (170 °C) in the presence of polyisobutene (polymeric surfactant) and decalin (decahydronaphthalene) solvent in a nitrogen atmosphere [45]. Moreover, organometallic precursors with cationic metal centers usually undergo thermal decomposition to directly produce metal oxide particles. Rockenberger and coworkers [58] reported the formation of γ-Fe_2O_3, Mn_3O_4, and Cu_2O particles by the thermal decomposition of $FeCup_3$, $MnCup_2$, and $CuCup_2$ as precursors, respectively. Sun and coworkers [69] reported the size-controlled synthesis of magnetite nanoparticles at high temperature

(265 °C) using iron (III) acetylacetonate $Fe(acac)_3$ as precursor, in phenyl ether in the presence of alcohol, oleic acid, and oleylamine. Recently, compact $Ag@Fe_3O_4$ core-shell nanoparticles were synthesized by a temperature-paused single-step thermal decomposition method [70]. These nanoparticles showed a silver nucleus wrapped in a compact magnetite shell. Therefore, owing to the curious rectangular shape, they were represented as bricklike nanoparticles (BLNs). The interesting feature of this synthesis lies in the introduction of a temperature pause in the single-step protocol to separate the growth of silver (zone 1) from the proper thermal decomposition of the iron precursor (zone 2) (Fig. 4.2) and to avoid the formation of nonhomogeneous core-shell NPs.

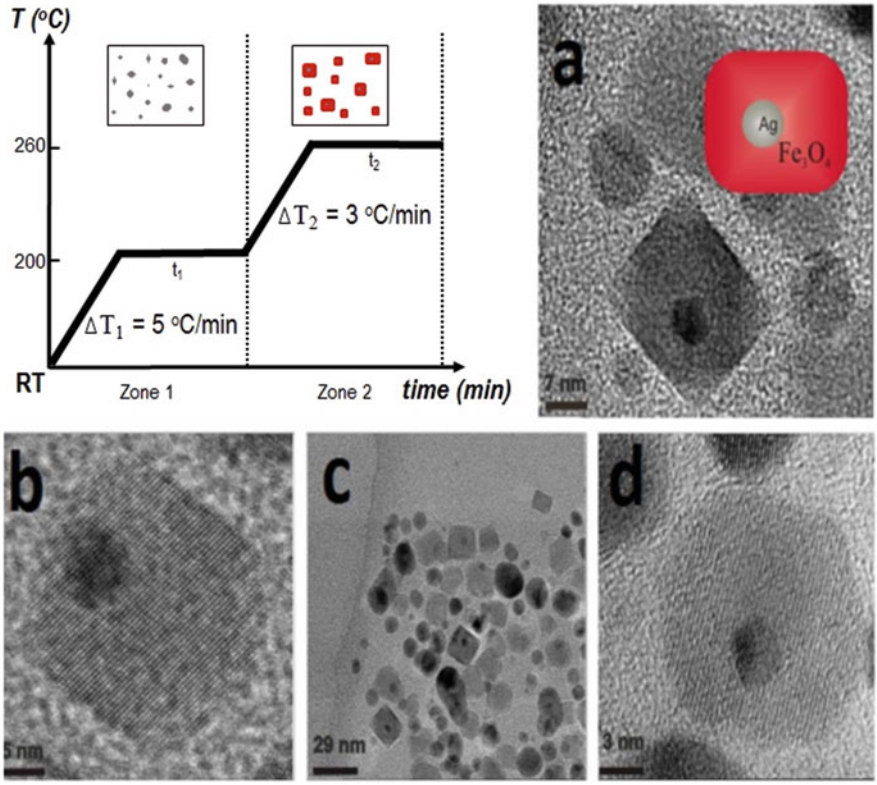

Fig. 4.2 Temperature profile of temperature-paused single-step thermal decomposition synthesis. *Boxes* sketch the expected predominant structures for each time zone. Typically, both waiting times are 120 min. Images: TEM images of BLNs obtained following the temperature-paused single-step protocol. Ag corresponds to a dark contrast, while lighter particles correspond to magnetite. Plain magnetite nanoparticles that form are also shown in (**c**). (**a**, **b**, **d**) Different amplifications of BLNs to understand the structure. Reproduced with permission from ref. [70]

4.2.1.3 Microemulsion

Microemulsion is a phenomenon that arises when two immiscible liquids (e.g., water and oil) are mixed together, and then a surfactant is added that stabilizes the dispersion of one of the phases (e.g., aqueous phase) in the other (e.g., organic phase). Surfactants are amphiphilic molecules that contain two well-differentiated hydrophobic and hydrophilic parts. They form a monolayer at the interface between the oil and water, with the hydrophobic tails of these molecules being dissolved in the oil phase and the hydrophilic head groups in the aqueous phase [71]. As a result, the surface tension between the two phases is reduced and the stable dispersion of one phase within the other is enabled through the formation of different structures, such as small drops, cylinders, and layers, depending on the mass relation between the aqueous and organic phases and surfactant [72]. Therefore, a microemulsion can be defined as a thermodynamically stable isotropic dispersion of two immiscible liquids (e.g., water and oil), where the microdomain of either or both liquids is stabilized by an interfacial film of surfactant molecules [45, 72]. In addition, Danielsson and coworker [73] defined a microemulsion as "a system of water, oil and amphiphile which is a single optically isotropic and thermodynamically stable liquid solution." Microemulsions are usually direct (oil dispersed in water, o/w) and reversed (water dispersed in oil, w/o). In the case of water-in-oil microemulsions, the aqueous phase is dispersed as microdroplets (usually 1–50 nm in diameter) surrounded by a monolayer of surfactant molecules in the continuous organic phase. The size of the reverse micelle is determined by the molar ratio of water to surfactant [45].

Micelles are aggregates of surfactant molecules dispersed in a liquid colloid (made of two immiscible liquids, e.g., water and oil). Like microemulsions, micelles can be normal-phase and reverse. Generally, micelles in aqueous solution form an aggregate with hydrophilic head parts in contact with surrounding solvent (water), and hydrophobic tail parts are extended in the micelle center (Fig. 4.3). These types

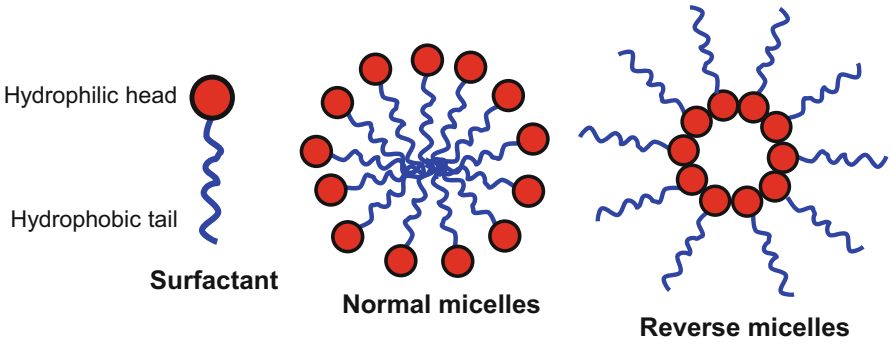

Fig. 4.3 Schematic representation of normal (*middle*) and reverse (*right*) micelles. Reproduced with permission from ref. [72]

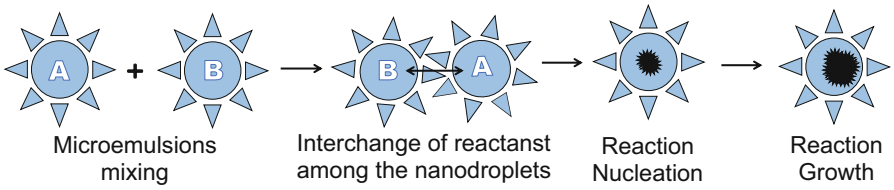

Fig. 4.4 Mechanism of formation of nanoparticles in microemulsions. Reproduced with permission from ref. [76]

of micelles are known as normal (oil-in-water) micelles [74]. Reverse micelles have head groups at the center with the tails extending out (water-in-oil micelle).

Micelles can be regarded as real nanoreactors, providing a suitable environment for controlled nucleation and growth. Therefore, microemulsion is a remarkable technique that provides very good control over the final particle size [45, 71, 74]. The mechanism of the microemulsion method is really simple and involves mixing two identical water-in-oil microemulsions containing appropriate reactants (e.g., A and B); the resulting microdroplets will continuously collide, coalesce, break up again, and interchange reactants, and finally a reaction will be occur to form a precipitate (nanoparticles) in the micelles (Fig. 4.4). By the addition of a solvent, such as acetone or ethanol, to a microemulsion, the precipitate can be extracted by filtering or centrifuging the mixture. In this regard, a microemulsion can be used as a nanoreactor for the formation of nanoparticles.

A water-in-oil microemulsion can be used to synthesize iron oxide, metallic iron nanoparticles, and silica-coated iron oxide nanoparticles employing several surfactants such as sodium dodecyl sulfate (SDS), cetyltrimethylammonium bromide (CTAB), and polyvinylpyrrolidone (PVP) [71]. The spinel MFe_2O_4 (M: Mn, Co, Ni, Cu, Zn, Mg, or Cd) ferrites are among the most important magnetic materials and have been widely used in electronic applications. Spinel ferrites can also be synthesized by microemulsions and reverse micelles. For instance, $MnFe_2O_4$ nanoparticles with controlled sizes from about 4–15 nm have been synthesized through the formation of water-in-toluene reverse micelles with sodium dodecylbenzenesulfonate (NaDBS) as surfactant [75]. In addition, Hashim and coworkers [76] reported the synthesis of manganese ferrite nanoparticles through the formation of water-in-cyclohexane reverse micelles, using cetyltrimethyl-ammonium bromide (CTAB) as surfactant and isoamylalcohol as the cosurfactant phase. In this synthesis, they schematically illustrated the preparation of $Mn^{3+}{}_xMn^{2+}Fe_{2-x}O_4$ ferrite nanoparticles by a reverse microemulsion method, as shown in Fig. 4.5, which is a remarkable representation of the synthesis of nanoparticles through the formation of reverse micelles and more easily understood by readers.

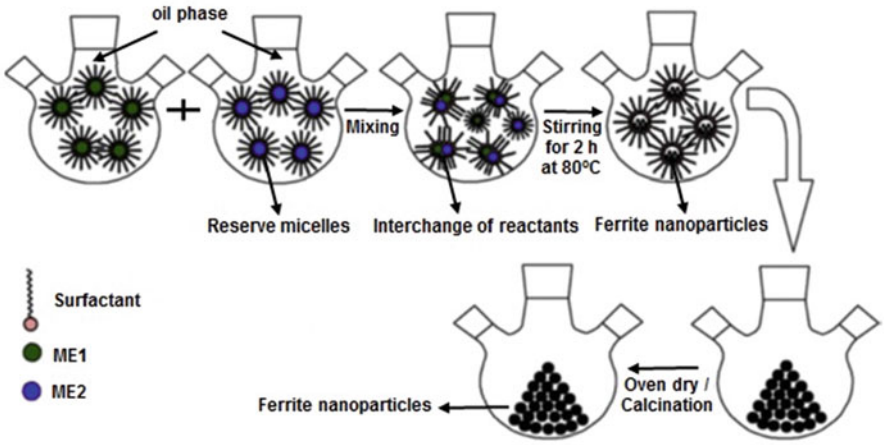

Fig. 4.5 Schematic representation of preparation of $Mn^{3+}{}_{x}Mn^{2+}Fe_{2-x}O_4$ ferrite synthesized by reverse microemulsion. Reproduced with permission from ref. [76]

4.2.1.4 Hydro(Solvo)Thermal Synthesis

Hydro(solvo) thermal synthesis usually refers to heterogeneous or homogeneous chemical reactions in water or nonaqueous media in an autoclave (a sealed thick-walled steel vessel with a Teflon cup) at high temperatures and high vapor pressure with subsequent growth of single crystals or crystallization of substances from the solution (e.g., aqueous solution). This method can be used to prepare different kinds of geometries, including thin films (e.g., nanostructured TiO_2 thin films) [77], bulk powders (e.g., zinc oxide powders) [78], single crystals (e.g., 3D metal–organic framework based on a lower-rim acid-functionalized calix[4]arene) [79], and nanocrystals (e.g., highly crystalline Fe_3O_4 nanoparticles) [80].

An excellent example of hydrothermal conditions is an aqueous medium over 100 °C and 1 bar pressure, which occurs in nature. Therefore, numerous minerals have been formed under these conditions. Through simulations in the laboratory, geologists and mineralogists have already been able to determine the conditions necessary for mineral formation and have thus contributed to the knowledge of geological processes [81]. Hydrothermal processes play an important role in industry, especially hydrometallurgy, for example, the classic Bayer process [81] for the decomposition of bauxite.

The material nature of the vessel (autoclave) should be chosen to be compatible with reaction media and conditions in hydrothermal synthesis. Therefore, the corrosive properties of the solution under the desired conditions as well as the danger of undesirable contamination of the reaction product must be considered. It has been found that certain metallic vessels, such as copper and nickel in particular, as well as titanium, vanadium, chromium, and iron, are attacked by alkaline solutions at 400 °C. Borosilicate and quartz glasses are quite stable toward neutral

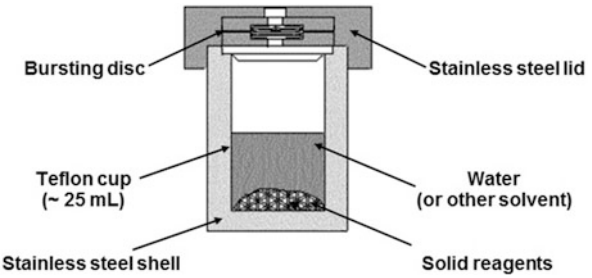

Fig. 4.6 Schematic of Teflon-lined stainless steel autoclave typically used in laboratories for hydrothermal synthesis. Reproduced with permission from ref. [82]

and acidic solutions, with the exception of hydrogen fluoride (HF) [81]. Therefore, in a neutral or acidic medium as well as within a limited pressure and temperature range, glass or quartz glasses are well suited for hydrothermal synthesis. In addition, Teflon is usually stable toward acids, even hydrogen fluoride, basic, and oxidizing media, but should be used within the temperature limit to avoid its melting. Thus, Teflon-lined stainless steel autoclave is the most common vessel [82] and is typically used in the laboratory for hydrothermal synthesis (Fig. 4.6).

A Teflon lining is important to avoid contamination from steel. As far as hydro(solvo)thermal synthesis in the laboratory is concerned, the filling factor of autoclave is important, and it should be sufficient to provide the necessary pressure, so filling factors of approximately 70% are normally used (i.e., 70% of the autoclave should be filled with reaction content). For most hydrothermal syntheses, only moderate temperatures between 100 and 250 °C are used, meaning that the hydrothermal conditions are below the supercritical region. Moreover, a minimum solubility of 2–5% is necessary for the least soluble reaction precursors [81, 82]. The autoclave is usually heated either by placing it in an oven or by using microwaves.

The specific reaction medium (solvent) and adjustment of reaction conditions, for example, temperature, pressure, and pH, are important for the preparation of specific materials using the solvothermal method. In the case of nanoparticles, the size, shape distribution, and crystallinity of the particles are precisely controlled by tuning the parameters, such as temperature, pressure, and reaction time. The solvent choice is not just limited to water; organic solvents, such as ethanol, can also be used in this method. Nevertheless, water remains the most widely used solvent. In addition, in hydro(solvo)thermal synthesis, some organic additives or surfactants with specific functional groups, for example, oleic acid (OA) [80], polyethylenimine (PEI) [83], and cetyltrimethylammonium bromide (CTAB), are generally added along with reaction precursors to achieve simultaneous control over the crystalline phases, sizes, and morphologies, as well as the surface functional groups, for the resulting nanoparticles.

The broad range of nanostructured materials can be synthesized by the hydro(solvo)thermal method, using optimized reaction conditions, for example, temperature, pressure, and pH. Li and coworkers [80] reported a generalized approach of the hydrothermal method for synthesizing a variety of different nanocrystals, for example, nanocrystals of metal (e.g., Ag, Au, Pd, Pt), magnetite

and spinel ferrites (e.g., MFe_2O_4, M^{2+}: Co, Mg, Mn, Zn), rare-earth fluorides (e.g., $NaYF_4$, YF_3, LaF_3) and semiconductors (e.g., CdS, ZnS, CdSe), by a liquid–solid solution reaction. This general hydrothermal approach consists of metal linoleate (solid), an ethanol–linoleic acid (liquid phase), and water–ethanol (solution) at different reaction temperatures under hydrothermal conditions. Later on the same method was applied by several authors to synthesize controlled size and morphology, highly crystalline Fe_3O_4 nanocrystals with a modification using different fatty acids, such as oleic acid and metal oleate solid precursor instead of linoleic acid and metal linoleate, and optimizing the hydrothermal parameters [3]. In this case the oleic acid acted as stabilizer to prevent particle agglomeration and to prevent the oxidation of Fe_3O_4 in air atmosphere.

Schüth and coworkers [45] summarized the four previously mentioned synthetic methods on the basis of their advantages and disadvantages in a convenient way (Table 4.1). Coprecipitation is usually considered the preferred route because of its simplicity of the synthesis. As far as the control of the size and morphology of nanoparticles is concerned, thermal decomposition seems like the best method developed to date. Alternatively, microemulsions can also be used to synthesize monodispersed nanoparticles with various morphologies. However, this method requires a large amount of solvent and the resulting yield of nanoparticles is comparatively low. Hydrothermal synthesis is a relatively little explored method for the synthesis of MNPs, although it allows for the synthesis of high-quality nanoparticles.

A literature review shows that MNPs prepared from coprecipitation and thermal decomposition methods have been extensively studied, and they can be prepared on a large scale. In addition, a broad range of particles of different chemical compositions, such as metals, luminescent rare-earth fluorides, rare earth–doped metal oxides, QDs, and semiconductors, can also be prepared by coprecipitation, thermal decomposition, and hydrothermal methods.

4.2.2 Synthesis of Luminescent and Magnetic Nanomaterials

Generally, the fabrication of luminescent and magnetic nanomaterials is categorized into three kinds of approaches. The first one is the preparation of optical and magnetic core-shell nanomaterials, based on coating or LBL deposition of rare-earth phosphors or QDs on the magnetic core nanoparticles. The second approach is based on combining luminophores and magnetic nanocrystals in single nanostructures assisted by crosslinking molecules. The third approach is the SiO_2-assisted synthesis of photoluminescent and magnetic nanomaterials using iron oxide as core nanoparticles and rare-earth-ion and transition-metal-ion complexes or fluorescent dyes as luminescent centers.

Table 4.1 Summary comparison of synthetic methods

Synthetic method	Synthesis	Reaction temp. [8 °C]	Reaction period	Solvent	Surface-capping agents	Size distribution	Shape control	Yield
Coprecipitation	Very simple, ambient conditions	20–90	Minutes–hours	Water	Needed, added during or after reaction	Relatively narrow	Not good	High/scalable
Thermal decom-position	Complicated, inert atmosphere	100–320	Hours–days	Organic compound	Needed, added during reaction	Very narrow	Very good	High/scalable
Microemulsion	Complicated, ambient conditions	20–50	Hours	Organic compound	Needed, added during reaction	Relatively narrow	Good	Low
Hydrothermal synthesis	Simple, high pressure	100–220	Hours-days	Water–ethanol	Needed, added during reaction	Very narrow	Very good	Medium

From [45] reproduced with permission

4.2.2.1 Optical and Magnetic Core-Shell Nanomaterials

Luminescent and magnetic core-shell nanomaterials are usually prepared by coating or LBL deposition of rare earth ion (RE^{3+})–doped compounds (e.g., $LaF_3:Ce^{3+},Tb^{3+}$, or $Y_2O_3:Eu^{3+}$) or QD (e.g., CdSe) shells on magnetic core nanoparticles (e.g., Fe_3O_4), using, for example, coprecipitation, thermal decomposition, or hydrothermal method, as discussed earlier in detail in Sects. 4.2.1.1, 4.2.1.2, and 4.2.1.4. Other interesting bifunctional nanostructures are based on the conjugation of QDs and MNPs. Several reports have focused on the preparation and characterization of these bifunctional nanomaterials. Zhang and coworkers [3] reported the stepwise synthesis of mesoporous multifunctional upconversion luminescent and magnetic nanorattles with controlled size and morphology for application in targeted chemotherapy (Fig. 4.7) and provided a good example of the fabrication of core-shell nanomaterials. Initially, they prepared $Fe_3O_4@SiO_2@Y_2O_3:Yb^{3+},Er^{3+}$ nanoparticles by thermal treatment of the $Fe_3O_4@SiO_2@Y(OH)CO_3{\cdot}H_2O:Yb^{3+},Er^{3+}$ precursor at 550 °C, which was obtained from Fe_3O_4/SiO_2 nanoparticles, $Y(NO_3)_3$, $Yb(NO_3)_3$, $Er(NO_3)_3$, and urea starting materials by the hydrothermal method. Furthermore, in the last step they treated the $Fe_3O_4@SiO_2@Y_2O_3:Yb^{3+},Er^{3+}$ nanomaterials with NaF and HF aqueous solutions at 80 °C to synthesize the $Fe_3O_4@SiO_2@\alpha$-$NaYF_4:Yb^{3+},Er^{3+}$ nanorattles through an ion-exchange process.

Tong and coworkers [84] have also studied luminescent and magnetic core-shell $Fe_3O_4@SiO_2@Y_2O_3:Eu^{3+}$ composites by annealing precursor material at 800 °C. The precursor was obtained from $Fe_3O_4@SiO_2$ nanoparticles, YCl_3, and $EuCl_3$ by

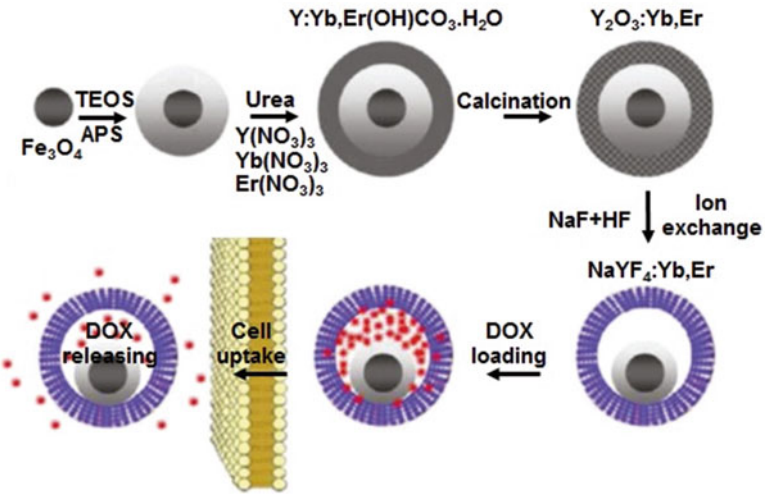

Fig. 4.7 Synthetic procedure for drug-loaded $Fe_3O_4@SiO_2@\alpha$-NaYF/Yb,Er nanorattles (DOX-MUC-F-NR). Reproduced with permission from ref. [3]

the hydrothermal method. The main disadvantage of annealing at high temperature (> 400 °C) is the oxidation of magnetite (Fe_3O_4) to hematite (α-Fe_2O_3), which greatly affects magnetic properties, causing a drastic decrease in the magnetization of the bifunctional nanomaterials. Moreover, owing to a sensitivity to oxidation, magnetite (Fe_3O_4) is usually transformed into maghemite (γ-Fe_2O_3) in the presence of oxygen, so magnetite core nanoparticles are stabilized with coating agents, for example, silica, organic compounds (e.g., oleic acid), or polymers, before use and an inert atmosphere is employed during the preparation of a luminescent shell (e.g., α-$NaYF_4$:Yb^{3+},Er^{3+}) on these nanoparticles. The pH of the reaction medium also affects the Fe_3O_4; under acidic and anaerobic conditions, surface Fe^{2+} ions are desorbed as hexaaqua complexes in solution. Therefore, acidic pH levels should be avoided during the synthesis of luminescent and magnetic core-shell nanomaterials.

Generally, core-shell optical and magnetic nanomaterials contain Fe_3O_4@$NaGdF_4$:Yb/Er@$NaGdF_4$:Yb/Er [85], Fe_3O_4@LaF_3:Yb^{3+},Er^{3+} [86], Fe_3O_4@YF_3:Ce^{3+},Tb^{3+} [87], and other compounds. (Table 4.2). In addition, various optical and magnetic nanostructures comprised of magnetic core nanoparticles and QDs as luminophores have been also extensively studied. These bifunctional nanomaterials include Fe_3O_4@CdSe [88], Fe_3O_4@C@CdTe [89], Fe_3O_4@ZnS [90], Co/CdSe [11], FePt@CdS, CdS-FePt [91], and other core-shell nanostructures and microspheres (Table 4.2).

Table 4.2 Summary of reported luminescent and magnetic core-shell nanomaterials

Magnetic species (core)	Luminophore (shell)	Method/conditions	Reference
Fe_3O_4	GdF_3:Er^{3+},Yb^{3+}	Coprecipitation	[92]
Fe_3O_4	Gd_2O_3:Eu^{3+}	Heating at 90 °C/calcination	[93]
Fe_3O_4	LaF_3:Ce^{3+},Tb^{3+}	Coprecipitation	[94]
Fe_3O_4	LaF_3:Yb^{3+},Er^{3+}	Coprecipitation/heating at 400 °C under N_2	[86]
Fe_3O_4	$NaGdF_4$: Yb^{3+},Er^{3+}	Thermolysis process	[85]
Fe_3O_4	α-$NaYF_4$:Yb^{3+},Er^{3+}	Hydrothermal/calcination/ion exchange	[3]
Fe_3O_4	YF_3:Ce^{3+},Tb^{3+}	Coprecipitation	[87]
Fe_3O_4	Y_2O_3:Eu^{3+}	Hydrothermal/calcination	[84]
Fe_3O_4	Y_2O_3:Tb^{3+}	Hydrothermal/calcination	[95]
Fe_3O_4	Y_2O_3:Yb^{3+},Er^{3+}	Heating/calcination under N_2	[96]
$FeYO_3$	Y_2O_3:Eu^{3+}	Hydrothermal/calcination/melamine/N_2	[97]
$CoFe_2O_4$	Y_2O_3:Eu^{3+}	Electrospinning technique/calcination	[98]
Fe_3O_4	YVO_4:Eu^{3+}	Coprecipitation	[99]
Fe_3O_4	CdSe	Thermal decomposition	[88]
Fe_3O_4	CdTe	Reduction using $NaBH_4$/heating	[100]
FePt	CdS	Thermal decomposition	[91]
Fe_3O_4	ZnS	Thermal decomposition	[101]

4.2.2.2 Crosslink-Assisted Synthesis of Luminescent and Magnetic Hybrid Nanostructures

A notable strategy to prepare bifunctional nanomaterials based on MNPs (e.g., Fe_3O_4) and luminescent compounds (e.g., $NaYF_4:Yb^{3+},Er^{3+}$) involves the use of crosslinking molecules, such as organic compounds, macrocycles (e.g., calixarene), and polymers (e.g., polyacrylic acid), which coassemble together the corresponding luminescent and magnetic entities into single nanostructures. The main difficulty in the combination of luminophores and MNPs is luminescence quenching, which occurs via an energy transfer process when a luminescent center (e.g., RE^{3+} ion) is in direct contact with or in proximity to a magnetic metal oxide surface (e.g., Fe_3O_4). To avoid this phenomenon, an intermediate layer or spacer is usually added to separate the MNPs and luminophores. Therefore, crosslinking molecules, such as organic macrocycles and polymers, may be good candidates for producing stable spacing layers between luminescent centers (e.g., RE^{3+} ions) and quenchers (e.g., Fe_3O_4) and also conjugating luminescent compounds with MNPs to produce bifunctional nanostructures. Several peer-reviewed articles have been published on these kinds of luminescent and magnetic nanomaterials, examining such aspects as their chemical synthesis and surface engineering for biomedical applications.

Yan and coworkers [102] reported superparamagnetic and upconversion emitting $Fe_3O_4/NaYF_4:Yb^{3+},Er^{3+}$ heteronanoparticles, prepared by a crosslinking–assisted strategy. In this synthesis, they used 1,10-decanedicarboxylic acid or 11-mercaptoundecanoic acid as crosslinkers to anchor the Fe_3O_4 nanoparticles onto the surface of $NaYF_4:Yb^{3+},Er^{3+}$ upconversion luminescent nanoparticles. Other interesting bifunctional nanoscale materials are green light–emitting superparamagnetic koosh nanoballs [103], which contain luminescent $LaPO_4:Ce^{3+}:Tb^{3+}$ and magnetic Fe_3O_4 nanoparticles assembled together by *p*-sulfonato-calix[6]arene macrocycle. Recently, Khan and coworkers [1] reported red-green–emitting and superparamagnetic nanomarkers based on Fe_3O_4 nanoparticles and rare-earth complexes conjugated together by *p*-tetrakis(carboxymethyl)calix-4-arene tetrol macrocycle (Fig. 4.8). In this work, the authors functionalized in situ Fe_3O_4 nanoparticles with *p*-tetrakis(carboxymethyl)calix-4-arene tetrol macrocycle via coprecipitation, then linked them to rare-earth complexes in one-pot syntheses.

Cheng and coworkers [4] described a novel class of multifunctional optical and magnetic nanomaterials based on upconversion luminescent $NaYF_4:Y^{3+}:Yb^{3+}:Er^{3+}$ and iron oxide nanoparticles. These nanomaterials are prepared by a LBL self-assembly procedure. In this procedure, ultrasmall superparamagnetic dopamine–modified iron oxide (Fe_3O_4) nanoparticles are adsorbed onto the surface of polyacrylic acid (crosslinking)–modified $NaYF_4:Y^{3+},Yb^{3+},Er^{3+}$ nanoparticles by electrostatic attraction to produce $NaYF_4:Y^{3+},Yb^{3+},Er^{3+}/Fe_3O_4$ nanostructures, and on top of which a thin gold shell is formed by seed-induced reduction growth.

Polymer-assisted assembly or encapsulation of MNPs and luminophores, for example fluorescent dyes or QDs, together into the same particles, on the basis of the methods used for the preparation of magnetic or fluorescent polymeric

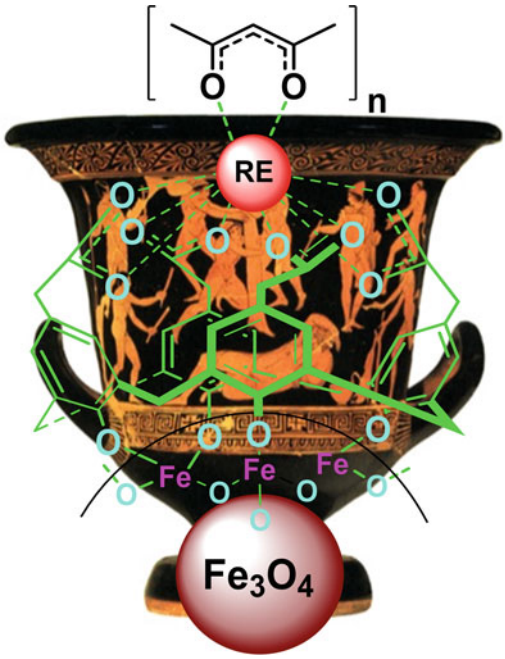

Fig. 4.8 Schematic illustration of structure of luminescent and magnetic nanoparticles containing Fe_3O_4 functionalized with RE^{3+} complex of β-diketonate and calixarene as ligands—Fe_3O_4@calix-RE(TTA or ACAC). Reproduced with permission from ref. [1]

particles, is widely used for the preparation of luminescent and magnetic nanomaterials. MNPs and fluorophores encapsulated together in nano- or micron-sized polymer particles can be fabricated by, for example, emulsion or miniemulsion polymerization, LBL self-assembly, solvent evaporation, or a microfluidic device for large-scale production (Table 4.3). Although the fluorescent and magnetic nanomaterials prepared by this concept can prevent MNPs from leaching into media and, consequently, maintain their magnetic properties, the luminescence quenching that occurs because of the close proximity of MNPs (quencher) to fluorophores is a serious concern. On the other hand, coating the polymer on single or aggregated magnetic core nanoparticles before introducing luminophores offers a promising solution to prevent the quenching effect.

Recently, Chen and coworkers [112] reported on a remarkable approach to coassemble MNPs with fluorescent QDs to form colloidal magnetofluorescent supernanoparticles. This strategy is based on combining CdSe-CdS core-shell QDs with Fe_3O_4 MNPs in the presence of dodecyltrimethylammonium bromide (DTAB) as a surfactant to produce QD-MNP micelles. Subsequent encapsulation of the QD-MNP micelles in PVP and ethylene glycol (EG) results in the formation of magnetofluorescent core-shell supernanoparticles. Additional thermal treatment transforms the randomly assembled Fe_3O_4 core nanoparticles into a periodic assembly with an fcc superlattice, producing magnetofluorescent core-shell supernanoparticles with a supercrystalline magnetic core.

Table 4.3 Bifunctional nanomaterials prepared by organic compound/polymer–assisted integration of luminophores with magnetic nanoparticles

Crosslinker (organic compound/polymer)	Magnetic species	Luminophore	Method	Reference
Calix	Fe_3O_4	$LaPO_4:Ce^{3+}:Tb^{3+}$	Coprecipitation/self-assembly process	[103]
Calix	Fe_3O_4	Eu^{3+} and Tb^{3+} complexes	Coprecipitation/RE^{3+} complex synthesis	[1]
1,10-Decanedicarb-oxylic acid or 11-mercaptoundecanoic acid,	Fe_3O_4	$NaYF_4:Yb^{3+},Er^{3+}$	Crosslink anchoring strategy	[102]
Poly(St-co-GMA)/Poly(St-NIPAM)	Fe_3O_4	Eu^{3+} complex ($Eu(AA)_3Phen$)	Two-step seed emulsifier–free emulsion polymerization technique	[104, 105]
PEG-diacid/polyethyleneglycol-bis-carboxymethyl ether	Fe_3O_4	$YPO_4:Eu^{3+}$	Covalent conjugation via amide bond formation	[106]
PEG	Fe_3O_4	$CaMoO_4:Eu^{3+}$	Encapsulation of $CaMoO_4$: Eu^{3+} and Fe_3O_4 in PEG by ultrasonication	[107]
Polyacrylic acid	Fe_3O_4	$NaYF_4:Y^{3+}:Yb^{3+}:Er^{3+}$	Polymer-assisted LBL deposition	[4]
PLGA	Fe_3O_4	Mn:ZnS QDs	Emulsion evaporation method	[108]
PSS and PAH	Fe_3O_4	CdTe QDs	LBL technique	[109, 110]
Commercial polymer having −SH and −COOH	γ-Fe_2O_3	CdSe/ZnS	Organic/water two-phase mixture	[111]

(continued)

Table 4.3 (continued)

Crosslinker (organic compound/polymer)	Magnetic species	Luminophore	Method	Reference
Polyvinylpyrrolidone/Ethylene glycol	Fe_3O_4	CdSe-CdS	Micelle process and encapsulation of QD-MNP micelles in PVP/EG	[112]
PS-co-AA	Fe_3O_4	PMI	Three-step miniemulsion process	[8]
PCL-b-PMAA	$MnFe_2O_4$	Pyrene	Nanoemulsion method	[113]
EG-diacrylate/PSSS/PAH	Fe_3O_4	Rhodamine B	Microfluidic device-based method/LBL	[114, 115]
PS	Janus magnetic emulsion	1-Pyrene carboxaldehyde	Swelling diffusion method	[116]
CS	γ-Fe_2O_3	FITC	Coating of FITC-CS onto γ-Fe_2O_3 surface	[117, 118]
P(HEMA)@P(NIPAAMco-AA)	Fe_3O_4	FITC	Combination of sol-gel, distillation precipitation polymerization (DPP), and RAFT polymerization process	[119]
PEG	$MnFe_2O_4$	1-Pyrene butyric acid	Self-assembly	[120]
Poly(styrene/divinylbenze-ne/acrylic acid) and CS	Fe_3O_4	FITC	Miniemulsion polymerization	[121]

4.2.2.3 SiO_2-Assisted Synthesis of Luminescent and Magnetic Nanomaterials

Silanization is a remarkable technique for the surface modification of MNPs that gives to nanoparticles biocompatibility and greater chemical and mechanical stability against variations in pH or temperature. The surface of a silica shell can be further functionalized with fluorescent dye molecules and also introduce specific ligand functional groups to graft with the luminescent metal complexes to produce multifunctional optical and magnetic nanomaterials.

Two essential methods for the coating of MNPs with silica are employed, acidic hydrolysis of silicate in aqueous solution and base-catalyzed hydrolysis of silicate (e.g., tetraethyl orthosilicate) in a mixture of organic solvent (e.g., ethanol) and water such as in a modified Stöber method [122]. In addition, a base-catalyzed silica coating of magnetic iron oxide nanoparticles was also reported by a water-in-cyclohexane microemulsion method, using a surfactant such as Triton X-100 [123], by which, generally, monodisperse uniform core-shell MNPs are obtained.

The silica coating of MNPs with the Stöber method is usually required in the pretreatment of these nanoparticles with small amounts of silicate in an aqueous solution in order to avoid their aggregation. Nevertheless, direct silica coating with TEOS in a mixture of ethanol and aqueous ammonia produces MNP clusters embedded in large silica aggregates. Moreover, the concentration of pretreated magnetic particles should be less than 12 mg L^{-1}; otherwise, large aggregates of nanoparticles may form.

Further detailed studies of coating nanoparticles with TEOS have revealed that this process is highly sensitive to experimental conditions such as ethanol/water ratio, concentration of ammonia and TEOS, and temperature. Silica coating using the Stöber method usually requires approximately 12–48 h of mechanical stirring at room temperature to obtain a uniform silica shell on the surface of MNPs. However, heating of the reaction mixture causes large MNP–silica aggregates with irregular morphology.

Recently, Pogorilyi and coworkers [124] reported that base-catalyzed silica coating by the Stöber method causes the oxidation of magnetite (Fe_3O_4) into maghemite (γ-Fe_2O_3). They observed that the larger the amount of TEOS used, the longer the reaction takes to complete, and so the deeper is the oxidation of the original magnetite phase, and in the end there will no longer be magnetite (Fe_3O_4), but predominantly maghemite (γ-Fe_2O_3). In addition, there is no visible transformation of magnetite into nonmagnetic hematite (α-Fe_2O_3), so the material remains strongly magnetic and effectively attracted to the magnet in dispersion and solid phases.

A variety of bifunctional optical and magnetic nanomaterials have been reported, on the basis of a modified Stöber method, using silica-coated magnetic iron oxide nanoparticles functionalized or grafted with luminescent rare-earth or transition-metal complexes and fluorescent dyes. Zhang and coworkers [125] reported the preparation of bifunctional nanocomposites by grafting a Tb^{3+} *N*-(4-benzoic acid-yl),*N*′-(propyltriethoxysilyl) urea) complex to SiO_2-coated Fe_3O_4 nanoparticles via

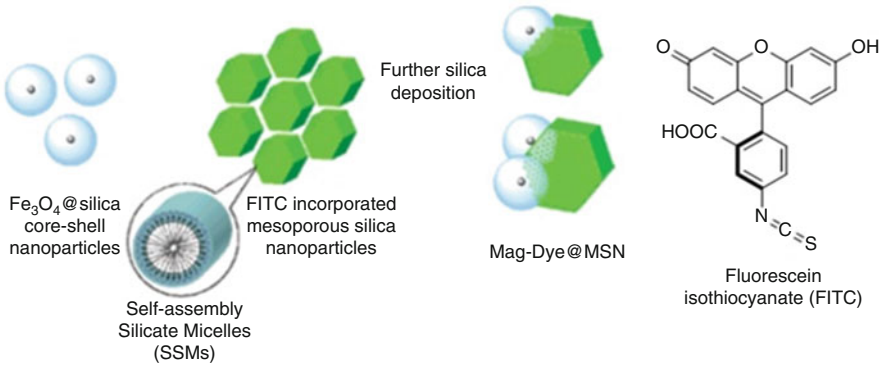

Fig. 4.9 Synthetic procedure of tumblerlike mesoporous silica nanocomposites (Mag-Dye@MSN). Reproduced with permission from ref. [13]

the Stöber method. Subsequently, Fu and coworkers extended the same method to produce Nd- and Yb-based luminescent (NIR) and magnetic nanocomposites using the same ligand and magnetic nanoparticles [126].

Mou and coworkers [13] prepared multifunctional nanocomposites, based on SiO_2-assisted assembly of fluorescent *N*-1-(3-trimethoxy-silylpropyl)-*N*-fluoresceyl thiourea (FITC-APTMS) with magnetic Fe_3O_4@SiO_2 nanoparticles through a self-assembled silicate micelle process (Fig. 4.9), using conditions similar to those of the Stöber method. In addition, bifunctional nanomaterials were reported by the encapsulation or incorporation of iron oxide nanoparticles and metal complexes [e.g., $Ru(bpy)_3Cl_2{\cdot}6H_2O$ complex] [14] in silica matrix through a modified Stöber or base-catalyzed microemulsion method.

4.3 Magnetism

By the 1930s, the magnetic characteristics of materials were extensively exploited owing to their key importance in some of the most significant inventions in modern technology, including magnetic sound recording and magnetic storage. Nothing was more representative of the modern world than the new marvels of radio and television, which incorporated magnetic components as important features of their design. The materials are usually either diamagnetic or paramagnetic and ferromagnetic. Diamagnetism is a phenomenon shown only by atoms that have no net magnetic moment as a result of their shells being filled or have all paired electrons classified as diamagnetic. On the other hand, diamagnetism is overshadowed by much stronger interactions such as paramagnetism and ferromagnetism, which occur in materials that have net magnetic moments due to the presence of unpaired electrons, giving them the classification as paramagnetic and ferromagnetic materials.

Remarkable advances in nanoscience and nanotechnology have led to a revolution in the research area of magnetism and applications of magnetic nanomaterials in different modern technologies having high efficiency. Common computer disks consist of granular magnetic materials, such as CoPtCr, with admixtures of boron or tantalum for recording and storing data. Recently, magnetic nanoscale materials have been widely explored to use in biomedical sciences, such as in drug delivery and the selective destruction of cancer cells through magnetic hyperthermia with photothermal support, still hot topics of research. Therefore, the scientific understanding of magnetism or the magnetic properties of materials remains rudimentary. Therefore, we attempt to explain simply the basic concept of magnetism in materials in a way that can be easily understood by nonspecialist readers.

4.3.1 Origin of Magnetism

Magnetism in materials is a consequence of *magnetic moments* associated with individual electrons. Moving electrons in atoms contain both an orbital magnetic moment $\mathbf{m}_l$, corresponding to their orbital angular momenta (**l**), and a spin magnetic moment $\mathbf{m}_s$, which is proportional to their spin angular momenta (**s**), as shown by Eqs. 4.3 and 4.4. To facilitate understanding, we establish a link between Ampère's ideas about circulating currents and the electronic structure of atoms. We can deduce that it is the angular momenta of electrons in atoms that correspond to Ampère's circulating currents and give rise to the magnetic dipole moment. In fact, the magnetic moment of a free atom in the absence of a magnetic field consists of *two* contributions. One is the motion of electrons in an orbit around the nucleus that give rise to their orbital angular momenta (**l**), and the other is the spin of electrons around their own axis, leading to their spin angular momenta (**s**). The spin and orbital angular momenta combine to produce the observed magnetic moment of atoms, which is measured in *Bohr magneton* (B.M.); consequently, each atom behaves like a tiny magnet:

$$\boldsymbol{m_l} = g_l \mathbf{l} \ \text{(B.M.)}\,, \tag{4.3}$$

$$\boldsymbol{m_S} = g_{SB} \mathbf{s} \ \text{(B.M.)}\,, \tag{4.4}$$

where g_l and g_S are orbital and spin *g-factors,* **s** is the *spin* of an electron, μ_B is *Bohr magneton* (9.274×10^{-24} J T^{-1}) and can be defined in terms of fundamental constants as $\mu_B = \text{B.M.} = \frac{eh}{4\pi mc}$, where e is the electron charge, h Planck's constant, m electron mass, and c the speed of light.

The magnetic moments of atoms, ions, and molecules are usually expressed in B.M., as explained earlier. In addition, the magnetic moment of a single electron is given according to wave mechanics by Eq. 4.5:

$$\mu_B \,(in \ \text{B.M.}) = g\sqrt{S\,(S+1)}, \tag{4.5}$$

where S is simply the absolute value of the spin quantum number (total spin of unpaired electrons in atom or ion) and g is the gyromagnetic ratio, more familiarly known as the g-factor; for a free electron its value is 2. This equation is also known as a "spin-only formula" [12]. The magnetic moment of transition elements is due to the presence of unpaired electrons, so the preceding Eq. 4.5 can be expressed as $\mu_{\text{spinonly}} = \sqrt{4S(S+1)}$ if only the entire spin of unpaired electrons is taken into account. In addition, it can also be related to the number of unpaired electrons n by the following Eq. 4.6:

$$\mu_{\text{spinonly}} = \sqrt{4S(S+1)} \approx \sqrt{n(n+2)}. \tag{4.6}$$

The orbital angular momentum of 3d transition metal ions is usually quenched by other surrounding ions in solid materials. This phenomenon is a consequence of the interaction of electric fields generated by surrounding ions with the 3d orbitals of metal ions restricting the orbital motion of the electrons. It is relevant that these electric fields cause the orbitals of metal ions to be coupled strongly to the crystal lattice, so that they are not able to reorient in response to an applied field and not contribute to the observed magnetic moment. On the other hand, the spins are only weakly coupled to the lattice, so they contribute to the magnetization process and, consequently, to the resultant magnetic moment of the material. In addition, if the orbital angular momentum makes a full contribution to the magnetic moment, then it can be calculated by Eq. 4.7:

$$\mu_{\text{LS}} = \sqrt{g^2 S(S+1) + L(L+1)} \approx g\sqrt{J(J+1)}. \tag{4.7}$$

Therefore, for first-row transition-metal ions in the periodic table, the measured magnetic moment is closer to the calculated one if the *orbital* angular momentum of the electrons is completely ignored. Table 4.4 lists the valuesof the measured and

Table 4.4 Calculated and measured effective magnetic moments for first-row transition-metal ions

Ion	Configuration	Fundamental level	$g\sqrt{J(J+1)}$	$g\sqrt{S(S+1)}$	m/μ_B
Ti^{3+}, V^{4+}	$3d^1$	$^2D_{3/2}$	1.55	1.73	1.8
V^{3+}	$3d^2$	$^3F_2$	1.63	2.83	2.8
Cr^{3+}, V^{2+}	$3d^3$	$^4F_{3/2}$	0.77	3.87	3.8
Mn^{3+}, Cr^{2+}	$3d^4$	$^5D_0$	0.00	4.90	4.9
Fe^{3+}, Mn^{2+}	$3d^5$	$^6S_{5/2}$	5.92	5.92	5.9
Fe^{2+}	$3d^6$	$^5D_4$	6.70	4.90	5.4
Co^{2+}	$3d^7$	$^4F_{9/2}$	6.63	3.87	4.8
Ni^{2+}	$3d^8$	$^3F_4$	5.59	2.83	3.2
Cu^{2+}	$3d^9$	$^2D_{5/2}$	3.55	1.73	1.9

From [127]. Reproduced with permission of John Wiley & Sons

calculated magnetic moments of 3d transition-metal ions using formulas considering the total angular momenta (J) and spin only. It is obvious that values calculated using a spin-only formula are in close agreement with experimental ones compared to values calculated using a formula taking into account the total angular momentum (J). This phenomenon is known as *quenching* of the orbital angular momentum, which is a consequence of the electric field generated by surrounding ions in solid materials. However, in rare-earth elements (from lanthanum to lutetium), there is no *quenching* of the orbital angular momentum, and hence both spin and orbital motions of 4f electrons contribute to the magnetic moment.

4.3.1.1 Magnetic Properties of Trivalent Rare-Earth Ions

Rare-earth ions are paramagnetic owing to the presence of unpaired electrons, with the exception of La^{3+}, Lu^{3+}, and Y^{3+} ions. The magnetic properties of rare-earth ions are determined entirely by the ground state (except for Sm^{3+} and Eu^{3+} ions) because their ground state is well separated by several hundred per centimeter from the next higher lying state (Fig. 4.10) owing to spin–orbit coupling and are thermally inaccessible. Unlike the d electrons of transition-metal ions, the 4f electrons of rare-earth ions are almost unaffected by the chemical environment, and 4f energy levels are the same as in free ions because of the very effective shielding by external filled $5s^2$ and $5p^6$ subshells. Consequently, rare-earth ions in compounds act in the same way as free ions, so their orbital angular momenta are not quenched by electric fields of the chemical environment, which effectively contributes to their magnetic moments (μ_{eff}).

Therefore, the magnetic moments of RE^{3+} ions are calculated in terms of the total angular momentum quantum number (J) by the use of HUND's formula (Eq. 4.8):

$$\mu_{\text{eff}} = g_j \sqrt{J\,(J+1)}, \tag{4.8}$$

where the Landé g-factor is defined by $g_J = \frac{S(S+1)+3J(J+1)-L(L+1)}{2J(J+1)}$.

The theoretical values of the magnetic moments of RE^{3+} ions, calculated with HUND's formula [128], are generally in good agreement with the experimental magnetic moments, with the exception of Sm^{3+} (f^5) and Eu^{3+} (f^6) ions, where the experimentally determined magnetic moments vary considerably with temperature. For these two ions the first excited J state is sufficiently close in energy to the ground state to be considerably populated at room temperature. Since these excited states have higher J values than the ground state, the actual magnetic moments are higher than those calculated by the use of Eq. 4.8 with the value of J for the ground state. Therefore, in the case of Sm^{3+} ions, the thermal population of the higher lying $^6H_{7/2}$ state leads to a magnetic moment of around $1.6\,\mu_B$, rather than $0.845\,\mu_B$, which would be expected if just the $^6H_{5/2}$ ground state were responsible (Table 4.5). Similarly, if the magnetic property of Eu^{3+} ions were determined solely by

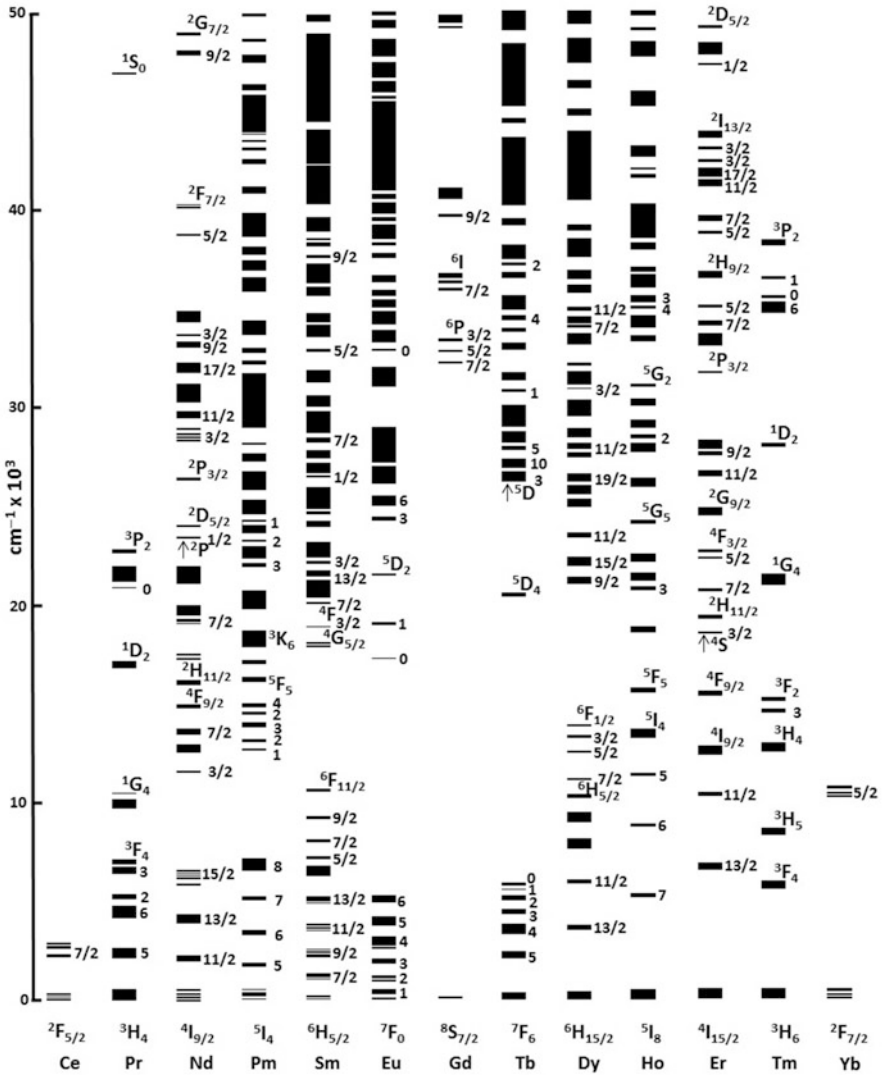

Fig. 4.10 Energy-level structure of Ln^{3+}:LaF_3 based on computed crystal field energies in range 0–50,000 cm^{-1} with labels of ^{2S+1}L and/or J, where the dominant character of the levels can be clearly assigned. This energy-level diagram was reproduced with permission from ref. [28]

the $^7F_0$ ground state, its compounds would be diamagnetic, whereas contributions from thermally accessible levels such as $^7F_1$ and $^7F_2$ [using a Boltzmann factor of exp.$(-\Delta E/kT)$] lead to an observed room-temperature magnetic moment at 3.5 μ_B.

Comparison of the values of the effective magnetic moment (μ_{eff}) calculated from the empirical HUND formula, which is known to fit well with observed magnetic moments for all RE^{3+} except Sm^{3+} and Eu^{3+} ions [129], and by

Table 4.5 Electronic structure and magnetic properties of trivalent rare-earth ions

Z	RE^{3+}	Config. ($4f^n$)	Fund. level	First excited level	ΔE (cm^{-1})	g_J	μ_{calc} spin	μ_{eff} J-Hund	μ_{eff} Van Vleck	μ_{eff} Exp.
57	La	$4f^0$	($^1S_0$)	–	–	–	–	–	–	–
58	Ce	$4f^1$	($^2F_{5/2}$)	($^2F_{7/2}$)	2200	0.86	1.73	2.54	2.56	2.3–2.5
59	Pr	$4f^2$	($^3H_4$)	($^3H_5$)	2100	0.80	2.83	3.58	3.62	3.4–3.6
60	Nd	$4f^3$	($^4I_{9/2}$)	($^4I_{11/2}$)	1900	0.73	3.87	3.62	3.68	3.5–3.6
61	Pm	$4f^4$	($^5I_4$)	($^5I_5$)	1600	0.60	4.90	2.68	2.83	2.7
62	Sm	$4f^5$	($^6H_{5/2}$)	($^6H_{7/2}$)	1000	0.29	5.92	0.84	**1.55–1.65**	**1.5–1.6**
63	Eu	$4f^6$	($^7F_0$)	($^7F_1$)	300	0	6.93	0	**3.40–3.51**	**3.4–3.6**
64	Gd	$4f^7$	($^8S_{7/2}$)	($^6P_{1/2}$)	32,000	2.00	7.94	7.94	7.94	7.8–8.0
65	Tb	$4f^8$	($^7F_6$)	($^7F_5$)	2000	1.50	6.93	9.72	9.7	9.4–9.6
66	Dy	$4f^9$	($^6H_{15/2}$)	($^6H_{13/2}$)	3300	1.33	5.92	10.60	10.6	10.4–0.5
67	Ho	$4f^{10}$	($^5I_8$)	($^5I_7$)	5300	1.25	4.90	10.61	10.6	10.3–0.5
68	Er	$4f^{11}$	($^4I_{15/2}$)	($^4I_{13/2}$)	6500	1.20	3.87	9.58	9.6	9.4–9.6
69	Tm	$4f^{12}$	($^3H_6$)	($^3H_4$)	5800	1.17	2.83	7.56	7.6	7.1–7.4
70	Yb	$4f^{13}$	($^2F_{7/2}$)	($^2F_{5/2}$)	10,000	1.14	1.73	4.54	4.54	4.4–4.9
71	Lu	$4f^{14}$	($^1S_0$)	–	–	–	–	–	–	–

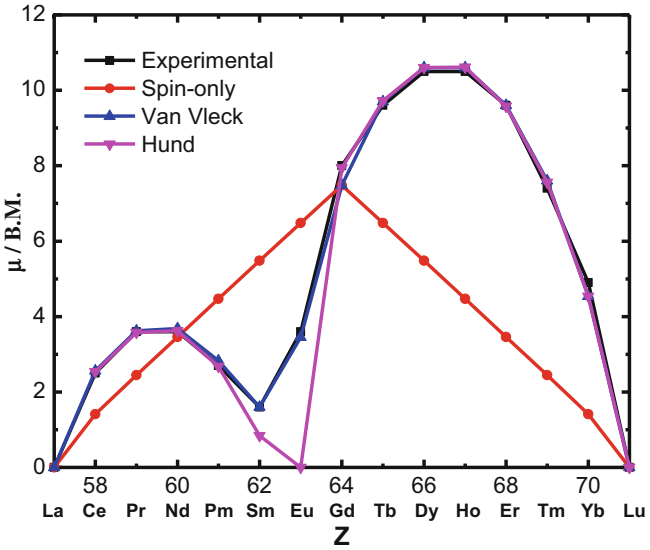

Fig. 4.11 Effective magneton number at room temperature for sequence of trivalent rare-earth ions in configurations $4f^0$, 4f, $4f^2$, ..., $4f^{14}$. Reproduced with permission from ref. [129]

means of the Van Vleck formula [128] gives calculated values that are generally in good agreement with the experimental magnetic moments for all rare-earth ions (Fig. 4.11). The Van Vleck formula describes the dependence of magnetic susceptibility on temperature and is one of the cornerstone relationships in magnetochemistry:

$$\chi(T) = \frac{N\sum_n \left[\frac{\left(E_n^{(1)}\right)^2}{KT} - 2E_n^{(2)} \right] \exp\left(-\frac{E_n^{(0)}}{KT}\right)}{\sum_n \exp\left(-\frac{E_n^{(0)}}{KT}\right)} \tag{4.9}$$

The effective Bohr magneton number (commonly defined as the effective magnetic moment) μ_{eff} is usually deduced from the magnetic susceptibility by the relation

$$\mu_{\text{eff}} = \left(\frac{3K_b \chi^T}{\mu_0 N_A \mu_B^2} \right)^{1/2}. \tag{4.10}$$

The experimental magnetic moments of rare-earth ions in the second half of the series are greater than in the first half (Table 4.5). For RE^{3+} ions, the magnetic moments are attributed to the J ground state values, where $J = L - S$ is lower if the electron number is less than half the $4f^7$ configuration ($n < 7$), and $J = L + S$

is larger if the electron number is greater than 7 in the $4f^n$ configuration ($n > 7$). Thus, the total angular momentum (J) has a key role during the calculation of the magnetic moments in rare-earth ions, and as a result, the spin-only formula cannot be applied to rare-earth ions (Fig. 4.11).

It is noteworthy that the rare-earth elements are good candidates for designing permanent magnets owing to the higher values of their magnetic moments. Therefore, neodymium magnets are the strongest permanent magnets, commercially available, and used in modern technologies such as hard disk drives. This magnet is an alloy of neodymium, iron, and boron, represented by the formula $Nd_2Fe_{14}B$, and has a tetragonal crystalline structure. In addition, among the common magnetic compounds are metal oxides, which are chemically bonded compositions of metals with oxygen, such as iron oxides and ferrites.

4.3.2 Magnetic Induction and Magnetization

When a magnetic field, $\boldsymbol{H}$, is applied to a material, the response of the material is called its *magnetic induction*, $\boldsymbol{B}$. The relationship between $\boldsymbol{B}$ and $\boldsymbol{H}$ is a property of the material and can be expressed by Eq. 4.11 (in centimeter–gram–second, or cgs, units) [127]:

$$\boldsymbol{B} = \boldsymbol{H} + 4\pi\boldsymbol{M}, \tag{4.11}$$

where $\boldsymbol{M}$ is the *magnetization* of the medium and is usually defined as the magnetic moment ($\boldsymbol{m}$) per unit volume ($\boldsymbol{V}$), as shown by Eq. 4.12:

$$\boldsymbol{M} = \frac{\boldsymbol{m}}{\boldsymbol{V}} \frac{\text{emu}}{\text{cm}^3}. \tag{4.12}$$

$\boldsymbol{M}$ is a property of the material and depends on both the individual magnetic moments of the constituent ions, atoms, or molecules and on how these dipole moments interact with each other. The cgs unit of magnetization is the emu/cm^3.

It is sometimes more convenient to express the value of magnetization in unit mass rather than unit volume. The mass of a small sample can be measured more accurately than its volume; moreover, the mass is independent of temperature, whereas the volume changes with temperature owing to thermal expansion. The specific magnetization $\boldsymbol{\sigma}$ is defined as the magnetic moment ($\boldsymbol{m}$) per unit mass ($\boldsymbol{w}$), as given by the expression

$$\boldsymbol{\sigma} = \frac{\boldsymbol{m}}{\boldsymbol{W}} = \frac{\boldsymbol{m}}{\boldsymbol{V}\boldsymbol{\rho}} = \frac{\boldsymbol{m}}{\boldsymbol{\rho}} \frac{\text{emu}}{\text{g}}, \tag{4.13}$$

where $\boldsymbol{V}$ is the volume and $\boldsymbol{\rho}$ the density.

Magnetization can also be expressed as the magnetic moment per mole, per unit cell, per formula unit, and so forth. When dealing with small volumes, such as the

unit cell, the magnetic moment is often given in the Bohr magneton, μ_B, where 1 Bohr magneton $= 9.27 \times 10^{-21}$ erg/Oe.

In SI units the relationship between $\boldsymbol{B}$, $\boldsymbol{H}$, and $\boldsymbol{M}$ is given by the expression [127]

$$\boldsymbol{B} = \boldsymbol{\mu}_0 (\boldsymbol{H} + \boldsymbol{M}), \tag{4.14}$$

where μ_0 is the permeability of free space. The units of $\boldsymbol{M}$ are obviously the same as those of $\boldsymbol{H}$ (A/m), and those of μ_0 are weber/(A m), also known as henry/m. Therefore, the units of $\boldsymbol{B}$ are weber/m^2, or tesla (T); 1 gauss $= 10^{-4}$ T.

Magnetic materials are usually composed of small regions, known as domains, and in each domain the individual magnetic moments of the constituent atoms are aligned with one another and point in the same direction. Magnetic domains are formed in materials that have magnetic ordering, that is, their dipoles spontaneously align owing to the exchange interaction. These materials include ferromagnetic, ferromagnetic, and antiferromagnetic materials. In paramagnetic and diamagnetic materials, the dipoles are aligned in response to an external applied magnetic field and cannot align spontaneously; therefore, they have no magnetic domains. The magnetic domain structure is responsible for the formation of permanent magnets and the attraction of ferromagnetic and ferrimagnetic materials to a magnetic field.

In the case of permanent magnets, the magnetic moments of all or most domains are aligned in a uniform direction to exhibit a net magnetization. In contrast, an unmagnetized magnet possesses domains that are randomly oriented with respect to each other, giving a net magnetization of zero. However, this unmagnetized magnet material can be magnetized if an external high magnetic field $\boldsymbol{H}$ is applied to it; consequently, the domains' magnetic moments are aligned with $\boldsymbol{H}$ to yield a net magnetization $\boldsymbol{M}$ and give an externally observable field whose strength depends on the nature of the magnet material.

4.3.2.1 Magnetization Curves

Irreversible changes in the magnetization of ferrimagnetic and ferromagnetic materials are measured by applying cyclic positive and negative values of the magnetic fields to these materials, yielding curves known as *hysteresis loops*. These measurements initially give a so-called *virgin curve* since the materials come from an unmagnetized or virgin state, which is formed as a result of the magnetization of these materials in the initial stage as the applied field is increased. Then the magnetic structure of the materials is irreversibly altered, preventing this virgin curve from forming, and it is usually withdrawn during experiments.

The magnetization curve of ferrimagnetic and ferromagnetic materials can be illustrated as a graph of $\boldsymbol{B}$ (or $\boldsymbol{M}$) versus $\boldsymbol{H}$, which is also called a *hysteresis loop* (Fig. 4.12). In this case, the magnetic material is started at the origin in an unmagnetized or virgin state, and magnetic induction ($\boldsymbol{B}$) follows the curve from the value of 0 to $\boldsymbol{B}_s$ as the applied magnetic field ($\boldsymbol{H}$) is increased in the positive direction, where $\boldsymbol{B}_s$ is known as *saturation induction* (or $\boldsymbol{M}_s$: *saturation*

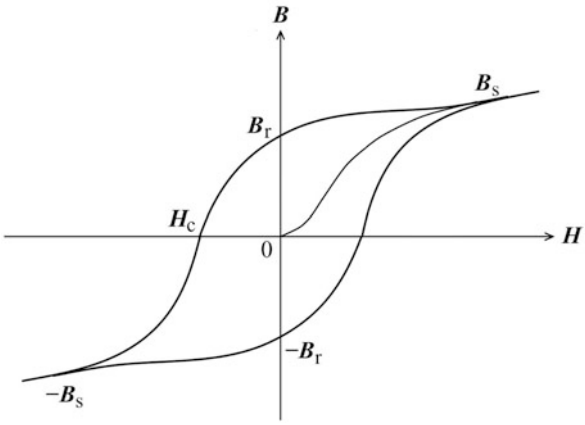

Fig. 4.12 Hysteresis loop for a ferro- or ferrimagnet. Reproduced with permission from ref. [127]

magnetization), which is essentially the limit value to which the curve tends within a high-field region and is reached when all a domain's magnetic moments in a material are aligned with the external field. However, the magnetization ($\boldsymbol{M}$) is constant after saturation, but $\boldsymbol{B}$ continues to increase because $\boldsymbol{B} = \boldsymbol{H} + 4\pi\boldsymbol{M}$ [127]. When $\boldsymbol{H}$ is reduced to zero after saturation, the induction decreases from $\boldsymbol{B}_s$ to $\boldsymbol{B}_r$: *residual induction* (or $\boldsymbol{M}_r$: *remanent magnetisation*), i.e., the material does not recover its unmagnetized state, retaining a certain amount of magnetization at the zero field owing to continued alignment of the domain's magnetic moments in the positive direction. A reversed field in the negative direction that is required to reduce the induction or magnetization to zero is called *coercivity* ($\boldsymbol{H}_C$). Depending on the value of the coercivity, ferromagnetic materials are classified as either hard or soft. Hard magnetic materials require a large field to reduce their induction or magnetization to zero, whereas soft materials are easily saturated but also easily demagnetized. When the reversed field is increased further, saturation is achieved in the reverse or negative direction, which leads to the formation of a hysteresis loop. In the case of superparamagnetic nanoparticles, the magnetization curves show almost zero *remanent magnetization* ($\boldsymbol{M}_r$) and zero *coercivity* ($\boldsymbol{H}_C$) values.

4.4 Luminescence

The term *luminescence* was introduced in 1888 by German physicist Eilhard Wiedemann; it can be explained as the emission of light by certain materials at relatively low temperatures (cold light), to be distinguished from emissions owing to incandescence (hot light), such as fire light, candles, oil lamps, and gas light. Incandescence is usually produced by the direct heating of matter to high temperatures, which results in the emission of light over a continuous range of energies (wavelenghts) in correlation with temperature. Luminescence, by contrast, is the emission of radiation at normal, lower temperatures when luminescent

materials are excited with often invisible energy sources such as ultraviolet light, electric fields, X-rays, energetic particles from radioactive decay, and so on.

Therefore, on the basis of the nature of the exciting source, luminescence is subdivided into a number of categories. Some of the most studied ones are *photoluminescence* (emission after excitation by irradiation with electromagnetic radiation), *electroluminescence* (emission by a recombination of electrons and holes under the influence of an electric field), *radioluminescence* (emission of light upon excitation owing to ionizing radiation), *cathodoluminescence* (emission after excitation with cathode rays), *chemiluminescence* (nonthermal production of light by a chemical reaction), or *triboluminescence* (emission observed by applying mechanical stress to crystals or by the fracture of crystals). Solid materials that give luminescence are called phosphors or, latterly, luminescent materials.

In this chapter, we discuss the luminescence spectroscopy of rare-earth ions (RE^{3+}), and, following the conventions of the International Union of Pure and Applied Chemistry, we usually use *fluorescence* in connection with processes that occur without changes in spin, typically $S_1 \rightarrow S_0$ ($\Delta S = 0$) or Yb^{3+} ($^2F_{5/2} \rightarrow {}^2F_{7/2}$) transitions, and *phosphorescence* for transitions implying a change in spin [130], typically $T_1 \rightarrow S_0$ ($\Delta S \neq 0$) or Eu^{3+} ($^5D_0 \rightarrow {}^7F_J$) transitions.

4.4.1 Rare-Earth Luminescence

Rare-earth elements include lanthanides, ranging from lanthanum to lutetium (Ln: La, Ce, Pr, Nd, Pm, Sm, Eu, Gd, Tb, Dy, Ho, Er, Tm Yb, Lu), scandium (Sc), and yttrium (Y). These elements have similar physical and chemical properties. The similarity of trivalent lanthanide ions to each other, especially to their neighbors, are due to their general adaptation of the +3 oxidation state in aqueous solution, which causes their separation to be an extremely difficult process. The rare earths usually occur in compounds as RE^{3+} ions; other oxidation states are stable only when an empty ($4f^0$), half-filled ($4f^7$), or full ($4f^{14}$) subshell is produced. The predominant oxidation state is trivalent (Ln^{3+}, Sc^{3+}, Y^{3+}), though divalent (Sm^{2+}, Eu^{2+}, Tm^{2+}, Yb^{2+}) and tetravalent states (Ce^{IV}, Pr^{IV}, Tb^{IV}) can also be encountered. The electronic configuration of RE^{3+} ions is represented by $[Xe]4f^n$, which shows a gradual increase in the number of electrons n with increasing the atomic numbers of the ions [31], ranging from $4f^0$ to $4f^{14}$ for La^{3+} to Lu^{3+} ions.

RE^{3+} ions exhibit a number of features in their chemistry that differentiate them from the d-block metals: (1) high coordination numbers (generally between 6 and 12); (2) coordination geometries that are determined by ligand steric factors rather than ligand field effects; (3) formation of labile "ionic" complexes that undergo facile exchanges of ligands; (4) small ligand field splitting and very narrow emission and absorption bands in comparison with d-block metals; (5) a preference for anionic ligands with donor atoms even of high electronegativity (e.g., N, O, F); (6) ready formation of hydrated complexes (on account of the high hydration energy of the small Ln^{3+} ion).

The remarkable feature of RE^{3+} ions is their photoluminescence behavior; some of them show luminescence in the visible or NIR spectral regions under a UV irradiation lamp. The color of the emitted light depends on the RE^{3+} ion. For instance, Eu^{3+} emits in red, Tb^{3+} in green, Sm^{3+} in orange, and Tm^{3+} in blue light. Yb^{3+}, Nd^{3+}, and Er^{3+} ions are well known for their NIR luminescence [25]. In addition, Pr^{3+}, Sm^{3+}, Dy^{3+}, Ho^{3+}, and Tm^{3+} ions also show transitions in the NIR region, and Gd^{3+} emits in the UV region.

4.4.1.1 Luminescence Spectroscopy of Rare-Earth Ions

The optical properties of rare-earth ions are fascinating and originate in the special features of the electronic $[Xe]4f^n$ configurations ($n = 0$–14). The more common oxidation states are +3, +2, and +4. However, the +3 oxidation state is characteristic of all rare-earth ions that show a $4f^n$ configuration. These 4f configurations generate a rich variety of electronic levels whose number is given by $[(4l + 2)!/(4l + 2 - n)n!]$, yielding 3003 sublevels for Eu^{3+} and Tb^{3+} ions. They are characterized by three quantum numbers, S, L, and J within the frame of a Russell–Saunders spin–orbit coupling scheme [32]. The energies of these levels are well defined owing to the shielding of 4f electrons by the filled $5s^25p^6$ subshells, and they are not very sensitive to the chemical environments in which the rare-earth ions are placed. Therefore, in RE^{3+} complexes the ligands in the first and second coordination spheres perturb and split the $^{2S+1}L_J$ energy levels of the RE^{3+} ions only slightly. This shielding is responsible for the specific properties of the rare-earth luminescence, more particularly the narrow emission bands and the long lifetimes of the excited states owing to forbidden 4f–4f transitions. Moreover, in particular, Ce^{3+} ions show intense broad emission bands due to the allowed f–d transitions, and the position of the emission maximum strongly depends on the ligand environment of the Ce^{3+} ions [131]. The 4f–4f transitions are parity forbidden; however, Laporte's rule is slightly relaxed for these transitions owing to the mixing of opposite parity electronic configurations produced by the odd components of a noncentrosymmetric ligand field. Moreover, ligand polarization effects have been shown to be of considerable importance for 4f–4f transitions.

The existence of different energy levels (Fig. 4.10) for rare-earth ions is a consequence of different interactions operating in the $4f^n$ electronic configuration of ions. Depending on the number, the electrons can distribute in many ways over the $4f^n$ configurations; however, some distributions are energetically more favorable. Each different electronic arrangement is called a *microstate*. For systems with more than one $4f^n$ electron, such as Eu^{3+} ions ($4f^6$) [132], the degeneracy of the $4f^n$ configuration is partly or totally lifted by several perturbations acting on the RE^{3+} ions: electron repulsion, spin–orbit coupling, ligand field perturbation, and eventually the Zeeman effect (Fig. 4.13). Electron repulsion is the electrostatic interaction between different electrons in a 4f subshell. Spin–orbit coupling results from interactions between the spin magnetic moment and the orbital magnetic moment of electrons. The ligand field effect is caused by interactions between 4f

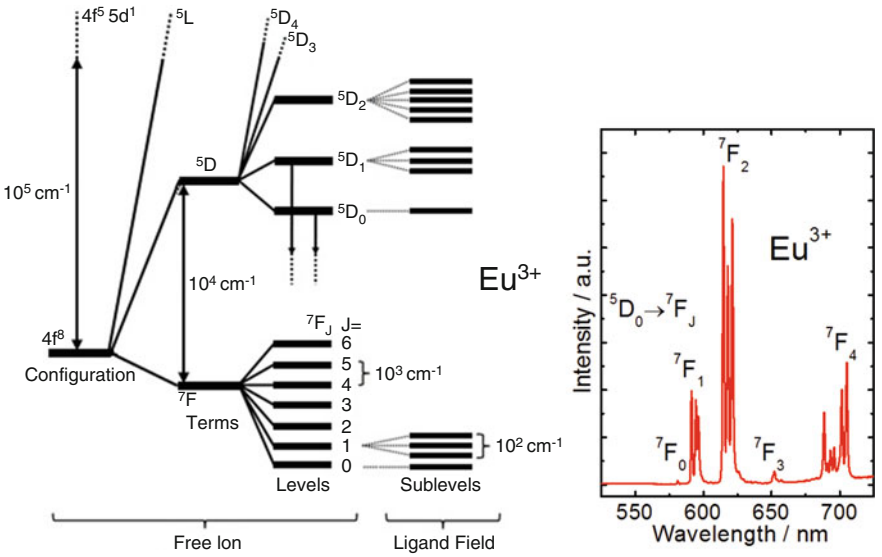

Fig. 4.13 Partial energy diagram of Eu^{3+} ($4f^6$) (*left*) showing relative magnitude of interelectronic repulsion (terms), spin–orbit coupling (levels), and crystal-field effects (sublevels). The *downward arrows* indicate the excited states $^5D_0$ and $^5D_1$ from which luminescence occurs. Reproduced with permission from ref. [132]. Emission spectrum (*right*) of Eu^{3+} complex

electrons and electrons of the ligands. The Zeeman effect is the splitting of energy levels by an external magnetic field.

Electrostatic repulsion splits the electronic configuration into spectroscopy terms labeled by "^{2S+1}L" according to the spin multiplicity $2S + 1$ and the total angular momentum L with a separation at around 10^4 cm^{-1} (Fig. 4.13). The terms are usually denoted by capital letters of the Latin alphabet, for example, S ($L = 0$), P ($L = 1$), D ($L = 2$), F ($L = 3$), G ($L = 4$), H ($L = 5$), I ($L = 6$), K ($L = 7$), L ($L = 8$), M ($L = 9$). Notice that the letter J is not used as a term label. The nomenclature for spin multiplicity is singlet, doublet, triplet, quartet, quintet, sextet, and septet for $2S + 1 = 1, 2, 3, 4, 5, 6, 7$, respectively [132]. The spin–orbit interaction (between two magnetic dipoles) removes the degeneracy of the ^{2S+1}L spectroscopy terms into J levels of free ions characterized by L, S, J quantum numbers and labeled by $^{2S+1}L_J$ levels. These levels are relatively higher (10^3 cm^{-1}) because of the heavy rare-earth nucleus (Fig. 4.13). The energy levels of a *free ion* can be described by $^{2S+1}L_J$ levels, where $2S + 1$ represents the total spin multiplicity, L the total orbital angular momentum, and J the total angular momentum of 4f electrons.

On placing RE^{3+} ions in a chemical environment, such as organic ligands or inorganic matrices, the spherical symmetry of free ions is destroyed and each spectroscopic level (J-levels) further splits under the influence of the asymmetric electric field produced by the chemical environment, called a ligand field or crystal field. This interaction removes, to a certain degree, the degeneracy of free-ion levels.

The magnitude of the splitting of the $^{2S+1}L_J$ energy levels was first parameterized in the simplest way assuming a point charge electrostatic model (PCEM) generated by the chemical environment around the rare-earth ions. The ligand field effect (H_{LF}) further lifts the $(2J + 1)$ degeneracy of the J levels in free ions, depending exclusively on the point of symmetry about the RE^{3+} ions [31], which are called crystal-field levels (or Stark levels). The splitting of the energy levels by the ligand field effect is of the order of a few hundred per centimeter (around 10^2 cm^{-1}).

Luminescence originating from intraconfigurational d transitions is quite different from that of 4f–4f ones. The spectra of d metals are much poorer in the number of observed pure zero-phonon transitions since d^n configurations have much fewer microstates than $4f^n$ ones. The vibronic interaction is much stronger than those of 4f–4f transitions. In addition, for d-transition elements, the ligand field interaction is at least one order of magnitude greater due to the nonscreened and more extended d radial distribution. These facts produce very broad d–d transition bands [29]. Transition-metal complexes usually have lower coordination numbers (4 and 6) than f elements. In the case of fourfold tetrahedral coordination, d–p mixing relaxes Laporte's rule, allowing for d–d transitions, while in the case of octahedral coordination Laporte's rule is not relaxed, except for vibronic interactions that instantaneously break down the center of inversion and allow for the d–d transitions, with much weaker intensities than in the tetrahedral case. Ligand polarization effects on d–d transitions, to our knowledge, have not yet been investigated.

4.5 Biomedical Applications

4.5.1 Bioimaging

Multimodal imaging may play an important role in the diagnoses of diseases and perhaps replace conventional single imaging techniques in the near future, such as magnetic resonance imaging (MRI), X-ray computed tomography (CT), positron emission tomography (PET), single-photon emission computed tomography (SPECT), and fluorescent imaging (FI) [133]. Bifunctional optical and magnetic nanomaterials can be used as agents to combine both magnetic resonance and fluorescent imaging, in order to record multiple images of the anatomical and physiological processes of the body at the same time with enhanced resolution and quality. In this case, the magnetic property of bifunctional nanomaterials can be used as a contrast agent for MRI and the photonic behavior as a tool for fluorescent imaging. However, to the best of our knowledge, little research has been dedicated to multimodal imaging, and MRI is still popular in medical diagnosis.

Magnetic resonance imaging, also known as magnetic resonance tomography (MRT), is a noninvasive medical imaging technique used in diagnosis to capture detailed three-dimensional images of the anatomy of various organs of the body in both health and disease without the use of deleterious radiation. MRI operates on the basis of applying a strong magnetic field and radio frequency waves, so

proton nuclei are decayed by transverse magnetization (T_2 relaxation) in order to recover the longitudinal magnetization (T_1 relaxation), which produce electrical radio signals. The durations of T_1 and T_2 relaxations vary in different tissues depending on their composition and nature. However, the relaxation times of various tissues, tumors, and physiological process are superimposed on each other, which makes the dynamic scan and resolution of images difficult to measure. Therefore, to enhance the clarity of imaging, various contrast agents are used to increase or decrease the T_1 and T_2 relaxation times. Functionally, MRI contrast agents can be divided into two groups: T_1 and T_2 contrast agents. Among the T_1 contrast agents, generally Gd^{3+} chelates and, to a lesser extent, Mn^{2+} chelates are widely used; however, gadolinium in the free ionic state is toxic and causes several clinical diseases [134], such as severe allergic reactions, nephrogenic system fibrosis, and kidney failures.

Bifunctional optical and magnetic nanomaterials have been studied for application in MRI, for instance, $Fe_3O_4@SiO_2@GdVO_4:Eu^{3+}$ (5 mol%) nanomaterial shows intense red luminescence and strong magnetism with no cytotoxicity against human erythrocytes and has been proposed as a good candidate for MRI [135]. Recently, Chen and coworkers [136] have reported on bifunctional Poly(MMA-HEMA $Eu(AA)_3Phen)/Fe_3O_4$ nanospheres as a good T_2-weighted MRI contrast agent and for optical imaging with good biocompatibility and 85% cell viability, even at concentrations has high as 1240 $\mu g\ mL^{-1}$. In addition, multifunctional magnetic/upconversion luminescent $Fe_3O_4@LaF_3:Yb^{3+},Er^{3+}$ mesoparticles show efficient T_2 enhancement in MRI with a T_2 relaxivity coefficient (r^2) value of 229 $mM^{-1}S^{-1}$ [86]. In vivo study of multifunctional $NaYF_4:Yb^{3+},Tm^{3+}@Fe_xO_y$ with histological analysis and MTT assays suggest these materials show low toxicity, good biocompatibility, and enhanced T_2 MRI [137]. Moreover, multifunctional $Fe_3O_4@NaLuF_4:Yb^{3+},Er^{3+}/Tm^{3+}$ nanostructures have exhibited good T_2-enhanced MRI with an r^2 value of 21.63 $s^{-1}\ mM^{-1}$ at 0.5 T and low cytotoxicity [138].

In different experiments, owing to the large magnetic moment of superparamagnetic Fe_3O_4, various multifunctional nanomaterials, such as $Fe_3O_4@Y_2O_3:Eu^{3+}$ /PMMA [139], Fe_3O_4-decorated $YPO_4:Eu^{3+}$ hybrid nanostructures by covalent bridging of carboxyl PEGylated Fe_3O_4 and amine-functionalized $YPO_4:Eu^{3+}$ particles [106], $Fe_3O_4@LaF_3:Ce^{3+},Tb^{3+}$ composite nanoparticles [140], $Fe_3O_4@SiO_2@GdVO_4:Dy^{3+}$ [141], $NaYF_4:Yb^{3+},Er^{3+}@Fe_3O_4@Au$ [142], and $Fe_3O_4/SiO_2/NH_2/PAA/CeF_3:Gd^{3+}$ (10%),Tb^{3+} (10%) [143], have been proposed as promising candidates for magnetic resonance contrast agents.

4.5.2 Hyperthermia

Hyperthermia, also known as thermotherapy, compared to conventional radiotherapy is the most potent medical treatment of cancer by magnetically generated heat from MNPs administered at a desired site such as a tumor. It is also known as

thermoradiotherapy when it is combined with radiation therapy [144]. In hyperthermia, when the desired site containing MNPs is exposed to an alternating current magnetic field (ACMF) within a proposed safe frequency range of approximately 100–400 kHz, nanoparticles begin to emit heat via Néel and Brownian pathways [145, 146], increasing the temperature of the surrounding tissue, which either kills the cells or makes them more susceptible to further radiation or drug treatment.

Ideally the viability of cancerous cells can be reduced to a large extent in a temperature range of 42–46 °C. On the basis of the generated temperature variability, there are two types of hyperthermia therapy: (1) thermal ablation at a temperature of >50 °C for a short time period of 10–30 min and (2) mild hyperthermia at a temperature of 42–45 °C for 30 min [147]. Hyperthermia therapy also acts by damaging the blood vasculature, impairing nutrient and oxygen supplies, or dilating blood vessels, where increased blood flow can carry large amounts of drug and oxygen, which is a potent radio sensitizer that makes tumor cells more susceptible to radiotherapy. It also causes a deterioration of tumor cells by the entropy of cellular structures [148, 149], such as DNA and protein, and immunological cells kill them as well, leading to tissue necrosis.

Note that the specific absorption rate (SAR) and the particle size are more important for achieving an adequate temperature in hyperthermia treatment. Therefore, MNPs are designed in such a way as to give a reasonably small size and maximum SAR [150]. The power released by the MNPs is assessed by their SAR or their specific losses per cycle (SLPC) denoted by A, linked by the equation $\mathrm{SAR} = Af_{\mathrm{exc}}$, where A is the area of the hysteresis loop and f the sweeping frequency of the magnetic field. An increase in SAR above 1 kW g^{-1} could be beneficial regarding several aspects of hyperthermia applications, but it represents a significant challenge.

Recently, significant research interest has been dedicated to designing bifunctional nanomaterials with efficient luminescent and magnetic properties for cancer therapy with hyperthermia. The luminescence properties of these nanomaterials can act as an internal thermometer to monitor changes in temperature of the surrounding tissues due to the heat generated by these magnetic particles deposited in corresponding tissues under the influence of an AC magnetic field. Therefore, several attempts have been made to develop multifunctional nanocomposites showing high thermal energy transfer capability, combining efficient magnetic and optical material in a single biocompatible nanostructure entity.

Among these nanomaterials, $YPO_4:Tb^{3+}@Fe_3O_4$ has been studied for magnetic hyperthermia, which produces a temperature of 42 °C with an SAR value of 39.22 W g^{-1} under an AC magnetic field of 110 Oe and 425 kHz frequency in 10 min [151]. Fe_3O_4–$CaMoO_4:Eu^{3+}$ hybrid MNPs present a good heating capacity, achieving 42 °C temperature in 9 min under the 300 A applied current and within 4.3 min, using 400 A applied current with 19 W g^{-1} and 26 W g^{-1} SARs values, respectively [107]. In addition, SnO_2:5Tb/Fe_3O_4 nanoparticles generate 42 °C at 300 and 400 A in 149 and 57 s with SAR values of 37 and 53 W g^{-1}, respectively [152]. Hybrid nanomaterials of $CaF_2:Eu^{3+}$, Mn^{2+}, and Fe_3O_4 have demonstrated the an ability to produce a temperature of 42 °C under an AC magnetic field

of 265 kHz and 335 Oe with a very high SAR of 283 W g^{-1} [9], while with Fe_3O_4@YPO_4:Eu^{3+} a hyperthermia temperature of 42 °C was obtained at a 400 A current within 10 min [153]. Therefore, these previously reported results suggest that optical and magnetic nanomaterials may be strong candidates for magnetic hyperthermia with self-monitoring temperature capability but will still represent a challenge in the field of medical therapies for cancer.

4.5.3 Drug Delivery

Drug delivery is engineered technology for the controlled administration of pharmaceutical compounds to a tissue of interest in order to achieve the maximum concentration of therapeutic agents while reducing the concentration in other tissues. Initial attempts to manipulate devices in the body with extracorporeal magnets began in the 1950s. Thus, owing to recent advancements in nanotechnology, interest in magnetic drug targeting has grown significantly [154], including the use of iron oxides—magnetite (Fe_3O_4) and maghemite (γ-Fe_2O_3) nanoparticles—as drug delivery vehicles for therapeutic applications exploiting magnetic systems.

Drug carrier MNPs are usually based on a core of iron oxide coated with silica, gold, or polymer, for example, to functionalize and load easily with the corresponding drug molecules. Maghemite (γ-Fe_2O_3) is one of the most suitable materials for the core of MNPs because it is causes fewer health hazards, and Fe^{3+} ions are widely found in the human body. On the other hand, the use of magnetite (Fe_3O_4) nanoparticles can be detrimental owing to the release of Fe^{2+} ions, which generate toxic hydroxyl radicals via Fenton reactions [155]. Drug molecules are loaded in various ways to magnetic iron oxide–based drug delivery vehicles: they are (1) linked directly to the activated surfaces of iron oxide nanoparticles, (2) encapsulated together in stimulus-responsive hydrogel/polymer frameworks, (3) trapped in magnetoliposomes, and (4) loaded in the polymer interspace of magnetic nanoclusters [156]. These cargo particles are guided by an external magnetic field to the target tissues, where they are unloaded by different mechanisms, such as varying the pH, osmolality, temperature generated by an external alternating magnetic field (e.g., for superparamagnetic iron oxide nanoparticles), heating with shortwave radio-frequency fields, irradiation with ultraviolet, visible light or NIR light, and by enzymatic activity.

Recently, multifunctional nanomaterials coassembling luminescent and magnetic features into single nanoparticles are the subject of great research interest owing to their therapeutic application as targeted drug delivery vehicles. In this case, the superparamagnetic and luminescent properties of these nanoparticles allow for the visualization of targeted locations (e.g., tumors) using T_2-wieghted MRI and fluorescent imaging [157], whereas magnetic behavior can also be utilized to manipulate and deliver a drug to a target with extracorporeal magnets, providing a new tool for understanding the physiochemical process of cells in developing cancer tissues.

Multifunctional magnetic iron oxide nanoparticles functionalized with inorganic materials, lipids, or polymers not only act as carriers of targeted drugs but also have potential in therapeutic and diagnostic applications. For instance, multifunctional (SPION–DOX–PEG–FA) nanoparticles have been studied as bimodal cancer cell imaging agents [158] and in bimodal cancer treatment through hyperthermia effects and targeted drug delivery. Iron oxide nanoparticles not only act as drug carriers but also as vehicles for targeted gene delivery. Qiu and coworkers [159] reported on stearic-LWPEI-SPIO nanoparticles, which showed a high binding capacity for minicircle DNA (mcDNA), protection efficiency from enzymatic degradation, and a controlled release property in the presence of polyanionic heparin. In addition, stearic-LWPEI-SPIO nanoparticles have been employed successfully in MRI visible delivery of mcDNA.

Upconversion luminescent nanoparticles (UCNPs) have emerged as promising candidates for traceable drug delivery because of their upconversion luminescence and biocompatible properties. On the basis of a drug loading procedure, UCNPs can be classified into three categories: (1) hydrophobic drugs (e.g., doxorubicin), which are encapsulated into hydrophobic pockets generated by polyethylene glycol (PEG)–grafted amphiphilic polymers that are bounded to ligands (e.g., oleic acid) via van der Waals interactions on the surfaces of $NaYF_4$:Yb^{3+},Er^{3+} UCNPs. The release of drug is then controlled by varying the pH in acidic tumor cells [160]; (2) drugs (e.g., ibuprofen) that are deposited in the pores of mesoporous silica shells coated onto the surface of β-$NaYF_4$:Yb^{3+},Er^{3+} UCNPs fibers [161]; (3) drugs that are commonly loaded in hollow spheres created by mesoporous UCNP shells made of rare earth ion–doped $NaYF_4$ materials [162] containing inner MNPs.

Carbon nanotubes (CNTs) decorated with MNPs have also gained attention as promising nanocarriers for targeted drug delivery thanks to their distinct characteristics such as enhanced cellular specificity and uptake, high surface area, and easy conjugation with great therapeutic value and diminished side effects. For instance, Singh and coworkers [163] have reported on the use of magnetic CNTs unsheathed with mesoporous silica to facilitate the loading of bioactive molecules. Mesoporous and magnetic hybrid CNTs exhibited excellent magnetic properties and a high loading capacity for therapeutic molecules, including the drug gentamicin and the protein cytochrome C. In addition, genetic molecules, such as small interfering RNA (siRNA), have also loaded effectively and then released over a period of several days to a week. Consequently, multifunctional magnetic nanomaterials are efficient candidates not only for targeted delivery of drugs but also for targeted delivery of genetic molecules.

4.5.4 Biosensors

Biosensors are composite analytical devices consisting of highly sensitive biological or biologically derived recognition components that interact with target analytes and physiochemical components (transducers) that generate signals. They are used to

detect and monitor various biochemical and physiological life processes [164]. The working principle of these devices involves the binding of desired target species to biorecognition elements fixed on a suitable support matrix connected to a transducer. The binding of analytes causes changes in the physical or chemical properties of bioreceptive elements together with the support matrix, which can then be sensed by a transducer to generate an electrical signal. This generated signal quantifies the amount of analyte deposited on the system.

Nanotechnology-based nanobiosensors utilizing nanocantilevers as transducers can provide extreme sensitivity in the detection of targeted species such as biomolecules down to the level of a single particle [164, 165]. Biosensing strategies based on MNPs offer great advantages over other sensing techniques. For instance, MNPs are inexpensive to prepare, physically and chemically stable, biocompatible, and environmentally safe. In addition, biological samples usually exhibit no magnetic background; therefore, highly sensitive measurements can be performed in turbid or otherwise visually obscured samples without further processing [166]. MNP-based sensing has remarkable applications in tissue matching, gene analysis, detection of genetic disorders, forensic applications, and for taking immediate action against infectious agents or onsite emergent contaminations. These biosensors are virtually designed via the immobilization of biological recognition elements of DNA, for example, enzymes, tissue, antibodies, microorganisms, cell receptors, and organelles on the surface of magnetic nanoparticles. In addition, to date, numerous methods have been developed to sense biomolecules using magnetic labels. These methods include various techniques that use magnetometers, such as SQUID, magnetoresistive sensors, and Hall sensors to directly detect magnetic particles.

CNTs are also among the most studied materials in sensing and biosensing applications since they have a large surface area, controlled nanostructure, chemical and thermal stability, and good electronic and optical features. Recently, Fe_3O_4@SiO_2-decorated multiwalled carbon nanotube (MWCNT) nanocomposites have been employed to fabricate a modified carbon-paste electrode (CPE) for the sensing of uric acid [167]. In addition, multifunctional nanostructures based on Fe_3O_4 nanoparticles and carbon nanomaterials, such as graphene oxide (GO) and reduced graphene oxide (rGO), have been used for a variety of applications. Teymourian and coworkers [168] reported on Fe_3O_4-decorated rGO nanosheets for the electrochemical sensing of various analytes, such as ascorbic acid, uric acid, dopamine, NADH, and nitric acid.

Rare-earth materials are promising candidates for biodetection and bioimaging, owing to their low toxicity, high photothermal stability, notable electronic structures, long luminescence lifetimes, and tunable emission colors from UV (Gd^{3+}) to visible (Sm^{3+}, Eu^{3+}, Tb^{3+}, Dy^{3+}) and NIR (Nd^{3+}, Yb^{3+}, Er^{3+}) regions [32, 169]. Moreover, they have the capability for time-resolved fluorescence imaging in the quantitative detection of genes, tissue-specific transcripts, and antigens and can be used effectively for the noninvasive, nondestructive, and real-time in vivo diagnosis of various diseases. Nichkova and coworkers [170] reported on the application of poly(L-lysine)-encapsulated Gd_2O_3:Eu^{3+} nanoparticles as fluorescent labels in competitive fluorescence microarray immunoassays to detect phenoxybenzoic acid.

$YVO_4:Eu^{3+}$ nanoparticles have also been used as luminescent probes for the detection of rabbit immunoglobulin G (IgG) analyte [171] through a sandwich immunoassay strategy.

Upconversion luminescent materials are generally more advantageous for biosensing because they produce no autofluorescence from cells and tissues and are excited by nondeleterious NIR light that has strong penetration ability and high detection sensitivity [172]. Niedbala and coworkers [173] have reported the application of upconversion phosphors to detect amphetamine, the opiate methamphetamine, and phencyclidine in saliva, utilizing a lateral flow–based strip assay. In addition, MnO_2-modified $NaYF_4:Yb^{3+},Tm^{3+}@NaYF_4$ upconversion nanoparticles have also been used for the selective and abrupt sensing of glutathione in living cells [174]. On the basis of these reported results, it can be suggested that in the future, highly sensitive biosensor devices will be designed by combining highly target-specific biological sensing elements, such as antibodies and magnetic luminescent nanomaterials, in a nanoprobe. This system will be operational on the basis of principles involving changes in either the optical or magnetic properties of nanoprobes as target materials are attached to biorecognition elements. These changes will be measurable by optical or magnetic sensors fixed in the devices, which remains a challenge in nanobiotechnology and medical diagnosis.

4.6 Conclusions

The reduction in the size of materials to the nanoscale level leads to profound changes in internal structures, which in turn greatly modifies the electronic, optical, and magnetic properties of the materials in comparison with their bulk counterparts. Thus, various research groups in science and engineering disciplines are focusing on nanoscale materials. In addition, hundreds of peer-reviewed articles have been published in various scientific journals on bifunctional nanomaterials that coassemble magnetic and photonic features into single-entity nanostructures, examining their magnetic and luminescent properties as well as their applications in various fields, from biomedical diagnosis and therapy to materials science. These bifunctional nanomaterials are usually based on MNPs and trivalent rare-earth ions or iron oxide nanoparticles functionalized with QDs, fluorescent dyes, and luminescent complexes. In this chapter, we provided a concise presentation of various strategies adopted in the design of bifunctional nanomaterials, including synthesis methods of magnetic core nanoparticles, magnetism and luminescence behaviors, and multimodal biomedical applications of bifunctional nanomaterials. To the best of our knowledge, this is the first time detailed information on bifunctional luminescent and magnetic nanomaterials has been summarized in chapter form. We hope the chapter will prove beneficial to both nonspecialists and those working on optical and magnetic nanomaterials.

Acknowledgments The authors are grateful for the financial support of the Coordenação de Aperfeiçoamento de Pessoal de Nível Superior (CAPES, Brazil), Conselho Nacional de Desenvolvimento Científico e Tecnológico (CNPq, Brazil), the World Academy of Sciences (TWAS) for the advancement of science in developing countries, and Fundação de Amparo à Pesquisa do Estado de São Paulo (FAPESP, Brazil). Priscila V. Khan is gratefully acknowledged for her assistance in the preparation of the figures.

References

1. Khan LU, Brito HF, Hölsä J, Pirota KR, Muraca D, Felinto MCFC, Teotonio EES, Malta OL (2014) Red-green emitting and superparamagnetic nanomarkers containing Fe_3O_4 functionalized with calixarene and rare earth complexes. Inorg Chem 53:12902–12910
2. Li X, Zhao D, Zhang F (2013) Multifunctional upconversion-magnetic hybrid nanostructured materials: synthesis and bioapplications. Theranostics 3:292–305; Khan LU, Muraca D, Brito HF, Pirota KR, Felinto MCFC, Teotonio EES, Malta OL (2016) Optical and magnetic nanocomposites containing $Fe_3O_4@SiO_2$ grafted with Eu^{3+} and Tb^{3+} complexes. J Alloys Compd 686:453–466
3. Zhang F, Braun GB, Pallaoro A, Zhang Y, Shi Y, Cui D, Moskovits M, Zhao D, Stucky GD (2012) Mesoporous multifunctional upconversion luminescent and magnetic "nanorattle" materials for targeted chemotherapy. Nano Lett 12:61–67
4. Cheng L, Yang K, Li Y, Chen J, Wang C, Shao M, Lee S-T, Liu Z (2011) Facile preparation of multifunctional upconversion nanoprobes for multimodal imaging and dual-targeted photothermal therapy. Angew Chemie Int Ed 50:7385–7390
5. Cheng L, Yang K, Li Y, Zeng X, Shao M, Lee S-T, Liu Z (2012) Multifunctional nanoparticles for upconversion luminescence/MR multimodal imaging and magnetically targeted photothermal therapy. Biomaterials 33:2215–2222
6. Son A, Dhirapong A, Dosev DK, Kennedy IM, Weiss RH, Hristova KR (2008) Rapid and quantitative DNA analysis of genetic mutations for polycystic kidney disease (PKD) using magnetic/luminescent nanoparticles. Anal Bioanal Chem 390:1829–1835
7. Espinosa A, Di Corato R, Kolosnjaj-Tabi J, Flaud P, Pellegrino T, Wilhelm C (2016) Duality of iron oxide nanoparticles in cancer therapy: amplification of heating efficiency by magnetic hyperthermia and photothermal bimodal treatment. ACS Nano 10:2436–2446
8. Shi D, Sadat ME, Dunn AW, Mast DB (2015) Photo-fluorescent and magnetic properties of iron oxide nanoparticles for biomedical applications. Nanoscale 7:8209–8232
9. Singh LP, Srivastava SK, Mishra R, Ningthoujam RS (2014) Multifunctional hybrid nanomaterials from water dispersible $CaF_2:Eu^{3+},Mn^{2+}$ and Fe_3O_4 for luminescence and hyperthermia application. J Phys Chem C 118:18087–18096
10. Gai S, Yang P, Li C, Wang W, Dai Y, Niu N, Lin J (2010) Synthesis of magnetic, up-conversion luminescent, and mesoporous core-shell-structured nanocomposites as drug carriers. Adv Funct Mater 20:1166–1172
11. Kim H, Achermann M, Balet LP, Hollingsworth JA, Klimov VI (2005) Synthesis and characterization of Co/CdSe core/shell nanocomposites: bifunctional magnetic-optical nanocrystals. J Am Chem Soc 127:544–546
12. Kaewsaneha C, Tangboriboonrat P, Polpanich D, Elaissari A (2015) Multifunctional fluorescent-magnetic polymeric colloidal particles: preparations and bioanalytical applications. ACS Appl Mater Interfaces 7:23373–23386
13. Lin Y-S, Wu S, Hung Y, Chou Y, Chang C, Lin M, Tsai C, Mou C-Y (2006) Multifunctional composite nanoparticles: magnetic, luminescent, and mesoporous. Chem Mater 18:5170–5172

14. Zhang L, Liu B, Dong S (2007) Bifunctional nanostructure of magnetic core luminescent shell and its application as solid-state electrochemiluminescence sensor material. J Phys Chem B 111:10448–10452
15. Laurent S, Forge D, Port M, Roch A, Robic C, Vander Elst L, Muller RN (2008) Magnetic iron oxide nanoparticles: synthesis, stabilization, vectorization, physicochemical characterizations, and biological applications. Chem Rev 108:2064–2110
16. Sharma R, Bansal S, Singhal S (2015) Tailoring the photo-Fenton activity of spinel ferrites (MFe_2O_4) by incorporating different cations (M = Cu, Zn, Ni and Co) in the structure. RSC Adv 5:6006–6018
17. Sun S, Zeng H, Robinson DB, Raoux S, Rice PM, Wang SX, Li G (2004) Monodisperse MFe_2O_4 (M = Fe, Co, Mn) nanoparticles. J Am Chem Soc 126:273–279
18. Zhang Y, Shi Q, Schliesser J, Woodfield BF, Nan Z (2014) Magnetic and thermodynamic properties of nanosized Zn ferrite with normal spinal structure synthesized using a facile method. Inorg Chem 53:10463–10470
19. Blanco-Gutiérrez V, Gallastegui JA, Bonville P, Torralvo-Fernández MJ, Sáez-Puche R (2012) MFe_2O_4 (M: Co^{2+}, Ni^{2+}) nanoparticles: mössbauer and X-ray absorption spectroscopies studies and high-temperature superparamagnetic behavior. J Phys Chem C 116:24331–24339
20. Jacintho GVM, Brolo AG, Corio P, Suarez PZ, Rubim JC (2009) Structural investigation of MFe_2O_4 (M = Fe, Co) magnetic fluids. J Phys Chem C 113:7684–7691
21. Kim KJ, Lee HS, Lee MH, Lee SH (2002) Comparative magneto-optical investigation of d–d charge–transfer transitions in Fe_3O_4, $CoFe_2O_4$, and $NiFe_2O_4$. J Appl Phys 91:9974
22. Fontijin WFJ, van der Zang PJ, Devillers MAC, Metselaar R (1997) Optical and magneto-optical Kerr spectra of Fe_3O_4 and Mg^{2+}-or Al^{3+}-substituted Fe_3O_4. Phys Rev B 56:5432–5442
23. Tilley RJD (2010) Colour and the optical properties of materials. Wiley, Chichester
24. Yu C-J, Wu S-M, Tseng W-L (2013) Magnetite nanoparticle-induced fluorescence quenching of adenosine triphosphate–BODIPY conjugates: application to adenosine triphosphate and pyrophosphate sensing. Anal Chem 85:8559–8565
25. Binnemans K (2009) Lanthanide-based luminescent hybrid materials. Chem Rev 109:4283–4374
26. Borges AS, Dutra JDL, Freire RO, Moura RT, Da Silva JG, Malta OL, Araujo MH, Brito HF (2012) Synthesis and characterization of the europium(III) pentakis(picrate) complexes with imidazolium counter cations: structural and photoluminescence study. Inorg Chem 51:12867–12878
27. Bünzli J-CG, Eliseeva SV (2013) Intriguing aspects of lanthanide luminescence. Chem Sci 4:1939–1949
28. Carnall WT, Goodman GL, Rajnak K, Rana RS (1989) A systematic analysis of the spectra of the lanthanides doped into single crystal LaF_3. J Chem Phys 90:3443–3457
29. Brito HF, Malta OL, Felinto MCFC, Teotonio EES (2009) Luminescence phenomena involving metal enolates. In: Zabicky J (ed) The chemistry of metal enolates—part 1. Wiley, Chichester, pp 131–184
30. de Sá GF, Malta OL, de Mello DC et al (2000) Spectroscopic properties and design of highly luminescent lanthanide coordination complexes. Coord Chem Rev 196:165–195
31. Bünzli J-CG (2015) On the design of highly luminescent lanthanide complexes. Coord Chem Rev 293–294:19–47
32. Bünzli JCG (2010) Lanthanide luminescence for biomedical analyses and imaging. Chem Rev 110:2729–2755
33. Cotton S (2005) Electronic and magnetic properties of the lanthanides. In: Lanthanide and actinide chemistry. Wiley, West Sussex. pp 61–83
34. Frison R, Cernuto G, Cervellino A et al (2013) Magnetite-maghemite nanoparticles in the 5-15 nm range: correlating the core-shell composition and the surface structure to the magnetic properties. A total scattering study. Chem Mater 25:4820–4827
35. Piao Y, Kim J et al (2008) Wrap–bake–peel process for nanostructural transformation from β-FeOOH nanorods to biocompatible iron oxide nanocapsules. Nat Mater 7:242–247

36. Prado Y, Daffé N, Michel A et al (2015) Enhancing the magnetic anisotropy of maghemite nanoparticles via the surface coordination of molecular complexes. Nat Commun 6:10139
37. Lacroix L, Lachaize S, Falqui A et al (2009) Iron nanoparticle growth in organic superstructures. J Am Chem Soc 131:549–557
38. Tadic M, Panjan M, Damnjanovic V, Milosevic I (2014) Magnetic properties of hematite (α-Fe_2O_3) nanoparticles prepared by hydrothermal synthesis method. Appl Surf Sci 320: 183–187
39. Lu Y, Lu X, Mayers BT et al (2008) Synthesis and characterization of magnetic Co nanoparticles: a comparison study of three different capping surfactants. J Solid State Chem 181:1530–1538
40. Peng S, Wang C, Xie J, Sun S (2006) Synthesis and stabilization of monodisperse Fe nanoparticles. J Am Chem Soc 128:10676–10677
41. Huber D (2005) Synthesis, properties, and applications of iron nanoparticles. Small 1: 482–501
42. Chen HM, Hsin CF, Chen PY et al (2009) Ferromagnetic $CoPt_3$ nanowires: structural evolution from fcc to ordered $L1_2$. J Am Chem Soc 131:15794–15801
43. Colak L, Hadjipanayis GC (2009) Chemically synthesized FePt nanoparticles with controlled particle size, shape and composition. Nanotechnology 20:485602
44. Ghosh Chaudhuri R, Paria S (2012) Core/shell nanoparticles: classes, properties, synthesis mechanisms, characterization, and applications. Chem Rev 112:2373–2433
45. Lu A-H, Salabas E, Schüth F (2007) Magnetic nanoparticles: synthesis, protection, functionalization, and application. Angew Chemie Int Ed 46:1222–1244
46. Hasany F, Ahmed S et al (2013) Systematic review of the preparation techniques of iron oxide magnetic nanoparticles. Nanosci Nanotechnol 2:148–158
47. Jolivet J-P, Chanèac C, Tronc E (2004) Iron oxide chemistry. From molecular clusters to extended solid networks. Chem Commun 5:481–483
48. Barbosa HP, Kai J, Silva IGN et al (2015) Luminescence investigation of R^{3+}-doped alkaline earth tungstates prepared by a soft chemistry method. J Lumin 170:1–7
49. Yi G, Lu H, Zhao S et al (2004) Synthesis, characterization, and biological application of size-controlled nanocrystalline $NaYF_4$:Yb,Er infrared-to-visible up-conversion phosphors. Nano Lett 4:2191–2196
50. Ximendes EC, Rocha U, Jacinto C et al (2016) Self-monitored photothermal nanoparticles based on core–shell engineering. Nanoscale 8:3057–3066
51. Gribanov NM, Bibik EE, Buzunov OV, Naumov VN (1990) Physico-chemical regularities of obtaining highly dispersed magnetite by the method of chemical condensation. J Magn Magn Mater 85:7–10
52. Boistelle R, Astier JP (1988) Crystallization mechanisms in solution. J Cryst Growth 90: 14–30
53. Knobel M, Nunes WC, Socolovsky LM et al (2008) Superparamagnetism and other magnetic features in granular materials: a review on ideal and real systems. J Nanosci Nanotechnol 8:2836–2857
54. Tresilwised N, Pithayanukul P, Plank C (2005) Factors affecting sizes of magnetic particles formed by chemical co-precipitation. Pharmacy Mahidol Ac Th 32:71–76
55. Kim DK, Zhang Y, Voit W et al (2001) Synthesis and characterization of surfactant-coated superparamagnetic monodispersed iron oxide nanoparticles. J Magn Magn Mater 225:30–36
56. Vayssières L, Chanéac C, Tronc E, Jolivet JP (1998) Size tailoring of magnetite particles formed by aqueous precipitation: an example of thermodynamic stability of nanometric oxide particles. J Colloid Interface Sci 205:205–212
57. Li Y, Afzaal M, O'Brien P (2006) The synthesis of amine-capped magnetic (Fe, Mn, Co, Ni) oxide nanocrystals and their surface modification for aqueous dispersibility. J Mater Chem 16:2175
58. Rockenberger J, Scher EC, Alivisatos AP (1999) A new nonhydrolytic single-precursor approach to surfactant-capped nanocrystals of transition metal oxides. J Am Chem Soc 121:11595–11596

59. Hyeon T (2003) Chemical synthesis of magnetic nanoparticles. Chem Commun 927–934
60. Chen X, Liu Y, Tu D (2014) Lanthanide-doped luminescent nanomaterials. Springer, Berlin
61. Mahalingam V, Vetrone F, Naccache R et al (2009) Colloidal Tm^{3+}/Yb^{3+}-doped $LiYF_4$ nanocrystals: multiple luminescence spanning the UV to NIR regions via low-energy excitation. Adv Mater 21:4025–4028
62. Chen G, Ohulchanskyy TY, Kumar R et al (2010) Ultrasmall monodisperse $NaYF_4$:Yb^{3+}/Tm^{3+} nanocrystals with enhanced near-infrared to near-infrared upconversion photoluminescence. ACS Nano 4:3163–3168
63. Naccache R, Vetrone F, Mahalingam V et al (2009) Controlled synthesis and water dispersibility of hexagonal phase $NaGdF_4$:Ho^{3+}/Yb^{3+} nanoparticles. Chem Mater 21:717–723
64. Liu Q, Sun Y, Yang T et al (2011) Sub-10 nm hexagonal lanthanide-doped $NaLuF_4$ upconversion nanocrystals for sensitive bioimaging in vivo. J Am Chem Soc 133:17122–17125
65. Vetrone F, Mahalingam V, Capobianco JA (2009) Near-infrared-to-blue upconversion in colloidal $BaYF_5$:Tm^{3+},Yb^{3+} nanocrystals. Chem Mater 21:1847–1851
66. Yang D, Li C, Li G et al (2011) Colloidal synthesis and remarkable enhancement of the upconversion luminescence of $BaGdF_5$:Yb^{3+}/Er^{3+} nanoparticles by active-shell modification. J Mater Chem 21:5923–5927
67. Yi G, Peng Y, Gao Z (2011) Strong red-emitting near-infrared-to-visible upconversion fluorescent nanoparticles. Chem Mater 23:2729–2734
68. Sun X, Zhang Y-W, Du Y-P et al (2007) From trifluoroacetate complex precursors to monodisperse rare-earth fluoride and oxyfluoride nanocrystals with diverse shapes through controlled fluorination in solution phase. Chem A Eur J 13:2320–2332
69. Sun S, Zeng H (2002) Size-controlled synthesis of magnetite nanoparticles. J Am Chem Soc 124:8204–8205
70. Brollo MEF, López-Ruiz R, Muraca D et al (2014) Compact $Ag@Fe_3O_4$ core-shell nanoparticles by means of single-step thermal decomposition reaction. Sci Rep 4:6839
71. Liz-Marzán LM, Kamat PV (2003) Nanoscale materials, 1st edn. Springer, New York
72. Langevin D (1992) Micelles and microemulsions. Annu Rev Phys Chem 43:341–369
73. Danielsson I, Lindman B (1981) The definltion of microemulsion. Colloids Surf 3:391–392
74. Malik MA, Wani MY, Hashim MA (2012) Microemulsion method: a novel route to synthesize organic and inorganic nanomaterials. Arab J Chem 5:397–417
75. Liu C, Zou B, Rondinone AJ, Zhang ZJ (2000) Reverse micelle synthesis and characterization of superparamagnetic $MnFe_2O_4$ spinel ferrite nanocrystallites. J Phys Chem B 104:1141–1145
76. Hashim M, Shirsath SE, Meena SS et al (2015) Manganese ferrite prepared using reverse micelle process: structural and magnetic properties characterization. J Alloys Compd 642:70–77
77. Dongale TD, Shinde SS, Kamat RK, Rajpure KY (2014) Nanostructured TiO_2 thin film memristor using hydrothermal process. J Alloys Compd 593:267–270
78. Xu H, Wang H, Zhang Y et al (2004) Hydrothermal synthesis of zinc oxide powders with controllable morphology. Ceram Int 30:93–97
79. Lee E, Kim Y, Heo J, Park K-M (2015) 3D metal–organic framework based on a lower-rim acid-functionalized calix[4]arene: crystal-to-crystal transformation upon lattice solvent removal. Cryst Growth Des 15:3556–3560
80. Wang X, Zhuang J, Peng Q, Li Y (2005) A general strategy for nanocrystal synthesis. Nature 437:121–124
81. Rabenau A (1985) The role of hydrothermal synthesis in preparative chemistry. Angew Chemie Int Ed 24:1026–1040
82. Einarsrud M-A, Grande T (2014) 1D oxide nanostructures from chemical solutions. Chem Soc Rev 43:2187–2199
83. Cai H, An X, Cui J et al (2013) Facile hydrothermal synthesis and surface functionalization of polyethyleneimine-coated iron oxide nanoparticles for biomedical applications. ACS Appl Mater Interfaces 5:1722–1731

84. Tong L, Shi J, Liu D, Li Q (2012) Luminescent and magnetic properties of Fe_3O_4@SiO_2@Y_2O_3:Eu^{3+} composites with core–shell structure. J Phys Chem C 116:7153–7157
85. Zhong C, Yang P, Li X et al (2012) Monodisperse bifunctional Fe_3O_4@$NaGdF_4$:Yb/Er@$NaGdF_4$:Yb/Er core–shell nanoparticles. RSC Adv 2:3194–3197
86. Zhang L, Wang Y-S, Yang Y et al (2012) Magnetic/upconversion luminescent mesoparticles of Fe_3O_4@LaF_3:Yb^{3+},Er^{3+} for dual-modal bioimaging. Chem Commun 48:11238–11240
87. Peng H, Liu G, Dong X et al (2012) Magnetic, luminescent and core–shell structured Fe_3O_4@YF_3:Ce^{3+},Tb^{3+} bifunctional nanocomposites. Powder Technol 215–216:242–246
88. Jie G, Yuan J (2012) Novel magnetic Fe_3O_4@CdSe composite quantum dot-based electrochemiluminescence detection of thrombin by a multiple DNA cycle amplification strategy. Anal Chem 84:2811–2817
89. Wang H, Sun L, Li Y et al (2011) Layer-by-layer assembled Fe_3O_4@C@CdTe core/shell microspheres as separable luminescent probe for sensitive sensing of Cu^{2+} ions. Langmuir 27:11609–11615
90. Yu X, Wan J, Shan Y et al (2009) A facile approach to fabrication of bifunctional magnetic-optical Fe_3O_4@ZnS microspheres. Chem Mater 21:4892–4898
91. Gu H, Zheng R, Zhang X, Xu B (2004) Facile one-pot synthesis of bifunctional heterodimers of nanoparticles: a conjugate of quantum dot and magnetic nanoparticles. J Am Chem Soc 126:5664–5665
92. Liu G, Peng H, Wang J, Dong X (2012) Fe_3O_4@GdF_3:Er^{3+},Yb^{3+} nanoparticles: synthesis and bifunctional properties. J Optoelectron Adv Mater 14:205–209
93. Wu T, Pan H, Chen R et al (2016) Effect of solution pH value changes on fluorescence intensity of magnetic-luminescent Fe_3O_4@Gd_2O_3:Eu^{3+} nanoparticles. J Rare Earths 34:71–76
94. He H, Xie MY, Ding Y, Yu XF (2009) Synthesis of Fe_3O_4@LaF_3:Ce,Tb nanocomposites with bright fluorescence and strong magnetism. Appl Surf Sci 255:4623–4626
95. Atabaev T, Kim H-K, Hwang Y-H (2013) Fabrication of bifunctional core-shell Fe_3O_4 particles coated with ultrathin phosphor layer. Nanoscale Res Lett 8:357
96. Yu X, Shan Y, Li G, Chen K (2011b) Synthesis and characterization of bifunctional magnetic–optical Fe_3O_4@SiO_2@Y_2O_3:Yb^{3+},Er^{3+} near-infrared-to-visible up-conversion nanoparticles. J Mater Chem 21:8104–8109
97. Wu A, Zhang Z (2015) Luminescent and magnetic properties of carbon-based $FeYO_3$/Y_2O_3:Eu^{3+} nanocomposites. Appl Surf Sci 356:1077–1081
98. Bi F, Dong X, Wang J, Liu G (2014) Coaxial electrospinning preparation and properties of magnetic–photoluminescent bifunctional $CoFe_2O_4$@Y_2O_3:Eu^{3+} coaxial nanofibers. J Mater Sci Mater Electron 25:4259–4267
99. Peng H, Liu G, Dong X et al (2011) Preparation and characteristics of Fe_3O_4@YVO_4:Eu^{3+} bifunctional magnetic–luminescent nanocomposites. J Alloys Compd 509:6930–6934
100. Sun P, Zhang H, Liu C et al (2010) Preparation and characterization of Fe_3O_4/CdTe magnetic/fluorescent nanocomposites and their applications in immuno-labeling and fluorescent imaging of cancer cells. Langmuir 26:1278–1284
101. Du GH, Liu ZL, Lu QH et al (2006) Fe_3O_4/CdSe/ZnS magnetic fluorescent bifunctional nanocomposites. Nanotechnology 17:2850–2854
102. Shen J, Sun L-D, Zhang Y-W, Yan C-H (2010) Superparamagnetic and upconversion emitting Fe_3O_4/$NaYF_4$:Yb,Er hetero-nanoparticles via a crosslinker anchoring strategy. Chem Commun 46:5731–5733
103. Fang J, Saunders M, Guo Y et al (2010) Green light-emitting $LaPO_4$:Ce^{3+}:Tb^{3+} koosh nanoballs assembled by p-sulfonato-calix[6]arene coated superparamagnetic Fe_3O_4. Chem Commun 46:3074–3076
104. Zhu H, Tao J, Wang W et al (2013) Magnetic, fluorescent, and thermo-responsive Fe_3O_4/rare earth incorporated poly(St-NIPAM) core–shell colloidal nanoparticles in multimodal optical/magnetic resonance imaging probes. Biomaterials 34:2296–2306

105. Zhu H, Shang Y, Wang W et al (2013) Fluorescent magnetic Fe_3O_4/rare earth colloidal nanoparticles for dual-modality imaging. Small 9:2991–3000
106. Barick KC, Sharma A, Shetake NG et al (2015) Covalent bridging of surface functionalized Fe_3O_4 and YPO_4:Eu nanostructures for simultaneous imaging and therapy. Dalt Trans 44:14686–14696
107. Parchur AK, Ansari AA, Singh BP et al (2014) Enhanced luminescence of $CaMoO_4$:Eu by core@shell formation and its hyperthermia study after hybrid formation with Fe_3O_4: cytotoxicity assessment on human liver cancer cells and mesenchymal stem cells. Integr Biol 6:53–64
108. Ye F, Barrefelt Å, Asem H et al (2014) Biodegradable polymeric vesicles containing magnetic nanoparticles, quantum dots and anticancer drugs for drug delivery and imaging. Biomaterials 35:3885–3894
109. Hong X, Li J, Wang M et al (2004) Fabrication of magnetic luminescent nanocomposites by a layer-by-layer self-assembly approach. Chem Mater 16:4022–4027
110. Gaponik N, Radtchenko IL, Sukhorukov GB, Rogach AL (2004) Luminescent polymer microcapsules addressable by a magnetic field. Langmuir 20:1449–1452
111. Wang D, He J, Rosenzweig N, Rosenzweig Z (2004) Superparamagnetic Fe_2O_3 beads−CdSe/ZnS quantum dots core−shell nanocomposite particles for cell separation. Nano Lett 4:409–413
112. Chen O, Riedemann L, Etoc F et al (2014) Magneto-fluorescent core-shell supernanoparticles. Nat Commun 5:5093
113. Yang J, Lim E-K, Lee HJ et al (2008) Fluorescent magnetic nanohybrids as multimodal imaging agents for human epithelial cancer detection. Biomaterials 29:2548–2555
114. Gallagher JJ, Tekoriute R, O'Reilly J-A et al (2009) Bimodal magnetic-fluorescent nanostructures for biomedical applications. J Mater Chem 19:4081–4084
115. Yuet KP, Hwang DK, Haghgooie R, Doyle PS (2010) Multifunctional superparamagnetic janus particles. Langmuir 26:4281–4287
116. Kaewsaneha C, Bitar A, Tangboriboonrat P et al (2014) Fluorescent-magnetic Janus particles prepared via seed emulsion polymerization. J Colloid Interface Sci 424:98–103
117. Chekina N, Horák D, Jendelová P et al (2011) Fluorescent magnetic nanoparticles for biomedical applications. J Mater Chem 21:7630–7639
118. Ge Y, Zhang Y, He S et al (2009) Fluorescence modified chitosan-coated magnetic nanoparticles for high-efficient cellular imaging. Nanoscale Res Lett 4:287–295
119. Torkpur-Biglarianzadeh M, Salami-Kalajahi M (2015) Multilayer fluorescent magnetic nanoparticles with dual thermoresponsive and pH-sensitive polymeric nanolayers as anticancer drug carriers. RSC Adv 5:29653–29662
120. Lim E-K, Yang J, Dinney CPN et al (2010) Self-assembled fluorescent magnetic nanoprobes for multimode-biomedical imaging. Biomaterials 31:9310–9319
121. Kaewsaneha C, Opaprakasit P, Polpanich D et al (2012) Immobilization of fluorescein isothiocyanate on magnetic polymeric nanoparticle using chitosan as spacer. J Colloid Interface Sci 377:145–152
122. Stöber W, Fink A, Bohn E (1968) Controlled growth of monodisperse silica spheres in the micron size range. J Colloid Interface Sci 26:62–69
123. Santra S, Tapec R, Theodoropoulou N et al (2001) Synthesis and characterization of silica-coated iron oxide nanoparticles in microemulsion: the effect of nonionic surfactants. Langmuir 17:2900–2906
124. Pogorilyi RP, Melnyk IV, Zub YL et al (2014) New product from old reaction: uniform magnetite nanoparticles from iron-mediated synthesis of alkali iodides and their protection from leaching in acidic media. RSC Adv 4:22606–22612
125. Yu S-Y, Zhang H-J, Yu J-B et al (2007) Bifunctional magnetic-optical nanocomposites: grafting lanthanide complex onto core-shell magnetic silica nanoarchitecture. Langmuir 23:7836–7840

126. Yu S, Fu L, Zhou Y, Su H (2011) Novel bifunctional magnetic-near-infrared luminescent nanocomposites: near-infrared emission from Nd and Yb. Photochem Photobiol Sci 10:548–553
127. Spaldin NA (2010) Magnetic materials. Fundamentals and applications. Cambridge University Press, New York
128. Kurzen H, Bovigny L, Bulloni C, Daul C (2013) Electronic structure and magnetic properties of lanthanide 3+ cations. Chem Phys Lett 574:129–132
129. Van Vleck JH (1978) Quantum mechanics-key understanding magnetism. Rev Mod Phys 50:181–189
130. Bünzli J-CG, Piguet C (2005) Taking advantage of luminescent lanthanide ions. Chem Soc Rev 34:1048–1077
131. Dorenbos P (2002) Light output and energy resolution of Ce^{3+}-doped scintillators. Nucl Instrum Methods Phys Res A 486:208–213
132. Binnemans K (2015) Interpretation of europium(III) spectra. Coord Chem Rev 295:1–45
133. Xu W, Park JY, Kattel K et al (2012) A T_1, T_2 magnetic resonance imaging (MRI)-fluorescent imaging (FI) by using ultrasmall mixed gadolinium–europium oxide nanoparticles. New J Chem 36:2361–2367
134. Li C, Li YX, Law GL et al (2006) Fast water-exchange Gd^{3+}-(DO3A-like) complex functionalized with Aza-15-crown-5 showing prolonged residence lifetime in vivo. Bioconjug Chem 17:571–574
135. Szczeszak A, Ekner-Grzyb A, Runowski M et al (2015) Synthesis, photophysical analysis, and in vitro cytotoxicity assessment of the multifunctional (magnetic and luminescent) core@shell nanomaterial based on lanthanide-doped orthovanadates. J Nanopart Res 17:143
136. Hu C, Xia T, Gong Y et al (2016) Emulsifier-free emulsion polymerized poly(MMA-HEMA-$Eu(AA)_3$Phen)/Fe_3O_4 magnetic fluorescent bifunctional nanospheres for magnetic resonance and optical imaging. Chinese J Polym Sci 34:135–146
137. Xia A, Gao Y, Zhou J et al (2011) Core-shell $NaYF_4$:Yb^{3+},Tm^{3+}@Fe_xO_y nanocrystals for dual-modality T_2-enhanced magnetic resonance and NIR-to-NIR upconversion luminescent imaging of small-animal lymphatic node. Biomaterials 32:7200–7208
138. Zhu X, Zhou J, Chen M et al (2012) Core–shell Fe_3O_4@$NaLuF_4$:Yb,Er/Tm nanostructure for MRI, CT and upconversion luminescence tri-modality imaging. Biomaterials 33:4618–4627
139. Guo R, Wang J, Dong X et al (2014) A new tactics to fabricate flexible nanobelts with enhanced magnetic-luminescent bifunction. J Mater Sci Mater Electron 25:2561–2568
140. Leyu W, Zhihua Y, Yi Z, Lun W (2009) Bifunctional nanoparticles with magnetization and luminescence. J Phys Chem C 113:3955–3959
141. Li B, Fan H, Zhao Q, Wang C (2016) Synthesis, characterization and cytotoxicity of novel multifunctional Fe_3O_4@SiO_2@$GdVO_4$:Dy^{3+} core-shell nanocomposite as a drug carrier. Materials 9:149
142. Sukumar UK, Bhushan B, Dubey P et al (2013) Emerging applications of nanoparticles for lung cancer diagnosis and therapy. Int Nano Lett 3:1–17
143. Runowski M, Lis S (2015) Synthesis, surface modification/decoration of luminescent–magnetic core/shell nanomaterials, based on the lanthanide doped fluorides (Fe_3O_4/SiO_2/NH_2/PAA/LnF_3). J Lumin 170:484–490
144. Sonuga-Barke E, Brandeis D, Cortese S et al (2013) Response to Chronis-Tuscano et al. and Arns and Strehl. Am J Psychiatry 170:800–802
145. Roland S, Thomas W, Yitzhak R et al (1957) Targeted magnetic hyperthermia. Ther Deliv 2:815–838
146. Walter A, Billotey C, Garofalo A et al (2014) Mastering the shape and composition of dendronized iron oxide nanoparticles to tailor magnetic resonance imaging and hyperthermia. Chem Mater 26:5252–5264
147. Lepock JR (2003) Cellular effects of hyperthermia: relevance to the minimum dose for thermal damage. Int J Hyperth 19:252–266

148. Xie J, Zhang Y, Yan C et al (2014) High-performance PEGylated Mn-Zn ferrite nanocrystals as a passive-targeted agent for magnetically induced cancer theranostics. Biomaterials 35:9126–9136
149. Thrall DE, Larue SM, Pruitt AF et al (2006) Changes in tumour oxygenation during fractionated hyperthermia and radiation therapy in spontaneous canine sarcomas. Int J Hyperth 22:365–373
150. Gazeau F, Lévy M, Wilhelm C (2008) Optimizing magnetic nanoparticle design for nanothermotherapy. Nanomedicine (Lond) 3:831–844
151. Luwang MN, Chandra S, Bahadur D, Srivastava SK (2012) Dendrimer facilitated synthesis of multifunctional lanthanide based hybrid nanomaterials for biological applications. J Mater Chem 22:3395–3403
152. Singh LP, Singh NP, Srivastava SK (2015) Terbium doped SnO_2 nanoparticles as white emitters and SnO_2:5Tb/Fe_3O_4 magnetic luminescent nanohybrids for hyperthermia application and biocompatibility with HeLa cancer cells. Dalt Trans 44:6457–6465
153. Prasad AI, Parchur AK, Juluri RR et al (2013) Bi-functional properties of Fe_3O_4@YPO_4:Eu hybrid nanoparticles: hyperthermia application. Dalton Trans 42:4885–4896
154. Kempe H, Kates SA, Kempe M (2011) Nanomedicine's promising therapy: magnetic drug targeting. Expert Rev Med Devices 8:291–294
155. Marcu A, Pop S, Dumitrache F et al (2013) Magnetic iron oxide nanoparticles as drug delivery system in breast cancer. Appl Surf Sci 281:60–65
156. Hola K, Markova Z, Zoppellaro G et al (2015) Tailored functionalization of iron oxide nanoparticles for MRI, drug delivery, magnetic separation and immobilization of biosubstances. Biotechnol Adv 33:1162–1176
157. Mohapatra S, Rout SR, Das RK et al (2016) Highly hydrophilic luminescent magnetic mesoporous carbon nanospheres for controlled release of anticancer drug and multimodal imaging. Langmuir 32:1611–1620
158. Bao Y, Wen T, Samia ACS et al (2015) Magnetic nanoparticles: material engineering and emerging applications in lithography and biomedicine. J Mater Sci 51:513–553
159. Wan Q, Xie L, Gao L et al (2013) Self-assembled magnetic theranostic nanoparticles for highly sensitive MRI of minicircle DNA delivery. Nanoscale 5:744–752
160. Wang C, Cheng L, Liu Z (2011) Drug delivery with upconversion nanoparticles for multifunctional targeted cancer cell imaging and therapy. Biomaterials 32:1110–1120
161. Gambhir SS, Weiss S (2005) Quantum dots for live cells, in vivo imaging, and diagnostics. Science 307:538–544
162. Xu H, Cheng L, Wang C et al (2011) Polymer encapsulated upconversion nanoparticle/iron oxide nanocomposites for multimodal imaging and magnetic targeted drug delivery. Biomaterials 32:9364–9373
163. Singh RK, Patel KD, Kim JJ et al (2014) Multifunctional hybrid nanocarrier: magnetic CNTs ensheathed with mesoporous silica for drug delivery and imaging system. ACS Appl Mater Interfaces 6:2201–2208
164. Snyder P, Joshi A, Serna JD (2014) Modeling a nanocantilever-based biosensor using a stochastically perturbed harmonic oscillator. Int J Nanosci 13:1450011
165. Justino CIL, Rocha-Santos TAP, Cardoso S et al (2013) Strategies for enhancing the analytical performance of nanomaterial-based sensors. TrAC Trends Anal Chem 47:27–36
166. Haun JB, Yoon T-J, Lee H, Weissleder R (2010) Magnetic nanoparticle biosensors. Wiley Interdiscip Rev Nanomed Nanobiotechnol 2:291–304
167. Arvand M, Hassannezhad M (2014) Magnetic core-shell Fe_3O_4@SiO_2/MWCNT nanocomposite modified carbon paste electrode for amplified electrochemical sensing of uric acid. Mater Sci Eng C 36:160–167
168. Teymourian H, Salimi A, Khezrian S (2013) Fe_3O_4 magnetic nanoparticles/reduced graphene oxide nanosheets as a novel electrochemical and bioeletrochemical sensing platform. Biosens Bioelectron 49:1–8
169. Dou Q, Idris NM, Zhang Y (2013) Sandwich-structured upconversion nanoparticles with tunable color for multiplexed cell labeling. Biomaterials 34:1722–1731

170. Nichkova M, Dosev D, Gee SJ et al (2005) Microarray immunoassay for phenoxybenzoic acid using polymer encapsulated Eu:Gd_2O_3 nanoparticles as fluorescent labels. Anal Chem 77:6864–6873
171. Shen J, Sun LD, Zhu JD et al (2010b) Biocompatible bright YVO_4:Eu nanoparticles as versatile optical bioprobes. Adv Funct Mater 20:3708–3714
172. Idris NM, Li Z, Ye L et al (2009) Tracking transplanted cells in live animal using upconversion fluorescent nanoparticles. Biomaterials 30:5104–5113
173. Niedbala RS, Feindt H, Kardos K et al (2001) Detection of analytes by immunoassay using up-converting phosphor technology. Anal Biochem 293:22–30
174. Deng R, Xie X, Vendrell M et al (2011) Intracellular glutathione detection using MnO_2-nanosheet-modified upconversion nanoparticles. J Am Chem Soc 133:20168–20171

Chapter 5
X-Ray Absorption Spectroscopy: Element-Selective Tools to Characterize Magnetic Nanoparticles

Adriana I. Figueroa

5.1 Introduction

Synthesis and research in nanomaterials has attracted the attention of the scientific community in recent decades, mostly as a consequence of the ongoing miniaturization of devices. They also constitute ideal systems for studying finite-size and surface effects, those yielding new physical phenomena and enhanced properties with respect to their bulk counterparts. The intrinsic high surface-to-volume ratio of nanoparticles (NPs), for instance, make them very attractive for various applications in diverse fields, from biomedical sciences to engineering. In the field of magnetism, NPs have both scientific and technological importance owing to the overwhelming variety of structures with interesting physical properties, ranging from naturally occurring nanomagnets to comparatively easy-to-produce bulk nanocomposites. Nanomagnetism has opened the door to completely new technologies, and nanoscale magnetic materials are already found in applications as sensors of low magnetic fields, computer hard disk read heads, magnetoresistive RAM chips, and advanced filters for telecommunications, to cite a few examples.

The development of new technologies and fundamental research on magnetic NPs require characterization techniques that provide a full map of the magnetization at nanometer-length scales and subnanosecond time scales, as well as access to buried layers and interfaces [1]. Element-sensitive structural, chemical, and magnetic characterization is essential for understanding and unraveling the behavior of magnetic NPs. This is where advanced characterization techniques that make use of large facilities, such as advanced neutron and photon sources, play an important role. They offer high-resolution power to study the structural and magnetic properties of NP systems. The unique properties of synchrotron radiation, such as broad

A.I. Figueroa (✉)
Magnetic Spectroscopy Group, Diamond Light Source, Didcot OX11 0DE, UK
e-mail: aifigueg@gmail.com

© Springer International Publishing AG 2017

S.K. Sharma (ed.), *Complex Magnetic Nanostructures*,
DOI 10.1007/978-3-319-52087-2_5

energy spectrum, variable light polarization, and flexible time structure, have made it an enormously powerful tool in the study of magnetic phenomena and structure of materials. Extensive characterization of magnetic NPs has been carried out in recent decades with synchrotron-based spectroscopic techniques demonstrating their possibilities [2].

X-ray absorption spectroscopy (XAS) techniques in synchrotron radiation facilities are some of the spectroscopic characterization methods that are widely used nowadays to study nanomaterials. This chapter is devoted to presenting an overview of such techniques and to illustrate how these powerful methods provide unparalleled information for research on magnetic NP systems owing to their element-specific and local character. Various spectroscopic approaches can provide information about the relation between electronic structures and magnetism in condensed matter. Here we focus on three techniques: X-ray absorption near edge structure (XANES), extended X-ray absorption fine structure (EXAFS), and X-ray magnetic circular dichroism (XMCD). The combination of XAS experiments and theoretical calculations make these techniques such compelling tools for characterizing and understanding the electronic, structural, and magnetic behavior of the atoms that compose particles. We will start with an introductory description of synchrotron radiation facilities and continue with a brief overview of each technique. Finally, we will give some examples of magnetic NP systems where XAS techniques have been very useful for unraveling their microscopic properties.

5.2 X-ray Absorption Spectroscopy in Synchrotron Radiation Facilities

Several experimental techniques based on the interaction of radiation with matter require highly intense, bright, continuous, and tunable light sources [3, 4]. These requirements are easily fulfilled with synchrotron radiation sources (SRSs). They are shared regional research facilities that, with a few exceptions, are operated under government support. They are based on technology originally developed for high-energy physics experiments but were subsequently adapted to reliably produce high-energy electromagnetic radiation such as X-rays with certain desirable spectral characteristics [5].

5.2.1 Synchrotron Radiation Sources

Synchrotron radiation has a broad spectrum from microwaves to hard X-rays, so that it is a tunable radiation source. Its high-intensity photon beam of approximately 10^{18}–10^{20} photons/s/mm^2 (compared to the 10^8 photons/s/mm^2 of a conventional X-ray tube) allows for very rapid experiments. It is highly brilliant and coherent,

has a very small divergence, is very stable (submicron source stability) and naturally polarized, and has a time structure (on the picosecond time scale) that allows researchers to explore time-dependent processes from catalytic reactions to magnetization dynamics. Third-generation synchrotron radiation facilities are the most powerful currently operating SRSs and have become one of the essential tools for basic and applied scientific research around the world. Fourth-generation facilities, known as free electron lasers (FELs), are being developed and are opening up new ways to explore ultrarapid phenomena thanks to their subpicosecond temporal resolution, high coherence, and unprecedented peak brightness.[1]

SRS comprise a particle accelerator, a series of beamlines and peripheral laboratories to provide support for experiments performed at the beamlines. Synchrotron radiation is generated when the accelerated particles (electrons or protons), moving nearly at speed of light into an orbit, are deflected from their trajectory. According to the electromagnetic theory, an electric charge irradiates energy when accelerated: a radiation that is emitted tangentially to the circular trajectory of the electric charge.

The synchrotron light generation starts in an electron gun, where a cathode produces free electrons released to a linear accelerator or LINAC. The LINAC feeds a booster ring, where electrons receive a boost in energy from approximately 250 MeV to approximately 1.5–8 GeV from microwaves generated in a radio frequency cavity as they circulate in the ring. The booster increases the speed of the electrons close to the speed of light. When the electrons have enough energy to produce light, an injection system transfers them from the booster ring to the storage ring, which consists of a tube with straight and circular sections kept in ultra high vacuum, with quadrupole and sextupole magnets designed to focus the electron beam. This is where the accelerated particles are deflected from their flow direction using dipole magnets (bending magnets, BM) or insertion devices (ID) such as wigglers or undulators. ID consist of periodic magnetic structures that stimulate highly brilliant, forward-directed synchrotron radiation emission by forcing the stored charged particle beam to perform wiggles, or undulations, as they pass through the device. The magnet arrays are designed in such a way that the emitted radiation interferes constructively to produce a very intense and concentrated beam in narrow energy bands in the spectrum.

After the electron beam is deflected by a BM or ID there is a photon port to allow the light to travel down the beamlines to the research stations. Each beamline has an optics, experimental and control hutch. The optics hutch has optical instruments used to tailor the type of radiation to have the characteristics for each experiment. The experimental hutch contains the support mechanism and the environment for the sample study. Different instruments and detectors record the information produced from the interaction of the synchrotron light and the sample. The control cabin allows the researchers to operate the experimental station, perform the experiments and collect the data.

[1]For more information visit http://www.lightsources.org/.

5.2.2 X-ray Absorption Process

X-ray absorption spectroscopy benefits from the high intensity and tunable properties of X-ray beams produced in a SRS. XAS is a core-level spectroscopy, that is, it refers to the details of how X-rays are absorbed by an atom at energies near and above its core-level binding energies. Thus, it provides sensitivity to a specific chemical element by tuning the X-rays to the resonance energy of the core to valence transition. The absorbing process is illustrated in Fig. 5.1a. An X-ray photon reaches the absorbing atom (in pink) and disappears. Whenever the energy of an X-ray is greater than the binding energy of one of the absorbing atom's core electrons, a photoelectron is emitted. Depending on the energy of the incident X-ray photon, different processes occur. If the binding energy (ionization potential E_0) of a certain electron in the absorbing atom is equal to the X-ray photon energy E, there is a sharp increase in the absorption cross section, called the absorbing edge, corresponding to an emission of the photoelectron to the continuum states, as indicated in Fig. 5.1b. With the absorption of a photon of energy, the electron undergoes a transition to an unbound state in the continuum and, by the conservation of energy, acquires a kinetic energy $(E - E_0)$ [6].

The absorption edges are named according to the principal quantum number of the electron that is excited, that is, K, L, M, N, and O refer to $n = 1, 2, 3, 4$, and 5, respectively. The subscripts 1, 2, 3, 4, 5, 6, and 7 correspond to the electronic orbital shells as $s_{1/2}$, $p_{1/2}$, $p_{3/2}$, $d_{3/2}$, $d_{5/2}$, $f_{5/2}$, and $f_{7/2}$, respectively. The energies at which edges appear are unique for each element, which is the key to its element-selectivity nature. Figure 5.1c shows the spectrum for a Pt foil measured at the Pt L_3 edge, which corresponds to $2p_{3/2} \rightarrow 5d$ transitions.

X-rays have energies ranging from less than 1 keV to greater than 100 keV. Hard X-rays are the highest-energy X-rays, while the lower-energy ones are referred to as soft X-rays, with the boundary between both regions being around 2–3 keV. Soft X-rays cover the $3d$ transition metal $L_{2,3}$ ($2p \rightarrow 3d$), $4d$ and $5d$ transition metal $M_{2,3}$ ($3p \rightarrow d$), and lanthanide $M_{2,3}$ ($3p \rightarrow 5d$) and $M_{4,5}$ ($3d \rightarrow 4f$) edges. Hard X-rays cover the $3d$ and $4d$ transition metal K ($1s \rightarrow p$), $4d$ and $5d$ transition metal, and lanthanide $L_{2,3}$ ($2p \rightarrow d$) edges. Intense absorption jumps at an edge are known as *white lines*, which refers to the sharp lines observed on photographic plates used in the early days of X-ray spectroscopy.

The X-ray absorption process can be treated semiclassically, describing the X-ray photon in terms of a classical electromagnetic field but using a quantum mechanical description of the electron. This consists of a transition from an initial state with an X-ray, a core electron, and no photoelectron, to a final state with no X-ray, a core hole, and a photoelectron. According to Fermi's golden rule for dipolar transitions (following the dipole selection rules $\Delta\ell = \pm 1$ and $\Delta s = 0$), the transition probability between two electronic states, per unit time, is defined as

$$W_{if} = \frac{2\pi}{\hbar}\left(\frac{eE_0}{2}\right)^2 |\langle i|\,\hat{\varepsilon}\cdot\mathbf{r}\,|f\rangle|^2 \rho(E_f), \tag{5.1}$$

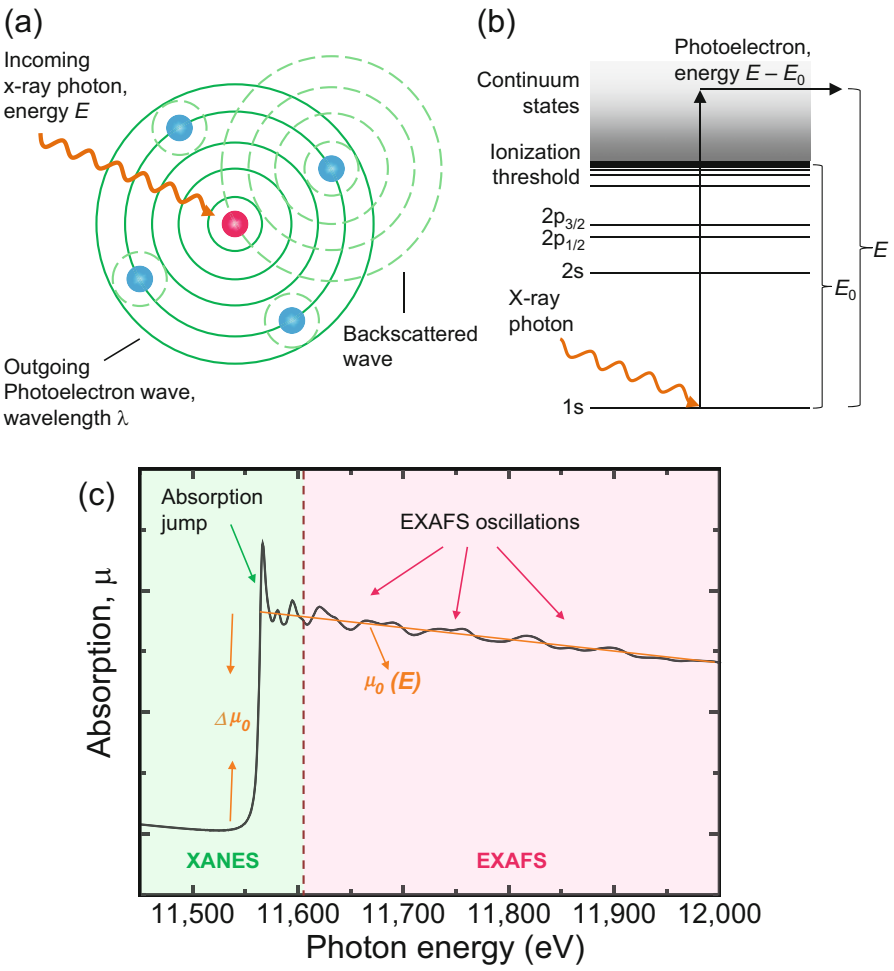

Fig. 5.1 (**a**) Schematics of X-ray absorption process. An absorbing atom (*pink*) is shown here surrounded by several other atoms (*blue*). (**b**) Energy-level diagram of an absorbing atom showing atom's first few core electron orbitals: $1s$, $2s$, $2p_{1/2}$, and $2p_{3/2}$ [6]. (**c**) XAFS spectrum recorded at Pt L_3 edge for Pt foil at 300 K. The main regions of the spectrum are depicted. The background function μ_0 and the measured jump at the absorption at the threshold energy E_0, $\Delta\mu_0$, are also shown . Figure reprinted/adapted with permission from [2]

where $\rho(E_f)$ is the density of the final states, $\langle i|$ the initial state of the core electron, $|f\rangle$ the final state of the photoelectron, and $\hat{\varepsilon} \cdot \mathbf{r}$ the dipole operator. Since the core-level electron is very tightly bound to the absorbing atom, the initial state will not be altered by the presence of the neighboring atom. The final state, on the other hand, will be affected by the neighboring atom since the photoelectron will be able to "see" it. The absorption coefficient $\mu(E)$ is proportional to the sum of possible

final states f of the transition probability in Eq. (5.1). It is calculated according to the first-order approximation of time-dependent perturbation theory, based on the interaction between the electromagnetic field and the atom potential.

5.2.3 X-ray Absorption Fine Structure

X-ray absorption fine structure (XAFS) is a specific structure observed in XAS [6, 7]. A typical XAFS spectrum is plotted in Fig. 5.1c, where the two spectral regions are depicted: the near edge region XANES, typically within 50 eV of the main absorption edge, and the extended fine structure (EXAFS), which spans from 50 to 2000 eV above the edge. The physical principles to describe both regimes are basically the same. EXAFS results from interference in the single scattering process of a photoelectron scattered by interaction with the surrounding atoms (Fig. 5.1a), and it provides information on the local structure such as distances between neighbors, coordination, and thermal and structural disorder in a material. Information on the geometry of the local structure is obtained by an analysis of the multiple scattering peaks in the XANES spectra. However, XANES is harder to describe in a quantitative way, so it usually requires comparison with single-particle or atomic multiplet calculations. For a review of different theoretical approaches used to calculate XAS spectra, see, for example, [8].

5.2.3.1 EXAFS Equation

Quantitative analysis of the EXAFS region is possible thanks to the parameterization of this region with the so-called EXAFS equation [5]. As observed in Fig. 5.1c, the spectrum reflects oscillatory variation of $\mu(E)$, as a function of photon energy beyond the absorption edge. We define the EXAFS fine structure function, $\chi(E)$, as

$$\chi(E) = \frac{\mu(E) - \mu_0(E)}{\Delta\mu_0(E)}, \tag{5.2}$$

where $\mu(E)$ is the absorption coefficient, $\mu_0(E)$ a smooth background function representing the absorption of an isolated atom, and $\Delta\mu_0(E)$ the measured jump in the absorption $\mu(E)$ at the threshold energy E_0. These parameters are also represented in Fig. 5.1c. $\chi(E)$ is proportional to the amplitude of the scattered photoelectron at the absorbing atom. Therefore, EXAFS is best understood in terms of the wavelike nature of the photoelectron created in this process. Thus, it is common to convert the X-ray energy to k, the wave number of the photoelectron, being $k^2 = 2m(E - E_0)/\hbar^2$, and m the electron mass. The primary quantity for EXAFS is then $\chi(k)$, the oscillations being a function of the photoelectron wave number. To emphasize the oscillations, $\chi(k)$ is often weighted by a power of k,

typically k^2 or k^3. The different frequencies composing these oscillations correspond to different near-neighbor coordination shells, described and modeled according to the EXAFS equation

$$\chi(k) = \sum_j \frac{N_j S_0^2 F_j(k) \exp(-2k^2\sigma_j^2) \exp\left(-\frac{2R_j^2}{\lambda_j(k)}\right)}{kR_j^2} \sin(2kR_j + \delta_j(k)), \qquad (5.3)$$

where $F_j(k)$ is the backscattering amplitude from each of the N_j neighboring atoms, $\delta_j(k)$ is the total phase shift experienced by the photoelectron, R_j is the distance to the neighboring atom j, σ_j^2 is the disorder in the neighbor distance, a parameter usually known as the Debye–Waller factor, and S_0^2 is the amplitude reduction due to many body effects. The term $\exp(-2R_j^2/\lambda_j(k))$ is due to inelastic losses in the scattering process, with λ_j being the electron mean free path. The EXAFS equation allows us to determine N, R, and σ^2 knowing the scattering amplitude $F(k)$ and phase shift $\delta(k)$ for each path. Furthermore, since these scattering factors depend on the atomic number, Z, of the neighboring atom, EXAFS is also sensitive to the atomic species of the neighborhood.

The EXAFS $\chi(k)$ is usually Fourier transformed into a radial structure function $\chi(R)$ that represents the data in terms of distances from the absorbing atom. Peak positions in this radial structure function roughly correspond to the radii of the scattering shells. Diverse tools to model and fit $\chi(k)$ or $\chi(R)$ have been developed (e.g., [9]) to extract all relevant information about the local environment of a given atom.

5.2.3.2 XAFS Experimental Details

EXAFS experiments are performed with hard X-rays since the extended region is better explored at the K edges of an atom [5]. On a beamline designed for XAFS and EXAFS experiments, synchrotron light passes through an entrance slit, which helps collimate the radiation before entering into a double crystal monochromator. The X-rays diffract off the crystals' lattice planes, which are aligned at an angle θ with respect to the incoming beam. Because of the Bragg scattering condition $n\lambda_j = 2d\sin\theta$, only X-rays of energy $E_n = nhc/\lambda_j$ can reflect off the crystals. Different energies can be selected by changing the angle θ of the crystals. The monochromatic beam passes through an ion chamber that monitors the beam intensity I_0 by absorbing part of it. The beam then passes through the sample, and the intensity of the transmitted X-ray I is measured by a second ion chamber. Taking the natural log of the ratio of I/I_0 yields the absorption as $\mu(E) = \frac{\ln(I/I_0)}{x}$, with x the sample thickness. The sample's absorption can also be determined by measuring the intensity of its X-ray fluorescence, I_f, with a detector that is outside of the beam path, usually oriented at 45° with respect to the sample. In this case $\mu(E)$ is proportional

to I/I_f, that is, without taking the natural log. Finally, the beam passes through a reference sample whose absorption edge is used to help correct for uncertainties in the beam's energy.

5.2.4 X-ray Magnetic Circular Dichroism

Some synchrotron radiation techniques take advantage of the natural polarization of this light in the plane of the electron orbit in order to perform polarization-dependent measurements. This is the case with X-ray magnetic circular dichroism (XMCD), where the difference between two X-ray absorption spectra recorded in a magnetic field, one measured with right circularly polarized light (+1 helicity), the other with left circularly polarized light (−1 helicity), is performed. The XMCD is then defined as

$$\text{XMCD}(E) = \mu^- - \mu^+, \tag{5.4}$$

where μ^- and μ^+ are the absorption coefficients with left and right circularly polarized light, respectively. The differences in the absorption of light with opposite helicities arise from an additional dipole selection rule for dipolar transitions, $\Delta m_j = \pm 1$ for +1 and −1 helicity, respectively, in Eq. (5.1); the dipole operator, $\hat{\varepsilon} \cdot \mathbf{r}$, must also be expressed as dependent on the light polarization. XMCD reflects the difference in the density of empty states with different spin moments, so that information on the magnetic properties of the absorbing atom, such as its spin and orbital magnetic moment, can be obtained.

In a simple atomic monoelectronic picture, XMCD may be understood in terms of the two-step approach described by Schütz et al. [10]. In the first step, a circularly polarized photon excites a spin-polarized electron from a spin-orbit split core level, for example, $2p_{3/2}$ (L_3 edge) and $2p_{1/2}$ (L_2 edge), as illustrated in Fig. 5.2a. When absorbing a circularly polarized photon, some of the orbital moment of the photon can be transferred via the spin-orbit coupling to the electron spin. This results in an effective spin polarization of the excited electrons, a process known as the Fano effect [11]. From the $2p_{3/2}$ state, 62.5% of excited electrons carry a spin of $m_s = +1/2$ and only 37.5% carry a spin of $m_s = -1/2$. From the $2p_{1/2}$ state, 75% of the excited electrons carry a spin of $m_s = -1/2$ and only 25% carry a spin of $m_s = +1/2$. Note that the sign of spin polarization is different for the different $2p$ states, given their different spin-orbit couplings: $(\ell + s)$ in the $p_{3/2}$ state and $(\ell - s)$ in the $p_{1/2}$ state. If there were no spin-orbit splitting, that is, no energy gap between $2p_{3/2}$ and $2p_{1/2}$ states, the averaged spin polarization would be zero.

With these spin and orbital polarized excited electrons, the polarization of the unoccupied final states is probed in the second step of this model. Any imbalance in either spin or orbital momentum in the final states will give rise to a dichroic effect. Thus, in a magnetic material, exchange splitting leads to a splitting of the

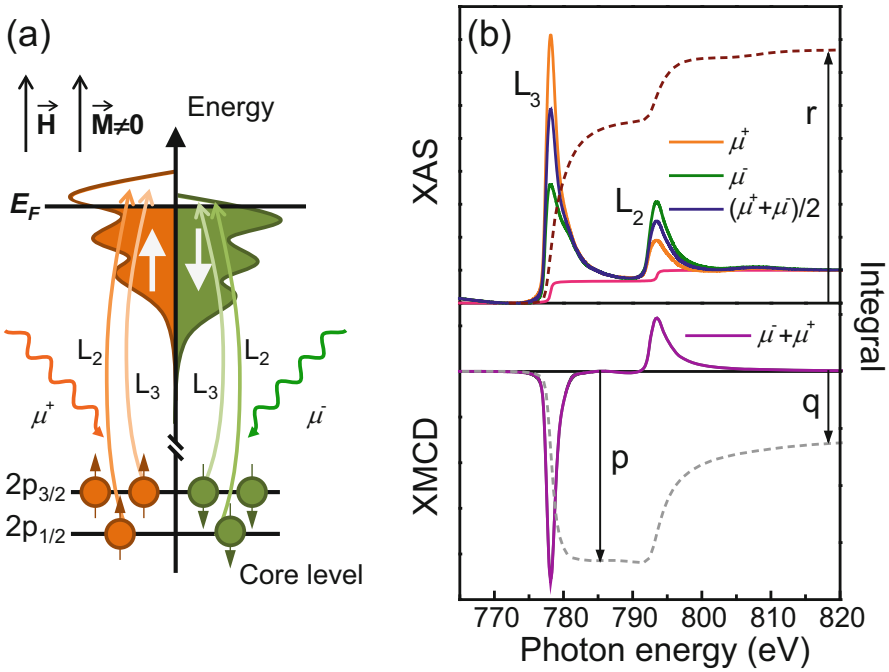

Fig. 5.2 (**a**) Diagram of two-step picture of XMCD for single electron in resonant excitation process for magnetic material. (**b**) XAS and XMCD at Co $L_{2,3}$ for right (μ^+) and left (μ^-) circular polarization together with their integrated intensities. *Arrows* indicate values for p, q, and r used in sum rules. Figure reprinted/adapted with permission from [8]

valence band, lowering the energy for electrons with one spin orientation (majority electrons) and raising it for the other (minority electrons), as illustrated in Fig. 5.2a. The transition probability of electrons in a dipole transition are proportional to the unoccupied density of states, as expressed in Eq. (5.1). If this density of states is different for different spin orientations and the electrons are spin polarized, the absorption spectra will change when the spin polarization is inverted, owing to the change in helicity of the incoming light. This results in such spectra as the one represented in Fig. 5.2b, where XAS recorded with right and left circularly polarized X-rays at the Co $L_{2,3}$ edges in Co-Pt NPs is plotted together with the resulting XMCD signal. The strong core spin-orbit interaction at the transition metal $L_{2,3}$ and lanthanide $M_{4,5}$ edges gives a large dichroism like the one observed for Co in this case, leading to a high sensitivity of the technique (better than the 0.005 monolayer at the surface). Soft X-ray excitations have the additional benefit of giving huge resonances owing to dipole-allowed transitions directly to the magnetic valence state.

5.2.4.1 Sum Rules

Quantitative analysis of the integrated intensities of the XAS and XMCD signal yields element-specific local moments through the application of magneto-optical sum rules for spin-orbit split absorption edges. The derivation of these sum rules by Thole et al. [12] and Carra et al. [13] have transformed XMCD into the powerful standard technique that it is today.

The XMCD sum rules complement the earlier sum rules for isotropic XAS, which relate the total integrated intensity at the $L_{2,3}$ to the number of valence holes, and they relate the core-level spin-orbit split branching ratio [14], B, to the angular part of the spin-orbit interaction, $\langle \ell \cdot s \rangle$, as

$$B \equiv \frac{I(L_3)}{I(L_3) + I(L_2)} = B_0 + \frac{\langle \ell \cdot s \rangle}{n_h}, \tag{5.5}$$

where B_0 is the branching ratio value without spin-orbit interaction and n_h is the number of d holes. B is thus proportional to the ground-state expectation value of the angular part of the spin-orbit interaction per d hole.

The sum rules for the orbital, m_L, and effective spin, $m_{S_{\text{eff}}}$, moments are expressed as

$$m_L = -\frac{4}{3}\frac{q}{r} n_h \tag{5.6}$$

and

$$m_{S_{\text{eff}}} = -\frac{6p - 4q}{r} n_h, \tag{5.7}$$

where p and q are the integrated XMCD intensities for the L_3 and $L_3 + L_2$ edges, respectively. r is the XAS integrated intensity at $L_3 + L_2$, defined as $r = \mu^- + \mu^+$ and calculated after removing the unwanted transitions into higher unoccupied states or into the continuum in the absorption spectra. It is usually performed by subtracting a hyperbolic step function with one step at the L_3 and one at the L_2 edge [15]. Figure 5.2b depicts p, q, r, and this step function for spectra measured at the Co $L_{2,3}$ edges.

The *effective* spin moment in the spin sum rule, Eq. (5.7), is defined as $m_{S_{\text{eff}}} = m_S + m_D$, which takes into account a dipolar term m_D. The latter is expressed as a function of the expectation value of the intra-atomic magnetic dipole operator $\langle T_z \rangle$ [16], $m_D = -7\langle T_z \rangle \mu_B/\hbar$, which reflects the asphericity of the spin moment distribution around the absorbing atom. To determine m_S, one option is to assume that the angle-averaged $\langle T_z \rangle$ is much smaller than the spin moment and can be neglected, as in the case where the absorbing atom is in a cubic (undistorted) symmetry. In the case of lower symmetries or distorted systems, $\langle T_z \rangle$ may be obtained from angle-dependent experiments or be theoretically approximated [16, 17]. For instance, XMCD recorded at the so-called magic angle of 54.7^o with respect to

the sample normal yields $m_{S_{\text{Seff}}} = m_S$. For noncubic structures, $\langle T_z \rangle$ might have a maximum value of $\langle S_z \rangle / 3$, corresponding to the Lorentz local field at the absorbing atom site. However, the angle-averaged of $\langle T_z \rangle$ with this approximation in the whole sample usually cancels out as well.

For a precise estimation of m_L and m_S, one must separate the L_3 and L_2 contributions of the spectrum, which is fairly easy for the heavier $3d$ and for $4d$ and $5d$ elements since the spin-orbit split increases with the nuclear charge of the atom. An interesting analysis of the validity of these sum rules can be found in [17]. Moreover, the number of d holes in the probing atom needs to be known, but there exists no straightforward experimental determination procedure. This drawback may be resolved either by obtaining n_h from band structure calculations or by expressing the sum rule results as magnetic moments per d hole.

From Eqs. (5.6) and (5.7), the orbital-to-spin magnetic moment ratio can be calculated as

$$\frac{m_L}{m_{S_{\text{eff}}}} = \frac{2}{3} \frac{q}{3p - 2q}, \tag{5.8}$$

which is independent of n_h and the r integral.

5.2.4.2 XMCD Experimental Details

To observe XMCD, the magnetization of the sample must have at least a component parallel to the incoming light. The inversion of the magnetization has the same effect on the absorption process as the inversion of the photon polarization. Thus, XMCD measurements can be performed in two equivalent ways: either by changing the helicity while keeping the applied magnetic field constant or by changing the direction of the magnetic field at a constant helicity of the light.

XMCD measurements are performed on beamlines dedicated to polarization-dependent X-ray absorption and excitation spectroscopies. Some beamlines make use of undulators to produce polarized light by longitudinal phasing of the magnetic arrays, which allows for changing the polarization from linear to elliptical and circular. Other beamlines use BMs, with the polarization of the light being controlled by changing the vertical position of the beam emitted: light coming out of the BM is linearly polarized when observed in the bending plane, while out of this plane the polarization is elliptical and can be decomposed into its horizontal and vertical components.

The energy of the beam is selected by setting the angle of incidence of the beam onto a crystal (hard X-rays) or a diffraction grating (soft X-rays) monochromator. Polarized and monochromatized X-rays are directed through the sample, which is located at the center of a magnet. The magnetic field is usually applied along the direction of the incoming beam. The detection of the polarization-dependent X-ray absorption spectra may be performed by fluorescence yield (FY) or total electron yield (TEY), the latter being regularly used in the soft X-ray regime.

TEY detection is similar to FY in that it indirectly measures absorption events by detecting the decay products when the core hole is refilled. In the case of FY, it is photons that are detected, while for TEY one measures the electrons emitted from the surface of the sample. The relatively short path length ($\sim$1000 Å) makes this detection technique surface-sensitive, which can be useful for studies of near-surface phenomena. It also can be beneficial for avoiding "self-absorption" effects that can occur in fluorescence mode [5, 8].

5.3 Examples

Hundreds of works in the literature could be cited to illustrate the benefits of using X-ray spectroscopy to investigate magnetic NPs. Interesting reviews can be found in [18–21]. In what follows, we describe some representative recent examples that combine XAS, EXAFS, and XMCD in their research to study ferrite NPs, magnetic semiconductor NPs, core-shell NP systems, noble-metal NPs, and other assemblies.

5.3.1 Iron Oxide and Ferrite NPs

Iron oxide NPs are probably the most commonly studied particulate systems because of their relatively easy production by chemical routes, low toxicity, and fascinating magnetic properties. Magnetite, Fe_3O_4, and its oxidized phase maghemite, γ-Fe_2O_3, are two iron oxide systems that are regularly studied. Both phases have an inverse spinel crystal structure with Fe cations distributed among octahedral, O_h, and tetrahedral, T_d, sites. In Fe_3O_4, Fe^{2+}, and Fe^{3+} cations occupy octahedral sites, while the tetrahedral ones are only occupied by Fe^{3+}. Maghemite is a fully trivalent (Fe^{3+} cations occupying all Fe sites in the structure) iron oxide.

X-ray spectroscopic methods have become valuable techniques in the characterization of the electronic properties of these mixed-valence nanomaterials. In fact, each specific cation in the lattice structure generates a unique XMCD signature determined by its valence state, site symmetry, and moment direction, which can be computed using atomic multiplet calculations (Fig. 5.3). Fe $L_{2,3}$ XMCD is therefore routinely used to determine the relative magnetic contributions of the cations at O_h and T_d sites. By fitting a weighted sum of these calculated spectra to the measured XMCD signal, the site occupations of the Fe cations can be obtained. This approach is very useful for obtaining information about the valency and location of Fe ions within a structure, even if the main focus of the research is not on their magnetism. In addition, comparison with the local coordination obtained from EXAFS analysis provides a complete picture of the Fe sites in the structure. Using magnetite as a starting point, other doped ferrites, such as $Fe_{3-x}Ti_xO_4$, $Fe_{3-x}Zn_xO_4$, and $Fe_{3-x}Co_xO_4$, have been studied. XMCD analysis on some of these systems is reviewed in [8].

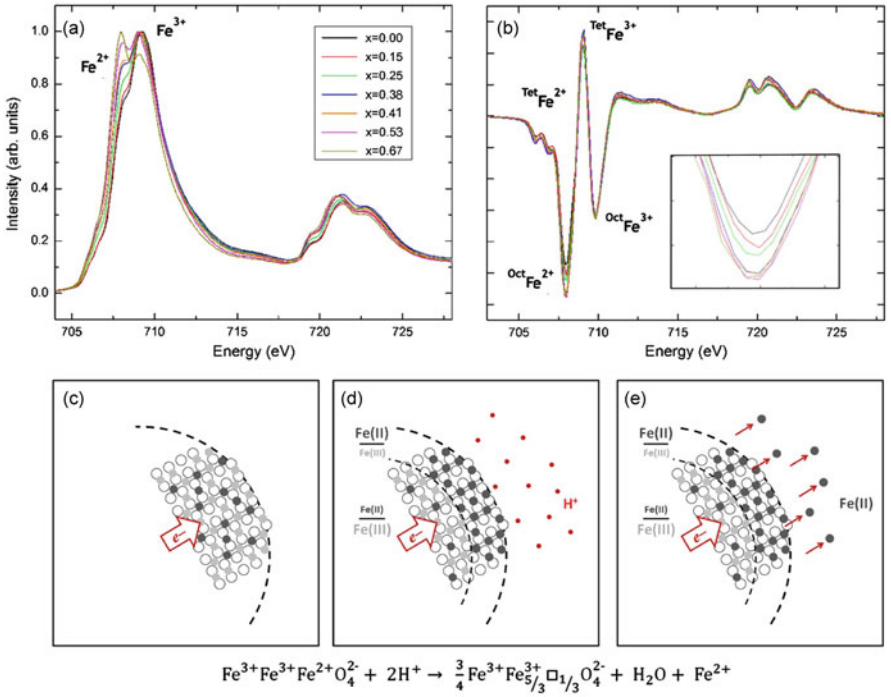

Fig. 5.3 (**a**) XAS and (**b**) XMCD at Fe $L_{2,3}$ edges for $Fe_{3-x}Ti_xO_4$ NPs ($x = 0$–0.67). Inset in (**b**) shows details of octahedral Fe2+ component. The XMCD spectra are normalized to the intensity of the Fe3+ octahedral site for comparison. (**c**)–(**e**) illustrate the conceptual model for Fe2+(aq) release from the particles. Figure reprinted/adapted with permission from [22]

Pearce et al. [22] used XANES, EXAFS, and XMCD to study a series of $Fe_{3-x}Ti_xO_4$ NPs synthesized in aqueous solutions. They obtain NP systems with a tunable built-in Fe^{2+}/Fe^{3+} ratio based on Ti^{4+} substitution for Fe^{3+} in the lattice, both on O_h and T_d sites. Figure 5.3a, b shows Fe $L_{2,3}$ XAS and XMCD for samples with varying Ti concentration. Notice how the characteristic features for Fe^{2+} and Fe^{3+} on the XAS and XMCD spectra change with Ti incorporation. A clever combination of bulk-sensitive aspects of Fe *K* XANES and EXAFS with the surface-sensitive character of Fe $L_{2,3}$ XAS and XMCD techniques allowed the researchers to obtain a complete picture of the inner and surface structure of the $Fe_{3-x}Ti_xO_4$ NPs. Comparison of measurements before and after dissolution enabled them to discriminate between different Fe^{2+} reservoirs based on the observed spontaneous decrease in Fe^{2+} in the bulk NP structure, Fe^{2+} enrichment in the near-surface, and release of Fe^{2+} into solution. This model is illustrated in Fig. 5.3c, e. This suggests an apparent distribution of Fe^{2+} at the NP/solution interface and the persistence of surface Fe^{2+} enrichment through NP oxidation by acidic dissolution.

Similarly, the combination of EXAFS and XMCD analysis of $ZnFe_2O_4$ nanocrystals prepared by forced hydrolysis in polyols allowed Ammar et al. [23] to

investigate the cation distribution in O_h and T_d sites. Their findings differ from the characteristic cation structure of the bulk material as a result of nano-size effects. Fe^{3+} cations are therefore observed in a ratio that depends on the crystallite size, which has important consequences for the magnetic properties of these particles.

Guyodo et al. [24] have also used this methodology of combining diverse XAS techniques to demonstrate unambiguously the presence of tetrahedrally coordinated Fe^{3+} in the mineral structure of ferrihydrite, an important iron oxyhydroxide for earth and environmental sciences, biology, and technology. XMCD and EXAFS measurements and analysis on small crystalline particles allowed them to answer a long-standing open question about the quantification of the presence—or absence—of a substantial amount of tetrahedrally coordinated Fe^{3+}. They found a concentration of 20–30% of Fe^{3+} in T_d sites. Moreover, an antiferromagnetic coupling between tetrahedral and octahedral sublattices was observed, with the octahedral sublattice parallel to the external magnetic field.

Gilbert et al. [25] also used several spectroscopic techniques to characterize the products of oxidizing uncoated and oleic acid–coated magnetite NPs in air. They showed that ferrous iron sites within ferric iron oxide NPs coated by an organic ligand could persist under ambient conditions. Their results are highly relevant as their NPs have the potential to perform or catalyze technologically useful redox reactions through interfacial electron transfer. Similar studies followed (e.g., [26]), where XAS techniques were crucial to understand these redox mechanisms.

5.3.2 Magnetic Semiconductor NPs

Dilute magnetic semiconductors (DMSs) are materials that play an important role in interdisciplinary nanoscience and the future of spintronics because of the integration of charge and spin degrees of freedom with which new technologies for information storage and processing are expected to emerge. Several systems are being explored in this direction, both theoretically and experimentally, with GaN and semiconducting metal oxides, such as ZnO, TiO_2, and SnO_2, attracting great interest owing to the theoretical results predicting room-temperature ferromagnetism for a correct level of dopant Mn, Fe, or Co atoms [27].

The nanostructures of DMSs are particularly interesting owing to their potential in the miniaturization of electronic devices. Moreover, surface defects such as Zn and O vacancies with broken chemical bonds and charge imbalance may influence and mediate the magnetic coupling between dopants. Surprisingly, ZnO NPs capped with different molecules (trioctylphosphine-TOPO, dodecylamine-AMINE, and dodecanethiol-THIOL) and ZnS/ZnO heterostructures exhibit interesting magnetic properties in the absence of 3*d* magnetic atoms [28]. XAS techniques, and XMCD at both $L_{2,3}$ and K edges in Zn in particular, have been decisive in demonstrating that the magnetism in these ZnO NP materials is intrinsic and located at the ZnO conduction band. These techniques have also allowed researchers to investigate the

structural, magnetic, and electronic structure of Co-doped ZnO NPs, revealing a successful incorporation of Co^{2+} dopants into Zn sites in the lattice, which account for their observed intrinsic ferromagnetism at room temperature [29].

5.3.3 Core-Shell NPs

XAS and XMCD measurements in the total electron yield mode are surface-sensitive and can be employed to extract the contribution of buried interfaces. This feature has been particularly useful for investigating core-shell NP systems with interesting magnetic properties, such as exchange bias (EB) effects. Studies of EB in a ferromagnetic Co core—antiferromagnetic CoO shell NPs using XMCD have revealed important features to unravel the magnetic behavior at the Co/CoO interface [30]. XMCD measurements at the Co $L_{2,3}$ edges and comparison with multiplet calculations of the contribution from the CoO shell, both plotted in Fig. 5.4, revealed a sizeable ferromagnetic signal originating from the CoO shell. This contribution cannot be attributed to the canted antiferromagnetic spins of polycrystalline Co/CoO core-shell systems owing to the large anisotropy energy of the Co^{2+} ion. Instead, these results give direct evidence for the existence of rotatable interfacial uncompensated Co spins in the nominally antiferromagnetic CoO shell, thereby supporting the uncompensated spin model as a microscopic description of the EB mechanism. Similar Fe/FeO interfaces in NP systems have been studied with Fe $L_{2,3}$ XMCD [31], where EB effects originating at the interface between Fe core and FeO shell/matrix were also observed.

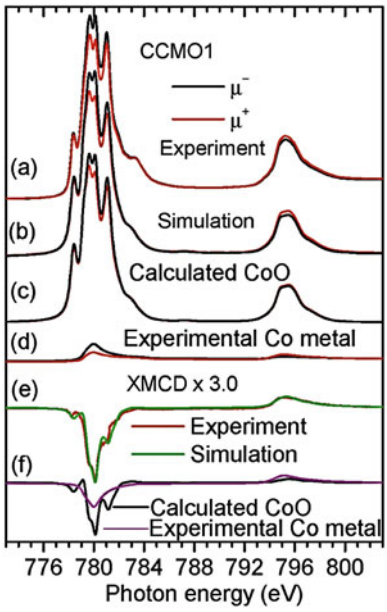

Fig. 5.4 (**a**) Experimental μ^+ and μ^- spectra of core-shell Co/CoO NPs. (**b**) Simulated μ^+ and μ^- spectra by a superposition of calculated data for CoO shown in (**c**) and experimental data for Co metal shown in (**d**). (**e**) Comparison of experimental XMCD spectrum of core-shell NPs and simulated XMCD spectrum by superposition of calculated XMCD from CoO shell (*black line* shown in (**f**)) and experimental Co metal XMCD (*magenta line* shown in (**f**)). Figure reprinted/adapted with permission from [30]

Interdiffusion at the core/shell interface has a critical role on the properties of these core-shell NPs. However, quantitative and direct information about interdiffused intermediate shells is not easily accessed with conventional techniques. Using X-ray spectroscopies, Juhin et al. [32] have overcome this drawback and have been able to evidence the existence of a 1.1 nm thick $(Fe, Mn)_3O_4$ interface in nominally γ-Fe_2O_3-Mn_3O_4 core-shell NPs. Their study exploits the unparallel advantages of hard X-rays, which provides chemical selectivity, bulk sensitivity, and low self-absorption at the *K* pre-edge. A combination of magneto-spectroscopic techniques including resonant inelastic X-ray scattering and XMCD performed in synchrotron radiation facilities, with transmission electron microscopy and electron energy loss spectroscopy, allowed them to quantitatively elucidate the buried internal structure of these complex core-shell nano-objects.

5.3.4 Noble-Metal NPs

It has been demonstrated that reducing the dimension of transition metals leads to novel electronic and magnetic phenomena as a consequence of the narrowing of the valence *d* bands in low-dimensional *d* metals, which results in a nonnegligible magnetic moment [2, 33]. The increase in the density of states at the Fermi level, E_F, opens up the possibility of detecting magnetic phenomena in materials that are nonmagnetic in bulk, as in the case of noble metals: Pd, Ag, Pt, and Au. The element selectivity of XAS and XMCD techniques have proved to be determinant in demonstrating that the origin of the detected magnetic moments is in the noble-metal atoms.

Magnetism in Au NPs is surprising since their bulk counterpart has a diamagnetic character. However, several reports have demonstrated the magnetic behavior of Au NPs, with features that the usual rules of magnetism are unable to explain. A review of magnetic Au NPs can be found in [34]. The largest XMCD signal in Au NPs has been detected on Au particles of around 2 nm in size deposited on a template of the *Sulfolobus acidocaldarius* S-layer [35]. The magnetic moment per particle was determined from Langevin fitting of the field-dependent Au $L_{2,3}$ XMCD measurements and was estimated to be several μ_B. The presence of sulfur (S) atoms at the template surface binding the Au particle seems to be of paramount importance for the magnetism at the particle, since Au NPs deposited on a *Bacilus sphaericus* S-layer, where there is no S present, do no exhibit the same magnetic properties. On each Au particle thiols and other groups present in the S-layer supply holes to the 5*d* band. Their spins are ferromagnetically coupled by spin-spin exchange interactions. In addition, an appreciable orbital moment is generated by spin-orbit interaction. Hund's third rule is satisfied and the orbital moment is parallel to the spin. The magnetic behavior of the particle is paramagnetic, with very low anisotropy. Thus, the external field sets the common alignment direction of the magnetization of all particles. The very large magnetic moment per Au atom observed in the XMCD

originates from the large charge transfer from the S-layer supporting template to the Au surface atoms and the reshuffling of holes to the particle core [35].

Bartolomé et al. [36] used XANES and XMCD to study the magnetic properties of Pt_{13} and hydrogenated $Pt_{13}Hm$ clusters dispersed in NaY zeolite. Similar to the case of Au NPs, the total magnetic-moment field-dependent Pt $L_{2,3}$ XMCD was measured and scaled to the absolute value of the average moment per Pt atom after application of the magneto-optical sum rules to the high field spectra. A magnetic moment per cluster of $m = 3.7\mu_B$ for Pt_{13} and 3.0 μ_B for $Pt_{13}Hm$ was obtained. The orbital to spin moment was found to be $m_L/m_S = 0.32$, that is, a very important fraction of the magnetic moment is of orbital origin. This is ascribed to the contribution of the predominant surface Pt atoms in the Pt_{13} clusters, which have a very different Pt near-neighbor surrounding than in bulk or in a Pt thin film. Electronic structure calculations have indicated the existence of surface states in these kinds of clusters, similar to surface bands in films, which may support an enhanced orbital momentum or anisotropy [36].

In both the previously described Au and Pt NP systems, EXAFS measurements and analysis were used to confirm the metallic character and structure of the noble metals within the particles [35, 36].

5.3.5 NP Assemblies

Bimetallic magnetic NPs of 3*d* ferromagnets and heavy metals are very attractive systems for magnetic storage applications because they offer new possibilities for tuning material performance aiming to control the magnetic anisotropy energy. X-ray spectroscopy has been extensively used to study such systems given the interplay between the electronic, structural, and magnetic properties of such bimetallic NP assemblies.

Using XANES, EXAFS, and XMCD, the properties of Co-M NPs, with M = Au, Ag, Cu, W, Pt, and Pd, have been thoroughly investigated [37–40]. These granular films consist of self-organized lattices of nanometer-sized Co magnetic clusters (1–4 nm in diameter) prepared by sequential sputtering deposition of Al_2O_3 and Co layers on a Si substrate. Depending on the metal used for capping, the magnetic anisotropy of the Co NP is modified either via hybridization at the Co/M interface, as in the case of M = Au, Ag, and Cu, or by the presence of a Co-M alloy, which is the case for M = W, Pt, and Pd (see Fig. 5.5a, d for illustrations of the Co-M NP structure in each case). Co-Pt and Co-Pd alloy granular systems exhibit perpendicular magnetic anisotropy, which is highly relevant for applications in perpendicular magnetic media.

XANES at the Co *K* and M L_3 edges (M = W, Pt, and Pd) revealed important changes in the electronic structure of both 3*d* and 4*p* bands in Co and *d* bands in the M atoms due to hybridization. The presence of short-range order alloys within NPs and their important consequences in their magnetic properties was demonstrated

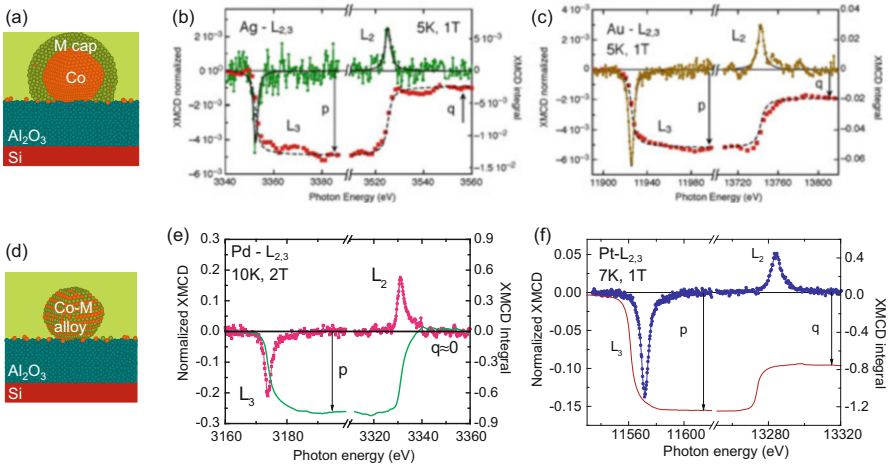

Fig. 5.5 (**a**) Illustration of M-capped Co NP for M = Ag, Au. (**b**, **c**) XMCD signal and integrated intensity at Ag and Au $L_{2,3}$ edges for Co-Ag and Co-Au NPs, respectively. (**d**) Illustration of Co-M alloy NP for M = W, Pd, Pt. (**e**, **f**) XMCD signal and integrated intensity at Pd and Pt $L_{2,3}$ edges for Co-Pd and Co-Pt NPs, respectively. The higher limit for the *p* and *q* integrals, used for the sum rules analysis, is given

with EXAFS. XMCD measurements at the $L_{2,3}$ edges of the corresponding M capping layer revealed sizeable magnetic polarization effects at the Au, Ag, Cu, W, Pt, and Pd atoms in contact with Co in these NP assemblies. Figure 5.5 shows the XMCD results for four metal-capped Co NPs, namely, Co-Ag, Co-Au, Co-Pd, and Co-Pt NPs. In all cases the nonzero XMCD signal indicates that the ferromagnetic Co has polarized the M atoms with the total moment parallel to the Co magnetization direction. In the case of Ag and, even more, in Pd, the orbital moment is practically quenched, while it is at least one order of magnitude larger in the Au and Pt cases. This feature is probably related to the fact that the spin-orbit coupling constant is larger in the Au and Pt cases [2, 33].

Similarly, the influence of local chemical composition, structure, and surface modifications on the magnetic properties of Fe_xPt_{1-x} NPs have been studied by means of XAS by Schmitz-Antoniak et al. [20, 41, 42]. EXAFS and XMCD allowed them to investigate the local structure around Fe and Pt atoms and to determine the spin and orbital magnetic moments of the two atomic species, respectively. The detailed atomistic picture deduced from their experimental results was compared to calculations within density functional theory, which makes it possible to state design rules for the preparation of NPs with the desired magnetic properties. This approach opens up ways of tailoring nanomagnets with desired magnetic properties to diverse and customized applications.

Table 5.1 Summary of information extracted with X-ray absorption spectroscopy techniques

Technique	Energies	Information
XANES	Soft	Valence and local coordination of atoms; electron transfer and hybridization; comparison with atomic multiplet calculations yields quantitative information on valence and coordination
	Hard	Valence and local coordination of atoms; electron transfer and hybridization; comparison with calculations yields quantitative information on valence and coordination
EXAFS	Hard	Interatomic distances and local environment of absorbing atom; number and identity of near neighbors; coordination environment; for doped systems, location of dopants in lattice
XMCD	Soft	Determination of spin and orbital magnetic moments of absorbing atoms through application of sum rules; comparison with multiplet calculations yields relative occupation and magnetic contribution of cations in octahedral and tetrahedral sites in, e.g., Fe oxide NPs
	Hard	Determination of spin and orbital magnetic moments through application of sum rules; characterization and quantification of *d*-band magnetic polarization in noble-metal NPs (e.g., Ag, Pd, Pt, Au)

5.4 Summary and Conclusion

We recapitulate the main microscopic information that XANES, EXAFS, and XMCD techniques yield in Table 5.1. Soft and hard X-ray regions are defined as described in Sect. 5.2.2.

X-ray spectroscopies are powerful techniques for the characterization of materials. In the field of magnetic NPs, the combination of experiment and theory has provided invaluable information about the electronic state, local structure, and magnetic properties of the atoms composing the particles. It is clear that research in this field has benefited from these compelling techniques and will continue to make important advances thanks to their use.

Acknowledgements The author would like to acknowledge the work of all her collaborators and colleagues who have contributed to the subject of magnetic NPs and XAS. In particular, she is grateful to Prof. Juan Bartolome, Dr. Luis Miguel Garcia, and Prof. Gerrit van der Laan for all their support and helpful discussions.

References

1. Srajer G, Lewis LH, Bader SD, Epstein AJ, Fadley CS, Fullerton EE, Hoffmann A, Kortright JB, Krishnan KM, Majetich SA, Rahman TS, Ross CA, Salamon MB, Schuller IK, Schulthess TC, Sun JZ (2006) Advances in nanomagnetism via X-ray techniques. J Magn Magn Mater 307:1–31

2. Figueroa AI (2015) Magnetic nanoparticles. A study by synchrotron radiation and RF transverse susceptibility. Springer Theses, Springer International Publishing AG, Cham
3. Hollas JM (2004) Modern spectroscopy. Wiley, New York
4. Hof M (2005) Basics of optical spectroscopy. Wiley, Weinheim
5. Bunker G (2010) Introduction to XAFS. A practical guide to X-ray absorption fine structure spectroscopy. Cambridge University Press, Cambridge
6. Conradson S (2000) XAFS. A technique to probe local structure. Los Alamos Sci 26:422
7. Newville M (2004) Fundamentals of XAFS. University of Chicago, Chicago
8. van der Laan G, Figueroa AI (2014) X-ray magnetic circular dichroism–a versatile tool to study magnetism. Coord Chem Rev 277–278:95–129
9. Ravel B, Newville M (2005) ATHENA, ARTEMIS, HEPHAESTUS: data analysis for X-ray absorption spectroscopy using IFEFFIT. J Synchrotron Radiat 12:537–541
10. Schütz G, Knülle M, Wienke R, Wilhelm W, Wagner W, Kienle P, Frahm R (1988) Z Phys B Condens Matter 73(1):67–75
11. Fano U (1969) Spin orientation of photoelectrons ejected by circularly polarized light. Phys Rev 178:131–136
12. Thole BT, Carra P, Sette F, van der Laan G (1992) X-ray circular dichroism as a probe of orbital magnetization. Phys Rev Lett 68:1943
13. Carra P, Thole BT, Altarelli M, Wang X (1993) X-ray circular dichroism and local magnetic fields. Phys Rev Lett 70:694
14. Thole BT, van der Laan G (1988) Branching ratio in X-ray absorption spectroscopy. Phys Rev B 38:3158
15. Chen CT, Idzerda YU, SLin H-J, Smith NV, Meigs G, Chaban E, Ho GH, Pellegrin E, Sette F (1995) Experimental confirmation of the X-ray magnetic circular dichroism sum rules for iron and cobalt. Phys Rev Lett 75:152
16. Stohr J, König H (1995) Determination of spin- and orbital-moment anisotropies in transition metals by angle-dependent X-ray magnetic circular dichroism. Phys Rev Lett 75:3748–3751
17. Piamonteze C, Miedema P, de Groot MF (2009) Accuracy of the spin sum rule in XMCD for the transition-metal l edges from manganese to copper. Phys Rev B 80:184410
18. Bansmann J, Baker SH, Binns C, Blackman JA, Bucher JP, Dorantes Dávila J, Dupuis V, Favre L, Kechrako D, Kleibert A, Meiwes-Broer KH, Pastor GM, Perez A, Toulemonde O, Trohidou KN, Tuaillon J, Xie Y (2005) Magnetic and structural properties of isolated and assembled clusters. Surf. Sci. Rep. 56:189–275
19. Baker SH, Roy M, Gurman SJ, Binns C (2009) Extended X-ray absorption fine structure studies of the atomic structure of nanoparticles in different metallic matrices. J Phys Condens Matter 21:183002
20. Schmitz-Antoniak C (2015) X-ray absorption spectroscopy on magnetic nanoscale systems for modern applications. Rep Prog Phys 78:062501
21. López-Ortega A, Estrader M, Salazar-Alvarez G, Roca AG, Nogués J (2015) Applications of exchange coupled bi-magnetic hard/soft and soft/hard magnetic core/shell nanoparticles. Phys Rep 553:1–32
22. Pearce CI, Qafoku O, Liu J, Arenholz E, Heald SM, Kukkadapu RK, Gorski CA, Henderson CMB, Rosso KM (2012) Synthesis and properties of titanomagnetite (Fe3xTixO4) nanoparticles: a tunable solid-state Fe(II/III) redox system. J Colloid Interface Sci 387:24–38
23. Ammar S, Jouini N, Fiévet F, Stephan O, Marhic C, Richard M, Villain F, Cartier dit Moulin Ch, Brice S, Sainctavit P (2004) Influence of the synthesis parameters on the cationic distribution of $ZnFe_2O_4$ nanoparticles obtained by forced hydrolysis in polyol medium. J Non-Cryst Solids 345–346:658–662
24. Guyodo Y, Sainctavit P, Arrio MA, Carvallo C, Penn RL, Erbs JJ, Forsberg BS, Morin G, Maillot F, Lagroix F, Bonville P, Wilhelm F, Rogalev A (2012). X-ray magnetic circular dichroism provides strong evidence for tetrahedral iron in ferrihydrite. Geochem Geophys Geosyst 13:Q06Z44

25. Gilbert B, Katz JE, Denlinger JD, Yin Y, Falcone R, Waychunas GA (2010) Soft X-ray spectroscopy study of the electronic structure of oxidized and partially oxidized magnetite nanoparticles. J Phys Chem C 114:21994–22001
26. Byrne JM, van der Laan G, Figueroa AI, Qafoku O, Wang C, Pearce CI, Jackson M, Feinberg J, Rosso KM, Kappler A (2016) Size dependent microbial oxidation and reduction of magnetite nano- and micro-particles. Sci Rep 6:30969
27. Dietl T, Ohno H, Matsukura F, Cibert J, Ferrand D (2000) Zener model description of ferromagnetism in zinc-blende magnetic semiconductors. Science 287:1019
28. Guglieri C, Laguna-Marco MA, Garcia MA, Carmona N, Céspedes E, García-Hernández M, Espinosa A, Chaboy J (2012) XMCD proof of ferromagnetic behavior in ZnO nanoparticles. J Phys Chem C 116(11):6608
29. Kumar S, Song TK, Gautam S, Chae KH, Kim SS, Jang KW (2015) Structural, magnetic and electronic structure properties of Co doped ZnO nanoparticles. Mater Res Bull 66:76–82
30. Ge C, Wan X, Pellegrin E, Hu Z, Valvidares M, Barla A, Liang W-I, Chu Y-H, Zoua W, Dua Y (2013) Direct observation of rotatable uncompensated spins in the exchange bias system Co/CoO–MgO. Nanoscale 5:10236
31. Kaur M, Qiang Y, Jiang W, Pearce C, McCloy JS (2014) Magnetization measurements and XMCD studies on ion irradiated iron oxide and core-shell iron/iron-oxide nanomaterials. IEEE Trans Magn 50(11):4800305
32. Juhin A, Lopez-Ortega A, Sikora M, Carvallo C, Estrader M, Estrade S, Peiro F, Baro MD, Sainctavit P, Glatzel P, Nogues J (2014) Direct evidence for an interdiffused intermediate layer in bi-magnetic core–shell nanoparticles. Nanoscale 6:11911
33. Bartolomé J, Figueroa AI, Bartolomé F, García LM, Wilhelm F, Rogalev A (2013) d-Band magnetism of Ag, Au, Pd and Pt studied with XMCD. Solid State Phenom 194:92–97
34. Nealon GL, Donnio B, Greget R, Kappler J-P, Terazzi E, Gallani J-L (2012) Magnetism in gold nanoparticles. Nanoscale 4:5244
35. Bartolomé J, Bartolomé F, García LM, Figueroa AI, Repollé s A, Martínez MJ, Luis F, Magén C, Selenska-Pobell S, Pobell F, Reitz T, Schonemann R, Herrmannsdorfer T, Merroun M, Geissler A, Wilhelm F, Rogalev A (2012). Strong paramagnetism of gold nanoparticles deposited on a Sulfolobus acidocaldarius S layer. Phys Rev Lett 109:247203
36. Bartolomé J, Bartolomé F, García LM, Roduner E, Akdogan Y, Wilhelm F, Rogalev A (2009) Magnetization of Pt_{13} clusters supported in a NaY zeolite: a XANES and XMCD study. Phys Rev B 80:014404
37. Bartolomé J, García LM, Bartolomé F, Luis F, Lopez-Ruiz R, Petroff F, Deranlot C, Wilhelm F, Rogalev A, Bencok P, Brookes NB, Ruiz L, Gonzalez-Calbet JM (2008) Magnetic polarization of noble metals by Co nanoparticles in M-capped granular multilayers (M = Cu, Ag, and Au): an X-ray magnetic circular dichroism study. Phys Rev B 77:184420
38. Figueroa AI, Bartolomé J, García LM, Bartolomé F, Magen C, Ibarra A, Ruiz L, Gonzalez-Calbet JM, Petroff F, Deranlot C, Pascarelli S, Bencok P, Brookes NB, Wilhelm F, Rogalev A (2011) Structural and magnetic properties of amorphous Co-W alloyed nanoparticles. Phys Rev B 84:184423
39. Figueroa AI, Bartolomé J, García LM, Bartolomé F, Bunau O, Stankiewicz J, Ruiz L, Gonzalez-Calbet JM, Petroff F, Deranlot C, Pascarelli S, Bencok P, Brookes NB, Wilhelm F, Smekhova A, Rogalev A (2014) Structural and magnetic properties of granular Co-Pt multilayers with perpendicular magnetic anisotropy. Phys Rev B 90:174421
40. Vivas LG, Rubin J, Figueroa AI, Bartolomé F, García LM, Deranlot C, Petroff F, Ruiz L, Gonzalez-Calbet JM, Pascarelli S, Brookes NB, Wilhelm F, Chorro M, Rogalev A, Bartolomé J (2015) Perpendicular magnetic anisotropy in granular multilayers of CoPd alloyed nanoparticles. Phys Rev B 93(17), 174410
41. Antoniak C, Warland A, Darbandi M, Spasova M, Trunova A, Fauth K, Aziz EF, Farle M, Wende H (2010) X-ray absorption measurements on nanoparticle systems: self-assembled arrays and dispersions. J Phys D Appl Phys 43(47):474007
42. Schmitz-Antoniak C (2013). Characterisation of FePt nanomagnets by X-ray absorption spectroscopy. Phys Status Solidi A 210(7):1298–1304

Chapter 6
Spin Polarization and Small Size Effect in Bare Silver Nanoparticles

Wen-Hsien Li and Chi-Hung Lee

6.1 Introduction

6.1.1 Magnetism of Noble Metals in Bulk Form

The term *noble metal* in chemistry refers to those transition-metal elements that are resistant to corrosion and oxidation in humid environments [1]. This class of elements includes the 3*d*, 4*d*, and 5*d* transition metals of ^{29}Cu, ^{44}Ru, ^{45}Rh, ^{46}Pd, ^{47}Ag, ^{76}Os, ^{77}Ir, ^{78}Pt, and ^{79}Au. Among these, the *d* bands of Ru, Rh, Pd, Os, Ir, and Pt are partially filled, giving rise to a nonzero atomic magnetic moment for each of these six elements. The atomic moments in these elements do not interact with each other but will respond to an external magnetic field, generating no spontaneous magnetic ordering but paramagnetic moments. In physics, the definition of a noble metal is restricted to those transition-metal elements with a completely filled *d* band [2]. From this perspective, only Cu, Ag, and Au are noble metals. The completely filled *d* bands give zero magnetic moments for Cu, Ag, and Au. In this chapter we follow the definition used in physics and focus on the magnetic properties of the noble metals Cu, Ag, and Au.

It is known that the magnetic behavior of a material is a direct consequence of the electron configuration. The band structures and Fermi surfaces of noble metals have been comprehensively studied both theoretically and experimentally. Generally speaking, the band structures of the 3*d*, 4*d*, and 5*d* transition metals are similar [3, 4]. Near the Fermi level, there is a broad, nearly free-electron-like *s*–*p* band that overlaps the relatively narrow *d* band in specific crystallographic directions [4]. The Fermi level of most transition metals falls into the *d*-band complex, but the

W.-H. Li (✉) • C.-H. Lee
Department of Physics, National Central University, Jhongli 32001, Taiwan
e-mail: whli@phy.ncu.edu.tw

© Springer International Publishing AG 2017

S.K. Sharma (ed.), *Complex Magnetic Nanostructures*,
DOI 10.1007/978-3-319-52087-2_6

completely filled *d* bands of Cu, Ag, and Au lie far below the Fermi energy, so that the *s–d* hybridization is negligibly small. The filled ion core and *d* bands give rise to a diamagnetic response to an applied magnetic field, whereas conduction electrons behave as a Pauli paramagnet. It appears that the diamagnetic responses are stronger than the Pauli paramagnetic ones in Cu, Ag, and Au, which gives rise to the diamagnetic character in their bulk forms.

6.1.2 Magnetism of Nanosized Noble Metals

Nanoparticle (NP) is a term used to indicate materials having sizes in the nanometer scale in all three spatial dimensions. Depending on their actual size, NPs may or may not exhibit properties that differ significantly from those observed in their bulk form [5]. Generally speaking, size-dependent properties will be revealed in NPs with diameters smaller than, say, 50 nm. The study of small NPs of various types is currently an area of intense scientific interest with regard to their fundamental properties as well as their practical applications for the next generation of devices [6, 7]. There are many ways to fabricate metal NPs, but the nucleation of atoms through chemical or physical processes is frequently employed for the fabrication of macroscopic amounts of small NPs. NPs fabricated through chemical processes are unavoidably capped by the organic molecules used as the reduction agents. These capping molecules not only stabilize the NP in the core but will also interact with the surface atoms. This interaction affects the physical properties of the NP. Studies conducted using surfactant-capped NPs reflect the physical properties of NP-surfactant complexes, rather than those of the NPs themselves. For example, it has been suggested [8] that the appearance of magnetic moments in thiol-capped Au NPs is associated with the 5*d* localized holes created through the covalent Au–S bonding between the surface Au ions and the S ions of the capping thiols. It is the strong affinity between Au and S ions, rather than the size effects themselves, that induces a noticeable charge transfer from the surface Au ions to the S ions that triggers the covalent Au–S bonding for the magnetism in Au NPs [9, 10]. Undoubtedly, NPs free from capping agents are needed for the investigation of the results of the size reduction itself. Metal NPs without capping agents may be fabricated by breaking down the bulk metal or building up from the atoms. The breakdown of bulk metals can be achieved by mechanical milling. This is a good way to fabricate particles with a high melting point, but it is difficult to control the particle size or produces particles smaller than 100 nm in diameter. The building-up method involves the assembly of atoms into small particles, which can be achieved through thermal evaporation coupled with cold condensation in an inner gas atmosphere [11].

An NP consists of a limited number of atoms, with a large fraction of them being on the surface where the coordinate number is much reduced. Obviously, the electronic properties of NPs will be affected by the broken symmetry and the disruption of lattice periodicity at the surface [12–15] and by the quantum

confinement of the conduction electrons [16–18]. Many novel magnetic, electronic, optical, and catalytic properties have been found in NPs [19–24]. In particular, a great variety of magnetic phenomena, such as giant paramagnetism, super-paramagnetism, spontaneous ferromagnetic moments, quantum-confined Brillouin magnetization, and thermally induced magnetization, have all been observed in noble-metal NPs [20, 25–38]. However, most studies conducted on the magnetic behavior of noble-metal NPs were performed using polymer-capped particles, with only a limited number of studies focusing on the magnetic properties of noble-metal NPs themselves.

6.1.3 Size Effects

It is known that the atomic environment of the atoms on the surface of a particle is different from those in the interior. Clearly, the physical and chemical behaviors of surface atoms will differ from those in the interior. In particular, surface atoms are relatively loosely bonded to the particle, which can be chemically very active with extrinsic stimulation. This surface effect is revealed in particles with sizes on the order of a few hundred nanometers, where the ratio between the number of surface and core atoms is no longer negligible [12]. The small size effect marks results from the disruption of the lattice periodicity at the particle surface. In addition to softening of the phonon modes from the weakening of the lattice rigidness at the surface, surface phonon modes will be revealed at low frequency when the total amount of surface atoms is not negligible [13–15]. Small size effects can be expected in particles a few dozen nanometers in diameter. Furthermore, a significant amount of electron charge redistribution will also occur if the lattice periodicity is severely limited. For example, there are 25 lattice periodicities along each crystallographic axis direction in a 10 nm Au NP, with two unit cells at the surface. Rearrangement of the electron charge distribution to accommodate the surface disruption can be anticipated. This electron charge redistribution can give rise to the significantly different physical characteristics of NPs compared to bulk materials.

Quantum confinement will be encountered if the spatial dimensions of the NPs are further reduced. Spatial confinement restricts the spatial motions of electrons, which results in a splitting of the electron energy bands near the Fermi energy into discrete narrow subbands [16–18]. The average electron band separation, known as the Kubo gap, is inversely proportional to the density of states at the Fermi energy $D(E_F)$ [16, 18]. In the free electron approximation [16], it takes the form

$$\Delta = \frac{1}{D\left(E_F\right)} = \frac{2\pi^2\hbar^2}{m(3\pi^2 n)^{1/3}V}, \tag{6.1}$$

where $\hbar$ is Planck's constant divided by 2π, m is the electron mass, n is the free electron density, and V is the volume of the NP. Apparently, the size of the Kubo

gap that opens up at the Fermi level depends very strongly on the diameter d of the NP and is inversely proportional to d^3. Quantum confinement governs the electronic behavior of particles smaller than 10 nm in diameter, but not larger. For example, the Kubo gap in a 10 nm Ag NP, estimated according to the Kubo formula, is only 0.23 meV, which corresponds to a thermal energy of 2.7 K, which will be barely visible at temperatures as low as 10 K. The Kubo gaps for other metals are even smaller as their free electron densities are lower.

In this study, we discuss the magnetic properties of capping-free noble-metal NPs, with an emphasis on the property changes originating from the reduction of particle size but avoiding the complications that might arise from the capping agents. Comprehensive discussion of the magnetic properties of bare Au NPs through magnetization studies are available in [11, 35], and confirmation of the existence of an intrinsic magnetic moment in 4 nm Au NPs using neutron diffraction can be found in [36]. Connections between the development of ferromagnetic superspins and the occurrence of electron charge redistribution in bare Cu NPs can be found in [37]. Here we focus on the magnetic properties of ultrasmall bare Ag NPs with diameters in a range of 2–35 nm. In the next section, we will present (a) details of the fabrication and characterization of the bare Ag NPs used in the present study, (b) the theoretical background for understanding the isofield and isothermal magnetization, (c) lattice relaxation and electron charge density, and (d) magnetic superspins in small Ag NPs a few nanometers in diameter.

6.2 Materials

6.2.1 Sample Fabrication

The Ag NPs used in the present study are fabricated using the gas condensation method. The basic concepts behind this method include (1) producing an atom vapor, (2) nucleation through collisions, (3) controlling the growth rate by introducing inner gas into the evaporation chamber, and (4) reducing the kinetic energies of the atoms to prevent interparticle fusion using a cold collector. Atom vapor can be produced by passing an electric current through bulk ingots until they reach their melting temperature. The source temperature and, hence, the evaporation rate can be controlled by adjusting the strength of the heating current. The kinetic energies of the evaporated atoms are reduced through collisions with the surrounding inert gas atoms. Argon gas is commonly used as the kinetic energy reducer. The cold collector acts as a cold trap for the collection of NPs. A collector maintained at 77 K can effectively prevent interparticle fusion for the formation of small NPs. Several physical parameters are important for controlling the mean size and size distribution of the resultant NPs: the strength of the electric current heating the metal ingots, the Ar pressure in the chamber during nucleation, the temperature of the collector,

and the distance between source and collector. A schematic plot of a typical gas condensation chamber for the fabrication of small NPs may be found in Fig. 14 of [11].

The Ag NP powders used in the present study are fabricated using the gas condensation method. The mean particle size and size distribution are controlled by the proper choice of chamber pressure and source temperature. High-purity Ag spheres (approx. 0.5 g, 99.99% pure, and 2 mm in diameter) are heated by a current source (65–90 A) and are evaporated at a rate of 0.05 Å/s in an Ar atmosphere under various pressures (0.1–5 torr). The evaporated particles are collected on a nonmagnetic SS316 stainless-steel plate placed 20 cm above the evaporation source and maintained at 77 K. After restoration to room temperature, the NPs, which are only loosely attached to the collector, are stripped off. The samples thus fabricated are in powdered form and consist of macroscopic amounts of individual Ag NPs. There is no substrate or capping molecules on the NPs. The resultant powders are no longer sliver sheen but dark black, indicating that the absorption bands of the powders have blue shifted to the invisible region, as is the case with most metallic NPs. It appears that the samples are quite stable against exposure to air for a limited time since the X-ray diffraction patterns and magnetization curves of the as-grown sample and the sample exposed to the air for 5 days are indistinguishable. However, the samples used in the present study were kept in a vacuum at all times, after being stripped off from the collector and loaded into the sample holders for measurements.

6.2.2 Sample Characterization

X-ray diffraction is currently the most commonly used and most effective tool for the determination of the crystalline structure and chemical composition of powdered compounds. In the Bragg formulation, crystals are viewed as being made of many parallel planes of ions, known as the lattice planes. In general, many sets of parallel lattice planes may be identified in a crystalline structure. The Miller indices h, k, and l are used to label the interplanar spacing d_{hkl} for reflection from the (hkl) lattice planes. Constructive interference of the diffracted X-ray of wavelength λ will occur whenever Bragg's law $2d_{hkl}\sin\theta = n\lambda$ is met, which gives the angle θ, known as the Bragg angle, for coherence scattering from crystal lattices. Identifying the d_{hkl} in the lattice allows for the construction of the crystalline structure. In addition, the width of the diffraction peak reflects the spatial extension of the lattice periodicity, which in the present case corresponds to the size of the NPs. The diffraction peaks from the NPs are broader than the instrumental width owing to the incomplete interference of the scattered waves. An easy way to extract the mean particle diameter of an NP assembly is to employ the Scherrer equation [39], which relates the peak width to the particle size but is formulated assuming a monodispersed particle assembly. The line profile of a diffraction peak from a size-dispersed assembly is the result of a superposition of the diffraction profiles from all the sizes in the assembly, which can be used to extract the size distribution of the assembly.

Atomic force microscopy (AFM) and transmission electron microscopy (TEM) images can reveal the shape and size of each individual NP, making them feasible to obtain the size distribution in an NP assembly, provided it has been properly sampled. In sampling the images, NPs must be very dispersedly deposited on a special sample holder for mapping of the morphology. The sampling must also be conducted over a substantial amount of individual NPs with no artificial preference to obtain a reliable signature of the size distribution. Stacking or aggregation of the NPs results in poor images for size or shape determination. The process is frequently troublesome and can be time consuming compared to the X-ray diffraction technique, in which a macroscopic amount of NPs in an assembly is automatically sampled. Proper analysis of the line profile of X-ray diffraction peaks allows one to extract the size distribution of the assembly.

6.2.3 *Diffraction Profile of a Size-Dispersed Nanoparticle Assembly*

The line profile of a diffraction peak from a size-dispersed NP assembly is produced from a combination of the diffraction profiles contributed from each individual NP in the assembly. It is clear that the resultant profiles will depart from the instrumental resolution function. Poor fits, especially at the tails and centers of the diffraction peaks, will emerge when the diffraction profiles of an NP assembly are fitted with the instrumental resolution function, as illustrated in Fig. 6.1. The intensities at the tails are contributed mainly from small particles, while those at the centers are from large particles. The diffraction profile contains information about the size distribution of the NP assembly. Unfortunately, it is not feasible to combine all the profiles from every individual NP since there are so many of them.

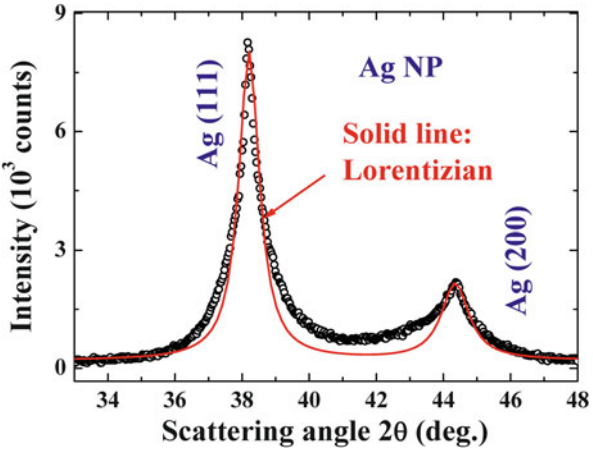

Fig. 6.1 X-ray diffraction peaks from representative Ag NP assembly. The *solid curve* indicates the results of fits of the diffraction peaks to Lorentizian profiles. Poor fits are obtained especially in the tail regions of the peaks

However, the problem can be largely reduced by assuming that the size distribution of the assembly may be represented by an analytical expression that can be described by two parameters. Formulation of the line profiles of the diffraction peaks of a size-dispersed assembly is then feasible. Generally speaking, an analytical function that reflects the instrumental resolution and specifies the peak position, peak width, and peak height is needed to describe the diffraction peak from an assembly of monosized particles. The peak positions in the diffraction pattern are the scattering angles $2\theta_{hkl}$ of the (*hkl*) Bragg reflection; in terms of the full width at half maximum, the peak width w_i of the (*hkl*) Bragg reflection for particles of diameter d_i can be formulated [39] as

$$w_i = \frac{0.94\lambda}{d_i \cos\theta_{hkl}} \tag{6.2}$$

for spherical particles, and the peak height is proportional to the number n_i of particles of diameter d_i in the assembly. In many cases, the diffraction profile from a single particle can be satisfactorily described by a Lorentzian function:

$$L_i\left(2\theta, w_i, n_i\right) = \frac{2n_i}{\pi}\left[\frac{w_i}{4(2\theta - 2\theta_{hkl})^2 + w_i^2}\right]. \tag{6.3}$$

The diffraction intensity of the (*hkl*) Bragg reflection of a multidispersed NP assembly is the superposition of $L_i(2\theta,w_i,n_i)$ from all n_i in the assembly:

$$I_{hkl}\left(2\theta\right) = C\sum_{n_i} L_i\left(2\theta, w_i, n_i\right), \tag{6.4}$$

where C is the instrumental scale factor that accounts for the setup of the diffractometer. In the case of an assembly consisting of quantum NPs, a log-normal size distribution is often found, so that

$$n_i\left(d_i\right) = \frac{1}{d_i\sqrt{2\pi}\sigma}\exp\left\{-\frac{(\ln d_i - \ln d_{\mathrm{m}})^2}{2\sigma^2}\right\}, \tag{6.5}$$

where d_{m} represents the mean particle diameter for the size distribution of the assembly and σ is the standard deviation of the size distribution.

6.2.4 X-Ray Diffraction and AFM Measurements

The X-ray diffraction measurements were conducted on a Bruker D8 ADVANCE diffractometer with K_α radiation and source wavelengths of $K_{\alpha1} = 1.5406$ Å and $K_{\alpha2} = 1.5443$ Å from a copper target. An accelerating voltage of 40 kV and a beam

current of 40 mA were employed. The Bruker LynxEye linear position-sensitive detector (PSD) captured a scattering angle of 4°, and a Ni filter was placed before the PSD to screen the K_β radiation. The diffraction patterns were taken in the reflection geometry, where a correct positioning of the sample to the zero-scattering-angle line is extremely important to avoid misjudgment of the diffraction angle. The sample temperature was controlled using a He-gas closed-cycle refrigeration system, equipped with a high-power heater. The AFM images were taken using a Digital Instruments Nanoscope III operated in tapping mode, with the cantilever oscillating to avoid trapping the NPs on the tip, at a scanning speed of three lines per second.

6.2.5 Size Distribution of Ag NP Assemblies

The size distributions and mean particle diameters of the Ag NP assemblies were determined by fitting the diffraction peaks to the diffraction profiles of finite size particles. Figure 6.2a shows an X-ray diffraction pattern of representative Ag NPs fabricated using a current source of 65 A and a chamber Ar pressure of 3 torr, taken at room temperature. As expected, the diffraction peaks appear to be much broader than the instrumental resolution, reflecting the broadening of the peak profiles owing to the finite size effect. The X-ray diffraction patterns can be associated with a face-centered cubic Ag structure. No traces of oxidation phases or elements other than Ag may be identified from the diffraction patterns. The solid curves in Fig. 6.2a indicate the fitted pattern, assuming a Lorentzian function for the diffraction profile (Eq. (6.3)), together with a log-normal size distribution (Eq. (6.5)), with the center at $d_m = 2.5$ nm and a standard deviation of $\sigma = 0.55$, as shown by the solid curve in Fig. 6.2b. This size distribution agrees well with that [bars in Fig. 6.2b] obtained from the AFM images, as illustrated in Fig. 6.2c.

6.3 Methods

6.3.1 Particle Superspin

Randomly oriented crystallized domains of sizes in the range of several hundred nanometers are frequently formed in bulk materials. The energy and stress buildup at the domain boundaries acts against the formation of a domain structure composed of domains smaller than a few hundred nanometers. Frequently, a single-domain structure is formed in an NP a few dozen nanometers in diameter. An isolated single-spin-domain NP can be treated as a superspin [40, 41], where the magnetic behavior is expressed by the net magnetic moment of the NP, namely, the particle magnetic moment μ_p, having several hundreds or thousands of Bohr magnetons. Thermal

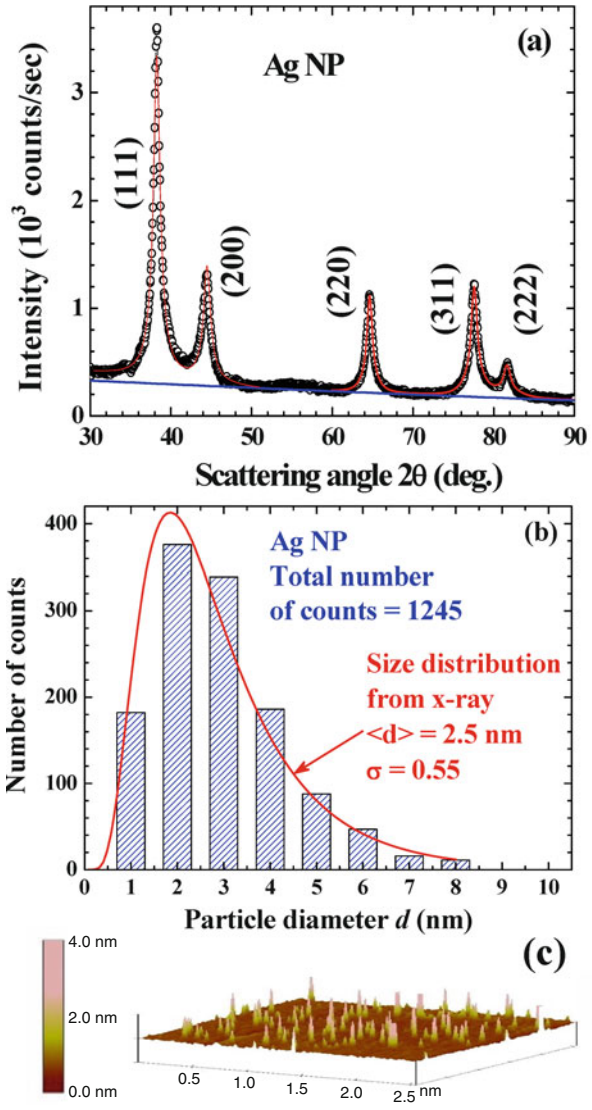

Fig. 6.2 (**a**) X-ray diffraction pattern of Ag NP assembly at 300 K, revealing a face-centered cubic crystalline structure. The *solid curves* indicate the calculated profiles of the diffraction peaks, assuming a log-normal size distribution with a center at 2.5 nm and a standard deviation width of 0.55. (**b**) Size distributions obtained from X-ray diffraction profile (*solid curve*) and from AFM images (*vertical bars*). (**c**) Portion of AFM images of Ag NPs

agitation will reduce the μ_p of each NP. The magnetic ordering temperature of the superspin, which frequently persists up to well above room temperature, depends strongly on the particle size.

Magnetization marks the density of the magnetic dipole moment of materials; it is the most commonly used parameter for revealing the magnetic character. An assembly of loosely packed magnetic NPs, where interparticle interactions are insignificant, is currently described as a superparamagnetic system that consists of a collection of many randomly oriented noninteracting superspins [42, 43].

The magnetization M at a finite temperature T of an NP assembly consisting of many individual well-separated (interaction-free) superspins will be zero when the NPs are naturally packed and the particle moments are randomly oriented, as illustrated in Fig. 6.3a. An applied magnetic field H_a drives the individual μ_p to align along the field direction. It is known that the magnetic field inside the NP that is experienced by the μ_p is a combination of the applied magnetic field, the magnetocrystalline anisotropy, and the molecular field. This effect is represented by the dimensionless permeability α such that αH_a indicates the net magnetic field inside the NP. It takes the form of $\alpha = 1 + \left(\mu_0 M_P^2/2K\right)$ for uniaxial spheres [44], where K is the energy density associated with the magnetocrystalline anisotropy, μ_0 is the magnetic permeability of the free space, and M_P is the spontaneous saturation magnetization. The Boltzmann statistics that balance the competition between the magnetic interaction energy $\mu_p \alpha H_a$ and the thermal agitation energy $k_B T$ give rise to a Langevin profile for the dependency of M on H_a and T [45]: $M_L(H_a,T) = M_P(T)L(x)$, where $M_P(T)$ indicates the saturation particle magnetization at temperature T

$$L(x) \equiv \coth(x) - \frac{1}{x} \tag{6.6}$$

is known as the Langevin function with $x \equiv \alpha \mu_p H_a / k_B T$, and k_B is Boltzmann's constant. The Langevin $M_L(H_a,T)$ profile is understood to be a randomly oriented assembly of many interaction-free superspins, with an average magnetic moment μ_p at temperature T, that are being aligned by the applied magnetic field, as illustrated in Fig. 6.3b.

6.3.2 *Quantum Confined Zeeman Condensation*

An applied magnetic field will split the energy degenerate spin-up and spin-down bands into two separated spin-polarized bands, with a Zeeman splitting energy of $g\mu_B \alpha H_a$, where g is the Lande g-factor and μ_B is the Bohr magneton. Magnetization contributed from the condensation of electrons into the Zeeman split spin-polarized states will appear. This H_a-induced magnetization is contributed mainly from the conduction electrons. The effect can be substantial in NPs, where the discrete nature of the electron level spacing is significant. Under the assumption of an even band separation for all Kubo gaps, it is the available density of states for the thermal excitation that measures the contribution to the Zeeman magnetization since thermal excitation for the conduction electrons into the first excited band and for the valence electrons into the conduction band is equally probable. The Zeeman magnetization of quantum spins follows a Brillouin profile [45]: $M_B(H_a,T) = M_Z(T)B_J(y)$, where $M_Z(T)$ represents the induced saturation magnetization,

$$B_J(y) \equiv \frac{2J+1}{2J} \mathrm{ctnh}\left[\frac{(2J+1)\,y}{2J}\right] - \frac{1}{2J} \mathrm{ctnh}\left(\frac{y}{2J}\right) \tag{6.7}$$

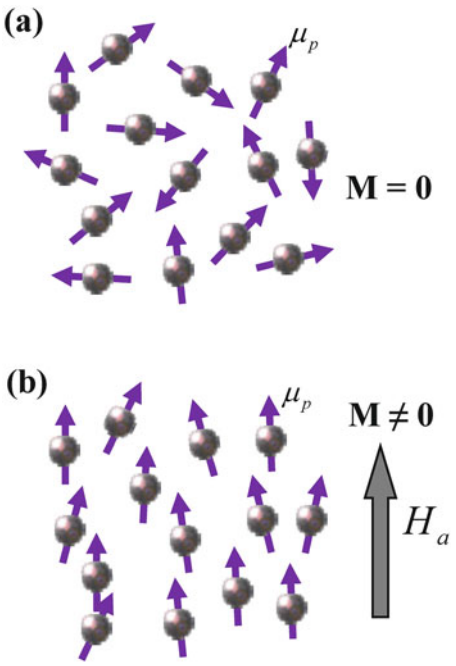

Fig. 6.3 Schematic illustration of configuration of superspins in NP assembly at finite temperature. Each NP carries a superspin moment μ_p (**a**) without and (**b**) with the presence of an applied magnetic field H_a

is the Brillouin function of order J, and $y \equiv g\mu_B\alpha H_a/k_BT$. Note that the Brillouin function reduces to a Langevin function when $J = \infty$, that is, $B_\infty(y) = L(y)$, and it reduces to a hyperbolic tangent function when $J = 1/2$, that is, $B_{1/2}(y) = \tanh(y)$. Competition between the thermal agitation and field alignment results in a Langevin profile for the magnetization $M_L(H_a,T)$, whereas thermal excitation of valence and conduction electrons into the Zeeman split spin-polarized states gives rise to a Brillouin profile for the magnetization $M_B(H_a,T)$.

6.3.3 *Generalized Magnetization Profile for a Size-Dispersed Nanoparticle Assembly*

It is very difficult to measure the physical properties of an individual NP at the currently available instrumental resolutions. Measurement is limited by the extremely weak signals that an NP can generate for detection. Thus measurement is nowadays performed on an assembly of NPs for signal enlargement. However, it is difficult to fabricate a monodispersed NP assembly. Consequently, the signals detected during measurement contain the responses from all sizes of NPs that appear in the assembly. It has been demonstrated that ignoring the influence of size dispersion in the NP assembly can result in unphysical conclusions [46]. When considering the magnetization profile for an NP assembly, the contributions from

particles of different sizes must be taken into account. Assuming that there are n_i NPs having a particle magnetic moment μ_{pi} and a magnetic permeability α_i in the assembly, the Langevin magnetization then takes the form of the summation of contributions from all sizes of n_i:

$$M_L(H_a, T) = \sum_i n_i \mu_{pi} L\left(\frac{\mu_{pi}\alpha_i H_a}{k_B T}\right) = \sum_i n_i \mu_{pi} L\left(\frac{\mu_{pi}\alpha H_a}{k_B T}\right) \tag{6.8}$$

taking the same value α for the magnetic permeability of all NPs in the assembly for simplicity. This simplified expression can be justified for narrowly dispersed assemblies. It is unphysical to extract all the parameters associated with the preceding expression from the observed $M_L(H_a,T)$ unless the number of free parameters can be reduced further.

Even though the size distribution of an NP assembly can be determined from the diffraction profile, as discussed in Sect. 2.5, extraction of the size distribution from the magnetization data is also feasible by specifying a distribution function for the particle size. Specification of the distribution function reduces the free parameters associated with the size dispersity into two, the mean size and the distribution width. In the case of an assembly consisting of quantum NPs, a log-normal size distribution is often found, as expressed in Eq. (6.5). Cross examination of the size distributions obtained from the magnetization and from the diffraction can then be used to check the physical quality of the fits. Likewise, by taking an analytical expression for the dependency of the particle magnetic moment μ_{pi} on the particle diameter d_i, the free parameters associated with the moment dispersity reduce into three: the maximum particle moment μ_{pm}, the mean particle diameter for the moment distribution d_c, and the standard deviation of the moment distribution w. In the case of a log-normal type of size dependency for the particle moment, it can be expressed as

$$\mu_{pi}(d_i) = \frac{\mu_{pm}}{d_i\sqrt{2\pi}w} \exp\left\{-\frac{(\ln d_i - \ln d_c)^2}{2w^2}\right\}. \tag{6.9}$$

A plot of $n_i\mu_{pi}$ against d_i using the parameters obtained from the fit gives the contribution from particles of each size to the saturation magnetization of the NP assembly.

6.3.4 Magnetization Measurements

The magnetization measurements were performed on a Physical Property Measurement System, manufactured by Quantum Design (San Diego, CA, USA), employing the standard setups. The magnetization M was measured by detecting the induced voltage in the detector coils as the sample moves through them. The NPs must be very loosely packed for these measurements, so that they reveal mainly the magnetic

responses from individual NPs without significant contributions from interparticle interactions. To avoid any aggregation that might arise among the NPs, the assembly is shaken at 50 Hz for 5 min using a Vortex-Genie Mixer (Bohemia, NY, USA). The NPs (approximately 60 mg each) are packed into a nonmagnetic cylindrical holder provided by Quantum Design. The packing fraction f, which marks the ratio between the mass densities of the NP assembly in the holder and that of the bulk Ag, is used to quantify the average interparticle separation that signals the significance of interparticle interactions in the NP assembly. The packing fraction chosen for all NP assemblies used in the present studies is approximately 6%, which corresponds to an average interparticle separation, from edge to edge, of 1.25 times the particle diameter. The holder produces a smooth temperature curve and a background signal that is approximately 2% of the signal from samples.

6.4 Lattice Relaxation

6.4.1 Size Effect

The structural ordering of atoms within a solid is formed by the lattice interaction. Generally speaking, a stronger lattice interaction gives rise to a shorter lattice separation, specified by the lattice constants that indicate the spatial extension of the lattice unit cell. The formation of a face-centered cubic structure in noble metals is known to be driven by metallic bonding, where appreciable electrons are distributed throughout the interstitial regions and the atomic connection is not restricted to within the nearest neighbors but can extend to several unit cells. Larger lattice constants can be anticipated for ultrasmall NPs having sizes smaller than the lattice interaction can reach. The lattice constant of Ag NPs increases progressively when the size is reduced to below 20 nm in diameter, which is accompanied by a building up of negative stress in the NPs (Fig. 6.4). Interestingly, the enlargement of the lattice constant a and stress σ with the reduction in particle diameter d may be described using an exponential profile (solid curves in Fig. 6.4), with decay constants of $d_0 = 5.6(4)$ nm for the lattice constant and $d_S = 3.9(4)$ nm for the stress. The $a_0 = 4.079(4)$ Å obtained from the fit indicates the lattice constant for large particles, which agree very well with the value known for bulk Ag. The lattice constant of 2.3 nm Ag NP at 300 K ($a = 4.102$ Å) is approximately 0.56% larger than that of bulk Ag ($a_0 = 4.079$ Å). This 0.56% relaxation of the lattice constant corresponds to a temperature change of 298 K in thermal expansion, when estimated using the linear thermal expansion coefficient of 18.9×10^{-6} K^{-1} at 300 K for bulk Ag. Note that a 298 K temperature change corresponds to a 25 meV change in thermal energy, which is significant when compared with the energy associated with lattice vibrations of Ag. Lattice relaxation is clearly revealed in the 12 and 16 nm Ag NPs. There are 30 unit cells in each crystallographic axis direction of the 12 nm Ag NP. The observation of a larger lattice constant for the 12 nm Ag NP than for

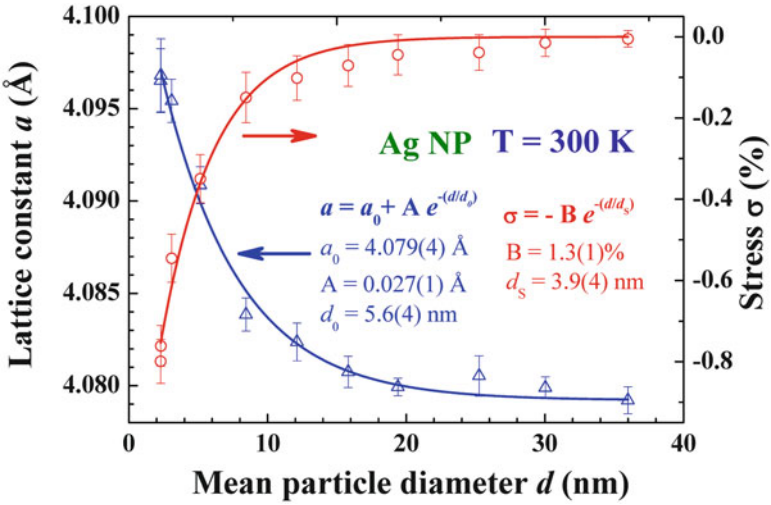

Fig. 6.4 Variations in lattice constant (*open circles*) and stress (*open triangles*) with particle diameter of Ag NPs. The *solid curves* indicate the results of fits to the expression listed in the plot

the bulk Ag shows that lattice interaction in bulk Ag extends at least over 15 unit cells, which corresponds to a length of 6 nm. The effects from quantum confinement are insignificant for 12 nm Ag NPs at 300 K since the Kubo gap opening is only 0.13 meV, which is invisible at 300 K. It is the small size effect that governs the lattice relaxation in Ag NPs.

6.4.2 Electron Charge Density

It is remarkable to see that the small size effect significantly alters the distribution of the electron charge density (ECD) of silver. This is illustrated in the ECD contour plots of the (000) (Fig. 6.5) and (0, 0, 0.2) (Fig. 6.6) lattice planes for the 3.5 nm Ag NPs and 2 mm Ag ingots. These ECD maps were obtained by employing the GSAS program, starting with profile refinement of the X-ray diffraction patterns, followed by calculation of the inverse Fourier transforms of the structure factors to extract the ECD distribution. The ECD contour map of a specific plane was then obtained by slicing the electron density in the vicinity, including 0.025 Å below and above the lattice plane. The ECD along a specific crystallographic direction was then obtained by cutting the density map along the selective direction. The contour plots reveal an approximately spherically symmetric ECD around the lattice sites, but with distortion near the regions of contact between two neighboring atoms [Fig. 6.5b, d], reflecting the characteristics of metallic bonding in both 3.5 nm Ag NPs and 2 mm Ag ingots.

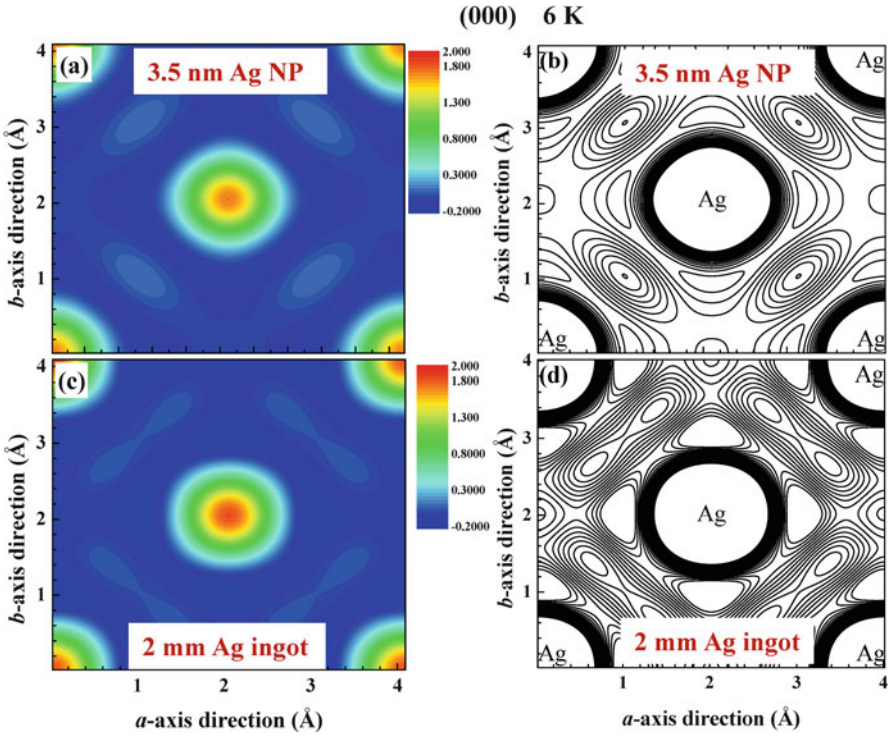

Fig. 6.5 Electron charge densities in (000) crystallographic plane of (**a**) 3.5 nm Ag NPs and (**c**) 2 mm Ag ingot, as inferred from X-ray diffraction data; the color bars are in units of $e/Å^3$. Contour plots of electron charge density in (000) crystallographic plane of (**b**) 3.5 nm Ag NPs and (**d**) 2 mm Ag ingot

However, several distinct differences may be identified between the ECD of the 3.5 nm Ag NPs and the 2 mm Ag ingots. First, the ECDs around the lattice sites of the 3.5 nm Ag NPs are noticeably lower and less extensively distributed [Fig. 6.5a, c]. The amount of reduction is larger for smaller NPs; the reduction can be as large as 5% in the 3.5 nm NPs compared with that of the 2 mm Ag ingots [Fig. 6.7a, b]. In addition, the amount of change in the ECD upon reducing the particle size from 8 to 3.5 nm is significantly less than for a reduction from 2 mm to 8 nm, showing that quantum size effect plays a less important role than the small size effect does in renormalizing the electron charge distribution. This is understandable since quantum confinement renormalizes the band configuration near the Fermi level for the conduction electrons but has less of an effect for the core electrons. On the other hand, the ECD in the contact regions between two neighboring atoms of the NPs is considerably higher (Fig. 6.7). Apparently, a portion of the electron charges shifts from being near the lattice sites to the contact regions between two neighboring atoms. Second, the spherical ECD contours of the 3.5 nm Ag NPs extend from the lattice sites further into the contact regions of two neighboring atoms [Fig.

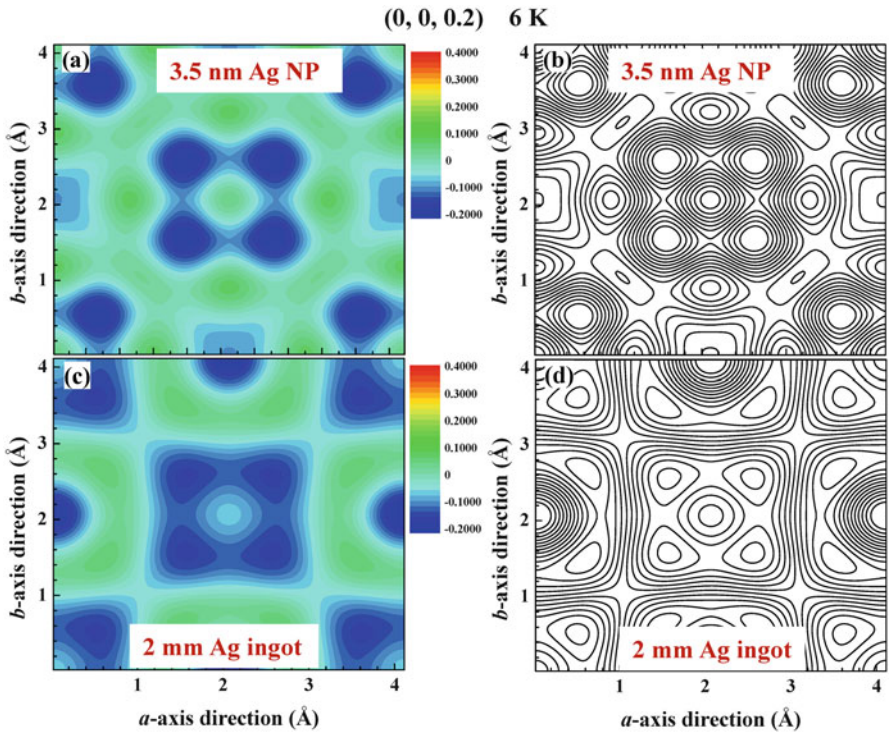

Fig. 6.6 Electron charge densities in (0,0,0.2) crystallographic plane of (**a**) 3.5 nm Ag NPs and (**c**) 2 mm Ag ingot, as inferred from X-ray diffraction data. The color bars are in units of $e/Å^3$. Contour plots of electron charge density in (0,0,0.2) crystallographic plane of (**b**) 3.5 nm Ag NPs and (**d**) 2 mm Ag ingot

6.5b, d]. Third, the most pronounced differences appear near the regions of contact between two neighboring atoms. The dumbbell-shaped contours that appear in the contact regions of the two nearest neighboring atoms in the 2 mm Ag ingots [Fig. 6.5d] renormalize into elliptical contours in the 3.5 nm Ag NPs [Fig. 6.5b]. This characteristic is more clearly revealed in the ECD contours away from the lattice sites, as shown in Fig. 6.6. The ECD contours in the (0, 0, 0.2) lattice plane [Fig. 6.6b, d] of the 3.5 nm NPs are more densely distributed in the contact regions along the [110] crystallographic direction but much more loosely distributed in the contact regions along the [100] crystallographic direction. Fourth, the ECD distributions in the NPs are not evenly extended along all crystallographic directions but reveal less electronic connection with its neighbors along specific directions, such as along the [100] direction, while having a better connection along the others, such as along the [110] direction.

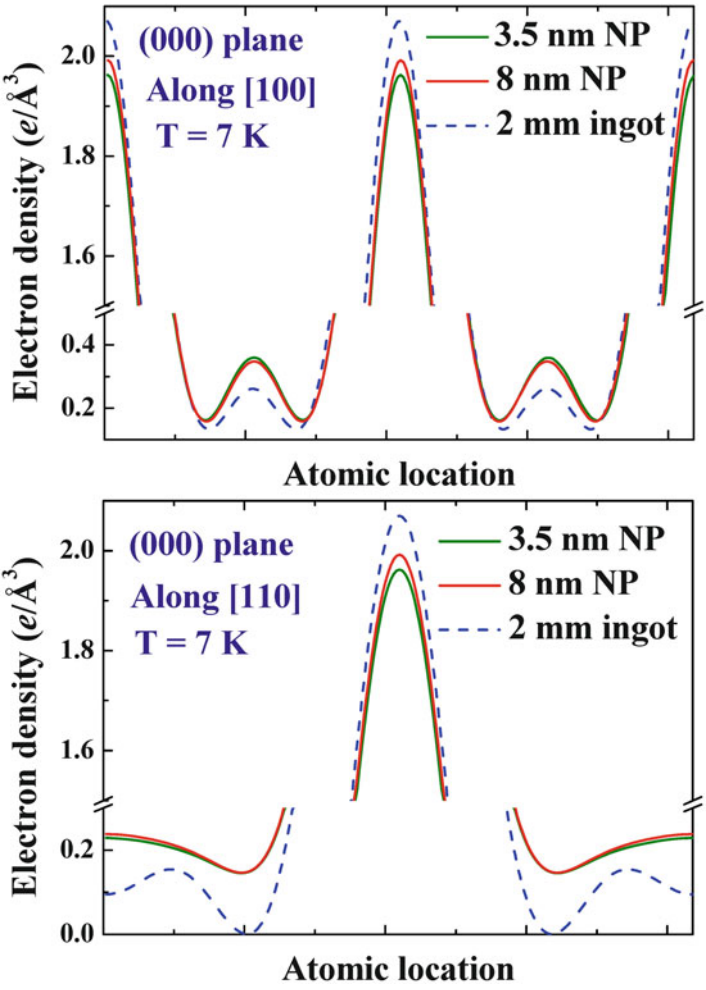

Fig. 6.7 Direct comparison of electron charge densities in (000) lattice plane along (**a**) [100] and (**b**) [110] crystallographic directions of 3.5 nm (*dotted curve*), 2 nm (*dashed curve*), and 8 nm (*solid curve*) Ag NPs at 7 K

6.4.3 Electron Charge Redistribution

It is clear that a reduction of the particle size to the nanometer scale can cause a significant change in the ECD distribution. These changes are better revealed in the difference density plots, where the electron density of the 2 mm ingot is subtracted from that of the 3.5 nm NP. Such difference density plots for the (000) and (0, 0, 0.2) crystallographic planes are illustrated in Figs. 6.8 and 6.9, respectively. The atomic positions with negative values of difference density represent the locations

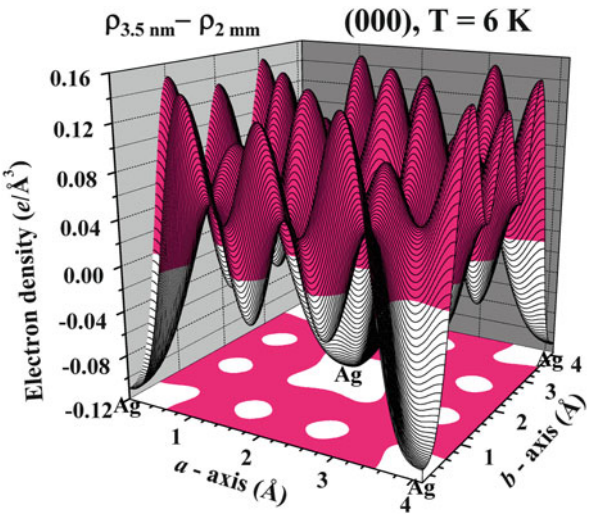

Fig. 6.8 Difference in ECD in (000) lattice plane between 3.5 nm Ag assembly and 2 mm Ag ingot at 6 K. Color-filled regions indicate locations having a positive difference charge density, where the charge density of the NPs is higher than that of the 2 mm ingot. The projection of the ECD onto the lattice plane is shown at the bottom

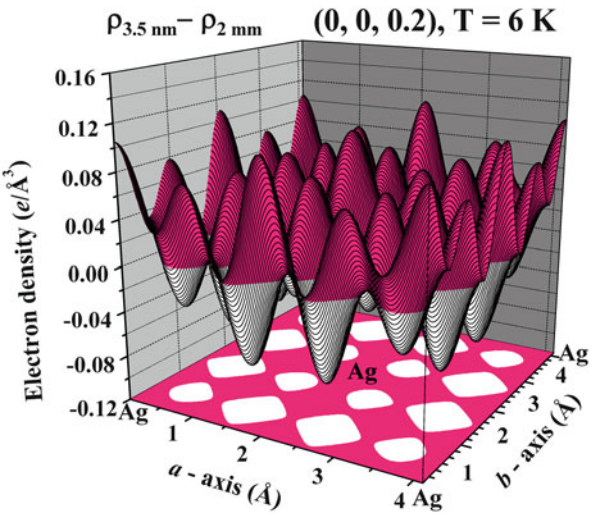

Fig. 6.9 Difference in electron charge density in (0,0,0.2) lattice plane between 3.5 nm Ag assembly and 2 mm Ag ingot at 6 K. Color-filled regions indicate locations having a positive difference charge density, where the charge density of the NPs is higher than that of the 2 mm ingot. The projection of the ECD onto the lattice plane is shown at the bottom

of lesser electron charges in the NP but are redistributed to the positions with positive values. The color-filled regions in Figs. 6.8 and 6.9 indicate the positions having a positive difference density. These positions can be more clearly seen in the projection of the difference density onto the lattice plane shown at the bottoms of Figs. 6.8 and 6.9. More electron charges in the NPs are found between the two nearest neighbors, but less around the lattice sites in the (000) plane (Fig. 6.8). The situation is different in the (0, 0, 0.2) plane, where a five-peak structure across the unit cell along the [110] crystallographic direction is seen in the difference pattern of the (0, 0, 0.2) plane (Fig. 6.9) but a three-peak structure is revealed in the (000) plane (Fig. 6.8). This spatially uneven change of the ECD over the crystallographic

directions cannot be associated only with the redistribution of the *s* electrons but requires the redistribution of the *d* or *p* electrons as well.

It is known that the inner electrons in the core (1*s* to 4*d* electrons) of each Ag ion in a crystallized face-centered cubic structure extend from the lattice site to cover a spatial region with a radius of approximately 7.5% of a lattice unit, where the 4*d* orbital extends to the outermost area of the inner core region and the 5*s* orbital is slightly within. Interestingly, the electron density of the inner core is noticeably lower in the NPs, and this region of fewer electrons in the NPs extends into the 5*s* orbital. Remarkably, reducing the size of Ag to the nanometer scale results in more electrons being distributed in the central regions of the two nearest neighbors, up to a spatial region of approximately 10% of a lattice constant below and above the lattice plane. Further away from this the electron density in the NPs becomes less intense. It is clear that the spatially extended distribution of the electron charge in the NPs is not isotopically extended in all crystallographic directions, but rather a portion of the electrons shifts from specific regions to the others. The redistribution involves not only spherically distributed 5*s* electrons but also includes directional 4*d* electrons. It is known that although the band structure of Ag can be separated into 5 narrow 4*d* bands and one broad 5*s* band to accommodate the 11 outer electrons, at some values of wave vector all 6 electron bands are closer together [1]. Apparently, the disruption of lattice periodicity at the Ag NP surfaces results in a greater degree of mixture between the 4*d* and 5*s* bands and the electrons are distributed toward the center locations of the neighboring atoms, especially in between the nearest neighbors.

6.5 Superspin Magnetism

6.5.1 Spontaneous Magnetic Moment

Three components may be anticipated to appear in the magnetization of an Ag NP assembly: a Langevin component M_L that describes the alignment of the superspins of Ag NPs by the applied magnetic field H_a, a Brillouin component M_B from H_a-induced Zeeman splitting near the Fermi level that appears when the Kubo splitting from quantum confinement is significant, and a diamagnetic component M_D from the Lenz responses to the application of H_a. These components have all been observed in Au [35] and Cu [37] NPs. They are visible in the isothermal magnetization curves $M(H_a)$ of the present Ag NP assemblies as well. Several features are seen in the isothermal $M(H_a)$ curves of the representative 2.5 nm Ag NP assembly shown in Fig. 6.10. (1) In the low-H_a regime, M increases rapidly with increasing H_a, revealing the appearance of an M_L that becomes saturated at H_a ~3 kOe; M_L is clearly visible even at 300 K; it appears that the thermal agitations at 300 K only slightly affect the strength of the superspins, showing a critical temperature that is much higher than 300 K for the superspins in 2.5 nm Ag NPs.

(2) In addition to M_L being saturated above 3 kOe, at 2 K, M continues to increase with increasing H_a, showing the appearance of M_B. This component is largely reduced at 10 K, showing that the thermal populations from the down-spin state to the up-spin state have nearly decompensated for the H_a-induced magnetization. (3) Lenz diamagnetic responses are clearly revealed in the high-H_a regime in the $M(H_a)$ curves above 15 K, such that M decreases linearly with increasing H_a. Stronger diamagnetic responses are seen at higher temperatures, reflecting that the mean square distance of the core electrons from the nucleus becomes larger at higher temperatures. Note that the thermal increase rate of the diamagnetic response becomes smaller as the temperature is increased.

A macroscopic amount of the monodispersed NP assembly is barely available. Results of size dispersion in the NP assembly must be accounted for when analyzing the $M(H_a)$ curves measured for an NP assembly [46]. The solid curves in Fig. 6.10 indicate the results of the fits for $M(H_a, T) = M_L(H_a, T) + M_B(H_a, T) + \chi_D H_a$, using the size distribution of the assembly obtained from the X-ray diffraction [solid curve in Fig. 6.2b] and assuming a log-normal type of particle moment dependency on the particle size (Eq. (6.8)), with $\alpha\mu_{pm}$, d_c, w, and χ_D being the fitting parameters. Unfortunately, the permeability α and maximum particle moment μ_{pm} cannot be separated in this fit since they are coupled parameters in the Langevin expression. Good agreement between the observations and fits is obtained at all the temperatures studied from 2 to 300 K. The size dependencies of the particle moments at various temperatures obtained from the fits are shown in Fig. 6.11. Note that $\alpha\mu_p$ of Ag NPs with sizes other than 2.5 nm can also be extracted from the analysis, which

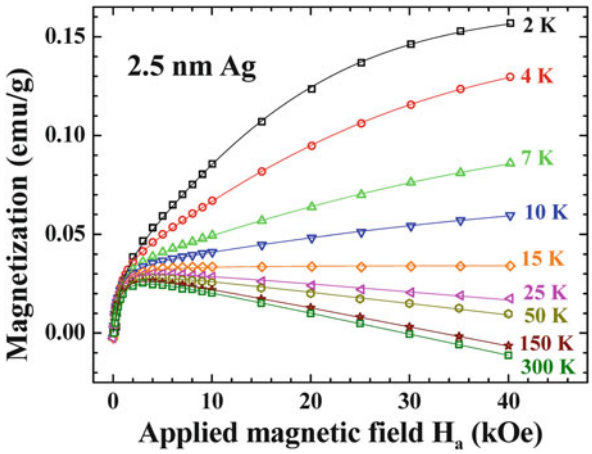

Fig. 6.10 Field profile of magnetization of 2.5 nm Ag NP assembly, taken in field-increasing loops at nine representative temperatures. The Langevin profile is seen in the $M(H_a)$ curves at all temperatures. The Lenz diamagnetic components are clearly revealed in the $M(H_a)$ curves taken above 15 K. An additional Zeeman Brillouin component appears in the high H_a regime of the $M(H_a)$ curves taken below 15 K. The *solid curves* indicate the results of fits for a Langevin profile plus a Brillouin profile plus a Lenz profile

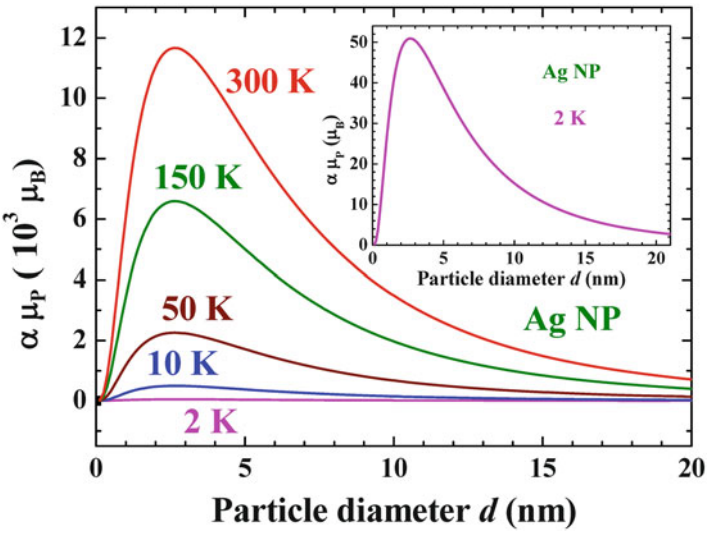

Fig. 6.11 Size dependence of $\alpha\mu_p$ obtained from $M(H_a)$ curve of 2.5 nm Ag NP assembly at 2 K, where α is the dimensionless permeability and μ_p the average particle moment. The *inset* shows the curve at 2 K using an expanded scale for clarity of presentation

is a direct consequence of the assumption made that the variation of superspin moment with particle diameter can be expressed by an analytical function. The intrinsic superspins of Ag NPs are represented by the $T = 2$ K curve (inset in Fig. 6.11), where thermally induced magnetization [47–50] does not severely affect the superspin moments. Accordingly, the maximum superspin moment of Ag will appear in the 2.6 nm NP with $\alpha\mu_p = 50\mu_B$, and $\alpha\mu_p$ drops to below $1\mu_B$ for particles larger than 25 nm in diameter. We remark that the $M(H_a)$ curves fit well to a Langevin profile without considering the size-dispersed nature of the assembly but gives $\alpha\mu_p = 39\mu_B$ at 2 K. This is the average $\alpha\mu_p$ for the assembly, ignoring the uneven nature of the number fractions. The μ_p obtained when ignoring the size dispersion is 22% smaller.

6.5.2 *Thermally Induced Magnetization*

It is interesting to see that the superspin moment μ_p of Ag NPs increases with increasing temperature for all sizes (Fig. 6.11). Generally speaking, the reduced coordination number and the cluster symmetry are the two fundamental factors for the onset of magnetism in small bare NPs. No sign of severe structural distortion is identified in the present face-centered cubic Ag NPs. The reduction of coordination number of the Ag ions on the particle surface, namely from the small size effect, is the main source for the development of superspins in Ag NPs. The electron charge

redistribution that enhances the band mixture near the Fermi level, triggered by small size effect, has been discussed (Figs. 6.8 and 6.9). It is very likely that the developments of superspins in Ag NPs are closely linked to the enhanced band mixture near the Fermi level. However, it is difficult to account for the increase of the superspin moments by a factor of more than two orders of magnitude upon warming from 2 to 300 K (Fig. 6.11) owing solely to the thermally induced band mixture that may occur upon lattice expansion on warming.

Nevertheless, thermally induced magnetization [47–50] can be used to understand the extremely large increases of the superspin moment through thermal excitations. In this scenario, a ferrimagnetic-like alignment of the core macromoment $\mathbf{m_c}$ and the surface macromoment $\mathbf{m_s}$ is needed. This structure of separated macromoments for the core and surface ions can be justified since their coordination numbers are different. In addition, if the core and surface ions of an NP gather the same number of electrons, the Fermi energy of the surface electrons is then slightly higher than that of the core electrons because the surface ions are more closely packed owing to the appearance of surface stress, which deforms the surface of the NP into a curved one. Electron transfer from the surface region into the core can be anticipated for matching the Fermi energy of the two regions, which can result in noticeably different electron densities in the core and surface regions. This transfer of charges from the surface ions to the core has been found to be energetically favorable to stabilizing the core [49–51]. Thermal excitations of spin-precession modes in these ferrimagnetic-like NPs will result in a decrease in the difference between the moment directions of $\mathbf{m_c}$ and $\mathbf{m_s}$, which in turn gives rise to an increase in μ_p [47, 52], as illustrated in Fig. 6.12.

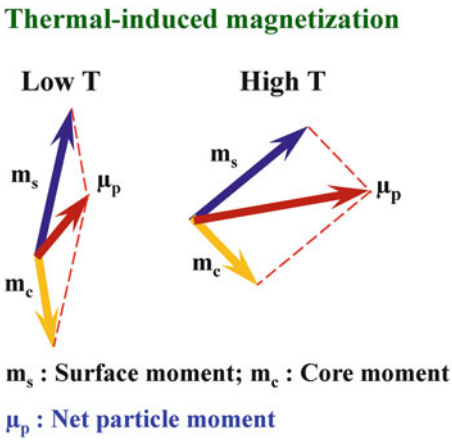

Fig. 6.12 Schematic illustration of configurations of surface and core superspin moments at finite temperatures

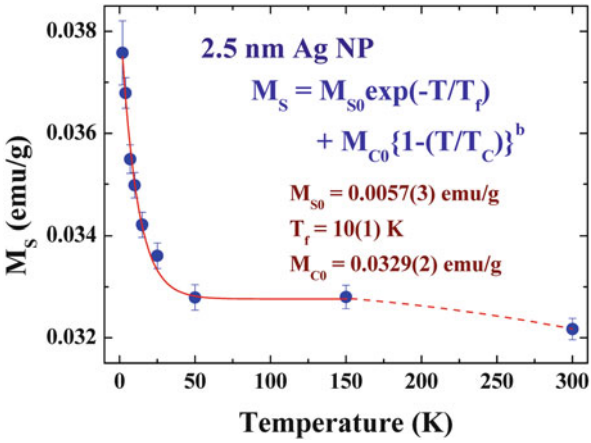

Fig. 6.13 Temperature dependencies of saturation spontaneous magnetization of 2.5 nm Ag NP assembly. The *solid curves* indicate the results of fits for the expression listed in the plot

6.5.3 Surface and Core Saturation Magnetizations

The intrinsic magnetic moments of NPs are expressed in the Langevin magnetization (Eq. (6.8)), where the saturation magnetization M_S may be obtained by

$$M_S = \sum_i n_i \mu_{pi}, \tag{6.10}$$

using the parameters n_i and μ_{pi} extracted from the fits of the X-ray diffraction pattern (Fig. 6.2) and $M(H_a)$ curves (Fig. 6.10). This M_S marks the saturation magnetization of the NP assembly, where the size-dispersed nature of the assembly has been accounted for. M_S will in general be different from one assembly to the next since every NP assembly has its own size-dispersion characteristics. Two components are clearly revealed in the temperature dependence of M_S of the 2.5 nm Ag NP assembly, as illustrated in Fig. 6.13. M_S drops rapidly with increasing temperature below 50 K, above which the thermal reduction rate of M_S is largely reduced. Interestingly, M_S reduces by only 2% upon warming from 50 to 300 K, showing that the transition temperature of the superspin is significantly higher than 300 K. The large difference observed in the thermal reduction rates below and above 50 K shows that they are associated with different origins. It is known that the coordination numbers of the Ag ions on the surface of an NP are different from those in the core. It can be anticipated that the superspin moments developed on the surface of an Ag NP will be different in strength from those developed in the core. In addition, it can be anticipated that the superspin moments on the surface will be weaker than those in the core, leading to a higher thermal reduction rate and a lower transition temperature for the surface superspins than for the core superspins. It is likely that the thermal profile of M_S at low temperature mainly reflects the thermal

characteristics of the surface superspins, whereas the high-temperature profile is linked to the Ag ions in the core. The sharp turn at 50 K in the $M_S(T)$ curve (Fig. 6.13) separates the effects resulting from the surface superspins from those of the core superspins.

It has been suggested that the thermal excitations of surface superspins can be described by the exponential reduction profile of $\exp(-T/T_f)$ for the magnetization characterized by the surface superspin freezing temperature T_f [53, 54]. On the other hand, the thermal excitations of core superspins are frequently described by taking the power law of $[1 - (T/T_C)^b]$ for magnetization, where T_C is the transition temperature and the exponent b is linked to the type of spin ordering [55]. Accounting for the contributions from the surface superspins as well as from the core superspins, the saturation magnetization can be expressed as

$$M_S(T) = M_{S0} \exp\left(-\frac{T}{T_f}\right) + M_{C0}\left[1 - \left(\frac{T}{T_C}\right)^b\right], \tag{6.11}$$

where M_{S0} and M_{C0} are the saturation magnetizations of the surface and core superspins at zero temperature. In this expression the saturation magnetization at zero temperature is $M_S = M_{S0} + M_{C0}$. Unfortunately, the nearly flat thermal reduction rate observed in $M_S(T)$ above 50 K prevents conclusive extraction of T_C and b for the core superspins in the 2.5 nm Ag NP assembly. The solid curve in Fig. 6.13 indicates the results of the fits of $M_S(T)$ for Eq. (6.11), giving $M_{S0} = 0.0057(3)$ emu/g, $T_f = 10(1)$ K, and $M_{C0} = 0.0329(2)$. Note that we choose not to call the values obtained for T_C and b since large uncertainties result for the two parameters as the direct results of lack of data at higher temperatures.

A field-induced magnetization M_B as large as 0.13 emu/g is revealed for the 2.5 nm Ag NP assembly at 2 K (Fig. 6.14). This M_B at 2 K is 3.4 times larger than the saturation magnetization M_S. M_B becomes hard to detect at 15 K, which

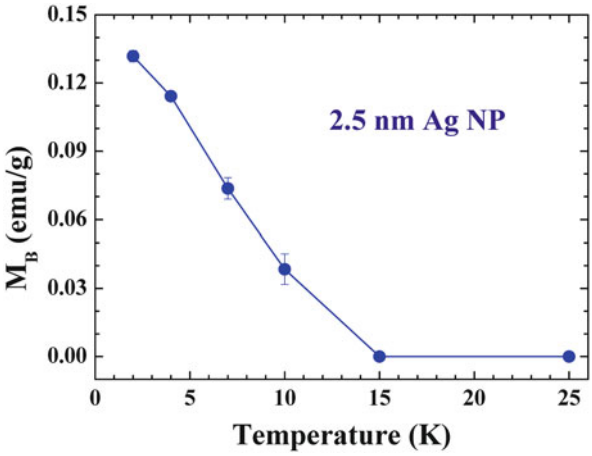

Fig. 6.14 Temperature dependence of Brillouin saturation magnetization of 2.5 nm Ag NP assembly. The Brillouin component disappears above 15 K. The *solid curve* is a guide for the eye only

indicates that at this temperature the thermal population from the down-spin states onto the up-spin states has decompensated for the Zeeman magnetization induced by H_a. It is known that the thermal reductions of M_B are linked to the creation of thermal magnons. The large reduction rate of M_B upon warming at low temperatures indicates small excitation energies for the associated thermal magnons.

6.5.4 Size Dependence

It is clear that both the intrinsic (Langevin) and field-induced Zeeman (Brillouin) magnetizations depend strongly on the particle size. The critical particle size for the appearance of field-induced Zeeman magnetization can be estimated using the Kubo formalism (Eq. (6.1)). Unfortunately, there is no theoretical basis available for estimating the critical particle size for the development of spontaneous magnetic moments in Ag NPs. Experimentally, the dependency of the superspin moment on particle diameter $\mu_p(d)$ obtained from the $M(H_a)$ curves of the 2.5 nm NP assembly (Fig. 6.11) shows that the maximum superspin moment will appear in 2.6 nm Ag particles. Figure 6.15 displays the $M(H_a)$ curves of four representative Ag NP assemblies at 2 K. Comparing the $M(H_a)$ curves of the 2 and 2.5 nm NP assemblies reveals that the particle superspin moment (dM/dH_a in the low-field regime) of the

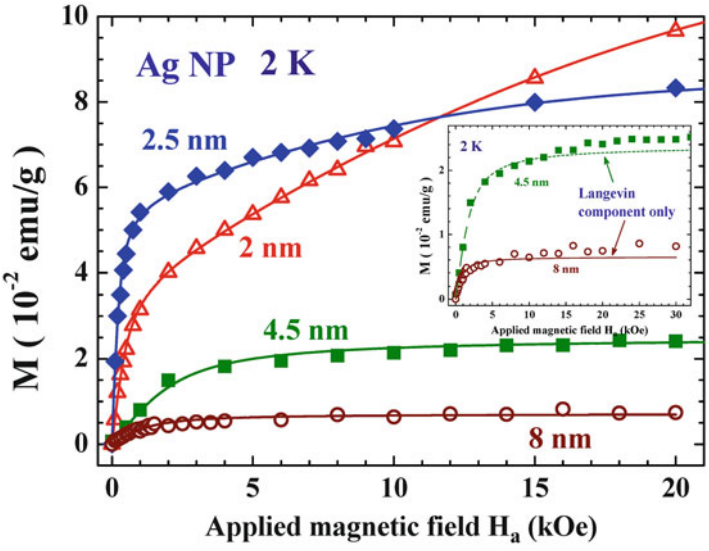

Fig. 6.15 Isothermal $M(H_a)$ curves of four representative Ag NP assemblies at 2 K. The *inset* shows the 4.5 and 8 nm assemblies using an expanded scale for clarity of presentation. Field-induced Brillouin magnetization is revealed even in the 8 nm assembly. The *solid curves* indicate the results of fits for the expression discussed in the text

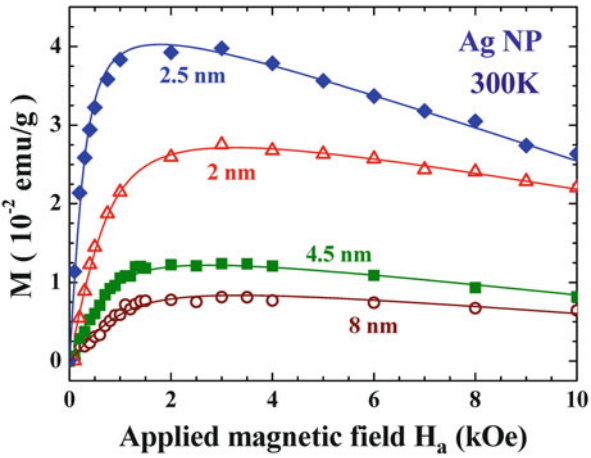

Fig. 6.16 Isothermal $M(H_a)$ curves of four representative Ag NP assemblies at 300 K. Spontaneous magnetization is clearly revealed in all assemblies. The *solid curves* indicate the results of fits for the expression discussed in the text

2.5 nm NP assembly is larger, while the Zeeman moment (dM/dH_a in the high-field regime) of the 2 nm NP assembly is larger. A small but visible Zeeman moment can still be seen in the 8 nm NP assembly at 2 K (inset in Fig. 6.15). A Kubo gap of $\Delta = 0.45$ meV is expected for the 8 nm Ag NPs when estimated using the Kubo formula (Eq. (6.1)), assuming the same electron density as for bulk Ag for the NPs. Apparently, the thermal energy at 2 K may be enough to equally populate the up-spin and down-spin states in the 8 nm Ag NPs.

The magnetization, on the other hand, indicates the total magnetic moment per unit mass of the assembly, where both the superspin moments (Eq. (6.9)) and the numbers of NPs (Eq. (6.5)) in the assembly must be accounted for. Generally speaking, the magnetizations of two multidispersed NP assemblies of the same mean particle diameter but having different size distributions will be different. The intrinsic magnetic moments of ultrasmall Ag NPs can still be seen even at 300 K (Fig. 6.16), where larger Lenz diamagnetic responses for the 2.5 nm assembly than for the 2 nm assembly are also visible. The solid curves in Fig. 6.16 indicate the results of the fits for $M(H_a, T) = M_L(H_a, T) + \chi_D H_a$. Good agreements between the observations and the fits are obtained for all sets of NP assemblies. It is remarkable to find that the size dependencies of the superspin moment thus obtained from the four sets of NP assemblies agree very well. A direct comparison of the representative $\alpha\mu_p(d_i)$ curves obtained from the $M(H_a)$ curves of 2.5 and 8 nm assemblies at 300 K can be made in Fig. 6.17. The superspin moment will be reduced to below $350\mu_B$ in the 20 nm Ag NPs, which is barely detectable using conventional means.

6.6 Concluding Remarks

In this chapter, we focused on identifying the intrinsic magnetic moments that developed in nanosized bare Ag NPs. Eleven sets of bare Ag NP assemblies were fabricated employing the gas condensation method, adopting a physical process

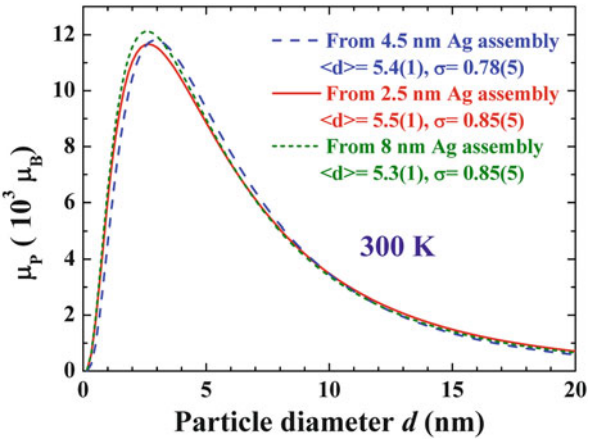

Fig. 6.17 Direct comparison of size dependence of μ_p obtained from $M(H_a)$ curves of 2.5 nm (*solid curve*), 4.5 nm (*dashed curve*), and 5 nm (*dotted curve*) particle assembly at 300 K. The three $\mu_p(d)$ curves match reasonably well

involving the self-nucleation of atoms to form capping-free Ag NPs. The mean particle diameters and size distributions of the NP assemblies were extracted from the line profiles of the X-ray diffraction peaks. Lattice relaxation is clearly revealed in the Ag NPs with diameters smaller than 12 nm, reflecting that lattice interaction in bulk Ag extends to at least over 6 nm, which corresponds to 15 unit cells long. It is the small size effect that governs the lattice relaxation in Ag NPs since the Kubo gap opening near the Fermi level of a 12 nm Ag particle is only 0.13 meV, which is invisible at 300 K with a thermal energy of 25 meV. The disruption of lattice periodicity at the particle surface causes a significant change in the distribution of the electron charge of the silver, in such a way that the electron charges are more extensively distributed toward the central regions of two nearest neighbors. The extension of the electron charge distribution is not isotopic in all crystallographic directions, revealing that redistribution involves not only the spherically distributed 5*s* electrons but also includes the directional 4*d* electrons. Apparently, the small size effect results in a higher degree of mixture between the 4*d* and 5*s* bands of the ultrasmall silver NPs.

The diamagnetic responses from the filled narrow *d* band that are stronger than the Pauli paramagnetic responses from the half-filled free electron *s* band in Cu, Ag, and Au give rise to a diamagnetic character for these noble-metal elements in their bulk forms. A spontaneous magnetic moment, described using particle superspin, develops in particles when their sizes are reduced to several nanometers in diameter. The isothermal magnetization of superspins can be described by the Langevin field profile. Contributions from the differently sized particles in the NP assemblies to the magnetization are considered when analyzing the $M(H_a)$ curves, which allows us to extract the dependency of the particle moment on the particle diameter $\mu_p(d)$. The $\mu_p(d)$ curves obtained from different sets of Ag NP assemblies match nicely, showing that the analysis is reasonably sound. Accordingly, the maximum superspin moment of Ag will appear in 2.6 nm particle with a superspin moment of $\alpha\mu_p = 139$ μ_B at 2 K. Thermal variation of the saturation magnetization of the superspin

moments displays very different thermal reduction rates at temperatures below and above 50 K, revealing that the superspin moments that develop on the surface of an Ag NP are different in strength from those developed in the core. In addition, magnetic field–induced Zeeman magnetization from the quantum confined Kubo gap opening near the Fermi level was also observed in Ag NPs smaller than 8 nm in diameter. Isothermal Zeeman magnetization can be described by the Brillouin field profile. The large reduction rate of Zeeman magnetization upon warming indicates small excitation energies for the associated thermal magnons.

The general picture established so far for the development of magnetic moments in polymer-capped Au NPs is based on the occurrence of electron charge transfer, triggered by the strong chemical affinity between the capping molecules and Au atoms. This creates localized 5*d* holes in the surface region of the NP. Ferromagnetism is thus associated only with the atoms on the surface. In this picture, coupling between the capping molecules and atoms on the particle surface is a prerequisite for the appearance of spin-polarized moments in noble-metal NPs. The present study demonstrates further that magnetic moments do develop in bare Ag NPs, and both surface atoms and core atoms contribute to superspin moments. Clearly, the sources for the development of magnetic moments in capping-free bare Ag NPs are fundamentally different from those developed in polymer-capped NPs. It is known that if the surface and core atoms of an NP gather the same number of electrons, the Fermi energy of the surface electrons will be higher than that of the core electrons because the surface atoms are more closely packed. Electron transfer from the surface region to the core can be anticipated for matching the Fermi energy of the two regions from the small size effect. Although the superspin moments developed in Ag NPs are relatively weak, localized 4*d* holes do exist, which reveals ferromagnetism. The present observations of the existence of superspins in Ag NPs involve both conduction 5*s* electrons and localized 4*d* holes. This can happen only when the 5*s* and 4*d* bands in Ag NPs are energetically close to each other.

Acknowledgement This work was supported by the National Science Council of Taiwan under Grant MOST 104-2112-M-008-007-MY3.

References

1. Holleman A, Wiberg N (1985) Lehrbuch der Anorganischen Chemie, de Gruyter, 33rd edn, p 1486
2. Hüger E, Osuch K (2005) Making a noble metal of Pd. Europhys Lett 71:276
3. Fuster G, Tyler JM, Brener NE, Callaway J (1990) Phys Rev B 42:7332
4. Ashcroft NW, Mermin ND (1976) Solid state physics. Saunders College, Philadelphia, pp 288–293
5. Buzea C, Pacheco II, Robbie K (2007) Nanomaterials and nanoparticles: sources and toxicity. Biointerphases 2:MR17–MR71
6. Andres RP, Bielefeld JD, Henderson JI, Janes DB, Kolagunta VR, Kubiak CP, Mahoney WJ, Osifchin RG (1996) Science 273:1690

7. Volokitin Y, Sinzig J, de Jongh LJ, Schmid G, Vargaftik MN, Moiseev II (1996) Nature (London) 384:621
8. Crespo P, Litrán R, Rojas TC, Multigner M, de la Fuente JM, Sánchez-López JC, García MA, Hernando A, Penedés S, Fernández A (2004) Phys Rev Lett 93:087204
9. Zhang P, Sham TK (2003) X-ray studies of the structure and electronic behavior of alkanethiolate-capped gold nanoparticles: the interplay of size and surface effects. Phys Rev Lett 90:245502
10. López-Cartes C, Rojas TC, Litrán R, Martínez-Martínez D, de la Fuente JM, Penadés S, Fernández A (2005) J Phys Chem B 109:8761
11. Li C-Y, Karna SK, Wang C-W, Li W-H (2013) Spin polarization and quantum spins in Au nanoparticles. Int J Mol Sci 14:17618–17642
12. Prutton M (1994) Introduction to surface physics. Clarendon Press, Oxford, pp 108–138
13. Dickey JM, Paskin A (1968) Phonon spectrum changes in small particles and their implications for superconductivity. Phys Rev Lett 21:1441–1443
14. Knorr K, Barth N (1970) Superconductivity and phonon spectra of disordered thin films. Solid State Commun 8:1085
15. Novotny V, Meincke PPM, Watson JHP (1972) Effect of size and surface on the specific heat of small lead particles. Phys Rev Lett 28:901–903
16. Kubo R (1962) Electronic properties of metallic fine particles. I. J Physical Soc Japan 17:975–986
17. Kawabata A, Kubo R (1966) Electronic properties of fine metallic particles. II. plasma resonance absorption. J Physical Soc Japan 21:1765–1772
18. Halperin WP (1986) Quantum size effects in metal particles. Rev Mod Phys 58:533–606 and references therein
19. Hung C-H, Lee C-H, Hsu C-K, Li C-Y, Karna SK, Wang C-W, Wu C-M, Li W-H (2013) Unusual large magnetic moments in the normal state and superconducting state of Sn nanoparticles. J Nanopart Res 15:1905
20. Litrán R, Sampedro B, Rojas TC, Multigner M, Sánchez-López JC, Crespo P, López-Cartes C, García MA, Hernando A, Fernández A (2006) Magnetic and microstructural analysis of palladium nanoparticles with different capping systems. Phys Rev B 73:054404
21. Garcia MA, Merino JM, Fernández Pinel E, Quesada A, de la Venta J, Ruíz González ML, Castro GR, Crespo P, Llopis J, González-Calbet JM, Hernando A (2007) Magnetic properties of ZnO nanoparticles. Nano Lett 7:1489–1494
22. Karna SK, Li C-Y, Wu C-M, Hsu C-K, Wang C-W, Li W-H (2011) Observations of large magnetic moments in icosahedral Pb nanoparticles. J Phys Chem C 115:8906–8910
23. Garitaonandia JS, Insausti M, Goikolea E, Suzuki M, Cashion JD, Kawamura N, Ohsawa H, de Muro IG, Suzuki K, Plazaola F, Rojo T (2008) Nano Lett 8:661
24. Li W-H, Wu SY, Yang CC, Lai SK, Lee KC, Huang HL, Yang HD (2002) Phys Rev Lett 89:135504
25. Hori H, Teranishi T, Nakae Y, Seino Y, Miyake M, Yamada S (1999) Phys Lett A 263:406
26. Hori H, Yamamoto Y, Iwamoto T, Miura T, Teranishi T, Miyake M (2004) Phys Rev B 69:174411
27. Yamamoto Y, Miura T, Suzuki M, Kawamura N, Miyagawa H, Nakamura T, Kobayashi K, Teranishi T, Hori H (2004) Phys Rev Lett 93:116801
28. de la Presa P, Multigner M, de la Venta J, García MA (2006) J Appl Phys 100:123915
29. García MA, Merino JM, Fernández Pinel E, Quesada A, de la Venta J, Ruíz González ML, Castro GR, Crespo P, Llopis J, González-Calbet JM, Hernando A (2007) Nano Lett 7:1489
30. Zhang P, Sham TK (2002) Appl Phys Lett 81:736
31. Jadzinsky PD, Calero G, Ackerson CJ, Bushnell DA, Kornberg RD (2007) Structure of a thiol monolayer-protected gold nanoparticles at 1.1 Å resolution. Science 318:430–433
32. Carmeli I, Leitus G, Naaman R, Reich S, Vager Z (2003) Magnetism induced by the organization of self-assembled monolayers. J Chem Phys 118:10372–10375
33. Dutta P, Pal S, Seehra MS, Anand M, Roberts CB (2007) Magnetism in dodecanethiol-capped gold nanoparticles: role of size and capping agent. Appl Phys Lett 90:213102

34. De la Venta J, Pucci A, Fernández Pinel E, García MA, de Julián Fernández C, Crespo P, Mazzoldi P, Ruggeri G, Hernando A (2007) Magnetism in polymers with embedded gold nanoparticles. Adv Mater 19:875–877
35. Wu C-M, Li C-Y, Kuo Y-T, Wang C-W, Wu S-Y, Li W-H (2010) Quantum spins in Mackay icosahedral gold nanoparticles. J Nanopart Res 12:177
36. Li C-Y, Wu C-M, Karna SK, Wang C-W, Hsu D, Wang C-J, Li W-H (2011) Intrinsic magnetic moments of gold nanoparticles. Phys Rev B 83:174446–174450
37. Batsaikhan E, Chen Y-C, Lee C-H, Li H-C, Li W-H (2015) Development of ferromagnetic superspins in bare Cu nanoparticles by electronic charge redistribution. Int J Mol Sci 16:23165–23176
38. Shih P-H, Li W-H, Wu SY (2015) Surface spin polarization induced ferromagnetic Ag nanoparticles. J Magn Magn Mater 406:30–34
39. Warren BE (1990) X-ray diffraction. Dover Publications, Dover, pp 251–314
40. Sahoo S, Petracic O, Kleemann W, Nordblad P, Cardoso S, Freitas PP (2003) Aging and memory in a superspin glass. Phys Rev B 67:214422
41. Nakamae S (2014) Out-of-equilibrium dynamics in superspin glass state of strongly interacting magnetic nanoparticle assemblies. J Magn Magn Mater 355:225
42. Bean CP, Livingston JD (1959) Superparamagnetism. J Appl Phys 30:S120–S129
43. Skomski R (2003) Nanomagnetics. J Phys Condens Matter 15:R841–R896
44. Craik D (1995) Magnetism-principles and applications. Wiley, New York, pp 99–100
45. Blundell S (2001) Magnetism in condensed matter. Oxford University Press, Oxford, pp 23–30
46. Silva NJO, Carlos LD, Amaral VS (2005) Phys Rev Lett 94:039707
47. Mørup S, Frandsen C (2004) Thermoinduced magnetization in nanoparticles of antiferromagnetic materials. Phys Rev Lett 92:217201
48. Mørup S, Hansen BR (2005) Uniform magnetic excitations in nanoparticles. Phys Rev B 72:024418
49. Pereiro M, Baldomir D (2005) Determination of the lowest-energy structure of Ag_8 from first principles calculations. Phys Rev A 72:45201
50. Pereiro M, Baldomir D, Arias JE (2007) Unexpected magnetism of small silver clusters. Phys Rev A 75:063204
51. Chang CM, Chou MY (2004) Phys Rev Lett 93:133401
52. Harris JGE, Grimaldi JE, Awschalom DD, Chiolero A, Loss D (1999) Excess spin and the dynamics of antiferromagnetic ferritin. Phys Rev B 60:3453–3456
53. Aquino R, Depeyrot J, Sousa MH, Tourinho FA, Dubois E, Perzynski R (2005) Magnetization temperature dependence and freezing of surface spins in magnetic fluids based on ferrite nanoparticles. Phys Rev B 72:184435
54. Shendruk TN, Desautels RD, Southern BW, van Lierop J (2007) The effect of surface spin disorder on the magnetism of γ-Fe_2O_3 nanoparticle dispersions. Nanotechnology 18:455704
55. Kittel C (1996) Introduction to solid state physics, 7th edn. Wiley, New York, p 446

Chapter 7
Multifunctional Magnetic Nanostructures: Exchange Bias Model and Applications

Sarveena, Navadeep Shrivastava, M. Singh, and Surender Kumar Sharma

7.1 Introduction

Over the past two decades, research in magnetic nanomaterials (MNPs) has been crucial. Exploring the applications of even iron oxide in only biological research has shown the importance of the MNPs as magnetic biosensor systems [1], separation immunoassays [2, 3], local heat sources for cancer treatment by hyperthermia [4–7], drug carriers [8–13], contrast agents for magnetic resonance imaging (MRI) [3, 13–17] and magnetic particle imaging (MPI) [18, 19], parasite diagnostic assays [20, 21], and nano bridging substances for surgery and wound healing [16, 22]. Various important biological applications are presented in Fig. 7.1. Using bare iron oxide nanoparticles (NPs) causes aggregation, which is addressed using coating methods, for example, oleic acid or carbon. These coating methods help against aggregation by minimizing the interparticle interactions in magnetic materials [23].

Sarveena • M. Singh
Department of Physics, H. P. University, Shimla 171005, India

N. Shrivastava
Department of Physics, Federal University of Maranhão, Av. dos Portugueses, 1966—Vila Bacanga, São Luis, MA 65085-580, Brazil

Institute of Chemistry, University of São Paulo, Av. Prof. Lineu Prestes, 748—Vila Universitaria, São Paulo, SP 05508-000, Brazil

S.K. Sharma (✉)
Department of Physics, Federal University of Maranhão, Av. dos Portugueses, 1966—Vila Bacanga, São Luis, MA 65085-580, Brazil

Department of Physics, H. P. University, Shimla 171005, India
e-mail: surender76@gmail.com

© Springer International Publishing AG 2017

S.K. Sharma (ed.), *Complex Magnetic Nanostructures*,
DOI 10.1007/978-3-319-52087-2_7

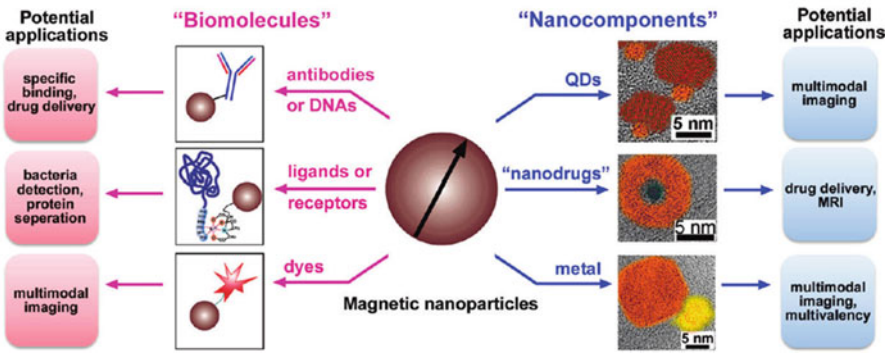

Fig. 7.1 Scheme illustrating fabrication of multifunctional MNPs and their potential applications in biomedicine. Reproduced with permission from [65]

The increasing use of new technologies demands the invention of new magnetic materials. Mainly these new materials depend on structural behavior in space at different length scales and various time scales [24]. This gives rise to NPs, nanowires, thin films, nanobowls, nanobeads, and nanocubes, for example. Proceeding from magnetic nanostructures, the synthesis and fabrication of different morphologically structured magnetic nanomaterials leads to complex structures and morphologies. The term *multifunctional* usually denotes a complex structure. Multifunctionality enables the integration of two or more functional NPs into a single nanoentity. This enables tailoring the properties of complex magnetic nanostructures to length scales. These novel magnetic materials cause dynamical magnetic properties to evolve over various timescales [24]. This in turn has prompted researchers to explore a variety of new phenomena starting from slower processes to faster processes. In other words, depending on the mechanism, it has been observed that various processes exist in complex magnetic nanosystems, such as domain walls and magnetic vortex dynamics [25–27], spin wave propagation and localization [28–30], ultrafast demagnetization [27, 31–34], and relaxation [33, 35, 36]. These multifunctional complex structures introduce magnetic structures at various length scales such as nanodots [37], microdisks [38], magnetic nanowires [3, 39], and nanostripes [40]. In addition to the preparation method of various MNPs, the synthesis of quantum dots [41, 42], silver NPs [43–45], gold NPs [9, 46, 47], nanosilicas, and lanthanides [46, 48] has improved. Recently, new advanced preparation techniques offer an opportunity to fabricate several-nanometer-length magnetic particles with narrow size distributions and different compositions through a variety of procedures, either embedded in a solid matrix or diluted in organic solvents. Depending on the material and structural synthesis, different types of MNP systems have been developed, for

example, Janus NPs [34, 49, 50], core-shell [51, 52], dumbbell [53, 54], flower [55–57], dimers/trimers [58–60], and multicomponent hybrid types of nanostructures [59, 61–64] called multifunctional MNPs. Jointly, these bifunctional MNPs manifest unique combinations of magnetic and optical/plasmonic/electronic properties and have shown great potential for different applications [64].

The two main features that dominate the magnetic properties of NPs are finite-size effects [18, 27, 42, 66–69] and surface effects [18, 31, 70–75]. The finite size effect lead to the quantum confinement of electrons, single domain, and superparamagnetism. The surface effects result from the breaking of symmetry of the crystalline structure at the surface of a particle. The existence of surfactants [76, 77], oxidation [78–80], organic and weak bonds, and surface strain, along with different physicochemical structures of different types of NPs [57, 73, 74, 81–83] furnish their special properties related to structural, electronic, optical, and magnetic behavior. These NPs can display interesting features associated either with the intrinsic characteristics of individual particles, such as finite-size and surface effects, or with the collective properties of NP ensembles, such as dipolar interactions and exchange-mediated couplings.

The shape, size, surface, and chemical effect in magnetic noble-metal single nanostructures can lead to the exciting phenomenon of exchange bias (EB) and a magnetic proximity effect. These have a significant impact on the industrial application of magnetic nanostructures in device fabrication. An example is core-shell MNPs used as storage media for magnetic recording, which are appealing because of their substantially improved thermal stabilities. This fact was brought out in a report by Skumryev et al. [84] showing that a superparamagnetic (SPM) limit could be exceeded by means of an EB effect, which raised hopes that storage devices could be further miniaturized. In particular, the exchange coupling at any ferromagnetic (FM)/antiferromagnetic (AFM) interface may induce unidirectional anisotropy in the FM when the system is cooled (or grown) in a static magnetic field above the Neél temperature (T_N) of the AFM (with the Curie temperature, T_C of the FM lower than T_N) causing a shift in the hysteresis loop along the magnetic field axis. This phenomenon is known as the exchange bias effect [85]. Exchange coupling between any FM/AFM systems produces a system with a stable order and high anisotropy owing to the large exchange parameter of FM, which makes the FM order stable at high temperatures, particularly if the dimensions are in nanometers and large anisotropies and, consequently, very stable orientations of AFM [86]. In addition to AFM/FM interfaces, EB is also observed in other types of interfaces involving a ferrimagnetic (FiM) (e.g., FiM/AFM, FiM/FM) or involving a spin-glass (SG) phase (e.g., FM/SG, AFM/SG, and FI/SG) and antiferromagnet/diluted ferromagnetic semiconductor (AFM/DFMS), reflecting its diverse origin [87, 88]. EB materials in thin film nanostructures have been widely studied for device applications. Materials in thin film form have been the basis of many interesting EB and related phenomena, for example, AFM thickness, coercivity enhancement, training effects, dilution effects, and interface disorder or orientation dependence of the exchange bias field (H_E). EB or exchange anisotropy has mostly been studied in bilayers (or multilayers) of magnetic materials [88]. These multifunctional

interfaces are usually achieved by artificially designed phase inhomogeneity, for example, by making artificial magnetic bilayers or mixing magnetic particles with a different matrix (granular systems). In these systems the interface can be controlled and characterized effectively. On the other hand, recent studies in FM/AFM/FM trilayers show a simple method of controlling EB by a simple structural modification from the bilayers to the trilayers; these studies have probed internal AFM spin distributions using EB [89].

Fundamentally, the preparation method for different NPs is the bottom-up solvent-based chemical reaction. The next and most important step is to control the nucleation and growth of the reaction products in the reaction under confined ambient conditions. They can also be manipulated by controlling the reaction mechanism via binding of appropriate ligands dynamically over the surface of the so-called core particle. Microemulsion and organometallic synthesis procedures are the most powerful way to prepare complex MNPs having good size distributions and stable colloids [90]. Microemulsion-based syntheses are usually done at low temperatures and can be utilized to prepare large amounts of material. Since the nucleation of a reaction is slow and occurs at low temperatures, it can present challenges. Synthesized NPs may be less crystalline and polydisperse [76, 91–93]. Organometallic-based synthesis is becoming more common in the preparation of particles with high quality, good crystallinity, and monodispersibility [94]. High-temperature (150–350 °C) thermal decomposition of organometallic precursors is common in this process [80, 95]. It is also feasible to use the reduction mechanism of metal salts in high-boiling-point solvents in the presence of stabilizers [33, 74]. The benefit from the temperature in this type of reaction is to remove the crystalline defect to obtain good-quality, multifunctional MNPs. The major issue is to use materials in biological applications because there may be toxicity issues owing to solvents, precursors, and ligands [90]. Obviously advances in controlling the functional characterization and functionalization of magnetic materials provide a pathway for developing complex structures or complex composite nanomaterials [96–98]. Finally, the application of these NPs depends on, for example, the structure, composition, stability, dispersity, and toxicity under a wide range of constraints [90]. Ligand exchange and ligand adsorption are general methods for making surface modifications to complex magnetic particles [31, 46, 80, 83, 99]. In this case, ligand exchange means changing a hydrophobic ligand into a hydrophilic one. Generally, these ligands consist of hydrophilic groups and linking groups. Linking groups can combine with the surface of MNPs, at which point the hydrophilic groups are exposed to the surrounding environment and make the MNPs disperse in the aqueous solution. The key to designing a successful ligand exchange is to select linking groups that have the strongest combination with the surface of the MNPs.

In this chapter, we shall discuss the synthesis of core-shell and dumbbell types of complex MNPs and focus to a lesser degree on bilayer thin films. The techniques that are widely employed in characterizations or multifunctional complex MNPs will be summarized. These techniques include X-ray diffraction (XRD), transmission electron microscopy (TEM), atomic force microscopy, small-angle X-ray scattering (SAXS), superconducting quantum interference device (SQUID),

AC susceptibility, Mössbauer spectroscopy, small-angle neutron scattering (SANS), X-ray magnetic circular dichroism (XMCD) spectroscopy, ferromagnetic resonance (FMR), and photoluminescence (PL). The surface chemistry and main factors affecting the properties of these NPs will also be taken into account. Applications in various fields of magnetic devices and catalysis are also explored. Furthermore, the models and a numerical survey of properties of MNPs, with a focus on EB easily observed in core-shell types of nanostructures, will also be presented.

7.2 Experimental Characterization Techniques

One of the most fundamental characteristics of NPs is their high surface-to-volume ratio. This can lead to novel and unexpected atomic arrangements and may also have dramatic effects on other physical and chemical characteristics. The precise determination of the structure and properties of nanomaterials can result in the development of new multifunctional nanomaterials for various multidisciplinary applications. Therefore, many techniques are required to measure the structural, magnetic, and optical/electronic properties of these materials. A description of the entire spectrum of experimental techniques employed for characterization is certainly beyond the scope of this chapter, so some of the most commonly used techniques and the main information they provide are summarized in the following subsections.

7.2.1 X-Ray Diffraction

XRD, based on wide-angle elastic scattering of X-rays, is a rapid analytical technique used primarily to determine the phases, crystallographic structure, lattice distortion, and average size of NPs. A fundamental principle and technical description of XRD is available in the literature [100]. The size of particles can be determined from the width of X-ray peaks using Scherrer's formula [100]. Characterization of individual particles is usually not possible, so it provides information on the average behavior of NP samples. This is limited to crystalline materials, and the X-ray coherence length does not allow this technique to be used for particles that are too small (<1 nm).

7.2.2 Transmission Electron Microscopy

TEM is a very informative and very frequently used technique to visualize and determine the morphology and structure of nanomaterials in electron microscopy (EM). TEM provides a real space image of atomic distribution in nanocrystals and over its surface. It produces direct images and chemical information of nanomaterials at a

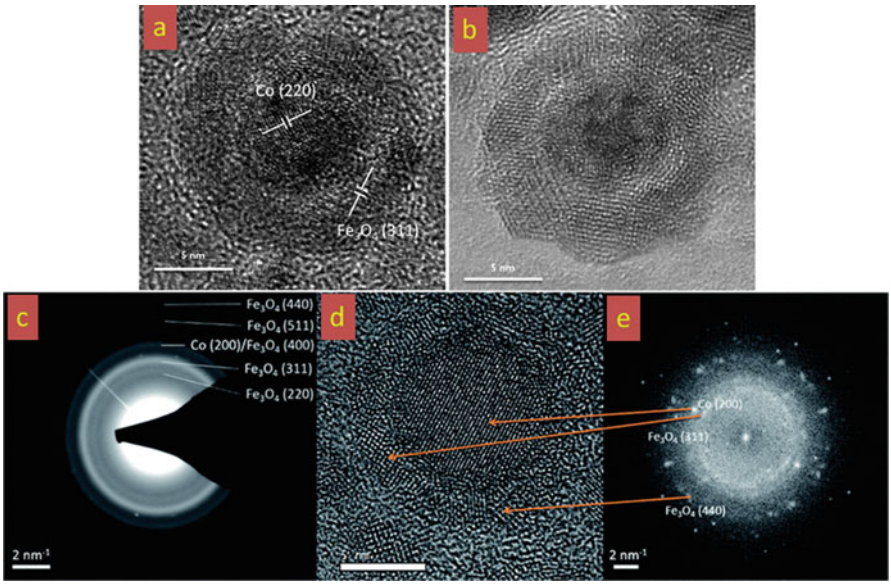

Fig. 7.2 (**a**, **b**) HRTEM images showing fringes in core and shell of a particle. (**c**) SAED image of sample region containing multiple core-shell NPs, shown alongside a TEM image of an individual NP (**d**) with corresponding FFT (**e**). Reproduced with permission from [102]

spatial resolution down to the level of atomic dimensions (<1 nm). In this technique, a specimen is illuminated by a beam of monochromatic electrons, some of which are transmitted through the objective lens and then projected onto a viewing screen to produce an image [101]. High-resolution transmission electron microscopy (HRTEM) gives information on the crystal planes of particles and measures lattice distances. HRTEM is very useful for complex structures such as core-shell or those consisting of an alloy. Selected area electron diffraction (SAED) patterns obtained by TEM yield information about the orientations, atomic arrangements, and structures of narrow regions of interest in nanomaterials. Figure7.2 explains the TEM imaging of the Co@Fe_3O_4 core-shell nanostructure. The oleic acid–capped Co NPs yielded two distinct types of particle: small uniform NPs and larger core-shell structures. Figure 7.2a highlights the 0.216 nm d-spacing of the (220) reflection of metallic Co in the core and the 0.251 nm d-spacing of the (311) reflection of Fe_3O_4 in the shell, while Fig. 7.2b shows the petal-like structure of the shell caused by multiple nucleation sites. Further, SAED from a large region containing NPs is given in Fig. 7.2c. The rings present in the pattern reveal the lattice spacing in the polycrystalline sample. The experimental values of 3.01, 2.56, 2.11, 1.71, and 1.51 Å correspond to the Fe_3O_4 (220), Fe_3O_4 (311), Fe_3O_4 (400)/Co (220), Fe_3O_4 (511), and Fe_3O_4 (440) reflections. Based on this analysis, it can be concluded that Co is present in a metallic, nonoxidized form, and the presence of γ-Fe_2O_3 is ruled out on the basis of its different lattice parameters.

A wide variety of analytical techniques, like energy dispersive x-ray spectroscopy (EDS) and electron energy loss spectroscopy (EELS), can be coupled with

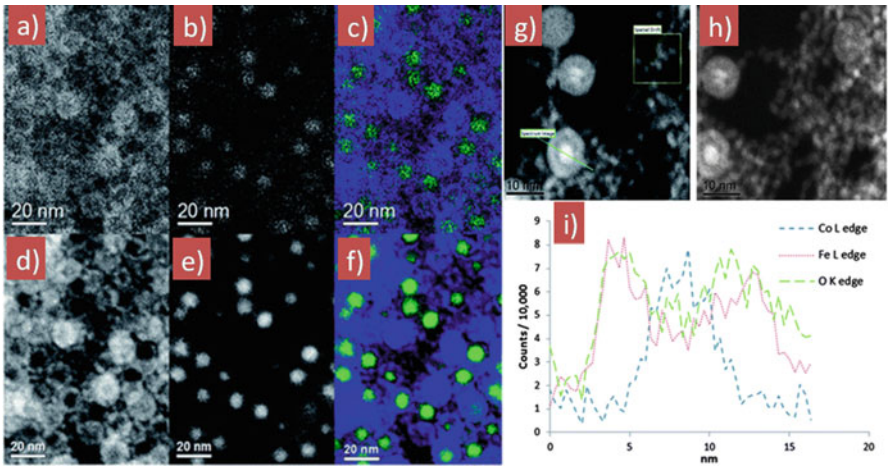

Fig. 7.3 EFTEM images of Co@Fe_3O_4 core-shell particles, both before (**a–c**) and after (**d–f**) Multivariate statistical analysis (MSA). (**a, d**) EFTEM Fe $L_{2,3}$ map; (**b**, **e**) EFTEM Co $L_{2,3}$ map; (**c, f**) overlay of Co and Fe maps, with Co in *green* and Fe in *blue*. (**g–i**) EELS line scan of a core-shell particle. (**g**) STEM-HAADF image showing square region (*yellow box*) selected for spatial drift correction and position of line scan (*green line*); (**h**) acquisition region postscan; (**i**) graph showing EELS signal intensity after MSA for Co, Fe, and O across diameter of particle. Reproduced with permission from [102]

TEM for different applications. EELS can be used for the microanalysis of materials and provide information about electron structure, whereas EDS can be used to quantify the chemical composition of a particular system. EELS spectroscopy is helpful in exploring rich information about bonding in crystals and at interfaces. The energy loss near-edge structure (ELNES), a unique transmission characteristic of EELS, is a sensitive tool to analyze crystalline structures and may serve as a fingerprint to identify compounds. Energy-filtered transmission electron microscopy (EFTEM) is a rapidly developing technique for high-spatial chemical imaging [103]. Wet scanning transmission electron microscopy (STEM) can be used for determining the particle size, dispersion, aggregation/agglomeration, and dynamic displacement of nanomaterials in an aqueous environment. Thus, wet mode STEM permits observation at a nanoscale resolution and high contrast, even through several micrometers of water, without adding contrast agents and stains [104]. Figure 7.3 shows EFTEM and EELS analyses for Co@Fe_3O_4 core-shell NP.

7.2.3 Atomic Force Microscopy

Atomic force microscopy provides 3D topographical images of NPs with sub-nanometer resolution by measuring forces between a sharp probe (radius less than 10 nm) and surface at very short distance (0.2–10 nm probe-sample separation). Atomic force microscopy techniques are used to measure surface properties such

as the frictional force on the nanoscale, hardness of surfaces, surface charge distribution, adhesion, surface magnetization, yield stress, elasticity, and the plastic deformation dynamics of nanomaterials [105]. Such imaging can be carried out in air, liquid, vacuum, and gas. Atomic force microscopy is gaining importance owing to its capability to image a variety of biomaterials by observing the interaction of nanomaterials with supported lipid bilayers in real time without causing appreciable damage to many types of native surfaces, which is the advantage of atomic force microscopy over other EM techniques [104]. An example is given in Fig. 7.4, which shows the atomic force microscopy images of Co-Py bilayers. It can be seen that the obtained short-range-ordered and disordered alumina templates are quite different. In the disordered case, the pores appear smaller, irregular, and not well delimited, while they are clearly visible in the short-range ordered templates.

7.2.4 Small-Angle X-Ray Scattering

SAXS is helpful in analyzing either crystalline or amorphous materials from polymers and proteins to nanomaterials. This analytical technique can be used to evaluate the size/size distribution, shape, orientation, and structure of a variety of polymers and nanomaterial-bioconjugate systems in solution [104]. The particle size estimated by SAXS is statistically more reliable as compared to other EM methods because the particle size distribution obtained by the SAXS is typically estimated over a large number of NPs, while the size distribution obtained by EM methods is based on the measurements of a few hundred or thousand. It is also useful to determine inhomogeneities within amorphous materials and pore sizes in porous materials. SAXS also provides information on long-range ordering or interparticle distances in an assembly of nanocrystals or in polymeric materials [107].

In SAXS profile information may be extracted from three distinct regions: Guinier, Fourier, and Porod [108], explained in Fig. 7.5a. The Guinier region provides information on the radius of gyration. The radius of gyration will be greatly affected by the aggregation of particles, polydispersity, and improper subtraction of background or buffer. A nonlinear Guinier plot is a strong indication of poor sample quality. Improper background subtraction, the presence of attractive or repulsive interparticle effects, and sample polydispersity result in deviations from linearity. When particles are highly polydisperse, a Guinier plot will show a curvature instead of a straight line [109]. In the Fourier region, the pair distribution function may be determined by an indirect Fourier transformation of the experimental form factor, providing significant information on particle shape. In the Porod region, the Porod invariant can be determined; it provides surface information, such as the surface-to-volume ratio and specific surface estimation for compact particles. Some information about the particle shape may be obtained from the asymptotic behavior in the Porod region.

Figure 7.5b shows SAXS patterns of M_5^T, M_8, and M_{19}^{O2} iron oxide NP samples [110]. Here M_8 is approximately 8 nm in size and synthesized at 290 °C, M_5^T is

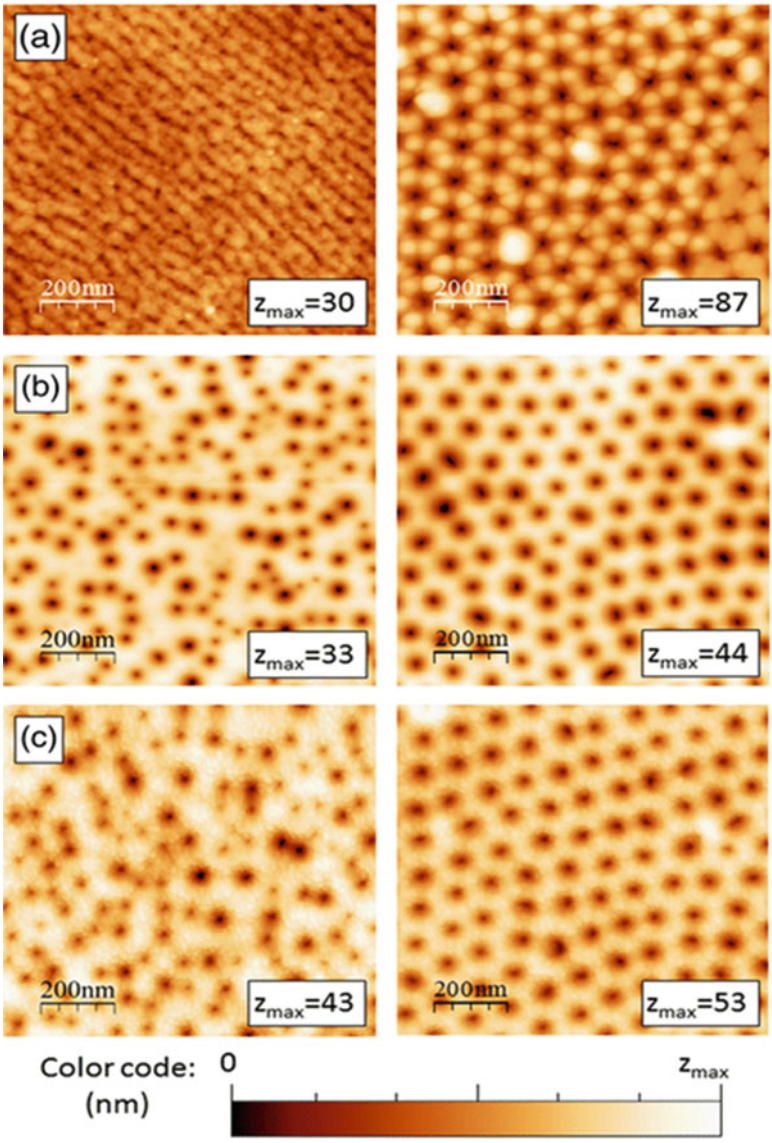

Fig. 7.4 Typical atomic force microscopy images of the antidot array surface: (**a**) initial templates before planarization, (**b**) templates after planarization, (**c**) final samples after thin film deposition (Co20Py27). *Left* disordered antidots, *right* ordered antidots. The maximum height variation in the atomic force microscopy image is indicated (nm). Reproduced with permission from [106]

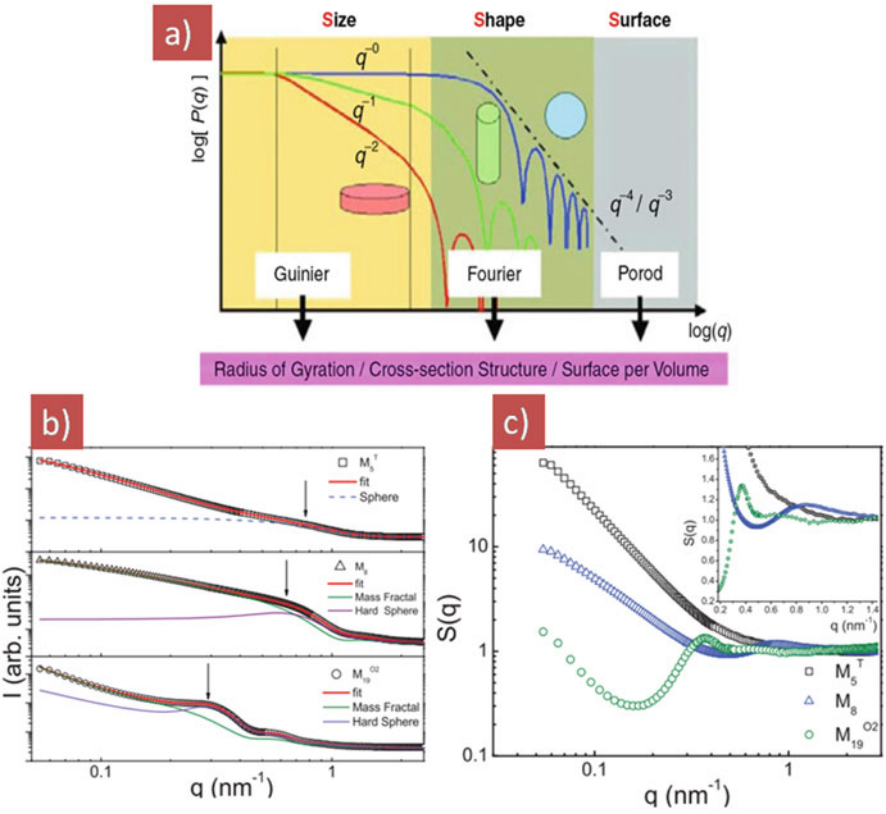

Fig. 7.5 (**a**) Regions of SAXS profile and data that may be extracted from each profile. Reproduced with permission [108]. (**b**) Log-log representation of colloid scattering curves expressed as intensity (I) vs. scattering vector modulus q of M_5^T, M_8, and M_{19}^{O2} colloids. Solid lines are the model functions (Eq. 2 of [110]) that best fit the experimental SAXS measures. (**c**) Log-log plot of structure function $S(q)$; inset shows a zoom in which power law and interference between particle dependence can be seen for low and high range q values respectively. Reproduced with permission [110]

approximately 5 nm in size and synthesized at 240 °C, and M_{19}^{O2} is 19 nm in size and obtained at 290 °C under varying pressure in the presence of oxygen. The scattered intensity (I) as a function of q displays three main features related to the aforementioned synthesized NP size, size dispersity, interparticle interference, and aggregation. Figure 7.5c shows log-log plots of $S(q)$. This plot is the ratio of experimental scattering intensity and the intensity scattered for the particles in a diluted state [110].

A monolayer of colloidal gold NPs deposited on a flexible Mylar foil by a modified Langmuir–Schaefer method was tested in situ under external uniaxial stress by the SAXS technique [111]. Figure 7.6 shows the size distribution of gold NPs dispersed in *n*-hexane measured by SAXS. The SAXS pattern (Fig. 7.6a) was

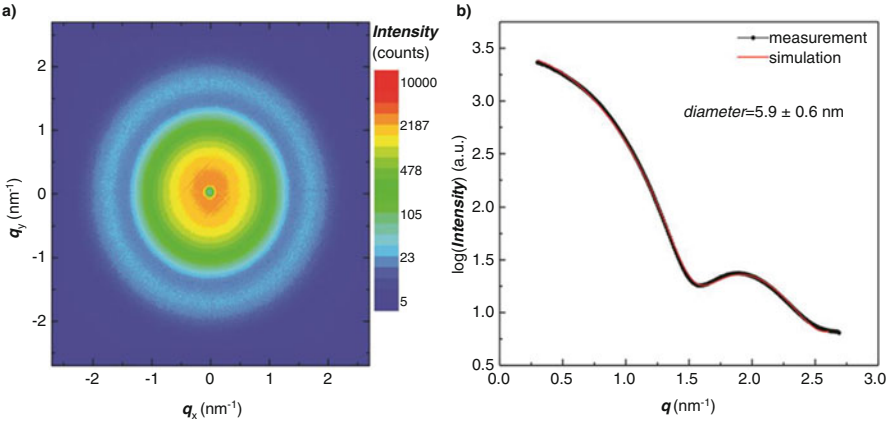

Fig. 7.6 SAXS pattern (**a**) and azimuthally averaged radial intensity distribution (**b**) of colloidal gold NPs dispersed in *n*-hexane. The *red solid line* in (**b**) is the best fit of the experimental intensity distribution according to the Rayleigh scattering model. Reproduced with permission from [111]

azimuthally averaged and fitted using a Rayleigh scattering model with a polynomial background. The NP form factor is a decreasing function at 0.91 nm^{-1} (Fig. 7.6b). The fit of the SAXS curve revealed a NP diameter of 5.9 ± 0.6 nm.

7.2.5 Magnetic Characterization

The most commonly used technique to study the magnetic properties of materials is the plot of magnetization (M) as a function of magnetic field intensity (H), that is, M-H hysteresis loops. Hysteresis loops have been measured using a wide variety of instruments, most commonly superconducting quantum interference device (SQUID), vibrating sample magnetometer, Kerr effect, and loop tracers. The main information obtained from these techniques is the saturation magnetization, retentivity, coercivity, and loop shift. Loop shift is the indication of the EB effect in any FM/AFM systems. It is noteworthy that from hysteresis loops and other DC experiments (e.g., torque), only the lower limit of the AFM/FM interface coupling is obtained. However, larger values are obtained from certain AC measurements that rely on small oscillations of the FM magnetization from its remanent or saturated state, such as magnetoresistance, AC susceptibility, or Brillouin light scattering. The shape of hysteresis loops provides information about anisotropies [88]. From SQUID, the blocking temperature (T_B) of a sample can be determined from a standard zero-field-cooled (ZFC) and field-cooled (FC) measurement of the magnetization. Complementary information, such as the monodispersity of a sample, size and anisotropy of particles, formation of an oxide layer on an

the intermetallic sample, and the magnetic (dipole–dipole) interaction between particles, can be obtained from blocking temperature [101].

Figure 7.7L shows magnetization hysteresis loops recorded at 2 and 300 K in ZFC and FC mode in a field of 30 kOe from 2–300 K for partially oxidized FeO NPs prepared using the thermal decomposition of iron acetylacetonate at high temperature [112]. At 300 K, particles are in a SPM state showing zero coercivity (H_C) and retentivity (inset b, Fig. 7.7L) without saturation up to a field of 70 kOe, whereas at 2 K, the coercivity is approximately 2.5 kOe (ZFC mode) with a high field of irreversibility, >50 kOe. Moreover, the loops in both ZFC and FC conditions are not saturated, even in a high field of 140 kOe, a clear indication of a strong internal interaction and coexistence of different magnetic phases into individual particles. Here the EB shift is quantified by exchange field parameters, $H_{EB} = -(H_R + H_L)/2$, while coercivity is defined as $H_C = (H_R - H_L)/2$, with H_R and H_L being the points where the loop intersects the field axis. The corresponding value of H_{EB} is approximately 2.3 kOe (at 2 K) and FC coercivity, $H_C^{FC} \approx 3.4$ kOe, which is more than the corresponding value observed in the ZFC condition. However, all these EB-related effects disappear at T close to or above a T_N of approximately 198 K, where the AFM core becomes paramagnetic.

Other techniques for magnetic characterizations are Mössbauer spectroscopy, AC susceptibility, and small-angle neutron scattering (SANS). In AC susceptibility, the change in magnetic flux produced due to the presence of an alternating field is measured as a function of the applied AC and DC fields, temperature, or frequency. The Mössbauer technique is very sensitive to the local atomic configuration. It can give very precise information about the chemical, structural, magnetic, and time-dependent properties of a material. The Mössbauer effect provides information about the local environment of Mössbauer nuclei (i.e., ^{57}Fe or ^{119}Sn) in a sample [113]. For MNPs, the magnetic hyperfine field splitting into Mössbauer spectra begins right below the blocking temperature, where the relaxation rate of particles slows down sufficiently for the reversal energy to exceed the thermal energy [101]. In FM/AFM layers, Mössbauer effects can be studied by introducing a radioactive isotope of one of the materials in the AFM or FM layer. The Mössbauer parameters allow the identification of nonequivalent iron positions in a crystal lattice and the identification of compounds and phases. Figure 7.7R shows a room-temperature Mössbauer spectrum of Au-Fe_3O_4 NPs (AIONPs) prepared using a thermal decomposition method oxidized at (a) 125 °C (AIO125), (b) 150 °C (AIO150), (c) 200 °C (AIO200), and 250 °C (AIO 250) for 30 min during cooling from 315 °C [47]. These Mössbauer spectra reflect collective magnetic excitations. Sample AIO125 shows SPM relaxation (approximately 42% of area fraction), consistent with its smallest size (approximately 9 nm). This sample also presents 50% of the area fraction with collective magnetic excitation phenomena. AIO150, AIO200, and AIO250 show only a magnetite (Fe_3O_4) phase with no traces of paramagnetic Fe (II) and Fe (III). Mössbauer analyses indicate that the increase in the oxidation temperatures resulted in only the magnetite (Fe_3O_4) phase. In other words, the Mössbauer study proved to be very useful in the determination of iron oxide phases present in the sample.

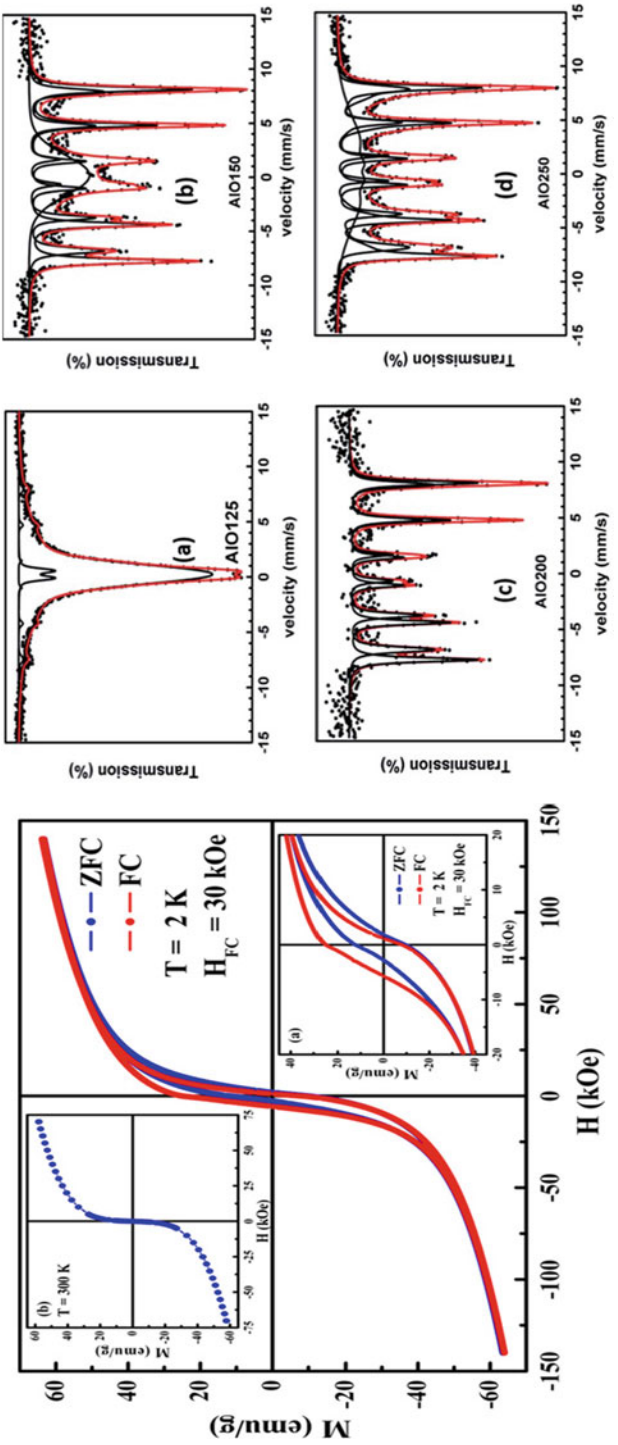

Fig. 7.7 (*Left panel L*) Hysteresis loops taken in ZFC and FC modes at 2 K. (**a**) Corresponding low field region. (**b**) Hysteresis curve taken at 300 K. Reproduced with permission from [112]. (*Right panel R*) Mössbauer spectrum of gold iron oxide NPs performed at 300 K. Reproduced with permission from [47]

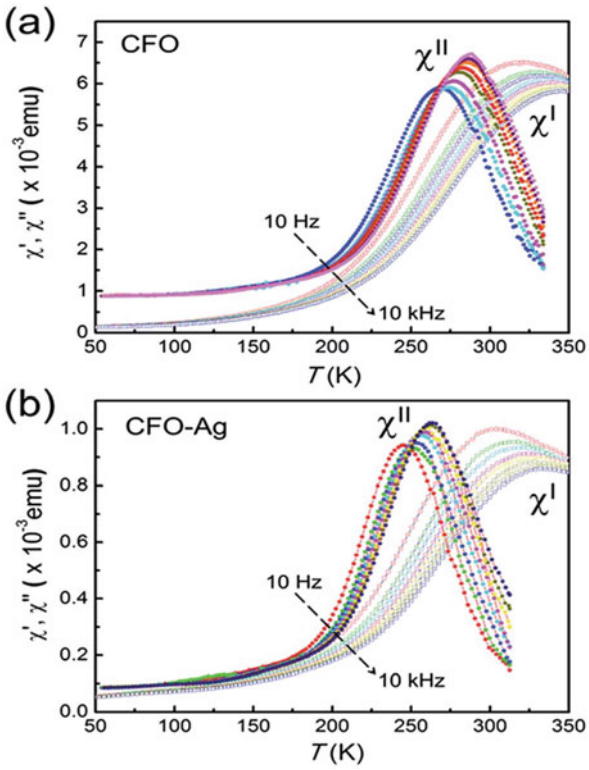

Fig. 7.8 (**a**, **b**) T dependence of real (χ', *open squares*) and imaginary (χ'', *closed circles*) components of AC susceptibility for CFO (**a**) and CFO–Ag (**b**) under an external field H_{ac} of 5 Oe. Reproduced with permission from [114]

Figure 7.8 shows the T dependence of the real $\chi'(T)$ and imaginary $\chi''(T)$ parts of the susceptibility for $CoFe_2O_4$ (CFO) (Fig. 7.8a) and $CoFe_2O_4$–Ag (CFO-Ag) (Fig. 7.8b) under a field H_{ac} of 5 Oe (50 K < T < 350 K) [114]. The blocking temperature, T_B, shifts toward a higher temperature and decreases in height with increasing frequency, which shows the expected behavior of blocking processes at T_B. Further, an ensemble of NPs in which the interparticle magnetic interactions are sufficiently weak shows SPM behavior, as described by the Néel–Brown model. On the contrary, when interparticle interactions are non-negligible, the system eventually shows collective behavior, which overcomes the individual anisotropy properties of the particles. The data were analyzed using the Vogel–Fulcher law [115] and the calculated fitted parameters were obtained for CFO ($E_B/k_B = 876$ K, $\tau_o = 10^{-8}$ s, $T_0 = 256$ K) and CFO–Ag ($E_B/k_B = 1846$ K, $\tau_o = 10^{-9}$ s, $T_0 = 201$ K) (Fig. 7.8). These values become comparable to those observed for SG systems. The analysis reveals that the energy barrier (E_B/k_B) for CFO–Ag is enhanced twice in comparison with CFO, together with a decrease in the effective temperature ($T_0 = 201$ K for CFO–Ag, $T_0 = 256$ K for CFO). The obtained static and dynamic magnetic behavior of CFO–Ag leads to the conclusion that under DC or low AC fields, the presence of Ag NPs enhances the magnetic relaxation of bulk CFO–Ag heterocomposite, a phenomenon that leads to a weakening of the magnetocrystalline

anisotropy. In contrast, at high frequencies of AC fields, CFO–Ag damping effects emerge in the relaxation behavior.

SANS can be used to evaluate various parameters including the radius of gyration, the particle surface area, shape of the scattering particles, magnetic structure, magnetic correlation, alignment of NPs, and their response to an external magnetic field [101]. Contrast variation data in SANS provide information about the shape and internal structure of multicomponent particles (e.g., core-shell NPs) [116].

7.2.6 X-Ray Magnetic Circular Dichroism Spectroscopy

X-ray absorption spectroscopy (XAS) has become one of the most fundamental and widely used techniques for studying the local structure and oxidation states in catalysts and other chemical complexes. Recently XMCD has attracted much attention, providing detailed information on the electron and magnetic structure of NPs, molecular materials, single-molecule magnets, and organometallic complexes. It is likely to become a significant tool in the inorganic and bioinorganic communities. The XMCD spectrum is obtained as the difference between the two XAS spectra with the circular polarization vector parallel and antiparallel to the external magnetic field [117]. Interpretation of the spectra provide quantitative information about the distribution of spin and orbital momentum in transition metal complexes (from sum rule analysis), determine spin orientations from the sign of the XMCD signal, infer spin states from magnetization curves, and separate magnetic and nonmagnetic components in heterogeneous samples. Figure 7.9 shows Fe and Ni $L_{3,2}$-edge XAS with the corresponding XMCD signal ($\mu^+ - \mu^-$) for Si/SiO_2/IrMn/FeNi/Pt films with 20 and 30 nm IrMn [118]. The Mn $L_{3,2}$-edge XAS with the corresponding XMCD signal for a 30 nm IrMn sample is shown in the inset of Fig. 7.9a. Figure 7.9c shows the value of spin moments (m_{spin}) and orbital moments (m_{orb}) of Fe and Ni as functions of IrMn thickness calculated from the XMCD sum rule [119]. The error was estimated to be 0.04 μ_B and 0.03 μ_B for the spin moment of Fe and Ni and 0.006 μ_B for the orbital moment, from sum rule–based analyses. The spin moments for films are much lower than that of the bulk for Fe and Ni. The spin moment of Ni shows little variation (by 0.01 μ_B), and when the thickness of the AFM film increases from 20 to 30 nm, the spin moment of Fe increases significantly (by 0.18 μ_B). The simultaneous changes in EB and magnetic moment indicate that the spin moment change is induced by EB. This shows that there is strong exchange coupling between Fe and the AFM layer around the interface, while it is weaker between Ni and the AFM layer.

XMCD provides a unique probe for the valency determination of the constituents in ternary oxides, the depth and field profiling of magnetic constituents, magnetic origin determination in dilute magnetic semiconductors, and the study of electron correlation effects in the electronic structure. XMCD used for magnetic imaging

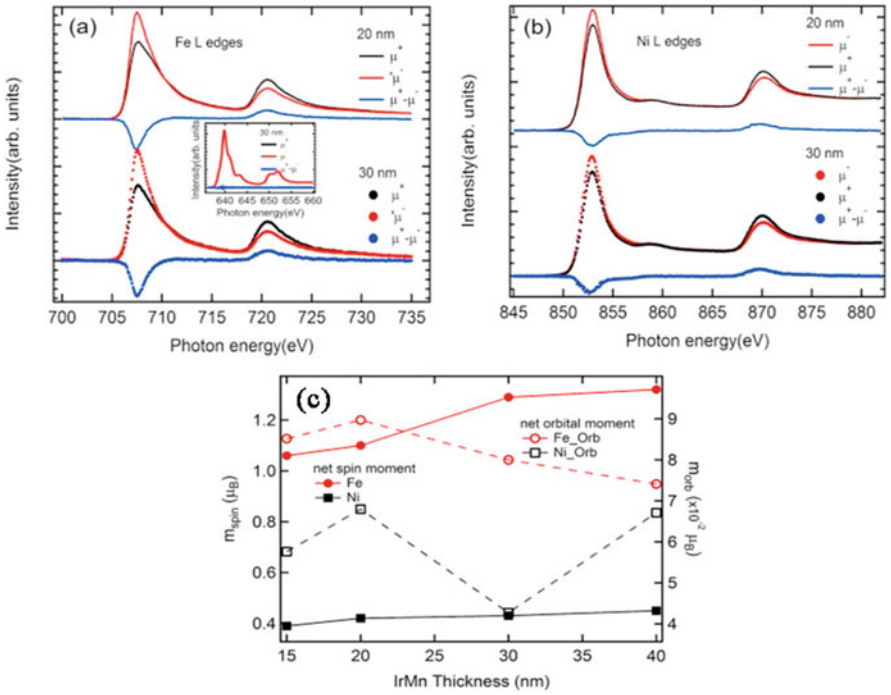

Fig. 7.9 (**a**) Fe $L_{3,2}$ edge. (**b**) Ni $L_{3,2}$-edge XAS for 20 nm (*line*) and 30 nm (*dot*) IrMn samples. The inset in (**a**) shows Mn $L_{3,2}$-edge XAS with corresponding XMCD signal for 30 nm IrMn sample and (**c**) the spin moment and orbital moment of Fe and Ni calculated from XMCD results. Reproduced with permission from [118]

offers surface sensitivity, time domain resolution, and elemental specificity, together with the capability for studying buried layers [120, 121].

7.2.7 Ferromagnetic Resonance

In FMR samples mounted in a microwave cavity are subjected to a high-frequency (GHz) magnetic field while a DC field is swept through resonance. From the resonance positions and line shapes it is possible to extract the EB and anisotropies. Under certain conditions, spin wave resonances (SWRs) are observed in AFM-FM bilayers, and from the position of the SWR the FM stiffness, A_{FM}, is obtained [88]. Most FMR measurements imply that the magnetization of the FM layer is not homogeneous throughout the thickness of the layer, that is, although the spins on the top of the FM layer are aligned with the field, the spins close to the interface may have other orientations. FMR spectra give evidence of two resonance modes attributed to the two asymmetrical non-interacting NiFe layers.

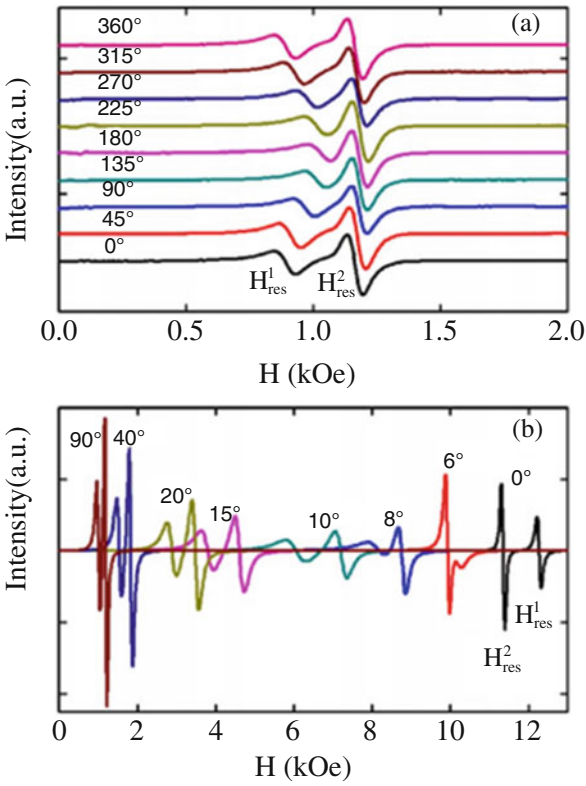

Fig. 7.10 In-plane (**a**) and out-of-plane (**b**) FMR spectra of NiFe/FeMn/NiFe trilayers. The inset numbers refer to the orientations of the applied magnetic field ϕ_H in (**a**) and θ_H in (**b**). Reproduced with permission from [122]

In conclusion, the perpendicular FMR spectrum of each NiFe/FeMn/NiFe trilayer shows two resonance modes due to two non-interacting asymmetrical magnetic layers with distinct effective magnetizations and absorption fields [122]. Both two resonance fields H_{res} vary with the azimuthal angle of the applied field, H, for in-plane FMR spectra (Fig. 7.10a). Around $H = 180°$ and in the low-magnetic-field region, a small step is observed. The two resonance peaks H^1_{res} and H^2_{res} denoting low absorption intensity (wider line width) and high absorption intensity (narrow line width), respectively, are attributed to the two NiFe layers and $H^1_{res} < H^2_{res}$ at all H. For the out-of-plane FMR spectra (Fig. 7.10b), the two resonance fields leans to low magnetic fields with increasing angle between the normal direction of the film plane and the applied magnetic field (θ_H).

7.2.8 Optical Measurement

The spontaneous emission of light from a material under optical excitation is called photoluminescence (PL). This is another powerful technique to evaluate

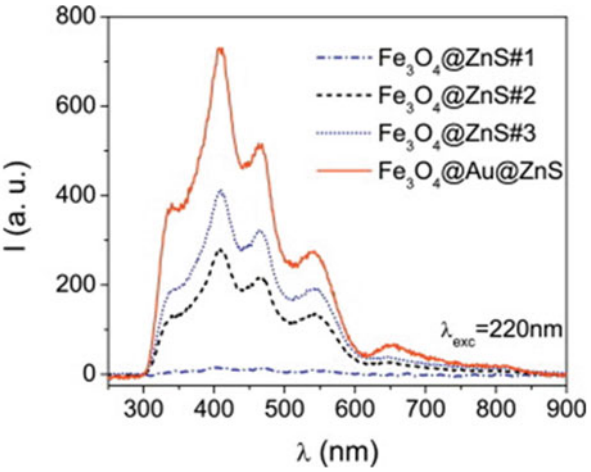

Fig. 7.11 Recorded PL spectra of core-shell samples with excitation at wavelength of 220 nm (E_1 transition). Reproduced with permission from [125]

the optical/electronic properties of multifunctional nanomaterials. PL investigations can be used to characterize a variety of material parameters, including quality of surfaces and interface in different type of nanosystems [11, 74, 123, 124]. PL spectroscopy is a selective and very sensitive probe of discrete electronic states to identify surface, interface, and impurity levels and even gauge alloy disorder and interface roughness. Under pulsed excitation, the transient PL intensity yields the lifetime of non-equilibrium interface and bulk states. The electric field at the surface of NPs can be mapped under the variation in the PL intensity. In addition, thermally activated processes cause changes in PL intensity with temperature. The fundamental limitation of PL analysis is its reliance on radiative events. Materials with poor radiative efficiency, such as low-quality indirect band gap semiconductors, are difficult to study via ordinary PL. Although PL is a very sensitive probe of radiative levels, one must rely on secondary evidence to study states that couple weakly with light [124]. Figure 7.11 represents the PL spectra of the core-shell of Fe_3O_4@ZnS and Fe_3O_4@Au@ZnS nanomaterials [125]. Upon excitation by UV light, these core-shell NPs show visible violet to blue luminescence with variable intensity. The band gap shifts toward the blue region owing to the Au layer. The improvement in the intensity might be due to interaction with resonance plasmonic modes at the surface of the Au shell over the Fe_3O_4 core particle.

7.3 Nanoparticle Systems

Magnetic properties for different nanoscale applications have been a major challenge for two decades, and the issue is whether they should be used in ferrofluids, recording media, recording taps, or biomedicine and catalysis [126–130]. Additionally, assemblies of nanoscale magnetic granular NPs are used to design permanent

magnets, nanocrystalline soft materials, and hard disk recording media [130]. When the dimension of materials drops to 100 nm and less, then new characteristics and phenomena are observed, such as exchange-coupled dynamics, giant magnetoresistance (GMR), enhanced magnetic moments, and quantized spin waves [131–137]. These characteristics enable applications in data storage devices, magnetic refrigeration systems, permanent magnets, contrast agents for MRI, catalysis, and targeted drug delivery [101, 138–152]. The exploitation of these unique features showing the multifunctionality of magnetic nanostructures start with the material synthesis and fabrication [90]. We will discuss the different heterostructured materials like dumbbell and core-shell etc. in which EB is also observed very easily. We will focus on their chemical synthesis and the effects of chemical treatment. Like bi-/trilayer thin films, heterostructured NPs are ideal structures for the study of interface effects such as magnetic proximity effects and EB effects. Better control of the quality of the interface between FM-AFM systems, along with the thickness of the material components and easy applications in connection with various technological aspects, are the reasons to explore heterostructure EB. There are various important examples of heterostructured nanomaterials in combinations of magnetic–magnetic, magnetic–noble metals, and noble metals–magnetic NPs.

Heterogeneous NPs are two or more different functional units in close conjugation due to their unique optoelectronic, magnetic, and catalytic properties [41, 153, 154]. The nanoscale heterojunction between metals and metal oxides is responsible for modifications in properties compared to bulk materials, and many factors, for example, surface reconstruction, lattice mismatch, and electron interaction, participate in this process. Nevertheless, tailoring material properties via heterogeneous conjugation largely relies on the epitaxial linkage between the two different types of materials [154].

7.3.1 Synthesis

Various synthesis procedures are used for magnetic NPs. Chemical- or solvent-based bottom-up synthesis provides flexibility to synthesize complex magnetic systems of materials; in addition, it represents the most cost-effective method and allows for large-scale production. Solvent-based synthesis resolves various challenges in NP synthesis including monodispersity of size and shape control, structure and crystallinity of materials, and stability in the atmosphere over time [150]. In the chemical method, the particle size can be well controlled in a range from a few nanometers to micrometers. In chemical synthesis, a short burst of nucleation followed by slow controlled growth is critical to producing monodisperse particles [150].

7.3.1.1 Core-Shell Nanoparticles

Multicomponent nanostructures are best exemplified by core-shell NPs, which were originally used in semiconductor devices leading to charge carrier confinement probability depending on the band alignment of two semiconductors with different gap energies. Core-shell magnetic NPs have attracted particular attention because of their physical and chemical properties, which are strongly dependent on the structure of the core, shell, and interface. It is now well known that the values of magnetic anisotropies in small particles exceed the corresponding bulk magnetocrystalline ones by orders of magnitude. Another interest in magnetic core-shell NPs arises because of the possibility to tune the surface strain anisotropy on the magnetic core through core-shell interface microstructure manipulation [150]. We can divide magnetic core-shell NPs into three groups: magnetic core with nonmagnetic shell, ferromagnetic core with FM shell, and FM core with AFM shell. Converse arrangements are equally valid. To date, various reports have been published, and research interest continues on nonmagnetic and magnetic core-shell structures, their stabilization, and surface effects after functionalization [150]. The EB effect is possible if an AFM shell is coated over an FM core. This interfacial effect, due to undercompensated spins, can result in unidirectional anisotropy. It can be easily seen owing to the shifting of the M-H curve, which presents its dependency on cooling field (H_{FC}) directionality. In the AFM/FM core-shell structure, the Curie temperature (T_c) of the FM must be higher than the Neél temperature (T_N) and the system must be cooled from a starting temperature between the two in the presence of an applied field, H_{FC}. It has been shown that the EB in core-shell magnetic particles provides a path for improvements in the thermal stability of a core [84]. EB has been observed in NPs for a variety of materials and morphologies, which can be divided into three categories: (1) single-phase FM or AFM oxides, (2) NPs deposited in AFM matrices, and (3) NPs with a core-shell structure. It has also been shown that EB-like hysteresis shifts can be observed in FM NPs, in which the surface behaves like a SG, which is formed owing to finite-size and surface effects [25]. EB in core-shell NPs has been found in many types of systems, for example, in Co/CoO, NiCo/NiCoO, Co/MnO, $Co_{80}Ni_{20}$/oxide, and CoPt/CoO [150].

Examples of the chemistry of core-shell MNPs are explained as follows. Bimagnetic core-shell FePt@Fe_3O_4 NPs were synthesized by the reductive decomposition of Fe $(acac)_3$ in the presence of monodisperse FePt NPs. Other core-shell NPs with a variety of material combinations (magnetic and noble metal) have also been synthesized using similar approaches. The core-shell Fe_3O_4@Au is a multifunctional nanomaterial. The magnetic functionality is provided by the core Fe_3O_4, and an Au shell provides a compatibility for biomolecule functionalization, which facilitates optical imaging plasmonically. The synthesis procedure can be seen in Ref. [59], which utilizes oleylamine as reducing agent and $HAuCl_4$ as precursor for Au NPs. Finally, this core-shell structure is made water soluble by treatment with CTAB and sodium citrate. The thickness of the shell can be manipulated. Further, Fe_3O_4@Au can be used as precursor for the synthesis of Fe_3O_4@Au@Ag. By the sequential

growth of CoS_2 porous nanoshells on FePt, core-shell NPs of FePt@COS_2 were also synthesized.

Furthermore, core-shell MNPs showing multifunctionality are illustrated by the following examples. The synthesis of bifunctional core-shell Fe_3O_4@Au colloidal nanoparticles (CNPs) was carried out by linking through chemical bonds to two NPs prepared separately by Bao [155]. The iron oxide particles they used in this study were much larger (>20 nm). Furthermore, Fe_3O_4@Au CNPs can be easily modified with other functional molecules to realize various bioapplications, but the colloidal stability issue prohibits this [156]. Considering the size reduction and, hence, improved property (magnetization and EB), Caruntu et al. reported a two-step synthesis procedure by attaching Au NPs (2–3 nm) onto the surface of Fe_3O_4 core NPs (10 nm) [157]. The synthesis procedure of Fe_3O_4 NPs combines a stable colloidal methanolic solution and a coating with amino-terminated silane to cover the particles with positive charges. A negatively charged solution of Au NPs was used as the shell for Fe_3O_4. These CNPs show that there is no quantified effect of Au NPs over the magnetic properties of Fe_3O_4, and they were highly stable against separation. Another "two-step" synthesis method was proposed for Fe_3O_4@Au NPs that uses high-temperature synthesis [47, 158]. The thermal decomposition method was used to synthesize Fe_3O_4 NPs (3.2 nm) Fe $(acac)_3$ precursor in the presence of oleic acid and oleylamine at a high temperature. The same protocol was used to cover Fe_3O_4 with a gold layer using gold (III) acetate and a coating of oleic acid to allow the formation of Fe_3O_4@Au CNPs. The 1:1 mixture of carboxy-terminal ligand and glucose terminal ligand leads these NPs to exchange ligand ions and make them soluble in water. Seed-mediated growth methods are also used to prepare core-shell Fe_3O_4@Au CNPs. The procedure includes Ag- or Au-decorated Fe_3O_4 nanohybrids as seeds. The seeds are coated by dropping them in the gold growth solution [159, 160]. The role of Ag ions is to manipulate the crystal growth direction, and they can form star-shaped core-shell Fe_3O_4@Au NPs.

Beyond the a forementioned approach to synthesizing Fe_3O_4@Au CNPs, a polymer-mediated self-assembly approach can also be used to generate Fe_3O_4@Au CNPs with good water dispersibility, colloidal stability, and biocompatibility. Zhang et al. prepared Fe_3O_4/polypyrrole (PPy)/Au core-shell NPs by coating PPy onto the preformed Fe_3O_4 NPs through the chemical oxidative polymerization of pyrrole and subsequent assembly of plentiful Au NPs on the surface of Fe_3O_4/PPy [161]. Cai et al. developed a convenient approach to assembling dendrimer trapped Au NPs (Au DENPs) onto Fe_3O_4 core NPs through a layer-by-layer (LbL) self-assembly technique and dendrimer chemistry [162]. In this work, a controlled coprecipitation synthesis was used for positively charged Fe_3O_4 NPs. Further, multilayering PGA/PLL/PGA using electrostatic LbL assembly of poly(γ-glutamic acid) (PGA) and poly(L-lysine) (PLL) was performed over Fe_3O_4 NPs and then this material was covered by Au DENPs formed using amine-terminated generation 5 (G5) poly (amidoamine) dendrimers.

The polymer-mediated assembly synthesis to prepare core-shell Fe_3O_4@Au CNPs contains multiple steps. A so-called one-pot hydrothermal synthesis for Fe_3O_4@Au CNPs with good water dispersibility and colloidal stability involves polyethylenimine (PEI) partially modified with poly(ethylene glycol) monomethyl

ether (mPEGPEI.NH_2) along with Fe (II) salt in a basic aqueous solution and autoclaved at elevated temperature and pressure [156]. This process leads to the formation of Fe_3O_4/Au CNPs with abundant PEI surface amines [7]. After further acetylation of the PEI amines, the final Fe_3O_4/Au CNPs are formed. The mPEG modification and the final acetylation are intended to improve the biocompatibility of these CNPs for biomedical imaging applications [156]. Recently, Sharma et al. [47] demonstrated the successful thermal decomposition synthesis of core-shell Au@Fe_3O_4 NPs and the effect of oxidation temperature on shape anisotropy, phase purity, and the growth of core-shell heterostructures and, consequently, their effect on structure–property relationships.

Core-shell $Fe_{1-x}O@Fe_{3-\delta}O_4$ nanocubes, with an average edge length of 17 ± 2 nm, were synthesized by the decomposition of iron pentacarbonyl $Fe(CO)_5$ in a mixture of 1-octadecene, oleic acid, and sodium oleate [163]. These nanocubes were transferred into water by exchanging their original surfactants with gallic acid, a derivative of the α-ω-diaminopropyl-poly(ethylene glycol) polymer. It was illustrated that without losing their functional molecular binding activity, these biotin-functionalized core-shell nanocubes showed a small phase transformation through self-oxidation. The core-shell Co@CoO were synthesized by preparing Co NPs through thermal decomposition of $Co_2(CO)_8$ using oleic acid and trioctylphosphine oxide surfactants, and these were oxidized by heating in different temperatures to form a core-shell [164]. The thermolysis of manganese (II) acetylacetonate was used to prepare $MnO_x@MnO_y$. It synthesizes the MnO, which after passing air (oxidizing) results in (FiM)Mn_3O_4 shell [79]. Further, core-shell $FeO_x@MnO_x$ particles were synthesized using iron oxide NPs as seeds for the shell growth of manganese oxide. These iron oxide seeds can be synthesized by thermolysis of the iron (III) oleate, which results in soft (FiM)Fe_3O_4 NPs. Again, the thermolysis of manganese (II) acetylacetonate using Fe_3O_4 NPs as seed results in a hard FM layer of Mn_3O_4 [79]. Core-shell NPs of $Co_{0.3}Fe_{0.7}O@Co_{0.6}Fe_{2.4}O_4$ AFM)-(FI) (diameter 6–18 nm) were prepared by a thermal decomposition process. They were originated by topotaxialoxidation of the core region and form a highly monodisperse single inverted AFM@FiM core-shell system with a variable AFM-core diameter and constant FiM-shell thickness (approximately 2 nm) [78]. The synthesis of $Fe_3O_4@CoFe_2O_4$ core-shell NPs without oleic acid was done in diethylene glycol (DEG) NPs synthesized by the method described earlier without oleic acid adding procedure [165]. Core-shell Fe_3O_4@ZnS NPs were prepared by a seed-mediated growth method by depositing a ZnS semiconductor over the surface of the Fe_3O_4 NPs through chemical precipitation of zinc acetate ($Zn(OAc)_2$) and thioacetamide (TAA) by sequentially adding precursors [125]. Further, like the previous method, Au was used a transition shell between Fe_3O_4 and ZnS to form a core-shell structure of Fe_3O_4@Au@ZnS NPs [125].

7.3.1.2 Dumbbell Nanoparticles

A dumbbell-like NP consists of a strongly interacting heterostructure with two particles separated at the ends [81, 154]. These two different functional NPs look like a dumbbell structure and are in intimate contact with each [81]. Dumbbell NPs are a little difficult to synthesize, although they are obtained by the sequential growth of a second component on pre-synthesized NP seeds [82, 166]. This is similar to the synthesis of core-shell NPs. But the major difference between them is that the nucleation and growth are anisotropically centered on only one specific crystal plane around the seed NPs. Hence, in general, the improved synthesis of dumbbell NPs is achieved by biased heterogeneous nucleation. The few major factors that control this synthesis are tuning of the seed-to-precursor ratio, heating profile control, and heterogeneous reaction. During growth, both lattice matching and mismatching are feasible for the fabrication of dumbbell NPs. For epitaxial nucleation of the second component, lattice spacing of the two components is generally well matched to lower the energy required. Lattice mismatch may also be used as a tool for synthesis of dumbbell NPs. In general, the surface dewetting process of the core-shell structure is used. Again, to control the morphology, electron transfer at the interface of two components in the nucleation process is important and can be affected by the properties of the solvent [14, 57, 61, 62, 74, 166, 167].

The most extensively studied dumbbell structure is that of Au–Fe_3O_4 NPs. The thermal decomposition method was used to break-down iron pentacarbonyl, $Fe(CO)_5$, over the surface of the presynthesized seeds of Au NPs [73, 168]. It is then oxidized in air. There are two ways to control the size of Au NPs: mapping the ratio of $HAuCl_4$ to oleylamine or controlling the injection temperature for $HAuCl_4$. Again, the Fe_3O_4 size is manipulated by adjusting the $Fe(CO)_5$/Au ratio. This gives rise to the dumbbell-like structure. Similarly, dumbbell NPs of Pt-Fe_3O_4 can be produced by controlled nucleation and growth of Fe on Pt NPs, followed by oxidation in air [81, 166]. FePt–Au NPs were prepared by the growth of Au over FePt NPs.

Other dumbbell NPs composed of various combinations of metals (Au, Ag, Pt, or Ni) and oxides (Fe_3O_4 or MnO) were synthesized from the thermal decomposition of mixtures of metal-oleate and metal-oleylamine complexes [9, 14, 64, 81, 154, 166, 167]. In this case, noble-metal NP seeds were formed first using oleylamine as a reductant. Then MnO or Fe_3O_4 components grew on the noble-metal NP seeds by a seed-mediated growth process at 300 °C through the thermal decomposition of the relevant oleate complex, resulting in heterostructured metal oxide NPs. The sequential growth of CdX (X = S or Se) onto FePt NPs at a lower reaction temperature results in the formation of FePt@CdX core-shell NPs [64, 65]. However, owing to the dewetting of CdX from the FePt surface at a higher reaction temperature, the core-shell FePt/CdX NPs can be converted to FePt-CdX dumbbell NPs [64]. This synthesis has been extended to γ-Fe_2O_3–MS (M = Zn, Cd, Hg) NPs. Note that Fe_3O_4–CdSe NPs show an emission wavelength peak at 610 nm, with a quantum yield of approximately 38%. The resulting fluorescent MNPs have two attractive features, superparamagnetism and fluorescence, which allow them to be controlled using magnetic force and to be imaged using a fluorescence microscope.

Ag–Fe_3O_4 nanodumbbells were made with a micellar structure by ultrasonication of a heterogeneous solution of as-prepared Fe_3O_4 NPs in an organic solution and $AgNO_3$ in water. The sonication provides the energy required to form a microemulsion, which is stabilized by the NPs that self-assemble at the liquid–liquid interface. Fe (II) in the NPs acts as a catalytic center for the reduction of Ag^+ to Ag NPs. The partial exposure of the NPs to the aqueous phase and the self-catalyzed reduction of Ag^+ and nucleation of Ag have been proposed as two factors that lead to a heterodimer morphology. The synthesis can be readily extended to make Ag–FePt NPs as well. Using combinations of the chemistry described earlier, more exotic dumbbell NPs that contain a noble metal, MNPs, and QD scan be made. For example, PbS–Au–Fe_3O_4 NPs were obtained by mixing Au–Fe_3O_4 NPs with a Pb–oleate complex and elemental S. The competition between the adsorption of S onto the Au surface and reaction with the Pb–oleate to form PbS NPs led to the heterogeneous nucleation of PbS on the Au surface.

Krylova et al. [166] proposed a general nucleation and growth model to explain the mechanism of the formation of $CoPt_3$-Au, FePt-Au, and Pt-Au nanodumbbells. It was found that a nucleation event occurs as a result of the reduction of Au^+ ions by partially oxidized surface Pt atoms. In cases where Au^{3+} is used as a gold precursor, the surface of seeds should be terminated by ions (e.g., Co^{2+}, Pb^{2+}) that can reduce Au^{3+} to Au^+ ions, which can further participate in the nucleation of the gold domain. Further growth of the gold domain is a result of the reduction of both Au^{3+} and Au^+ by hexamethylenediamine (HAD) at the surface of gold nuclei.

Factors affecting dumbbell NPs: Various factors affect the structure and properties of metal-magnetic nanodumbbells. The effects of, for example, size, morphology, temperature, time of reactions, polarity of solvent used in reactions, ratio of precursors, and concentration of surfactants are the major factors affecting the characteristics of dumbbell structures.

Nanomaterials have a higher specific surface area and, hence, are more likely to be in contact with reacting agents [57, 81]. This enhances optical activity characteristics and helps in synthesis to be used as seed [154]. Zhang et al. [81] studied these factors in detail. The temperature and reaction time should be carefully controlled according to the properties of the reactants with appropriate component sizes and narrow size distribution. The morphology of dumbbell-like NPs can be influenced by the polarity of the reaction solvent, the ratio of the precursors correlating to the two components in the dumbbell-like structure, the lattice mismatch between the two materials of the dumbbell-like NPs, and the surfactant concentration used in synthesizing the dumbbell-like NPs. In addition to these factors, suitable precursors and reducing or oxidizing agents, the operating environment, and many other factors can affect the results of the synthesis of dumbbell-like NPs. It will be meaningful to discover other synthetic methods to obtain dumbbell-like NPs consisting of more element species and to study the applications of these uniquely structured catalysts for the catalytic combustion of more gases.

Until recently, the major focus of synthesis was multifunctional magnetic heterostructures and core-shell and dumbbell NPs. These are still open fields of

research. Magnetic thin films, in particular nanometer-scale structures, have been the subject of numerous studies by different groups. Magnetic phenomena, such as oscillating exchange coupling, GMR, and surface anisotropy, have been extensively investigated. In particular, the structure and morphology of magnetic (M = Fe, Co, Ni or permalloy)/nonmagnetic (NM = Cu, Pd, Ag, and Au noble metals) multilayers with disordered interfaces has attracted growing interest. A typical thin film deposition process includes the production of the appropriate atomic, molecular, or ionic species, the transport of these species to the substrate through a medium, and condensation on the substrate, either directly or via a chemical or electrochemical reaction, to form a solid deposit. A detailed description of the synthesis method or thin film growth methods is beyond the scope of this chapter. The two methods, physical and chemical, are used for the deposition process for thin oxide films. Physical deposition processes include vacuum evaporation, laser ablation, molecular beam epitaxy, and sputtering. Chemical deposition processes consist of gas phase deposition methods and solution techniques. The gas phase methods are chemical vapor deposition (CVD) and atomic layer epitaxy (ALE), while spray pyrolysis sol-gel, spin, and dip coating are other methods employing precursor solutions. Further, thin film growth modes in materials can be characterized in three modes: Volmer–Weber (VW) or island growth, Frank–van der Merwe (FV) or layer-by-layer growth, and Stranski–Krastanov (SK) or mixed type growth.

7.4 Applications in Magnetic Industry

Novel multifunctional NPs have attracted much attention because of their ability to carry diverse functionalities in various fields. Biocompatibility, biodistribution, and reproducibility are the main concerns in biomedical applications. More specifically, research into targeted drug delivery, therapeutic and pharmaceutical agents is at the forefront of nanomedicine, as scientists and engineers, along with physicians, strive to meet a long list of requirements from the laboratory to the pharmacy. The applications of EB effects include permanent magnets, magnetic recording media, and domain stabilizers in recording heads based on anisotropic magnetoresistance. Since the discovery of exchange-biased GMR spin valves, a variety of devices have been built and proposed, such as read heads, magnetic sensors, and magnetoresistive (MR) memories. Any structure with metal–magnetic interfaces display a GMR effect [169]. The basic GMR structure is shown in Fig. 7.12. It is beyond the scope of this chapter to cover all biomedical and magnetic applications; hence, we will focus mainly on the application of multifunctional nanostructures in magnetic sensors, magnetic read heads, magnetic storage devices, and catalysis.

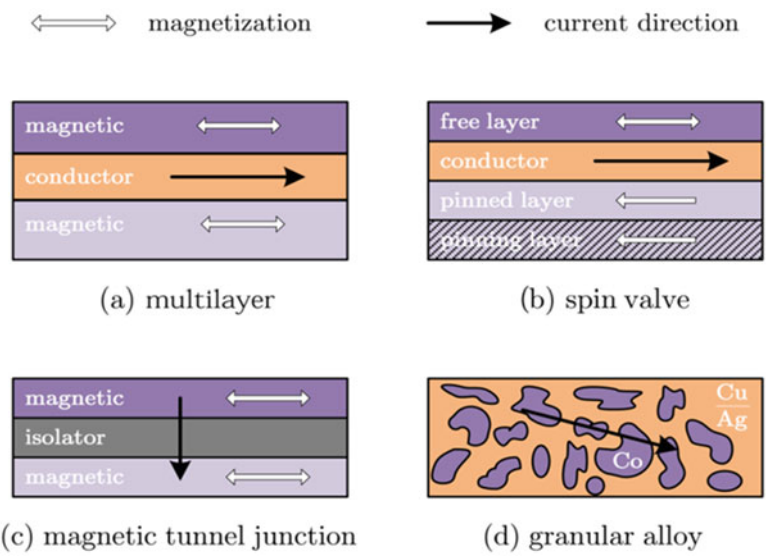

Fig. 7.12 Basic GMR structures in multilayer spin valve, magnetic tunnel junction, and granular nanostructures illustrating direction of magnetic field and electric current. Reproduced with permission from [169]

7.4.1 Magnetic Sensors

Magnetic sensing or imaging applications require an external applied magnetic bias field that decreases the possible spatial resolution and adds a noise source, thereby lowering the signal-to-noise ratio. Sensors without EB fail to detect low-frequency signals. Due to the limitation arising from an external magnetic bias field, an internal magnetic biasing of the magnetostrictive component within a magnetoelectric composite is in demand and offers many additional combinations of properties that make these systems more useful for applications in sensors. MR sensors are linear magnetic field transducers based either on the intrinsic magnetoresistance of the FM material [sensors based on the spontaneous resistance anisotropy in 3D ferromagnetic alloys, also called anisotropic magnetoresistance (AMR) sensors] or on FM/nonmagnetic heterostructures [GMR multilayers and spin valve and tunneling magnetoresistance (TMR) devices] [170]. The GMR effect, discovered by Fert and Grünberg, offers interesting new possibilities for sensor applications. GMR structures display sensitivities that exceed those of their counterpart AMR or Hall sensors. GMR is a quantum mechanical magnetoresistance effect where the relative orientation of the magnetization moments of the magnetic layers surrounding a thin nonmagnetic layer strongly affects the electric current flowing in such multilayers under the application of an external magnetic field. The reorientation of the magnetic moments alters both the electronic structure and the scattering of the conduction electrons in these systems, causing changes in the resistance [171]. Functional

GMR structures are usually composed of multilayer engineered structures based on nanometric to subnanometric thick magnetic layers separated by a nonmagnetic spacer. GMR spin valves are a particular configuration of a sandwich structure. In spin valves, an additional AFM (pinning) layer is added to the top or bottom part of the structure. Several kinds of structures can show a GMR effect, but for engineering applications, multilayer structures are preferred because of their integration feasibility. The fabrication of GMR devices can be carried out by means of traditional deposition (e.g., sputtering), CVD, UV lithography systems, and many other advanced synthesis techniques. The interfacial character of the EB effect gives rise to the reciprocal dependency of the EB on the thickness of the coupled FM layer [172].

An upper limit on FM layer thickness is set by the domain-wall width. Consequently, only a multilayer stack design is capable of exchange biasing many individual magnetostrictive layers having an accumulated thickness in the micrometer range. In self-biased composites the $Ta/Cu/Mn_{70}Ir_{30}/Fe_{50}Co_{50}$ or $Ta/Cu/Mn_{70}Ir_{30}/Fe_{70.2}Co_{7.8}Si_{12}B_{10}$ thickness of the FM layers and angle dependency of the EB field used to adjust the shift of the magnetostriction curve show high sensitivity to AC magnetic fields, with a maximum magnetoelectric coefficient of 96 Vcm^{-1} Oe^{-1} at mechanical resonance [172]. In the oil and gas industry nondestructive eddy current testing (ECT) technique of GMR sensors is widely used for continuous monitoring of growth defects in pipeline systems by increasing the measurement accuracy and scope of the inspections possible using ECT techniques. This technique offers many advantages over other nondestructive testing methods, such as its high sensitivity to small defects for tests that require fast scanning inspection, and it additionally requires no physical contact between the probe and the test subject. This technique is useful in diverse types of inspection, including surface and subsurface material defect inspections, thickness and coating measurements, electrical conductivity measurements for material classification, and conductive monitoring during material heat treatment [173]. Exchange coupling strength and blocking temperature, being the important parameters in MR sensors, can also be controlled by the insertion of a thin layer of controlled concentrations of nonmagnetic impurities between the AFM and FM layers. In top and bottom pinned systems comprising 5 nm thick $Co_{40}Fe_{40}B_{20}$ and 6.5 nm thick $Ir_{22}Mn_{78}$ films, controlled concentrations of Ru impurities at different concentrations in the $Ir_{22}Mn_{78}$ layer (AFM layer) produced blocking temperatures ranging from 220 to 100 °C and EB fields from 200 to 60 Oe [174].

A sensor geometry in which the current flows perpendicular to the plane of shields offers various advantages over current-in-plane (CIP) geometry, for example, it eliminates signal-shunting paths in nonactive layers and the magnetic shields can naturally be used as electrical leads for the sensor, which eliminates the need to electrically insulate the sensor from the shield with a gap insulator. Figure 7.13 shows a disk-view schematic of a typical thin film multilayer stack for a Current-perpendicular-to-plane (CPP) sensor [175]. An improved signal-to-noise ratio has been reported in current-perpendicular-to-plane giant-magnetoresistance sensors (CPP-GMR) using strong exchange-biased reference layers. Increases in the

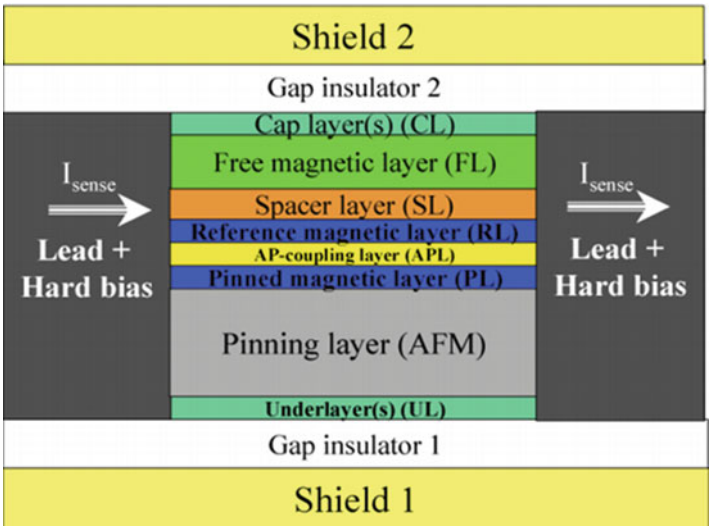

Fig. 7.13 Disk-view schematic of typical thin film multilayer stack for a CPP sensor. The current flows vertically between the shield regions. Reproduced with permission from [175]

pinning strength improves the spin transfer torque (STT) stability of the reference layer via increases in reference layer pinning fields and in the effective damping constant [176].

In automotive and industrial environments, magnetic sensors are often preferred because of their robustness, insensitivity to dirt, and contactless method of sensing. In automotive and industrial environments, the main basic applications of GMR sensors are position, angle, and rotation-speed sensing. GMR sensors are very suitable for analog angle sensing because of their intrinsic angle dependence [177]. Figure 7.14 shows the variation of the signal of the sensor according to the cosine of the angle of the external field with respect to the fixed layer. If the magnetization of the soft and hard layers are aligned parallel, resistance is minimum, and maximum if antiparallel [178]. Therefore, the principal objective is to produce sensors having enhanced MR effects, and various patents exist [179–181] on sensors based on spin valve, demonstrating GMR sensors and their usefulness.

7.4.2 Magnetic Read Heads

EB spin valves are used in the read head of the magnetic hard disk drives of personal computers for reading stored information. They are based on the GMR mechanism [171]. GMR multilayers offer more sensitive MR responses. The MR element is situated between the two magnetic soft shields that confine the length of the region along a track to which the MR element is sensitive to essentially the bit length.

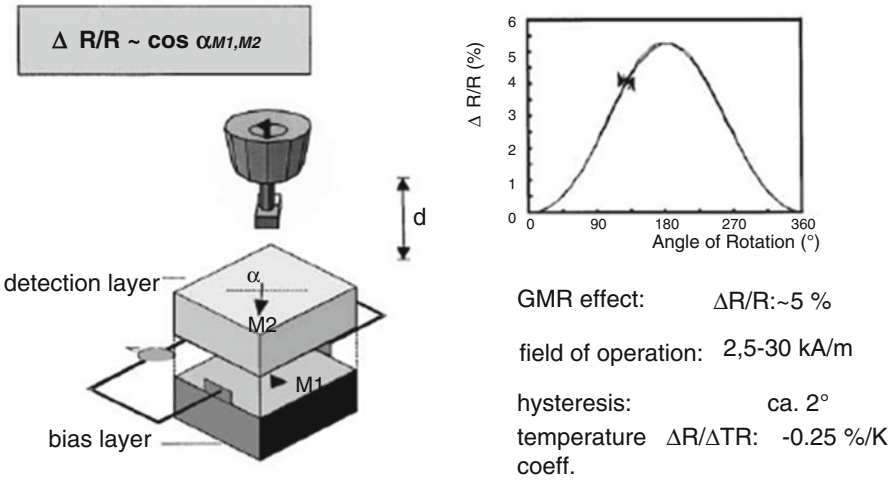

Fig. 7.14 Spin valve setup of GMR sensor for contactless position detection with typical sensor signal. Reproduced with permission from [178]

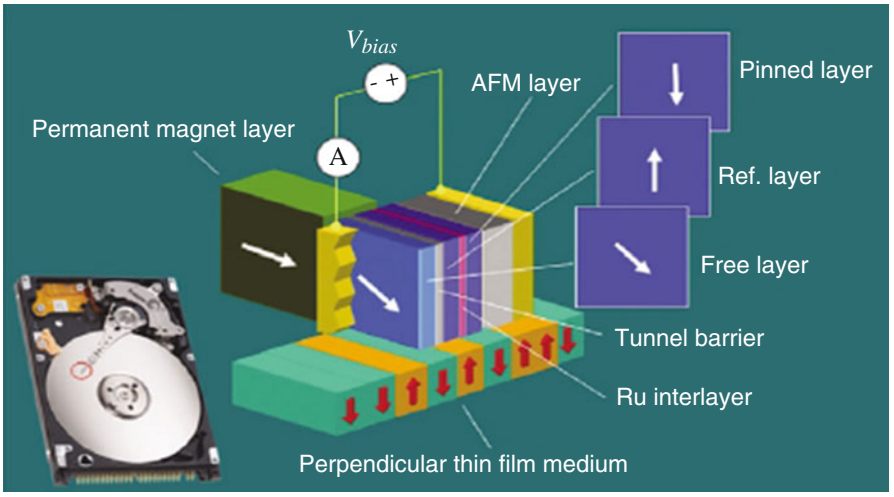

Fig. 7.15 Magnetic tunnel junction read head in a hard disk drive. Reproduced with permission from [183]

For this purpose the distance between the shields is approximately two times the bit length. In addition to MR material, the read heads contains two dielectric gap layers that electrically isolate the MR material from the metallic shields [182].

The detailed structure of a magnetic tunnel junction (MTJ) read head in a hard disk drive (HDD) [183] is illustrated in Fig. 7.15. One of the magnetic electrodes of the tunnel junction, referred to as the free layer, senses magnetic flux and its

magnetization rotates freely in response to the medium signal field. The other magnetic electrode is known as the reference layer and its magnetic moment is "fixed" through the interlayer magnetic coupling and functions as a reference to the free layer magnetization orientation. The purpose of the pinned layer is to compensate the stray field from the reference layer. Hence, the magnetic moment of the pinned layer is always opposite to that of the reference layer. This is achieved by introducing a strong antiparallel coupling between them by choosing a particular metallic interlayer of adequate thickness. A practical synthetic antiferromagnet (SAF) in use is CoFe (∼25 Å)/Ru(8 Å)/CoFe (∼25 Å). A pair of permanent magnets maintains the single-domain state of the free layer in the MTJ.

For a read head, the magnetization of the free layer needs to be sufficiently "free" in response to the signal flux from the recorded disk medium. This requires a sufficiently low magnetostriction coefficient. This can be obtained by making the free layer a composite free layer with a thin, high-spin polarization layer next to the barrier layer and a relatively thick layer of $Ni_{81}Fe_{19}$ alloy, which has zero magnetostriction coefficients. The two layers, by coupling ferromagnetically, act as a single magnetic entity. This composite free layer scheme has been successfully employed in read heads in commercial hard disk drive products with either AlO_x- or TiO_x-based MTJ [183].

The problem in manufacturing a magnetic read head is overcome by a liftoff technique, as claimed in Patent US 6842969 B [184]. The structure of magnetic read heads based on bottom spin valves is very difficult to manufacture. The inventors overcame this problem using a liftoff technique to form, on the free layer, a buffer layer having a trapezoidal cross section, sloping side walls, and a central area of uniform thickness whose width defines the read track. A suitable bias layer and leads are then deposited on this buffer layer. Patent US 6185078 B1 [185] demonstrates a spin valve read head with an AFM oxide film as longitudinal bias layer and a portion of the first read gap. The invention has a read head with an AFM stabilization scheme employed in a magnetic head to magnetically stabilize the free layer of the spin valve. This is accomplished utilizing an AFM oxide film below a spin valve sensor in a read region and first and second lead layers in end regions and an FM film in each of the lead layers that exchange couples with the AFM oxide film in the end regions. The FM films are pinned with their magnetic moments oriented parallel to an air-bearing surface (ABS) of the magnetic head. When the free layer is subjected to magnetic incursions from a rotating disk in a disk drive, the free layer maintains a stable magnetic condition so that resistance changes in the free layer are not altered by the differing magnetic conditions of the free layer.

Horizontal biasing plays an important role in all magnetoresistive heads (MRHs) in stabilizing the single domain against all reasonable perturbations such as external magnetic fields and thermal and mechanical stresses. The nondependency of the output voltage on scan velocity is the reason for the widespread applications of MRHs in digital tape and small-diameter hard disk drives. The simplicity of construction of vertical MRHs, compared with that of inductive heads, makes them the preferred transducer. Vertical heads that have or are simply called unshielded MRHs are used in many banks and credit card readers [186]. Advances in the

development of GMR spin valve materials and highly sensitive read heads have resulted in continuous increases in the areal density on hard disk drives. The synthetic FiM spin valve and specular spin valve enable an increased read-back output of the spin valve head. The specular spin valve enhance the GMR ratio because of the enhanced specular reflection at the oxide interface and an interesting oscillation of the interlayer coupling field and is an essential candidate for use as an advanced read head for magnetic recording beyond 100 Gbit/in^2 [187]. Advances in the development of media and read head materials have increased areal storage densities at an unprecedented rate. The exchange-biased spin valve, which is a multilayer GMR device, is the most promising candidate for read head applications.

7.4.3 Magnetic Storage Devices

In accordance with the current growth of information technology, the need for faster, smaller, higher-density, reliable memory storage and nonvolatile electronics is paramount. In memory storage applications, the storage material should be made up of particles that are stable and possess a switchable magnetic state that is able to represent the information stored in the form of bits, and these should not be readily affected by fluctuations in temperature. For memory storage applications the storage material should not demagnetize rapidly and have uniform magnetization abilities. To increase data storage density, the grain needs to be small but result in SPM behaviors. Overcoming the SPM limit is currently a prime concern for the hard disk industry, and many novel approaches are being considered. The magnetic exchange coupling induced at the interface between FM and AFM layers (EB effect) can provide an extra source of anisotropy leading to magnetization stability [188]. Recently, several concepts for next-generation devices for information processing and storage have been developed. Exchange-biased MTJ structures have been shown to have useful properties for forming magnetic memory storage elements. In TMR, the most important elements are nonvolatile tunnel junction random access memories (TJRAM) and read heads for very high-density magnetic storage. GMR-based exchange-biased MTJ holds the promise of improving the capabilities of existing charge-based memories by offering the combination of nonvolatility, speed, and density in a single technology resulting in novel device architecture. The basic MTJ contains one or two pinned (or reference) layers, an intervening tunnel barrier, and one or two free (or storage) layers. Typically, a pinned layer consists of an FM film deposited in intimate contact with an AFM film. These two films act to establish a stable magnetic orientation for magnetic fields up to several hundred oersted. A free layer consists of either a simple thin film of FM material (for Stoner–Wohlfarth switching) or a multilayer structure comprising magnetic and spacer layers (for toggle switching, also referred to as rotational switching). The tunnel barrier is formed by the oxidation of a thin metal film (usually an Al or Mg film), which is grown between the pinned and free layers [189]. Self-assembled FM FePt NP arrays are also promising as basic building blocks for constructing high-density

data storage media, indicating that the FM FePt NP assembly can indeed support magnetization reversal transitions [190].

Various systems have been successfully exploited in memory storage devices. In MTJs a structure such as a bottom FM electrode of the form 50ÅTa/250ÅAl/40Å$Ni_{60}Fe_{40}$/100Å$Mn_{54}Fe_{46}$/40ÅCo/7ÅRu/30ÅCo/, a tunnel barrier of the form 7Å Al, and a top electrode consisting of 75Å$Ni_{60}Fe_{40}$/250ÅAl/75ÅTa is used, and resistance can be varied over a very wide range, which makes it possible to impedance match such MTJ memory elements with the required semiconductor solid-state circuit devices, even for very dense memories of gigabit and greater sizes [191]. The size and aspect ratios of devices play an important role in determining the switching field. The nature of magnetization reversal in small, patterned magnetic devices is of particular importance for the successful operation of MRAM. Current MRAM prototypes rely on magnetic field pulses to switch between two stable states of the magnetic device [192].

The storage cells are MTJs, in which the storage layer is exchange biased and in a vortex configuration. A concept of multilevel thermally assisted magnetoresistive random-access memory (TA-MRAM) design based on exchange-biased vortex configurations was proposed and investigated by micromagnetic simulations [193]. The most practical one comprises an SAF reference layer in a single-domain configuration in which the thicknesses of the two antiferromagnetically coupled FM layers are adjusted to minimize the stray field on the storage layer. This type of cell should allow one to store at least 40 different states per cell, representing more than five bits per cell. Figure 7.16 shows the storage layer in a vortex configuration (3 nm thick) and a thinner reference (R) layer in the single-domain state. A vortex shift is observed in the storage layer due to the dipolar interaction with the reference layer (Fig. 7.16a). The vortex in the storage (S) layer is then centered in the initial state as a result of the reduced magnetostatic interaction with an SAF layer (Fig. 7.16b). The reference layer now consists of two antiferromagnetically coupled CoFe layers separated by a 0.9 nm Ru spacer providing an AFM RKKY exchange coupling assumed to be equal to 1 mJ/cm^2. The different CoFe layer thicknesses in the two layers constituting the SAF layer (1.2 nm for the layer closest to the storage layer and 1.8 nm for the other layer) make it possible to decrease the dipolar interaction with the storage layer while maintaining a net magnetization in the reference layer, which is necessary for magnetization rotation, under an external rotating magnetic field, during the readout process. The obtained TMG signals under a 10 mT rotating read field are shown in Fig. 7.16c.

The leakage field in TbFeCo/CoFe double-layer film was reported to be reduced to almost zero owing to the net magnetization of the rare earth–dominant TbFeCo layer being antiparallel to the FeCo sublattice magnetization, which is parallel to the magnetization of the CoFe layer owing to the strong exchange interaction of the TM metal in it [194]. In wafers comprising an Si substrate/Ta/PtMn/CoFe/Ru/CoFe/NiFe/IrMn (variable thickness)/Ru/Ta, a strong temperature dependence of the writing field is ensured by exchange coupling the storage layer of a tunnel junction with an AFM layer [195]. In nonvolatile memory devices using Au NPs and reduced graphene oxide (rGO) sheets fabricated in both

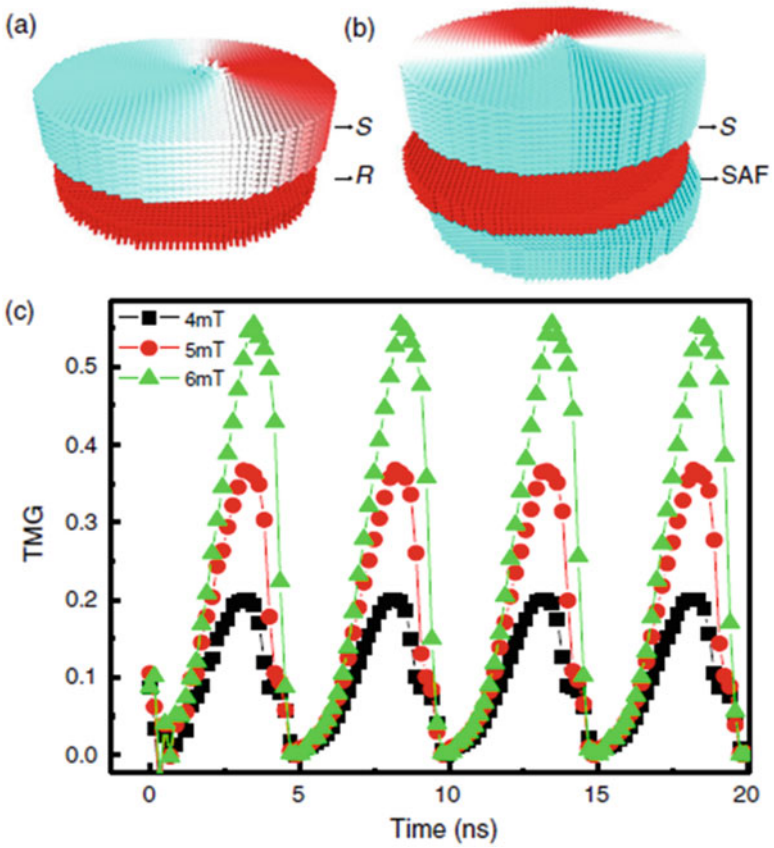

Fig. 7.16 (**a**) Remanent state when the reference layer consists of a single FM layer 1.2 nm thick. (**b**) Remanent state when the reference layer is part of a SAF layer. (**c**) Time evolution of TMG signal under rotating read field of 10 mT for three radial positions of storage-layer vortex core obtained by field cooling in 4, 5, and 6 mT. Reproduced with permission from [193]

horizontal and vertical structures, vertical AuNP-rGO memory devices showed a large current ON/OFF ratio and high stability, making them potentially applicable in nonvolatile memory electronics [196]. Hence, putting all the existing technologies together one may expect to build the next-generation data storage device.

7.4.4 Catalysis

Catalysis is one of the pioneer applications of NPs combining the advantageous characteristics of both homogeneous and heterogeneous catalysis while reducing their respective drawbacks. The variable and particle-specific catalytic activity of

NPs is due to their heterogeneity and their individual differences in size and shape. Nanocatalysis has high catalytic activity and selectivity, like homogeneous catalysis, recyclization (easily recovered), and separation of catalyst after the completion of a reaction, making it more like heterogeneous catalysis [197]. Various elements and materials, like aluminum, iron, titanium dioxide, clays, and silica, have been used as catalysts at the nanoscale for many years. The fine tuning of nanocatalysts, in terms of composition (bimetallic, core-shell type, or use of supports), shape, size, surface composition and electronic structure, and thermal and chemical stability of individual nanocomponents, has accomplished greater selectivity [198]. The field of catalysis has undergone explosive growth during the past decade, and efforts have been made to develop recoverable and reusable catalysts for economic and environmental reasons. MNPs with a core-shell structure have recently received increased attention in various catalytic processes and offer sustainable solutions to current energy problems. The shell consists of catalytically active species, and the magnetic core can act as an anchor to separate and recycle the catalyst. The strain and ligand effect between the core and surrounding shell can be exploited for tailoring the catalytic activity and selectivity of core-shell nanocatalysts. The most commonly used catalyst supports are iron oxide, often coated with a layer of robust shell, such as silica or a polymer shell, to protect the iron oxide core from unexpected corrosion and to facilitate catalyst coupling.

Shape- and size-controlled metal oxide nanocrystals and the confinement effects of nanospace and the structure along the interface between the phases can give rise to a unique set of properties that make nanocomposite materials a potential candidate for innovative multifunctional nanocatalyst design. The cubic shape of nanocrystals is best for assembling metal–metal oxide interfaces with a large contact area. Yamada et al. [199] fabricated a nanocrystal bilayer structure consisting of CeO_2–Pt–SiO_2 using a Langmuir–Blodgett method. Figure 7.17 shows the strategy they used to achieve the so-called tandem bilayer structure with nanocubes of metal and metal oxide. The capping agents of the nanocrystals were removed by ultraviolet/ozone treatment to form clean metal–metal oxide interfaces. After removal of the capping agent, the vertical clefts between the nanocrystals ensured access to both catalytic interfaces and provided a high surface area in the close-packed array.

Figure 7.18a shows time-dependent propanal formation from ethylene hydroformylation with in situ MeOH decomposition over the CeO_2–Pt–SiO_2 tandem catalyst at 190 °C. The CeO_2–Pt interface decomposed methanol into CO and H_2, which were used by the Pt–SiO_2 interface to hydroformylate ethylene. This represents a powerful approach for designing high-performance, multifunctional nanostructured catalysts for multiple-step chemical reactions, such as those proposed for artificial photosynthesis.

A large variety of catalysts, metal NPs, semiconductors, organic molecules, metal−organic complexes, and enzymes have been grafted onto magnetic NP supports for various organic reactions [200]. For instance, by coating precious metal catalysts (e.g., Au, Pt, or Pd) as a monolayer on the surfaces of non-precious-metal-based nanomaterials (e.g., Ni, Fe or Co), atom-economical and cost-effective

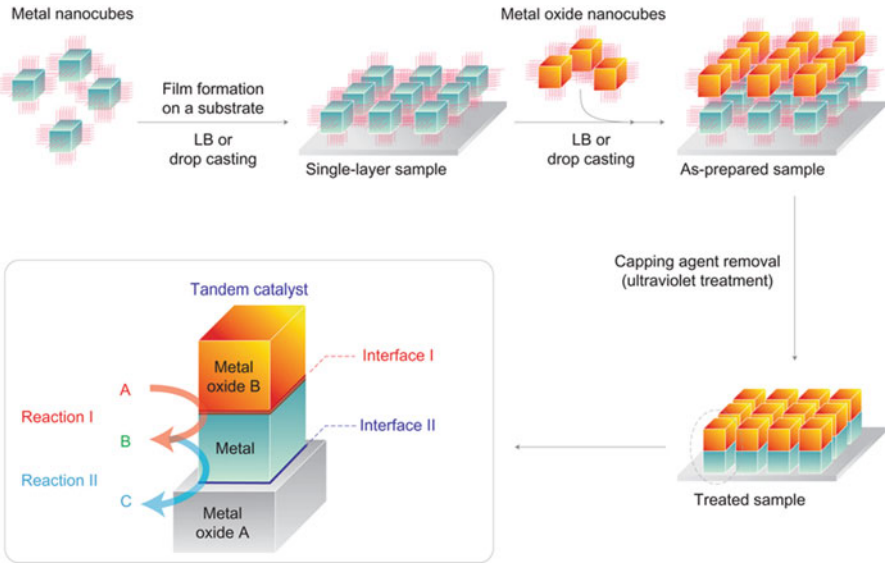

Fig. 7.17 Assembly process for preparation of nanocrystal bilayer tandem catalyst. Single layers of metal nanocubes and metal oxide cubes were deposited sequentially. Capping agents of NPs were removed by ultraviolet treatment. Reproduced with permission from [199]

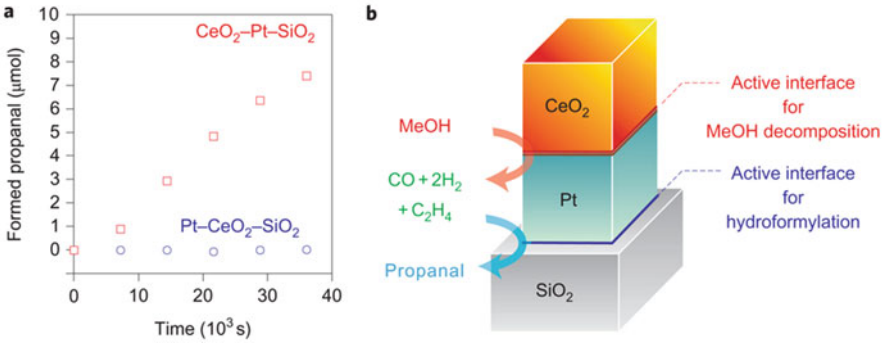

Fig. 7.18 Ethylene hydroformylation with MeOH over a tandem catalyst. (**a**) Propanal produced as a function of reaction time over CeO_2–Pt–SiO_2 and Pt–CeO_2–SiO_2 bilayers at 190 °C from ethylene and MeOH. *Open squares* CeO_2–Pt–SiO_2; *open circles* Pt–CeO_2-SiO_2. (**b**) Illustration of CeO_2–Pt–SiO_2 tandem catalyst. Reproduced with permission from [199]

core–shell with good catalytic efficiency can be produced [201]. Various multifunctional structures, such as Fe_3O_4-Au/pSiO_2 [202], Pd@IRMOF-3 [203], Fe_3O_4@SiO_2-M [204], Fe_3O_4@SiO_2@Dendritic-SiO_2 [205], Au-Fe_3O_4@MOF [206], and Pd-Fe_3O_4/Bpei [207], exhibit excellent catalytic activity and convenient recovery. In catalysis, ceria (CeO_2) and mixed-oxide-based formulations are indispensable as supports of transition-metal catalysts for ever growing numbers of

industrial processes. The major catalytic functions of CeO_2 are generally related to the high mobility of its lattice oxygen and the corresponding oxygen storage capacity, occurring via the reversible creation and healing of oxygen vacancies, accompanied by an easy switch between the Ce^{3+} and Ce^{4+} oxidation states [208]. Copper (Cu) and Cu-based NPs based on earth-abundant and inexpensive copper metal may be useful options in heterogeneous catalysis/nanocatalysis, benign sustainable protocols, and cost-effective methods may be useful in the near future [209]. Research in nanotechnology and nanoscience is expected to have a great impact on the development of new multifunctional catalysts with the ability to meet challenges related to energy use and sustainability.

7.5 Exchange Bias Model

In this section, we will discuss some theoretical aspects and models of EB relevant to nanostructures. Further, we will go through specifically developed EB models for core-shell nanostructures. In addition, we will discuss the effects of size/shape/structure of a system that can affect the main-stream EB theories. For thin film nanostructures, various reports were published following Coehroon's classification [27] considering macroscopic, mesoscopic, and microscopic lateral lengths [31].

Macroscopic models: In these models, only those nanostructures are taken into account that are not dependent on the lateral magnetic structure of layers. These models are usually applied in thin film nanostructures considering homogeneous layers in the x-y planes. Further, the spin of AFM materials in layered nanostructures have nonzero magnetization but are parallel to the interface plane. Even though some models in this category have net spin in the *z*-direction perpendicular to the x-y plane of the FM/AFM layers but undergo no change in spin structure in the x-y plane. The Meiklejohn and Bean model [210] is considered the simplest model and shows a coherent rotation of magnetization and parallel easy axes of FM/AFM nanostructures. The first and major modification and contribution in this model was proposed by Neél [31, 211], who coined the term *domain wall formation/partial domain wall formation* in either the FM or AFM layer parallel to the FM-AFM interface system, when the magnetic field is reversed, instead of having a sharp-edge magnetic interface. Further, various reports [212–217] and experimental results strengthened this argument and added the domain wall role to the originally proposed energy formulation. This introduction of a domain wall will suppress energy due to the configuration of magnetic equilibrium at the AFM/FM interface and lower the effective coupling value. Hence, depending on the foregoing considerations, in the strong interface coupling limit approach, the obtained loop shift changes accordingly,

$$H_{\mathrm{E}} \propto \sqrt{(K_{\mathrm{AFM}} A_{\mathrm{FM}} / M_{\mathrm{FM}} t_{\mathrm{FM}})}\,, \tag{7.1}$$

depending on whether the domain wall is formed on the AFM or FM side of the interface, where A_{AFM} and A_{FM} are the exchange stiffness of the AFM and FM layers, respectively. When substituting suitable values for the anisotropy and the exchange, the new value for H_{E} is usually much closer to experimentally observed loop shifts.

Mesoscopic model: This model explains the spin configuration difference in the x-y plane. Kouvel [31, 218] and Fulcomer and Charap [219] were the first in a series of developments in these models. The model presented by Kouvel [218] was for CuMn alloys (inhomogeneous) showing the formation of domains in an AFM system. It was further used for thin film systems. The effects of grain size distribution in EB were introduced by Fulcomer and Charap [219]. The different grains couple differently to ferromagnetically and small antiferromagnetic grains, showing the tendency toward SPM characteristics. Few models and theoretical approaches, including partial domain walls or perpendicular coupling in the AFM grains, have been incorporated into basic models. The model presented by Stiles and McMichael was best fitted for the wide ranging results in FM-AFM fine particle nanocomposites, and in this case there were different observed results due to various nanostructure contributions. The model given by Malozemoff [220–222] was inspired by the ideas of Irmy and Ma [223] and Meiklejohn and Bean [224]. It does not consider the ideal flat interface of AFM–FM layers. In the model, it was assumed that roughness or defects at the interface is the cause of a random field and leads to the breakup of the AFM layer into domains with domain walls perpendicular to the interface. The sizes are given by an approximate formula:

$$\pi (A_{\mathrm{AFM}} / K_{\mathrm{AFM}})^{1/2}. \tag{7.2}$$

Microscopic models: These include mainly three approaches: Monte Carlo (MC) simulations, micromagnetic calculations, and spin-lattice models. As an overview, these microscopic models consider the atomic spin configuration in detail spread over a volume in the *x*-, *y*-, and *z*-directions. In spin-lattice models, a different approach has been developed to find the minimum energy spin configurations. Most of the aforementioned approaches use the simplest uniaxial AFM approach (FeF_2). Koon assumed that minimum energy spin configuration for a compensated AFM and FM could couple the FM and AFM spins perpendicular to each other [215]. This is called *spin flop*. Thus, a new energy term, $J'(m_{\mathrm{AFM}} m_{\mathrm{FM}} \cos\theta)^2$, has been formulated, which is very significant. Schulthess and Butler explained simultaneously the loop shift and coercivity enhancement in FM-AFM bilayer systems by arguing perpendicular coupling with uncompensated spins at the interface [31]. MC simulations have been used by various groups [225–230] to investigate uncompensated spins at interfaces due to the coupling of FM-AFM layers with defects in the bulk of the AFM layer. Formation of domains was perpendicular to interface of AFM-FM in the bulk of AFM. Another interesting model was proposed

by Suess et al. [24, 231, 232]; it includes the concept of perpendicular coupling and randomly distributed and exchange-coupled grains. It contains an EB term as a function of the domain walls between AFM grains consisting of the energy in different orientations. Using the concept of coupling of two AFM sublattices in different ways, which can increase the EB, many experimental results containing FM/FeF_2 bilayer systems are explained [233].

Except for these fundamental works regarding macroscopic, microscopic, and mesoscopic theoretical calculations and models to achieve real interfaces, additional reports were made on the prediction of different features of the EB effect. Not all features and characteristics of EB in different systems are explained sufficiently by these theoretical models, for various reasons—distribution of size, length, and time. Recent advances in the development of theoretical models, especially for bilayer systems and core-shell nanomaterials, to tackle the challenges of the EB mechanism mainly depend on MC simulation using the Metropolis algorithm. We will discuss a theoretical approach to bilayer systems and focus on core-shell nanostructures.

There are simulations using an MC algorithm on the bilayers of an FM/AFM system with an uncompensated interface. These simulations considered the crystal structures of both FM and AFM layers either body centered cubic (BCC) or simple cubic (SC). Finally, the system was explained by the following Hamiltonian equation:

$$H = -J_{\mathrm{F}} \sum_{<R,r>\epsilon FM} S_R.S_r - K_{\mathrm{F}} \sum_{R\epsilon \mathrm{FM}} \left(S_R^z\right)^2 - \sum_{<R,r>\epsilon AFM} J_{\mathrm{AF}}\left(R-r\right) S_R.S_r$$
$$- K_{\mathrm{A}} \sum_{R\epsilon \mathrm{AFM}} \left(S_R^y\right)^2 - J_{\mathrm{eb}} \sum_{<R,r>\frac{\epsilon \mathrm{FM}}{\mathrm{AFM}}} S_R.S_r - h \sum_R S_R^y, \tag{7.3}$$

where S_R and S_r represent the classical Heisenberg spins located at the position vectors of the lattice, J_{F} and J_{AF} are exchange constants for the FM and AFM layers, respectively, K_{F} and K_{A} are anisotropy constants of the FM and AFM, respectively, J_{eb} is the coupling strength of the exchange coupling between the FM and AFM at the interface, and h is an external magnetic field along the y-axis. Using this equation, it was summarized that an EB field could be evaluated in two ways: (1) based on the stability of the first plane of the AFM near the FM/AFM interface and (b) by the intrinsic pinning of the domain walls parallel to the interface. This calculation depends on the ratio of AFM film anisotropy and its exchange interaction. Suess et al. [231] studied uncompensated and compensated interfaces using micromagnetic calculations and additional MC simulations. For the compensated interface in polycrystalline IrMn/NiFe bilayers, an MC simulation was carried out over a FC state. The predicted EB field was of the same order of the experimental result. In the latter case of an uncompensated state [24], it was concluded that the formation of domain walls between the exchange-coupled granular structures controlled the shift of the field cooling hysteresis loop and coercivity and explained the training effect. To create a more realistic model of the EB and coercivity of polycrystalline FM/AFM bilayers, Landau–Lifschitz–Gilbert

(LLG) equations were combined with MC simulation [232]. Thickness-dependent MC simulations of EB were well satisfied by experimental results [234]. The time evaluation analyses of FM moments using LLG equations for each degree of freedom were performed, and the origin of EB in a polycrystalline AFM/FM system was explained. An EB model in AFM/FM polycrystalline materials with uncompensated spins and granular interfaces were developed by simulating magnetization loops of an IrMn/Co bilayer system [234]. To explain the origin of EB and training effects in FM/AFM heterostructures using an MC dynamical method, a unified nonequilibrium theory was put forward by Kai-Cheng and Bang Gui [235]. Furthermore, various studies using MC simulations and experimental results were carried out to explain different nanostructures. Most of them are related to thin films and bilayers/trilayers.

7.5.1 Theoretical Model for Core-Shell Nanoparticles

Some theoretical models explain the EB phenomenon, especially in bilayer systems, by considering a few constraints and assumptions, various numerical methods, and MC simulations. However, most of them are not sufficient to explain the complete phenomenon in systems. Bilayer systems can be compared with core-shell types of nanostructures very easily because the characteristics of EB are very similar. Thus, the MC simulation method is most efficient and effective at explaining most EB features in core-shell NPs. Still today, there are few reports explaining EB in the core-shell nanostructure. To understand EB, one must have magnetic structures at the FM/AFM interface. The interface of core-shell nanostructures contains roughness and uncompensated spin, from which magnetization originates. The most general model is presented and explained by Iglesias et al. [236]. Recently, Lemos et al. [237] studied the properties of a finite system to model MNPs. It was formed by a reduced number of magnetic dipole moments due to the spin of atoms. The core-shell type NP, where the shell was formed by spins interacting through an AFM exchange coupling, while for spins belonging to the core the coupling was FM. The interaction between spins at the core-shell interface could be either FM or AFM.

The model developed by Iglesias et al. [236] contains most of the realistic assumptions that are necessary for EB observation. The core-shell structure in Fig. 7.19 (top left panel) considers atomic spins on the nodes of simple cubic structures. A complete particle is built by assuming spins inside a sphere of radius R ($R = \mathrm{na}, n = 1, 2, 3 \ldots$ and "a" is a unit cell dimension). There are three regions: (1) core of radius R, (2) shell thickness $\mathrm{R_s} = R - R_c$, and (3) core-shell interface formed by core-shell spins with nearest spins of the shell/core, i.e., FM core, AFM shell, and core-shell interface. Hence, anisotropy and exchange constants are taken into account to establish realistic EB properties. They considered $R = 12\mathrm{a}$ and $R_s = 3\mathrm{a}$. The MC simulation and theoretical study by Iglesias et al. [236] were based on a microscopic Hamiltonian equation explaining Heisenberg classical spins $\overrightarrow{S}$. This equation was used for the finite values of anisotropy in real core-shell structures:

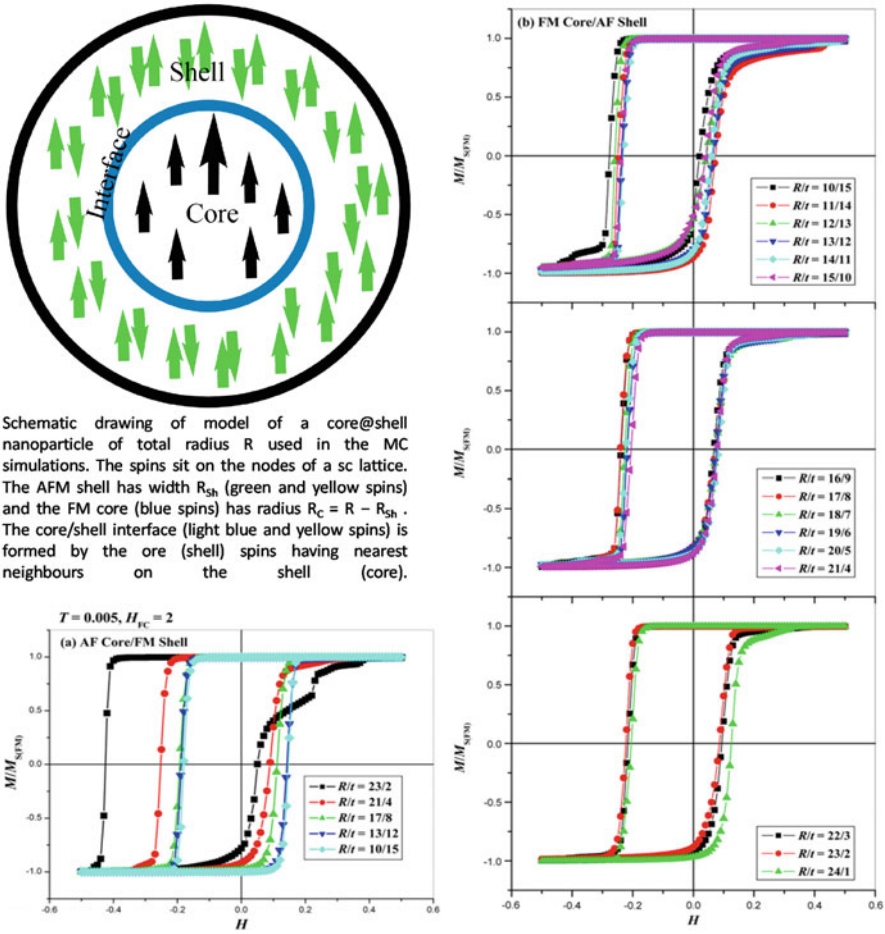

Fig. 7.19 Schematic diagram of core-shell model of NP (*top left panel*). FM hysteresis loops in NPs with opposite core-shell structures and representative core-shell relative dimensions at low temperature after field cooling, where M_s (FM) is a saturated value of FM magnetization. Reproduced with permission from [85]

$$
\begin{aligned}
H \Big/ k_{\mathrm{B}} = & -J_C \sum_{<i,j>\in C} \vec{S}_i . \vec{S}_j - J_C \sum_{<i,j>\in Sh} \vec{S}_i . \vec{S}_j - J_{\mathrm{Int}} \sum_{<i\in C, j\in \mathrm{Sh}>} \vec{S}_i . \vec{S}_j \\
& - k_{\mathrm{C}} \sum_{i\in C} \left(S_i^z\right)^2 - k_{\mathrm{Sh}} \sum_{i\in \mathrm{Sh}} \left(S_i^z\right)^2 - \sum_{i}^{N} \vec{h} . \vec{S}_i .
\end{aligned} \tag{7.4}
$$

Here, the first three terms explain the nearest-neighbor exchange interactions between spins with different exchange constants, available at the FM core surface, AFM shell surface, and core-shell (FM-AFM) interface. The fourth and fifth terms

show the on-site uniaxial anisotropy of the core and shell with anisotropy constants, K_C and K_{Sh}, respectively related to values in real units through the following relations:

$$k_c = \frac{K_C V}{N_C}, k_{Sh} = \frac{K_{Sh} S}{N_{Sh}}, \tag{7.5}$$

where V and S are the volume and surface of the particles respectively. The last term is due to the Zeeman energy coupling of the spin magnetic moment with an external magnetic field H, where $h = \mu H/k_B$ and μ is the magnetic moment of the spin. The $J_c(>0)$, $J_s(<0)$, and $J_{Int}(-J_c<J_{Int}<+J_c)$ are the exchange constants of FM core spins, AFM shell spins, and interface spins, respectively. K_C and K_{Sh} are the anisotropy constants in units of energy per unit volume (V) or surface (S) of the particle.

Using a complete Hamiltonian equation (Eq. (7.4)), MC simulation was performed in several steps. The FC states of the core-shell NPs were evaluated. Due to the roughness at the interface, the magnetic ordering and geometric structure of the interface for a core-shell (FM/AFM) nanomaterial are more complex compared to FM-AFM bilayers. This roughness constitutes interfacial spins, which may be surrounded by different neighbors depending on their position; hence, this results to some extent in a local compensated/uncompensated magnetic order at the shell interface. The simulation of FC hysteresis loops indicates that they can be associated with a small portion of uncompensated spins at the core-shell interface, which remains fixed during a field cycle procedure. The net magnetization of the interfacial shell spins and the magnitude of the EB field were analyzed quantitatively, and the interrelations between them were discussed. As there are various reversal mechanisms in both branches of the M-H loop of core-shell (FM-AFM) NPs, asymmetries arise in the hysteresis loop. A vertical shift in the core-shell (FM-AFM) was observed due to spin groups at the interface, aligned in the transverse direction of the magnetic field and difference in different reverse mechanisms. It is suggested that different important parameters, for example, particle size distribution, anisotropy direction randomness, presence of disordered surface spins, and the interparticle dipolar interaction of a particle assembly, should also be considered in theoretical calculations to match the theoretical calculations of the EB effect with those of the experiments.

To study the effect of the bimagnetic core-shell relative dimension on EB in FM/AFM NPs, Hu et al. [85] used a modified Metropolis MC simulation. The core-shell MNPs were modeled using an SC lattice of classical Heisenberg spins with unit vectors. Taking the lattice constant as 1 and a constant core radius of $R_0 = 25$, with shell thickness t, in the simulation, R increases while t decreases, and vice versa under an external magnetic field (H). The Hamiltonian is expressed as

$$H = -K \sum_i \left(S_i^z\right)^2 - J \sum_{<ij>} S_i S_j - H \sum_i S_i, \tag{7.6}$$

where $S_{i(j)}$ represents an atomic spin at site $i(j)$. The first term gives core-shell single-site anisotropy energies with an easy axis along the z-axis. The second term denotes the exchange energies between spins in the core, shell, and interfaces, commonly related to the Curie points of materials, and finally the third term contains the Zeeman energy and H is applied along the given z-axis.

The results explained by Hu et al. [85] are summarized. The EB field is inversely proportional to the FM shell thickness in AFM (core)/FM (shell) NPs, while in NPs with an opposite core-shell structure, the exchange bias behavior is complex and distinct in different ranges of the FM core radius. In other words, in AFM (core)/FM (shell) NPs, H_E is inversely proportional to t_{FM} owing to the large J_{IF} and the negligible K_{FM}, which cause an FM magnetization reversal by nucleation and domain wall propagation at the decreasing branch of the hysteresis loop while at the increasing branch by coherent rotation. For NPs with an FM (core)/AFM (shell) structure, H_E with R/t is divided into three kinds of behavior determined by different mechanisms. An oscillatory behavior is first observed for small values of R/t after the FM hysteresis loops are closed, probably due to the single-domain state in the FM core. With increasing R/t, a roughly linear relation between H_E and R_{FM} is found. However, H_E might deviate from this trend once the AFM shell loses its stability owing to the too-small thicknesses (Fig. 7.19a, b).

Lemos et al. [237] explain the properties of a finite magnetic system to model an MNP, which is formed by a reduced number of magnetic dipole moments owing to the spin of atoms. This model was studied in a lattice with square symmetry (Fig. 1 of [237]), using the MC method along with the Metropolis suggestions. The results show that the system deviates from an ordered state toward a disordered state at a definite temperature without an external magnetic field or exchange anisotropy. The EB phenomenon is observed in the influence of external magnetic fields. The expected shift/displacement of the M-H loops is due to the introduction of the exchange anisotropy term in the Hamiltonian equation. Also, this shift is dependent on the core and shell sizes, as well as on the magnitude of the coupling between the shell and core moments.

The Hamiltonian used in the model is explained as follows. A 2-D square lattice of spins of core-shell MNPs, which can continuously point in any direction in the x-y plane, is the base and consists of an XY model. The core-shell NPs in the XY model (Fig. 1 of [237]) have (1) a core (the exchange interaction between first neighbor spins is FM) and (2) a shell (contains the core created by spins whose exchange interaction between first neighbors is AFM). An exchange interaction between spins located in the last layer of the core with spins in the first layer of the shell gives rise to a coupling of the core-shell.

Lemos et al. [237] considered a magnetocrystalline anisotropy term pointing in the x-direction to ensure a favored direction for particle magnetization (easy axis), which is the same for all spins belonging to particles. The external magnetic field H is necessary to construct the hysteresis curves and can point in any direction in the x-y plane. By considering the aforementioned entities, Hamiltonian is given as

$$H = -\sum_{i,j} J_{ij} \overrightarrow{\sigma_i} . \overrightarrow{\sigma_j} - D \sum_i \left(\overrightarrow{\sigma_i} . \overrightarrow{e_x} \right)^2 - \sum_i \overrightarrow{H} . \overrightarrow{\sigma_i}, \tag{7.7}$$

where J_{ij} (>0 in core, <0 in shell, and $\pm$ at interface) is the magnitude of the exchange interaction between spins $\overrightarrow{\sigma_i}$ and $\overrightarrow{\sigma_j}$. The double sum is for only between first-neighbor pairs of spins, considering the different forms of interaction, while the sum in the second and third terms are over all spins of the lattice. The spins are written in terms of x-y components: $\overrightarrow{\sigma} = \overrightarrow{\sigma_x} i + \overrightarrow{\sigma_y} j$, with $\sigma_x = \cos(\theta)$ and $\sigma = \sin(\theta)$, angle θ is measured with respect to the x-axis taking into account $|\overrightarrow{\sigma}| = 1$. The magnetocrystalline anisotropy defines the easy magnetization axis $\overrightarrow{e_x}$ chosen to point along the x-direction with magnitude D. Finally, the uniform external magnetic field is presented by $\overrightarrow{H}$.

The coordination number of the spins depends on its location in the lattice structure. This concept is very important in this model as it explains the different sizes of core-shell NPs and it studies the relative sizes of the core with variations in shell thickness.

A few other major works are summarized here to show the current status of theoretical modeling in core-shell nanostructures to interpret EB properties. The atomic level MC simulation method was preferred by Vasilakaki et al. [238, 239] to explain the reasons of horizontal and vertical shifts of M-H curves and the training effect due to EB in FM/AFM (core-shell) NPs. As a result, vertical shift was due to the contribution from whole shell spins while the horizontal shift resulted from the core–shell interface, and the training effect was observed due to the contribution from the interface, core, shell, and size of NPs. They also interpreted the effect of interparticle dipole interactions on the EB characteristics of core (FM)-shell (AFM) nanostructures. Evans et al. [240] modeled the time evolution of FM/AFM core-shell nanomaterials using an LLG equation with Langevin dynamics. In addition, the role of interface roughness in the hysteric behavior of FM core/AFM shell NPs was also explored. The dependence of size, random field, and temperature on the EB field was studied by Wu et al. [241] theoretically using MC simulations on FM core/AFM shell NPs and the EB field was increased by increasing the shell thickness and reducing the core radius. The oscillatory behavior of the EB field was found to be dependent on the core radius. Further, Wu et al. [241] demonstrated a monotonic reduction of the EB field with an increase in temperature and random field inside NPs.

Hence, MC simulation with LLG equations is very useful and promising for theoretical calculations and modeling of the EB mechanism in core-shell NPs and bilayer systems. MC simulations are important not only in detailed analyses of interfacial spin structures but also in fluctuation studies. LLG equations support the modeling of spin magnetic moment dynamics in 3-D space using the time-evolution approach.

7.6 Conclusion

Multifunctional complex magnetic nanostructures are at the leading edge and promise to deliver high-yield applications. These applications are equally important in device engineering and biomedicine. Synthesis conditions play a crucial role in controlling the properties of multifunctional nanostructures. Organometallic and microemulsion synthesis protocols for multifunctional core-shell or dumbell nanostructures are challenging itself. Further, these synthesis techniques require advancement to fabricate multifunctional nanodevices in conjunction with magnetic and optical/plasmonic/electronic features. Core-shell and dumbbell nanostructures and "eye watch" multifunctionality of these anisotropic structures have led to many exotic interface phenomena like EB effects, which has enabled rapid technological advances in important commercial applications owing to their GMR spin valve devices. The theoretical calculations and modeling of different nanostructures using MC simulations to evaluate the magnetic characteristics are providing solutions and experimental challenges for designing devices at the nanoscale.

Acknowledgements SKS and NS are grateful for financial support from CAPES, CNPq, and FAPEMA, Brazil. Sarveena and MS are thankful to DST, India.

References

1. Strömberg M, Zardán Gómez de la Torre T, Nilsson M, Svedlindh P, Strømme M (2014) A magnetic nanobead-based bioassay provides sensitive detection of single- and biplex bacterial DNA using a portable AC susceptometer. Biotechnol J 9:137–145. doi:10.1002/biot.201300348
2. Niedbala RS, Feindt H, Kardos K, Vail T, Burton J, Bielska B, Li S, Milunic D, Bourdelle P, Vallejo R (2001) Detection of analytes by immunoassay using up-converting phosphor technology. Anal Biochem 293:22–30. doi:10.1006/abio.2001.5105
3. Haun JB, Yoon TJ, Lee H, Weissleder R (2010) Magnetic nanoparticle biosensors. Wiley Interdiscip Rev Nanomed Nanobiotechnol 2:291–304. doi:10.1002/wnan.84
4. Espinosa A, Di Corato R, Kolosnjaj-Tabi J, Flaud P, Pellegrino T, Wilhelm C (2016) Duality of iron oxide nanoparticles in cancer therapy: amplification of heating efficiency by magnetic hyperthermia and photothermal bimodal treatment. ACS Nano 10:2436–2446. doi:10.1021/acsnano.5b07249
5. Singh LP, Srivastava SK, Mishra R, Ningthoujam RS (2014) Multifunctional hybrid nanomaterials from water dispersible CaF_2:Eu^{3+}, Mn^{2+} and Fe_3O_4 for luminescence and hyperthermia application. J Phys Chem C 118:18087–18096. doi:10.1021/jp502825p
6. Labiadh H, Ben Chaabane T, Sibille R, Balan L, Schneider R (2015) A facile method for the preparation of bifunctional Mn:ZnS/ZnS/Fe_3O_4 magnetic and fluorescent nanocrystals. Beilstein J Nanotechnol 6:1743–1751. doi:10.3762/bjnano.6.178
7. Lacroix L-M, Delpech F, Nayral C, Lachaize S, Chaudret B (2013) New generation of magnetic and luminescent nanoparticles for in vivo real-time imaging. Interface Focus 3:20120103. doi:10.1098/rsfs.2012.0103
8. Gai S, Yang P, Li C, Wang W, Dai Y, Niu N, Lin J (2010) Synthesis of magnetic, up-conversion luminescent, and mesoporous core-shell-structured nanocomposites as drug carriers. Adv Funct Mater 20:1166–1172. doi:10.1002/adfm.200902274

9. Leung KC-F, Xuan S, Zhu X, Wang D, Chak C-P, Lee S-F, Ho WK-WK-W, Chung BC-TC-T (2012) Gold and iron oxide hybrid nanocomposite materials. Chem Soc Rev 41:1911–1928. doi:10.1039/c1cs15213k
10. Kempe H, Kates SA, Kempe M (2011) Nanomedicine's promising therapy: magnetic drug targeting. Expert Rev Med Devices 8:291–294. doi:10.1586/erd.10.94
11. Mangaiyarkarasi R, Chinnathambi S, Karthikeyan S, Aruna P, Ganesan S (2016) Paclitaxel conjugated Fe_3O_4@LaF3:Ce^{3+}, Tb^{3+} nanoparticles as bifunctional targeting carriers for Cancer theranostics application. J Magn Magn Mater 399:207–215. doi:10.1016/j.jmmm.2015.09.084
12. Sukumar UK, Bhushan B, Dubey P, Matai I, Sachdev A, Packirisamy G (2013) Emerging applications of nanoparticles for lung cancer diagnosis and therapy. Int Nano Lett 3:1–17. doi:10.1186/2228-5326-3-45
13. Ye F, Barrefelt A, Asem H, Abedi-Valugerdi M, El-Serafi I, Saghafian M, Abu-Salah K, Alrokayan S, Muhammed M, Hassan M (2014) Biodegradable polymeric vesicles containing magnetic nanoparticles, quantum dots and anticancer drugs for drug delivery and imaging. Biomaterials 35:3885–3894. doi:10.1016/j.biomaterials.2014.01.041
14. Comby S, Surender EM, Kotova O, Truman LK, Molloy JK, Gunnlaugsson T (2014) Lanthanide-functionalized nanoparticles as MRI and luminescent probes for sensing and/or imaging applications. Inorg Chem 53:1867–1879. doi:10.1021/ic4023568
15. Zhu X, Zhou J, Chen M, Shi M, Feng W, Li F (2012) Core–shell Fe_3O_4@$NaLuF_4$:Yb,Er/Tm nanostructure for MRI, CT and upconversion luminescence tri-modality imaging. Biomaterials 33:4618–4627. doi:10.1016/j.biomaterials.2012.03.007
16. Yigit MV, Moore A, Medarova Z (2012) Magnetic nanoparticles for cancer diagnosis and therapy. Pharm Res 29:1180–1188. doi:10.1007/s11095-012-0679-7
17. Liu C, Zou B, Rondinone AJ, Zhang ZJ (2000) Reverse micelle synthesis and characterization of superparamagnetic $MnFe_2O_4$ spinel ferrite nanocrystallites. J Phys Chem B 104:1141–1145. doi:10.1021/jp993552g
18. Issa B, Obaidat IM, Albiss BA, Haik Y (2013) Magnetic nanoparticles: surface effects and properties related to biomedicine applications. Int J Mol Sci 14:21266–21305. doi:10.3390/ijms141121266
19. Gaponik N, Radtchenko IL, Sukhorukov GB, Rogach AL (2004) Luminescent polymer microcapsules addressable by a magnetic field. Langmuir 20:1449–1452. doi:10.1021/la035914o
20. Krishnamurthy N, Gupta CK (2016) Extractive metallurgy of rare earth. Taylor and Francis, Boca Raton, FL
21. Bünzli J-CG (2010) Lanthanide luminescence for biomedical analyses and imaging. Chem Rev 110:2729–2755. doi:10.1021/cr900362e
22. Moscoso-Londoño O, Gonzalez JS, Muraca D, Hoppe CE, Alvarez VA, López-Quintela A, Socolovsky LM, Pirota KR (2013) Structural and magnetic behavior of ferrogels obtained by freezing thawing of polyvinyl alcohol/poly(acrylic acid) (PAA)-coated iron oxide nanoparticles. Eur Polym J 49:279–289. doi:10.1016/j.eurpolymj.2012.11.007
23. Gutiérrez L, Costo R, Grüttner C, Westphal F, Gehrke N, Heinke D, Fornara A, Pankhurst QA, Johansson C, Morales MP (2015) Synthesis methods to prepare single- and multicore iron oxide nanoparticles for biomedical applications. Dalton Trans 44:2943–2952. doi:10.1039/c4dt03013c
24. Suess D, Kirschner M, Schrefl T, Fidler J, Stamps RL, Kim J-V (2003) Exchange bias of polycrystalline antiferromagnets with perfectly compensated interfaces. Phys Rev B 67:54419. doi:10.1103/PhysRevB.67.054419
25. Bader SD (2006) Colloquium: opportunities in nanomagnetism. Rev Mod Phys. vol 78. doi:10.1103/RevModPhys.78.1
26. Coey JMD (2010) Magnetism and magnetic materials. Cambridge University Press, New York
27. Bedanta S, Petracic O, Kleemann W (2015) Supermagnetism. In: Buschow KHJ (ed) Handbook of magnetic materials, vol 23. Elseveir, Oxford

28. Kim J-V, Stamps RL, Camley RE (2016) Spin wave power flow and caustics in ultrathin ferromagnets with the Dzyaloshinskii-Moriya interaction. Phys Rev Lett 117:197204. doi: https://doi.org/10.1103/PhysRevLett.117.197204
29. Kharissova OV, Kharisov BI, Jiménez-Pérez VM, Flores BM, Ortiz Méndez U (2013) Ultrasmall particles and nanocomposites: state of the art. RSC Adv 3:22648. doi:10.1039/c3ra43418d
30. Brosseau C, Malĺgol S, Quéffélec P, Youssef JB (2007) Electromagnetism and magnetization in granular two-phase nanocomposites: a comparative microwave study. J Appl Phys 101:034301. doi:10.1063/1.2432871
31. Nogués J, Sort J, Langlais V, Skumryev V, Suriñach S, Muñoz JS, Baró MD (2005) Exchange bias in nanostructures. Phys Rep 422:65–117. doi:10.1016/j.physrep.2005.08.004
32. Liz-Marzán LM, Kamat PV (2003) Nanoscale materials. Springer, New York. doi:10.1007/b101855
33. Lavorato GC, Peddis D, Lima E, Troiani HE, Agostinelli E, Fiorani D, Zysler RD, Winkler EL (2015) Magnetic interactions and energy barrier enhancement in core-shell bimagnetic nanoparticles. J Phys Chem C 119:15755–15762. doi:10.1021/acs.jpcc.5b04448
34. Palneedi H, Annapureddy V, Priya S, Ryu J (2016) Status and perspectives of multiferroic magnetoelectric composite materials and applications. Actuators 5:9. doi:10.3390/act5010009
35. Mejía-López J, Altbir D, Schuller IK (2003) Relaxation times in exchange-biased nanostructures. Appl Phys Lett 83:332–334. doi:10.1063/1.1592637
36. Vargas JM, McBride AA, Plumley JB, Fichou Y, Memon TA, Shah V, Cook NC, Akins BA, Rivera AC, Smolyakov GA, JR O'B, Adolphi NL, HDC S, Osiński M (2011) Synthesis and characterization of core/shell Fe_3O_4/ZnSe fluorescent magnetic nanoparticles. J Appl Phys 109:7B536–7B5363. doi:10.1063/1.3565190
37. Enders A, Skomski R, Honolka J (2010) Magnetic surface nanostructures. J Phys Condens Matter 22:433001. doi:10.1088/0953-8984/22/43/433001
38. Yan C, Zhao H, Perepichka DF, Rosei F (2016) Lanthanide ion doped upconverting nanoparticles: synthesis, structure and properties. Small 12:3888–3907. doi:10.1002/smll.201601565
39. Sun P, Zhang H, Liu C, Fang J, Wang M, Chen J, Zhang J, Mao C, Xu S (2010) Preparation and characterization of Fe_3O_4/CdTe magnetic/fluorescent nanocomposites and their applications in immuno-labeling and fluorescent imaging of cancer cells. Langmuir 26:1278–1284. doi:10.1021/la9024553
40. Moya C, Iglesias Ó, Batlle X, Labarta A (2015) Quantification of dipolar interactions in $Fe_{3-x}O_4$ nanoparticles. J Phys Chem C 119:24142–24148. doi:10.1021/acs.jpcc.5b07516
41. Gu H, Zheng R, Zhang X, Xu B (2004) Facile one-pot synthesis of bifunctional heterodimers of nanoparticles: a conjugate of quantum dot and magnetic nanoparticles. J Am Chem Soc 126:5664–5665. doi:10.1021/ja0496423
42. Dabbousi BO, Rodriguez J, Mikulec FV, Heine JR, Mattoussi H, Ober R, Jensen KF, Bawendi MG (1997) (CdSe)ZnS core–shell quantum dots: synthesis and characterization of a size series of highly luminescent nanocrystallites. J Phys Chem B 101:9463–9475. doi:10.1021/jp971091y
43. Brollo MEF, López-Ruiz R, Muraca D, SJA F, Pirota KR, Knobel M (2014) Compact Ag@Fe_3O_4 core-shell nanoparticles by means of single-step thermal decomposition reaction. Sci Rep 4:6839. doi:10.1038/srep06839
44. Ding S-J, Nan F, Liu X-N, Liu X-L, Zhang Y-F, Liang S, Yao D-Z, Zhang X-H, Wang Q-Q (2015) Largely enhanced optical nonlinear response of heavily doped Ag:CdTe nanocrystals around the excitonic band edge. J Phys Chem C 119:24958–24964. doi:10.1021/acs.jpcc.5b06408
45. Yao D, Liu H, Liu Y, Dong C, Zhang K, Sheng Y, Cui J, Zhang H, Yang B (2015) Phosphine-free synthesis of Ag–In–Se alloy nanocrystals with visible emissions. Nanoscale 7:18570–18578. doi:10.1039/C5NR04856G
46. Wolfbeis OS (2015) An overview of nanoparticles commonly used in fluorescent bioimaging. Chem Soc Rev 44:4743–4768. doi:10.1039/c4cs00392f

47. Sarveena MD, Zelis PM, Javed Y, Ahmad N, Vargas JM, Moscoso Londoño O, Knobel M, Singh M, Sharma SK (2016) Surface and interface interplay on the oxidizing temperature of iron oxide and Au–iron oxide. RSC Adv 6:70394–70404. doi:10.1039/C6RA15610J
48. Teo RD, Termini J, Gray HB (2016) Lanthanides: applications in cancer diagnosis and therapy. J Med Chem 59:6012–6024. doi:10.1021/acs.jmedchem.5b01975
49. Kaewsaneha C, Bitar A, Tangboriboonrat P, Polpanich D, Elaissari A (2014) Fluorescent-magnetic Janus particles prepared via seed emulsion polymerization. J Colloid Interface Sci 424:98–103. doi:10.1016/j.jcis.2014.03.011
50. Bi F, Dong X, Wang J, Liu G (2015) Tuned magnetism–luminescence bifunctionality simultaneously assembled into flexible Janus nanofiber. RSC Adv 5:12571–12577. doi:10.1039/C4RA10022K
51. Atabaev T, Kim H-K, Hwang Y-H (2013) Fabrication of bifunctional core-shell Fe_3O_4 particles coated with ultrathin phosphor layer. Nanoscale Res Lett 8:357. doi:10.1186/1556-276X-8-357
52. Leszczyński B, Hadjipanayis GC, El-Gendy AA, Załski K, Śniadecki Z, Musiał A, Jarek M, Jurga S, Skumiel A (2016) The influence of oxidation process on exchange bias in egg-shaped FeO/Fe_3O_4 core-shell nanoparticles. J Magn Magn Mater 416:269–274. doi:10.1016/j.jmmm.2016.05.023
53. Mélinon P, Begin-Colin S, Duvail JL, Gauffre F, Boime NH, Ledoux G, Plain J, Reiss P, Silly F, Warot-Fonrose B (2014) Engineered inorganic core-shell nanoparticles. Phys Rep 543:163–197. doi:10.1016/j.physrep.2014.05.003
54. Urbanova V, Magro M, Gedanken A, Baratella D, Vianello F, Zboril R (2014) Nanocrystalline iron oxides, composites, and related materials as a platform for electrochemical, magnetic, and chemical biosensors. Chem Mater 26:6653–6673. doi:10.1021/cm500364x
55. Lv R, Yang G, He F, Dai Y, Gai S, Yang P (2014) LaF_3:Ln mesoporous spheres: controllable synthesis, tunable luminescence and application for dual-modal chemo-/photo-thermal therapy. Nanoscale 6:14799–14809. doi:10.1039/c4nr04336g
56. Chang C-J, Lee Z, Wei M, Chang C-C, Chu K-W (2015) Photocatalytic hydrogen production by magnetically separable Fe_3O_4@ZnS and $NiCo_2O_4$@ZnS core-shell nanoparticles. Int J Hydrog Energy 40:11436–11443. doi:10.1016/j.ijhydene.2015.01.151
57. Frey NA, Srinath S, Srikanth H, Wang C, Sun S (2007) Static and dynamic magnetic properties of composite. IEEE Trans Magn 43:3094–3096. doi:10.1109/TMAG.2007.893846
58. Boistelle R, Astier JP (1988) Crystallization mechanisms in solution. J Cryst Growth 90:14–30. doi:10.1016/0022-0248(88)90294-1
59. Nguyen T-D, Tran T-H (2014) Multicomponent nanoarchitectures for the design of optical sensing and diagnostic tools. RSC Adv 4:916–942. doi:10.1039/c3ra44056g
60. Zhu H, Hu MZ, Shao L, Yu K, Dabestani R, Zaman MB, Liao S (2014) Synthesis and optical properties of thiol functionalized CdSe/ZnS (core-shell) quantum dots by ligand exchange. J Nanomater. doi:10.1155/2014/324972
61. Zeng H, Sun S (2008) Syntheses, properties, and potential applications of multicomponent magnetic nanoparticles. Adv Funct Mater 18:391–400. doi:10.1002/adfm.200701211
62. Shevchenko EV, Bodnarchuk MI, Kovalenko MV, Talapin DV, Smith RK, Aloni S, Heiss W, Alivisatos AP (2008) Gold/iron oxide core/hollow-shell nanoparticles. Adv Mater 20:4323–4329. doi:10.1002/adma.200702994
63. Wang H, Sun L, Li Y, Fei X, Sun M, Zhang C, Li Y, Yang Q (2011) Layer-by-layer assembled Fe_3O_4@C@CdTe core-shell microspheres as separable luminescent probe for sensitive sensing of Cu^{2+} ions. Langmuir 27:11609–11615. doi:10.1021/la202295b
64. Hao R, Xing R, Xu Z, Hou Y, Goo S, Sun S (2010) Synthesis, functionalization, and biomedical applications of multifunctional magnetic nanoparticles. Adv Mater 22:2729–2742. doi:10.1002/adma.201000260
65. Gao J, Gu H, Xu B (2009) Multifunctional magnetic nanoparticles: design, synthesis, and biomedical applications. Acc Chem Res 42:1097–1107. doi:10.1021/ar9000026
66. Wei C (2006) Quantum size effects in nanostructures: lecture notes to course organic and inorganic nanostructures. APS Meet Abstr. doi:10.3402/nano.v1i0.5117

67. Jain M, Bøtter-Jensen L (2014) Luminescence instrumentation. In: Virk HS (ed) Luminescence: basic concepts, applications and instrumentation. Trans Teck Publications, Stafa-Zurich
68. Einarsrud M-A, Grande T (2013) 1D oxide nanostructures from chemical solutions. Chem Soc Rev 43:2187–2199. doi:10.1039/c3cs60219b
69. Kolen'ko YV, Bañobre-López M, Rodríguez-Abreu C, Carbó-Argibay E, Sailsman A, Piñeiro-Redondo Y, Cerqueira MF, Petrovykh DY, Kovnir K, Lebedev O, Rivas J (2014) Large-scale synthesis of colloidal Fe_3O_4 nanoparticles exhibiting high heating efficiency in magnetic hyperthermia. J Phys Chem C 118(16):8691–8701. doi:10.1021/jp500816u
70. Sun Q-C, Birkel CS, Cao J, Tremel W, Musfeldt JL (2012) Spectroscopic signature of the superparamagnetic transition and surface spin disorder in $CoFe_2O_4$ nanoparticles. ACS Nano 6:4876–4883. doi:10.1021/nn301276q
71. Gargas DJ, Chan EM, Ostrowski AD, Aloni S, Altoe MVP, Barnard ES, Sanii B, Urban JJ, Milliron DJ, Cohen BE, Schuck PJ (2014) Engineering bright sub-10-nm upconverting nanocrystals for single-molecule imaging. Nat Nanotechnol 9:300–305. doi:10.1038/nnano.2014.29
72. Pankhurst QA, Pollard RJ (1991) Origin of the spin-canting anomaly in small ferrimagnetic particles. Phys Rev Lett 67:248–250. doi:10.1103/PhysRevLett.67.248
73. Feygenson M, Bauer JC, Gai Z, Marques C, Aronson MC, Teng X, Su D, Stanic V, Urban VS, Beyer KA, Dai S (2015) Exchange bias effect in Au-Fe_3O_4 dumbbell nanoparticles induced by the charge transfer from gold. Phys Rev B 92:54416. doi:10.1103/PhysRevB.92.054416
74. Chaudhuri RG, Paria S (2012) core-shell nanoparticles: classes, properties, synthesis mechanisms, characterization, and applications. Chem Rev 112:2373–2433. doi:10.1021/cr100449n
75. Chauhan S, Singh AK, Srivastava SK, Chandra R (2016) Study of magnetic behavior in hexagonal-$YMn_{1-x}Fe_xO_3$ (x=0 and 0.2) nanoparticles using remanent magnetization curves. J Magn Magn Mater 414:187–193. doi:10.1016/j.jmmm.2016.04.074
76. Santra S, Tapec R, Theodoropoulou N, Dobson J, Hebard A, Tan W (2001) Synthesis and characterization of silica-coated iron oxide nanoparticles in microemulsion: the effect of nonionic surfactants. Langmuir 17:2900–2906. doi:10.1021/la0008636
77. Kim DK, Zhang Y, Voit W, Rao KV, Muhammed M (2001) Synthesis and characterization of surfactant-coated superparamagnetic monodispersed iron oxide nanoparticles. J Magn Magn Mater 225:30–36. doi:10.1016/S0304-8853(00)01224-5
78. Lottini E, López-Ortega A, Bertoni G, Turner S, Meledina M, Van Tendeloo G, De Julián Fernández C, Sangregorio C (2016) Strongly exchange coupled core-shell nanoparticles with high magnetic anisotropy: a strategy toward rare-earth-free permanent magnets. Chem Mater 28:4214–4222. doi:10.1021/acs.chemmater.6b00623
79. Estradé S, Yedra L, López-Ortega A, Estrader M, Salazar-Alvarez G, Baró MD, Nogués J, Peiró F (2012) Distinguishing the core from the shell in MnO_x/MnO_y and FeO_x/MnO_x core-shell nanoparticles through quantitative electron energy loss spectroscopy (EELS) analysis. Micron 43:30–36. doi:10.1016/j.micron.2011.04.002
80. Laurent S, Forge D, Port M, Roch A, Robic C, Vander Elst L, Muller RN (2008) Magnetic iron oxide nanoparticles: synthesis, stabilization, vectorization, physicochemical characterizations and biological applications. Chem Rev 108:2064–2110. doi:10.1021/cr068445e
81. Huang Q, Li W, Lin Q, Pi D, Hu C, Shao C, Zhang H (2016) A review of significant factors in the synthesis of hetero-structured dumbbell-like nanoparticles. Chinese J Catal 37:681–691. doi:10.1016/S1872-2067(15)61069-5
82. Hu J, Zhou S, Sun Y, Fang X, Wu L (2012) Fabrication, properties and applications of Janus particles. Chem Soc Rev 41:4356–4378. doi:10.1039/c2cs35032g
83. Salgueiriño-Maceira V, Correa-Duarte MA (2007) Increasing the complexity of magnetic core-shell structured nanocomposites for biological applications. Adv Mater 19:4131–4144. doi:10.1002/adma.200700418
84. Skumryev V, Stoyanov V, Zhang Y, Hadjipanayis G, Givord D, Nogues J (2003) Beating the superparamagnetic limit with exchange bias. Nature 423:850–853. doi:10.1038/nature01687

85. Hu Y, Liu Y, Du A, Shi F (2014) Dependence of exchange bias on core-shell relative dimension in ferromagnetic/antiferromagnetic nanoparticles. Phys Lett A 378:1667–1674. doi:10.1016/j.physleta.2014.04.015
86. Stamps RL (2001) Mechanisms for exchange bias. J Phys D Appl Phys 33:R247–R268. doi:10.1088/0022-3727/34/3/501
87. Passamani EC, Larica C, Marques C, Proveti JR, Takeuchi AY, Sanchez FH (2006) Exchange bias and anomalous vertical shift of the hysteresis loops in milled Fe/MnO_2 material. J Magn Magn Mater 299:11–20. doi:10.1016/j.jmmm.2005.03.014
88. Nogues J, Schüller IK (1999) Exchange bias. J Magn Magn Mater 192:203–232. doi:10.1016/S0304-8853(98)00266-2
89. Chi X, Hu Y (2015) Role of antiferromagnetic bulk exchange coupling on exchange-bias propagation. IEEE Int Magn Conf INTERMAG 379:2772–2776. doi:10.1109/INTMAG.2015.7156539
90. Lin XM, Samia ACS (2006) Synthesis, assembly and physical properties of magnetic nanoparticles. J Magn Magn Mater 305:100–109. doi:10.1016/j.jmmm.2005.11.042
91. Danielsson I, Lindman B (1981) The definition of microemulsion. Colloids Surf 3:391–392
92. Langevin D (1992) Micelles and microemulsions. Annu Rev Phys Chem 43:341–369. doi:10.1146/annurev.physchem.43.1.341
93. Malik MA, Wani MY, Hashim MA (2012) Microemulsion method: a novel route to synthesize organic and inorganic nanomaterials. 1st Nano Update. Arab J Chem 5:397–417. doi:10.1016/j.arabjc.2010.09.027
94. Wang X, Zhuang J, Peng Q, Li Y (2005) A general strategy for nanocrystal synthesis. Nature 437:121–124. doi:10.1038/nature03968
95. Hyeon T (2003) Chemical synthesis of magnetic nanoparticles. Chem Commun:927–934. doi:10.1039/B207789B
96. Wu W, He Q, Jiang C (2008) Magnetic iron oxide nanoparticles: synthesis and surface functionalization strategies. Nanoscale Res Lett 3:397–415. doi:10.1007/s11671-008-9174-9
97. Wegner KD, Lanh PT, Jennings T, Oh E, Jain V, Fairclough SM, Smith JM, Giovanelli E, Lequeux N, Pons T, Hildebrandt N (2013) Influence of luminescence quantum yield, surface coating, and functionalization of quantum dots on the sensitivity of time-resolved fret bioassays. ACS Appl Mater Interfaces 5:2881–2892. doi:10.1021/am3030728
98. Lu AH, Salabas EL, Schüth F (2007) Magnetic nanoparticles: synthesis, protection, functionalization, and application. Angew Chem Int Ed 46:1222–1244. doi:10.1002/anie.200602866
99. Li Y, Afzaal M, O'Brien P (2006) The synthesis of amine-capped magnetic (Fe, Mn, Co, Ni) oxide nanocrystals and their surface modification for aqueous dispersibility. J Mater Chem 16:2175–2180. doi:10.1039/b517351e
100. Dinnebier RE, Billinge SJL (2008) Powder diffraction theory and practice. The Royal Society of Chemistry, Cambridge
101. Thanh NTK, Robinson I, Tung LD (2007) Magnetic nanoparticles for biomedical applications: synthesis, characterization and uses. Dekker Encyclopedia of Nanoscience and Nanotechnology 1:1–10. doi:10.1081/E-ENN-120042172
102. Knappett BR, Abdulkin P, Ringe E, Jefferson DA, Lozano-Perez S, Rojas TC, Fernández A, AEH Wheatley (2013) Characterisation of Co@Fe_3O_4 core-shell nanoparticles using advanced electron microscopy. Nanoscale 5:5765–5772. doi:10.1039/c3nr33789h
103. Wang ZL (2000) Characterization of nanophase materials. Willey VCH-Verlag GmbH, Weinheim
104. Lin P-C, Lin S, Wang PC, Sridhar R (2014) Techniques for physicochemical characterization of nanomaterials. Biotechnol Adv 32:711–726. doi:10.1016/j.biotechadv.2013.11.006
105. Butt H-J, Cappella B, Kappl M (2005) Force measurements with the atomic force microscope: technique, interpretation and applications. Surf Sci Rep 59:1–152. doi:10.1016/j.surfrep.2005.08.003
106. Béron F, Kaidatzis A, Velo MF, Arzuza LCC, Palmero EM, del Real RP, Niarchos D, Pirota KR, García-Martín JM (2016) Nanometer scale hard/soft bilayer magnetic antidots. Nanoscale Res Lett 11:86. doi:10.1186/s11671-016-1302-3

107. Rao CNR, Biswas K (2009) Characterization of nanomaterials by physical methods. Annu Rev Anal Chem 2:435–462. doi:10.1146/annurev-anchem-060908-155236
108. Boldon L, Laliberte F, Liu L (2015) Review of the fundamental theories behind small angle X-ray scattering, molecular dynamics simulations, and relevant integrated application. Nano Rev 6:25661. doi:10.3402/nano.v6.25661
109. Li T, Senesi AJ, Lee B (2016) Small angle X-ray scattering for nanoparticle research. Chem Rev 16:11128–11180. doi:10.1021/acs.chemrev.5b00690
110. Orozco-Henao JM, Coral DF, Muraca D, Moscoso-Londoño O, Mendoza Zélis P, Fernandez Van Raap MB, Sharma SK, Pirota KR, Knobel M (2016) Effects of nanostructure and dipolar interactions on magnetohyperthermia in iron oxide nanoparticles. J Phys Chem C 120:12796–12809. doi:10.1021/acs.jpcc.6b00900
111. Vegso K, Jergel M, Siffalovic P, Kotlar M, Halahovets Y, Hodas M, Pelletta M, Majkova E (2016) Real-time SAXS study of a strain gauge based on a self- assembled gold nanoparticle monolayer. Sensors Actuators A Phys 241:87–95. doi:10.1016/j.sna.2016.02.021
112. Sharma SK, Vargas JM, Pirota KR, Kumar S, Lee CG, Knobel M (2011) Synthesis and ageing effect in FeO nanoparticles: transformation to core–shell FeO/Fe_3O_4 and their magnetic characterization. J Alloys Compd 509:6414–6417. doi:10.1016/j.jallcom.2011.03.072
113. Dickson DPE, Berry FJ (1986) Mössbauer spectroscopy. Cambridge University Press, Melbourne
114. Sharma SK, Vargas JM, Vargas NM, Castillo-sep S, Altbir D, Pirota KR, Zboril R, Zoppellaro G, Knobel M (2015) Unusual magnetic damping effect in a silver–cobalt ferrite hetero nanosystem. RSC Adv 5:17117–17122. doi:10.1039/C4RA14960B
115. Vargas JM, Srivastava A, Yourdkhani A, Zaldivar L, Caruntu G, Spinu L (2011) Tuning the thermal relaxation of transition-metal ferrite nanoparticles through their intrinsic magnetocrystalline anisotropy. J Appl Phys 110:064304. doi:http://dx.doi.org/10.1063/1.3638053
116. Petoukhov MV, Svergun DI (2006) Joint use of small-angle X-ray and neutron scattering to study biological macromolecules in solution. Eur Biophys J 35:567–576. doi:10.1007/s00249-006-0063-9
117. van der Laan G, Figueroa AI (2014) X-ray magnetic circular dichroism—a versatile tool to study magnetism. Coord Chem Rev 277:95–129. doi:10.1016/j.ccr.2014.03.018
118. Yin X, Sun W, Soh WT, Yang P, Yu X, Breese MBH, Wee ATS, Rusydi A, Ong CK (2017) Unraveling the magnetic coupling in the interface of the exchange-biased IrMn/permalloy multilayers. Mater Lett 187:133–135. doi:10.1016/j.matlet.2016.10.051
119. Chen CT, Idzerda YU, Lin H-J, Smith NV, Meigs G, Chaban E, Ho GH, Pellegrin E, Sett F (1995) Experimental confirmation of the X-ray magnetic circular dichroism sum rules for iron and cobalt. Phys Rev Lett 75:152–155. doi:https://doi.org/10.1103/PhysRevLett.75.152
120. Stöhr J (1995) X-ray magnetic circular dichroism spectroscopy of transition metal thin films. J Electron Spectrosc Relat Phenom 75:253–272. doi:10.1016/0368-2048(95)02537-5
121. Funk T, Deb A, George SJ, Wang H, Cramer SP (2005) X-ray magnetic circular dichroism—a high energy probe of magnetic properties. Coord Chem Rev 249:3–30. doi:10.1016/j.ccr.2004.05.017
122. Yuan SJ, Xu K, Yu LM, Cao SX, Jing C, Zhang JC (2007) Ferromagnetic resonance investigation in as-prepared. NiFe/FeMn/NiFe trilayer 101:113915. doi:10.1063/1.2738387
123. Shi D, Sadat ME, Dunn AW, Mast DB (2015) Photo-fluorescent and magnetic properties of iron oxide nanoparticles for biomedical applications. Nanoscale 7:8209–8232. doi:10.1039/c5nr01538c
124. Gfroerer TH (2000) Photoluminescence in analysis of surfaces and interfaces. In: Encyclopedia of analytical chemistry. Wiley, Chichester, pp 9209–9231. doi:10.1002/9780470027318.a2510

125. Stefan M, Leostean C, Panaa O, Sorana ML, Suciua RC, Gautronb E, Chauvet Z (2014) Synthesis and characterization of Fe_3O_4@ZnS and Fe_3O_4@Au@ZnS core-shell nanoparticle. Appl Surf Sci 288:180–192. doi:10.1016/j.apsusc.2013.10.005
126. McDonagh BH, Singh G, Hak S, Bandyopadhyay S, Augestad IL, Peddis D, Sandvig I, Sandvig A, Glomm WR (2016) L-DOPA-coated manganese oxide nanoparticles as dual MRI contrast agents and drug-delivery vehicles. Small 12:301–306. doi:10.1002/smll.201502545
127. Baek SH, Jang HW, Folkman CM, Li YL, Winchester B, Zhang JX, He Q, Chu YH, Nelson CT, Rzchowski MS, Pan XQ, Ramesh R, Chen LQ, Eom CB (2010) Ferroelastic switching for nanoscale non-volatile magnetoelectric devices. Nat Mater 9:309–314. doi:10.1038/nmat2703
128. Zhai YM, Zhai JF, Zhou M, Dong SJ (2009) Ordered magnetic core-manganese oxide shell nanostructures and their application in water treatment. J Mater Chem 19:7030–7035. doi:10.1039/b912767d
129. Tartaj P (2006) Nanomagnets-From fundamental physics to biomedicine. Curr Nanosci 2:43–53. doi:10.2174/157341306775473818
130. Kodama RH (1999) Magnetic nanoparticles. J Magn Magn Mater 200:359–372. doi:10.1016/S0304-8853(99)00347-9
131. Dimitrov DV, Zhang S, Xiao JQ, Hadjipanayis GC, Prados C (1998) Effect of exchange interactions at antiferromagnetic/ferromagnetic interfaces on exchange bias and coercivity. Phys Rev B 58:12090–12094. doi:10.1103/PhysRevB.58.12090
132. Leighton C, Morellon L, Leighton C, Ibarra MR, Schuller IK (2000) Antiferromagnetic spin flop and exchange bias. Phys Rev B 61:6455–6458. doi:https://doi.org/10.1103/PhysRevB.61.R6455
133. Roy S, Fitzsimmons MR, Park S, Dorn M, Petracic O, Roshchin IV, Li Z, Batlle X, Morales R, Misra A, Zhang X, Chesnel K, Kortright JB, Sinha SK, Schuller IK (2005) Depth profile of uncompensated spins in an exchange bias system. Phys Rev Lett 95:47201. doi:10.1103/PhysRevLett.95.047201
134. Krishnan KM, Pakhomov AB, Bao Y, Blomqvist P, Chun Y, Gonzales M, Griffin K, Ji X, Roberts BK (2006) Nanomagnetism and spin electronics: materials, microstructure and novel properties. J Mater Sci 41:793–815. doi:10.1007/s10853-006-6564-1
135. Ali M, Adie P, Marrows CH, Greig D, Hickey BJ, Stamps RL (2007) Exchange bias using a spin glass. Nat Mater 6:70–75. doi:10.1038/nmat1809
136. Chandra S (2013) Magnetization dynamics and related phenomena in nanostructures. Dissertation, University of South Florida.
137. Yang J, Liu H (2015) Metal-based composite nanomaterials. Springer, London. doi:10.1007/978-3-319-12220-5
138. Fantechi E, Innocenti C, Zanardelli M, Fittipaldi M, Falvo E, Carbo M, Shullani V, Mannelli LDC, Ghelardini C, Ferretti AM, Ponti A, Sangregorio C, Ceci P (2014) A smart platform for hyperthermia application in cancer treatment: cobalt-doped ferrite nanoparticles mineralized in human ferritin cages. ACS Nano 8:4705–4719. doi:10.1021/nn500454n
139. Chandra S, Huls NAF, Phan MH, Srinath S, Garcia MA, Lee Y, Wang C, Sun S, Iglesias O, Srikanth H (2014) Exchange bias effect in Au-Fe_3O_4 nanocomposites. Nanotechnology 25:055702. doi:10.1088/0957-4484/25/5/055702
140. Phan M, Alonso J, Khurshid H, Lampen-kelley P, Chandra S, Repa KS, Nemati Z, Das R, Iglesias O, Srikanth H (2016) Exchange bias effects in iron oxide based nanoparticle systems. Nanomaterials 6:221. doi: 10.3390/nano6110221
141. Gun'ko YK, Brougham DF (2011) Magnetic nanomaterials as MRI contrast agents. Nanotechnol Life Sci. doi:10.1002/9783527610419.ntls0166
142. Leung CW (2002) Metallic magnetic heterostructures. Metallic magnetic heterostructures. Dissertation, St. John College Cambridge
143. Fraile Rodríguez A, Basaran AC, Morales R, Kovylina M, Llobet J, Borrisé X, Marcus MA, Scholl A, Schuller IK, Batlle X, Labarta A (2015) Manipulation of competing ferromagnetic and antiferromagnetic domains in exchange-biased nanostructures. Phys Rev B 92:174417. doi:10.1103/PhysRevB.92.174417

144. Obaidat IM, Issa B, Haik Y (2015) Magnetic Properties of Magnetic Nanoparticles for Efficient Hyperthermia. Nanomaterials 5:63–89. doi:10.3390/nano5010063
145. Rukat T, Walker-Samuel S, Reinsberg SA (2015) Dynamic contrast-enhanced MRI in mice: an investigation of model parameter uncertainties. Magn Reson Med 73:1979–1987. doi:10.1002/mrm.25319
146. Vaz B, Salgueiriño V, Pérez-Lorenzo M, Correa-Duarte MA (2015) Enhancing the exploitation of functional nanomaterials through spatial confinement: the case of inorganic submicrometer capsules. Langmuir 31:8745–8755. doi:10.1021/acs.langmuir.5b00098
147. Yang C, Hou Y-L, Gao S (2014) Nanomagnetism: principles, nanostructures, and biomedical applications. Chinese Phys B 23:57505. doi:10.1088/1674-1056/23/5/057505
148. Walter A, Billotey C, Garofalo A, Ulhaq-Bouillet C, Lefèvre C, Taleb J, Laurent S, Elst LV, Muller RN, Felder-Flesch D, Begin-Colin S (2014) Mastering the Shape and Composition of dendronized iron oxide nanoparticles to tailor magnetic resonance imaging and hyperthermia. Chem Mater 26:5252–5264. doi:10.1021/cm5019025
149. Estrader M, López-Ortega A, Estradé S, Golosovsky IV, Salazar-Alvarez G, Vasilakaki M, Trohidou KN, Varela M, Stanley DC, Sinko M, Pechan MJ, Keavney DJ, Peiró F, Suriñach S, Baró MD, Nogués J (2013) Robust antiferromagnetic coupling in hard-soft bi-magnetic core-shell nanoparticles. Nat Commun 4:2960. doi:10.1038/ncomms3960
150. Bedanta S, Barman A, Kleemann W, Petracic O, Seki T (2013) Magnetic nanoparticles: a subject for both fundamental research and applications. J Nanomater 2013:1–22. doi:10.1155/2013/952540
151. Zoppellaro G, Tuček J, Herchel R, Šafářová K, Zbořil R (2013) Fe_3O_4 nanocrystals tune the magnetic regime of the Fe/Ni molecular magnet: a new class of magnetic superstructures. Inorg Chem 52:8144–8150. doi:10.1021/ic4008729
152. Krug IP (2008) Magnetic proximity effects in highly-ordered transition metal oxide heterosystems studied by Soft X-Ray Photoemission Electron Microscopy. Dissertation, Forschungszentrum Jülich, Germany
153. Frey NA, Phan MH, Srikanth H, Srinath S, Wang C, Sun S (2009) Interparticle interactions in coupled Au–Fe_3O_4 nanoparticles. J Appl Phys 105:07B502. doi:10.1063/1.3056582
154. Wang C, Yin H, Dai S, Sun S (2010) A general approach to noble metal-metal oxide dumbbell nanoparticles and their catalytic application for CO oxidation. Chem Mater 22:3277–3282. doi:10.1021/cm100603r
155. Bao J, Chen W, Liu T, Zhu Y, Jin P, Wang L, Liu J, Wei Y, Li Y (2007) Bifunctional Au-Fe_3O_4 nanoparticles for protein separation. ACS Nano 1:293–298.
156. Hu Y, Li J-C, Shen M-W, Shi X-Y (2014) Formation of multifunctional Fe_3O_4/Au composite nanoparticles for dual-mode MR/CT imaging applications. Chinese Phys B 23:78704. doi:10.1088/1674-1056/23/7/078704
157. Caruntu D, Cushing BL, Caruntu G, Connor CJO (2005) Attachment of gold nanograins onto colloidal magnetite nanocrystals. Chem Mater 17(13):3398–3402
158. Vetrone F, Mahalingam V, Capobianco JA (2009) Near-infrared-to-blue upconversion in colloidal $BaYF_5$:Tm^{3+}, Yb^{3+} nanocrystals. Chem Mater 21:1847–1851. doi:10.1021/cm900313s
159. Bhana S, Wang Y, Huang X (2015) Nanotechnology for enrichment and detection of circulating tumor cells. Nanomedicine 10:1973–1990. doi:10.2217/nnm.15.32
160. Hu Y, Meng L, Niu L, Lu Q (2013) Highly cross-linked and biocompatible polyphosphazene-coated superparamagnetic Fe_3O_4 nanoparticles for magnetic resonance imaging. Langmuir 29(29):9156–9163. doi:10.1021/la402119s
161. Zhang H, Zhong X, Xu J-J, Chen H-Y (2008) Fe_3O_4/Polypyrrole/Au nanocomposites with core-shell/shell structure: synthesis, characterization, and their electrochemical properties. Langmuir 24:13748–13752. doi:10.1021/la8028935
162. Cai H, An X, Cui J, Li J, Wen S, Li K, Shen M, Zheng L, Zhang G, Shi X (2013) Facile hydrothermal synthesis and surface functionalization of polyethyleneimine-coated iron oxide nanoparticles for biomedical applications. ACS Appl Mater Interfaces 5:1722–1731. doi:10.1021/am302883m

163. Lak A, Niculaes D, Anyfantis GC, Bertoni G, Barthel MJ, Marras S, Cassani M, Nitti S, Athanassiou A, Giannini C, Pellegrino T (2016) Facile transformation of FeO/Fe_3O_4 core-shell nanocubes to Fe_3O_4 via magnetic stimulation. Sci Rep 6:33295. doi:10.1038/srep33295
164. Inderhees SE, Borchers JA, Green KS, Kim MS, Sun K, Strycker GL, Aronson MC (2008) Manipulating the magnetic structure of Co core/CoO shell nanoparticles: implications for controlling the exchange bias. Phys Rev Lett 101:117202. doi:10.1103/PhysRevLett.101.117202
165. Yelenich OV, Solopan SO, Greneche JM, Belous AG (2015) Synthesis and properties MFe_2O_4(M=Fe,Co) nanoparticles and core-shell structures. Soild State Sciences 46:19–26. doi:10.1016/j.solidstatesciences.2015.05.011
166. Krylova G, Giovanetti LJ, Requejo FG, Dimitrijevic NM, Prakapenka A, Shevchenko EV (2012) Study of nucleation and growth mechanism of the metallic nanodumbbells. J Am Chem Soc 134:4384–4392. doi:10.1021/ja211459p
167. Ray PC, Khan SA, Singh AK, Senapati D, Fan Z (2012) Nanomaterials for targeted detection and photothermal killing of bacteria. Chem Soc Rev 41:3193–3209. doi:10.1039/c2cs15340h
168. Chen X, Zhu J, Chen Z, Xu C, Wang Y, Yao C (2011) A novel bienzyme glucose biosensor based on three-layer Au-Fe_3O_4@SiO_2 magnetic nanocomposite. Sensors Actuators B Chem 159:220–228. doi:10.1016/j.snb.2011.06.076
169. Reig C, Cubells-Beltran M-D, Muñoz DR (2009) Magnetic field sensors based on giant magnetoresistance (GMR) technology: applications in electrical current sensing. Sensors (Basel) 9:7919–7942. doi:10.3390/s91007919
170. Freitas PP, Ferreira R, Cardoso S, Cardoso F (2007) Magnetoresistive sensors. J Physics Condensed Matter 19:165221. doi:10.1088/0953-8984/19/16/165221
171. Cubells-Beltrán MD, Reig C, Madrenas J, De Marcellis A, Santos J, Cardoso S, Freitas PP (2016) Integration of GMR sensors with different technologies. Sensors 16:939. doi:10.3390/s16060939
172. Lage E, Kirchhof C, Hrkac V, Kienle L, Jahns R, Knöchel R, Quandt E, Meyners D (2012) Exchange biasing of magnetoelectric composites. Nat Mater 11:523–529. doi:10.1038/nmat3306
173. Rifai D, Abdalla AN, Ali K, Razali R (2016) Giant magnetoresistance sensors: a review on structures and non-destructive eddy current testing applications. Sensors 16:298. doi:10.3390/s16030298
174. Sharma PP, Albisetti E, Monticelli M, Bertacco R, Petti D (2016) Exchange bias tuning for magnetoresistive sensors by inclusion of non-magnetic impurities. Sensors 16:1030. doi:10.3390/s16071030
175. Childress JR, Jr REF (2005) Magnetic recording read head sensor technology. Comptes Rendus Physique 6:997–1012. doi:10.1016/j.crhy.2005.11.001
176. Mihajlovic G, Read JC, Smith N, van der Heijden P, Tsang CH, Childress JR (2016) Improved signal-to-noise ratio in current-perpendicular-to-plane giant-magnetoresistance sensors using strong exchange-biased reference layers. IEEE Magn Lett 7:1–4. doi:10.1109/LMAG.2016.2620119
177. Lenssen KMH, Adelerhof DJ, Gassen HJ, Kuiper AET, Somers GHJ, Van Zon JBAD (2000) Robust giant magnetoresistance sensors. Sensors Actuators A Phys 85:1–8. doi:10.1016/S0924-4247(00)00342-3
178. Rieger G, Ludwig K, Hauch J, Clemens W (2001) GMR sensors for contactless position detection. Sensors Actuat A Phys 91:7–11. doi:10.1016/S0924-4247(01)00480-0
179. Wang J-P, Li Y (2014) Gmr sensor. US Patent 20140099663 A1
180. Heim DE, Parkin SSP (1995) Magnetoresistive spin valve sensor with improved pinned ferromagnetic layer and magnetic recording system using the sensor. U.S. Pat. No. US 5465185 A
181. Dieny B, Gurney BA, Lambert SE, Mauri D, Steven E, Mauri D, Parkin SSP, Speriosu VS, Wilhoit DR (1993) Magnetoresistive sensor based on the spin valve effect. U. S. Pat. No. US 5206590 A
182. Buschow KHJ (2003) Handbook of Magnetic Materials. Elsevier B.V. The Netherlands

183. Zhu J-G (Jimmy), Park C (2006) Magnetic tunnel junctions (MTJs). Mater Today 9:36–45. doi:10.1016/S1369-7021(06)71693-5
184. Dovek M, Wang P-K, Chien C-J, Torng C-J, Li Y-F (2005) Process for manufacturing a magnetic read head. U.S. Pat. No. US 6,842,969 B2
185. Lin T, Mauri D (2001) Spin valve read head with antiferromagnetic oxide film as longitudinal bias layer and portion of first read gap. U.S. Pat. no.6,185,078 B1
186. Mohammed E, Assaj A, Patil PB, Chaudhari YA, Jagtap PP, Bendre ST (2013) GMR materials: a new generation of miniaturizated technology. ISOR J Appl Phys 5:76–81
187. Kanai H, Noma K, Hong J (2001) Advanced spin-valve GMR head. Fujitsu Sci Tech J 37:174–182
188. Gubin SP (2009) Magnetic nanoparticles. WILEY-VCH Verlag GmbH & Co. KGaA, Weinheim
189. Abraham DW, Trouilloud PL, Worledge DC (2006) Rapid-turnaround characterization methods for MRAM development. IBM J Res Dev 50:55–67. doi:10.1147/rd.501.0055
190. Sun S (2006) Recent advances in chemical synthesis, self-assembly, and applications of FePt nanoparticles. Adv Mater 18:393–403. doi:10.1002/adma.200501464
191. Parkin SSP, Roche KP, Samant MG, Rice PM, Beyers RB, Scheuerlein RE, O'Sullivan EJ, Brown SL, Bucchigano J, Abraham DW, Lu Y, Rooks M, Trouilloud PL, Wanner RA, Gallagher WJ (1999) Exchange-biased magnetic tunnel junctions and application to nonvolatile magnetic random access memory (invited). J Appl Phys 85:5828–5833. doi:10.1063/1.369932
192. Kaka S, Russek SE (2002) Precessional switching of submicrometer spin valves. Appl Phys Lett 80:2958–2960. doi:10.1063/1.1470704
193. CIL DA, Alves SG, Dieny B (2016) Multilevel thermally assisted magnetoresistive random-access memory based on exchange-biased vortex configurations. Phys Rev Applied 6:024015. doi:10.1103/PhysRevApplied.6.024015
194. Nishimura N, Hirai T, Koganei A, Ikeda T, Okano K, Sekiguchi Y, Osada Y (2002) Magnetic tunnel junction device with perpendicular magnetization films for high-density magnetic random access memory. J Appl Phys 91:5246–5249. doi:10.1063/1.1459605
195. Prejbeanu IL, Kula W, Ounadjela K, Sousa RC, Redon O, Dieny B, Nozières J-P (2004) Thermally assisted switching in exchange-biased storage layer magnetic tunnel junctions. IEEE Trans Magn 40:2625–2627. doi:10.1109/TMAG.2004.830395
196. Cui P, Seo S, Lee J, Wang L, Lee E, Min M, Lee H (2011) Nonvolatile memory device using gold nanoparticles covalently bound to reduced graphene oxide. ACS Nano 5:6826–6833. doi:10.1021/nn2021875
197. Bergmann CP, De Andrade MJ (2011) Nanostructured materials for engineering applications. Springer, Berlin, Heidelberg. doi:10.1007/978-3-642-19131-2
198. Olveira S, Forster SP, Seeger S (2014) Nanocatalysis: academic discipline and industrial realities. J Nanobiotechnol 2014:1–19. doi:10.1155/2014/324089
199. Yamada Y, Tsung C-K, Huang W, Huo Z, Habas SE, Soejima T, Aliaga CE, Somorjai GA, Yang P (2011) Nanocrystal bilayer for tandem catalysis. Nat Chem 3:372–376. doi:10.1038/nchem.1018
200. Wu L, Mendoza-garcia A, Li Q, Sun S (2016) Organic phase syntheses of magnetic nanoparticles and their applications. Chem Rev 116:10473–10512. doi:10.1021/acs.chemrev.5b00687
201. Gawande MB, Goswami A, Asefa T, Guo H, Biradar AV, Peng D, Zboril R, Varma RS (2015) Core–shell nanoparticles: synthesis and applications in catalysis and electrocatalysis. Chem Soc Rev 44:7540–7590. doi:10.1039/C5CS00343A
202. Chen F, Chen Q, Fang S, Sun Y, Chen Z, Xie G, Du Y (2011) Multifunctional nanocomposites constructed from Fe_3O_4–Au nanoparticle cores and a porous silica shell in the solution phase. Dalton Trans 40:10857–10864. doi:10.1039/c1dt10374a
203. Zhao M, Deng K, He L, Liu Y, Li G, Zhao H, Tang Z (2014) Core–shell palladium nanoparticle@metal–organic frameworks as multifunctional catalysts for cascade reactions. J Am Chem Soc 136:1738–1741. doi:10.1021/ja411468e

204. Walker JM, Zaleski JM (2016) A simple route to diverse noble metal-decorated iron oxide nanoparticles for catalysis. Nanoscale 8:1535–1544. doi:10.1039/C5NR06700F
205. Sun Z, Li H, Cui G, Tian Y, Yan S (2016) Multifunctional magnetic core-shell dendritic mesoporous silica nanospheres decorated with tiny Ag nanoparticles as a highly active heterogeneous catalyst. Appl Surf Sci 360:252–262. doi:10.1016/j.apsusc.2015.11.013
206. Ke F, Wang L, Zhu J (2014) Multifunctional Au-Fe_3O_4@MOF core-shell nanocomposite catalysts with controllable reactivity and magnetic recyclability. Nanoscale 7:1201–1208. doi:10.1039/C4NR05421K
207. Wen X, Qiao X, Han X, Niu L, Huo L, Bai G (2015) Multifunctional magnetic branched polyethylenimine nanogels with in-situ generated Fe_3O_4 and their applications as dye adsorbent and catalyst support. J Mater Sci 51:3170–3181. doi:10.1007/s10853-015-9627-3
208. Bruix A, Neyman KM (2016) Modeling ceria-based nanomaterials for catalysis and related applications. Catal Lett 146:2053–2080. doi:10.1007/s10562-016-1799-1
209. Gawande MB, Goswami A, Felpin F-X, Asefa T, Huang X, Silva R, Zou X, Zboril R, Varma RS (2016) Cu and Cu-based nanoparticles: synthesis and applications in catalysis. Chem Rev 116:3722–3811. doi:10.1021/acs.chemrev.5b00482
210. Meiklejohn WH, Bean CP (1957) New magnetic anisotropy. Phys Rev Lett 105:904–913. doi:10.1103/PhysRev.105.904
211. Danan H, Gengnagel H, Steinert J, Linzen A (1971) Exchange coupling investigations on epitaxial deposited and superficially oxidized co and ni monocrystalline films. J Phys Colloques 32:C1-131–C1-133. doi:10.1051/jphyscol:1971142
212. Mauri D, Siegmann HC, Bagus PS, Kay E (1987) Simple model for thin ferromagnetic films exchange coupled to an antiferromagnetic substrate. J Appl Phys 62:3047–3049. doi:10.1063/1.339367
213. Kiwi M (2001) Exchange bias theory. J Magn Magn Mater 234:584–595. doi:10.1016/S0304-8853(01)00421-8
214. Kiwi M, Mejía-López J, Portugal RD, Ramírez R (2000) Positive exchange bias model: Fe/FeF2 and Fe/MnF2 bilayers. Solid State Commun 116:315–319. doi:10.1016/S0038-1098(00)00333-1
215. Kiwi M, Mejía-López J, Portugal RD, Ramírez R (1999) Exchange bias model for Fe/FeF2: role of domains in the ferromagnet. Europhys Lett 48:573–579. doi:https://doi.org/10.1209/epl/i1999-00522-9
216. Geshev J (2000) Analytical solutions for exchange bias and coercivity in ferromagnetic/antiferromagnetic bilayers. Phys Rev B - Condens Matter Mater Phys 62:5627–5633. doi:10.1103/PhysRevB.62.5627
217. Kim J-V, Stamps RL, McGrath BV, Camley RE (2000) Angular dependence and interfacial roughness in exchange-biased ferromagnetic/antiferromagnetic bilayers. Phys Rev B 61:8888–8894. doi:10.1103/PhysRevB.61.8888
218. Morup S (1985) Spin-flop in antiferromagnetic microcrystals. Surf Sci 156:888–892. doi:10.1016/0039-6028(85)90263-8
219. Fulcomer E, Charap SH (1972) Thermal fluctuation aftereffect model for some systems with ferromagnetic-antiferromagnetic coupling. J Appl Phys 43:4190–4199. doi:10.1063/1.1660894
220. Malozemoff AP (1988) Mechanisms of exchange anisotropy (invited). J Appl Phys 63:3874–3879. doi:10.1063/1.340591
221. Imry Y (1984) Random external fields.J. Stat Phys 34:849–862. doi:10.1007/BF01009444
222. Malozemoff AP (1987) Random-field model of exchange anisotropy at rough ferromagnetic-antiferromagnetic interfaces. Phys Rev B 35:3679–3682. doi:https://doi.org/10.1103/PhysRevB.35.3679
223. Imry Y, Ma S-K (1975) Random-field instability of the ordered state of continuous symmetry. Phys Rev Lett 35:1399–1401. doi:10.1103/PhysRevLett.35.1399
224. Meiklejohn WH (1962) Exchange Anisotropy—A Review. J Appl Phys 33:1328. doi:10.1063/1.1728716

225. Nowak U, Misra A, Usadel KD (2001) Domain state model for exchange bias. J Appl Phys 89:7269–7271. doi:10.1063/1.1358829
226. Misra A, Nowak U, Usadel KD (2003) Control of exchange bias by diluting the antiferromagnetic layer. J Appl Phys 93:6593–6595. doi:10.1063/1.1543880
227. Misra A, Nowak U, Usadel KD (2004) Structure of domains in an exchange-bias model. J Appl Phys 95:1357–1363. doi:10.1063/1.1638888
228. Miltényi P, Gierlings M, Keller J, Beschoten B, Güntherodt G, Nowak U, Usadel KD (2000) Diluted antiferromagnets in exchange bias: proof of the domain state model. Phys Rev Lett 84:4224–4227. doi:10.1103/PhysRevLett.84.4224
229. de Wijs GA, Fang CM, Kresse G, de With G (2002) First-principles calculation of the phonon spectrum of $MgAl_2O_4$ spinel. Phys Rev B 65:94305. doi:10.1103/PhysRevB.65.094305
230. Beckmann B, Nowak U, Usadel KD (2003) Asymmetric reversal modes in ferromagnetic/antiferromagnetic multilayers. Phys Rev Lett 91:187201. doi:10.1103/PhysRevLett.91.187201
231. Suess D, Kirschner M, Schrefl T, Scholz W, Dittrich R, Forster H, Fidler J (2003) Micromagnetic calculations of bias field and coercivity of compensated ferromagnetic antiferromagnetic bilayers. J Appl Phys 93:8618–8620. doi:10.1063/1.1557859
232. Kirschner M, Suess D, Schrefl T, Fidler J, Chapman JN (2003) Micromagnetic calculation of bias field and coercivity of polycrystalline ferromagnetic/antiferromagnetic layers. IEEE Trans Magn 39:2735–2737. doi:10.1109/TMAG.2003.815580
233. Lederman D, Ramírez R, Kiwi M (2004) Monte Carlo simulations of exchange bias of ferromagnetic thin films on FeF_2(110). Phys Rev B 70:184422. doi:10.1103/PhysRevB.70.184422
234. van Driel J, De Boer FR, Lenssen KMH, Coehoorn R (2000) Exchange biasing by $Ir_{19}Mn_{81}$: dependence on temperature, microstructure and antiferromagnetic layer thickness. J Appl Phys 88:975–982. doi:10.1063/1.373764
235. Kai-cheng Z, Bang-gui L (2009) Unified nonequilibrium dynamical theory for exchange bias and training effects. Chenese Phys B 18:3960–3965. doi:10.1088/1674-1056/18/9/056
236. Iglesias O, Labarta AA, Batlle X (2008) Exchange bias phenomenology and models of core-shell nanoparticles. J Nanosci Nanotechnol 8:2761–2780. doi:10.1166/jnn.2008.015
237. Lemos CGO, Figueiredo W, Santos M (2015) Exchange bias for core-shell magnetic nanoparticles. Phys A Stat Mech its Appl 433:148–160. doi:10.1016/j.physa.2015.03.073
238. Vasilakaki M, Eftaxias E, Trohidou KN (2008) Monte Carlo study of the exchange bias and the training effect in nanoparticles with core-shell morphology. Phys Status Solidi Appl Mater Sci 205:1865–1871. doi:10.1002/pssa.200723671
239. Eftaxias E, Vasilakaki M, Trohidou KN (2007) A Monte Carlo study of the exchange bias effects in magnetic nanoparticles with ferromagnetic core/antiferromagnetic shell morphology. Mod Phys Lett B 21:1169–1177. doi:10.1142/S0217984907013870
240. Evans RFL, Bate D, Chantrell RW, Yanes R, Chubykalo-Fesenko O (2011) Influence of interfacial roughness on exchange bias in core-shell nanoparticles. Phys Rev B Condens Matter Mater Phys 84:092404. doi:10.1103/PhysRevB.84.092404
241. Wu MH, Li QC, Liu J-M (2007) Monte Carlo simulation of size, random field and temperature dependences of exchange bias in a core-shell magnetic nanoparticle. J Phys Condens Matter 19:186202. doi:10.1088/0953-8984/19/18/186202

Chapter 8
Role of Magnetic Nanoparticles in Providing Safe and Clean Water to Each Individual

Ekta Roy, Santanu Patra, Paramita Karfa, Rashmi Madhuri, and Prashant K. Sharma

8.1 Introduction

Environmental pollution is one of the greatest problems facing the world today. It is increasing with every passing year and causing grave and irreparable damage to the earth. Environmental pollution consists of five basic types of pollution, most commonly air, water, soil, noise, and light. Because of these kinds of pollution, the temperature of the environment increases daily, which is causing unusually warm weather, ocean warming, a rise in sea levels, coastal flooding, warming of Arctic and Antarctic zones, changes in air patterns, and others. These consequences of pollution have created serious health hazards.

Among all basic needs, water is one of the basic requirements for sustaining life, the main essential fluid on which all life depends but now a days due to our activity it has changed to global garbage cans, **i.e.,** ***water pollution.***

With the evolution of human civilization, the purity of pure drinking water has undergone dramatic changes. Water is recognized as a symbol for the origin of life and for its medicinal value; originally, it was not designated as a carrier of diseases. In the seventeenth century, Anton van Leeuwenhoek's discovery of the microscope opened a new door in the field of purity: humans were empowered to see beyond suspended particles, for example, tiny material particles, to microorganisms. The discoveries of Louis Pasteur in the study of microorganism-based diseases and

E. Roy • S. Patra • P. Karfa • R. Madhuri (✉)
Department of Applied Chemistry, Indian Institute of Technology (Indian School of Mines), Dhanbad, Jharkhand, 826 004, India
e-mail: rshmmadhuri@gmail.com

P.K. Sharma
Functional Nanomaterials Research Laboratory, Department of Applied Physics, Indian Institute of Technology (Indian School of Mines), Dhanbad, Jharkhand, 826 004, India

© Springer International Publishing AG 2017

S.K. Sharma (ed.), *Complex Magnetic Nanostructures*,
DOI 10.1007/978-3-319-52087-2_8

those of John Snow in identifying the cause of the spread of cholera in London revealed that the quality of drinking water was changing [1]. Thus, the era of water purification had begun.

Along with industrialization and urbanization came water pollution, and according to the World Health Organization (WHO), around 1.8 million people die every year due to diseases caused by water pollution, for example, typhoid, diarrhea, and hepatitis. Water pollution is a primary cause of death mostly in developing countries as a result of unsafe water supplies, inadequate sanitation, and deficient hygiene. The WHO also reports that 1.1 billion people living in rural areas are not able to access sufficiently clean water [2]. Modern society is growing very fast but because of these developments, we have contaminated not only the surface water but groundwater as well. As a result, both water used for daily nondrinking needs and drinking water sources are becoming highly contaminated.

8.1.1 Causes of Water Pollution

In ancient times, water resources contained natural contaminants, particularly inorganic contaminants that arise from natural phenomena like water flows, volcanoes, and anthropogenic pollution [3]. In general, groundwater is comparatively more protected from pollution than surface waters. Groundwater becomes contaminated mainly as a result of human activities like discharges from industrial premises and sewage or runoff from agricultural land and hard surfaces such as roads [3]. There is also the possibility of leakage of chemicals from industry and slurries from intensive farm units that can contain pathogens. In some countries, poorly sited latrines and septic tanks are a significant source of contamination, especially of wells.

In short, there are so many ways to contaminate drinking water and groundwater that we do not even notice them, and contaminated water is not only toxic but sometimes lethal for humans and all living beings. Normal human activities are worse for nature than the greatest nuclear accidents in history.

Many regulatory bodies, such as the U.S. Environmental Protection Agency (USEPA), WHO, and the European Union (EU), have played a key role in developing regulations for many toxic species found in drinking water. The most common and chemical species responsible for water pollution are as follows (Fig. 8.1):

- Metal ions: cadmium, copper, lead, mercury, nickel, zinc, arsenic
- Nutrients: phosphate, ammonia, nitrate, nitrite
- Dyes used in industry: methylene blue (MB), rhodamine
- Biological materials: algae, viruses, bacteria, parasites
- Miscellaneous: cyanide, phenols and organic compounds, antibiotics

Therefore, it is essential to control the harmful effects of contaminants and improve the quality and quantity of fresh, clean water. In this regard, the purification of drinking water, treatment of sewage water, and protection of natural resources are among the urgent and challenging issues for government and researchers.

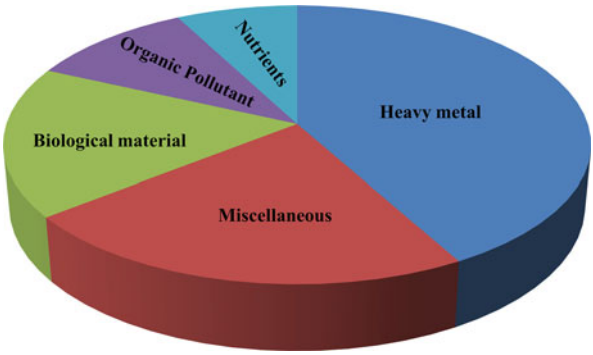

Fig. 8.1 Pie chart showing distribution of various water contaminants

8.1.2 Water Purification and Nanomaterials

Water contaminants exist either in dissolved forms or industrial effluents or in suspended forms as in sediments and surface and ground waters. Traditionally, dissolved contaminants have been removed from water sources by adsorption on activated carbon [4], ion exchange [5], and solvent extraction [6]. Common techniques used to remove suspended contaminants include pumping and treating, in situ adsorption on activated carbon, bioremediation, and stabilization and solidification [7]. In recent years, several methods have been proposed or used to make water clean and hygienic, for example, like adsorption, separation processing, photocatalytic oxidation, and bioremediation [7]. However, they have not been fully functional or adopted because of several restrictions, specifically restrictions related to efficiency, mode of operation, energy requirements, and, lastly, the methods' economic importance. The most popular of these techniques is the adsorption of contaminants on activated carbon, but this process suffers from mass transfer limitations, issues of bacterial growth, channeling, and difficulty in regeneration. In the case of sediment structures, carbon is often left behind in matrices being treated, which risks rerelease of adsorbed contaminants and the migration of contaminant-laden carbon to new areas. Given that carbon is concentrated in contaminants, the risk of rerelease is much greater than the risk posed by the initial contamination.

Nowadays, from the standpoint of resource preservation and environmental remediation, nanomaterials have been proposed as a very efficient, low cost, non-hazardous, and environmentally friendly alternative treatment. The highly efficient, modular, and multifunctional processes facilitated by nanomaterials could be used to provide pure drinking water treatment solutions [8]. Nanosized materials, especially nanosized ferric oxides, manganese oxides, aluminum oxides, titanium oxides, carbon-based material, magnesium oxides, and cerium oxides, are considered promising materials for use in the treatment and purification of water [9]. Nanomaterials possess a large surface-area-to-volume ratio caused by the size quantization effect, resulting in extraordinary optical, magnetic, and electrical properties [9]. Recent studies suggest that nanomaterials exhibit very favorable sorption properties

with respect to toxic materials present in water in terms of a high adsorption capacity and selectivity, which would result in effective and efficient removal of toxic materials. The application of nanomaterials for environmental remediation, though in its infancy, has great potential for remediating sites and effluents in a cost-effective manner.

As an alternative to existing remediation techniques, magnetic nanoparticles (MNPs) have attracted the attention of researchers and industrialists in connection with their role in water purification and treatment. Their superiority to activated carbon lies in the fact that they offer a high surface-area-to-volume ratio because of their nanosize [10]. In addition, they do not suffer from the limitations common to porous structures because the entire surface area lies outside the particles [10]. Furthermore, under external magnetic field gradients, the complete removal of particles from their medium of application is possible. Unlike activated carbon, which is left behind in the environment, it is now possible to isolate contaminant-rich adsorbents. These versatile MNPs can be applied to both treat effluents and remediate sediment matrices.

The greatest advantage of this process is that the net volume of disposal waste is reduced by concentrating contaminants from a large dilute volume to a small concentrated volume.

The advantages of using this alternative nanotechnology compared to existing methods are that it involves low-cost chemicals and magnets, can be implemented in a continuous manner for treating waste streams or as an in situ technique for remediating sediments, provides for the almost complete recovery of adsorbents owing to its magnetic properties, and it can be target specific. Additionally, MNPs can be reused after the contaminant has been stripped off. Though the proposed magnetic nanotechnology is applicable to both sediments and waste streams, the focus of this chapter is largely on the purification of drinking water. The general protocol used for the purification or treatment of water using MNPs is shown in Fig. 8.2.

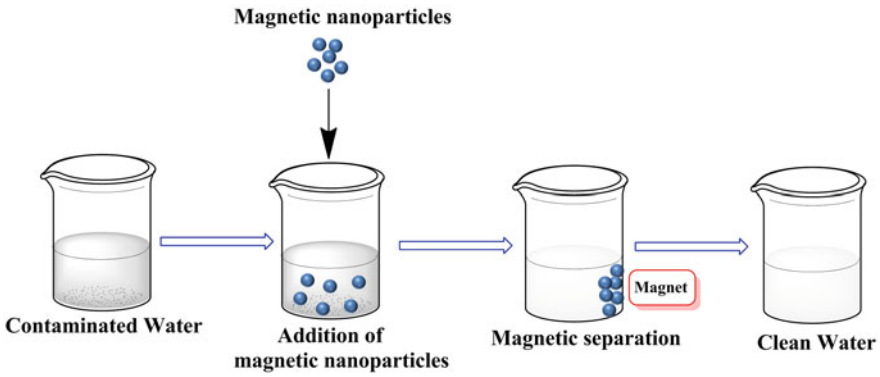

Fig. 8.2 General protocol for water purification using magnetic nanoparticles

Based on the applicability and worldwide application of MNPs in the field of water purification and treatment, several review articles have been published to compile the large world of MNPs in a small space. In 2010, Ambashta and Sillanpaa published a good review of water purification using magnetic materials [11]. In the same year, Xu et al. and Crane et al. published two reviews on the use of iron oxide nanomaterials in wastewater treatment [10] and water treatment technology based on nano zero-valent iron (nZVI) particles [12]. Recently, Fu et al. published a review on groundwater remediation and wastewater treatment using an nZVI particle [8]. Recent years have witnessed a surge of interest in the synthesis and use of MNPs due to their size in the nano range, high surface-area-to-volume ratios, large removal capacity, fast kinetics, and superparamagnetism. In addition to these properties, MNPs have a low toxicity, chemical inertness, and biocompatibility, which hold tremendous potential in combination with biotechnology. Magnetism is a unique physical property that independently helps in water purification by influencing the physical properties of contaminants in water. In addition, its combination with other processes enables an improvised efficient purification technology. MNPs, such as Fe_3O_4, and modified MNPs are good candidates as absorption materials in light of their main advantages [13]:

- The particles can be produced in large quantities using a simple method;
- They generally have a high adsorption capacity because of their large surface area;
- They have strong magnetic properties and low toxicity;
- Particles are superparamagnetic, which means a metal-laden sorbent can be easily separated from treated water via an external magnetic field.

Since most water pollutants are nonmagnetic, it is favorable that MNPs can be combined with pollutants efficiently and be collected rapidly and thoroughly following agglomeration with pollutants owing to their high ferromagnetism.

8.2 Magnetic Nanoparticles

In general, ferrite colloids, magnetite (Fe_3O_4), maghemite (γ-Fe_2O_3), and hematite (α-Fe_2O_3) are the most common and popular MNPs, which have so far received considerable attention in the fields of water purification and wastewater treatment [10]. Ferrite colloids are characterized by a spinel crystalline structure with oxygen ions forming a close-packed cubic lattice and iron ions located at the interstices. The magnetization of Fe_3O_4 arises from antiferromagnetic coupling (superexchange through oxygen) between Fe^{3+} ions in octahedral and tetrahedral interstices, making the magnetic moments of Fe^{2+} ions (in octahedral positions) responsible for the magnetization of the unit cell [10]. MNPs can be synthesized by physical, chemical, and biological methods. The physical methods [14, 15] include gas-phase deposition and electron beam lithography; the chemical methods include wet chemical preparation methods, such as sol−gel synthesis [16], oxidation method

[17], chemical coprecipitation [18], hydrothermal reactions [19], flow injection synthesis [20], electrochemical method [21], aerosol/vapor-phase method [22], sonochemical decomposition reactions [23], supercritical fluid method [24], and synthesis using nanoreactors [25]; and the biological methods comprise microbial methods [26]. Although the resulting MNPs are stable enough in their solid state and have various applications in such fields as catalysis and sensing, the major problem associated with MNPs is their poor stability in aqueous medium and high tendency toward aggregation. Naked MNPs are generally unstable in strong acidic solutions and undergo leaching, which strongly limits their reusability and reduces the lifetime of such materials. The large ratio of surface area to volume leads to another limitation, the aggregation of particles, and thus a minimization of their surface energy occurs owing to the strong magnetic attractions between particles, which limits their dispersion in aqueous solutions and matrices. The exposure of proteins/enzymes to such interfaces would result in a decrease or loss of activity. To enhance the stability of MNPs, several modifications to them have been reported using the following materials (Fig. 8.3):

- Surfactants, such as oleic acid, lauric acid, alkyl sulphonic acids, and alkyl phosphonic acids;

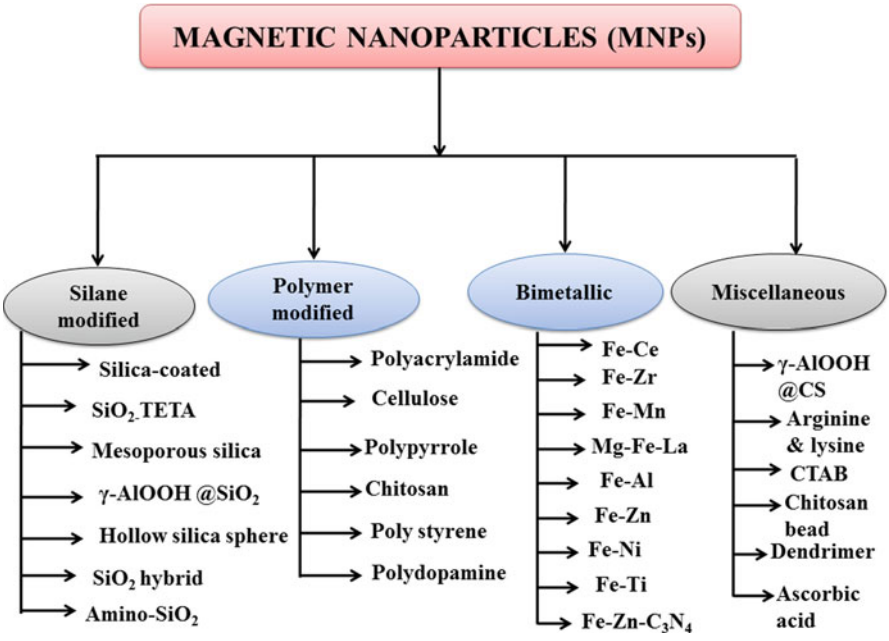

Fig. 8.3 Flowchart for different modifications of magnetic nanoparticles used for water purification

- Various polymers, such as polyethylene glycol, polyvinyl pyrrolidone, poly(ethylene-co-vinyl acetate), poly(lactic-co-glycolic acid), and polyvinyl alcohol (PVA), which have been used as coating materials in aqueous suspension;
- Natural dispersants, including gelatin, dextran, polylactic acids, starch, albumin, liposomes, chitosan, and ethyl cellulose;
- Silane compounds;
- Carbonaceous materials.

These techniques not only optimize the surface properties, such as biocompatibility, dispersibility, and biodegradability, of MNPs, they also provide an environment for the transferal of hydrophobic iron oxide nanoparticles to a hydrophilic system [27]. In this chapter we aim to assemble all aspects and roles of differentially modified MNPs in water purification and wastewater treatment. The chapter concludes with recent investigations on the issue of nanotoxicity and its implications for the future.

8.2.1 Removal of Heavy-Metal Ions

Metals are introduced mainly in aquatic systems as a result of the weathering of soils and rocks, from volcanic eruptions, and from a variety of human activities involving the mining, processing, or use of metals or substances that contain metal pollutants. The most common heavy-metal pollutants include zinc, arsenic, mercury, lead, and chromium. In this section we will discuss various modified MNPs and their role in the removal of heavy-metal ions. The role of MNPs in the removal of heavy-metal ions is summarized in the Table 8.1.

8.2.1.1 Silane-Modified MNPs

Surface silanization is undoubtedly the most widely used technique to introduce surface functional groups on bare MNPs owing to its characteristics such as satisfying responsivity, low cytotoxicity, high stability under acidic conditions, inertness to redox reactions, and ease of carrying out surface chemical modification [28]. The reaction can be carried out in either aqueous media or organic solvents at moderate temperatures, and no particular conditions or expensive equipment are required; therefore, it is considered an ideal method for the protection of the inner magnetic core. Silane molecules are first activated (hydrolyzed), followed by condensation reactions occurring between the Si–OH groups of silanol and OH groups of the surface (Fig. 8.4). This leads to the formation of a stable bond on the surface [29, 30]. According to the literature, silane-modified MNPs are the most popular nanoparticles used in the removal of heavy-metal ions from water systems [28]. Herein, we list the recent silane-modified MNPs used in the removal of uranyl, arsenic, chromium ions, and others.

Table 8.1 Magnetic nanoparticles used as adsorbent for removal of heavy metal ion from water samples

Serial number	Modification	Metal ion	Adsorption capacity	Reference
1.	3-Aminopropyl triethoxysiliane@Fe_3O_4	U^{6+}	12.33 mg g^{-1}	Sadeghi et al. [27]
2.	Fe_3O_4@SiO_2	U^{6+}	52.0 mg g^{-1}	Fan et al. [134]
3.	Polyacrylamide coated-Fe_3O_4	U^{6+}	220.9 mg g^{-1}	Song et al. [42]
4.	Poly(ethylene glycol)diacrylate modified α-Fe_2O_3	As^{3+}	3.0 mg g^{-1}	Savina et al. [43]
5.	PS-Fe_3O_4	As^{3+}	139.3 mg g^{-1}	Wei et al. [44]
6.	Fe_3O_4-PDA	Cu^{2+}, Ag^{+}, Hg^{2+}	112.9, 259.1, 467.3 mg g^{-1}	Zhang et al. [45]
7.	Mesoporous iron manganese bimetal oxides	As^{3+}, As^{5+}	67.8 and 93.5 mg g^{-1}	Wen et al. [47]
8.	Fe–Mn binary oxide nanowires	As^{3+}	171.0 mg g^{-1}	Cui et al. [49]
9.	Fe(III)–Al(III)	As^{5+}	54.5 mg g^{-1}	Basu et al. [50]
10.	Fe–Zr	As^{5+}, As^{3+}	46.1 and 120.0 mg g^{-1}	Ren et al. [51]
11.	Fe–Zr	PO_4^{-}	13.65 mg g^{-1}	Long et al. [53]
12.	Fe–Zr binary oxide	Sb^{5+}	51.0 mg g^{-1}	Li et al. [54]
13.	Goethite	As^{5+}	23.47 mg g^{-1}	Veličković et al. [55]
14.	Fe-MWCNT	As^{5+}, As^{3+}	1723 and 189 mg g^{-1}	Ntim and Mitra [56]
15.	Fe_3O_4 and MnO_2 nanoparticles modified graphene oxide	As^{5+}, As^{3+}	14.0 and 12.2 mg g^{-1}	Luo et al. [58]
16.	Chitosan-functionalized MWCNTs-$CoFe_2O_4$–NH_2	Pb^{2+}	140.1 mg g^{-1}	Zhou et al. [59]
17.	Amidoximated magnetite/graphene oxide	U^{6+}	1.197 mmol g^{-1}	Zhao et al. [60]
18.	Bio-based α-Fe_2O_3 impregnated chitosan beads	As^{3+}	9.3 mg g^{-1}	Liu et al. [64]

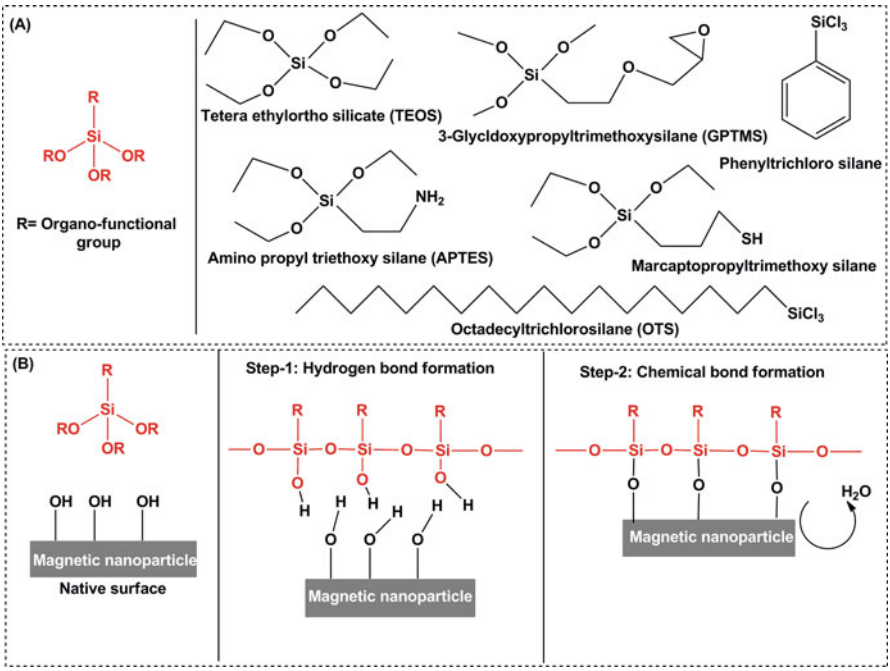

Fig. 8.4 Schematic representation showing various silanes and their interaction with magnetic nanoparticles

Uranium is a radioactive metallic element that is chemically active in its pure form. However, uranium and its compounds are highly toxic to humans and lead to kidney failure or even death. The WHO has established that the maximum uranium concentration in drinking water should be less than 15.0 $\mu g\ L^{-1}$, while this value in spring waters should be less than 20.0 $\mu g\ L^{-1}$ [27]. However, depending on the location, the level of uranium in water varies. It is difficult to determine directly the extremely low concentration of uranium in the presence of relatively high concentrations of other diverse ions. Therefore, a refined analytical method must be used to detect such low concentrations [31]. Sadeghi et al. reported on 3-aminopropyl triethoxysiliane (APTES)-coated MNPs modified with quercetin as a new solid-phase sorbent for the extraction of uranyl ions from water [27]. The absorption was explained by Langmuir isotherm, and the maximum monolayer adsorption capacity was found to be 12.33 mg g^{-1}. The synthesized sorbent was applied to the extraction of uranyl ions from different water samples. Fan and coworkers reported on the use of magnetic $Fe_3O_4@SiO_2$ composite particles to remove uranium ions from aqueous solution [28]. The experimental results were well fitted by a pseudo-second-order model and adsorption process was well described by Langmuir isotherm model and the maximum uranium sorption capacity onto magnetic $Fe_3O_4@SiO_2$ composite particles was estimated to be about 52.0 mg g^{-1} at 25 °C. The aforementioned

composite materials showed a good selectivity for uranium from aqueous solution in the presence of other interfering ions.

Another important, common, and harmful metal ion is chromium, which exists in the environment as Cr(III) and Cr(VI). The existence of a metal-ion oxidation state depends on the pH and redox conditions of the environment. Cr(III) is much less soluble and therefore less mobile than Cr(VI). Because of the greater solubility of Cr(VI), it can penetrate into plants, animals, and microorganisms, so exposure to certain levels of Cr(VI) can result in significant risks for human health [32]. Based on the significance of chromium metal ions on human health, their detection is very important, and several studies have been reported on the analysis of chromium ions in aqueous and solid samples. Prakash et al. reported on iron oxide–reduced graphene oxide hybrid materials. This material was used to detect Cr(III) in aqueous solution. The linear range of detection of Cr(III) is 0.2–2.0 nM [33]. Cui et al. reported on chitosan-modified MNPs used to detect Cr(III) and Cr(VI) in water, and the limits of detection were 0.02 and 0.03 ng mL^{-1} for Cr(III) and Cr(VI), respectively [34]. Cheng et al. reported on dithizone-modified MNPs, which used trace amounts of Cr(III) in environmental and biological samples. The linear range of detection of Cr(III) is 0.1–100.0 $\mu g\ L^{-1}$, with a limit of detection of 35.0 ng L^{-1} [35].

Arsenic (As) is a very toxic element. Pollution from As is mainly due to human activities that include the production of wood preservatives, agricultural uses such as pesticides and herbicides, and mining activity, burning coal, and copper smelting [36]. Industrial activities also contribute to As pollution. Arsenic exists in water in two main chemical forms, As(V) and As(III). The arsenite ion is more soluble in water and approximately 50 times more toxic than arsenate ions [37]. The total As level in drinking water should be below 10 ppb as established by WHO. In the literature, several works have been reported for the detection and removal of arsenite and its conversion to arsenate [37]. Saiz et al. reported a magnetic $Fe_3O_4@SiO_2$ composite nanoparticle functionalized with aminopropyl groups incorporating Fe^{3+} as adsorbents for removing arsenate from polluted groundwater. This material was easily regenerated under alkaline conditions and showed adsorption yields of arsenic of around 90% [38]. Kokate et al. reported a novel one-pot single-step synthesis of magnetite–silica nanocomposites that has various applications such as in tagging (attachment of fluorophores to rhodamine), entrapment matrices (zinc loading), and the removal of As for water purification [39].

In addition to these metal ions, other metal ions are also known for their toxic nature in the everyday life of living organisms, that is, copper, lead, cadmium, mercury, and zinc metal ions. MNPs were reported to be very effective for sensing and removing them from water samples. Mahmoud et al. have reported on nanosorbents, synthesized from the direct surface impregnation of magnetic iron oxide nanoparticles (nano-Fe_3O_4) with nano-silicon oxide (Nano-SiO_2) for the formation of (nano-Fe_3O_4–SiO_2) sorbents. They were further modified with target nitrogen donor atoms via covalent surface binding and immobilization of triethylenetetramine (TETA) for the formation of a (nano-Fe_3O_4–SiO_2–TETA) sorbent that selectively removes some heavy-metal ions such as Cu(II) and Pb(II) from water samples [40].

Wei et al. have reported on novel adsorbent γ-AlOOH (boehmite)@SiO_2/Fe_3O_4 porous magnetic microspheres with high adsorption capacity toward heavy-metal ions. The nanomaterial was found to be very useful for the simultaneous and selective electrochemical detection of five metal ions, Zn(II), Cd(II), Pb(II), Cu(II), and Hg(II), in drinking water [41].

8.2.1.2 Polymer-Modified MNPs

To increase the stability and sorption capacity of Fe_3O_4 nanoparticles, a variety of natural (e.g., cellulose, chitosan) and synthetic polymers (e.g., polyacrylamide, polydopamine, polystyrene) were also used as grafting/coating agents. Song and coworkers synthesized polyacrylamide-coated Fe_3O_4 magnetic composites applied as adsorbents to remove U(VI) from aqueous solutions and were able to separate it by a simple magnetic separation method [42]. The sorption isotherms were well fitted in the Langmuir sorption isotherm model, and the maximum sorption capacity of uranium (VI) at pH 5.0 was calculated to be 220.9 mg g^{-1}. Savina et al. reported a poly(ethylene glycol)diacrylate containing a-Fe_2O_3 and Fe_3O_4 nanoparticles prepared by cryopolymerization, and the resulting monolithic structure containing material showed a higher efficiency for the removal of As(III) from aqueous solution [43]. The experimental results revealed that the nanocomposite showed an excellent capability for the removal of trace concentrations of As(III) from solution, with a total capacity of up to 3.0 mg As/g of nanoparticles. Wei et al. [44] reported a polystyrene (PS)-supported nano-Fe_3O_4 for the removal of As from water [44]. The maximum adsorption capacity of this PS-Fe_3O_4 was 139.3 mg g^{-1}. Zhang and co-workers synthesized the polydopamine (PDA) modified MNPs (Fe_3O_4/PDA) and applied the nanomaterial for removal of multiple pollutants like methylene blue, tartrazine, Cu(II), Ag(I) and Hg(II) from water. The synthesized nanomaterial follow the Langmuir adsorption isotherm during binding study and shows the maximum capacity of 204.1, 100.0, 112.9, 259.1, and 467.3 mg g^{-1} for methylene blue, tartrazine, Cu(II), Ag(I) and Hg(II) respectively [45].

8.2.1.3 Bimetallic MNPs

Bimetallic MNPs (BMNPs) can also be used as substitutes to enhance the stability of nanoparticles. Bimetallic nanoparticles are prepared using iron as the principal metal to which a thin layer of transition metals such as palladium (Pd), copper (Cu), nickel (Ni), or platinum (Pt) is deposited by chemical reaction. Bimetallic nanoparticles have considerable potential in the removal of contaminants from water and have several potential advantages over single MNPs, such as faster reaction kinetics and slower deposition of corrosion products on the particle surface. The representative studies dealing with contaminant removal by BMNPs in water are summarized in what follows.

For example, Wen and coworkers reported on magnetic mesoporous iron cerium (MMIC) bimetallic oxides with large surface area and pore volume via a hard

template approach. The MMIC could separate As(III) very easily from water with an external magnetic field and was also proposed as a heterogeneous Fenton-like catalyst for the oxidation of As(III) [46]. The same group also synthesized mesoporous iron manganese (OMIM) bimetallic oxides via the hard template approach. The material showed excellent performance for As(III) removal owing to its large surface area and pore volume. The pH was significantly affected by the removal efficiency of As(III) and As(V), and the greatest removal occurred in acidic solutions for both As species. The adsorption isotherms for the aforementioned materials were well described by a Freundlich model, and the calculated adsorption capacities of As(III) and As(V) were 67.89 and 93.54 mg g^{-1}, respectively [47]. Kong and coworkers prepared an Fe–Mn binary oxide-laden zeolite (MFM), which was used in the removal of As from contaminated groundwater [48]. This bimetal is produced by an improved precipitation method and was easily separated from water by an external magnetic field after As adsorption. The adsorption kinetics was well fitted with a pseudo-second-order and Weber–Morris model, and this material can also be used to remove more than 99.0% As from water at a pH of 7.0. Cui et al. have also reported on magnetic porous Fe–Mn binary oxide nanowires with superior capability for the removal of As(III) from water [49]. The magnetic porous Fe–Mn binary oxide nanowires with an initial Fe:Mn molar ratio of 1:3 exhibited the highest absorption capacity for As(III), and the maximum adsorption capacity value was found to be 171.0 mg g^{-1} at pH 7.0. Basu and coworkers reported on agglomerated iron(III)–aluminum(III) mixed oxide nanoparticles (NIAO) for As(V) adsorption in the presence/absence of some common ions [50]. This nanomaterial showed the highest As(V) adsorption efficiency, 54.5 mg g^{-1} at pH = 7.0 and 30 °C. This nanocomposite was able to detect As(V) in a qualitative and quantitative way in groundwater. Ren and coworkers have reported on an Fe–Zr bimetallic type nanoparticle that was used as an adsorbent material for the removal of As from drinking water [51]. This adsorbent material was easily prepared using a coprecipitation method and shows the maximum adsorption for As(V) and As(III), 46.1 and 120.0 mg g^{-1}. Fu et al. reported on iron/aluminum (Fe/Al) bimetallic nanoparticles that are highly efficiency in the removal of Cr(VI) from aqueous solution [52]. The particles showed high stability and high removal efficiency for Cr(VI) in acidic, neutral, and alkaline solutions. Long et al. reported on a magnetic Fe–Zr binary oxide as adsorbent for removing phosphate from aqueous solution [53]. The specific surface area of the reported material was 106.2 m^2 g^{-1}. The result presented here follows pseudo-second-order kinetics and was well executed using a Langmuir isotherm model. The maximum adsorption capacity was found to be 13.65 mg g^{-1} at a pH value of 4.0. Additionally, the magnetic Fe–Zr binary oxide adsorbent could be regenerated using a 0.1 M NaOH solution as eluent, and the adsorption capacity reached as high as 66.7% of the original adsorption capacity after the fifth cycle. Li and coworkers synthesized an Fe–Zr binary oxide adsorbent

by the coprecipitation method that was able to remove antimonate [Sb(V)] from water [54]. The material showed a maximum adsorbent capacity of 51.0 mg g^{-1} at pH 7.0 with an initial Sb(V) concentration of 10.0 mg L^{-1}.

8.2.1.4 Magnetic Nanoparticles Modified with Carbonaceous Nanomaterials

Recently carbonaceous nanomaterials, like carbon nanotubes (CNTs) [single-walled (SWCNTs) and multiwalled carbon nanotubes (MWCNTs)], graphene, and others, were investigated as promising adsorbents for various organic pollutants and metal ions thanks to their large surface area, hollowness, and layered structure. They can be easily modified by chemical treatment to increase their adsorption capacity. To increase the unique surface property of the aforementioned carbonaceous nanomaterials, their modification with inorganic nanoparticles has been reported, in which MNPs are the most common materials. The modification of MNPs with carbonaceous nanomaterials not only increases the surface property but also enhances the adsorptive capacity and lifetime of prepared nanocomposites.

Veličković and coworkers [55] reported on ethylenediamine-functionalized MWCNTs laden with iron(III) oxide in goethite form, and these adsorbent materials were used to adsorb As from drinking water [55]. The adsorption procedure for As(V) was described by a pseudo-second-order kinetic model, and adsorption data were best fitted in the Langmuir adsorption isotherm model; the maximum adsorption capacity for As (V) was found to be 23.47 mg g^{-1}. Ntim and Mitra [56] reported the removal of trace-level arsenic from drinking water using an iron oxide (Fe-MWCNT) hybrid as a sorbent [56]. The Fe-MWCNT was effective in arsenic removal below standard drinking water levels of 10.0 μg L^{-1}. The absorption capacity of the aforementioned composite was 1723.0 μg g^{-1} and 189.0 μg g^{-1} for As(III) and As(V), respectively. Vadahanambi et al. reported a highly versatile and one-pot microwave route for the production of 3D graphene–CNT–iron oxide nanostructures for the efficient removal of arsenic from contaminated water [57]. Here, a unique 3D nanostructure shows that CNTs were stood vertically on graphene sheets and MNPs were tinted on both the graphene and CNTs. The material with MNPs showed excellent absorption performance toward arsenic removal from contaminated water due to its high surface-to-volume ratio and open pore network of the graphene–CNT–iron oxide 3D nanostructures. Similarly, a nanocomposite of graphite oxide (GO), MNPs, and manganese dioxide (MnO_2) nanoparticles was synthesized by Luo et al. using a coprecipitation method [58]. The nanocomposite was used for the removal of both As(III) and As(V) from water samples, and their maximum adsorption capacity for As(III) and As(V) was found to be 14.04 and 12.22 mg g^{-1}, respectively. Zhou and coworkers reported on MWCNTs coated with magnetic amino-modified $CoFe_2O_4$ ($CoFe_2O_4$–NH_2) nanoparticles via a simple one-pot polyol method. This MNP composite was further modified with chitosan (CTS) to obtain a chitosan-functionalized MWCNT-$CoFe_2O_4$–NH_2 hybrid material [59]. The adsorption of tetrabromobisphenol A was well represented by

the Freundlich isotherm model, and the absorption of Pb(II) was better described by the Langmuir model. This composite material showed maximum adsorption capacities for both tetrabromobisphenol A and Pb(II) of 42.48 and 140.1 mg g^{-1}, respectively. Zhao et al. reported on amidoximated modified magnetite/graphene oxide composites for the removal of uranium from wastewater and seawater. The sorption isotherm agreed well with the Langmuir model, and the maximum sorption capacity was found to be 1.197 mmol g^{-1} at pH = 5.0 and a temperature of 298 K [60].

Fu et al. reported on a water-dispersible MNP–graphene oxide (MGO) composite that was applied to remove selenium ions [both Se (IV) and Se (VI)] in an aqueous system [61]. They showed that for 1.0 g L^{-1} of metal ions the MGO showed >99.9% removal percentage for Se (IV) and approximately 80% for Se (VI) within 10 s. This material can be separated effectively under an external magnetic field and recycled for reuse in water treatment. Cong et al. reported on a facile one-step approach for the fabrication of macroscopic graphene/iron oxide hydrogels with 3D interconnected networks under the synergistic effects of the self-assembly of GO sheets. Metal oxide nanoparticles such as FeOOH nanorods and magnetic Fe_3O_4 nanoparticles were simultaneously in situ deposited on graphene sheets. This induced metal nanoparticles to act as a reducing agent to reduce the GO sheets under mild conditions. In this case, the compositions of graphene hydrogels could be easily changed by adjusting the pH value of the initial GO suspension with other conditions remaining constant. Low-cost graphene/metal oxide hydrogels exhibit an excellent capacity for the removal of heavy-metal ions and oils from water [62].

8.2.1.5 Molecularly Imprinting Polymer–Modified MNPs

Molecularly imprinted polymers (MIPs) containing tailor-made recognition sites exhibit the ability to rebind a target molecule with high specificity and selectivity in preference to analogous compounds. To fabricate specific binding sites, the copolymerization of functional and cross-linking monomers around a template molecule in a suitable porogenic solution is first conducted, which creates a 3D polymeric matrix. When the template is removed from the polymeric matrix by extraction or chemical reaction, a cavity is created in the polymer matrix that is highly specific and selective for the target analog. The schematic representation for the synthesis of MIPs is shown in Fig. 8.5.

Due to its high specificity and selectivity, as well as favorable thermal, mechanical, and chemical stability, MIPs have been widely used as artificial receptors in various applications, for example, solid-phase extraction [29], chromatography separation [63], and chemical sensing [30]. Additionally, they are also very popular in the field of environmental analysis or pollutant detection owing to their high selectivity and specificity toward their template molecules. It has been reported that nanosized MIPs perform better for the removal of organic pollutants from environmental samples at trace levels because their small particle sizes and high specific surface area could produce a large adsorption capacity and fast adsorption rate [30]. To further increase their adsorption capacity and removal efficiency, MNPs

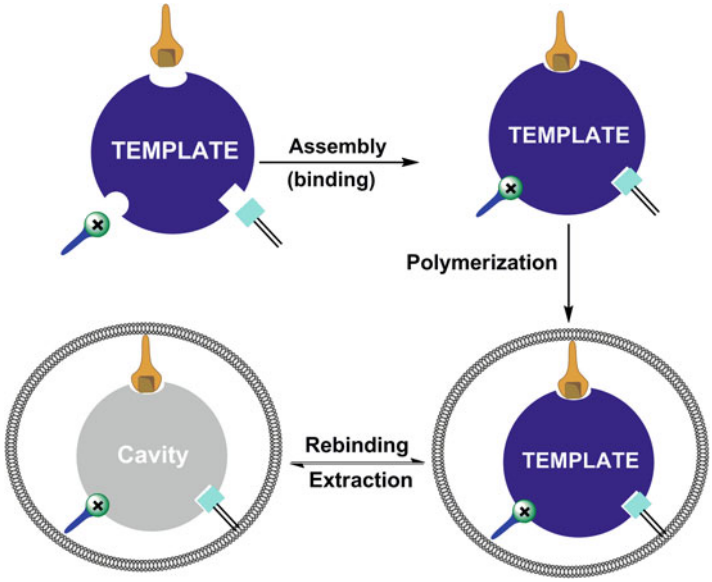

Fig. 8.5 Schematic representation showing synthesis procedure of molecularly imprinting polymer

have been incorporated into MIPs. Several works have reported on the combination of MIPs with MNPs to detect and remove pollutants and heavy-metal ions from water samples. Liu and coworkers reported on As(III)-imprinted bio-based α-Fe_2O_3 impregnated chitosan beads for the adsorption and removal of As(III) ions from aqueous solutions [64]. The kinetic data, obtained at the optimum pH of 5, could be fitted with a pseudo-second-order equation and the adsorption process could be well described by Langmuir adsorption isotherms. The maximum adsorption capacity calculated from the Langmuir equation was found to be 9.355 mg g^{-1}. Roy et al. have reported on the novel synthesis of reduced GO dendrite kind of nanomaterial that was used to detect europium metal ions in water [30]. The same research group also reported on the synthesis of GO and silane-modified MNP-based dendritic monomers for the synthesis of Eu(III)-imprinted polymers. This Eu(III)-imprinted polymer was developed on vinyl group–modified silica fiber and used as a substrate for solid-phase microextraction. The modified fiber was used for the extraction or separation of Eu(III) from the soil of coal-mining areas and the removal of Eu(III) contamination from wastewater [29].

8.2.1.6 Nanoscale Zero-Valent Iron

Since 1991, the nanoscale zero-valent iron (Fe^0 or nZVI) has been known for the removal of toxic metal ions like Pb(II), As(III), Cr(VI), Ni(II), Cu(II), and Co(II) [8], owing to their ability to reduce them, either directly or indirectly. Iron is present

in the environment in their most stable (thermodynamically) oxide form. But, in normal conditions, the nZVI is not very stable and is easily oxidized. The reduction of metal-ion contaminants involves several steps, and the prescribed pathways are given as follows [12, 65]:

1. By the direct reduction of metal ions at the surface of nZVI,
2. By catalytic reduction via Fe(II) at corrosion product surfaces,
3. By adsorption onto the surface of corrosion products.

It has been reported in the literature that nZVI have a core and shell type structure [66] in which the core is made up of metallic iron (α-Fe) and the shell is formed by oxides and hydroxides, resulting from the oxidation of iron. Here, the core is responsible for the reduction of metal ions. As the contaminants is reduced, the core becomes oxidized and several other reactants like iron (II), its oxides, and hydroxides, are produced [67]. On the one hand, iron oxides help to prevent contaminants from migrating to the core; on the other hand, they also form an electroconductive layer for better electron flow/migration [67]. Therefore, many research groups have reported the synthesis of differentially modified nZVI and explored their role in water purification and wastewater management. Torrey and coworkers reported nZVI mixed matrix membranes for water treatment applications. Upon oxidation of metallic iron to iron oxide hydroxide, FeO(OH), particles, a significant transformation in size and morphology had occurred. Spherical particles 100 nm in diameter are transformed into platelike crystalline particles with a hydrodynamic diameter greater than 450 nm. These nanoparticles are incorporated to the membrane at the time their synthesis and remain intact during filtration to ensure the production of safe drinking water [68]. Vernon et al. conducted a series of experiments on the interactions of nZVI and mercury (Hg) dissolved in aqueous solution [69]. Huang and coworkers reported on hybrid nZVI technology for removing selenium (Se), mercury (Hg), and nitrate from the wastewater of a coal-fired power plant. The hybrid was prepared by interaction between nZVI and magnetite or other Fe(II) species. The hybrid nZVI technology creates a self-sustaining highly reactive mixture that can achieve rapid reduction, transformation, immobilization, and mineralization of various heavy metals, oxy anions, and other impurities from aqueous streams in a neutral or near-neutral pH environment [70]. Ling et al. reported that nZVI is an effective agent for the treatment and removal of selenium (IV) from water [71]. The experimental results showed that Se(IV) was separated from water by nZVI via chemical reduction to Se(II) and Se(0). Herein, 1.3 mM selenite was quickly removed from water within 3 min using only a 5.0 g L^{-1} suspension of nZVI. Kim et al. have reported a composite of zeolite and nZVI that shows good potential to remove Pb(II) from water [72]. The surface area of the composite was found to be 80.37 m^2 g^{-1}, which was much greater than normal zeolite (1.03 m^2 g^{-1}) or nZVI (12.25 m^2 g^{-1}) alone. Moreover, 96% of the Pb(II) was removed from 100.0 mL of solution containing 100.0 mg L^{-1} Pb(II) within 140 min of mixing with 0.1 g composite material. Almeelbi and Bezbaruah have used nZVI particles for the removal of phosphate from aqueous solution [73]. They reported that the efficiency of the nZVI in phosphate removal was found to

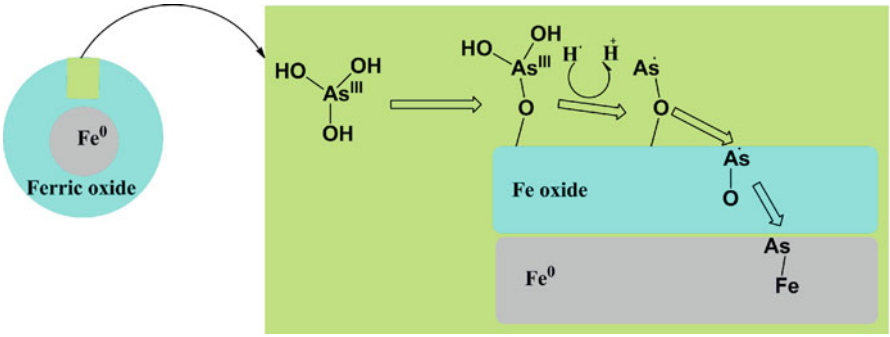

Fig. 8.6 Proposed reaction mechanism for removal of As(III) using nano zero-valent iron (nZVI)

be 13.9 times higher than micro-ZVI particles at the same concentration. Su et al. reported a magnetic sulfide-modified nZVI for the removal of cadmium from water [74]. Sulfide-modified nZVI had an optimal Cd(II) removal capacity of 85.0 mg g^{-1}, which was 100% higher than normal nZVI, with a 95% removal efficiency. Petala and coworkers reported a Mobil Composition of Matter No. 41 solid (MCM-41)-supported nZVI used for the removal of Cr(VI) from water [75]. The MCM-41 belongs to the M41S family and shows a regular hexagonal shaped arrangement of pores that looks like a cylinder and has a variable pore diameter in a range of 1.5–20 nm. The material shows high crystallinity as well as high thermal stability. Its large surface area (1000 m^2 g^1) as well as its high loading capacity towards metal cations, makes it ideal for catalytic applications. nZVI is also very popular in As removal owing to its specific and selective interaction with arsenic ions. The interaction mechanism of arsenic with nZVI is shown in Fig. 8.6. Thus, a number of research papers have been published on the removal and determination of different forms of arsenic using nZVI.

Zhou et al. reported on magnetic cellulose nanomaterials using nZVI for the removal of arsenite [76]. They reported that composites could be easily separated from solutions in 30 s through an external magnetic field. The experimental results showed that arsenite adsorption followed the pseudo-second-order kinetic model and Langmuir isotherm model. A maximum removal of 99.27% was observed for an initial concentration of 10.0 mg L^{-1} at pH 8.0 and an adsorbent dose of 1.0 g L^{-1}. The researchers stated that the maximum adsorption capacity of As(III) was approximately 19.93 mg g^{-1} at pH 6–7 at 25 °C. Chauhan et al. described the synthesis of chitosan/PVA/nZVI nanofibrous material that was used for the removal of As from water [77]. The experimental results showed that the aforementioned nanofiber was biodegradable and capable of removing 200.0 ± 10.0 mg g^{-1} As(V) and 142.9 ± 7.2 mg g^{-1} As(III) from aqueous solution of pH 7.0 under ambient conditions. In another work, the fabrication of nZVI nanoparticles was reported using two polymers, carboxymethyl cellulose and starch, as stabilizers [78]. The fabricated nanoparticles were able to remove both As(III) and As(V) from aqueous water samples in just 5 min. The pseudo-second-order kinetics and Langmuir

equation were followed by the adsorption phenomenon. Along with these, the maximum adsorption capacity for As(V) and As(III) was found to be 14.0 and 12.2 mg g^{-1}, respectively. Similarly, a GO-modified nanocomposite of nZVI was synthesized by Wang and coworkers for the removal of both forms of arsenic (III and V) with maximum adsorption capacities of 35.83 and 29.04 mg g^{-1} for As(V) and As(III), respectively [79].

8.2.1.7 Miscellaneous Magnetic Nanoparticles

In addition to popular methods of MNP modification, some different modifiers have also been used to enhance the stability of bare MNPs and remove heavy-metal ions from water. Zhang and coworkers synthesized Fe-coated bamboo charcoal for the removal of Pb(II) from water [80]. The material was easily synthesized by microwave-assisted reaction, and the resultant material showed an excellent porosity and absorption capacity for Pb(II). In this study, the researchers used bamboo charcoal as a low-cost supporting material for Fe oxides coated by a novel and simple synthetic approach. The proposed Fe-coated bamboo charcoal material follows the Langmuir adsorption isotherm model and showed the maximum adsorption capacity of 200.38 mg g^{-1}. Thanh and coworkers reported on a novel composite adsorbent by successfully incorporating a-MnO_2 nanorods and γ-Fe_2O_3 nanoparticles into the ball-milled expanded perlite carrier material for As(V) removal from aqueous solution [81]. The adsorption capacity of this material for As(V) was found to be highly pH dependent, and the adsorption kinetics followed the pseudo-second-order kinetic model. The Langmuir isotherm was found to be the best fitted to describe the adsorption of As(V) on both composites, and the adsorption capacity was found to be 4.64 and 7.09 mg g^{-1} for γ-Fe_2O_3- and a-MnO_2-containing adsorbents compared to 0.0025 mg g^{-1} for perlite alone, confirming that these composites retain the constituent nanomaterial properties.

Lee and coworkers fabricated unique sea-urchin-like magnetic iron oxide (mixed-Fe_2O_3/Fe_3O_4 phase) nanostructures (called u-MFN) with large surface areas (94.1 m^2 g^{-1}) and strong magnetic properties (57.9 emu g^{-1}), and the material was used in wastewater treatment [82]. The u-MFN had excellent removal capabilities with respect to the heavy-metal ions such as As(V) (39.6 mg g^{-1}), Cr(VI) (35.0 mg g^{-1}), and the organic pollutant Congo red (109.2 mg g^{-1}). Biswal et al. have reported the use of an inexpensive and natural seed based hydrogel. They have shown that natural seeds sabja (Ocimum basilicum) can absorb water to about 30 times their weight and can be easily loaded with nanoparticles of functional metal oxides such as visible light photo-catalyst N-doped TiO_2 or magnetite (Fe_3O_4). The material can be used for effective multiple water purification objectives such as efficient photocatalytic degradation of toxins or bacteria, heavy metal ion (AS^{3+}, Cr^{6+}, Pb^{2+}, Cd^{2+}) removal or simple particulate filtering [83]. Rao et al. have examined the removal of hexavalent chromium [Cr(VI)], an important groundwater pollutant, by phyto-inspired Fe^0/Fe_3O_4 nanocomposite-modified cells of Yarrowialipolytica. The maximum adsorption capacity was found to be

137.31 mg g^{-1} for a 1000.0 mg L^{-1} concentration of Cr (VI) [31]. Han and coworkers have investigated the removal of Hg(II) from water using FeS(s) with batch and continuous contact filtration systems. The results showed that in batch kinetic tests, FeS(s) was a good scavenger for Hg(II) and could rapidly remove the bulk of the Hg [84]. The material was also able to achieve complete Hg(II) removal after sufficient contact time, regardless of initial Hg concentration in the range studied (500–1250 μM).

Yuan et al. reported a new synthesis strategy for Fe_2O_3–ceramisite using sintering bentonite, iron powder, and activated carbon [85]. The materials showed a maximum removal efficiency of 17.5 and 7.4 mg g^{-1} for Pb(II) and Zn(II) at pH 5.0, respectively. Fan et al. described a nano-iron/oyster shell composite by an in situ synthesis method to detect the arsenic in wastewater [86]. The composite showed a good acid/alkali resistance and thermal endurance for the removal of As(III). Zelmanov and Semiat [87] reported iron oxide/hydroxide nanoparticles solution for removal of selenium from water [87]. The experimental results showed maximum adsorption capacities of 95.0 and 15.1 mg g^{-1} for Se(IV) and Se(VI), respectively. Cheng et al. have discussed the synthesis of MNPs by a dispersion–precipitation method involving acetone-promoted precipitation of colloidal hydrous MNPs and subsequent calcination of the precipitate at 250 °C [36]. This material was successfully used to remove arsenite from water. The experimental results showed that the adsorption obeyed pseudo-second-order kinetics and the data were well fitted in the Langmuir adsorption isotherm model, and the maximum adsorption found for arsenite was 46.5 mg g^{-1} at pH 7.0. Zhang et al. described a composite of arginine and lysine-modified Fe_3O_4 nanoparticles by a coprecipitation process used to remove trace arsenate [As(V)] from river water [88]. The modified adsorbents had maximum adsorption capacities of arginine MNPs and lysine MNPs of 29.14 and 23.86 mg g^{-1} and were found to be greater than the normal adsorption capacities found for bare MNPs (12.12 mg g^{-1}). Jing Wang and coworkers synthesized MNP-impregnated chitosan beads for the removal of As from water. It shows maximum adsorption capacities of 35.7 and 35.3 mg g^{-1} for As(V) and As(III) [89].

Jin and coworkers synthesized a cetyltrimethyl ammonium bromide–modified MNPs which has higher As(V) adsorption capacity from 7.59 to 23.07 mg g^{-1} [37]. Almost 95% of the As(V) (100.0 μg L^{-1}) was removed with 0.1 g L^{-1} modified composites within 2 min at pH 6. This composite could be regenerated with a simple alkalization–acidification process and more than 85% As(V) removal rates could be achieved even in the fifth adsorption/desorption cycle. Feng et al. reported on ascorbic acid–coated superparamagnetic iron oxide nanoparticles (SPIONs) by an environmentally friendly hydrothermal route [90]. The composite was used as an absorbent to remove As from wastewater and adsorption data well fitted in the Langmuir adsorption isotherm with a maximum adsorption capacity of 16.56 mg g^{-1} for As(V) and 46.06 mg g^{-1} for As(III).

Badruddoza et al. described novel nanoadsorbent, carboxymethyl-cyclodextrin-modified MNPs for the removal of copper ions from aqueous solution. The maximum adsorption capacity for these MNPs for Cu(II) was estimated and found

to be 47.2 mg g^{-1} at 25 °C [91]. Liu et al. reported on ethylene diamine tetracetate (EDTA)–functionalized MNPs as novel magnetic nanoadsorbents for the removal of Cu(II) from aqueous solution. Studies on the adsorption revealed that the adsorption process obeyed the pseudo-second-order kinetic model. The data were well fitted in the Langmuir adsorption isotherm model and the maximum adsorption was found to be 46.27 mg g^{-1} at pH 6.0 and 298 K [92]. Recently, a green synthesis approach was reported for the synthesis of MNPs using natural precursors. Prasad et al. described a new approach to synthesizing MNPs using the leaf extract of a mint plant (Menthaspicata L.) [93]. These green MNPs were used to remove arsenite and arsenate from aqueous solution. The sorption process fitted well with the Langmuir model and followed pseudo-second-order kinetics, and the maximum adsorption capacity of the prepared sorbent was found to be 86.53 for As(III) and 94.67 mg g^{-1} for As(V), respectively, at optimal experimental conditions.

8.2.2 *Microbial Contamination*

Contamination in drinking water by bacteria or viruses causing diarrheal disease is the most important aspect of drinking water quality. The bacteria and viruses that are mainly responsible for this type of diseases are *Escherichia coli*, *P. aeruginosa*, Salmonella, *B. subtilis*, polio virus, retro virus, and others. The common pathogenic species and their detection methods are portrayed in Fig. 8.7. Thus, in many parts of

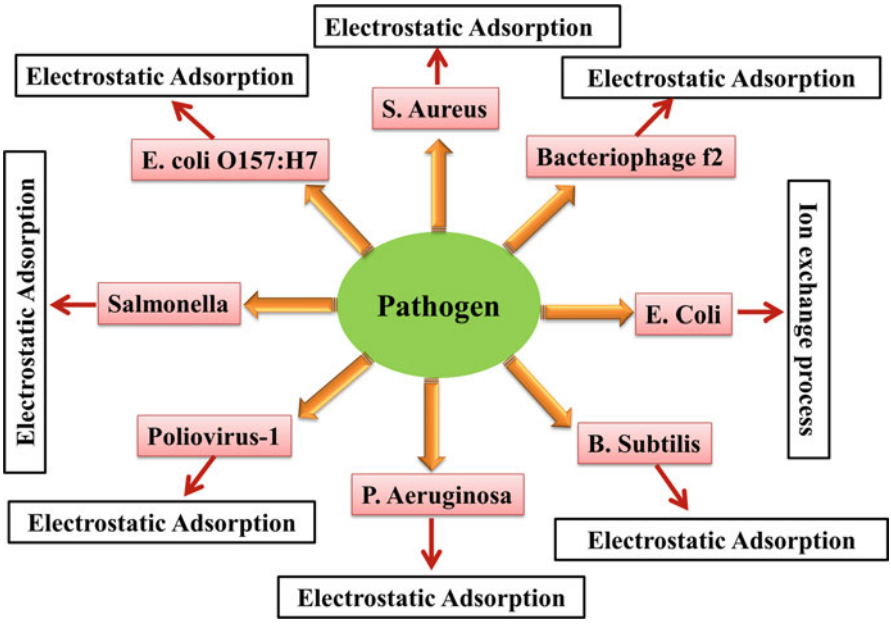

Fig. 8.7 List of popular analytical techniques used for detection of pathogens

the developing world contamination by pathogens remains a major cause of disease. It is therefore essential to prevent such pathogens from entering water sources or to treat drinking water to kill the pathogens. Many works have been published where bare or modified MNPs play an important role in the purification of drinking water from pathogens.

Zhan and coworkers synthesized aminosilane-functionalized MNPs (NH_2-MNPs) using a layer-by-layer method for the rapid removal of both pathogenic bacteria and viruses from water [94]. These prepared MNPs were able to capture a wide range of pathogens, including bacteriophage f2 and a virus (Poliovirus-1), as well as various bacteria, such as *S. aureus*, *E. coli* O157:H7, *P. aeruginosa*, Salmonella, and *B. subtilis* from wastewater. Sarika and coworkers reported on–COOH, $-NH_2$, and –SH group–modified MNPs by facile soft-chemical approaches for the removal of toxic metal ions [Cr(III), Co(II), Ni(II), Cu(II), Cd(II), Pb(II), and As(III)] and bacterial pathogens (*E. coli*) from water [95]. Depending on the surface functionality (−COOH, $-NH_2$, or –SH) magnetic nanoadsorbents can capture the different metal ions either by forming chelate complexes or undergoing an ion-exchange process or electrostatic interaction. Wei et al. have described $Ag@Fe_2O_3$–Gluyolk–shell multifunctional nanoparticles that provide a new platform for the simultaneous rapid detection of bacteria and safe decontamination treatment, which may have applications in water purification and food safety [96]. Nangmeny et al. described an Ag-modified Fe_2O_3 nanoparticle impregnated fiberglass by an aqueous hydrothermal synthetic approach [97]. The experimental results showed that the material was used to kill bacteria and viruses in water, and these new systems are less costly since a lower amount of nanoparticles is needed to achieve the same disinfection efficiency.

8.2.3 Other Widespread Water Pollutants

MNPs have been used in the purification or treatment of groundwater and wastewater contaminated with different types of materials besides heavy metals, like anions (nitrate) [98], chlorinated organic compounds [99], nitroaromatic compounds (NACs) [100], dyes [101], and phenol [102]. Recently, there has been great interest in the use of MNPs for the removal of contaminants from groundwater and wastewater, and many articles have been published recently on this topic. A summary of studies reported for removal of other water pollutants using MNPs is given in Table 8.2.

8.2.3.1 Anions as Water Contaminant

Recently, nitrate pollution in ground and surface water has become a serious problem in developing countries. The source of NO_3^- is the use of chemical fertilizers, pesticides, animal-feeding operations, petroleum products, and waste

Table 8.2 Estimation of anions, industrial dyes, pesticides, and aromatic organic contaminants using magnetic nanoparticles as adsorbent

Serial number	Material	Detection or adsorption	Adsorption capacity	Reference
1.	nZVI	Nitrate	–	Xu et al. [104]
2.	nZVI	Nitrate	–	Hwang et al. [98]
3.	Fe–Ti bimetallic oxide Fe_3O_4 particles	Fluoride	57.2 mg g^{-1}	Zhang et al. [106]
4.	γ-AlOOH@CS-MNPs	Fluoride	67.5 mg g^{-1}	Wan et al. [107]
5.	Polypyrrole (PPy)/Fe_3O_4	Fluoride	–	Bhaumik et al. [108]
6.	Mg–Fe–La tri metal composite	Fluoride	112.1 mg g^{-1}	Wang et al. [109]
7.	Fe–GAC	Bromate and perchlorate	–	Xu et al. [110]
8.	Fe^{3+}oxide/hydroxide nanoparticles	Phosphate	–	Zelmanov and Semiat [111]
9.	Chitosan MNPs	Humic acid	32.6 mg g^{-1}	Dong et al. [84]
10.	nZVI	Remazol Blue R, Acid Black 1	–	Chang et al. [118]
11.	nZVI	Acid Blue 129	–	Shirin and Balakrishnan [101]
12.	nZVI–UASB	Brilliant Red X-3B	–	Zhang et al. [119]
13.	nZVI and anaerobic sludge	Azo dye	–	Li et al. [54]
14.	Fe_3O_4@C core-shell nanoparticle	Methylene blue, Cresol red	44.3, 11.2 mg g^{-1}	Zhang and Kong [117]
15.	Fe_3O_4@HHSS	Methylene blue, Fuchsin dye	147.0, 124.6 mg g^{-1}	Zhang et al. [122]
16.	Magnetic TiO_2/montmorillonite/Fe_3O_4	Methylene blue	–	Zhang et al. [124]
17.	Graphene nanosheet-Fe_3O_4	Methylene blue	43.8 mg g^{-1}	Ai et al. [125]
18.	Polydopamine-graphene–Fe_3O_4	Methylene blue	365.3 mg g^{-1}	Han et al. [127]
19.	Fe_2O_3/MWCNTs/RGO	Rhodamine B	–	Pawer et al. [128]
20.	nZVI	2,4-Dichlorophenoxyacetic acid	–	Zhu et al. [131]
21.	Chitosan-Fe_3O_4	Carbamazepine	–	Zhang et al. [132]
22.	SPION	Tetracycline	12.1 mg g^{-1}	Dai et al. [133]
23.	Chitosan-Fe_3O_4	Alizarin red	40.1 mg g^{-1}	Fan et al. [134]
24.	Iron-polyphenol complex	Acid black 194	1.6 g g^{-1}	Wang [129]
25.	Fe_3O_4@SiO_2@TiO_2/graphene oxide	Rhodamine B	–	Chen et al. [114]
26.	$ZnFe_2O_4$−C_3N_4 hybrids	Orange II	–	Yao et al. [123]
27.	Magnetic ionic liquid modified MWCNTs	Aryloxyphenoxy-propionate	–	Luo et al. [130]
28.	nZVI	*p*-Nitrophenol	–	Nakatsuji et al. [113]

contamination through storm and urban runoff. Because of nitrate contamination, serious health problems like methemoglobinemia, carcinoma, malformation, and mutation defects have been observed. According to WHO, the minimum limit of nitrate in drinking water is 10.0 mg L^{-1} [103].

Although the chemical reduction of nitrate by MNPs was reported as early as 1964, it has not gained popularity until the last 10 years [103]. In recent years, MNPs have been intensively studied for their ability to reduce NO_3^- in water and groundwater. Nitrate can be reduced to NH_3, N_2, and NH_4^+, and iron may be oxidized to Fe^{2+}, Fe^{3+}, Fe_2O_3, or Fe_3O_4 depending on the reaction conditions. Several papers have been published where nitrate reduction was carried out using MNPs (Table 8.2). Xu et al. have reported that 95% of nitrate was rapidly removed by MNPs under strongly acidic conditions (pH < 2–3), while less than 50% of nitrate was removed at pH > 5 [104]. When Fe^{2+} is added, the reductive efficiency of nitrate by MNPs at neutral pH initially increased, accompanied by the generation of Fe_3O_4, which favored electron transfer on the surface of iron particles and accelerated the reductive denitrification rate of nitrate. Hwang and coworkers investigated the fate of nitrogen species during nitrate reduction by MNPs and related reaction mechanisms [98]. They reported that ammonia was the major product of nitrate reduction by MNPs and the nitrate was absorbed onto the surface of the nanoparticles, followed by reduction and desorption in sequential steps. On the other hand, some studies have concentrated on seeking a solution where nitrate was converted into N_2. Pan and coworkers investigated nitrate removal from solution by single (TiO_2 and Fe) and composite (Nano-TiO_2–Fe^0 composite) systems under UV illumination [105]. They found that the composite system could satisfactorily transform nitrate into N_2.

Similarly, MNPs were also used to remove fluoride contamination from drinking water. In this regard, Zhang and coworkers prepared a novel adsorbent by coating Fe–Ti bimetallic oxide on magnetic Fe_3O_4 particles by a coprecipitation method. The synthesized material was added to fluoride-containing water, and after adsorption, the material was easily separated within 2 min by an external magnet. The experimental data showed that the adsorption process should follow the Langmuir adsorption isotherm model, and the maximum adsorption capacity was found to be 57.22 mg g^{-1} [106]. Wen and coworkers synthesized a novel adsorbent of γ-AlOOH@CS (pseudoboehmite and chitosan shell) MNPs with magnetic separation capabilities to remove fluoride from drinking water, and the calculated adsorption capacity of the ACMN for fluoride was found to be 67.5 mg g^{-1} [107]. Bhaumik and coworkers prepared a polypyrrole (PPy)/Fe_3O_4 magnetic nanocomposite as a novel adsorbent via in situ polymerization of a Py monomer with $FeCl_3$ as oxidant in aqueous medium for fluoride removal from drinking water [108]. The equilibrium data were well described by Freundlich and Langmuir–Freundlich isotherm models, while the adsorption kinetics followed the pseudo-second-order model. The thermodynamic parameters confirmed the spontaneity as well as endothermic nature of the fluoride adsorption. Wang et al. described a novel Mg–Fe–La trimetal composite by coprecipitation for the removal of fluoride ions from water [109]. The adsorption process was fitted well with the Langmuir isotherm and pseudo-second-order kinetic models and showed a maximum absorption capacity of

112.17 mg g^{-1} toward fluoride. Xu and coworkers published a comparative study of nano-iron hydroxide–impregnated granular activated carbon (Fe–GAC) for bromate or perchlorate removal from water [110]. The experimental results showed that Fe–GAC exhibited a much greater removal capacity for bromate than perchlorate. Furthermore, Fe–GAC could remove bromate first through adsorption and then reduction to bromide, and it removed bromate (optimal pH 6–8) completely after 50 h. Zelmanov and Semiat [111] reported on an iron oxide/hydroxide nanoparticle–based agglomerate (AggFe) suspension that was used to remove phosphate ions from water [111]. The effect of inorganic ions on the removal of phosphate ions using AggFe, like HCO_3^-, Cl^-, and SO_4^{-2}, which were usually present in municipal and industrial wastewater, was also reported.

8.2.3.2 Aromatic Compounds

Aromatic compounds, mainly phenol and their derivatives, are common organic pollutants in water that are discharged by petrochemical and chemical companies, coking plants, oil refineries, and pharmaceutical companies. Similarly, carcinogenic organic compounds, such as chlorophenol and polychlorophenols, are produced during the chlorination process of drinking water. Waters containing aromatic compounds are highly toxic for most aquatic life and, indirectly, for humans as well. Therefore, the removal of phenol and other organic contaminants from wastewater is of central concern.

Shimizu and coworkers investigated the removal of phenol by MNPs. For this, the concentration of hydroxyl radical (•OH) was quantified via a Fenton reaction [102]. The Fenton reaction was mainly responsible for the removal of phenol. In the Fenton reaction, H_2O_2 or oxygen species (in acidic medium) reacts with Fe^{2+} and produces hydroxyl radicals (•OH) that have a strong oxidizing capability toward a variety of organic compounds:

$$Fe^0 + O_2 + 2H^+ \rightarrow Fe^{2+} + H_2O_2, \tag{8.1}$$

$$Fe^0 + H_2O_2 + 2H^+ \rightarrow Fe^{2+} + 2H_2O, \tag{8.2}$$

$$Fe^{2+} + H_2O_2 \rightarrow Fe^{3+} + \bullet OH + OH^-. \tag{8.3}$$

To reduce the presence of ferrous ions in solution, the role of nZVI was also studied by Babuponnusami et al. nZVI was used to advance the oxidation processes in Fenton reactions and remove phenol from water [112]. Nakatsuji and coworkers have also reported on nZVI to remove p-nitrophenol and its derivatives from aqueous solution [113]. Chen and coworkers have synthesized a quaternary nanocomposite of $Fe_3O_4@SiO_2@TiO_2$/graphene oxide for simultaneous adsorption and photocatalytic degradation of aromatically structured chemical pollutants [114].

Dong and coworkers prepared novel chitosan MNPs for the removal of humic acid from water using the Langmuir isotherm model, and the maximum absorption capacity was shown to be 32.6 mg g^{-1} at 25 °C [84].

8.2.3.3 Industrial Dyes

Dyes are widely used in various fields, mainly in the textile industry, and heavily implicated in water pollution. Dyes used for industrial purposes are toxic, carcinogenic, and teratogenic, and unfortunately most of them are stable and resistant to photodegradation, biodegradation, and other oxidizing agents [115, 116]. Based on their numerous advantages, such as high separation efficiency, simple manipulation process, benign operating conditions, and easy modifications, recently, magnetic nanoparticle loaded adsorbent materials have attracted special attention of the researcher for water purification [11, 117]. The reduction of nZVI in anoxic conditions has received much attention for the decolorization of the most used azo and anthraquinone dyes, and representative studies dealing with heavy-metal removal have been published. However, under anoxic conditions, the reduction of dyes by nZVI often has a low chemical oxygen demand (COD) removal ability. Numerous studies have reported that nZVI under aerobic conditions can generate strong oxidants and degrade dyes. Chang et al. reported that an nZVI/air process can decolorize remazol brilliant blue R and acid black 1 dyes more rapidly and significantly. Higher COD removals for both dyes were achieved (compared to Fenton oxidation) [118]. Shirin and coworkers have investigated the reduction of acid blue 129 dye by nZVI under aerobic conditions and identified novel reaction intermediates and products, including a genotoxic end product, 2,4,6-trimethylaniline [101].

Zhang et al. have developed an nZVI packed upflow anaerobic sludge blanket (ZVI–UASB) reactor to treat azo dye reactive brilliant red X-3B in wastewater that showed greater removal of COD and color [119]. Li et al. combined nZVI and anaerobic sludge to decolorize reactive blue 13 dyes and found that the wastewater treatment of azo dye was enhanced in an acidogenic reactor by nZVI dosing [120]. Zhang et al. have described novel magnetic Fe_3O_4@C core-shell nanoparticles as adsorbents for the removal of organic dyes such as MB and cresol red from polluted water [117]. The maximum adsorption capacities for MB and cresol red were found to be 44.38 and 11.22 mg g^{-1}, respectively. In another year, Zhang and Kong [121] examined magnetic Fe_3O_4@hierarchical hollow silica spheres (Fe_3O_4@HHSS) by a microemulsification method that had a high specific surface area, huge interior space, and robust magnetic properties. The Fe_3O_4@HHSS material showed good adsorption performance for the removal of MB from aqueous solution [121]. The same research group also developed a magnetic microsphere with an Fe_3O_4 core and a SiO_2−TiO_2 hybrid hollow shell by an aerosol process and subsequent etching treatment. This material showed maximum adsorption capacities of 147.0 mg g^{-1} for MB and 124.6 mg g^{-1} for fuchsin dye [122]. The adsorption should follow the pseudo-second-order model and the dye-saturated microspheres can be easily

recycled using an external magnet. The nanomaterial could be easily regenerated by 1–3 wt% aqueous NaOH solution. Yao et al. reported on magnetic $ZnFe_2O_4$−C_3N_4 hybrids through a simple reflux treatment of $ZnFe_2O_4$ nanoparticles (ca. 19.1 nm) with graphitic C_3N_4 sheets in methanol at 90 °C. This hybrid material exhibited stable performance without losing activity and holds promise as an application for the photo-oxidative degradation of organic contaminants [123].

Zhang et al. described a magnetic TiO_2/montmorillonite (MMT)/Fe_3O_4 nanocomposite prepared by a single-step hydrolysis method. This material showed adsorption and photocatalytic activity toward MB as contaminant. The results showed that 94% of the MB was decomposed by the aforementioned nanocomposite, and this material maintained a high degradation rate and revealed good reusability [124]. Ai et al. presented a facile one-step solvothermal method for the synthesis of a graphene nanosheet (GNS)/magnetite composite for the removal of MB from water [125] with a maximum adsorption capacity of 43.85 mg g^{-1}. Wang et al. described a magnetic hybrid nanomaterial (Fe_3O_4–MWCNT) for water purification. The prepared Fe_3O_4–MWCNT nanocomposites can be used as an effective catalyst in Fenton-like reactions for the purification of methylene blue–polluted water in a wide pH range [126]. Han et al. described polydopamine-functionalized graphene–Fe_3O_4 nanocomposites by a simple solution mixing method that has high adsorption capacities and easy separation ability. The synthesized nanocomposite was easily separated from polluted water and the adsorption capacity of these nanocomposites for MB was found to be 365.39 mg g^{-1}, which is much higher than that of graphene–Fe_3O_4 nanocomposite [127]. Pawer and coworkers synthesized an Fe_2O_3/MWCNT/RGO composite by a hydrothermal process. It exhibits photocatalytic activity in terms of the degradation of rhodamine B under visible irradiation [128]. In 2013, Wang [129] prepared iron-polyphenol complex nanoparticles (Fe−PNPs) using eucalyptus leaves. This material has an excellent adsorption−flocculation capacity and might have potential in the removal of acid black 194 from water [129]. The maximum adsorption−flocculation capacity of this material for acid black 194 has been observed at 1.6 g g^{-1} of Fe−P nanoparticles.

8.2.3.4 Pesticides

As the name suggests, pesticides are compounds used to kill pests, that is, organisms that are harmful to plants, animal, or humans. These are chemicals that are intentionally added to the environment to kill pests. They can be classified based on the type of organism they are used to kill:

1. Herbicides: used to kill weeds,
2. Insecticides: used to kill insects,
3. Fungicides: used to kill fungi,
4. Rodenticides: used to kill rodents and others.

Due to the effectiveness of these chemicals, they have become very popular in agricultural activities throughout the world. Their use is not restricted to agriculture; they are also very common in residential homes, on college campuses, in forests, and even on roadsides. As a consequence, pesticides are present in air, food, and drinks and inhaled, eaten, and drunk by all humans in the course of daily life. In the literature, several studies have been reported on the removal as well detection of pesticides from groundwater and drinking water using MNPs. The role of MNPs in the removal of such toxic materials is discussed in the next section. Mai Luo and coworkers have reported a sensitive, rapid, and environmentally friendly analysis procedure for the simultaneous detection of aryloxyphenoxy-propionate herbicides and their metabolites in water using magnetic ionic liquid–modified MWCNTs [130]. The limits of detection of herbicides and their metabolites were in a range of 2.8–14.3 and 9.8–43.2 $\mu g\ L^{-1}$, respectively. Zhu and coworkers have described nZVI particles, prepared by an in situ chemical reduction method, that were employed for 2,4-dichlorophenoxyacetic acid (2,4-D) hydrodechlorination. To do this, the researchers used a palladium/nickel foam (Pd/Ni foam) electrode [131]. The combination of electrochemistry and nZVI is a promising technology for the degradation of 2,4-D, which could control environmental pollution.

8.2.3.5 Other Toxic Chemicals

Other than these water pollutants, MNPs have also been applied to remove estradiol, aniline, phenolic estrogens, diclofenac (DFC), and carbamazepine (CBZ) from contaminated and sources of water. Zhang and coworkers reported a novel magnetic MIP based on chitosan-Fe_3O_4 for the fast separation of CBZ from water samples. This study can be regarded as a combination of selective adsorption and magnetic separation, and the obtained magnetic MIP exhibited higher specific recognition and selectivity to CBZ in the presence of various interferents [132]. Dai and coworkers have reported a novel effective technique for the preparation of MIP@SPION via atom transfer radical emulsion polymerization (ATREP). The as-prepared magnetic molecularly imprinted nanoparticles were evaluated as adsorbents for the selective recognition of tetracycline (TC) molecules from aqueous medium [133]. Fan et al. have reported a novel chitosan coating on the surface of magnetite for the adsorption and removal of alizarin red from aqueous solutions. It should follow the pseudo-second-order equation, and the adsorption process was well described by the Langmuir adsorption model. The maximum adsorption capacity was found to be 40.12 mg g^{-1} at pH 3 and 30 °C [134].

8.3 Toxicity of MNPs

The toxicity of MNPs to biological entities is highly dependent on its size and on a combination of factors related to the properties of the MNPs themselves, such as structural properties, dosage, and the intended use [135]. The chemical

composition of MNPs is naturally toxic. MNPs could elicit a cytotoxic response by interfering with the biological function of the cells but not when attached to the cell membrane [136]. However, when MNPs are attached to the surfaces of cells, they may interfere with cell surface interaction [136]. Furthermore, according to the size and shape of MNPs, they become aggregated and coagulate, which will evoke a toxic response in the physical properties like particle size, shape, and surface coating [137]. However, another issue arises when MNPs become degraded and the outcome of MNPs or MNP byproducts accumulate in various tissues and organs [137]. These degraded products are thought to react with various components of tissues or cells in the body. When MNPs enter a body, they come into direct contact with biological macromolecules such as proteins, lipids, and enzymes, which are found within biological fluids. These biological molecules interact with the surfaces of MNPs and form a complex layer over them called a *corona* [138]. The physical and chemical properties of MNPs, like surface coating, size, or functionalization, result in the formation of either a hard or weak corona [138]. When protein molecules are bound to a corona, various toxic outcomes could result. According to the literature, approximately 10–50 protein molecules could bind to the surfaces of MNPs simultaneously with high affinity [139]. The parameters affecting MNP–protein interactions include various physiochemical properties like surface properties, particle size, shape, charge, surface area, surface defects, smoothness or roughness, and functional groups of MNPs and the composition of the biological fluid [139]. The interaction of proteins with the surfaces of MNPs with different types of coatings is also an important factor when assessing in vitro toxicity. When MNPs are added to culture media, media proteins and other nutrients may be adsorbed onto the MNPs and thus be unavailable for cellular activities. In connection with the toxicity of MNPs, another effect is observed with MNPs, called *cell vision,* and was presented by Laurent et al. [140]. It occurs when the membrane constituents of cells, like proteins, sugars, and phospholipids, come into contact with MNPs. Different type of cells bind in different ways to MNPs. As a result, the binding of exogenous objects to MNPs may cause different responses and affect uptake and metabolism depending on cell type. Furthermore, another problem is posed by the sedimentation of MNPs, as this phenomenon effectively occurs when there is an apparent increase in MNP concentration at cell surfaces and so should be taken into account when performing toxicity assays [141].

8.4 Future Aspects of MNPs in Water Purification and Treatment

The application of nanotechnology to water and wastewater treatment is attracting significant attention. The unique properties of MNPs and their convergence with current treatment technologies present great opportunities to revolutionize water and wastewater treatment. The multifunctional applications of MNPs have been estab-

lished. However, the different structure of MNPs, like their micro- or nanoporous structures with nanometer SPIONs embedded within these structures, could offer alternative applications in different fields. They could be successfully applied to the remediation or treatment of drinking water, groundwater, and wastewater contaminated with chlorinated organic compounds, nitroaromatic compounds, arsenic, heavy metals, nitrate, dyes, fluoride, and phenols.

Although several aspects of MNPs were highlighted in this chapter, most of them are still at the laboratory research stage. Among them, very few are used as a guide in testing or have been commercialized. The stages in their research and development, commercial availability, the cost of nanomaterials involved, and their compatibility with the existing infrastructure will determine their full-scale application for the general population. The challenges faced in water or wastewater treatment by nanomaterials are important, but many of these challenges are only temporary, including technical handling, and high cost. To overcome these challenges, collaboration among research institutions, industry, government, and other stakeholders is essential. It is expected that advancing nanotechnology by careful handling to avoid unintended consequences can continuously provide robust solutions to water and wastewater treatment challenges.

Acknowledgments The authors are thankful to DST, BRNS, and ISM for sponsoring the research projects of Dr. Rashmi Madhuri (SERB/F/2798/2016-17, SB/FT/CS-155/2012, FRS/43/2013-2014/AC, 34/14/21/2014-BRNS) and Dr. Prashant K. Sharma (SR/FTP/PS-157/2011, FRS/34/2012-2013/APH, 34/14/21/2014-BRNS).

References

1. Thatai S, Khurana P, Boken J, Prasad S, Kumar D (2014) Nanoparticles and core–shell nanocomposite based new generation water remediation materials and analytical techniques: a review. Microchem J 116:62–76
2. WHO (2014) Progress on drinking water and sanitation. http://www.who.int/water_ sanitation_health/publications/2014/jmp-report/en/
3. Fawell J, Nieuwenhuijsen M-J (2003) Contaminants in drinking water. Br Med Bull 68: 199–208
4. Yapsakli K, Mertoglub B, Ferhan C (2010) Identification of nitrifiers and nitrification performance in drinking water biological activated carbon (BAC) filtration. Process Biochem 45:1543–1549
5. Dabrowski A, Hubicki Z, Podkoscielny P, Robens E (2004) Selective removal of the heavy metal ions from waters and industrial wastewaters by ion-exchange method. Chemosphere 56:91–106
6. Yang C, Qian Y, Zhang L, Feng J (2006) Solvent extraction process development and on-site trial-plant for phenol removal from industrial coal-gasification waste water. Chem Eng J 117:179–185
7. Bukhari AA (2008) Investigation of the electro-coagulation treatment process for the removal of total suspended solids and turbidity from municipal wastewater. Bioresour Technol 99: 914–921
8. Fu F, Dionysiou DD, Liu H (2014a) The use of zero-valent iron for groundwater remediation and wastewater treatment: a review. J Hazard Mater 267:194–205

9. Qu X, Alvarez P-JJ, Li Q (2013) Applications of nanotechnology in water and wastewater treatment. Water Res 47:3931–3946
10. Xu P, Zeng GM, Huang DL, Feng CL, Hu S, Zhao MH, Lai C, Wei Z, Huang C, Xie GX, Liu ZF (2012a) Use of iron oxide nanomaterials in wastewater treatment: a review. Sci Total Environ 424:1–10
11. Ambashta RD, Sillanpaa M (2010a) Water purification using magnetic assistance: a review. J Hazard Mater 180:38–49
12. Crane RA, Scott TB (2012) Nanoscale zero-valent iron: future prospects for an emerging water treatment technology. J Hazard Mater 211–212:112–125
13. Wu T, Pan H, Chen R, Luo D, Li Y, Wang L (2016) Preparation and properties of magnetic Fe_3O_4 hollow spheres based magnetic-fluorescent nanoparticles. J Alloys Compd 689:107–113
14. Rishton A, Lu Y, Altman RA, Marley AC, Bian Hahnes C, Viswanathan R, Xiao G, Gallagher WJ, Parkin SSP (1997) Magnetic tunnel junctions fabricated at tenth-micron dimensions by electron beam lithography. Microelectron Eng 35:249–252
15. Mathur S, Barth S, Werner U, Hernandez-Ramirez F, Romano-Rodriguez A (2008) Chemical vapor growth of one-dimensional magnetite nanostructures. Adv Mater 20:1550–1554
16. Itoh H, Sugimoto TJ (2003) Systematic control of size, shape, structure, and magnetic properties of uniform magnetite and maghemite particle. J Colloid Interface Sci 265:283–295
17. Vereda F, Rodríguez-González B, de Vicente J, Hidalgo-Álvarez RJ (2008) Evidence of direct crystal growth and presence of hollow microspheres in magnetite particles prepared by oxidation of $Fe(OH)_2$. J Colloid Interface Sci 318:520–524
18. Estévez M, Vargas S, Castaño VM, Rodríguez JR, Lobland HEH, Brostow W (2007) Novel wear resistant and low toxicity dental obturation materials. Mater Lett 61:3025–3029
19. Chen F, Gao Q, Hong G, Ni J (2008) Synthesis and characterization of magnetite dodecahedron nanostructure by hydrothermal method. J Magn Magn Mater 320:1775–1780
20. Salazar-Alvarez G, Muhammed M, Zagorodni AA (2006) Novel flow injection synthesis of iron oxide nanoparticles with narrow size distribution. Chem Eng Sci 61:4625–4633
21. Cabrera L, Gutierrez S, Menendes N, Morales MP, Herrasti P (2008) Magnetite nanoparticles: electrochemical synthesis and characterization. Electrochim Acta 53:3436–3441
22. Strobel R, Pratsinis SE (2009) Direct synthesis of maghemite, magnetite and wustite nanoparticles by flame spray pyrolysis. Adv Powder Technol 20:190–194
23. Enomoto N, Akagi J, Nakagawa Z (1996) Sonochemical powder processing of iron hydroxides. Ultrason Sonochem 3:97–103
24. Lam UT, Mammucari R, Suzuki K, Foster NR (2008) Processing of iron oxide nanoparticles by supercritical fluids. Ind Eng Chem Res 47:599–614
25. Liu JF, Lua MF, Chaia P, Fua L, Wang ZL, Cao XQ, Meng J (2007) The magnetic and structural properties of hydrothermal-synthesized single-crystal Sn1−xFexO2 nanograins. J Magn Magn Mater. 317:1–7
26. Narayanan KB, Sakthivel N (2010) Biological synthesis of metal nanoparticles by microbes. Adv Colloid Interface Sci 156:1–13
27. Sadeghia S, Azhdaria H, Arabib H, Moghaddam AZ (2012) Surface modified magnetic Fe_3O_4 nanoparticles as a selective sorbent for solid phase extraction of uranyl ions from water samples. J Hazard Mater 215–216:208–216
28. Fan F-L, Qin Z, Bai J, Rong W-D, Fan F-Y, Tian W, Wu X-L, Wang Y, Zhao L (2011) Rapid removal of uranium from aqueous solutions using magnetic $Fe_3O_4@SiO_2$ composite particles. J Environ Radioact 106:40–46
29. Patra S, Roy E, Kumar D, Madhuri R, Sharma PK (2015) Fast and selective preconcentration of europium from wastewater and coal soil by graphene oxide/silane@Fe_3O_4 dendritic nanostructure. Environ Sci Technol 49:6117–6126
30. Roy E, Patra S, Kumar D, Madhuri R, Sharma PK (2015) Multifunctional magnetic reduced graphene oxide dendrites: synthesis, characterization and their applications. Biosens Bioelectron 68:726–735

31. Rao TP, Metilda P, Gladias JM (2006) Preconcentration techniques for uranium(VI) and thorium(IV) prior to analytical determination-an overview. Talanta 68:1047–1064
32. Kotas J, Stasicka Z (2000) Chromium occurrence in the environment and methods of its speciation. Environ Pollut 107:263–283
33. Prakash A, Chandra S, Bahadur D (2012) Structural, magnetic, and textural properties of iron oxide-reduced graphene oxide hybrids and their use for the electrochemical detection of chromium. Carbon 50:4209–4219
34. Cui C, He M, Chen B, Hu B (2014a) Chitosan modified magnetic nanoparticles based solid phase extraction combined with ICP-OES for the speciation of Cr(III) and Cr(VI). Anal Methods 6:8577–8583
35. Cheng G, He M, Peng H, Hu B (2012) Dithizone modified magnetic nanoparticles for fast and selective solid phase extraction of trace elements in environmental and biological samples prior to their determination by ICP-OES. Talanta 88:507–515
36. Cheng W, Xu J, Wang Y, Wu F, Xu X, Li J (2015a) Dispersion–precipitation synthesis of nanosized magnetic iron oxide for efficient removal of arsenite in water. J Colloid Interface Sci 445:93–101
37. Jin Y, Liu F, Tonga M, Hou Y (2012) Removal of arsenate by cetyltrimethyl ammonium bromide modified magnetic nanoparticles. J Hazard Mater 227–228:461–468
38. Saiz J, Bringas E, Ortiz I (2014) New functionalized magnetic materials for As^{5+} removal: adsorbent regeneration and reuse. Ind Eng Chem Res 53:18928–18934
39. Kokate M, Garadkar K, Gole A (2013) One pot synthesis of magnetite-silica nanocomposites: applications as tags, entrapment matrix and in water purification. J Mater Chem A 1:2022–2029
40. Mahmoud ME, Abdelwaha MS, Fathallah EM (2013) Design of novel nano-sorbents based on nano-magnetic iron oxide–bound-nano-silicon oxide–immobilized-triethylenetetramine for implementation in water treatment of heavy metals. Chem Eng J 223:318–327
41. Wei Y, Yang R, Zhang YX, Wang L, Liu JH, Huang XJ (2011a) High adsorptive γ-AlOOH(boehmite)@SiO_2/Fe_3O_4 porous magnetic microspheres for detection of toxic metal ions in drinking water. Chem Commun 47:11062–11064
42. Song W, Liu M, Hu R, Tan X, Li J (2014) Water-soluble polyacrylamide coated-Fe_3O_4 magnetic composites for high-efficient enrichment of U(VI) from radioactive wastewater. Chem Eng J 246:268–276
43. Savina IN, English CJ, Whitby RLD, Zheng Y, Leistner A, Mikhalovsky SV, Cundy AB (2011) High efficiency removal of dissolved As(III) using iron nanoparticle-embedded macroporous polymer composites. J Hazard Mater 192:1002–1008
44. Wei J, Chen X, Niu Y, Pan B (2012) Spherical polystyrene-supported nano-Fe_3O_4 of high capacity and low-field separation for arsenate removal from water. J Hazard Mater 243:319–325
45. Zhang S, Zhang Y, Bi G, Liu J, Wang Z, Xu Q, Xu H, Li X (2014a) Mussel-inspired polydopamine biopolymer decorated with magnetic nanoparticles for multiple pollutants removal. J Hazard Mater 270:27–34
46. Wen Z, Zhanga Y, Dai C, Sun Z (2015) Nanocasted synthesis of magnetic mesoporous iron cerium bimetal oxides (MMIC) as an efficient heterogeneous Fenton-like catalyst for oxidation of arsenite. J Hazard Mater 287:225–233
47. Wen Z, Zhang Y, Dai C, Chen B, Guo S, Yu H, Wu D (2014) Synthesis of ordered mesoporous iron manganese bimetal oxides for arsenic removal from aqueous solutions. Microporous Mesoporous Mater 200:235–244
48. Kong S, Wanga Y, Hua Q, Olusegun AK (2014) Magnetic nanoscale Fe-Mn binary oxides loaded zeolite for arsenic removal from synthetic groundwater. Colloids Surf A Physicochem Eng Asp 457:220–227
49. Cui H-J, Caia J-K, Zhao H, Baoling Y, Ai C-L, Fu M-L (2014b) Fabrication of magnetic porous Fe–Mn binary oxide nanowires with superior capability for removal of As(III) from water. J Hazard Mater 279:26–31

50. Basu T, Gupta K, Ghosh UC (2012) Performances of As(V) adsorption of calcined (250 °C) synthetic iron(III)-aluminum(III) mixed oxide in the presence of some groundwater occurring ions. Chem Eng J 183:303–314
51. Ren Z, Zhang G, Chen JP (2011) Adsorptive removal of arsenic from water by an iron–zirconium binary oxide adsorbent. J Colloid Interface Sci 358:230–237
52. Fu F, Cheng Z, Dionysiou DD, Tang B (2015) Fe/Al bimetallic particles for the fast and highly efficient removal of Cr(VI) over a wide pH range: performance and mechanism. J Hazard Mater 298:261–269
53. Long F, Gong J-L, Zeng G-M, Chen L, Wang X-Y, Deng J-H, Niu Q-Y, Zhang H-Y, Zhang X-R (2011) Removal of phosphate from aqueous solution by magnetic Fe–Zr binary oxide. Chem Eng J 171:448–455
54. Li X, Dou X, Li J (2012) Antimony (V) removal from water by iron-zirconium bimetal oxide: performance and mechanism. J Environ Sci 24:1197–1203
55. Veličković Z, Vukovi'c GD, Marinkovi'c AD, Moldovan M-S, Peri'c-Gruji'c AA, Uskokovi'c PS, Ristic MĐ (2012) Adsorption of arsenate on iron(III) oxide coated ethylenediamine functionalized multiwall carbon nanotubes. Chem Eng J 181–182:174–181
56. Ntim SA, Mitra SJ (2011) Removal of trace arsenic to meet drinking water standards using iron oxide coated multiwall carbon nanotubes. Chem Eng Data 56:2077–2083
57. Vadahanambi S, Lee S-H, Kim W-J, Oh I-K (2013) Arsenic removal from contaminated water using three-dimensional graphene-carbon nanotube-iron oxide nanostructures. Environ Sci Technol 47:10510–10517
58. Luo X, Wang C, Luo S, Dong R, Tu X, Zeng G (2012) Adsorption of As (III) and As (V) from water using magnetite Fe_3O_4-reduced graphite oxide-MnO_2 nanocomposites. Chem Eng J 187:45–52
59. Zhou L, Ji L, Ma P-C, Shao Y, Zhang H, Gao W, Li Y (2014a) Development of carbon nanotubes/$CoFe_2O_4$ magnetic hybrid material for removal of tetrabromobisphenol A and Pb(II). J Hazard Mater 265:104–114
60. Zhao Y, Li J, Zhang S, Chen H, Shao D (2013) Efficient enrichment of uranium(VI) on amidoximated magnetite/graphene oxide composites. RSC Adv 3:18952–18959
61. Fu Y, Wang J, Liu Q, Zeng H (2014b) Water-dispersible magnetic nanoparticle–graphene oxide composites for selenium removal. Carbon 77:710–721
62. Cong H-P, Ren X-C, Wang P, Yu S-H (2012) Macroscopic multifunctional graphene-based hydrogels and aerogels by a metal ion induced self-assembly process. ACS Nano 6:2693–2703
63. Marquina C, de Teresa JM, Serrate D, Marzo J, Cardoso FA, Saurel D, Cardoso S, Freitas PP, Ibarra MR (2012) GMR sensors and magnetic nanoparticles for immuno-chromatographic assays. J Magn Magn Mater 324:3495–3498
64. Liu B, Dongfeng W, Li H, Xu Y, Zhang L (2011) As(III) removal from aqueous solution using α-Fe_2O_3 impregnated chitosan beads with As(III) as imprinted ions. Desalination 272:286–292
65. Noubactep CA (2008) A critical review on the process of contaminant removal in Fe^0–H_2O systems. Environ Technol 29:909–920
66. Li W-P, Liao P-Y, Su C-H, Yeh C-S (2014) Formation of oligonucleotide-gated silica shell-coated Fe_3O_4-Au core–shell nanotrisoctahedra for magnetically targeted and near-infrared light-responsive theranostic platform. J Am Chem Soc 136:10062–10075
67. Lu X, Li M, Tang C, Feng C, Liu X (2012) Electrochemical depassivation for recovering Fe^0 reactivity by Cr(VI) removal with a permeable reactive barrier system. J Hazard Mater 213–214:355–360
68. Torrey JD, Killgore JP, Bedford NM, Greenlee LF (2015) Oxidation behavior of zero-valent iron nanoparticles in mixed matrix water purification membranes. Environ Sci Water Res Technol 1:146–152
69. Vernon JD, Bonzongo J-CJ (2014) Volatilization and sorption of dissolved mercury by metallic iron of different particle sizes: implications for treatment of mercury contaminated water effluents. J Hazard Mater 276:408–414

70. Huang YH, Peddi PK, Tang C, Zeng H, Teng X (2013) Hybrid zero-valent iron process for removing heavy metals and nitrate from flue-gas-desulfurization wastewater. Sep Purif Technol 118:690–698
71. Ling L, Pan B, Zhang W-X (2015) Removal of selenium from water with nanoscale zero-valent iron: mechanisms of intraparticle reduction of Se(IV). Water Res 71:274–281
72. Kim SA, Kamala-Kannan S, Lee K-J, Park Y-J, Shea PJ, Lee W-H, Kim H-M, Oh B-T (2013) Removal of Pb(II) from aqueous solution by a zeolite–nanoscale zero-valent iron composite. Chem Eng J 217:54–60
73. Almeelbi T, Bezbaruah A (2013) Aqueous phosphate removal using nanoscale zero-valent iron. J Nanopart Res 14:900–914
74. Su Y, Adeleye AS, Keller AA, Huang Y, Dai C (2015) Magnetic sulfide-modified nanoscale zerovalent iron (S-nZVI) for dissolved metal ion removal. Water Res 74:47–57
75. Petala E, Dimos K, Douvalis A, Bakas T, Tucek J, Zboˇril R, Karakassides MA (2013) Nanoscale zero-valent iron supported on mesoporous silica: characterization and reactivity for Cr(VI) removal from aqueous solution. J Hazard Mater 261:295–306
76. Zhou S, Wang D, Sun H, Chen J, Wu S, Na P (2014b) Synthesis, characterization, and adsorptive properties of magnetic cellulose nanocomposites for arsenic removal. Water Air Soil Pollut 225:1945–1958
77. Chauhan D, Dwivedi J, Sankararamakrishnan N (2014) Novel chitosan/pva/zerovalent iron biopolymeric nanofibers with enhanced arsenic removal applications. Environ Sci Pollut Res 21:9430–9442
78. Mosaferi M, Nemati S, Khataee A, Nasseri S, Hashemi AA (2014) Removal of Arsenic (III, V) from aqueous solution by nanoscale zero-valent iron stabilized with starch and carboxymethyl cellulose. J Environ Health Sci Eng 12:74–85
79. Wang C, Luo H, Zhang Z, Wu Y, Zhang J, Chen S (2014a) Removal of As(III) and As(V) from aqueous solutions using nanoscale zero valent iron-reduced graphite oxide modified composites. J Hazard Mater 268:124–131
80. Zhang Z, Wang X, Wang Y, Xia S, Chen L, Zhang Y, Zhao J (2013a) Pb(II) removal from water using Fe-coated bamboo charcoal with the assistance of microwaves. J Environ Sci 25:1044–1053
81. Thanh DN, Singh M, Ulbrich P, Strnadova N, Šteˇpanek F (2011) Perlite incorporating c-Fe_2O_3 and a-MnO_2 nanomaterials: preparation and evaluation of a new adsorbent for As(V) removal. Sep Purif Technol 82:93–101
82. Lee HU, Lee SC, Lee Y-C, Vrtnik S, Kim C, Lee SG, Lee YB, Nam B, Lee JW, Park SY, Lee SM, Lee J (2013) Sea-urchin-like iron oxide nanostructures for water treatment. J Hazard Mater 262:130–136
83. Biswal M, Bhardwaj K, Singh PK, Singh P, Yadav P, Prabhune A, Rode C, Ogale S (2013) Nanoparticle-loaded multifunctional natural seed gel-bits for efficient water purification. RSC Adv 3:2288–2295
84. Dong C, Chena W, Liu C (2014) Preparation of novel magnetic chitosan nanoparticle and its application for removal of humic acid from aqueous solution. Appl Surf Sci 292:1067–1076
85. Yuan L, Liu Y (2013) Removal of Pb(II) and Zn(II) from aqueous solution by ceramisite prepared by sintering bentonite, iron powder and activated carbon. Chem Eng J 215–216: 432–439
86. Fan L, Zhang S, Zhang X, Zhou H, Lu Z, Wang S (2015) Removal of arsenic from simulation wastewater using nano-iron/oyster shell composites. J Environ Manage 156:109–114
87. Zelmanov G, Semiat R (2013) Selenium removal from water and its recovery using iron (Fe^{3+}) oxide/hydroxide-based nanoparticles sol (NanoFe) as an adsorbent. Sep Purif Technol 103:167–172
88. Zhang C, Shan C, Jin Y, Tong M (2014b) Enhanced removal of trace arsenate by magnetic nanoparticles modified with arginine and lysine. Chem Eng J 254:340–348
89. Wang J, Xu W, Chen L, Huang X, Liu J (2014b) Preparation and evaluation of magnetic nanoparticles impregnated chitosan beads for arsenic removal from water. Chem Eng J 251:25–34

90. Feng L, Cao M, Ma X, Zhu Y, Hu C (2013) Superparamagnetic high-surface-area Fe_3O_4 nanoparticles as adsorbents for arsenic removal. J Hazard Mater 217-218:439–446
91. Badruddoza AZM, Tay ASH, Tan PY, Hidajat K, Uddin MS (2011) Carboxymethyl-β-cyclodextrin conjugated magnetic nanoparticles as nano-adsorbents for removal of copper ions: synthesis and adsorption studies. J Hazard Mater 185:1177–1186
92. Liu Y, Chen M, Hao Y (2013) Study on the adsorption of Cu(II) by EDTA functionalized Fe_3O_4 magnetic nano-particles. Chem Eng J 218:46–54
93. Prasad KS, Gandhi P, Selvaraj K (2014) Synthesis of green nano iron particles (GnIP) and their application in adsorptive removal of As(III) and As(V) from aqueous solution. Appl Surf Sci 317:1052–1059
94. Zhan S, Yang Y, Shen Z, Shan J, Li Y, Yang S, Zhu D (2014) Efficient removal of pathogenic bacteria and viruses by multifunctional amine-modified magnetic nanoparticles. J Hazard Mater 274:115–123
95. Singh S, Barick KC, Bahadur D (2011) Surface engineered magnetic nanoparticles for removal of toxic metal ions and bacterial pathogens. J Hazard Mater 192:1539–1547
96. Wei Z, Zhou Z, Yang M, Lin C, Zhao Z, Huang D, Chen Z, Gao J (2011b) Multifunctional $Ag@Fe_2O_3$ yolk–shell nanoparticles for simultaneous capture, kill, and removal of pathogen. J Mater Chem 21:16344–16348
97. Nangmenyi G, Li X, Mehrabi S, Mintz E, Economy J (2011) Silver-modified iron oxide nanoparticle impregnated fiberglass for disinfection of bacteria and viruses in water. Mater Lett 65:1191–1193
98. Hwang YH, Kim DG, Shin HS (2011) Mechanism study of nitrate reduction by nano zero valent iron. J Hazard Mater 185:1513–1521
99. Dorathi PJ, Kandasamy P (2012) Dechlorination of chlorophenols by zero valent iron impregnated silica. J Environ Sci 24:765–773
100. Yin W, Wu J, Li P, Wang X, Zhu N, Wu P, Yang B (2012) Experimental study of zero-valent iron induced nitrobenzene reduction in groundwater: the effects of pH, iron dosage, oxygen and common dissolved anions. Chem Eng J 184:198–204
101. Shirin S, Balakrishnan VK (2011) Using chemical reactivity to provide insights into environmental transformations of priority organic substances: the Fe^0-mediated reduction of acid blue 129. Environ Sci Technol 45:10369–10377
102. Shimizu A, Tokumura M, Nakajima K, Kawase Y (2012) Phenol removal using zero-valent iron powder in the presence of dissolved oxygen: roles of decomposition by the Fenton reaction and adsorption/precipitation. J Hazard Mater 201–202:60–67
103. Ahn SC, Oh SY, Cha DK (2008) Enhanced reduction of nitrate by zero-valent iron at elevated temperatures. J Hazard Mater 156:17–22
104. Xu J, Hao ZW, Xie CS, Lv XS, Yang YP, Xu XH (2012b) Promotion effect of Fe^{2+} and Fe_3O_4 on nitrate reduction using zero-valent iron. Desalination 284:9–13
105. Pan JR, Huang C, Hsieh WP, Wu BJ (2012) Reductive catalysis of novel TiO_2/Fe^0 composite under UV irradiation for nitrate removal from aqueous solution. Sep Purif Technol 84:52–55
106. Zhang C, Chen L, Wang T-J, Su C-L, Jin Y (2014c) Synthesis and properties of a magnetic core–shell composite nano-adsorbent for fluoride removal from drinking water. Appl Surf Sci 317:552–559
107. Wan Z, Chen W, Liu C, Liu Y, Dong C (2015) Preparation and characterization of r-AlOOH@CS magnetic nanoparticle as a novel adsorbent for removing fluoride from drinking water. J Colloid Int Sci 443:115–124
108. Bhaumik M, Leswifi TY, Maity A, Srinivasu VV, Onyango MS (2011) Removal of fluoride from aqueous solution by polypyrrole/Fe_3O_4 magnetic nanocomposite. J Hazard Mater 186:150–159
109. Wang J, Kang D, Yu X, Ge M, Chen Y (2015) Synthesis and characterization of Mg–Fe–La trimetal composite as an adsorbent for fluoride removal. Chem Eng J 264:506–513
110. Xu J-h, Gao N-y, Zhao D-y, Yin D-q, Zhang H, Gao Y-q, Shi W (2015) Comparative study of nano-iron hydroxide impregnated granular activated carbon (Fe–GAC) for bromate or perchlorate removal. Sep Purif Technol 147:9–16

111. Zelmanov G, Semiat R (2015) The influence of competitive inorganic ions on phosphate removal from water by adsorption on iron (Fe^{+3}) oxide/hydroxide nanoparticles-based agglomerates. J Water Process Eng 5:143–152
112. Babuponnusami A, Muthukumar K (2012) Removal of phenol by heterogenous photo electro Fenton-like process using nano-zero valent iron. Sep Purif Technol 98:130–135
113. Nakatsuji Y, Salehi Z, Kawase Y (2015) Mechanisms for removal of p-nitrophenol from aqueous solution using zero-valent iron. J Environ Manage 152:183–191
114. Chen F, Yan F, Chen Q, Wang Y, Han L, Chen Z, Fang S (2014) Fabrication of Fe_3O_4@SiO_2@TiO_2 nanoparticles supported by graphene oxide sheets for the repeated adsorption and photocatalytic degradation of rhodamine B under UV irradiation. Dalton Trans 43:13537–13544
115. Qadri S, Ganoe A, Haik Y (2009) Removal and recovery of acridine orange from solutions by use of magnetic nanoparticles. J Hazard Mater 169:318–323
116. Qu S, Huang F, Yu S, Chen G, Kong J (2008) Magnetic removal of dyes from aqueous solution using multi-walled carbon nanotubes filled with Fe_2O_3 particles. J Hazard Mater 160:643–647
117. Zhang Z, Kong J (2011) Novel magnetic Fe_3O_4@C nanoparticles as adsorbents for removal of organic dyes 63-from aqueous solution. J Hazard Mater 193:325–329
118. Chang SH, Chuang SH, Li HC, Liang HH, Huang LC (2009) Comparative study on the degradation of I.C. Remazol Brilliant Blue R and I.C. Acid Black 1 by Fenton oxidation and Fe^0/air process and toxicity evaluation. J Hazard Mater 166:1279–1288
119. Zhang Y, Liu Y, Jing Y, Zhao Z, Quan X (2012) Steady performance of a zero valent iron packed anaerobic reactor for azo dye wastewater treatment under variable influent quality. J Environ Sci 24:720–727
120. Li WW, Zhang Y, Zhao JB, Yang YL, Zeng RJ, Liu HQ, Feng YJ (2013) Synergetic decolorization of reactive blue 13 by zero-valent iron and anaerobic sludge. Bioresour Technol 149:38–43
121. Zhang J, Li B, Yang W, Liu J (2014d) Synthesis of magnetic Fe_3O_4@hierarchical hollow silica nanospheres for efficient removal of methylene blue from aqueous solutions. Ind Eng Chem Res 53:10629–10636
122. Zhang H, Li X, He G, Zhan J, Liu D (2013b) Preparation of magnetic composite hollow microsphere and its adsorption capacity for basic dyes. Ind Eng Chem Res 52:16902–16910
123. Yao Y, Cai Y, Lu F, Qin J, Wei F, Xu C, Wang S (2014) Magnetic $ZnFe_2O_4-C_3N_4$ hybrid for photocatalytic degradation of aqueous organic pollutants by visible light. Ind Eng Chem Res 53:17294–17302
124. Zhang P, Mo Z, Han L, Zhu X, Wang B, Zhang C (2014e) Preparation and photocatalytic performance of magnetic tio_2/montmorillonite/Fe_3O_4 nanocomposites. Ind Eng Chem Res 53:8057–8061
125. Ai L, Zhang C, Chen Z (2011) Removal of methylene blue from aqueous solution by a solvothermal-synthesized graphene/magnetite composite. J Hazard Mater 192:1515–1524
126. Wang H, Jiang H, Wang S, Shi W, He J, Liu H, Huang Y (2014c) Fe_3O_4–MWCNT magnetic nanocomposites as efficient peroxidase mimic catalysts in a Fenton-like reaction for water purification without pH limitation. RSC Adv 4:45809–45815
127. Han X, Zhang L, Li C (2014) Preparation of polydopamine-functionalized graphene–Fe_3O_4 magnetic composites with high adsorption capacities. RSC Adv 4:30536–30541
128. Pawar RC, Choi D-H, Lee CS (2015) Reduced graphene oxide composites with MWCNTs and single crystalline hematite nano rhombohedra for applications in water purification, Int. J. Hydrogen Energy 40:767–778
129. Wang Z (2013) Iron complex nanoparticles synthesized by eucalyptus leaves. ACS Sustainable Chem Eng 1:1551–1554
130. Luo M, Liu D, Zhao L, Han J, Liang Y, Wang P, Zhou Z (2014) A novel magnetic ionic liquid modified carbon nanotube for the simultaneous determination of aryloxyphenoxy-propionate herbicides and their metabolites in water. Anal Chim Acta 852:88–96

131. Zhu K, Sun C, Chen H, Baig SA, Sheng T, Xu X (2013) Enhanced catalytic hydrodechlorination of 2,4-dichlorophenoxyacetic acid by nanoscale zero valent iron with electrochemical technique using a palladium/nickel foam electrode. Chem Eng J 223:192–199
132. Zhang Y-L, Zhang J, Daia C-M, Zhou X-F, Liu S-G (2013c) Sorption of carbamazepine from water by magnetic molecularly imprinted polymers based on chitosan-Fe_3O_4. Carbohydr Polym 97:809–816
133. Dai J, Pan J, Xu L, Li X, Zhou Z, Zhang R, Yan Y (2012) Preparation of molecularly imprinted nanoparticles with superparamagnetic susceptibility through atom transfer radical emulsion polymerization for the selective recognition of tetracycline from aqueous medium. J Hazard Mater 205-206:179–188
134. Fan L, Zhang Y, Li X, Luo C, Lu F, Qiu H (2012) Removal of alizarin red from water environment using magnetic chitosan with Alizarin Red as imprinted molecules. Colloid Surf, B 91:250–257
135. Markides H, Rotherham M, El Haj AJ (2012) Biocompatibility and toxicity of magnetic nanoparticles in regenerative medicine. J Nanomat 2012
136. Solanki A, Kim JD, Lee K-B (2008) Nanotechnology for regenerative medicine: nanomaterials for stem cell imaging. Nanomedicine 3:567–578
137. Sharifi S, Behzadi S, Laurent S, Forrest ML, Stroeve P, Mahmoudi M (2012) Toxicity of nanomaterials. Chem Soc Rev 41:2323–2343
138. Lundqvist M, Stigler J, Cedervall T (2011) The evolution of the protein corona around nanoparticles: a test study. ACS Nano 5:7503–7509
139. Yang WJ, Lee JH, Hong SC, Lee J, Lee J, Han D-W (2013) Difference between toxicities of iron oxide magnetic nanoparticles with various surface-functional groups against human normal fibroblasts and fibrosarcoma cells. Materials 6:4689–4706
140. Laurent S, Burtea C, Thirifays C, UO H, Mahmoudi M 2012 Crucial ignored parameters on nanotoxicology: the importance of toxicity assay modifications and “cell vision”. PLoS One 7(1):Article ID e29997
141. Mahmoudi M, Lynch I, Ejtehadi MR, Monopoli MP, Bombelli FB, Laurent S (2011) Protein−canoparticle interactions: opportunities and challenges. Chem Rev 111:5610–5637

Chapter 9
Magnetic Graphene Nanocomposites for Multifunctional Applications

Bhaskar Garg, Tanuja Bisht, and K.R. Justin Thomas

9.1 Introduction

Carbon, symbol C, is the 15th most abundant natural element found in the Earth's crust and the 4th most abundant element, after hydrogen, helium, and oxygen, by mass. The sun, stars, comets, and atmosphere of most planets are surrounded with profuse amounts of carbon, making carbon the chemical basis of all known life. Over the centuries, carbon allotropes, such as amorphous carbon or coal and, most familiar, graphite and diamonds, have been increasingly used for different applications. From providing energy to being the most expensive crystal ("popular among women" as well as an "the symbol of an indestructible relationship between two people") to meeting central needs in schools everywhere (in pencils), carbon does it all. The groundbreaking discoveries of buckministerfullerene (C_{60}) [1] and carbon nanotubes (CNTs) [2], with their mass scale availability and environmentally benign nature, opened up new horizons in different research areas at critical moments in time, ensuring that these carbonaceous materials will attract enormous scientific attention and that the scope of their utility will mature in the imminent carbon age. Indeed, over the last decade, the emergence of novel nanofabrication techniques and the rapid pace of research at the interface of nanotechnology and material chemistry for the development of highly efficient but practically applicable carbonaceous nanomaterials have indubitably justified earlier perspectives. Until the 20th century, the so-called carbon family had been conquered only by well-known

B. Garg (✉) • K.R. Justin Thomas
Department of Chemistry, Indian Institute of Technology Roorkee, Roorkee, 247667, Uttarakhand, India
e-mail: bhaskargarg111@gmail.com

T. Bisht
Department of Chemistry, Government Post Graduate College, Champawat, 262523, Uttarakhand, India

© Springer International Publishing AG 2017

S.K. Sharma (ed.), *Complex Magnetic Nanostructures*,
DOI 10.1007/978-3-319-52087-2_9

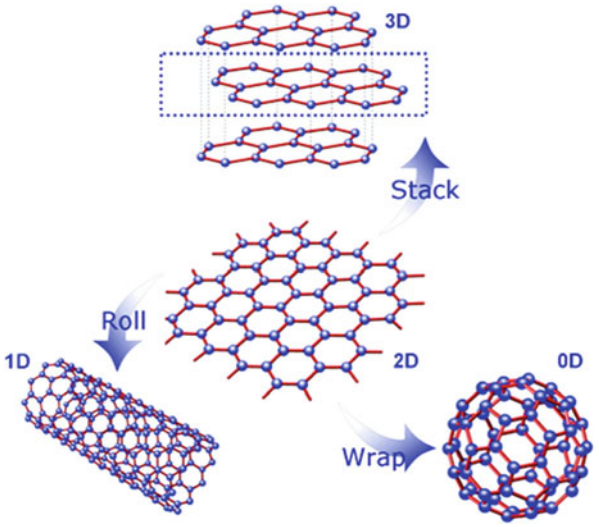

Fig. 9.1 Graphene: the basic building block for other carbon allotropes, graphite (3D), fullerene (0D), and CNT (1D). Reprinted with permission from Ref. [17]. Copyright (2012) American Chemical Society

materials like fullerenes and CNTs. However, this "aura" was lessened with the first serendipitous discovery of free-standing graphene in 2004 [3].

As a very strong and thin single-atom-thick two-dimensional (2D) sheet of sp^2-hybridized carbon atoms, graphene has become a rapidly rising star in the twenty-first century in materials science [4–6]. In a broader context, the hexagonal packed lattice structure of graphene, similar to that of a honeycomb, can be considered a potential building block of other related carbonaceous materials, namely, fullerenes (0D), CNTs (1D), and graphite (3D) (Fig. 9.1). Nevertheless, compared to its predecessor, the growing interest of scientists and researchers in graphene is mainly due to its exceptional properties such as the quantum Hall effect (QHE) [7], an ultrahigh electron mobility of approximately 200,000–250,000 $cm^2\ V^{-1}\ s^{-1}$ [8], good optical transparency of approximately 97.7% [9], a high Young's modulus of approximately 1 TPa [10], an excellent thermal conductivity of 3000–5000 $W\ m^{-1}\ K^{-1}$ [11], high physicochemical stability [12], flexibility [13], and biocompatibility [14]. Aside from these properties, graphene has a large theoretical specific surface area of 2630 $m^2\ g^{-1}$, twice that of CNTs and around 260 times larger than that of graphite [15]. Furthermore, graphene exhibits a fast electron transport property [16] with zero energy gap between the highest occupied molecular orbital (HOMO) and the lowest unoccupied molecular orbital (LUMO). Not surprisingly, therefore, in recent years, a variety of graphene-based materials have been increasingly used in optoelectronic [17], switching and information storage [18], energy conversion and storage [17, 19], photocatalysis or photovoltaic [20], biosensing [21, 22], and catalytic applications [23–28], to highlight just a few. Needless to say, an intelligent surface engineering of the graphene domain, in particular, graphene oxide (GO), plays a vital role in most of these applications [29]. For instance, the solubility (*thanks to the abundant*

hydrophilic groups on its surface) and biocompatibility of GO can be greatly enhanced after PEGylation, reducing the inherent toxicity of GO in vitro and in vivo, for biological applications [30]. Likewise, the specific high surface area of graphene or reduced graphene oxide (rGO) as well as single-layered GO further provides an outstanding opportunity to integrate them with high loadings of a variety of nanoscale structures, including, but not limited to, metal nanoparticles (NPs) (Pd, Pt, Fe, Au, and Ni) or their hybrids (Pd-Au/Ag/Ni/Pt/Fe) and metal oxides. These graphene-based nanocomposites have shown great potential in biomimetics, catalysis, and biomedical applications [20, 31–35].

Among many metal oxides, magnetite or iron oxide nanoparticles (IONPs) have emerged as promising candidates to decorate the graphene and its derivatives with improved intrinsic properties for multifunctional applications. Owing to their easy preparation, cost-effectiveness, active surface for adsorptions or immobilization, good chemical stability, facile separation by magnetic decantation [especially, in (bio)catalysis], and nontoxicity, various forms of IONPs, such as Fe_3O_4, Fe_2O_3 (iron III oxides), α-Fe_2O_3 (hematite), β-Fe_2O_3 (beta phase), and γ-Fe_2O_3 (maghemite), have been successfully deployed in the construction of magnetic graphene nanocomposites (MGNCs), which are significantly influencing current trends in heterogeneous catalysis, enzyme mimicry, bioanalytical chemistry, and molecular imaging in a more sustainable way. It is worth mentioning here that because of its poor dispersibility in water (no or fewer hydrophilic groups) and most organic solvents, a perfect graphene sheet (unlike rGO, which has some surface and edge defects) is usually chemically inert and rarely used as precursor for loadings of IONPs [36]. Nevertheless, exfoliated graphite oxide or GO has been considered as a convenient and excellent precursor for loadings of IONPs or other semiconductor NPs, using its abundant oxygen-rich surface functional groups as anchor points. In this milieu, it is critical to shed light on some important aspects of oxidation products of graphite, namely, graphite oxide and GO.

Graphite oxide was discovered as a way to measure the molecular weight of graphite. In 1859, Brodie [28, 37] heated a mixture of graphite and fuming HNO_3 in the presence of potassium chlorate. The repeated oxidations (four times) of the as-obtained product afforded the first sample of graphite oxide as a light yellow solid, which was called graphic acid, based on its dispersion behavior at different pH values. In 1958 [38], Hummers introduced $KMnO_4$ in a mixture of $NaNO_3$ and concentrated H_2SO_4, which resulted in a more heavily oxygenated form of graphite oxide. To this day, the Hummers' modified method is widely used by many researchers worldwide. Similar to that of its oxidative synthesis, the chemical structure of graphite oxide has been the subject of extensive research over the years. However, the Lerf–Klinowski (LK) model [39] of graphite oxide is the most popular one and is widely accepted in the graphene research community. As such, it is assumed that the basal plane of heavily oxygenated graphite oxide is highly populated with hydroxyl (–OH) and epoxide (C–O–C) functions, while the edge plane consists of carbonyl (C=O) and carboxylic acid (–COOH) groups. The coverage of the oxygen-rich functional groups in graphite oxide generates hole defects (nanovoids and vacancies) throughout the surface and causes it to

deviate from the state of pristine graphite [28]. Indeed, the presence of such features on the graphite oxide surface has recently been observed [40] using high-resolution transmission electron microscopy (HRTEM). Graphite oxide is chiefly composed of C, O, and H elements retaining a C/O ratio of between 1.8 and 2.5, while the most common C/O ratio for different samples is found to be approximately 2 [41, 42]. GO, an exfoliated form of graphite oxide, is an important intermediate between graphite and graphene and usually attained *via* mechanical (ultrasonication), chemical, or thermal treatment of graphite oxide. Whereas graphite oxide has a lamellar structure (consisting of layers of carbon from the original graphene lattice), GO largely exists as monolayer, bilayer, or at most a few layers (three to four) of graphene sheets. Nevertheless, despite being structurally different, both are chemically similar, having a complex cocktail of oxygen functionalities, rendering them hydrophilic in nature. As a consequence, water molecules can readily intercalate between layers, resulting in an increase of the interlayer distance and change of hybridization state (in oxidized carbons) from sp^2 (planar) to sp^3 (tetrahedral) [28]. It is commonly assumed that graphite oxide or GO, obtained by the "Hummers' modified method, contains significant Brønsted acid sites, making them an ideal candidate for acid-catalyzed reactions [28]." Furthermore, owing to the presence of oxygen-rich surface functional groups, both graphite oxide and GO can be used as powerful oxidants [23]. Consequently, GO can even oxidize Fe^{2+} into $FeCl_2$ or $FeSO_4$, leading to an in situ deposition of Fe_3O_4 NPs [magnetic NPs (MNPs) or IONPs] onto the rGO nanosheets (NSs) (owing to the self-reduction of GO into rGO) [36, 43]. The nucleation or loadings of IONPs onto the GO surface can be followed by both covalent and noncovalent interactions [44], making GO a preferred choice for use as a precursor in the synthesis of MGNCs, following different synthetic routes (as will be briefly covered later), including ex situ and in situ routes.

In this chapter, the state-of-the-art progress in the design, fabrication, and exploration of a variety of MGNCs with remarkable performances is comprehensively discussed. The aim is to cover not only synthesis, characterization, kinetics, and mechanisms, but also their potential applications in enzyme mimetics and biosensing, heterogeneous catalysis, and molecular imaging. Of note, because of certain technical restrictions, we have excluded studies and applications of MGNCs in photocatalysis [45], environmental science (adsorption and degradation or removal of dyes or organic pollutants) [46], and electrochemical energy conversion and storage [47]. Furthermore, abbreviations such as MNPs and IONPs for Fe_3O_4 NPs are not unified here, unless otherwise stated, and thus the organization of the chapter should be regarded as a flexible guide to the use of these terms. As such, the subject is broken down into the following three sections:

- MGNCs for enzyme mimics and biosensing applications (*peroxidase mimics*),
- MGNCs for catalytic applications (*carbon–carbon coupling*),
- MGNCs for biomedical applications (*molecular imaging*).

9.2 Overview of General Synthetic Routes for MGNCs

Given the size-controllable, handy, cost-effective, eco-friendly, and most large-scale synthesis of MGNCs, a variety of synthetic routes have been developed during the last decade. Most of these routes can be broadly categorized into in situ and ex situ methods. Typically, in the in situ approaches, the synthesis and decoration of IONPs on the surface of GO/rGO are performed in one step, reducing the need for any further steps. Thus far, in situ methods have appeared to provide much stronger interactions between IONPs and the graphene domain with an added advantage of uniform distribution of NPs on the carbon surface [48, 49]. On the other hand, in the ex situ approaches, the synthesis and decoration of IONPs on the surface of graphene domain are performed in individual steps [50, 51]. The hydrothermal or solvothermal [36, 52], thermal decomposition [53–55], coprecipitation, or chemical precipitation followed by thermal decomposition [56], microwave technology [57, 58], sol-gel [59], hydrolysis [60], and electrochemical approach [61] are some common methods to fabricate MGNCs that are significantly influencing nanofabrication techniques.

9.3 How We Characterize Magnetic Graphene Nanocomposites

MGNCs are small chemical entities with a large surface area, exhibiting characteristic physicochemical and biological properties that are significantly different from those of the same materials in bulk form. Consequently, the range of parameters that must be taken into account for the characterization of MGNCs is relatively large. Specifically, the shapes and sizes, preferably in the nano range (1–100 nm), of MGNCs are usually characterized by scanning electron microscopy (SEM) and TEM imaging. HRTEM, a more advanced technique, can further allow the observation of even a single NP (< 1 nm) and determine the structural morphology of both the graphene domain and decorated IONPs on its surface. Indeed, the sizes of magnetic particles on a graphene surface can significantly influence the particular application, for instance, catalysis. In general, smaller IONPs exhibit a high catalytic activity (due to the presence of a relatively large amount of catalytically active sites) compared to larger particles on the graphene surface. Aside from those of SEM and (HR)TEM, Fourier transform infrared spectroscopy (FT-IR), X-ray photoelectron spectroscopy (XPS), atomic force microscopy (AFM), X-ray diffraction (XRD), field-emission gun scanning electron microscopy and energy dispersive X-ray spectrometry (FEG-SEM-EDS), N_2 adsorption-desorption isotherms, inductively coupled plasma-atomic emission spectroscopy (ICP-AES), and Mössbauer spectroscopy, along with a superconducting quantum interference device (SQUID), are frequently used to determine the functional groups, binding energy (and oxidation state), average size diameter of NPs, crystalline phases

(along with orientation, structural properties, and atomic arrangements of NPs), morphology and particle composition, pore volume and diameter [in conjunction with Brunauer-Emmett-Teller (BET) surface area analysis], leaching of NPs, and magnetic properties of MGNCs, respectively.

9.4 Applications of Magnetic Graphene Nanocomposites

9.4.1 MGNCs for Enzyme Mimics and Biosensing Applications

Nature is the supreme engineer and the source of all inspiration. *Biomimetics*, a term coined by Otto Schmitt [62], is a highly multidisciplinary science and can be defined as

> "the study of the formation, structure, or function of biologically produced substances and materials (as enzymes or silk) and biological mechanisms and processes (as protein synthesis or photosynthesis) especially for the purpose of synthesizing similar products by artificial mechanisms which mimic natural ones."

Natural enzymes, most of which are proteins, represent linear chains of amino acids that can fold and self-assemble by making the use of multivalent interactions to produce a three-dimensional (3D) structure, a factor responsible for enzymes' specificity. Natural enzymes are delicate biocatalysts that exhibit very high catalytic activity (depending on the particular reaction) with high substrate specificity and selectivity under ambient atmospheric conditions [63, 64]. However, on exposure to relatively harsh environmental conditions, the enzyme structures unfold (denature), resulting in loss of their catalytic activity. Furthermore, the high costs involved in the preparation, purification, and storage of natural enzymes also hamper their practical utility. Consequently, artificial or human-made enzymes came into existence to overcome the shortcomings of natural enzymes [65, 66]. Artificial enzymes, a term invented by Ronald Breslow [67], is an exhilarating branch of biomimetics, which relies on the use of alternative molecules or materials to either reproduce the elusive structure of enzyme active sites or imitate the functions of natural enzymes [68–79]. Nanozymes, nanomaterials with enzyme-like personality, is an emerging research area in the field of artificial enzymes and have generated colossal scientific excitement owing to the exceptional properties of nanomaterials, including, but not limited to, an elegant response to external stimuli, specific large surface area, self-assembly capability, ease of synthesis, desirable functionalization, and, most importantly, size-dependent (overall surface charges, sizes, and shape) catalytic activities [80–83]. Intrigued by these properties, to date, researches have explored a variety of functional nanoscale materials, including carbonaceous nanomaterials, to mimic the structures and functions of various natural enzymes such as superoxide dismutase, peroxidase (POD), oxidase, catalase, and nuclease [84–89]. In the context of MGNCs, the literature is mostly limited to PODs, which is the only aspect that will be discussed here following an overview of PODs.

9.4.1.1 Overview of Peroxidases

PODs (EC 1.11.1.7), a group of oxidoreductases, belong to a family of isoenzymes and play a key role in different metabolic activities in living organisms. In general, a typical POD-catalyzed reaction involves the reduction of hydrogen peroxide (H_2O_2) or alkyl hydroperoxide with the simultaneous oxidation of an electron donor redox substrate (Scheme 9.1a). Among PODs, horseradish peroxidase (HRP) [90], isolated from the roots of perennial herb, namely, horseradish (*Armoracia rusticana*), is the most abundant isoenzyme and is frequently used for diverse applications [91]. Mechanistically, HRP functions like a ping-pong ball and bounces back and forth from an intermediate state (E*) to its standard state (E). Based on this feature, the mechanism is typically known as the ping-pong mechanism or double-displacement reaction, in which one substrate (A) is converted to the product (C) and dissociates or releases before the second substrate (B) binds to the enzyme. The overall process is shown in Scheme 9.1b. For a specific reaction, the POD-like activity of nanomaterials, for instance, MGNCs, can be evaluated by measuring the concentration of H_2O_2 using a variety of substrates such as 3,3′,5,5′-tetramethylbenzidine (TMB), 2,2′-azino-bis-(3-ethylbenzothiozoline-6-sulfonic acid) (ABTS), *o*-phenylenediamine (OPD), hydroquinone (HQ), amplex red (AR), *p*-aminophenol (PAP), 4-aminoatipyrene (4-AAP)-phenol, 1,2,3-trihydroxybenzene (THB), 3,3′-diaminobenzidine (DAB), and *N,N*-diethyl-*p*-phenylenediamine sulfate (DPD) [33]. For instance, the POD-catalyzed oxidation of TMB in the presence of H_2O_2 produces a typical blue color due to the formation of 3,3′,5,5′-tetramethylbenzidine diimine (TMBDI) (Scheme 9.1c). The rate of the reaction is usually determined by monitoring the absorbance intensity changes as a function of time followed by the determination of various kinetic parameters, namely, maximum turnover number (K_{cat}), reaction velocity (V_{max}), Michaelis–Menten constant (K_m), and double-reciprocal plots for different substrates. In an elegant work, Song et al. [89] discovered that single-layered GO can exhibit POD-like activity, similar to that of HRP. This study set a new direction and opened the door to the development of highly efficient MGNCs for their potential applications as POD nanozymes.

9.4.1.2 MGNCs as POD Nanozymes

In pioneering work, Dong et al. [92] synthesized a GO-Fe_3O_4 nanocomposite with POD-like activity by decorating Fe_3O_4 NPs onto the GO's surface. In a typical experiment, GO chips were dispersed in 1-methyl-2-pyrrolidone (NMP) by means of ultrasonication. To this suspension, tris(acetylacetonato)iron(III) was added dropwise and heated under constant stirring. The product was isolated and dried after subsequent washings with acetone. The TEM images indicated that the as-prepared GO-Fe_3O_4 contained magnetic Fe_3O_4 NPs (MNPs; 6–8 nm in size) on the surface of graphene layers, which acted as stabilizers against the fold of individual graphene sheets. The integration of GO with MNPs was evidenced by

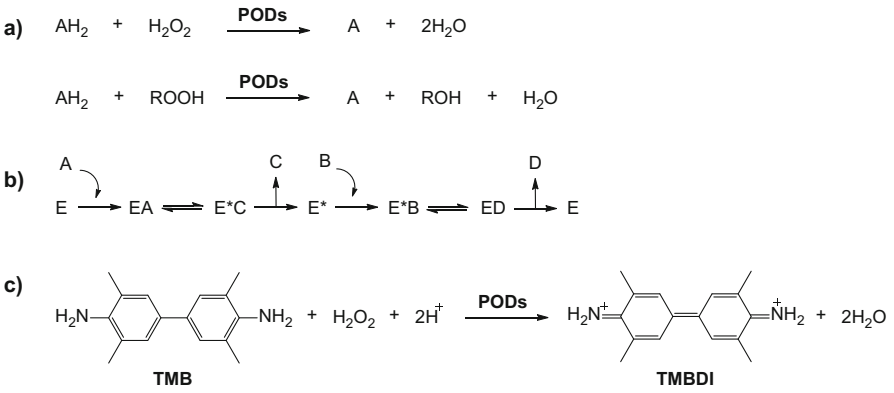

Scheme 9.1 (**a**) Representative reactions catalyzed by PODs. (**b**) Schematic of ping-pong mechanism. (**c**) Schematic for PODs-catalyzed oxidation of TMB into TMBDI, in the presence of H_2O_2

FT-IR spectrum, which showed a new absorption band at 578 cm^{-1} due to Fe-O stretching. Furthermore, the attenuated peak at 3425 cm^{-1} indicated that the –OH groups on the GO's surface were reduced completely after deposition of MNPs, while a complex formation occurred between –COOH groups of GO and iron atoms of MNPs as inferred by two new bands at 1435 and 1381 cm^{-1} in the FT-IR spectrum. The superparamagnetic behavior of GO-Fe_3O_4 was realized based on the S-like appearance of magnetization hysteresis loops as well as nearly zero magnetic coercivity or remanence. A saturation magnetization value of 16 emu g^{-1} clearly indicated that the GO-Fe_3O_4 composite could be quickly separated from the solution just by making use of an external magnet (Fig. 9.2a). The POD-like activity of GO-Fe_3O_4 was demonstrated by oxidation of TMB to TMBDI in the presence of H_2O_2. The experimental results indicated that the catalytic activity evolved from the GO-Fe_3O_4 but not due to leaching of iron ions. However, catalysis was found to be strongly dependent on pH, temperature, and concentrations of TMB, H_2O_2, and GO-Fe_3O_4, similar to HRP. The kinetic studies revealed that the K_m values of GO-Fe_3O_4 nanocomposite for H_2O_2 were 217 and 5.6 times lower than those of Fe_3O_4 NPs and bare GO, respectively, suggesting that the GO-Fe_3O_4 had a higher affinity for H_2O_2. The mechanism of GO-Fe_3O_4-induced POD catalysis was evaluated by measuring the activity of GO-Fe_3O_4 over a wide range of H_2O_2 and TMB concentrations. As shown in Fig. 9.2b, c, the parallel lines of the double-reciprocal plots suggest that the catalytic behavior of GO-Fe_3O_4 follows a typical ping-pong mechanism. Based on the intrinsic POD-like activity of GO-Fe_3O_4, a colorimetric assay was developed for the detection of H_2O_2 and glucose with respective detection limits of 0.32 and 0.74 μM. Furthermore, GO-Fe_3O_4 could exhibit a glucose selective color response even in the presence of higher concentrations of fructose, lactose, and maltose (Fig. 9.2d). The practical usability of this colorimetric assay was demonstrated to detect glucose in the urine of a diabetic person with average recoveries from 95.1 to

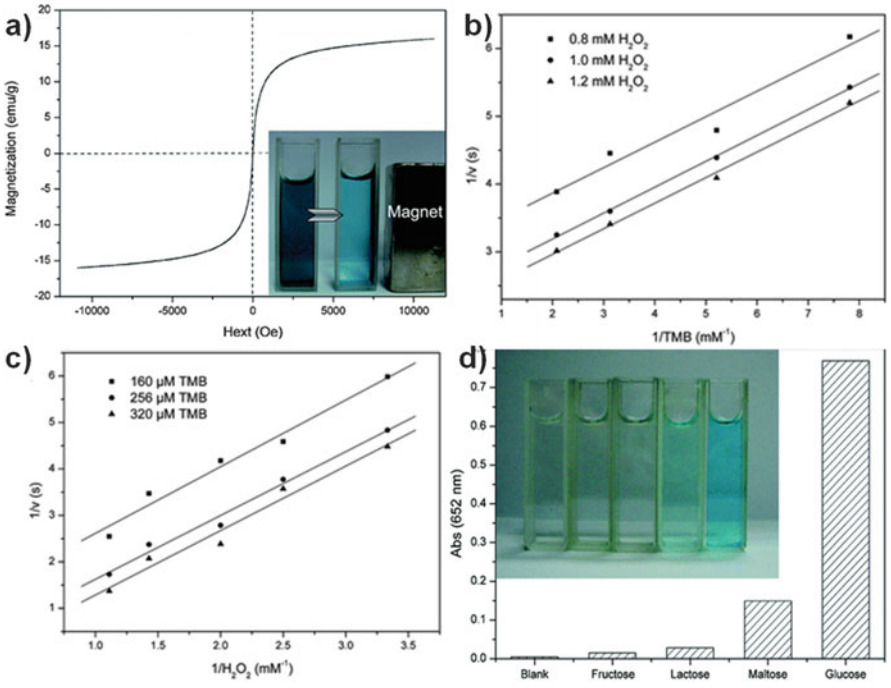

Fig. 9.2 (**a**) Magnetization curve of GO-Fe_3O_4 nanocomposites. *Inset*: image of solution before and after magnetic separation of GO-Fe_3O_4 nanocomposites. (**b**, **c**) Double reciprocal plots of activity of GO-Fe_3O_4 nanocomposite with concentration of one substrate (H_2O_2 or TMB) fixed and the other varied. The velocity (v) of the reaction was measured using 80 μg/mL GO-Fe_3O_4 nanocomposite in 5 mL of 25 mM NaH_2PO_4 with pH 4.0 at 40 °C. (**d**) Selectivity analysis for glucose detection by monitoring the absorbance at 652 nm. The analyte concentrations were as follows: 5 mM lactose, 5 mM fructose, 5 mM maltose, and 0.5 mM glucose. Inset: color change for different solutions. Reprinted with permission from Ref. [92]. Copyright (2012) Royal Society of Chemistry

104.1%. The easy preparation, facile separation, and superparamagnetic properties of the GO-Fe_3O_4 composite, along with the synergistic effects of both GO and Fe_3O_4 NPs, make it an excellent material for biochemical applications.

Hao et al. [93] demonstrated a facile method for the synthesis of cubic $CoFe_2O_4$ ferrite (CF)-rGO nanocomposite sheets (rGO-CFs) using poly(*N*-vinyl-2-pyrrolidone) (PVP)-functionalized rGO-FeOOH (rGO-IHO) as a precursor. In neutral aqueous solutions, PVP served as a stable capping agent on the surface of rGO-IHO. Owing to the capping agent and ethanol, which restrict the crystal growth of CF NPs, especially during the second step, the uniform and cubic nanostructured CF NPs on the rGO could be controlled and stabilized. It was found that even a slight change in the ethanol volume could lead to products with different morphologies. For instance, only an interconnected network with nanoplate subunits was obtained in a pure-water system. When the volume ratio of ethanol and water was increased

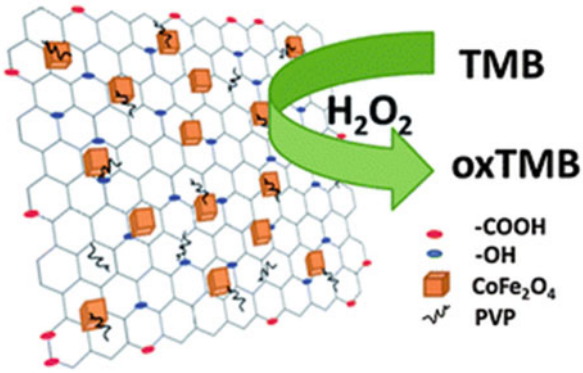

Fig. 9.3 Schematic illustration of POD-like activity of cubic $CoFe_2O_4$ ferrite-reduced graphene oxide nanocomposite sheets. Reproduced with permission from Ref. [93]. Copyright (2013) Royal Society of Chemistry

to 1:9, the resultant rGO-CFs contained only cubic NPs. With a further increase in the volume ratio (5:5), high loading of CF nanocubes onto rGO was observed, which decreased subsequently at a quite high volume ratio of 7:3. It is apparent that the formation of the cubic nanostructure in rGO-CFs depends primarily on the volume ratio of ethanol and water in the reaction system. The XRD pattern of rGO-CFs exhibited a single phase with a face-centered cubic spinel structure (JCPDS 22-1086) and high crystallinity. TEM images indicated the presence of a large quantity of uniformly distributed cubic NPs (approximately 30 nm in size) on the rGO's surface. Furthermore, lattice fringes were found perpendicular to the axis of the nanocubes, as inferred by HRTEM imaging. In acetate buffer (pH 4.0), rGO-CFs exhibited a typical POD-like activity and produced a blue color solution in the presence of a TMB-H_2O_2 system (Fig. 9.3). Under the optimized conditions, the rGO-CFs exhibited a higher catalytic efficiency, similar to that of HRP. Nevertheless, at a higher H_2O_2 concentration, the catalytic reaction failed to reach the maximum level of POD activity. A relatively larger K_m value for H_2O_2 than that of HRP was consistent with this observation. However, the rGO-CF-induced catalysis was found to be in accordance with typical Michaelis–Menten kinetics, following a ping-pong mechanism. On this basis, the rGO-CFs could be used as an effective POD-like catalyst in the colorimetric detection of H_2O_2 with a detection limit of 0.3 μM, which was found to be lower than that of bare Fe_3O_4 NPs (3 μM). Interestingly, in contrast to HRP, rGO-CFs can maintain 70% of its initial activity even after 2 h of incubation in different solvents.

Xing et al. [94] developed a 2D hybrid mesoporous Fe_2O_3-graphene nanostructure with an iron oxide content of ca. 57%. The as-obtained mFe_2O_3-G nanocomposite was well characterized by a combination of (HR)TEM, XRD, EDS, and N_2 adsorption-desorption analysis. Specifically, the TEM images of mFe_2O_3-G clearly indicated the surface coating of graphene by a thin film of Fe salt, as was also evidenced by EDS analysis. In the XRD pattern of the hybrid, all peaks could be indexed as a pure α-Fe_2O_3 (JCPDS 33-0664). The absence of a stacking peak of graphene clearly suggests that the surface coating of graphene by Fe_2O_3 can prevent them from restacking [95]. Further, the HRTEM imaging indicated the mesoporous

nature of the film. This was demonstrated by an adsorption-desorption curve, which showed a typical type IV isotherm with a type H3 hysteresis loop, which is characteristic of the presence of disordered mesopores within Fe_2O_3 film [96]. The POD-like activity of mFe_2O_3-G was examined using a TMB-H_2O_2 system. Under optimal conditions (pH 4.0, 45 °C, 500 mM H_2O_2), mFe_2O_3-G exhibited much higher activity than mFe_2O_3 and graphene itself, which is attributable to the synergistic features of both mFe_2O_3 and graphene. In particular, whereas mFe_2O_3 provides a large number of catalytically active sites (owing to the specific large surface area) and facilitates the diffusion of substrates, graphene favors the adsorption and enrichment of TMB within mesopores. Under the experimental conditions, H_2O_2 could be detected at 0.2 μM in a linear range of 0.2 to 10 μM. The protocol was further extended for the sensitive and selective detection of glucose with a detection limit of 0.5 μM, which was found to be lower than those of bare Fe_3O_4 NPs (10 μM) [97], Fe(III)-based coordination polymer (1 μM) [98], and GO-Fe_3O_4 nanocomposite (0.74 μM) [92]. The practical utility of this assay was realized by glucose detection in diluted blood serum with an estimated concentration of 6.15 mM. The mFe_2O_3-G nanocomposite exhibited good stability and could be reused (three runs) effectively in glucose biosensing.

The synergistic effect in MGNCs was also featured by Kim et al. [99] in a hybrid nanocomposite, GO_MNP-10-Pt-10 (the number represents the weight % of NPs), by integrating both MNPs and Pt NPs onto a GO surface. In a typical experiment, the deposition of catalytically active MNPs on GO was first achieved *via* the coprecipitation method. Pt NPs were subsequently incorporated onto the surface of as-obtained GO_MNP, following application of a polyol method [100]. The POD-like activity of GO_MNP-10-Pt-10 was demonstrated in conjunction with bare GO, MNPs, Pt NPs, and other GO-entrapping metal NPs such as GO_Pt-10, GO_MNP-10, GO_MNP-10/30, and GO_MNP-30-Pt-10, using TMB-H_2O_2 system. Among all nanocatalysts, the GO_MNP-10-Pt-10 exhibited the best volumetric activity (V_{max} 2180.9 nM S^{-1}), except bare Pt NPs (V_{max} 4002.2 nM S^{-1}), manifested in a color change from colorless to deep blue. The steady-state kinetic measurements suggested that the immobilization of MNPs and Pt NPs onto the GO surface substantially relieves the mass transfer limitations of NPs by the affirmative effect of GO. Since GO_MNP-10 showed only 13% V_{max} of GO_Pt-10, it is interesting to note that GO_MNP-10-Pt-10 showed 70% higher V_{max} than GO_Pt-10. This synergistic effect might be attributed to the facile electron transfer between Pt NPs and MNPs [101]. The GO_MNP-10-Pt-10 could be used to develop a sandwich-type immunoassay for colorimetric detection of target cancer cells (Fig. 9.4**,** left panel). In detail, GO_MNP-10-Pt-10 was conjugated with antibodies directed against human epidermal growth factor receptor 2 (HER2), a well-known breast cancer cell marker, using 1-Ethyl-3-(3-dimethylaminopropyl)carbodiimide-N-hydroxysulfosuccinimide (EDC-NHS) chemistry through anchored –COOH groups on the GO surface. The resultant antibody-conjugated GO_MNP-10-Pt-10 retained is original activity (>70%) and was used to detect human breast adenocarcinoma cells (SKBR-3), which overexpressed HER2, as model target cancer cells. Human melanoma cells (WM-266-4),

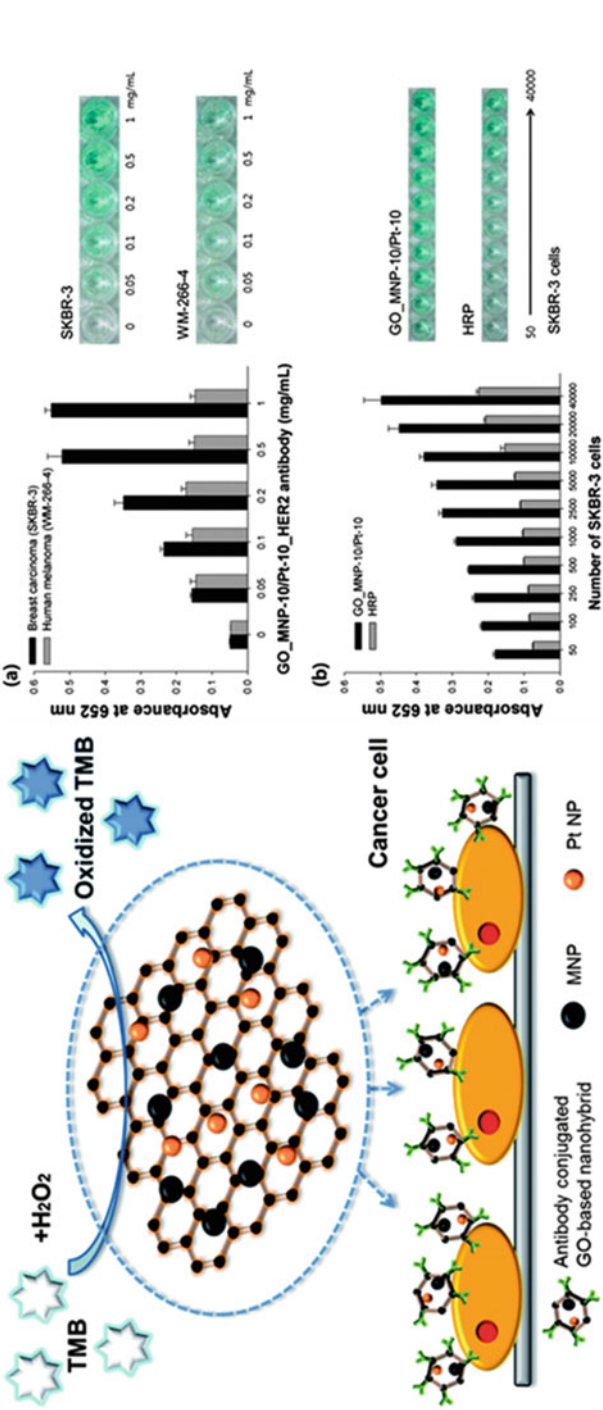

Fig. 9.4 *Left panel*: Schematic representation of colorimetric detection of target cancer cells based on hybrid nanocomposite entrapping both MNPs and Pt NPs on carboxyl-modified graphene oxide. *Right panel*: absorption intensities of *blue* color signal and their corresponding well plate images to (*a*) specifically detect SKBR-3 cells using a GO_MNP-10-Pt-10 nanohybrid and (*b*) quantitatively detect SKBR-3 cells using GO_MNP-10-Pt-10 nanohybrid and HRP. Error bars represent standard deviation of three independent measurements. Reprinted with permission from Ref. [99]. Copyright (2013) Royal Society of Chemistry

which lack HER2 expression, were used as negative control cells. As shown in Fig. 9.4a (right panel), specific blue color signals were generated within 5 min in the wells containing only SKBR-3 cells. However, the wells containing negative controls of WM-266-4 cells did not produce significant color changes, confirming the specific binding of the antibody-conjugated GO_MNP-10-Pt-10 to SKBR-3 cells. Furthermore, as the amounts of the cells were increased, the antibody-conjugated GO_MNP-10-Pt-10 exhibited a gradational blue color evolution with higher absorption intensity than HRP. The limit of detection for target SKBR-3 cells was found to be ca. 100 cells in a linear range from 100 to 1000 cells (Fig. 9.4b, right panel). The GO_MNP-10-Pt-10 conjugated with a HER2 antibody could be used in fluorescence visualization of target cancer cells (SKBR-3) by utilizing POD-mediated tyramide signal amplification to generate high-density fluorescent labeling of target biomolecules in situ. The present protocol using GO_MNP-10-Pt-10 nanocomposite may offer an efficient point-of-care detection in clinical diagnostics in the near future.

The EDC-NHS chemistry was also utilized by Bi et al. [102] in the synthesis of MNPs-GO-supported hemin (MNP-GO-hemin) as a POD mimic. Typically, in the first step, thiol-modified MNPs were treated with *S*-2-pyridylthio cysteamine hydrochloride to functionalize MNPs with disulfide bonds with an amino terminal. Meanwhile, GO was activated with EDC and NHS and reacted with the $-NH_2$ groups of modified MNPs to synthesize MNP-GO conjugates. In the final step, hemin was immobilized onto the GO surface by means of $\pi-\pi$ interactions. Based on the strong nucleophilicity of sulfhydryl, a colorimetric assay for thiols was developed using glutathione (GSH) as a model analyte. Upon the introduction of GSH to the MNP-GO-hemin, the disulfides could be readily reduced and released a GO-hemin hybrid into the solution. The as-released GO-hemin hybrid with POD-like activity could catalyze the oxidation of ABTS to form the green colored radical product, in the presence of H_2O_2. A broad linear dynamic range from 10^{-6} to 10^{-10} M GSH was achieved with good specificity and a detection limit of 8.2×10^{-11} M. Further, the hybrid could be successfully applied to protein and nonprotein thiol detection in the extracts of Ramos cells. Specifically, nonprotein thiols in Ramos extracts could be detected with as low as 500 cells.

Following a one-step solvothermal approach, Quin et al. [103] synthesized Fe_3O_4 nanosphere/rGO (Fe_3O_4 NSs/rGO) composite using diethylene glycol (DEG) as the solvent. The Fe_3O_4 NSs/rGO nanocomposite, in conjunction with Fe_3O_4 microspheres (MSs)/rGO, Fe_3O_4 nanopolyhedrons (NPHs)/rGO and bare Fe_3O_4 NSs, was thoroughly characterized by TEM, XRD, and FT-IR spectroscopy. In particular, the TEM images of the Fe_3O_4 NSs/rGO nanocomposite revealed that the graphene surface was homogeneously and densely covered with narrow distributed Fe_3O_4 NSs, while the pristine Fe_3O_4 NSs (with no rGO) were severely agglomerated due to their large surface-to-volume ratio [48]. Compared with Fe_3O_4 MSs/rGO and Fe_3O_4 NPHs/rGO, the Fe_3O_4 NSs/rGO nanocomposite exhibited the highest POD-like activity, as evidenced by the oxidation of TMB, in the presence of H_2O_2. This indicates that shape and size of MGNCs significantly affect their POD-mimicking activities. Based on the specific reaction of acetylcholine (ACh) esterase

and choline oxidase, the Fe_3O_4 NSs/rGO nanocomposite could be used to develop a colorimetric assay for the sensitive and selective detection of ACh, an important signal transmission molecule in the central nervous system, with a detection limit as low as 39 nM. Furthermore, the practical utility of the assay was demonstrated to detect ACh in milk with average recoveries of 87.9 to 115.2%.

Wang et al. [104] relied on the use of two carbon supports having high conductivity and electron-transfer capability. In a typical experiment, cube-shaped MNPs were first synthesized by the thermal decomposition of iron oleate complex [105] and subsequently stabilized in tetramethylammonium hydroxide solution for derivatization with amino functions. Meanwhile, GO was used as a surfactant to disperse –COOH-functionalized CNTs to create stable support, namely, GCNT (mass ratio of GO to CNTs being 1:10) in water. Finally, cubic MNPs were covalently loaded separately onto CNTs and GCNT by EDC-NHS chemistry, resulting in GCNT-Fe_3O_4 nanocomposites with higher aqueous stability. Figure 9.5a highlights the assessment of topological structures among different nanomaterials by TEM imaging. Specifically, MNPs were found to be well distributed and aligned on the GCNT-Fe_3O_4 with fair density [inset, Fig. 9.5a(D)]. In contrast, they were stacked and coagulated on the CNT-Fe_3O_4 nanocomplex. Compared to MNPs and CNT-Fe_3O_4, the GCNT-Fe_3O_4 could achieve much stronger POD-like catalysis due to the synergistic effects of two conductive carbon supports

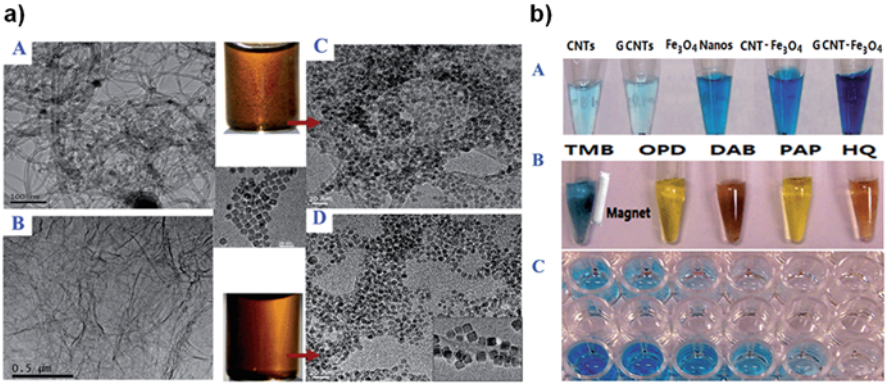

Fig. 9.5 (**a**) Typical TEM images of (*A*) CNTs, (*B*) GO, (*C*) CNT-Fe_3O_4 nanocomposite, and (*D*) GCNT-Fe_3O_4 nanocomposite (*inset*: partially amplified view of a nanocomposite) and free cubic Fe_3O_4 nanos (*middle*), including (*middle*, *top*, and *bottom*) photographs of CNT-Fe_3O_4 and GCNT-Fe_3O_4 suspensions indicated. (**b**) Colorimetric comparison investigations of catalysis activities of GCNT-Fe_3O_4 nanocatalysts. (*A*) Comparison of catalytic activities for TMB-H_2O_2 reaction (5.0 mM TMB and 2.0 mM H_2O_2) among CNTs, GCNTs, Fe_3O_4 nanos, CNT-Fe_3O_4, and GCNT-Fe_3O_4 materials normalized with same iron amount. (*B*) GCNT-Fe_3O_4-catalyzed H_2O_2 oxidization of various organic peroxidase substrates (2.0 mM) of TMB, OPD, DAB, PAP, and HQ. (*C*) Colorimetric detection of glucose (*top row*) and H_2O_2 (*bottom row*), ranging from 0.050 to 1.0 mM (*right* to *left*) using GOD-loaded GCNT-Fe_3O_4 and pure GCNT-Fe_3O_4 nanocatalysts (0.010 mg mL^{-1}), respectively. Reprinted with permission from Ref. [104]. Copyright (2014) Royal Society of Chemistry

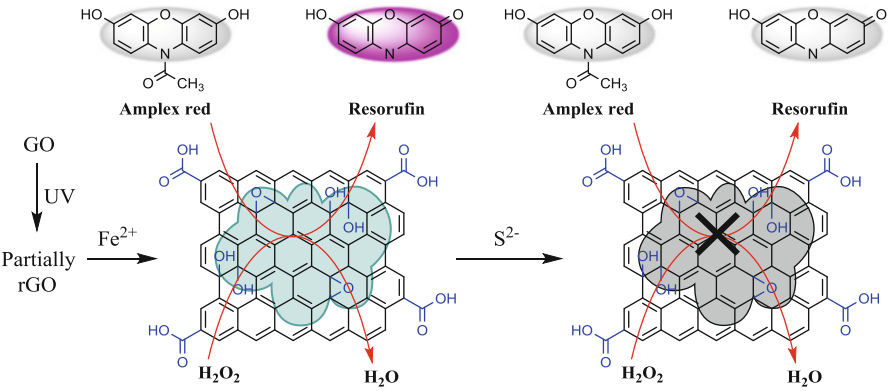

Fig. 9.6 Schematic representation of preparation of peroxidaselike FeO_xH-rGO nanocomposites for detection of sulfide ions based on inhibition of enzymatic activity. Adapted with permission from Ref. [106]. Copyright (2014) Royal Society of Chemistry

as well as effectively loaded cubic Fe_3O_4 nanocatalysts. As shown in Fig. 9.5b, GCNT-Fe_3O_4 nanocomposite-catalyzed oxidation of TMB, OPD, DAB, PAP, and HQ substrates produced different color reactions in the presence of H_2O_2. Kinetic measurements indicated that the K_m value of GCNT-Fe_3O_4 with H_2O_2 substrate (2.52 mM) was slightly lower than that of HRP (3.7 mM). However, the GCNT-Fe_3O_4 presented a much lower K_m value with a TMB substrate (0.118 mM) in comparison with HRP (0.434 mM), which indicates the higher affinity of GCNT-Fe_3O_4 toward TMB, presumably resulting from its carbon carriers with strong adsorption to TMB. The excellent POD-like activity of GCNT-Fe_3O_4 could be used for colorimetric detection of glucose and H_2O_2 with high sensitivities [Fig. 9.5b(C)]. Furthermore, the strong magnetism of GCNT-Fe_3O_4, leading to an easy recovery and recyclability, make it an ideal candidate in the fields of enzyme mimics and environmental chemistry.

Hsu et al. [106] prepared an FeO_xH-rGO nanocomposite by immobilizing amorphous FeO(OH) and $Fe(OH)_2$ on partially reduced GO. The FeO_xH-rGO nanocomposite exhibited high POD-like activity in the H_2O_2-induced oxidation of AR (10-acetyl-3,7-dihydroxyphenoxazine) to fluorescent resorufin (7-hydroxy-3*H*-phenoxazine-3-one) (Fig. 9.6). The catalytic mechanism of the FeO_xH-rGO nanocomposite was proposed to be similar to Fenton-like reactions owing to the presence of Fe^{2+}/Fe^{3+} in deposited FeO_xH [107]. The experimental results indicated that the POD-like activity of FeO_xH-rGO was ca. tenfold higher than that of FeO_xH-GO. This may be attributed to the fact that rGO has a higher conductivity and greater ability adsorb AR [108]. The AR-FeO_xH-rGO allowed facile detection of H_2O_2 under microwave irradiation (50 nM, 10 min). In the presence of sulfide (S^{2-}) anions, the catalytic activity of FeO_xH-rGO was found to be lower owing to the formation of FeS and Fe_2S_3 on the active sites of FeO_xH-rGO. This served as the basis for designing a sensitive and stable sensor probe for S^{2-}. Specifically,

the H_2O_2/AR-FeO_xH-rGO probe could be used to detect S^{2-} with high selectivity (>100-fold) and a detection limit of 50 nM. Furthermore, the practical utility of the probe was explored in the determination of S^{2-} levels in real environmental water samples such as stream, tap, and lake water, with average recoveries of 104.2 to 107.3%. In line with this, the H_2O_2/AR-FeO_xH-rGO probe also allowed the detection of S^{2-} in hot spring water samples (75.1–619.5 μM) and the results showed a good correlation ($r = 0.98$) with upshot from inductively coupled plasma mass spectrometry inductively coupled plasma mass spectrometry (ICP-MS).

Zheng et al. [109] employed a solvothermal method to fabricate a self-assembled 3D graphene nanohybrid (3DRGO) with in situ-formed Pd and MNPs on it. In a typical procedure, L-glutamic acid was added into graphene solution and sonicated to form the partial self-assembly of graphene. With the addition of $FeCl_3$ to DEG at pH 13, 3D graphene was formed by a metal-induced self-assembly process, followed by mixing with $PdCl_2$. After thermal reduction in DEG, further self-assembly of graphene occurred. Meanwhile, Pd and MNPs were grown on 3DRGO, and a part of Pd NPs were also loaded on MNPs using L-glutamic acid as linkers. The overall process is depicted in Fig. 9.7a. The morphology, crystallinity, and composition of as-prepared bimetallic 3DRGO_Fe_3O_4-Pd nanocomposite were carried out by SEM, TEM, EDS, XRD, FT-IR, XPS, and BET isotherm. The magnetization curve of 3DRGO_Fe_3O_4-Pd showed no remanence or coercivity, confirming their superparamagnetic character. Further, the saturation magnetization value of 7.6 emu g^{-1} demonstrated the quick recovery of nanocomposite from aqueous solutions. In the TMB-H_2O_2 system, the 3DRGO_Fe_3O_4-Pd produced a deep blue color, similar to PODs (Fig. 9.7b). In addition, the composite could also oxidize TMB substrate even in the absence of H_2O_2, as inferred by a solution color change from colorless to light blue (oxidaselike activity). This indicates that a 3DRGO_Fe_3O_4-Pd system can exhibit dual-enzyme activity. Nevertheless, the POD-like activity of 3DRGO_Fe_3O_4-Pd was found to be much higher than oxidase-like activity. Neither of the two monometallics, 3DRGO_Fe_3O_4 or 3DRGO-Pd, exhibited better POD-like activity than 3DRGO_Fe_3O_4-Pd, as demonstrated by time-dependent absorbance changes. The kinetic data revealed that the K_m value of 3DRGO_Fe_3O_4-Pd with H_2O_2 substrate was two times lower than those of GO and HRP, and ca. 30 times lower than GO-Fe_3O_4, which signifies that the incorporation of bimetallic NPs on 3DRGO can considerably improve the catalytic affinity toward H_2O_2. Based on these findings, a simple colorimetric method was developed to detect H_2O_2, GSH, and glucose with respective detection limits of 8.6×10^{-8}, 5.2×10^{-8}, and 1.3×10^{-7} M. Interestingly, the nanoprobe could be reused repeatedly and the catalytic activity was found to be greater than 90% after ten consecutive runs. Among several interfering substances such as KCl, uric acid, urea, fructose, lactose, and maltose, the probe could detect glucose with high selectivity in the diluted urine sample with recoveries of 98.0–102.0%.

Li et al. [110] reported an iron-self-catalysis method (in situ simultaneous reduction of Fe^{3+} and GO) for the synthesis of rGO-iron NP (rGO-INs) composites under mild conditions. During the chemical reduction, INs were in situ formed on

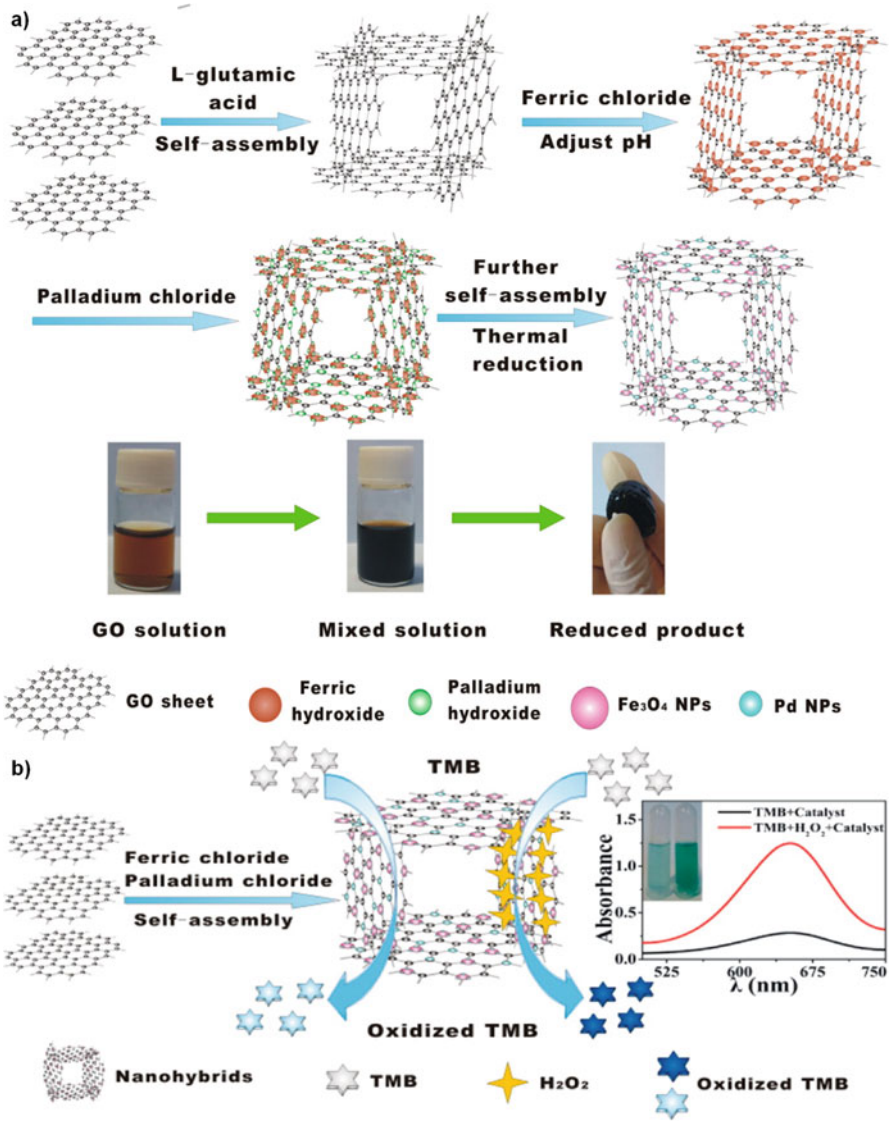

Fig. 9.7 (**a**) Schematic of preparation process for 3DRGO_Fe_3O_4-Pd nanohybrid. (**b**) Schematic representation of POD-like catalytic activity of 3DRGO_Fe_3O_4-Pd nanohybrid. *Inset*: UV-visible absorption spectra, exhibiting dual enzymatic activity of 3DRGO_Fe_3O_4-Pd nanohybrid. Reprinted with permission from Ref. [109]. Copyright (2015) American Chemical Society

the surface of rGO. Benefitting from the synergistic effects between rGO and INs, the rGO-INs could effectively catalyze the oxidation of TMB, OPD, and THB in the presence of H_2O_2 and produced typical color reactions. Similar to HRP, the POD-like activity of rGO-INs was also found to be dependent on pH, temperature, and

H_2O_2 concentration and could be used to develop the sensitive, selective, and cost-effective colorimetric assays for H_2O_2 and glucose with respective detection limits of 0.2 and 0.8 μM.

Zhang et al. [111] synthesized a strongly coupled Au-Fe_3O_4-GO nanocomposite by the direct anchoring of Au and MNPs onto GO (Fig. 9.8A). Owing to the introduction of a long PEG chain on the graphene surface, the Au-Fe_3O_4-GO could be easily dispersed in water. As shown in Fig. 9.8B(b), both Au NPs, with an average size of 5 nm, and MNPs, with an average size of 7 nm, were found to be uniformly dispersed on the GO surface. This observation was further supported by the selected area electron diffraction (SAED) pattern [inset in Fig. 9.8B(b)]. The homogeneous distribution of C, N, O, S, Fe, and Au in the nanocomposite was evidenced by element mapping images. In particular, compared with the C signal, the Fe, Au, S, and O signals were found to be located in nanometer-sized domains, while the signals of Au and S exhibited a one-to-one relationship [Fig. 9.8B(d–i)]. Magnetic property measurements indicated the superparamagnetic nature of Au-Fe_3O_4-GO, which did not change with the adsorption of Hg on the nanocomposite. However, the saturation magnetization value was found to have decreased by 54% (31.6 emu g^{-1}) in Au-Fe_3O_4-GO, which was attributable to the contributions from nonmagnetic Au-PEG-coated GO to the overall mass. The Au-Fe_3O_4-GO did not exhibit POD-like activity in a citric acid–disodium hydrogen phosphate buffer (CA-DHPB) solution (25 mM, pH 5.0). However, in the presence of a catalytic amount of Hg^{2+}, the activity was stimulated significantly, as observed in the color change of oxidized TMB. Under optimal conditions (pH 5.0, 298 K, 0.20 M H_2O_2 and TMB) in CA-DHPB solution (25 mM), the Au-Fe_3O_4-GO showed the best Hg^{2+}-stimulated POD-like activity relative to those of bare GO, Au NPs, Fe_3O_4 NPs, Au-GO, and Fe_3O_4-GO nanoscale structures. The unique affinity of Hg for Au undoubtedly allowed this method to be used for the ultrasensitive and selective detection of Hg^{2+} over other environmentally relevant metal ions, with a detection limit as low as 0.15 nM. The mechanism of Hg^{2+}-stimulated POD-like activity of Au-Fe_3O_4-GO can be understood in two steps (Fig. 9.8C). First, Hg^{2+} is reduced by citrate sodium to form Hg^0; second, Hg^0 disperses on the surface of Au NPs and thus changes the surface properties of the Au NPs, improving their POD-like activity [112]. The Hg^{2+}-stimulated Au-Fe_3O_4-GO presented a very low K_m value for both TMB and H_2O_2 with a large V_{max}, indicating its strong catalytic activity and higher affinity for TMB and H_2O_2. The Au-Fe_3O_4-GO in citric acid–disodium could be effectively used in removing Hg^{2+} from aqueous media (>99.96% of the 10 μM Hg^{2+}) within 30 min.

Very recently, Li et al. [113] synthesized a Pd-Fe_3O_4-PEI-rGO nanocomposite by dispersion of Pd NPs and MNPs on polyetheylenimine (PEI)-modified GO sheets. The nanohybrid was found to demonstrate excellent POD-like activity, as inferred by the catalytic reaction of a TMB-H_2O_2 system. Consequently, a sensing platform for colorimetric detection of H_2O_2 was developed with a detection limit of 0.1 μM. Compared with other hybrid systems, such as PEI-rGO, Fe_3O_4-PEI-rGO, and Pd-PEI-rGO, the Pd-Fe_3O_4-PEI-rGO nanocomposite exhibited a high POD-like activity with the added advantages of facile preservation and rapid separation.

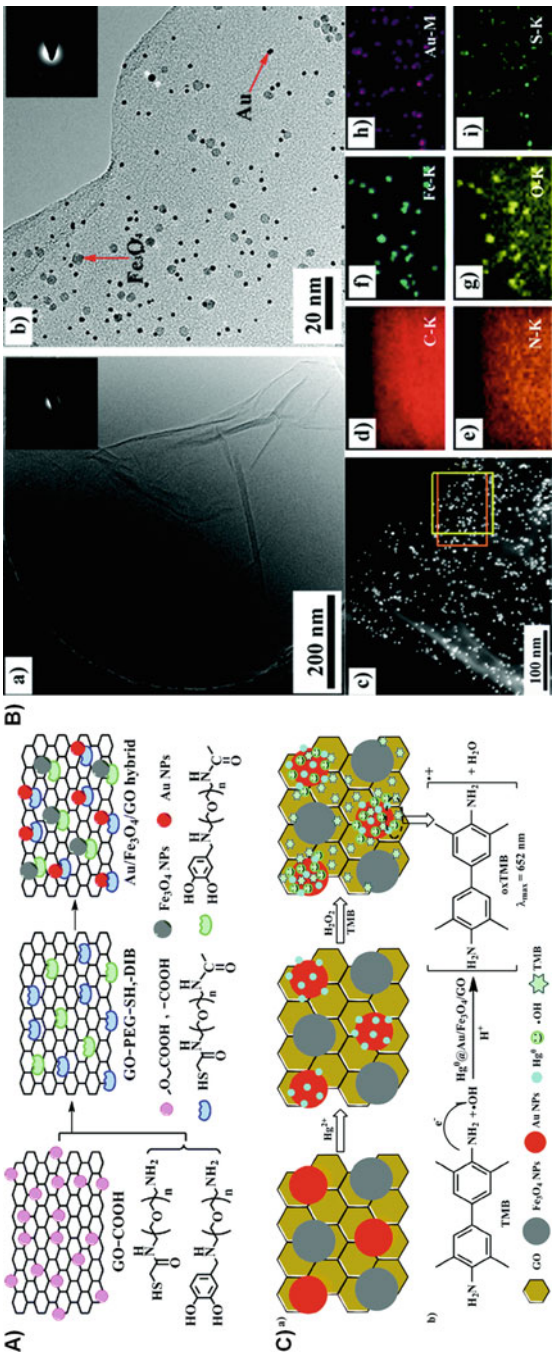

Fig. 9.8 (**A**) Schematic of preparation process for Au-Fe_3O_4-GO hybrid nanocomposite. (**B**) TEM images of (*a*) GO and (*b*) Au-Fe_3O_4-GO hybrid nanocomposite; *insets*: selected area electron diffraction of GO and Au-Fe_3O_4-GO nanocomposite. (*C*) Dark field STEM image and (*d–i*) element mapping images of Au-Fe_3O_4-GO hybrid nanocomposite. (**C**) (*a*) Mercury-enhanced POD-like activity of Au-Fe_3O_4-GO hybrid nanocomposite. (*b*) Reaction principles in this system. Reprinted with permission from Ref. [111]. Copyright (2015) Royal Society of Chemistry

9.4.2 MGNCs for Catalytic Applications

The principal source of energy on Earth is found in chemical bonds. Catalysis affords a way of changing the rates at which chemical bonds are formed and broken, making it possible to yield a desired product versus an undesired product, a phenomenon of chemical specificity. The petroleum, chemical, plastic, and pharmaceutical industries, essential to a healthy economy of any nation, rely heavily on catalysis. Not surprisingly, therefore, it lies at the heart of our quality of life [28]. Over the past few decades, the shift toward an emphasis on catalyst recoverability as well as reusability has resulted in extensive research efforts devoted to the development of solid or heterogeneous acid catalysts [resins, clay, zeolites, molecular sieves, silica, solid superacids, and (supported) metal oxides, sulfides, or triflates], which are easier to separate, recover, and reuse in a specific reaction [114–116]. However, despite their good catalytic efficiencies, these solid catalysts suffer from certain disadvantages, such as leaching, high mass transfer resistance, deactivation due to undesired deposits on their active sites, and toxicity of certain metals or metal oxides. In graphene research, semi-heterogeneous nanocatalysts, covering GO, rGO, and their derivatives, are usually recovered either through membrane filtration or centrifugation methods. However, these procedures are also quite tedious and time-consuming. The use of MNPs supported on a graphene domain has emerged as an ideal and the most logical solution to circumvention of the aforementioned problem. Owing to their efficient magnetic separation, synergistic features leading to high catalytic activity, and high dispersion and stability in aqueous solutions, MGNCs are being increasingly used as catalysts, especially in the past few years, and are significantly influencing current heterogeneous catalysis in the context of carbon–carbon (C–C) coupling reactions.

C–C coupling reactions are one of the most routinely used industrially useful transformations and are key in developing a wide range of bioactive molecules. Not surprisingly, therefore, they lie at the heart of catalysis, organic synthesis, and organometallic chemistry. The Mizoroki–Heck or Heck, Suzuki–Miyaura or Suzuki, Negishi, Sonogashira, Ullmann, and Kumada coupling reactions represent some well-known examples of C–C coupling reactions [117–124], which are usually executed in the presence of Pd catalysts with high selectivities, yields, reaction rates, and large turnover numbers (TONs) and frequencies (TOFs). Important milestones in the development of C–C coupling reactions were realized in 2010, when three carbon couplers, the late Prof. Richard Heck, Akira Suzuki, and Eiichi Negishi, were awarded the Nobel Prize in Chemistry.

In their pioneering work, Hu et al. [125] assembled Pd and MNPs on sulfonated graphene (s-G) using sodium dodecyl sulfate (SDS) as both surfactant and reducing agent. The as-fabricated Pd-Fe_3O_4-s-G nanocomposite, in conjunction with Pd-s-G, was suitably characterized by TEM, XRD, and EDX spectroscopy. Using ICP-AES, the Pd content in Pd-Fe_3O_4-s-G was determined to be 8.33 wt%. Further, the presence of crystalline structures of zero-valent Pd and Fe_3O_4 was evidenced by XRD patterns of nanocomposite. Pd-Fe_3O_4-s-G can be homogeneously dispersed in a water–ethanol mixture or even pure water and may be used as catalyst

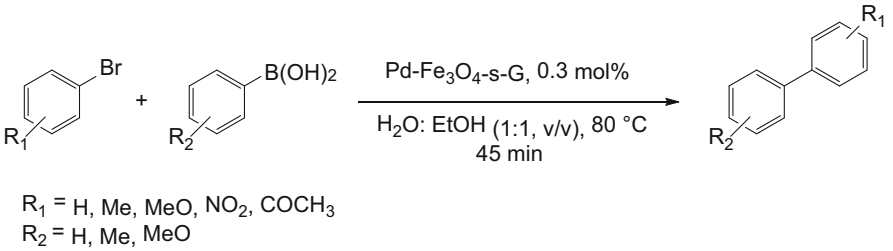

Scheme 9.2 Pd-Fe_3O_4-s-G-catalyzed Suzuki–Miyaura cross-coupling reaction

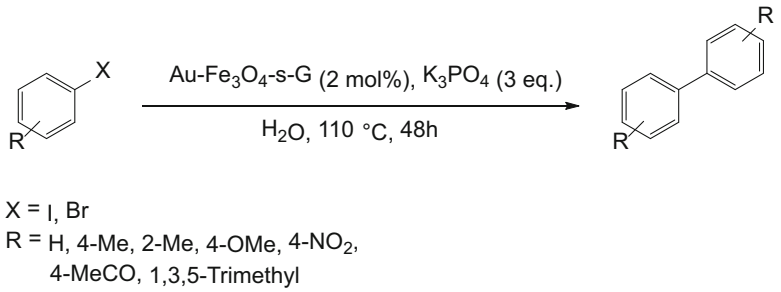

Scheme 9.3 Au-Fe_3O_4-s-G-catalyzed Ullmann coupling reaction

in Suzuki–Miyaura cross-coupling reactions. Specifically, the reactions of different aryl bromides, containing both electron-donating and electron-withdrawing groups, with arylboronic acids in the presence of Pd-Fe_3O_4-s-G composite catalyst in aqueous EtOH, afforded corresponding coupling products in 79–95% yields (Scheme 9.2). The higher catalytic activity of Pd-Fe_3O_4-s-G can be attributed to the homogeneously dispersed smaller-sized Pd NPs (2–5 nm) on Fe_3O_4/s-G matrix. The catalyst was found to be very stable in air and could be recycled eight times with minimal loss in activity.

Dabiri et al. [126] relied on Au NPs to prepare a magnetically separable Au-Fe_3O_4-s-G nanocomposite. In a typical procedure, MNPs were first deposited on s-G sheets by the coprecipitation method using $FeSO_4$ and $FeCl_3$. The as-obtained Fe_3O_4-s-G was finally decorated by Au NPs in the presence of SDS. The nanocomposite was extensively characterized by SEM, TEM, XPS, EDS, SAED, and Raman spectroscopy. Specifically, the Raman spectrum of Au-Fe_3O_4-s-G indicated signals of graphene and MNPs. However, the intensity of the Raman signals of graphene (D and G bands) were enhanced significantly following conjugation of Au NPs on the Fe_3O_4-s-G sheets. This may be attributed to the surface-enhanced Raman spectroscopy (SERS) of Au NPs. A relatively low saturation magnetization value of 10.06 emu g^{-1} of Au-Fe_3O_4-s-G could be attributed to the presence of magnetically inactive layers at NP surfaces. The Au-Fe_3O_4-s-G-catalyzed Ullmann coupling reaction with a variety of aryl halides afforded corresponding biaryls in good to excellent yields (Scheme 9.3). However, lower yields of homocoupling products were

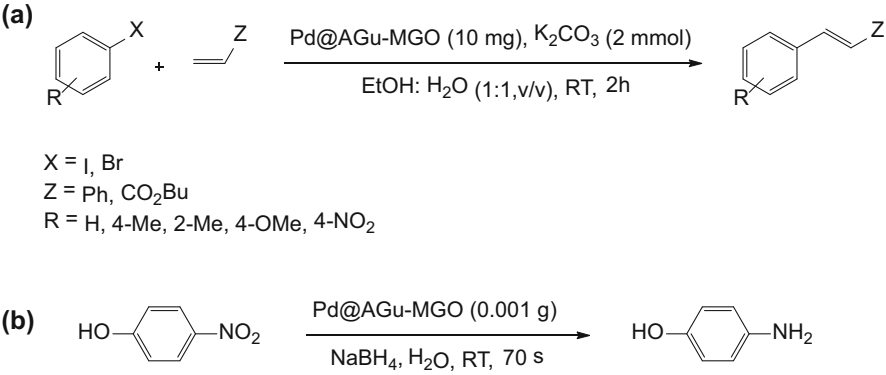

Scheme 9.4 Pd@AGu-MGO-catalyzed (**a**) Heck coupling reaction and (**b**) reduction of 4-nitrophenol

obtained with more hindered 2-iodotoluene and 2-iodo-1,3,5-trimethylbenzene. Similarly, the reactions were found to be silent with bromobenzene and aryl bromides, bearing both electron-donating and electron-withdrawing groups. The heterogeneous nature of the catalysis was demonstrated using a hot filtration test as well as atomic absorption spectroscopy (AAS). The catalyst could be reused in up to five consecutive runs. However, the catalytic activity of Au-Fe_3O_4-s-G dropped significantly after the third cycle. In follow-up work [127], the group designed and synthesized a magnetic-core–double-shell Fe_3O_4@rGO@Au@C architecture, in which magnetic-core–double-shell carbon with MNPs, rGO, and carbon layer works as the core, inner shell, and outer shell, respectively. This tailor-made structure acted as an excellent capsule for encapsulating Au NPs, preventing them from aggregation and leaching. The Fe_3O_4@rGO@Au@C was found to exhibit high catalytic activity in the reduction of nitroarenes and Suzuki coupling reactions of aryl halides with phenylboronic acid. The catalyst showed good stability and was easily recovered and reused ten times.

Ma'mani et al. [128] developed a heterogeneous Pd@AGu-MGO catalyst by deposition of Pd onto the surface of *N*-aminoguanidinium functionalized magnetic GO using DEG as an organic spacer. The loading of Pd on Pd@AGu-MGO was assessed to be 0.9 mmol g^{-1}, as inferred by ICP-AES and elemental analysis. The catalytic activity of Pd@AGu-MGO was demonstrated in Heck and Suzuki couplings of aryl halides as well as in the reduction of 4-nitrophenol (Scheme 9.4). The catalyst recovery results confirmed the excellent stability of Pd@AGu-MGO, allowing 10 consecutive runs for Heck and Suzuki couplings and 20 successive cycles in nitrophenol reduction with respective TONs of 1005 and 9565. In line with this, the calculated TOFs were found to be 500, 1000, and 22,770 for the Heck, Suzuki, and reductions reactions, respectively. Hoseini et al. [129] deposited Pd NPs onto a magnetic Fe_3O_4-rGO nanohybrid by the reduction of dichloropalladium (II) complex in water. The as-prepared Pd-Fe_3O_4-rGO nanocomposite was char-

acterized by FT-IR, XRD, and TEM imaging and could be used as a magnetically separable and reusable catalyst (eight runs) in the Suzuki–Miyaura coupling reaction of arylboronic acid with a variety of aryl bromides and chloride derivatives. Under the optimal reaction conditions (catalyst: 0.36 mol% of Pd, K_2CO_3, and water), corresponding coupling products were obtained in 77–99% yields.

Elazab et al. [130] developed catalytically active Pd-Fe_3O_4-G nanocomposites using Pd-Fe_3O_4 NPs as support. The synthesis approach was based on the microwave-induced reduction of Pd and ferric nitrates using $N_2H_4{\cdot}H_2O$ as reducing agent, in the presence of GO. Of the different systems, the Pd-Fe_3O_4-G containing 7.6 wt% Pd NPs with 4–6 nm in size and 30 wt% MNPs with 12–16 nm diameters exhibited remarkable catalytic activity for a Suzuki reaction with an extremely high TON of 9250 and TOF of 111,000 h^{-1} under microwave conditions at 80 °C. The Pd-Fe_3O_4-G catalysts also exhibited a greater recyclability of up to eight consecutive runs, achieving nearly 90% or higher yields of coupling products. However, a significant drop in the activity (to ca. 80% conversion) was realized during the ninth and tenth runs. The Pd-Fe_3O_4-G catalyst could also be used over a broad range of highly functionalized substrates in Heck reactions and afforded corresponding coupling products in 82–95% yields.

Yao et al. [131] reported a four-in-one strategy to construct rGO-Pd-Fe_3O_4@polypyrrole (PPy) nanocomposite catalyst by anchoring Pd and MNPs onto the rGO surface and wrapped in a PPy shell. Interestingly, the reduction of GO, synthesis and assembly of both Pd and MNPs, and preparation of PPy layer could all be done in just one step. In the rGO-Pd-Fe_3O_4@PPy system, the PPy layer not only prevented the aggregation of Pd and MNPs but also generated a synergistic effect with Pd^{2+}, which led to a high dispersity of Pd NPs. The rGO-Pd-Fe_3O_4@PPy catalyst exhibited a superparamagnetic nature owing to nearly no remanence or coercivity left, with a magnetization value of 8.1 emu g^{-1}. With even small loadings, for instance 1.1 μg, rGO-Pd-Fe_3O_4@PPy showed high catalytic activity toward the reduction of 4-nitrophenol at a constant rate as high as 0.191 min^{-1}. The catalyst was found to be recyclable for up to four runs without significant loss of catalytic activity.

In subsequent work [132], the group introduced Pd and γ-Fe_2O_3 NPs embedded between rGO sheets (rGS) and N-doped carbon sheets (NCS) using a two-step protocol. In a typical experiment, a GS/Prussian blue (PB)-Pd/PPy composite was first synthesized *via* a redox reaction using pyrrole monomer as reductant and $K_3Fe(CN)_6$ and $PdCl_2$ as oxidants in the presence of GS. Subsequently, the as-obtained GS-PB-Pd-PPy composite was calcinated in nitrogen. During the heat treatment, GS reduced to rGS, PPy carbonized to NCS, and nonmagnetic PB NPs converted into magnetic γ-Fe_2O_3 NPs simultaneously. The as-obtained rGS-Fe_2O_3-Pd-NCS nanocomposite exhibited good catalytic activity toward 4-nitrophenol reduction and could be reused four times without significant loss of activity.

Zhao and Liu [133] developed a magnetically separable $NiFe_2O_4$@GN-Pd nanocomposite under hydrothermal conditions. A schematic illustration for the synthesis of $NiFe_2O_4$@GN-Pd is shown in Fig. 9.9a. Specifically, the nanocomposite was constructed by spherically shaped $NiFe_2O_4$ and Pd NPs having average

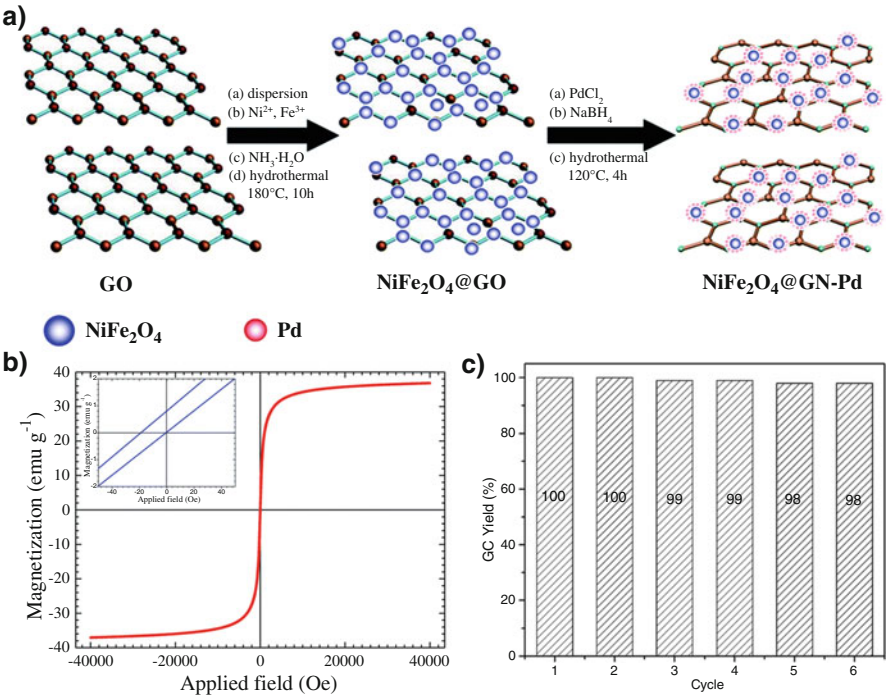

Fig. 9.9 (**a**) Schematic illustration for synthesis of $NiFe_2O_4$@GN-Pd magnetic composite. (**b**) Magnetic hysteresis curves of as-prepared $NiFe_2O_4$@GN-Pd nanocomposites measured at room temperature. *Inset*: zoomed-in view of curve near origin. (**c**) Reusability of $NiFe_2O_4$@GN-Pd nanocomposite achieved in Suzuki reaction of iodobenzene and phenylbronic acid. Reprinted with permission from Ref. [133]. Copyright (2015) Royal Society of Chemistry

particle sizes of 10–20 nm, which were nucleated homogeneously on certain sites of single-layer graphene through electrostatic interactions. The $NiFe_2O_4$@GN-Pd was characterized by FT-IR, XRD, XPS, TEM, and vibrating sample magnetometry (VSM). Magnetic measurement studies indicated that the $NiFe_2O_4$@GN-Pd exhibits a typical superparamagnetic behavior with a finite coercivity of 9.46 Oe. A low saturation magnetization value of 36.82 emu g^{-1} than that of the bulk $NiFe_2O_4$ particles (55 emu g^{-1}) further reflected the ultrafine nature of the nanocomposite (Fig. 9.9b). The catalytic activity of the nanocomposite was demonstrated in Suzuki coupling in aqueous ethanol. In most of the cases, the coupling products were obtained in good to excellent yields. However, moderate product yields were recognized with more challenging chloroarenes. The catalyst could be reused in up to six runs (Fig. 9.9c) with nearly no loss of catalytic activity, as demonstrated by ICP-MS analysis. In particular, the results indicated that only 0.2 wt% of Pd

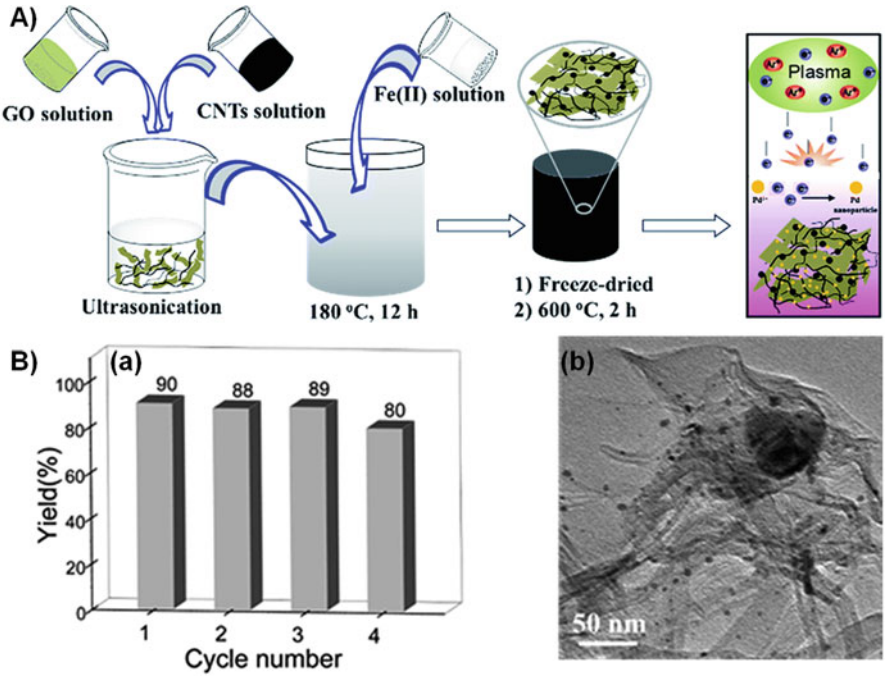

Fig. 9.10 (**A**) Synthesis process of GO/CNT-Fe_3O_4-supported Pd nanoparticles. (**B**) Yields for 4 cycles of Pd-3-catalyzed nitrobenzene hydrogenation reaction (*a*), and TEM image of Pd-3 catalyst after 4 cycles (*b*). Reprinted with permission from Ref. [135]. Copyright (2016) Royal Society of Chemistry

was leached after six runs. In another work [134], the group further reported a magnetically separable $NiFe_2O_4$@GO-Pd composite and effectively used in Heck reactions.

Yang et al. [135] synthesized GO-CNT-Fe_3O_4-supported Pd NPs (of varying sizes and loadings, designated as Pd-*n*, Pd-1 to Pd-5) using a gas–liquid interfacial plasma method with palladium acetate as precursor (Fig. 9.10A). Typically, the GO-CNT-Fe_2O_3 hybrid was first synthesized by the hydrothermal reaction of ferrous oxalate, GO, and CNTs. Second, GO-CNT-Fe_2O_3 was calcinated to a GO-CNT-Fe_3O_4 composite. Finally, Pd-*n* with size distributions of ca. 4 nm were supported onto the GO-CNT-Fe_3O_4 surface without destroying its microstructure. Whereas the introduction of Fe_3O_4 to GO-CNTs could effectively prevent NPs from restacking and aggregation, the GO-CNTs could modulate the hydrophobic–hydrophilic property of the GO-CNT-Fe_2O_3-Pd-*n* nanocomposite. As a result, the nanocomposite exhibited a remarkable catalytic activity in the hydrogenation of nitroarenes in water. In particular, the catalyst with Pd-3 and a GO-CNT ratio of 1:2 exhibited the best activity and afforded substituted anilines in 87–99% yields. Nevertheless, nitroarenes containing electron-withdrawing groups took a relatively longer time to attain the highest yield. The low reaction rate was attributed to the

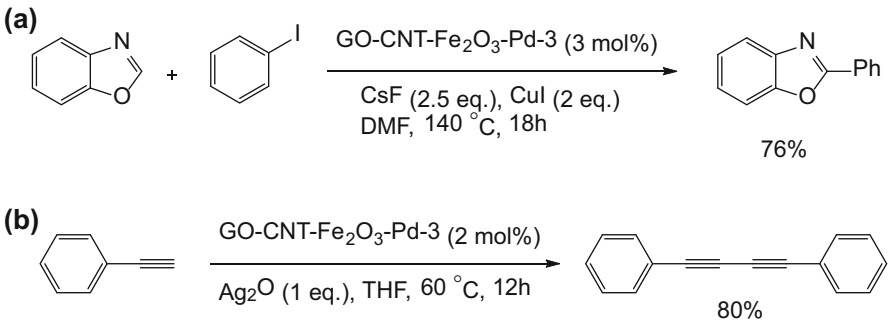

Scheme 9.5 GO-CNT-Fe_2O_3-Pd-3 nanocomposite-catalyzed (**a**) C–H bond functionalization and (**b**) Glaser coupling reaction

fact that these substrates are solid, and the reaction products are also water soluble. The recyclability of the nanocatalyst was demonstrated in the hydrogenation of nitrobenzene. As shown in Fig. 9.10B, the catalyst can be recycled and effectively reused in up to three runs. However, activity dropped considerably in the fourth run owing to the increase in particle size, as evidenced by TEM imaging. Furthermore, an ICP-AES experiment revealed no Pd leaching in the reaction mixture, indicating the truly heterogeneous nature of the catalysis. Aside from the reduction of nitroarenes, the GO-CNT-Fe_2O_3-Pd-*n* nanocomposite was successfully used in the C–H bond functionalization of benzoxazole with iodobenzene as well as the Glaser coupling reaction of phenylacetylene (Scheme 9.5).

Zhang et al. [136] prepared an Fe_3O_4-GO-Mo nanocomposite in three steps. Typically, GO was treated with $FeCl_3/FeCl_2$ to obtain a black colored Fe_3O_4-GO nanocomposite in the first step. The reaction of Fe_3O_4-GO with dopamine afforded amine-functionalized Fe_3O_4-GO in the second step. The addition of bis(acetylacetonato)dioxomolybdenum into the Fe_3O_4-GO suspension in methanol finally yielded Fe_3O_4-GO-Mo nanocomposite with 7.70% Mo, 55.2% Fe, and a saturation magnetization value of 28.6 emu g^{-1}, as revealed by ICP-MS analysis and magnetic property measurements, respectively. Under microwave irradiation in choline chloride(ChCl)-urea solution, the nanocomposite exhibited high catalytic activity in a one-pot, three-component reaction of isatins, malononitrile, and anilinolactones, affording spirooxiindole dihydropyridines in high to excellent yields (Scheme 9.6). The catalyst was easily recovered and reused eight times without significant loss of activity.

The other MGNCs, including the design and synthesis of Fe_3O_4-hierarchical-Mn_3O_4-GO [137], magnetic GO-polyvinyl alcohol composite gels [138], magnetic cobalt-graphene nanocomposite [139], magnetic manganese-GO composite [140], magnetic polysaccharide-GO (SCGO) composite [141], Fe_3O_4-GO/rGO composites [142], superparamagnetic graphene-Fe_3O_4-polydimethylsiloxane (G-F-PDMS) nanocomposites [143], nanomagnetite supported on poly(amidoamine)(PAMAM)-modified GO [144], and Ni NPs-rGO composites [145], while beyond the scope

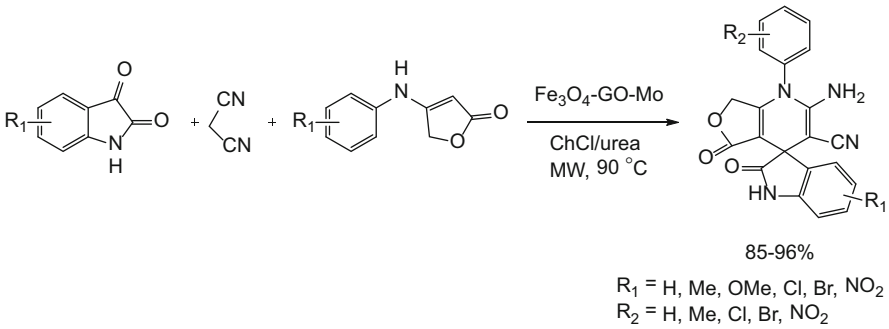

Scheme 9.6 Fe_3O_4-GO-Mo nanocomposite-catalyzed three-component reactions for synthesis of spirooxiindole dihydropyridines

of this chapter, offer further examples of a wide variety of MGNCs being used for different applications, including the degradation of certain dyes or organic pollutants.

9.4.3 MGNCs for Biomedical Applications

Since its initial discovery, graphene or rGO has emerged as a promising nano platform for biomedical applications and translational research because of its exceptional properties, as described earlier. Given an increasing consensus on synergistic aspects, the MGNCs are one of the most promising study areas at the bio–nano interface. In this section, we will highlight the status of current research on MGNC-based molecular imaging (MI) studies, which hold great promise in the areas of diagnostics, therapeutics, drug discovery and development, and personalized medicine [146, 147]. Generally speaking, MI is a real-time forecast, characterization, and measurement of different biochemical events at the cellular and molecular levels (within different living cells, tissues, and even intact objects) that can be valuably applied in the areas of biomedical science to understand nanoscale reactions. Computed tomography (CT), positron emission tomography (PET), magnetic resonance imaging (MRI), ultrasound, photoacoustic imaging (PAI), photothermal imaging (PTI), and optical imaging are the key MI modalities and will be discussed here within the framework of MGNCs.

Optical imaging is an inexpensive, highly sensitive, and routinely used imaging technique. In an elegant work, Wang et al. [148] used a noncovalent approach to fabricate a GO-MNP hybrid that could be used to illuminate graphene for optical imaging by employing the strong localized SPR (LSPR) light scattering of MNPs as an effective signal reporter. Advantageously, in cellular internalization, GO can prevent DNA from enzymatic cleavage and keep the integrality of the GO-MNP hybrid.

MRI, or imaging by magnet, is yet another widely applicable MI modality that largely works similarly to nuclear magnetic resonance spectroscopy. Because all ^{1}H nuclei are magnetically active, it is the most commonly used nucleus for clinical MRI. IONPs are well-studied T_2 contrast agents and can be effectively deposited onto the GO/rGO surface to achieve an enhanced MRI contrast effect, along with good biocompatibility and stability. In general, the formation of aggregates of MNPs results in an enhanced relaxation rate (r_2) [149]. Chen et al. [150] synthesized an aminodextran-coated MNP-GO composite (AMD-MNP-GO) *via* the formation of amide bonds in the presence of EDC. PB staining analysis indicated that AMD-MNP-GO nanocomposites can be internalized efficiently by Hela cells. Compared to bare MNPs, the AMD-MNP-GO composite exhibited significantly enhanced MRI, capable of detecting cells at iron concentrations of 5 and 20 μg/mL with respective cell densities of 2×10^5 and 1000 cells mL^{-1}.

Yang et al. [151] employed GO as a carrier to chemically deposit IONPs on the GO surface. Following basic treatment of GO with NaOH solution, Fe^{3+}/Fe^{2+} ions with a proper ratio were captured by the GO's carboxylate functions. The as-obtained GO-MNP hybrids were used as controlled targeted drug carriers. In a similar work, a simple in situ method was proposed by Cong et al. [152] for decorating rGO NSs with MNPs for MRI applications. The MNPs were found to be uniformly distributed on the surface of rGO with no magnetic particle aggregation. In another interesting study, an rGO-IONP-PEG nanoprobe was developed for in vivo multimodal (optical, PAI, and MRI) tumor (4T1) imaging and imaging-guided highly effective-photothermal therapy (PTT) [153]. The rGO-IONP-PEG probe was found to achieve ultraefficient tumor ablation using a rather lower laser power density at 0.5 W cm^{-2}.

Ma et al. [154] synthesized and used a GO-IONP-PEG nanocomposite for the loading of doxorubicin (DOX), a chemotherapy drug. The resultant GO-IONP-PEG-DOX enabled magnetically targeted drug delivery. The GO-IONP-PEG exhibited strong optical absorbance from the visible to near-infrared (NIR) region and could be used for localized photothermal ablation of cancer cells guided by a magnetic field. Furthermore, GO-IONP-PEG was also applied for in vivo MRI of tumor-bearing mice as the T_2 contrast agent.

Narayanan et al. [155] demonstrated that GO-MNP hybrids can be used as a contrast in dual mode imaging processes (T_2 MRI and optical). The deposition of $MnFe_2O_4$ NPs onto a GO through a mini-emulsion and solvent evaporation process resulted in an MGONC nanocomposite, which could be used as MRI T_2 contrast agent with r_2 values as high as 256.2 mM^{-1} s^{-1} [156].

Fan et al. [50] formulated an MNP-graphene nanocomposite as nanocarrier for pH-activated release of 5-fluorouracil (5-FU) (Fig. 9.11a). TEM imaging indicated that the nanocomposite could be internalized efficiently by HepG2 cells. Chen et al. [157] reported on the in situ growth of β-FeOOH nanorods onto PEGylated GO to synthesize a GO-PEG-β-FeOOH nanocomposite with an ultrahigh r_2 value of 303.81 mM^{-1} s^{-1}. In vitro cell viability tests demonstrated that the GO-PEG-β-FeOOH nanocomposite had minimum cellular toxicity. T_2-weighted MRI of mouse liver before and 0.5, 1, 2, and 4 h after intravenous administration of the GO-PEG-

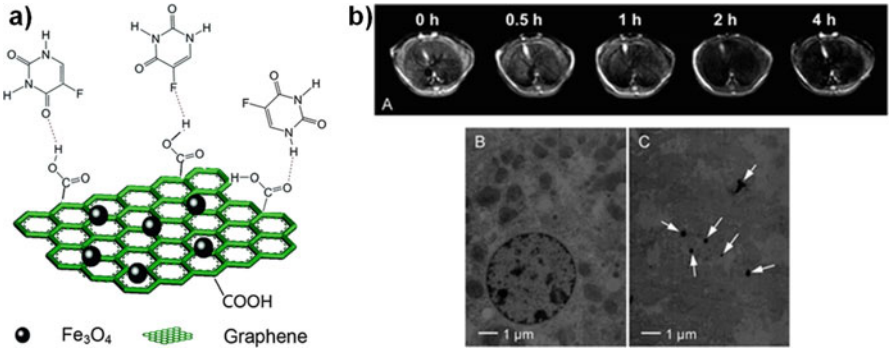

Fig. 9.11 (**a**) Schematic illustration of hydrogen-bonding interactions between MGNs and 5-fluorouracil (5-FU). (**b**) In vivo T_2-weighted MR images of liver before and after postintravenous administration of GO-PEG–β-FeOOH corresponding to 1.0 mg Fe/kg body weight of mice (0.5, 1, 2, and 4 h posttreatment); (*A*) TEM images of liver cells from mouse before and (*B*) after intravenous injection of GO-PEG–β-FeOOH. (*C*) *White arrows* point to aggregated GO-PEG–β-FeOOH inside liver cells from mouse. The mice were sacrificed 4 h after injection. Reprinted with permissions from Refs. [50, 157]. Copyright (2012, 2013) Royal Society of Chemistry

β-FeOOH nanocomposite showed significant darkening of the liver [Fig. 9.11b(A)]. The uptake of the GO-PEG-β-FeOOH nanocomposite in liver tissues was further confirmed by TEM imaging for mouse liver cells. As shown in Fig. 9.11b(B, C), aggregates of GO-PEG-β-FeOOH nanocomposite were observed inside the endosomes of the liver cells, indicating the preferential accumulation of GO-PEG-β-FeOOH nanocomposite in the liver of treated mice. The nanocomposite could be effectively used to load DOX, and the subsequently released DOX exhibited significantly higher efficacy for cellular apoptosis relative to free drug.

Because of the multimodal imaging capabilities of a "nanosack" (wrapping several NPs or their hybrids within graphene domains), Shi et al. [158] decorated GO with both Au and IONPs to synthesize a multifunctional magnetic and plasmonic GO-IONP-Au nanocomposite with superparamagnetism as well as significantly enhanced optical absorbance in the NIR region. Further, the PEGylated nanocomposite, GO-IONP-Au-PEG, exhibited high stability in physiological environments with no significant in vitro toxicity and could serve as a powerful PTT agent for in vitro cancer cell killing under molecular or magnetic targeting. In vivo dual model imaging–guided photothermal tumor destruction was further demonstrated in animal experiments, which showed the excellent tumor ablation therapeutic efficacy of GO-IONP-Au-PEG nanocomposite as PTT agent. In parallel with this work, Chen et al. [159] developed a rGO-Au-Fe_3O_4 nanosack and applied it to CT and MRI, using a carboxymethylcellulose gel. In contrast to the rGO-Fe_3O_4 nanocomposite, the rGO-Au-Fe_3O_4 nanosack indicated a reduced r_2 relaxivity of 114.0 mM^{-1} s^{-1} and a mean CT number of 25.6 at a concentration of 2000 μg/mL (Fig. 9.12a).

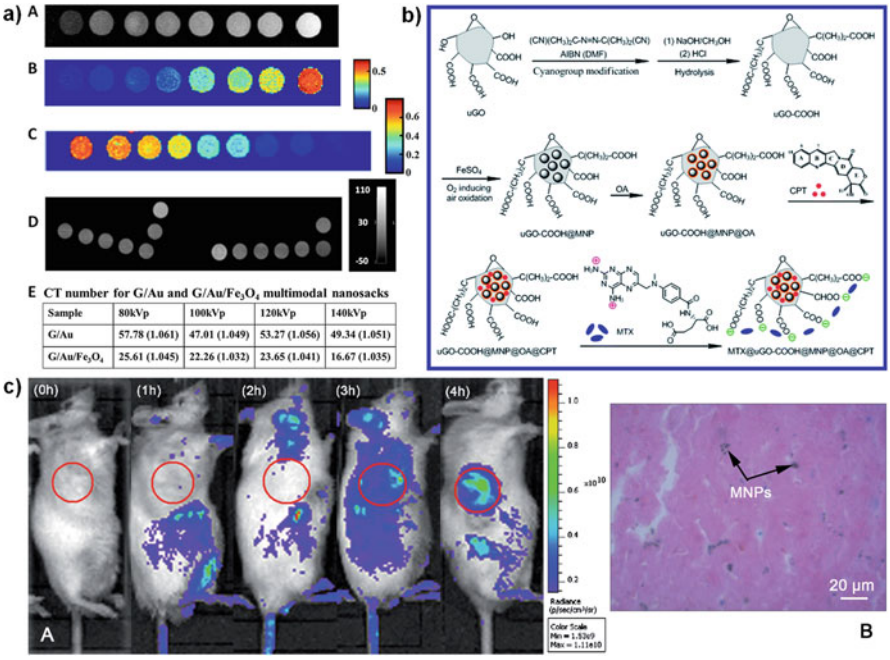

Fig. 9.12 (**a**) Clinical MRI and X-ray CT results showing contrast performance of rGO/Fe_3O_4, rGO/Au, and rGO/Au/Fe_3O_4 multifunctional probes. (*A*)T_2-weighted image (TE = 30 ms) of rGO/Fe_3O_4 nanosacks in CMC gel. Control (gel alone) is on right, with nanosack concentration increasing *right* to *left*: 0.5, 1, 2, 5, 10, 20, 50 μg/mL. (*B*) T_2 map computed from 24 echo image series. Color bar is T_2 in seconds. (*C*) MRI T_2 map of G/Au/Fe_3O_4 hybrid. Sack concentrations increase from *left* to *right* as 0.05, 0.1, 0.5, 1, 5, 10, 50, 100, and 500 μg/mL. (*D*) X-ray CT image (80 kVp) of G/Au nanosacks (right-hand L-shaped sequence) and free Au controls (left-hand L-shaped sequence). For G/Au nanosacks, sack concentrations (μg/mL) from *left* to *right* are 2000, 400, 200, 40, 20, gel control, H_2O control. For free Au, particle concentrations are (*left* to *right*) 400, 200, 40, 20, gel control with 2000 μg/mL sample at top, and a 200 μg/mL sample of empty sacks immediately beneath it. (*E*) Table of CT results shown as change in CT number with attenuation (relative to control gel sample) shown in parentheses. (**b**) Schematic diagram showing preparation of an MTX@uGO-COOH@MNP@OA@CPT nanocomposite. (**c**) (*A*) Typical in vivo images of male S-180 sarcoma-bearing Balb/c mice that have undergone magnetic guide at defined time periods (0, 1, 2, 3, and 4 h) postintravenous injection of RhB-labeled MTX@uGO-COOH@MNP@OA@CPT composite. *Red highlighted* sections are tumor sites. The system uses color coding of fluorescence with *red* for high levels of fluorescence and *blue* for low levels. Excitation = 570 nm, emission = 650 nm. (*B*) Representative microscope image of histochemical analysis of tumor tissue induced with magnetic field for 4 h after i.v. administration (H&E and Prussian blue stain, ×40). Reprinted with permission from Refs. [159, 160]. Copyright (2013) American Chemical Society & (2014) Royal Society of Chemistry

Shen et al. [160] proposed a novel method to synthesize MGNCs using ultrafine GO (uGO) and MNPs. The MGNC was fabricated by a combination of a simple and effective deposition with further oxidation of iron ions on a carboxylated uGO base, followed by oleic acid (OA) coating on MNPs. By making use of carboxyl terminals

of uGO, two anticancer drugs, camptothecin (CPT) and methotrexate (MTX), were separately bound to uGO sheets to afford a superparamagnetic and dual drug-loaded MTX@uGO-COOH@MNP@OA@CPT nanocomposite (Fig. 9.12b). In vitro release and apoptotic assay results indicated that the nanocomposite caused the apoptosis and death of HepG2 cells by preferentially releasing drugs to the tumor environment. The MTX@uGO-COOH@MNP@OA@CPT composite could target tumor tissue in vivo after labeling with Rh B. As can be seen in Fig. 9.12c, the uptake of Rh B-labeled MTX@uGO-COOH@MNP@OA@CPT was originally exhibited in the intraperitoneal organs with homogeneous distribution. PB staining of the tumor slice also clearly indicated that MNPs were uniformly scattered within the tumor tissue. In line with this, the tumor inhibitory rate of 73.9% in S-180 sarcoma–bearing Balb/c mice suggested that the combination of MTX@uGO-COOH@MNP@OA@CPT-mediated dual drug synergistic chemotherapy and PTT has excellent therapeutic potential against drug-resistant tumors. In their follow-up work [161], the group evaluated the safety of uGO-based MNPs and NSs both in vitro and in vivo. Specifically, at the organ level, explorations of biodistribution, MRI, and histopathology consistently showed that uGO-MNPs and uGO-MNSs were primarily trapped in the liver and spleen, while the heart, spleen, liver, and kidney were damaged. At the cellular level, blood compatibility and cytotoxicity studies demonstrated that uGO-MNSs possessed a higher toxicity than uGO-MNPs and resulted in ca. 47% (HepG2) and 48% (L02) loss of cell viability at their higher concentration.

Venkatesha et al. [162] prepared a series of GO-MNP composites by employing different amounts of GO [0.01 g (E1), 0.1 g (E2), and 0.2 g (E3)] and studied them as contrast agents in MRI. The observed trend in the proton relaxivity was found to be in the order E2 > E3 > E1, which contributed to the synergistic effect of the extent of reduction of GO as well as the arrangement of MNPs within the GO domain. It was generalized that a very high relaxivity value depends on both the large numbers of NPs and carboxylic functions on the GO surface.

Zhu et al. [163] developed a thermosensitive DOX-GO-IONP-PEI-gel using chitosan and β-glycerophosphate salt. Compared to the bare DOX, the DOX-GO-IONP-PEI-gel could efficiently pass through cell membranes, leading to more apoptosis and higher antitumor efficacy on MCF-7 cells in vitro. Moreover, intratumorally injected (*i.t.*) DOX-GO-IONP-PEI-gel showed high antitumor efficacy on tumor-bearing mice in vivo with no toxicity. Interestingly, the antitumor efficacy was found to be higher when combined with an alternating magnetic field (AMF). Chen et al. [164] synthesized an Fe_3O_4-PEG-GO nanocomposite by coupling reaction of *meso*-2,3,-dimercaptosuccinic acid (DMSA)-coated Fe_3O_4 NPs with PEGylated GO *via* EDC chemistry. The nanocomposite exhibited good physiological stability and did not affect cellular viability and proliferation. Compared to bare MNPs, the Fe_3O_4-PEG-GO nanocomposite showed significantly improved T_2-weighted MRI contrast. Furthermore, an efficient anticancer effect was realized with the DOX-loaded Fe_3O_4-PEG-GO nanocomposite as demonstrated by WST cytotoxicity experiments.

Very recently, Deng et al. [165] designed a hybrid microcapsule (h-MC) using a layer-by-layer technique, comprising polysaccharides, iron oxide, and GO. Elec-

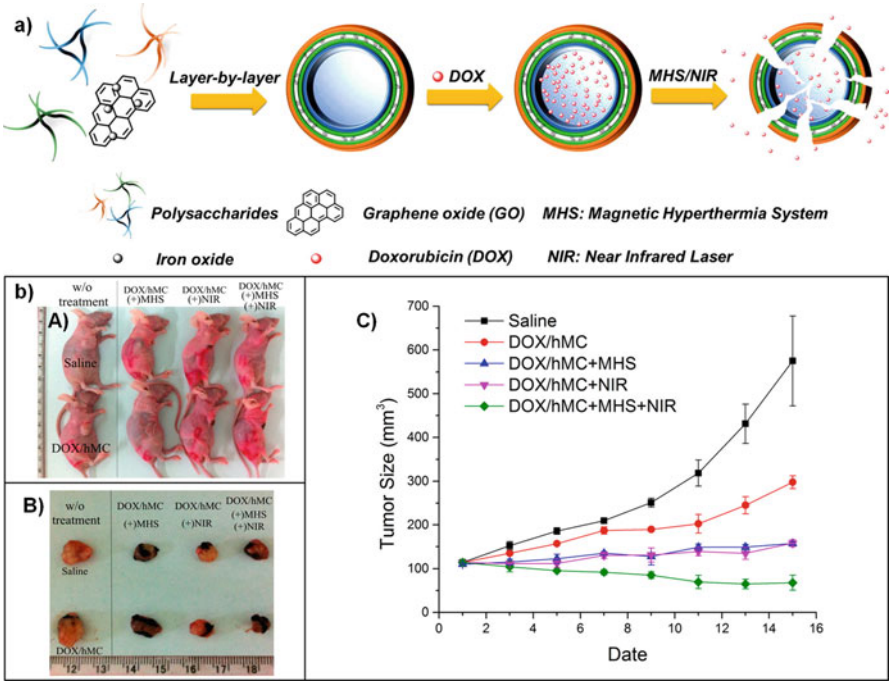

Fig. 9.13 (**a**) Schematic illustration of hybrid microcapsules (h-MC) created via layer-by-layer assembly. (**b**) in vivo study of h-MC capsules. (*A*) HeLa-bearing mice after injection of DOX-loaded h-MC (DOX/h-MC) with/without magnetic hyperthermia treatment (MHS) and NIR laser irradiation (NIR). (*B*) Tumor sizes after five rounds of treatment. (*C*) Tumor therapy using DOX-loaded h-MC with/without MHS and NIR. Reprinted with permission from Ref. [165]. Copyright (2016) American Chemical Society

trostatic assembly of the oppositely charged polysaccharides and graphene sheets provides a robust structure for pH-controlled drug loading and release. Whereas the polysaccharide components such as sodium alginate, chitosan, and hyaluronic acid, ensure high biocompatibility, bioavailability, and tumor cell targeting, the AMF and NIR laser-triggerable Fe_3O_4@GO components provide for dual high-energy and high-penetration hyperthermia therapy in vitro and in vivo (Fig. 9.13). On-demand drug release from h-MC could be achieved by synchronizing these external triggers, making the release highly controllable.

9.5 Conclusions

The aim of this chapter has been to illustrate the many magnetic graphene nanocomposites or systems that have been effectively utilized as biocatalysts, heterogeneous catalysts, and molecular imaging agents in enzyme mimics, carbon–

carbon coupling reactions, and biomedical applications, respectively. Besides the several distinctive advantages shared with other carbonaceous nanomaterials or their metal oxide/sulfide composites, such as nanodiamonds, carbon nanotubes, and carbon nanohorns, magnetic graphene nanocomposites are unique due to their specific large surface area, an exceptional physicochemistry for on-demand surface engineering, and synergistic features of individual components, enhancing their potential to be used in multifunctional applications. Given the fast pace in the area of sustainability, a variety of magnetic graphene nanocomposites (MGNCs) will certainly continue to thrive in the near future to address many physical, chemical, and biological processes, which were not previously accessible.

Acknowledgements Dr. B. Garg is thankful to the Science & Engineering Research Board (SERB), New Delhi, Government of India (YSS/2015/002036) for financial support. B. Garg additionally thanks to all the publishers, especially, Royal Society of Chemistry (RSC) for giving permissions to reuse the figures as illustrated in this chapter.

References

1. Kroto HW, Heath JR, O'Brien SC, Curl RF, Smalley RE (1985) C_{60}: Buckminsterfullerene. Nature 318:162–163
2. Iijima S (1991) Helical microtubules of graphitic carbon. Nature 354:56–58
3. Novoselov KS, Geim AK, Morozov SV, Jiang D, Zhang Y, Dubonos SV, Grigorieva IV, Firsov AA (2004) Electric field effect in atomically thin carbon films. Science 306:666–669
4. Geim AK, MacDonald AH (2007) Graphene: exploring carbon flatland. Phys Today 60: 35–41
5. Lee C, Wei X, Kysar JW, Hone J (2008) Science 321:385–388
6. Geim AK (2009) Graphene: status and prospects. Science 324:1530–1534
7. Bolotin KI, Ghahari F, Shulman MD, Stormer HL, Kim P (2009) Observation of the fractional quantum Hall effect in graphene. Nature 462:196–199
8. Bolotin KI, Sikes KJ, Jiang Z, Klima M, Fudenberg G, Hone J, Kim P, Stormer HL (2008) Ultrahigh electron mobility in suspended graphene. Solid State Commun 146:351–355
9. Nair RR, Blake P, Grigorenko AN, Novoselov KS, Booth TJ, Stauber T, Peres NMR, Geim AK (2008) Fine structure constant defines visual transparency of graphene. Science 320:1308–1308
10. Lee C, Wei XD, Kysar JW, Hone J (2008) Measurement of the elastic properties and intrinsic strength of monolayer graphene. Science 321:385–388
11. Balandin AA, Ghosh S, Bao W, Calizo I, Teweldebrhan D, Miao F, Lau CN (2008) Superior thermal conductivity of single-layer graphene. Nano Lett 8:902–907
12. Girit CO, Meyer JC, Erni R, Rossell MD, Kisielowski C, Yang L, Park CH, Crommie MF, Cohen ML, Louie SG, Zettl A (2009) Graphene at the edge: stability and dynamics. Science 323:1705–1708
13. Kim KS, Zhao Y, Jang H, Lee SY, Kim JM, Ahn JH, Kim P, Choi JY, Hong BH (2009) Large-scale pattern growth of graphene films for stretchable transparent electrodes. Nature 457:706–710
14. Chen H, Muller MB, Gilmore KJ, Wallace GG, Li D (2008) Mechanically strong, electrically conductive, and biocompatible graphene paper. Adv Mater 20:3557–3561
15. Chen XM, Wu GH, Jiang YQ, Wang YR, Chen X (2011) Graphene and graphene-based nanomaterials: the promising materials for bright future of electroanalytical chemistry. Analyst 136:4631–4640

16. Chen F, Tao NJ (2009) Electron transport in single molecules: from benzene to graphene. Acc Chem Res 42:429–438
17. Wan X, Huang Y, Chen Y (2012) Focusing on energy and optoelectronic applications: a journey for graphene and graphene oxide at large scale. Acc Chem Res 45:598–607
18. Chen Y, Zhang B, Liu G, Zhuang X, Kang E-T (2012) Graphene and its derivatives: switching ON and OFF. Chem Soc Rev 41:4688–4707
19. Dai L, Chang DW, Baek J-B, Lu W (2012) Carbon nanomaterials for advanced energy conversion and storage. Small 8:1130–1166
20. Huang X, Qi X, Boey F, Zhang H (2012) Graphene-based composites. Chem Soc Rev 41:666–686
21. Guo CX, Ng SR, Khoo SY, Zheng X, Chen P, Li CM (2012) RGD-peptide functionalized graphene biomimetic live-cell sensor for real-time detection of nitric oxide molecules. ACS Nano 6:6944–6951
22. Li Y, Wen T, Xue C, Han Q, Wang Y, Hong J, Zhou X, Jiang H (2013) RGO LBL modified biomimetic electrochemical sensor for detection of Sildenafil in herbal sexual health products. Biosens Bioelectron 42:287–292
23. Dreyer DR, Jia H-P, Bielawski CW (2010) Graphene oxide: a convenient carbocatalyst for facilitating oxidation and hydration reactions. Angew Chem Int Ed Engl 49:6813–6816
24. Machado BF, Serp P (2012) Graphene-based materials for catalysis. Cat Sci Technol 2:54–75
25. Su C, Loh KP (2013) Carbocatalysts: graphene oxide and its derivatives. Acc Chem Res 46:2275–2285
26. Garg B, Ling Y-C (2013) Versatilities of graphene-based catalysts in organic transformations. Green Mater 1:47–61
27. Navalon S, Dhakshinamoorthy A, Alvaro M, Garcia H (2014) Carbocatalysis by graphene-based materials. Chem Rev 114:6179–6212
28. Garg B, Bisht T, Ling Y-C (2014) Graphene-based nanomaterials as heterogeneous acid catalysts: a comprehensive perspective. Molecules 19:14582–14614
29. Shi S, Chen F, Ehlerding EB, Cai W (2014) Surface engineering of graphene-based nanomaterials for biomedical applications. Bioconjug Chem. 25:1609–1619
30. Zhang W, Guo ZY, Huang DQ, Liu ZM, Guo X, Zhong HQ (2011) Synergistic effect of chemo-photothermal therapy using PEGylated graphene oxide. Biomaterials 32:8555–8561
31. Julkapli NM, Bagheri S (2015) Graphene supported heterogeneous catalysts: an overview. Int J Hydrogen Energy 40:948–979
32. Fan X, Zhang G, Zhang F (2015) Multiple roles of graphene in heterogeneous catalysis. Chem Soc Rev 44:3023–3035
33. Garg B, Bisht T, Ling Y-C (2015) Graphene-based nanomaterials as efficient peroxidase mimetic catalysts for biosensing applications: An overview. Molecules 20:14155–14190
34. Zhang Y, Nayak TR, Hong H, Cai W (2012) Graphene: a versatile nanoplatform for biomedical applications. Nanoscale 4:3833–3842
35. Yang K, Feng L, Hong H, Cai W, Liu Z (2013) Preparation and functionalization of graphene nanocomposites for biomedical applications. Nat Protoc 8:2392–2403
36. Su J, Cao M, Ren L, Hu C (2011) Fe_3O_4-graphene nanocomposites with improved lithium storage and magnetism properties. J Phys Chem C 115:14469–14477
37. Brodie BC (1859) On the atomic weight of graphite. Philos Trans R Soc Lond A 149:249–259
38. Hummers WS Jr, Offeman RE (1958) Preparation of graphitic oxide. J Am Chem Soc 80:1339–1339
39. Lerf A, He H, Forster M, Klinowski J (1998) Structure of graphite oxide revisited. J Phys Chem B 102:4477–4482
40. Erickson K, Erni R, Lee Z, Alem N, Gannett W, Zettl A (2010) Determination of the local chemical structure of graphene oxide and reduced graphene oxide. Adv Mater 22:4467–4472
41. Hofmann U, Holst R (1939) Über die säurenatur und die methylierung von graphitoxyd. Ber Dtsch Chem Ges A/B 72:754–771
42. Szabó T, Tombácz E, Illés E, Dékány I (2006) Enhanced acidity and pH-dependent surface charge characterization of successively oxidized graphite oxides. Carbon 44:537–538

43. Xue YH, Chen H, Yu DS, Wang SY, Yardeni M, Dai QB, Guo MM, Liu Y, Lu F, Qu J, Dai LM (2011) Oxidizing metal ions with graphene oxide: the *in situ* formation of magnetic nanoparticles on self-reduced graphene sheets for multifunctional applications. Chem Commun 47:11689–11691
44. Singh V, Joung D, Zhai L, Das S, Khondaker SI, Seal S (2011) Graphene based materials: past, present and future. Prog Mater Sci 56:1178–1271
45. Upadhyay RK, Soin N, Roy SS (2014) Role of graphene/metal oxide composites as photocatalysts, adsorbents and disinfectants in water treatment: a review. RSC Adv. 4:3823–3851
46. Yusuf M, Elfghi FM, Zaidi SA, Abdullah EC, Khan MA (2015) Applications of graphene and its derivatives as an adsorbent for heavy metal and dye removal: a systematic and comprehensive overview. RSC Adv 5:50392–50420
47. Wang Z, Liu C-J (2015) Preparation and application of iron oxide/graphene based composites for electrochemical energy storage and energy conversion devices: current status and perspective. Nano Energy 11:277–293
48. Sun HM, Cao LY, Lu LH (2011) Magnetite/reduced graphene oxide nanocomposites: one step solvothermal synthesis and use as a novel platform for removal of dye pollutants. Nano Res 4:550–562
49. Zong PF, Wang SF, Zhao YL, Wang H, Pan H, He CH (2013) Synthesis and application of magnetic graphene/iron oxides composite for the removal of U(VI) from aqueous solutions. Chem Eng J 220:45–52
50. Fan XJ, Jiao GZ, Zhao W, Jin PF, Li X (2013) Magnetic Fe_3O_4-graphene composites as targeted drug nanocarriers for pH-activated release. Nanoscale 5:1143–1152
51. Li Y, Chu J, Qi JY, Li X (2011) An easy and novel approach for the decoration of graphene oxide by Fe_3O_4 nanoparticles. Appl Surf Sci 257:6059–6062
52. Shen XP, Wu JL, Bai S, Zhou HJ (2010) One-pot solvothermal syntheses and magnetic properties of graphene-based magnetic nanocomposites. Alloys Compd 506:136–140
53. Singh VK, Patra MK, Manoth M, Gowd GS, Vadera SR, Kumar N (2009) *in situ* synthesis of graphene oxide and its composites with iron oxide. New Carbon Mater 24:147–152
54. Yang S, Sun Y, Chen L, Hernandez Y, Feng X, Müllen K (2012) Porous iron oxide ribbons grown on graphene for high-performance lithium storage. Sci Rep 2:427–433
55. Kamiya K, Hashimoto K, Nakanishi S (2012) Instantaneous one-pot synthesis of Fe-N-modified graphene as an efficient electrocatalyst for the oxygen reduction reaction in acidic solutions. Chem Commun 48:10213–10215
56. Chandra V, Park J, Chun Y, Lee JW, Hwang IC, Kim KS (2010) Water-dispersible magnetite-reduced graphene oxide composites for arsenic removal. ACS Nano 4:3979–3986
57. Zhang M, Qu B, Lei D, Chen Y, Yu X, Chen L, Li Q, Wang Y, Wang T (2012) A green and fast strategy for the scalable synthesis of Fe_2O_3/graphene with significantly enhanced Li-ion storage properties. J Mater Chem 22:3868–3874
58. Karthikeyan K, Kalpana D, Amaresh S, Lee YS (2012) Microwave synthesis of graphene/magnetite composite electrode material for symmetric supercapacitor with superior rate performance. RSC Adv 2:12322–12328
59. Yu SH, Conte DE, Baek S, Lee DC, Park SK, Lee KJ, Piao YZ, Sung YE, Pinna N (2013) Structure-properties relationship in iron oxide-reduced graphene oxide nanostructures for Li-ion batteries. Adv Funct Mater 23:4293–4305
60. Zhou GM, Wang DW, Li F, Zhang LL, Li N, Wu ZS, Wen L, Lu GQ, Cheng HM (2010) Graphene-wrapped Fe_3O_4 anode material with improved reversible capacity and cyclic stability for lithium ion batteries. Chem Mater 22:5306–5313
61. Zhang WY, Zeng Y, Xu C, Tan HT, Liu WL, Zhu JX, Xiao N, Hng HH, Ma J, Hoster HE, Yazami R, Yan QY (2012) Fe_2O_3 nanocluster-decorated graphene as O_2 electrode for high energy Li-O_2 batteries. RSC Adv 2:8508–8514
62. Schmitt OH (1969) Some interesting and useful biomimetic transform. In: Proceedings of third internatioanl biophysics congress, Boston, MA, 29 August–3 September 1969, p 297

63. Wolfenden R, Snider MJ (2001) The depth of chemical time and the power of enzymes as catalysts. Acc Chem Res 34:938–945
64. Garcia-Viloca M, Gao J, Karplus M, Truhlar DG (2004) How enzymes work: analysis by modern rate theory and computer simulations. Science 303:186–195
65. Hennrich N, Cramer F (1965) Inclusion compounds. XVIII.1 the catalysis of the fission of pyrophosphates by cyclodextrin. A model reaction for the mechanism of enzymes. J Am Chem Soc 87:1121–1126
66. Klotz IM, Royer GP, Scarpa IS (1971) Synthetic derivatives of polyethyleneimine with enzyme-like catalytic activity (synzymes). Proc Natl Acad Sci U S A 68:263–264
67. Breslow R, Overman LE (1970) Artificial enzyme combing a metal catalytic group and a hydrophobic binding cavity. J Am Chem Soc 92:1075–1077
68. Bhabak KP, Mugesh G (2010) Functional mimics of glutathione peroxidase: bioinspired synthetic antioxidants. Acc Chem Res 43:1408–1419
69. Lin Y, Ren J, Qu X (2014) Catalytically active nanomaterials: a promising candidate for artificial enzymes. Acc Chem Res 47:1097–1105
70. Friedle S, Reisner E, Lippard SJ (2010) Current challenges of modeling diiron enzyme active sites for dioxygen activation by biomimetic synthetic complexes. Chem Soc Rev 39:2768–2779
71. Sumner JB (1926) The isolation and crystallization of the enzyme urease. J Biol Chem 69:435–441
72. Breslow R (1972) Centenary lecture. Biomimetic chemistry. Chem Soc Rev 1:553–580
73. Tabushi I (1982) Cyclodextrin catalysis as a model for enzyme action. Acc Chem Res 15:66–72
74. Takagishi T, Klotz IM (1972) Macromolecule-small molecule interactions; introduction of additional binding sites in polyethyleneimine by disulfide cross-linkages. Biopolymers 11:483–491
75. Tramontano A, Janda KD, Lerner RA (1986) Catalytic antibodies. Science 234:1566–1570
76. Breaker RR, Joyce GF (1994) A DNA enzyme that cleaves RNA. Chem Biol 1:223–229
77. Cuevas F, Di Stefano S, Magrans JO, Prados P, Mandolini L, de Mendoza J (2000) Toward an artificial acetylcholinesterase. Chem A Eur J 6:3228–3234
78. Kuah E, Toh S, Yee J, Ma Q, Gao Z (2016) Enzyme mimics: advances and applications. Chem A Eur J 22:8404–8430
79. Ragg R, Tahir MN, Tremel W (2016) Solid go bio: inorganic nanoparticles as enzyme mimics. Eur J Inorg Chem 2016:1906–1915
80. Manea F, Houillon FB, Pasquato L, Scrimin P (2004) Nanozymes: gold-nanoparticle-based transphosphorylation catalysts. Angew Chem Int Ed Engl 43:6165–6169
81. Wei H, Wang E (2013) Nanomaterials with enzyme-like characteristics (nanozymes): next-generation artificial enzymes. Chem Soc Rev 42:6060–6093
82. He W, Wamer W, Xia Q, Yin J-J, Fu PP (2014) Enzyme-like activity of nanomaterials. J Environ Sci Health C Environ Carcinog Ecotoxicol Rev 32:186–211
83. Wang X, Hu Y, Wei H (2016) Nanozymes in bionanotechnology: from sensing to therapeutics and beyond. Inorg Chem Front 3:41–60
84. Comotti M, Della Pina C, Matarrese R, Rossi M (2004) The catalytic activity of "naked" gold particles. Angew Chem Int Ed Engl 43:5812–5815
85. Wan Y, Qi P, Zhang D, Wu J, Wang Y (2012) Manganese oxide nanowire-mediated enzyme-linked immunosorbent assay. Biosens Bioelectron 33:69–74
86. Ali SS, Hardt JI, Quick KL, Kim-Han JS, Erlanger BF, Huang TT, Epstein CJ, Dugan LL (2004) A biologically effective fullerene (C60) derivative with superoxide dismutase mimetic properties. Free Radic Biol Med 37:1191–1202
87. Quick KL, Ali SS, Arch R, Xiong C, Wozniak D, Dugan LL (2008) A carboxyfullerene SOD mimetic improves cognition and extends the lifespan of mice. Neurobiol Aging 29:117–128
88. Song Y, Wang X, Zhao C, Qu K, Ren J, Qu X (2010) Label-free colorimetric detection of single nucleotide polymorphism by using single-walled carbon nanotube intrinsic peroxidase-like activity. Chem A Eur J 16:3617–3621

89. Song Y, Qu K, Zhao C, Ren J, Qu X (2010) Graphene oxide: Intrinsic peroxidase catalytic activity and its application to glucose detection. Adv Mater 22:2206–2210
90. Veitch NC (2004) Horseradish peroxidase: a modern view of a classic enzyme. Phytochemistry 65:249–259
91. Hamid M, Khalil-ur-Rehman (2009) Potential applications of peroxidases. Food Chem 115:1177–1186
92. Dong Y, Zhang H, Rahman ZU, Su L, Chen X, Hu J, Chen X (2012) Graphene oxide-Fe_3O_4 magnetic nanocomposites with peroxidase-like activity for colorimetric detection of glucose. Nanoscale 4:3969–3976
93. Hao J, Zhang Z, Yang W, Lu B, Ke X, Zhang B, Tang J (2013) *in situ* controllable growth of $CoFe_2O_4$ ferrite nanocubes on graphene for colorimetric detection of hydrogen peroxide. J Mater Chem A 1:4352–4357
94. Xing Z, Tian J, Asiri AM, Qusti AH, Al-Youbi AO, Sun X (2014) Two-dimensional hybrid mesoporous Fe_2O_3-graphene nanostructures: a highly active and reusable peroxidase mimetic toward rapid, highly sensitive optical detection of glucose. Biosens Bioelectron 52:452–457
95. Wu Z-S, Ren W, Wen L, Gao L, Zhao J, Chen Z, Zhou G, Li F, Cheng H-M (2010) Graphene anchored with Co_3O_4 nanoparticles as anode of lithium ion batteries with enhanced reversible capacity and cyclic performance. ACS Nano 4:3187–3194
96. Wang D, Li Y, Wang Q, Wang TJ (2012) Nanostructured Fe_2O_3–graphene composite as a novel electrode material for supercapacitors. Solid State Electrochem. 16:2095–2102
97. Wei H, Wang E (2008) Fe_3O_4 magnetic nanoparticles as peroxidase mimetics and their applications in H_2O_2 and glucose detection. Anal Chem 80:2250–2254
98. Tian J, Liu S, Luo Y, Sun X (2012) Fe(III)-based coordination polymernanoparticles: peroxidase-like catalytic activity and their application to hydrogen peroxide and glucose detection. Cat Sci Technol 2:432–436
99. Kim M II, Kim MS, Woo MA, Ye Y, Kang KS, Lee J, Park HG (2014) Highly efficient colorimetric detection of target cancer cells utilizing superior catalytic activity of graphene-oxidemagnetic-platinum nanohybrids. Nanoscale 6:1529–1536
100. Xing Y (2004) Synthesis and electrochemical characterization of uniformly-dispersed high loading Pt nanoparticles on sonochemically-treated carbon nanotubes. J Phys Chem B 108:19255–19259
101. Wang C, Daimon H, Sun S (2009) Dumbbell-like Pt-Fe_3O_4 nanoparticles and their enhanced catalysis for oxygen reduction reaction. Nano Lett 9:1493–1496
102. Bi S, Zhao T, Jia X, He P (2014) Magnetic graphene oxide-supported hemin as peroxidase probe for sensitive detection of thiols in extracts of cancer cells. Biosens Bioelectron 57:110–116
103. Qian J, Yang X, Jiang L, Zhu C, Mao H, Wang K (2014) Facile preparation of Fe_3O_4 nanospheres/reduced graphene oxide nanocomposites with high peroxidase-like activity for sensitive and selective colorimetric detection of acetylcholine. Sens Actuators B Chem 201:160–166
104. Wang H, Li S, Si Y, Sun Z, Li S, Lin Y (2014) Recyclable enzyme mimic of cubic Fe_3O_4 nanoparticles loaded on graphene oxide-dispersed carbon nanotubes with enhanced peroxidase-like catalysis and electrocatalysis. J Mater Chem B 2:4442–4448
105. Kovalenko MV, Bodnarchuk MI, Lechner RT, Hesser G, Schaffler F, Heiss W (2007) Fatty acid salts as stabilizers in size- and shape-controlled nanocrystal synthesis: the case of inverse spinel iron oxide. J Am Chem Soc 129:6352–6353
106. Hsu K, Lien CW, Lin CH, Chang HT, Huang CC (2014) Immobilization of iron hydroxide/oxide on reduced graphene oxide: peroxidase-like activity and selective detection of sulfide ions. RSC Adv 4:37705–37713
107. Wang S (2008) A comparative study of Fenton and Fenton-like reaction kinetics in decolourisation of wastewater. Dyes Pigments 76:714–720
108. Yun J-H, Ng YH, Wong RJ, Amal R (2013) Reduced graphene oxide: control of water miscibility, conductivity, and defects by photocatalysis. ChemCatChem 5:3060–3067

109. Zheng X, Zhu Q, Song H, Zhao X, Yi T, Chen H, Chen X (2015) *in situ* synthesis of self-assembled three-dimensional graphene-magnetic palladium nanohybrids with dual-enzyme activity through one-pot strategy and its application in glucose probe. ACS Appl Mater Interfaces 7:3480–3491
110. Li L, Zeng C, Ai L, Jiang J (2015) Synthesis of reduced graphene oxide-iron nanoparticles with superior enzyme-mimetic activity for biosensing application. J Alloys Compd 639:470–477
111. Zhang S, Li H, Wang Z, Liu J, Zhang H, Wang B, Yang Z (2015) A strongly coupled Au/Fe_3O_4/GO hybrid material with enhanced nanozyme activity for highly sensitive colorimetric detection, and rapid and efficient removal of Hg^{2+} in aqueous solutions. Nanoscale 7:8495–8502
112. Long YJ, Li YF, Liu Y, Zheng J-J, Tang J, Huang CZ (2011) Visual observation of the mercury-stimulated peroxidase mimetic activity of gold nanoparticles. Chem Commun 47:11939–11941
113. Li S, Li H, Chen F, Liu J, Zhang H, Yang Z, Wang B (2016) Strong coupled palladium nanoparticles decorated on magnetic graphene nanosheets as enhanced peroxidase mimetics for colorimetric detection of H_2O_2. Dyes Pigments 125:64–71
114. Mizuno N, Misono M (1998) Heterogeneous catalysis. Chem Rev 98:199–217
115. Okuhara T (2002) Water-tolerant solid acid catalysts. Chem Rev 102:3641–3666
116. Harmer MA, Farneth WE, Sun Q (1996) High surface area nafion resin/silica nanocomposites: a new class of solid acid catalyst. J Am Chem Soc 118:7708–7715
117. Yin L, Liebscher J (2007) Carbon-carbon coupling reactions catalyzed by heterogeneous palladium catalysts. Chem Rev 107:133–173
118. Miyaura N, Yamada K, Suzuki A (1979) A new stereospecific cross-coupling by the palladium-catalyzed reaction of 1-alkenylboranes with 1-alkenyl or 1-alkynyl halides. Tetrahedron Lett 20:3437–3440
119. Miyaura N, Suzuki A (1979) Stereoselective synthesis of arylated (E)-alkenes by the reaction of alk-1-enylboranes with aryl halides in the presence of palladium catalyst. J Chem Soc Chem Commun 19:866–867
120. Mizoroki T, Mori K, Ozaki A (1971) Arylation of olefin with aryl iodide catalyzed by palladium. Bull Chem Soc Jpn 44:581–581
121. Heck RF, Nolley JP Jr (1972) Palladium-catalyzed vinylic hydrogen substitution reactions with aryl, benzyl, and styryl halides. J Org Chem 37:2320–2322
122. Fanta PE (1974) The Ullmann synthesis of biaryls. Synthesis 1:9–21
123. Corriu RJP, Masse JP (1972) Activation of Grignard reagents by transitionmetal complexes. A new and simple synthesis of trans-stilbenes and polyphenyls. J Chem Soc Chem Commun 3:113–204
124. Tamao K, Sumitani K, Kumada M (1972) Selective carbon-carbon bond formation by cross-coupling of Grignard reagents with organic halides. Catalysis by nickel-phosphine complexes. J Am Chem Soc 94:4374–4376
125. Hu J, Wang Y, Han M, Zhou Y, Jiang X, Sun P (2012) A facile preparation of palladium nanoparticles supported on magnetite/s-graphene and their catalytic application in Suzuki-Miyaura reaction. Cat Sci Technol 2:2332–2340
126. Dabiri M, Shariatipour M, Movahed SK, Bashiribod S (2014) Waterdispersible and magnetically separable gold nanoparticles supported on a magnetite/s-graphene nanocomposite and their catalytic application in the Ullmann coupling of aryl iodides in aqueous media. RSC Adv 4:39428–39434
127. Dabiri M, Lehi NF, Movahed SK (2016) Fe_3O_4@rGO@Au@C composite with magnetic core and Au enwrapped in double-shelled carbon: an excellent catalyst in the reduction of nitroarenes and Suzuki-Miyaura cross-coupling. Catal Lett 146:1674–1686
128. Ma'mani L, Miri S, Mahdavi M, Bahadorikhalili S, Lotfi E, Foroumadi A, Shafiee A (2014) Palladium catalyst supported on N-aminoguanidine functionalized magnetic graphene oxide as a robust water-tolerant and versatile nanocatalyst. RSC Adv 4:48613–48620

129. Hoseini SJ, Heidari V, Nasrabadi H (2015) Magnetic Pd/Fe_3O_4/reducedgraphene oxide nanohybrid as anefficient and recoverable catalyst for Suzuki-Miyaura couplingreaction in water. J Mol Cat A Chem 396:90–95
130. Elazab HA, Siamaki AR, Moussa S, Gupton BF, El-Shall MS (2015) Highly efficient and magnetically recyclable graphene-supported Pd/Fe_3O_4 nanoparticle catalysts for Suzuli and Heck cross-coupling reactions. Appl Catal A Gen 491:58–69
131. Yao T, Wang H, Zuo Q, Wu J, Zhang X, Cui F, Cui T (2015) One step preparation of reduced graphene oxide/Pd-Fe_3O_4@polypyrrole composites and their application in catalysis. Chem Asian J 10:1940–1947
132. Yao T, Zhang J, Zuo Q, Wang H, Wu J, Zhang X, Cui T (2016) A simple way to prepare reduced graphene oxide nanosheets/Fe_2O_3-Pd/N-doped carbon nanosheets and their application in catalysis. J Colloid Interface Sci 468:62–69
133. Zhao X, Liu X (2015) A novel magnetic $NiFe_2O_4$@graphene-Pd multifunctional nanocomposite for practical catalytic application. RSC Adv 5:79548–79555
134. Liu X, Zhao X, Zhu J, Xu J (2016) One-pot synthesis of magnetic palladium-$NiFe_2O_4$-graphene oxide composite: an efficient and recyclable catalyst for Heck reaction. Appl Organomet Chem 30:354–359
135. Yang F, Feng A, Wang C, Dong S, Chi C, Jia X, Zhang L, Li Y (2016) Graphene oxide/carbon nanotubes-Fe_3O_4 supported Pd nanoparticles for hydrogenation of nitroarenes and C-H activation. RSC Adv 6:16911–16916
136. Zhang M, Liu Y-H, Shang Z-R, Hu H-C, Zhang Z-H (2017) Supported molybdenum on graphene oxide/Fe_3O_4: an efficient, magnetically separable catalyst for one-pot construction of spiro-oxindole dihydropyridines in deep eutectic solvent under microwave irradiation. Catal Commun 88:39–44
137. Yang B, Tian Z, Wang B, Sun Z, Zhang L, Guo Y, Li H, Yan S (2015) Facile synthesis of Fe_3O_4-hierarchical-Mn_3O_4/graphene oxide as a synergistic catalyst for activation of peroxymonosulfate for degradation of organic pollutants. RSC Adv 5:20674–20683
138. Cheng Z, Liao J, He B, Zhang F, Zhang F, Huang X, Zhou L (2015) One-step fabrication of graphene oxide enhanced magnetic composite gel for highly efficient dye adsorption and catalysis. ACS Sustain Chem Eng 3:1677–1685
139. Lin K-YA, Hsu F-K, Lee W-D (2015) Magnetic cobalt-graphene nanocomposite derived from self-assembly of MOFs with graphene oxide as an activator for peroxymonosulfate. J Mater Chem A 3:9480–9490
140. Du J, Bao J, Liu Y, Ling H, Zheng H, Kim SH, Dionysiou DD (2016) Efficient activation of peroxymonosulfate by magnetic Mn-MGO for degradation of bisphenol A. J Hazard Mater 320:150–159
141. Gao L, Wang Y, Yan T, Cui L, Hu L, Yan L, Wei Q, Du B (2015) A novel magnetic polysaccharide-graphene oxide composite for removal of cationic dyes from aqueous solution. New J Chem 39:2908–2916
142. Jiao T, Liu Y, Wu Y, Zhang Q, Yan X, Gao F, Bauer AJP, Liu J, Zeng T, Li B (2015) Facile and scalable preparation of graphene oxide-based magnetic hybrids for fast and highly efficient removal of organic dyes. Sci Rep 5:12451–12460
143. Zha J-W, Huang W, Wang S-J, Zhang D-L, Li RKY, Dang Z-M (2016) Difunctional graphene-Fe_3O_4 hybrid nanosheet/polydimethylsiloxane nanocomposites with high positive piezoresistive and superparamagnetism properties as flexible touch sensors. Adv Mater Interfaces 3:1500418–1500426
144. Liu X, Zhao T, Cheng H, Zhu C, Li S, Cui P (2015) In-situ synthesis of nanomagnetites on poly(amidoamine)-modified graphite oxides and their novel catalytic performances towards the degradation of p-nitroaniline. Appl Surf Sci 327:226–232
145. Hussain N, Gogoi P, Khare P, Das MR (2015) Nickel nanoparticles supported on reduced graphene oxide sheets: a phosphine free, magnetically recoverable and cost effective catalyst for Sonogashira cross-coupling reactions. RSC Adv 5:103105–103115

146. Garg B, Sung C-H, Ling Y-C (2015) Graphene-based nanomaterials as molecular imaging agents. WIREs Nanomed Nanobiotechnol 7:737–758
147. Yoo JM, Kang JH, Hong BH (2015) Graphene-based nanomaterials for versatile imaging studies. Chem Soc Rev 44:4835–4852
148. Wang Y, Zhen SJ, Zhang Y, Li YF, Huang CZ (2011) Facile fabrication of metal nanoparticle/graphene oxide hybrids: a new strategy to directly illuminate graphene for optical imaging. J Phys Chem C 115:12815–12821
149. Jaganathan H, Hugar DL, Ivanisevic A (2011) Examining MRI contrast in three-dimensional cell culture phantoms with DNA-templated nanoparticle chains. ACS Appl Mater Interfaces 3:1282–1288
150. Chen W, Yi P, Zhang Y, Zhang L, Deng Z, Zhang Z (2011) Composites of aminodextran-coated Fe_3O_4 nanoparticles and graphene oxide for cellular magnetic resonance imaging. ACS Appl Mater Interfaces 3:4085–4091
151. Yang XY, Zhang XY, Ma YF, Huang Y, Wang YS, Chen YS (2009) Superparamagnetic graphene oxide-Fe_3O_4 nanoparticles hybrid for controlled targeted drug carriers. J Mater Chem 19:2710–2714
152. Cong HP, He JJ, Lu Y, Yu SH (2010) Water-soluble magnetic-functionalized reduced graphene oxide sheets: *in situ* synthesis and magnetic resonance imaging applications. Small 6:169–173
153. Yang K, Hu L, Ma X, Ye S, Cheng L, Shi X, Li C, Li Y, Liu Z (2012) Multimodal imaging guided photothermal therapy using functionalized graphene nanosheets anchored with magnetic nanoparticles. Adv Mater 24:1868–1872
154. Ma X, Tao H, Yang K, Feng L, Cheng L, Shi X, Li Y, Guo L, Liu ZA (2012) Functionalized graphene oxide-iron oxide nanocomposite for magnetically targeted drug delivery, photothermal therapy, and magnetic resonance imaging. Nano Res 3:199–212
155. Narayanan TN, Gupta BK, Vithayathil SA, Aburto RR, Mani SA, Taha-Tijerina J, Xie B, Kaipparettu BA, Torti SV, Ajayan PM (2012) Hybrid 2D nanomaterials as dual-mode contrast agents in cellular imaging. Adv Mater 24:2992–2998
156. Peng E, Choo ESG, Chandrasekharan P, Yang C-T, Ding J, Chuang K-H, Xue JM (2012) Synthesis of manganese ferrite/graphene oxide nanocomposites for biomedical applications. Small 8:3620–3630
157. Chen M-L, Shen L-M, Chen S, Wang H, Chen X-W, Wang J-H (2013) *in situ* growth of β-FeOOH nanorods on graphene oxide with ultra-high relaxivity for in vivo magnetic resonance imaging and cancer therapy. J Mater Chem B 1:2582–2589
158. Shi X, Gong H, Li Y, Wang C, Cheng L, Liu Z (2013) Graphene-based magnetic palsmonic nanocomposite for dual bioimaging and photothermal therapy. Biomaterials 34:4786–4793
159. Chen Y, Guo F, Qiu Y, Hu H, Kulaots I, Walsh E, Hurt RH (2013) Encapsulation of particle ensembles in graphene nanosacks as a new route to multifunctional materials. ACS Nano 7:3744–3753
160. Shen J-M, Gao F-Y, Guan L-P, Su W, Yang Y-J, Li Q-R, Jin Z-C (2014) Graphene oxide-Fe_3O_4 nanocomposite for combination of dual-drug chemotherapy with photothermal therapy. RSC Adv 4:18473–18484
161. Shen J-M, Huang G, Zhou X, Zou J, Yang Y, Chen Y-F, Men S-K (2014) Safety evaluation of graphene oxide-based magnetic nanocomposites as MRI contrast agents and drug delivery vehicles. RSC Adv 4:50464–50477
162. Venkatesha N, Poojar P, Qurishi Y, Geethanath S, Srivastava C (2015) Graphene oxide-Fe_3O_4 nanoparticle composite with high transverse proton relaxivity value for magnetic resonance imaging. J Appl Phys 117:154702–154709
163. Zhu X, Zhang H, Huang H, Zhang Y, Hou L, Zhang Z (2015) Functionalized graphene oxide-based thermosensitive hydrogel for magnetic hyperthermia therapy on tumors. Nanotechnology 26:365103–365114

164. Chen W, Wen X, Zhen G, Zheng X (2015) Assembly of Fe_3O_4 nanoparticles on PEG-functionalized graphene oxide for efficient magnetic imaging and drug delivery. RSC Adv 5:69307–69311
165. Deng L, Li Q, Al-Rehili S, Omar H, Almalik A, Alshamsan A, Zhang J, Khashab NM (2016) Hybrid iron oxide-graphene oxide-polysaccharides microcapsule: a micro-matryoshka for on-demand drug release and antitumor therapy in vivo. ACS Appl Mater Interfaces 8:6859–6868

Chapter 10
Graphene-Based Multifunctional Magnetic Nanocomposites and Their Multimode Biomedical Applications

Trupti R. Das, Suryakanti Debata, Rashmi Madhuri, and Prashant K. Sharma

10.1 Introduction

10.1.1 A brief Introduction to Carbon Allotropes

The term *allotrope* explains the existence of a single element in two or different physical states. Carbon (C) is the frontline paradigm of allotropic elements. The valency of C is the central cause of different allotropic forms, including diamonds, graphite, lonsdaleite, C60 (Bucky ball), C540, C70, amorphous carbon, and carbon nanotubes. The allotrope C60, that is, the fullerene, was discovered in 1996 and earned a Nobel Prize. The structure of the fullerene looks like a soccer ball that contains 60 carbon atoms. The presence of 20 hexagons and 12 pentagons in the fullerene causes the surface to have a spherical shape. Nanotube is a one-dimensional (1D) cylindrical nanostructure that can be made by rolling graphene sheets. It was discovered in 1993 and has electronic and mechanical properties similar to those of graphene [1].

Graphite is a hexagonal form of carbon sheets stacked on each other, forming a three-dimensional (3D) structure. Previously, to conduct electrical measurements, it was necessary to isolate an individual sheet. However, early on that was somewhat difficult. In October 2004, the physics world was shocked by the news relating to the

T.R. Das • S. Debata • P.K. Sharma (✉)
Functional Nanomaterials Research Laboratory, Department of Applied Physics, Indian Institute of Technology (Indian School of Mines), Dhanbad, Jharkhand, 826004, India
e-mail: prashantnac@gmail.com

R. Madhuri (✉)
Department of Applied Chemistry, Indian Institute of Technology (Indian School of Mines), Dhanbad, Jharkhand, 826004, India
e-mail: rshmmadhuri@gmail.com

© Springer International Publishing AG 2017

S.K. Sharma (ed.), *Complex Magnetic Nanostructures*,
DOI 10.1007/978-3-319-52087-2_10

formation of two dimensional (2D) graphene sheets. Konstantin Novoselov, Andre Geim, and their collaborators revolutionized nanoscience and technology with the discovery of this youngest allotrope of graphite [1, 2].

10.1.2 Graphene and Graphene Oxide

Graphene is the tilling of benzene hexagon, with the carbon atoms of benzene being replaced by hydrogen atoms. Graphene consists of 2D nanostructures or the mother of all allotropic forms, i.e., a 0D fullerene, 1D carbon nanotubes, and 3D graphite. A graphene sheet can wrapped up into 0D fullerene, rolled up into a 1D carbon nanotube, and stacked on each other to give 3D graphite (Fig. 10.1). The 2D material contains a high crystalline quality. The charge carriers in 2D graphene have the capability of traveling thousand interatomic distances without scattering [2]. The carbon–carbon distance in 2D graphene is 0.142 nm.

Different methods can be used to synthesize graphene, for example, chemical vapor deposition, chemical exfoliation, epitaxial growth on SiC, or Scotch tape. The main obstacle to synthesizing graphene arises during the separation of bulk

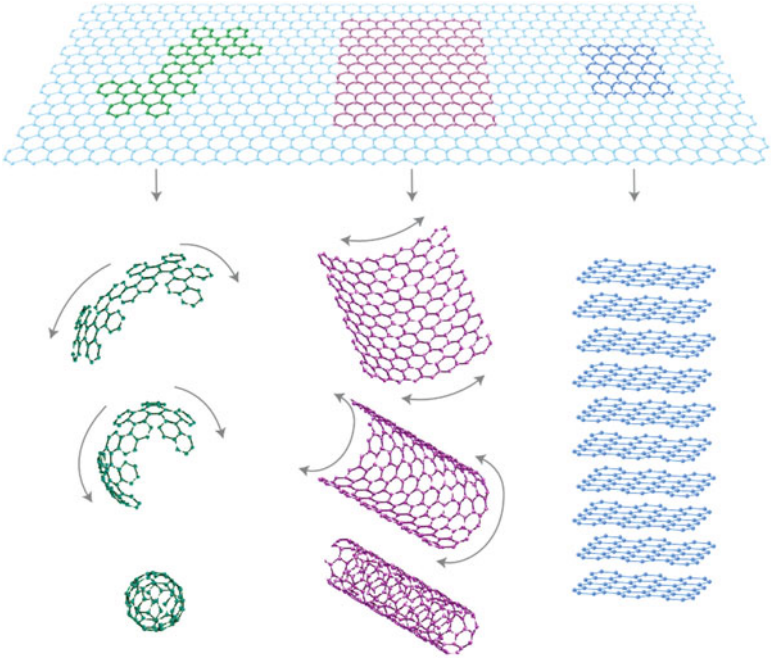

Fig. 10.1 Mother of all graphitic forms. Graphene is a 2D building material for carbon materials of all other dimensionalities. It can be wrapped up into 0D buckyballs, rolled into 1D nanotubes, or stacked into 3D graphite. Reproduced with permission from [2]

graphite against the van der Waal forces among the layers [3]. Graphene oxide (GO) is the best way to synthesize graphene using a chemical method. Owing to the presence of various oxygen functional groups in GO, it has become a suitable candidate for various applications through functionalization. To analyze the structure of graphite, in 1859, British chemist B.C. Brodie conducted an experiment using $KClO_3$ and HNO_3. He conclude with a material having a mass greater than that of graphite flakes containing carbon, hydrogen, and oxygen with a ratio of C:H:O::61.04:1.88:37.11. Brodie named the material graphic acid owing to its dispersibility in normal water and in basic water (not in acidic media). Forty years after this experiment, L. Staudenmair improved Brodie's method by adding chlorate in multiple aliquot over the course of the reaction. This resulted in a carbon-to-oxygen ratio of 2:1. Then, 60 years later, Hummers and Offeman developed an oxidation method by adding $KMnO_4$ and H_2SO_4 [4]. In the case of GO, different oxygen-containing functional groups, like carboxyl, hydroxyl, epoxy, and carbonyl, are present on its basal plane and in the edges. Normally carboxyl groups are found at the edges of 2D graphene sheets. Such oxygen-containing functional groups are the main reason for the binding of various nanoparticles on its surface through electrostatic attraction and covalent bonding.

10.1.2.1 Structure

GO and reduced GO are 2D nanosheets. In the case of graphene, the carbon atoms are sp^2-hybridized, whereas in the case of GO, the carbon atoms are sp^3-hybridized. The X-ray diffraction (XRD) study of GO and rGO explains the structural information on the materials. Krishnamoorthy et al. have studied the XRD spectra of GO with different degrees of oxidation. In the case of reduced GO, a peak arises at $2\theta = 26.3°$, which corresponds to an interplanar spacing of 0.34 nm. The researchers increased the degree of oxidation. It was observed that when the degree of oxidation was increased, the degree of intensity disappeared at then position $2\theta = 26.3°$, resulting in a peak at a lower diffraction angle. A peak at $2\theta = 13.3°$ corresponds to GO with large interplanar spacing [5].

10.1.2.2 Morphology

The 2D honeycomb lattice is formed by two carbon atoms joining with each other by a σ bond. Thus, there will be a π orbital in the carbon atom that contributes to a delocalized network of electrons. A transmission electron microscopy (TEM) study is very easy for such light atoms [6]. The edges of graphene have two different forms, a zigzag and an armchair [7]. In the armchair edge, elastic scattering occurs and the D band gives strong intensity in Raman studies [6]. The electronic property of graphene alters with the layer of graphene. The stacking of graphene sheets to make graphite occurs based on AA or AB stacking. For graphite AB stacking is stable. Bilayer graphene shows a parabolic band. In technical applications using

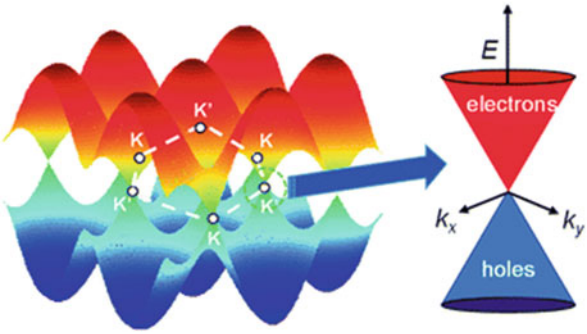

Fig. 10.2 Tight-binding band structure of graphene: energy ε as a function of momentum (k_x, k_y), where $-t$ is the nearest-neighbor hopping amplitude. There are the two cones in equivalent contact points at K and K', between the conduction (positive energy) and valence (negative energy) bands. In undoped graphene, the so-called Fermi surface consists of two points at K and K'. A zoom shows the linear dispersion of massless Dirac fermions near the K point. Reproduced with permission from [1]

an electric field, bilayer graphene can be open. As the layer increases, the number of charge carrier increases and the valence band overlaps the conduction band [8]. Chemically converted graphene is hydrophobic in nature, i.e., it appears to be insoluble in water and organic solvents. The ionization of carboxylic acid and phenolic hydroxyl groups is explained in a surface charge (zeta potential) study [9].

10.1.2.3 Electronic Properties

The 2D graphene shows exceptional electronic properties. The material is also called a zero band gap semiconductor due to its cone-shaped Fermi surface. As shown in Fig. 10.2, there are six double cones, the upper half representing the conduction band and the lower half the valence band.

If the graphene is undoped or intrinsic, then the tip of the cones represents its Fermi level. The low density of state at the tip lowers the electrical conductivity of the intrinsic graphene. With the application of an electric field the Fermi level of the material changes. The material becomes n-doped or p-doped depending on the polarity of the applied field. Three electrons in carbon of graphene always makes σ bonds and one electron contributes to a π bond. The π electron is responsible for electronic properties [10]. A Dirac-like equation is used in the case of the charge carrier. In a graphene the linear spectrum shows the different behavior of quasi-particles than that of the parabolic dispersion relation of metal and semiconductor. The intersection of the energy band resulting from two sublattices gives the conical spectrum. The chirality in a graphene originates from an additional phase gain of π during electron motion in a close contour called the *berry phase*.

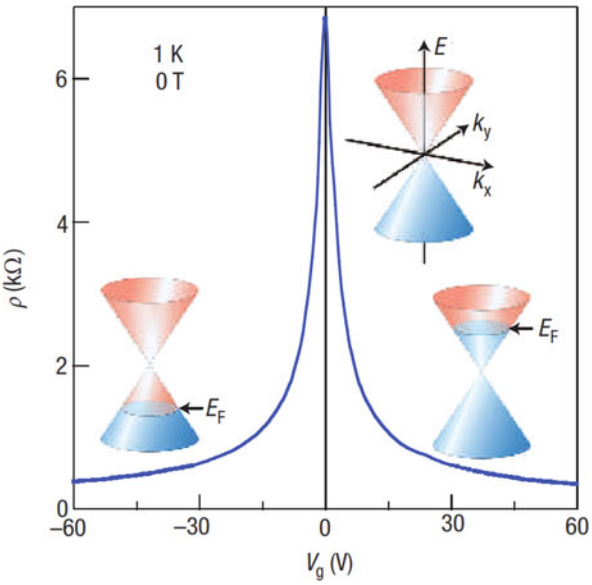

Fig. 10.3 Ambipolar electric field effect in single-layer graphene. The *insets* show its conical low-energy spectrum $E(k)$, indicating changes in the position of the Fermi energy E_F with changing gate voltage V_g. Positive (negative) V induces electrons (holes) in concentrations $n = aV_g$ where the coefficient a 7.2 × 10 g for field effect devices with a 300 nm SiO_2 layer used as dielectric. The rapid decrease in resistivity ρ on adding charge carriers indicates their high mobility (in this case, μ 5,000 cm^2 V^{-1} s and does not noticeably change when increasing the temperature to 300 K). Reproduced with permission from [2]

The ambipolar electric field effect (Fig. 10.3) clarifies the high mobility of electrons when resistivity decreases with the addition of charge carriers. A graphene shows a minimum conductivity of $\frac{e^2}{h}$ [6, 11]. At room temperature the mobility of charge carriers is as high as 1500 cm^2 V^{-1} S^{-1}. Graphene shows ultrahigh mobility at room temperature. The 2D material exhibits a half-integral quantum Hall effect with Hall conductivity $\sigma_{xy} = \pm\frac{4e^2}{\hbar}\left(N + \frac{1}{2}\right)$ (where N is the Landau level) and the energy quantization in the applied magnetic field $E_n = \pm v_f\sqrt{2e\hbar BN}$ [6].

10.1.2.4 Mechanical Properties

A nanoindentation study through atomic force microscopy (AFM) gives an idea about the elastic properties and intrinsic breaking strength of free-standing monolayer graphene. A Young's modulus of 1.0 TPa and a fracture strength of 130 GPa are shown by a defect-free graphene [6].

10.1.2.5 Application

The use of composites of graphene is very promising for detecting a variety of molecules. The chemical response is observed through the charge transport between adsorbed molecules and the material (graphene composites). The composite acts as donor or acceptor by changing its Fermi level, electrical resistance, and carrier density. According to a recent study, NH_3 and CO molecules are donor sites whereas H_2O and NO_2 are acceptors [6]. A large surface-to-volume ratio, high carrier mobility, and a high electron transfer rate have made this material highly suitable in sensor devices [12]. The large-scale and planar sp^2-hybridized carbon domain, high specific surface area (2630 $m^2\ g^{-1}$), and oxygen-containing group make GO a superior solution in biomedical applications. Nanoscale GO acts as a carrier that successfully transports anticancer drugs to cells [13]. Graphene and its derivatives have set milestones in destroying tumors and cancer cells. The graphene made from GO is toxic. To make it nontoxic, it is coated with biocompatible polymers such as polyethylene glycol (PEG). With the exceptional magnetic properties of GO-iron nanocomposites, several researchers have used this as a best guide to drug delivery and magnetic resonance imaging (MRI).

10.2 Importance of Magnetic Nanoparticles in Biomedicine

Nanoparticles showing various paramagnetic and superparamagnetic behaviors are categorized as magnetic nanoparticles. Today, magnetic nanoparticles are mostly used in such current research fields as detection, dye degradation, sensing, and biomedicine. It includes several oxide forms of several metals, like Fe, Ni, and Co, and it includes some rare earth–based metals like Gd and Er, for example. Their unique magnetic properties, facile surface modification, and biocompatibility are the main reasons for their special place in research. Magnetic nanoparticles have been used widely in MRI, drug delivery vehicles, hyperthemia agents, and magnetic separation [14]. Supermagnetic nanoparticles have an appropriate surface chemistry for various in vivo applications, such as tissue repair, immunoassays, detoxification of biological fluids, hyperthermia, drug delivery, and cell separation [15]. Magnetite is one of the promising magnetic nanoparticles that have occupied a special position in biomedicine. This material is very biocompatible in nature. In biomedical research, a homogeneous suspension called a fero fluid is produced by dispersing magnetic nanoparticles in a suitable solvent with a proper surface coating. Then, using an external magnetic field, these fero fluids are targeted to a special part of the body, making them easy to apply in MRI and cancer therapy. A few remarkable properties of magnetic nanoparticles are the main cause of their application in biomedical science, including the quantum size effect and large surface area. Based on their chemical, thermal, and mechanical properties, supermagnetic nanoparticles have had a significant effect in biomedical fields like cellular therapy, tissue repair, drug delivery, MRI, hyperthermia, and magnetofection [14, 16].

10.3 Overview of Multifunctional Magnetic Graphene Nanocomposites

10.3.1 Graphene and Graphene Oxide–Based Magnetic Nanoparticle Composites

We have already discussed the importance and application of graphene in various fields. In biomedicine, graphene and GO play a vital role owing to their large surface area, oxygen-containg functional groups, and tremendous mechanical and electrical properties. The composites of graphene and GO with different supermagnetic and paramagnetic nanoparticles have emerged as a superior solution in biomedicine compared to normal graphene and GO for fast response to drug delivery, drug loading, and different biomedical phenomena. The 2D material possesses the quality of being able to adsorb large aromatic biomolecules on its surface with the help of π–π stacking and electrostatic interactions. These phenomena are very important in drug loading and biosensing. The large oxygen-containing groups in GO are modified with targeting ligands for application in targeted imaging and drug delivery [17]. To be used in a biomedical application, the material must be biocompatible first. As the surface area of a nanoparticle is one of the important factors in biomedical applications, materials with large surface areas, for example, composites of magnetic nanoparticles with graphene and GO, are required. This is because the addition of such nanoparticles to the base material increases its surface area. The oxygen-containing functional groups on GO, i.e., carboxylic, epoxide, and hydroxyl groups improve the biocompatible and physiological stability of magnetic nanoparticles [18]. The hydrophilic functional groups are one of the most important factors in making for an easy dispersion of magnetic nanoparticle–decorated GO in solvent [6]. Such functional groups not only contribute to hydrophilicity but also modify GO with other molecules via covalent and noncovalent bonding [19]. Graphene or GO-based magnetic nanoparticles have a potential broad application in different biomedical fields. Chen et al. developed aminodextran-coated Fe_3O_4 nanoparticles and GO for cellular MRI. Good physiological stability, low cytotoxicity, and efficient cellular labeling have made the material a promising one in cellular MRI [18]. The nanocomposite Gd_2O_3/GO developed by Wang et al. has greater water dispersibility and gives a high T_1 relaxivity value due to the large effective surface area of Gd_2O_3/GO nanocomposites [20]. Magnetic nanoparticle/graphene and GO composites are also used as targeted drug nanocarriers [21] and in, for example, photothermal therapy [22], drug delivery [23], and cancer therapy [24].

10.3.2 Synthesis, Structural Properties, and Magnetic Response of Functional GO/rGO

Generally magnetic nanomaterials are less soluble and have low stability in physiological solutions. So these materials are functionalized with GO at its hydrophilic edges and hydrophobic basal planes and are applied in in vitro drug/gene delivery, biomedicines, and cellular imaging.

Cheng and coworkers have reported that a higher loading capacity and the presence of a huge hydrophilic group on GO-Fe $_3$ O $_4$ nanocomposites provide a superior platform for protein immobilization. In this report, the researchers prepared superparamagnetic Fe_3O_4, GO-Fe_3O_4, and rGO-Fe_3O_4 composites by a grafting method, which produced saturation magnetization values of 77.6, 33.0, and 36.9 emu g^{-1}, respectively. Although these saturation magnetization values are not very high, these kinds of superparamagnetic materials still provide sufficient magnetic response for separation from an aqueous solution. Taking a multidomain protein, bovine serum albumin (BSA), as a testing sample, they showed that, though the magnetic property increases by the addition of more and more Fe_3O_4, the adsorption of protein decreases gradually owing to the decrease of exposed surface area. Therefore they chose a typical weight ratio of GO-Fe_3O_4 of 1:1. The synthesis of this nanocomposite can be thought up to be possible for the intermediate reagent, (3-mercaptopropyl) trimethoxysilane (MPS). This acts as a good linking reagent between GO and Fe_3O_4 that possesses multitudinous bifunctional reactive groups. This forms a linkage with GO via the chemical bond between its trimethoxysilane head with hydroxyl and epoxy groups present on the surface of the GO and with Fe_3O_4 via the covalent bond between its mercapto tail with Fe atoms of Fe_3O_4. In this way a variety of structures and sizes of Fe_3O_4 is grafted onto the modified GO (GO-MPS) [25].

In many studies, different researchers have incorporated both Fe and Au on the GO surface to achieve superparamagnetism. Recently Shi and coworkers developed graphene-based plasmonic nanocomposites in which both iron oxide and gold nanoparticles are grown on GO sheets, forming a uniformly decorated GO-IONP-Au composite [26]. This nanomaterial has substantially lower stability and is less soluble in water. To overcome this deficiency, GO-IONP-Au was again modified with the growth of lipoic acid–modified PEG, which is a hydrophilic polymer, resulting in a GO-IONP-Au-PEG nanocomposite. The result of field-dependent magnetization measurements can be observed from Fig. 10.4a. The absence of a hysteresis loop indicates that GO-IONP-Au-PEG is superparamagnetic by nature. This novel material can be used in bioimaging as well as photothermal therapy for its rapid response to magnets. The concentration-dependent darkening effect of GO-IONP-Au-PEG is exhibited in T2-weighted magnetic resonance images taken by a 3T magnetic resonance scanner, showing a transverse relaxivity of 62.79 L $mmol^{-1}$ S^{-1} (Fig. 10.4b).

A layer-by-layer assemblage of gold nanoparticles on graphene sheets was achieved by a simple vacuum filtration method by Kong et al. The advantage

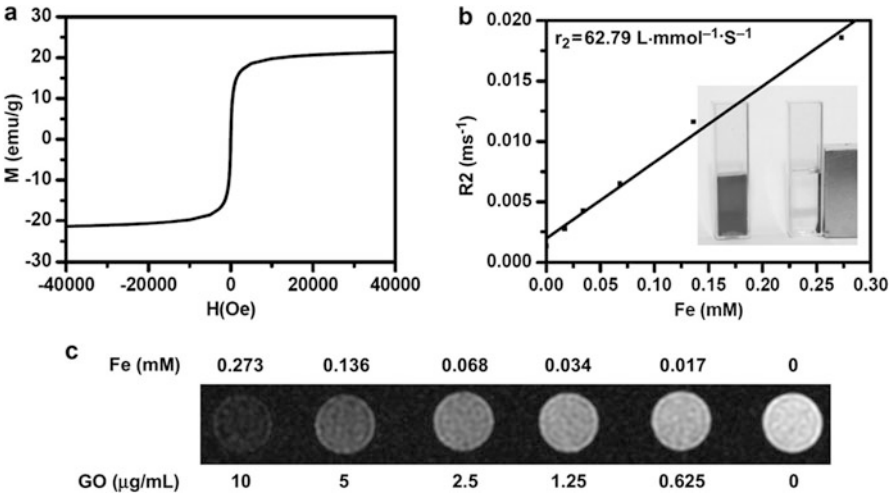

Fig. 10.4 Magnetic properties of GO-IONP-Au. (**a**) Hysteresis loop of GO-IONP-Au. (**b**) T2 relaxation rates (r2) of GO-IONP-Au at different Fe concentrations.*Inset*: Photos of GO-IONP-Au in aqueous solution with and without magnet. (**c**) T2-weighted magnetic resonance images of GO-IONP-Au aqueous solutions at different Fe concentrations. Reproduced with permission from [26]

of this method over the previously reported ones is that there is no requirement for external agents for the reduction of gold ions on graphene sheets. A TEM analysis showed that a large number of spherically shaped gold nanoparticles several nanometers in diameter were distributed throughout the graphene sheets [27]. Hollow nanomaterials with shapes like nanorings, nanocubes, nanotubes, prism-shaped nanoboxes, and multiwalled nanoshells or nanotubes are more effective than solid structures of the same shape and size because they provide more surface area for reactions with the surroundings. These types of materials are prepared using various methods like the Kirkendall effect, chemical etching, galvanic replacement, and a template-mediated approach [28–31].

Hollow plasmonic nanoparticles like gold nanoshells, gold nanorods, and gold nanocages furnished with GO have been reported as appropriate materials for photothermal therapy in the near-infrared (NIR) spectrum. As discussed by Lim et al., plasmonic nanoparticles like Au nanoshells and Au nanorods are coated with rGO to enhance the photothermal activity. High-resolution TEM (HRTEM) analysis revealed that the thickness of rGO coated on Au nanorods (2.5 nm) is more than that of rGO coated on Au nanoshells (1 nm). The effect of rGO-coated plasmonic nanomaterials is connected more with killing cells than that of unreduced GO-coated plasmonic nanomaterials [32].

Fan and his coworkers chose an eco-friendly reduction process of GO for the preparation of a drug delivery system based on magnetic Fe_3O_4-graphene nanocomposites (MGN) for cancer treatment. Scanning electron microscopy (SEM)

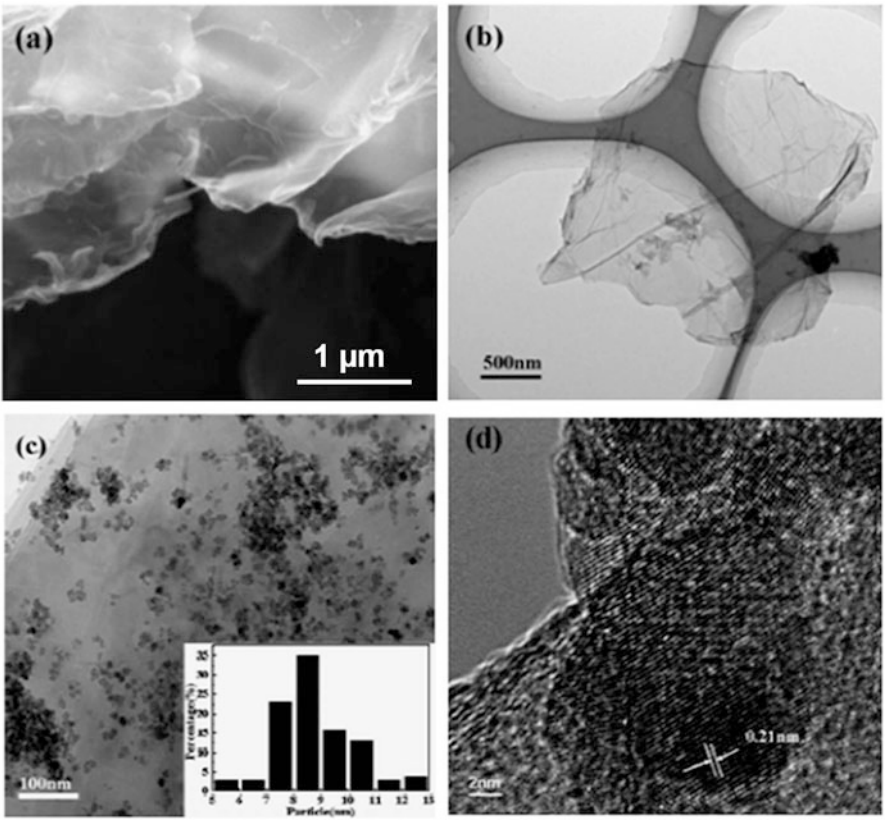

Fig. 10.5 SEM and TEM images of graphene prepared by Fan et al. (**a**, **b**), TEM and HRTEM images of MGNs The *inset* represents the size distribution of FE_3O_4 nanoparticles. Reproduced with permission from [21]

and TEM images of this nanocomposite clearly show a homogeneous distribution of Fe_3O_4 particles in the interlayer of graphene sheets with particle sizes of 5–13 nm, as shown in Fig. 10.5 below [21].

The magnetic property emerges from the covalently conjugated surface–modified Fe_3 O_4 on the graphene sheets. After the synthesis of MGN, the drug 5-Fluorouracil (5-FU) was loaded over the composite for the destruction of the solid tumors. MGNs with different concentrations were mixed with 5-FU solution and the unabsorbed 5-FU concentration was measured with UV-visible spectrophotometry, resulting in a wavelength of 265 nm. To test for the stability of the material in the aqueous solution, pH-dependent zeta potentials of the graphene sheets were measured for different pH values ranging from 3 to 11. It was found that the zeta potential value was − 2.1 mV for the solution with pH 3 and decreased with an increase in pH, with largest negative value of − 51.5 mV for pH 11. So it is evident that the graphene suspension shows very good stability in weakly acidic to basic solutions.

10.3.3 Mechanical Properties of Magnetic Graphene

Owing to its excellent mechanical properties, graphene has received significant attention across the world. Graphene, because of its 0.142 nm long strong carbon–carbon bonds, possesses a Young's modulus of 1 TPa, which is nearly 100 times greater than that of stainless steel. Graphene platelets (GPLs), the combination of a few layers of graphene sheets with a thickness of 2–8 nm, have extremely high tensile strength when incorporated with ceramics. Liu et al. prepared a GPL-Al_2O_3 nanocomposite by a pressureless sintering process, providing a positive biocompatibility with osteoblasts [33]. As reported by Kantar, the mechanical strength of chitosan hydrogen increases with the addition of GO, and this was studied by varying the amount of GO several times. From the measurement of the mechanical properties, the tensile strength of the chatoyant film without GO was found to be 17 ± 2 MPa and the modulus value to be 0.8 ± 0.1 MPa. After adding GO, the tensile strength of the film was increased by 12 MPa and the modulus value by 1.5 MPa. The improvement of this property supposedly arises from the strong hydrogen bonding as well as the polar-polar interaction between various functional groups present in the film. These interactions result in the formation of a compact structure of the nanomaterials inside the film, as shown in the following figure.

Intrinsic properties, like flexibility, durability, and physical adhesiveness, make the polymer nanocomposite useful for biomedical applications. Adopting the supporting film method, polysaccharide nanosheets are loaded onto a SiO_2 substrate. The resulting polymer, following removal of the SiO_2 substrate, comprised of very flexible, transparent, large, noncovalently bonded, free-standing nanosheets [31].

10.3.4 Optical Properties of Magnetic Graphene

Another important requirement of materials to be used in biomedical functions is their optical response. The UV-absorption peak of GO is observed at 231 nm and a gradual red shift toward 270 nm, while rGO shows an absorption maximum at 265 nm [9]. A single-walled carbon nanotube (SWCNT) gives the absorption maxima at 255 and 1050 nm. Zhang et al. have tested the UV-vis absorbance of sulfonated aluminum pthalocyanine ($AlPcS_4$) dye over the addition of GO, rGO, and SWCNT separately and observed a new band in the red region upon the addition of each of the mentioned materials [34]. Indeed the absorption measurement gives only the ground state interactions.

Fluorescence spectra were measured to study the excited state interactions of $AlPcS_4$ (Fig. 10.6). It was observed that $AlPcS_4$ emitted maximum fluorescence at a wavelength of 685 nm. On increasing the wavelength of incident light, the fluorescence of $AlPcS_4$ decreased exponentially with a lifetime of 5.68 ns. After adding rGO, the fluorescence intensity of $AlPcS_4$ decreases sharply with the band

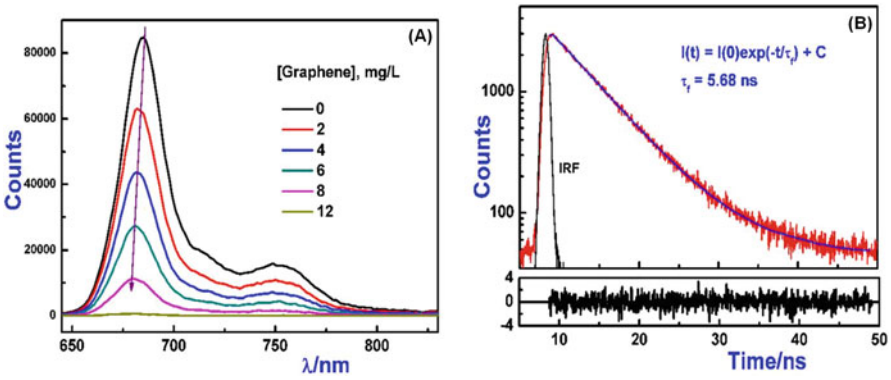

Fig. 10.6 (**a**) Decrease of fluorescence of $AlPcS_4$ after adding different concentrations of rGO, with excitation at 610 nm. (**b**) Exponential decay of $AlPcS_4$ with a lifetime of 5.68 ns. Reproduced with permission from [34]

position showing a slight blue shift. From this experiment it was found that the fluorescence intensity of $AlPcS_4$ is quenched very efficiently by the addition of rGO in a particular amount of 12 mg mL^{-1}.

Ligninsulfonate/graphene quantum dots (SL/GQDs), the core shell hybrids prepared by a citric acid (CA)–assisted simple hydrothermal method gives a fluorescence quantum yield of 23.3% with quinine sulfate as a standard. The fluorescence intensity of SL/GQD is found to be four times more than that of GQD when excited with a 362 nm UV beam. GQDs possess strong fluorescence by appropriate passivation treatment. In one experiment, partially carbonized citric acid was collected on the GQD surface by π–π interaction with the surface increasing its fluorescence property [9].

Roy and colleagues synthesized GO from a natural resource like tasar silk cocoon and tested the fluorescent properties of GO-containing carbon nanoparticles [35]. The sample product showed a fluorescent emission peak at 460 nm with excitation at 320 nm and the maximum peak was observed at an excitation of 380 nm. The fluorescence property was guessed to be originating from the carbenelike triple ground state ($\sigma^1 \pi^1$) at the zigzag sites of GO or due to the radiative recombination of electron-hole pairs produced at the localized sp^2 states. Smaller sized sp^2 clusters have demonstrated fluorescence in the UV-visible region, whereas larger ones have fluorescence in the NIR region. The hydrogen bonding between oxygen functional groups and carbon atom sites leads to the surface passivation effect.

Global environmental change and uncontrolled pollution play a vital role in the emergence of deadly bacteria and viruses, causing fatal diseases in human bodies. The traditional antibiotic therapies are becoming less efficient at getting rid of these antibiotic-resistant bacteria groups. Thus, the development of novel antibiotics to fight against harmful bacteria is essential.

Wu et al. have developed a graphene-based superparamagnetic nanocomposite by reducing and functionalized GO with magnetic nanoparticles [36]. The as-prepared magnetic reduced GO functionalized with glutaraldehide (MRGOGA) possesses the power of magnetic aggregation of material–bacteria conjugates by an externally applied magnetic field as well as the destruction of both Gram-positive *Staphylococcus aureus* (*S. aureus*) and Gram-negative *E. coli* bacteria by focusing a NIR laser beam. The saturation magnetization value of the superparamagnetic MRGAGO is 29 emu g^{-1} at 298 K. The glutaraldehyde-assisted magnetic reduced graphene oxide (MRGO) provides an excellent cross linkage with the peptidoglycan on the cell wall of bacteria and the bacterial protein and hence gains the ability to capture both Gram-positive and Gram-negative bacteria. MCNGA, a single-walled carbon nanotube functionalized with magnetic nanoparticles and GA, and MRGOGA were prepared separately with size of the functional magnetic nanomaterials ranging from 5 to 8 nm.

10.3.5 Toxicological Effects of Magnetic Graphene

The application of graphene-based functional nanomaterials in biomedicine essentially requires nontoxic behavior toward living cells and organelles. But till now there has been no report for the complete safety of the use of GO/rGO as a base material in drug delivery and biomedical applications. However, a literature review showed that magnetic nanoparticle–coated GO/rGO gives very fruitful results of application in biomedicine. Dextran coating on GO sheets (GO-DEX) provides a phenomenal lowering of cell toxicity of GO [37]. Dextran-biocompatible polymer is extremely stable in physiological solutions and can be applied in drug delivery.

Konwar et al. developed a novel coprecipitation method for the synthesis of chitosan-iron oxide–coated GO (CH-GIO) nanocomposite hydrogel to fight against Gram-positive and Gram-negative bacteria causing certain types of pneumonia, infection in wounds, and sexually transmitted diseases [38]. The cytotoxicity level of CH-GIO films toward mammalian cells was evaluated by 3-[4,5-dimethylthiazol-2-yl]-2,5-diphenyltetrazolium bromide dye conversion in mouse. Since the hemolytic potential increases with the exfoliation and growing size of GO, chitosan is used to coat bare GO to reduce such activities. In this experiment, GO was coated with iron oxide and then decorated on chitosan film, as shown in Fig. 10.6, dropping its toxic behavior toward red blood cells (RBCs). An in vitro cytotoxicity study revealed that the CH-GIO nanocomposite shows a concentration-dependent hemolysis for human RBCs. The major component of this film, chitosan, is a biocompatible polymer and the Fe_2O_3 is itself a bio-inert material. The prepared CH-GIO films are noncytotoxic in nature, which is the most essential property for biomedical applications. After treating on methicillin-resistant *Staphylococcus aureus* (MRSA) bacteria, CH-GIO presents excellent antibacterial activity due to the ionic interaction between the positive amino groups in chitosan and the negatively charged bacterial surface molecules, killing the bacterial cells (Fig. 10.7).

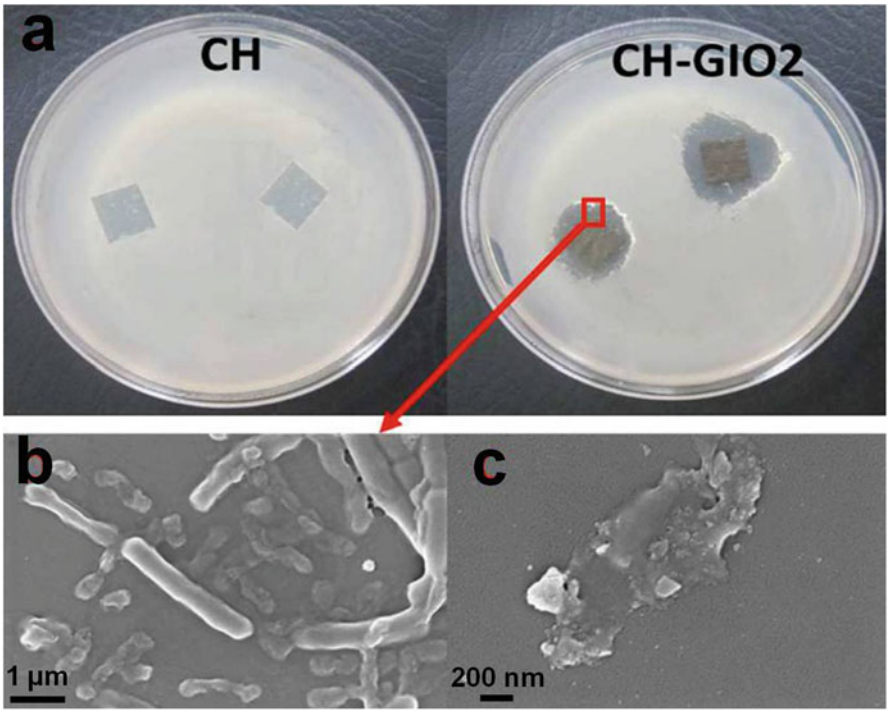

Fig. 10.7 (**a**) Antimicrobial activity of chitosan hydrogel nanocomposites against MRSA. (**b**) SEM image of dead bacterial shell after treatment of CH-GIO2. (**c**) Dead shell of MRSA bacteria after treatment with chitosan. Reproduced with permission from [38]

The biocompatibility of MGN was tested in vitro by Fan and his research team on Chang liver cells at 37 °C for 24 h [13]. The cells were set in different concentrations of MGN and the cell viability was measured for each condition. The study revealed that the incorporation of MGN in Chang liver cells, even at a higher concentration, maintained cell viability above 98%, as depicted in Fig. 10.8. So it is clear that superparamagnetic MGN acts as a noncytotoxic and biocompatible material.

Yang for the first time studied the in vivo characteristics of nanographene sheets (NGSs) coated with PEG in a tumor-bearing mouse model [38]. GO and nanographene oxide (NGO) as an efficient aromatic drug carrier was first reported by Dai et al., who conjugated the composite with PEG polymer and then loaded the anticancer drug onto it [39].

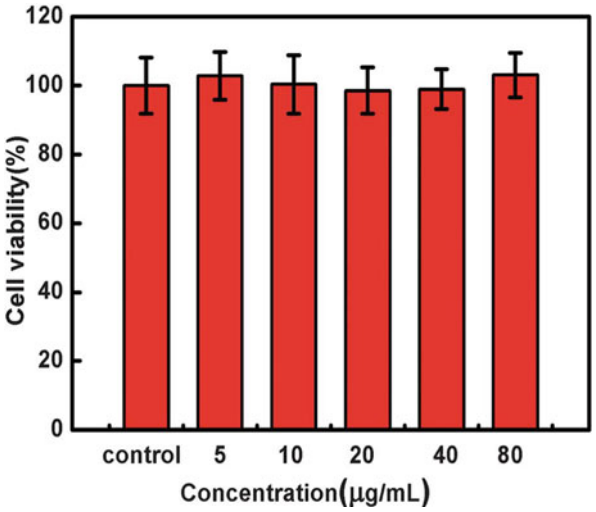

Fig. 10.8 Relative cell viability of MGNs against Chang liver cells at different concentrations. Reproduced with permission from [21]

10.4 Specific Requirements of Magnetic Nanoparticle–Decorated Graphene and GO Composites in Biomedical Applications

10.4.1 Biocompatibility

Nanoparticles entering the human body come in contact with various tissues and cells directly. So it is necessary to make such materials biocompatible. On the basis of a material's contact in the human body, its biocompatibility is further classified as follows.

10.4.1.1 Hemocompatibility

Nanoparticles come in contact with blood during applications like gene delivery and drug delivery, for example. Studies on blood cell aggregation and hemolysis are used to examine the blood compatibility of nanoparticles in vitro. The surface area, surface charge, hydrophobicity, and hydrophilicity of nanoparticles significantly affect blood compatibility [40].

10.4.1.2 Histocompatibility

This includes the tissue compatibility of nanoparticles. Microcytotoxicity assays are among the commonly used tests in histocompatibility analysis. This involves adding a sample of the donor or recipient cells containing major histocompatibility complex proteins to a serum known as antihuman leukocyte antigens.

10.4.2 Water Solubility of Nanoparticles

This is one of the important concerns in biomedical applications. Normally it is the conjugation of colloidally unstable nanoparticles with hydrophobic ligands. Water solubility of nanoparticles includes physical and chemically stable colloidal suspensions. In this case, nanoparticles do not aggregate, dissociate, or chemically react to the solvent or any dissolved gas with time [41]. GO-based magnetic nanoparticles possess the property of excellent aqueous processibility, amphiphilicity, and surface functionalizability. These properties are very likely to result in a well-dispersed nanoparticle solution [19].

10.4.3 Ionic Stabilization

During the binding of molecules to nanoparticles, charge particles reside outside of the nanoparticles, resulting in Coulomb repulsion. This leads to the dispersion of the nanoparticles. The stability of ligand cells and nanoparticles depends upon the ionic interaction of the nanoparticles with charged particles in the biological medium.

10.5 Promising Verities of Multifunctional Magnetic Graphene Nanocomposites for Biomedical Applications

Applications like drug delivery, gene delivery, photothermal therapy, MRI, and tissue engineering are some important fields in biomedicine. Wang et al. have developed a cobalt ferrite GO nanocomposite for application in MRI and drug delivery. They performed an in vitro study of MRI effects and cytotoxicity effects for investigating the bioimaging potential of the nanocomposite. The entire analysis was performed with the loading of an antitumor model drug of doxorubicin in the nanocomposite [42]. Pan et al. have developed a carboxymethyl chitosan–functionalized GO nanocomposite for application in drug delivery [43]. Wang et al. have developed a manganese ferrite/GO nanocomposite by a sonochemical method for application in drug delivery [44]. Gao et al. demonstrated the promising use of a graphene-based magnetic fluorescent hybrid, i.e., CdTe-Fe_3O_4/SiO_2, in the domain of drug delivery and cellular imaging. They prepared monodispersed magnetic Fe_3O_4 by a coprecipitation method and finally the amino-functionalized CdTe-Fe_3O_4/SiO_2 nanocomposite was prepared by a microemulsion method at room temperature [45]. Fan et al. have developed a magnetic Fe_3O_4/graphene composite for targeted drug delivery. The superparamagnetic Fe3O4 nanoparticles were obtained by chemical deposition and GO was synthesized by a modified Hummers method. The graphene was synthesized from GO by the sonication of GO in aqueous NaOH under nitrogen conditions. The magnetic stirring of the solution for 48 h resulted in 2D graphene. The researchers synthesized the final

Table 10.1 List of magnetic graphene and GO composites with their various applications

Material	Biomedical application	Reference
Ni-BiCP-G	Cell culture	[47]
Cobalt ferite/GO	MRI	[42]
	Drug delivery	
GO-CMC	Drug delivery	[43]
Fe_3O_4/rGO	Stimulus response	[48]
$MnFe_2O_4$/GO	Drug delivery	[44]
GO-CdTe-Fe_3O_4/SiO_2	Drug delivery	[45]
	Cellular imaging	
GO-CMC-FI-HA	Drug delivery	[49]
rGo/IO QD	Dual modality imaging	[50]
	Drug delivery	
	Photothermal therapy	
GO-PE	Gene delivery	[51]
	Bioimaging	
GO-IO-PEG	Thermochemosensitization	[46]
	MRI	
GQD-Cur	Drug delivery	[24]
RGO-IONP-PEG	Photothermal therapy	[22]
Fe_3O_4-graphene	Drug delivery	[21]
GO-IONP-PEG	MRI	[52]
	Drug delivery	
	Photothermal therapy	
CH-IO-GO	Antimicrobial film	[52]
Fe_3O_4/GO	MRI	[53]
Gd_2O_3/GO	MRI	[54]

composite magnetic Fe_3O_4/graphene by sonicating the two prepared samples with suitable proportion [21]. Yang et al. synthesized a biocompatible polymer (i.e., PEG)-functionalized GO-iron oxide nanocomposite for application in photothermal therapy [22]. Similarly, Sasikala et al. developed the same GO-iron oxide-PEG composite having application in MRI and thermochemosensitization. The functionalization of PEG with GO-IO nanocomposite improves the hydrophilicity, stability, and biocompatibility of the material [46]. The different types of magnetic graphene or GO nanocomposites with their applications are listed in Table 10.1.

Ni-BiCP-G nickel–doped biphasic calcium phosphate graphene nanoparticle composite, *Cobalt Ferite/GO* cobalt ferite GO composite, *GO-CMC* carboxymethyl chitosan–functionalized GO, *Fe_3O_4/rGO* magnetic reduced GO, *$MnFe_2O_4$/GO* manganese ferrite/GO composite, *GO-CdTe-Fe_3O_4/SiO_2* GO-based magnetic fluorescent hybrid, *GO-CMC-FI-HA* carboxymethyl chitosan–mediated hyaluronic acid targeted GO, *rGo/IO QD* reduced GO iron oxide quantun dot, *GO-PE* GO–polyethelene, *GQD-Cur* graphene quantum dot-curcumin, *RGO-IONP-PEG* polyethylene glycol–functionalized reduced GO iron oxide composite,

Fe_3O_4-graphene magnetic graphene, *GO-IONP-PEG* PEGylated iron oxide GO nanocomposite, *CH-IO-GO* chitosan iron oxide–coated GO, *Gd_2O_3/GO* gadolinium oxide decorated GO

10.6 Application of Graphene or GO-Based Magnetic Nanoparticles in Different Biomedical Fields

10.6.1 Magnetic Resonance Imaging

The technology that gives the picture of organ and structures inside the body using magnetic fields and pulses of radio wave energy is called magnetic resonance imaging, or MRI. Before starting an examination, the person is place in an MRI scanner. The part of the body to be imaged is kept in a zone of a strong magnetic field. The hydrogen atoms (proton) present in the human body are the important factors in MRI. When a magnetic field is applied to a normal human body, protons become excited, releasing radio waves. The radio waves are measured through a receiving coil. The position information is given by the radio signals by varying the magnetic field using gradient coils. Alternately switching it on and off creates the characteristic repetitive noise of an MRI scanner. So a contrast image can be recorded by the rate at which the excited atoms return to the equilibrium state.

High spatial resolution and good spatial tissue contrast are some promising features of MRI in medicine. MRI works based on the shortening of the longitudinal relaxation time (T_1) or the transverse relaxation time (T_2) of water protons. In blood pool imaging or in passive targeting, negative T_2 contrast agents are used, whereas positive T_1 contrasting agents are used as extracellular agents, blood cell agents, and hepatobiliary agents in clinical applications. A high longitudinal relaxation rate, low intake dose, and low cytotoxicity have made research on positive T_1 contrasting agents selective one.

Wang et al. have developed GO-based Gd_2O_3 nanocomposites that act as water-soluble MRI T_1 contrasting agents with high T_1 relaxivity values [53]. Hydrophobic–hydrophobic interaction or π–π stacking helps the adsorption of gadolinium nanoparticles on the hydrophobic basal plane. The material possesses a large effective surface area and can exhibit high T_1 relaxivity values. Researchers have used a 7T MRI scanner for measuring the magnetic relaxometric properties of GO-based Gd_2O_3 nanocomposites. T_1 relaxivity is influenced by two important factors, the number of surface Gd^{3+} ions and the distance between the paramagnetic center and the surrounding water protons. The larger surface-to-volume ratio is obtained by smaller gadolinium nanoparticles.

In a cytotoxicity study the researchers cultured breast cancer cells and put them in a GO-based Gd_2O_3 nanocomposite with different gadolinium concentrations for 24 h at 37 °C. Using the cell counting Kit-8 (CCK-8), the cell viability was calculated as shown in Fig. 10.9. Two types of material of GO-based Gd_2O_3 nanocomposite were tested.

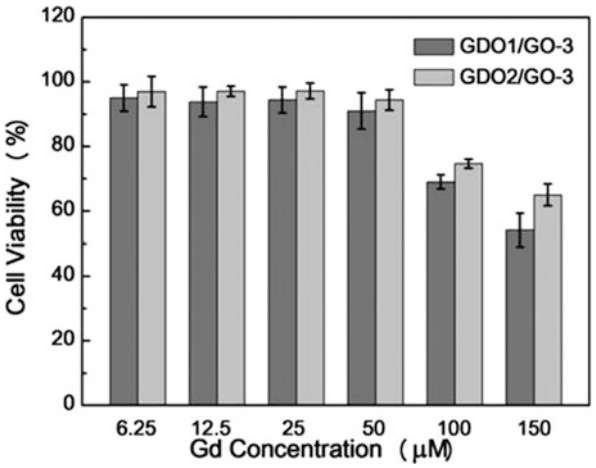

Fig. 10.9 Cell viability of breast cancer cell lines incubated at different concentrations of GO-based Gd_2O_3 nanocomposite. Reproduced with permission from [20]

Ma et al. synthesized GO-iron nanoparticle-PEG (GO-IONP-PEG) for MRI application. They injected GO-IONP-PEG into 4T1 tumor-bearing BALB/c mice. One day after injection they were imaged in a 3T clinical MRI scanner. Dark spots were localized in the tumor and lever areas by T_2 -weighted magnetic resonance images (Fig. 10.10 a, b). The magnetic resonance signal significantly decreased by 64 and 67% for the lever and tumor, respectively, as shown in Fig. 10.10c, d [52].

Wang et al. synthesized transferrin-functionalized gold nanoclusters/GO nanocomposites to turn ON NIR fluorescent bioimaging of cancer cells and small animals. In this work, two different human cancer cells, Hela and HepG-2, and one normal mouse cell, 3T3, were taken for the imaging study. All three cells were incubated in a fluorescent probe for 4 h. Significant fluorescence recovery of the activatable fluorescent was observed for Hela cancer cells.

From Fig. 10.11a it can be easily identified that the fluorescent probe is completely taken up by the Hela cells and, in the case of HepG-2 and 3T3 (Fig. 10.11b, c), the probe showed no fluorescent enhancement. In the case of Hela cells, the results indicate the protection of Tf from enzymolysis by GO and, after 4 h incubation, the maintenance of fluorescence by Tf-AuNC composite. The binding mechanism of GO and Tf-AuNCs is based on noncovalent bonding. For the imaging of tumors with turn on NIR fluorescence probe, the researchers injected the probe into tumor-bearing mice as shown in Fig. 10.12.

After 45 min, the NIR fluorescence signal was detected in the tumor-bearing mice and this signal continued for up to 12 h. Again the probe was subcutaneously injected into the same site of a normal nude mice. In this case the fluorescence signal observed at 3 h and disappeared after 8 h while in the tumor-bearing mice it was observed for up to 12 h. A slower clearance rate of a tumor site was observed in comparison to normal tissue; the high affinity of the Tf to target cancer cells shielded the probe from metabolism and degradation [55].

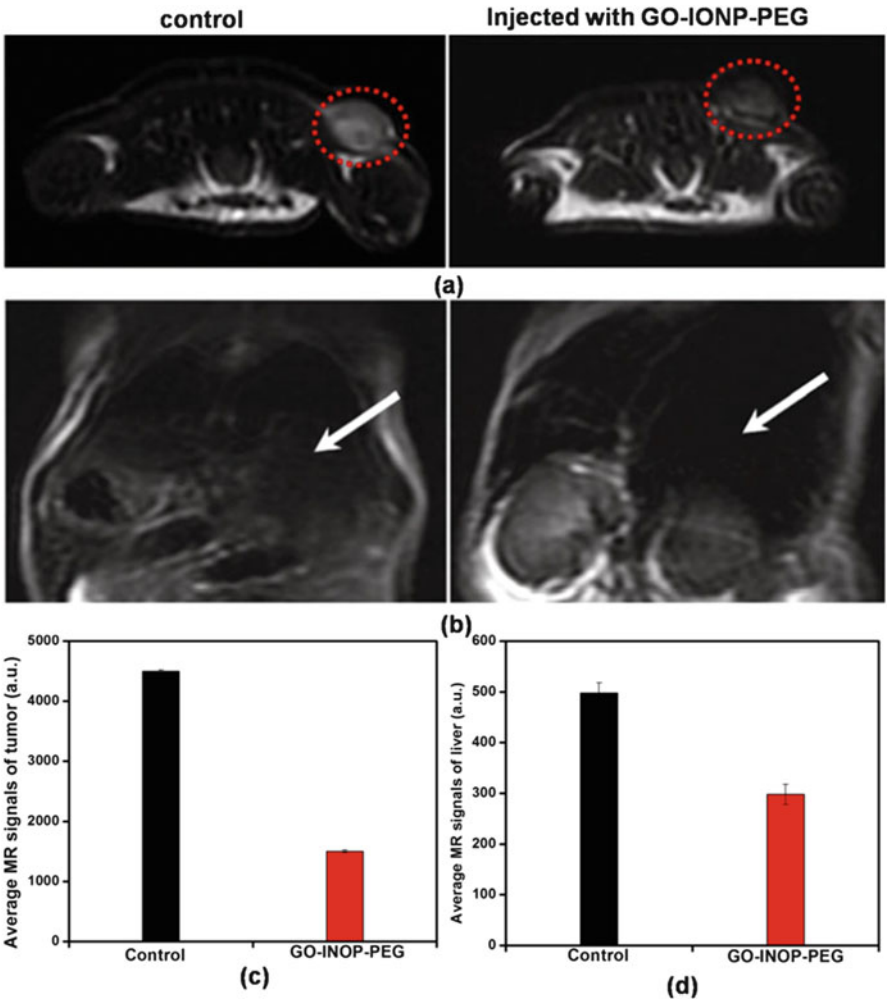

Fig. 10.10 (**a**) Transversal and (**b**) longitudinal T_2-weighted MR images. Quantitative analysis of T_2-weighted magnetic resonance signals from tumor (**c**) and lever (**d**) of mice. Reproduced with permission from [52]

10.6.2 Drug Delivery

To achieve various therapeutic applications in the human body, the delivery of a drug by various magnetic nanoparticles is one of the major applications in biomedicine. Different techniques have been implemented to achieve greater control over drug delivery as compared to traditional in vivo drug releasing systems. The large surface area and sp^2 carbon lattice increases the drug loading and drug delivery capability of graphene-based nanomaterials. The presence of functional groups covalently

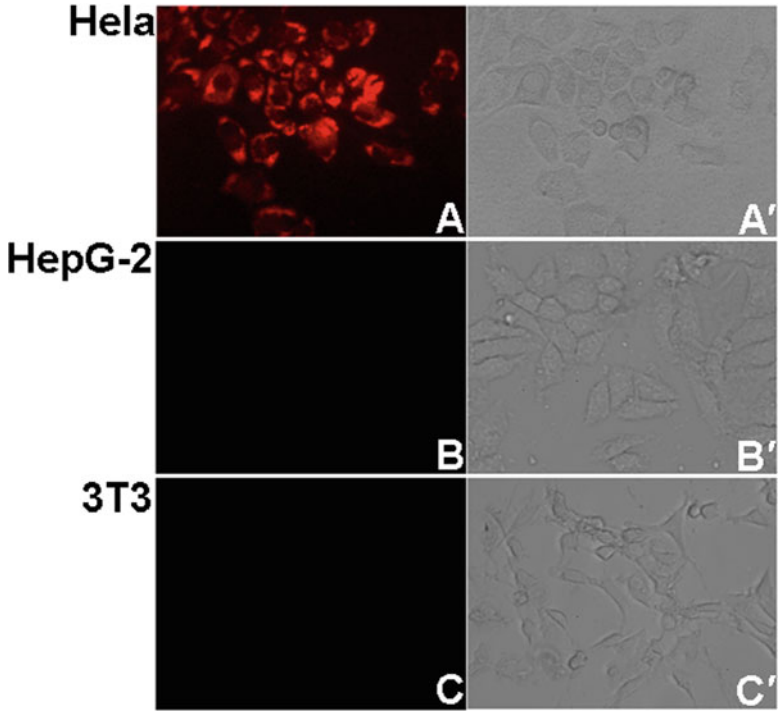

Fig. 10.11 (**a**–**c**) Fluorescence images of Hela, HepG2, and 3T3 cells after incubation. (**a′**–**c′**) The corresponding bright-field images. Reproduced with permission from [55]

modifies nanoparticles in targeted drug delivery, whereas the π electrons on the surface of 2D nanosheets strongly enables π–π interactions with the aromatic drug compound. The better adsorption properties of graphene-based materials in the blood stream is one of the important reasons for its use in drug loading or delivery applications. Normally drug-loaded GOs are modified through different cancer cell targeting antibodies or by functionalizing with various paramagnetic particles for magnetic direct delivery [24, 56].

Weaver et al. presented an electrically controlled drug delivery system based on GO nanoparticles, i.e., poly(pyrrole) (ppy) doped with GO for controlled delivery of anti-inflammatory drugs like Dexamethasone (DEX) (GO-ppy-DEX). They incorporated the nanoparticles with the conducting polymer. By responding to electrical stimulation, the drug-loaded conducting polymers released drug molecules. A conducting scaffold was formed by the conducting polymer matrix. Through the scaffold the electrical stimulation was applied to extract drug release from the nanocomposite. For the measurement of the drug-releasing activity of (GO-ppy-DEX) nanocomposite, voltage pulses were applied by immersing the nanoparticles in phosphate buffer solution. UV spectroscopy was used for the analysis of the amount of DEX expelled from the film.

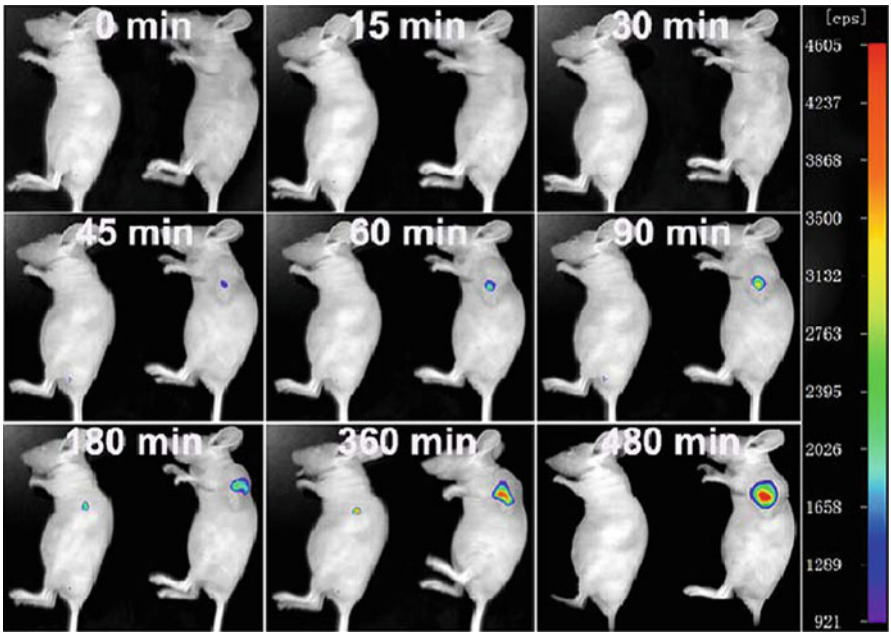

Fig. 10.12 Fluorescent probe imaging of tumor-bearing mice and normal nude mice. The fluorescent probe was intratumorally injected into the tumor-bearing mice (*right*) and subcutaneously injected into the left forelimb region of the normal nude mice (*left*). Reproduced with permission from [55]

A biphasic voltage pulse (− 2 V for 5 s followed by 0 V for 5 s) was used to stimulate the film for evaluating the DEX release (Fig. 10.13a). The drug released by the codoped GO and ppy was found to be 2.3 times of normal ppy. The process is completely surface dependent. For the study of maximum amount of drug release, a cumulative DEX release with stimulation was evaluated (Fig. 10.13b). After 600 stimulations the drug release gave a plateau like structures indicating the maximum release of drug from the sample. Milder electrical stimulations (e.g., − 0.5 V for 5 s followed by 0.5 V for 5 s) released small quantities of DEX from the nanocomposite film (Fig. 10.13c). It gave a drug release profile that was linear over 400 stimulations [56].

Some et al. have developed a curcumin (CUR)-graphene composite and applied it to the death of cancer cells (HCT 116) both in vitro and in vivo. The materials they used during the experiment included GO, double-oxidized graphene oxide (DGO), and GQDs for transporting the anticancer drug CUR. The GQD-CUR composite shows high anticancer activity. The composite contains large amounts of CUR owing to the large surface area and oxygen-containing functional groups. The researchers performed both in vitro and in vivo experiments (Fig. 10.14).

The quantitative analysis of drug loading was investigated in a basic to acidic range.

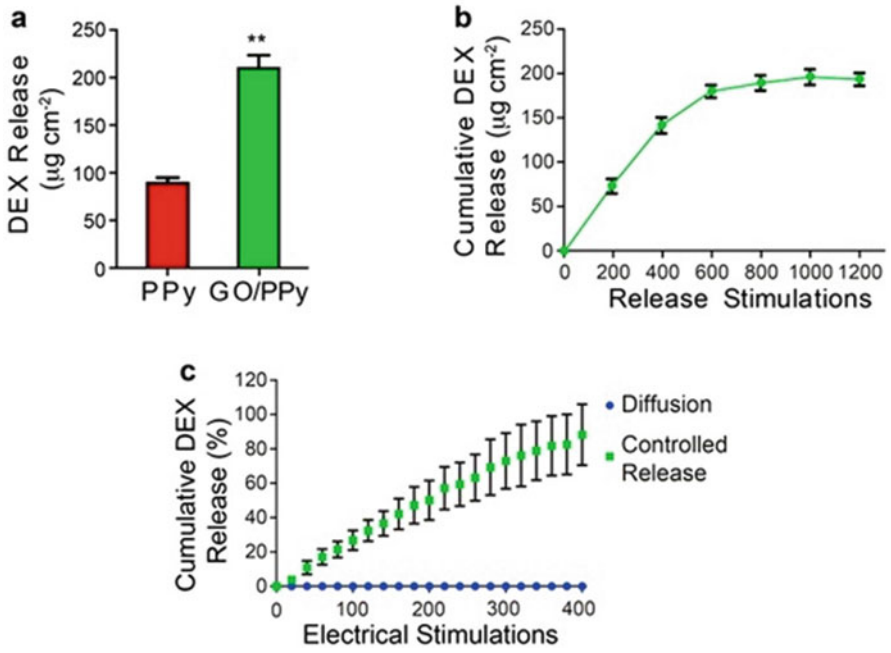

Fig. 10.13 Electrically controlled DEX release from GO-ppy nanocomposite film. (**a**) Comparison of DEX release from ppy or from GO-ppy film. (**b**) Cumulative release of drug with release stimulation. (**c**) Cumulative release of drug with electrical stimulation. Reproduced with permission from [56]

The amount of CUR loaded in graphene-based composites is pH dependent. From Fig. 10.15a, the loading factors of GO-CUR, DGO-CUR, and GQD-CUR were analyzed with values of 20.8, 38.8, and 40.8, respectively. The loading amount of CUR gradually decreases from a high amount to a very low amount when the pH is reduced from 9 to 7.5 to 5, as shown in Fig. 10.15b [24].

10.6.3 Photothermal Therapy

Photothermal therapy involves the damaging of tumor cells by light-absorbing agents under the exposure of NIR light. Ma et al. have developed a supermagnetic multifunctional graphene oxide–iron oxide nanocomposite (GO-IONP). For high stability in physiological solution, the material is functionalized with PEG. Because of the strong optical absorption of NIR windows, the GO-IONP-PEG material was utilized for the photothermal ablation of cancer cells. The researchers exposed GO-IONP-PEG to an 808 nm NIR laser with a power density of 1 W cm^{-2}. The temperature of the material gradually increased with time depending upon the

Fig. 10.14 Schematic representation of graphene-curcumin based composite used in cancer treatment. Reproduced with permission from [24]

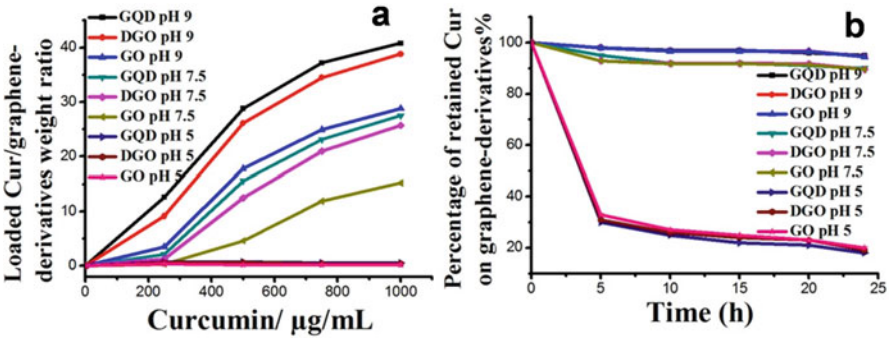

Fig. 10.15 (**a**) Loading of curcumin at different concentrations and different pH. (**b**) Curcumin retained on GO, DGO, and GQD versus time at constant pH (pH 5, 7.5, and 9). Reproduced with permission from [24]

concentration of the material (Fig. 10.16). For water no temperature changes were measured under the same conditions. The magnetic properties of GO-IONP-PEG were used for targeted photothermal therapy. For the ablation of cancer cells, 4T1 cells were incubated with GO-IONP-PEG for 2 h at 37 °C in the presence of a magnetic field. The cells near the magnet were destroyed, whereas those far from the magnet were unaffected [52].

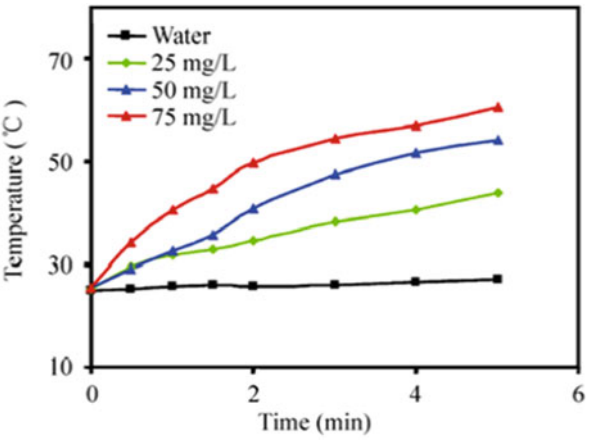

Fig. 10.16 Temperature changes of water and GO-IONP-PEG at different concentrations (25, 50, 75 mg L^{-1}). Reproduced with permission from [52]

10.6.4 Antimicrobial Applications

An agent that kills microorganisms and inhibits their growth is called antimicrobial. The extensive use of biopolymers in the biomediacal and food industries has prompted researchers to incorporate antimicrobial properties into polymers. Konwar et al. synthesized an antimicrobial biofilm from a chitosan iron oxide–coated GO (CH-GIO) nanocomposite hydrogel. Pathogenic bacteria, like methicillin-resistant *Staphylococcus aureus* (MRSA), *Staphylococcus aureus* (SA), *Escherichia coli* (*E. coli*), and the opportunistic dermal pathogen *Candida albicans* (CA), were investigated using a CH-GIO film. The researchers compared the antimicrobial properties of CH, CH-GO, chitosan–iron oxide (CH-IO), and chitosan–iron oxide–graphene oxide (CH-GOI2) composite films (Fig. 10.17). It can be observed that the antimicrobial activity of nanocomposite films differs in the previously mentioned four bacteria. But in all cases it was determined that the CH-GIO nanocomposite film showed higher antimicrobial properties compared to the other composite films [38].

10.6.5 Gene Delivery

Various genetic disorders, like cystic fibrosis, Parkinson's disease, and cancer, can be eradicated with the new technique of gene therapy. Gene delivery analysis is completely based on gene delivery carriers or gene vectors, which protect DNA from nuclease degradation and help in the uptake of DNA with high transfection efficiency [13 , 57]. Genetic diseases like diabetes, heart disease, obesity, ciliopathies, developmental disabilities, and hypertension are major problems in human societies. Gene therapy, initiated in 1972, is one of the promising methods of treatment of these genetic diseases. In gene therapy the segments of the selected

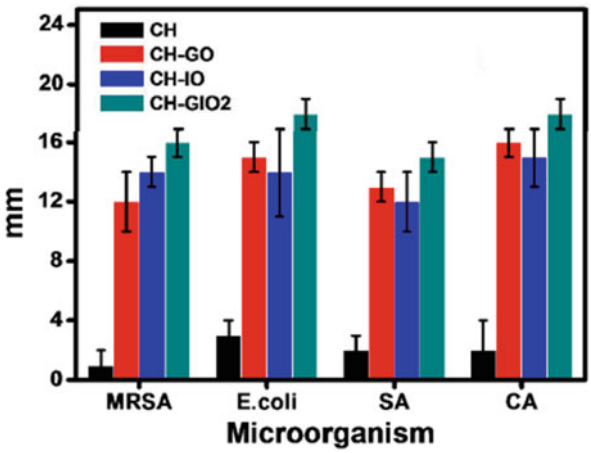

Fig. 10.17 Comparison of antimicrobial activity among CH, CH-GO, CH-IO, and CH-GOI2 nanocomposite films in different bacteria. Reproduced with permission from [38]

DNA, particularly genes, are directly launched into the tissues of the affected person to stop the mutation of the hereditary genes. The role of magnetic nanoparticles in gene delivery is to encapsulate a gene on a delivery platform and subsequently enhance cell uptake. Gene transfer is achievable for several kinds of gene vectors like polymeric, viral, and nonviral vectors. Viral vectors perform gene delivery very efficiently because they possess the capacity to launch DNA into the targeted cells and even into the nucleus. But it has its own limitation of carrying the viral vector has its own limitation of selecting a desired gene. Cationic nonviral vectors, such as liposomes, core-shell nanoparticles, micelles, and peptides, are less expensive, easily prepared, and safe tools for gene delivery. But these vectors show less efficiency for in vivo DNA delivery compared to viral vectors.

A process called *magnetofection*, initiated by Christian Plank and his coworkers, is used to enhance the gene transfer rate in an external magnetic field. In this method superparamagnetic nanoparticles containing nucleic acid are gathered together in the target cells under the influence of the applied magnetic field, resulting in an increased efficiency of gene vectors. For example, a superparamagnetic iron oxide coated with polyethylenimine, developed by Scherer et al. [58], was applied in both in vitro and in vivo gene delivery. Gene vectors (DNA) are associated with these magnetic nanoparticles by electrostatic interaction followed by a salt-induced colloid aggregation. In this process a major fragment of the DNA gets associated with the magnetic nanoparticles, i.e., in a weight ratio of 2:1. Magnetofection was in vivo tested by putting the nonviral and adenoviral vectors together with the malignancies present in ilea lumens of rats and stomach lumens of mice. From this test it was observed that in the presence of an external magnetic field, an X-gal staining in tissue transfaction resulted after 48 h, while there is much less transfaction in the absence of a magnetic field. This confirms that gene delivery is efficient in the presence of a magnetic field. Again this experiment was carried out under the same conditions with the β -galactosidase (LacZ) gene, applied to the lumen of the stomach. From this experiment it was found that less transfaction

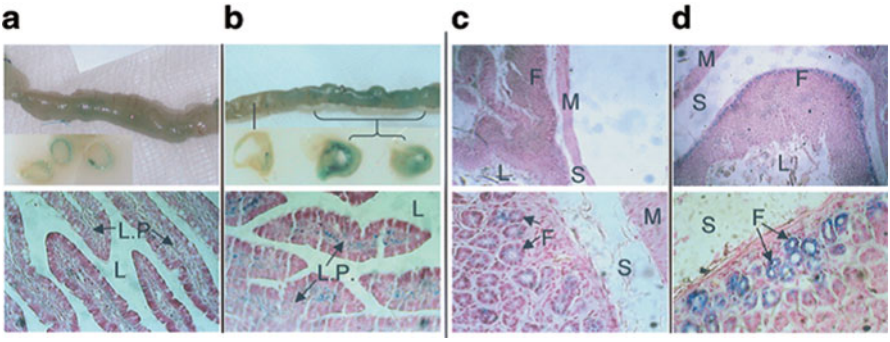

Fig. 10.18 In vivo magnetofection. (**a**, **b**) Ilea lumen of rat incorporating DNA-iron oxide–coated polyethylenimine: in absence of magnetic field (**a**) and after placement in magnetic field for 20 min (**b**). *Upper panel* (macroscopic level): intestinal tubes after X-gal stain, *insets*: cross section of tubes embedded in paraffin. *Lower panel* (microscopic level): paraffin sections counterstained with eosin. (**c**, **d**) Stomach lumen of mice incorporating LacZ-iron oxide–coated polyethylenimine: in absence of magnetic field (**c**) and after placement in magnetic field for 20 min (**d**). Magnetic field is due to Nd-Fe-B permanent magnets. L, lumen; LP, lamina propria; F, fundic glands; S, submucosa; M, muscularis. Reproduced with permission from [58]

occurs in the absence of a magnetic field and after placing the tissue in the applied magnetic field for 20 min, a widespread X-gal staining was observed in the crypts of fundic glands after four days of gene delivery (Fig. 10.18).

One of the most popular and convenient agents for gene delivery is light. Light beams with wavelengths in the UV or visible range suffer frequent absorption and scattering from animal tissues, hemoglobin, biomolecules, and water. Therefore, the practical uses of UV/visible light are not suitable especially for in vivo applications. Near infrared (NIR) lights are often used for photochemical internalization (PCI) gene transfer. The photothermal transfection (PTT) process, involving the break-down of endosomal or lysosomal cell membranes in the presence of NIR lights, initiates because of novel nanomaterials like gold, carbon nanotubes, and graphene. GO, as the parent material of graphene, is a promising material for gene delivery.

Luo et al. have developed a multifunctional photosensitizer grafted on PEG and polyethylenimine dual-functionalized nanographene oxide for cancer-targeted NIR imaging and synergistic phototherapy [59]. The researchers chemically conjugated a photodynamic therapy (PDT) photosensitizer (IR-808) with cancer-targeting ability and NIR sensitivity to both PEG- and branched polyethylenimine (BPEI)-functionalized NGO. The IR-808-conjugated NGO sheets (NGO-808, 20–50 nm) produced local hyperthermia as well as large reactive oxygen species (ROS) as a consequence of 808 nm laser irradiation. The tumor targeting of NGO-808 was examined in athymic nude mice bearing A549 tumor xenografts and C57 BL/6 mice bearing Lewis tumor xenografts. NGO-808 (0.5 mg kg^{-1}) was intravenously injected into the tumor-bearing mice. In vivo NIR fluorescence imaging was taken from 0 to 48 h after injection (Fig. 10.19).

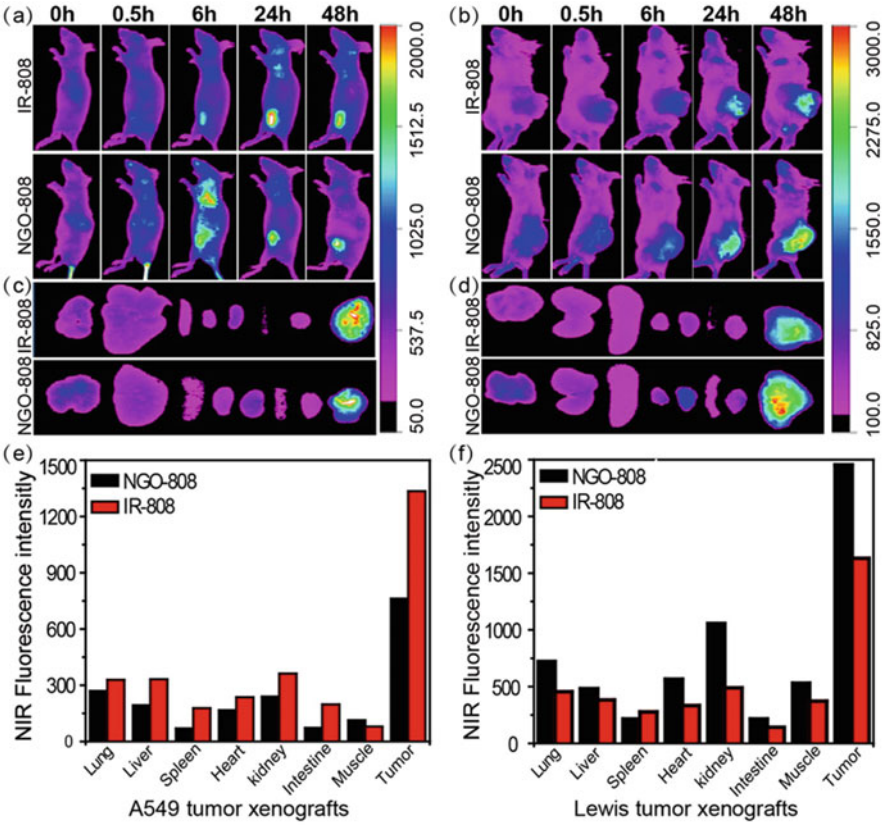

Fig. 10.19 In vivo tumor-targeted NIR imaging of NGO-808 on nude mice bearing A549 tumors and C57 mice bearing Lewis tumors. In vivo NIR images of (**a**) A549 tumor xenografts and (**b**) Lewis tumor xenografts from 0 to 48 h after injection of IR-808 or NGO-808. Ex vivo NIR images of dissected organs and tumors at 48 h postinjection [(**c**) A549 tumor xenografts. (**d**) Lewis tumor xenografts; *left* to *right*: lung, liver, spleen, heart, kidney, intestine, muscle, tumor.] (**e**, **f**) NIR fluorescence intensity of dissected organs and tumors between IR-808 and NGO-808. Reproduced with permission from [59]

With PEG- and BPEI-modified NGO as the carrier, the tumor cellular uptake of NGO-808 exhibited higher efficacy than that of strongly hydrophobic free IR-808. Through evaluation with both human and mouse cancer cells, NGO-808 was demonstrated to provide significantly enhanced PDT and PTT effects compared to individual PDT using IR-808 or PTT using NGO. Furthermore, NGO-808 preferentially accumulated in cancer cells as mediated by organic-anion transporting polypeptides (OATPs) over expressed in many cancer cells, providing the potential for highly specific cancer phototherapy [59].

Chemotherapy has become unsuitable for anticancer treatment according to recent medical trends because of its unendurable toxicity and resistance of

cancerous cells to traditional drugs. Therefore, different techniques, like launching multiple chemotherapeutic agents in different targets, multiple drug delivery in a single platform, and combined chemotherapy and gene therapy, have evolved for anticancer treatment.

10.6.6 Hyperthermia Application

The treatment of cancer at high temperature is called hyperthermia. The application involves the damaging of cancer cells by exposing the body tissue to high temperature. Microwave, radio frequency, and ultrasound are used as the source of heat in hyperthermia applications. Although these techniques are responsible for damaging cellular growth, additionally the treatment affects healthy tissues. To resolve this issue a new technique must be developed. Nanotechnology has led to the use of a new method, *magnetic hyperthermia*, of damaging cancer cells. This technique involves the release of heat by magnetic energy loss of magnetic nanoparticles under an oscillating magnetic field. Normally in this technique the magnetic nanoparticles have the ability to transform electromagnetic energy into heat energy, which increases the temperature of the tumor cells in human body. Such nanoparticles are called *nanoheaters*. The activation of such nanoheaters is controlled by tuning the oscillating magnetic field [60]. Bai et al. have studied the inductive heating property of GO nanosheet–iron oxide composite (GO-Fe_3O_4) hybrids in an AC magnetic field for localized hyperthermia.

Figure 10.20 shows the temperature dependence of GO-Fe_3O_4 nanocomposites with time in an AC magnetic field. After exposing the material for 500 s to an AC magnetic field, the temperature of the saline suspension containing GO-Fe_3O_4 is 92.8 °C [61]. In a temperature range of 41–46 °C in an external magnetic field, the implanted thermo seeds kill the tumor cells [61–63].

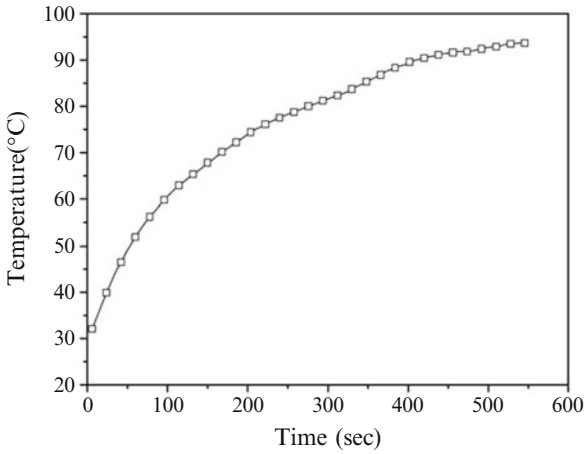

Fig. 10.20 Temperature-dependent curve of GO-Fe_3O_4 hybrid in AC magnetic field. Reproduced with permission from [61]

10.6.7 Bacterial/Pathogen Detection and Isolation

When pathogenic bacteria enter a human body, they immediately multiply into several new bacteria, causing rashes, fever, and headache and suppress the human immune system. These bacteria tend to grow very fast, contaminating blood components. Therefore it is essential to detect these bacteria and find ways of getting rid of these pathogens in time. Many undesirable signals arise from the interference of various biomolecules during the detection of bacteria in a patient's blood, which is to be reduced in order to attain higher detection efficiency. Several techniques, like fluorescence microscopy, UV absorption, immunomagnetic separation, matrix-assisted laser desorption ionization imaging mass spectroscopy (MALDI-IMS), antibody- and DNA-based tests, have been implemented. But these techniques have their own limitations in detection. Abdel Hamid et al. have demonstrated the feasibility of using chitosan for the development of multifunctional magnetic graphene nanosheet biosensors [64]. The novel material graphene-magnetic@chitosan (GMC) is chosen for the detection of pathogenic bacteria like *Pseudomonas aeruginosa* and *Staphylococcus aureus*, present in mouse blood samples. GMC has numerous functional abilities like fluorescent biosensing, fluorescent background suppression, nanoprobe enrichment, action as a comatrix, and superior magnetic separation, which make this nanomaterial useful for bacterial applications. In this experiment, both MALDI-IMS and fluorescence techniques were integrated for enhanced bacterial detection. Since pathogenic bacteria show a high affinity toward GMC, they can accumulate on the GMC and, hence, be easily separated.

For the enrichment and isolation of target compounds like proteins and peptides in MALDI-TOF-MS analysis, Liu et al. designed a very useful material, Fe_3O_4@SiO_2 @graphene microspheres, by solvothermal synthesis followed by a sol-gel method [65]. Graphene provides a very high loading capacity of biomolecules on its surface. Fe_3O_4@SiO_2@graphene as an adsorbent has advantages over previous magnetic nanoparticle decorated graphene sheets in that it avoids the agglomeration of graphene sheets and provides sufficient stable exposures for the adsorption process. The rapid and facile enrichment process and the reusability of Fe_3O_4@SiO_2@graphene make this material appropriate for MALDI-TOF-MS analysis.

In another study, monolayer graphene was integrated with silk fibroin films (Fig. 10.21), which were again incorporated into the electrode pattern by a shadow-mask-assisted electron beam evaporation of a gold technique to form an LRC resonance network [66]. This integrated network, set on enamel, has been extensively used for respiration monitoring and the detection of bacteria present in human saliva. For wireless communication, a gold inductive coil was used in the LRC circuit, where graphene acts as a resistive sensor. The structural and electronic properties of the graphene used in the sensor were investigated using Raman spectroscopy, which confirmed a successful biotransfer to tooth enamel.

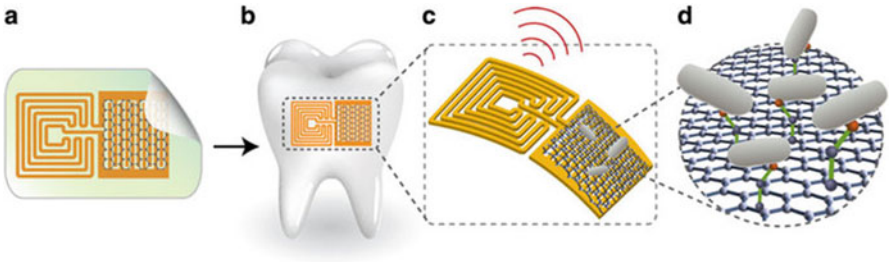

Fig. 10.21 Schematic diagram of biotransferable graphene wireless sensor. (**a**) Wireless contact of graphene on bioreversible silk. (**b**) Biotransfer of nanosensor on tooth enamel. (**c**) Magnified image of nanosensor, showing wireless readout. (**d**) Binding of pathogenic bacteria on graphene nanotransducer. Reproduced with permission from [66]

10.7 Conclusion

This chapter offers a comprehensive overview of the state of progress made in graphene-based multifunctional magnetic nanocomposites and their applications in various biomedical fields. The biocompatibility requirements and functionalization approach of these nanocomposites are also reviewed. The potential use of graphene-based multifunctional magnetic nanocomposites in living beings has led to remarkable developments in research as well as the theragnosis of various diseases. Graphene-based multifunctional magnetic nanocomposites, which are used in drug delivery and theragnosis, has played a momentous role in the emergence of the age of tailored medicine.

Acknowledgements The authors are thankful to the Department of Science and Technology, Government of India, for approving the Fast Track Research Project for Young Scientists for Dr. Prashant K. Sharma (SR/FTP/PS-157/2011) and Dr. Rashmi Madhuri (SB/FT/CS-155/2012). Dr. Sharma (FRS/34/2012-2013/APH) and Dr. Madhuri (FRS/43/2013-2014/AC) are also thankful to the Indian Institute of Technology (Indian School of Mines), Dhanbad, for a grant for a major research project under the Faculty Research Scheme. We are also thankful to the Board of Research in Nuclear Sciences (BRNS), Department of Atomic Energy, Government of India, for a major research project (Sanction 34/14/21/2014-BRNS/0295). The authors also sincerely acknowledge the facilities made available in the central research facility of the institute. Trupti and Suryakanti are thankful to the Indian Institute of Technology (Indian School of Mines), Dhanbad, for their Fellowships.

References

1. Arora VK, Bhattacharyya A (2013) Cohesive band structure of carbon nanotubes for applications in quantum transport. Nanoscale 5:10927–10935
2. Geim AK, Novoselov KS (2007) The rise of graphene. Nat Mater 6:183–191
3. Marcano DC, Kosynkin DV, Berlin JM, Sinitskii A, Sun Z, Slesarev A, Alemany LB, Lu W, Tour JM (2010) Improved synthesis of graphene oxide. ACS Nano 4:4806–4814

4. Dreyer DR, Park S, Beilawski CW, Ruoff RS (2010) Chemistry of graphene oxide. Chem Soc Rev 39:228–240
5. Krishnamoorthy K, Veerapandian M, Yun K, Kim S-J (2013) The chemical and structural analysis of graphene oxide with different degrees of oxidation. Carbon 53:38–49
6. Zhu Y, Murali S, Cai W, Li X, Suk JW, Potts JR, Ruoff RS (2010) Graphene and graphene oxide: synthesis, properties and applications. Adv Mater 22:1–19
7. Childres I , Jauregui LA , Park W , Cao H , Chen YP (2013) Raman spectroscopy of graphene and related materials. In: Jang JI (ed) New developments in photon and materials research, vol 1. Nova Science Publisher, Hauppauge (Chapter 19)
8. Terrones M, Botello-Mendez AR, Campos-Delgado J, Lopez-Urias F, Vega-Cantu YI, Rodriguez-Macias FJ, Elias AL, Munoz-Sandoval E, Cano-Marquez AG, Charlier J-C, Terrones H (2010) Graphene and graphite nanoribbons: morphology, properties, synthesis, defects and applications. Nano Today 5:351–372
9. Li D, Muller MB, Gilje S, Kaner RB, Wallace GG (2008) Processable aqueous dispersions of graphene nano sheets. Nat Nanotechnol 3:101–105
10. Fuhrer MS, Lau CN, MacDonald AH (2010) Graphene: materially better carbon. MRS Bull 35(4):289–295
11. Novoselov KS, Morozov SV, Mohinddin TMG, Ponomarenko LA, Elias DC, Yang R, Barbolina II, Blake P, Booth TJ, Jiang D, Giesbers J, Hill EW, Geim AK (2007) Electronic properties of graphene. Phys Stat Sol (b) 244:4106–4111
12. Liu J, Liu Z, Barrow CJ, Yang W (2015) Molecularly engineered graphene surfaces for sensing applications: a review. Anal Chim Acta 859:1–19
13. Shen H, Jhang L, Liu M, Zhang Z (2012) Biomedical application of graphene. Theranostics 2:283–294
14. Lee N, Choi Y, Lee Y, Park M, Moon WK, Choi SH, Hyeon T (2008) Water-dispersible ferrimagnetic iron oxide nanocubes with extremely high r2 relaxivity for highly sensitive in vivo MRI of tumors. Nano Lett 12:3127–3131
15. Laurent S, Forge D, Port M, Roch A, Robic C, Elst LV, Muller RN (2008) Magnetic iron oxide nanoparticles: synthesis, stabilization, vectorization, physicochemical characterizations, and biological applications. Chem Rev 108:2064–2110
16. Gupta AK, Gupta M (2005) Synthesis and surface engineering of iron oxide nanoparticles for biomedical applications. Biomaterials 26:3995–4021
17. Yang Y, Asiri AM, Tang Z, Du D, Lin Y (2013) Graphene based material for biomedical application. Mater Today 16:365–373
18. Chen W, Yi P, Zhang Y, Zhang L, Deng Z, Zhnag Z (2011) Composites of aminodextran-coated Fe3O4 nanoparticles and graphene oxide for cellular magnetic resonance imaging. ACS Appl Mater Interface 3:4085–4091
19. Chung C, Kim Y, Shin D, Ryoo S, Hong BH, Min D (2013) Biomedical applications of graphene and graphene oxide. Acc Chem Res 46:2211–2224
20. Wang F, Peng E, Zheng B, Li SFY, Xue JM (2015) Synthesis of water-dispersible Gd2O3/GO nanocomposites with enhanced MRI T1 relaxivity. J Phys Chem 119:23735–23742
21. Fan X, Jiao G, Zhao W, Jin P, Li X (2013) Magnetic Fe3O4–graphene composites as targeted drug nanocarriers for pH-activated release. Nanoscale 5:1143–1152
22. Yang K, Hu L, Ma X, Ye S, Cheng L, Shi X, Li C, Li Y, Liu Z (2012) Multimodal imaging guided photothermal therapy using functionalized graphene nanosheets anchored with magnetic nanoparticles. Adv Mater 24:1868–1872
23. Sun X, Liu Z, Welsher K, Robinson JT, Goodwin A, Zaric S, Dai H (2008) Nano-graphene oxide for cellular imaging and drug delivery. Nano Res 1:203–212
24. Some S, Gwon A, Hwang E, Bahn G, Yoon Y, Kim Y, Kim S, Bak S, Yang J, Jo D, Lee H (2014) Cancer therapy using ultrahigh hydrophobic drug-loaded graphene derivatives. Sci Rep 4:6314
25. Cheng G, Liu Y-L, Wang Z-G, Zhang J-L, Sun D-H, Ni J-Z (2012) The GO/rGO–Fe3O4 composites with good water-dispersibility and fast magnetic response for effective immobilization and enrichment of biomolecules. J Mater Chem 22:21998–22004

26. Shi X, Gong H, Li Y, Wang C, Cheng L, Liu Z (2013) Graphene-based magnetic plasmonic nanocomposite for dual bioimaging and photothermal therapy. Biomaterials 34:4786–4793
27. Kong B-S, Geng J, Jung J-T (2009) Layer-by-layer assembly of graphene and gold nanoparticles by vacuum filtration and spontaneous reduction of gold ions. Chem Commun 16:2174–2176
28. El Mel A-A, Nakamura R, Bittencourt C (2015) The Kirkendall effect and nanoscience: hollow nanospheres and nanotubes. Beilstein J Nanotechnol 6:1348–1361
29. Wang L, Yamauchi Y (2013) Metallic nanocages: synthesis of bimetallic Pt−Pd hollow nanoparticles with dendritic shells by selective chemical etching. J Am Chem Soc 135:16762–16765
30. Skrabalak SE, Chen J, Sun Y, Lu X, Au L, Cobley CM, Xia Y (2008) Gold nanocages: synthesis, properties, and applications. Acc Chem Res 41:1587–1595
31. Fujie T, Matsutani N, Kinoshita M, Okamura Y, Saito A, Tokeoka S (2009) Adhesive, flexible and robust polysaccharide nano sheets integrated for tissue-defect repair. Adv Funct Mater 19:2560–2568
32. Lim D-K, Barhoumi A, Wylie R, Reznor G, Langer R, Kohane DS (2013) Enhanced photothermal effect of plasmonic nanoparticles coated with reduced graphene oxide. Nano Lett 13:4075–4079
33. Liu J, Yang Y, Hassinin H, Jumbu N, Deng S, Zuo Q, Jiang K (2016) Graphene-alumina nanocomposites with Improved mechanical properties for biomedical applications. ACS Appl Mater Interfaces 8:2607–2616
34. Zhang XF, Shao X (2014) π–π binding ability of different carbon nano-materials with aromatic phthalocyanine molecules: comparison between graphene, graphene oxide and carbon nanotubes. J Photochem Photobiol 278:69–74
35. Roy M, Kusurkar TS, Maurya SK, Meena SK, Singh SK, Sethy N, Bhargava K, Sharma RK, Goswami D, Sarkar S, Das M (2014) Graphene oxide from silk cocoon: a novel magnetic fluorophore for multi-photon imaging. 3 Biotech 4:67–75
36. Wu M-C, Deokar AR, Liao J-H, Shih P-Y, Ling Y-C (2013) Graphene-based photothermal agent for rapid and effective killing of bacteria. ACS Nano 7(2):1281–1290
37. Zhang S, Yang K, Feng L, Liu Z (2011) In vitro and in vivo behaviors of dextran functionalized graphene. Carbon 49:4040–4049
38. Yang K, Zhang S, Zhang G, Sun X, Lee S-T, Liu Z (2010) Graphene in mice: ultrahigh in vivo tumor uptake and efficient photothermal therapy. Nano Lett 10:3318–3323
39. Li X, Wang L, Fan Y, Feng Q, Cui F-Z (2012) Biocompatibility and toxicity of nanoparticles and nanotubes. J Nanomater 2012:19
40. Thanh NTK, Green LAW (2010) Functionalisation of nanoparticles for biomedical applications. Nano Today 5:213–230
41. Wang G, Ma Y, Wei Z, Qi M (2016) Development of multifunctional cobalt ferrite/graphene oxide nanocomposites for magnetic resonance imaging and controlled drug delivery. Chem Eng J 289:150–160
42. Pan Q, Lv Y, Williams GR, Tao L, Yang H, Li H, Zhu L (2016) Lactobionic acid and carboxymethyl chitosan functionalized graphene oxide nanocomposites as targeted anticancer drug delivery systems. Carbohydr Polym 151:812–820
43. Wang G, Ma Y, Zhang L, Mu J, Zhang Z, Zhang X, Che H, Bai Y, Hou J (2016) Facile synthesis of manganese ferrite/graphene oxide nanocomposites for controlled targeted drug delivery. J Magn Magn Mater 401:647–650
44. Gao Y, Zou X, Zhao JX, Li Y, Su X (2013) Graphene oxide-based magnetic fluorescent hybrids for drug delivery and cellular imaging. Colloids Surf B Biointerfaces 112:128–133
45. Sasikala ARK, Thomas RG, Unnithan AR, Saravanakumar B, Jeong YY, Park CH, Kim CS (2016) Multifunctional nanocarpets for cancer theranostics: remotely controlled graphene nanoheaters for thermo-chemosensitisation and magnetic resonance imaging. Sci Rep 6:20543
46. Baradaran S, Moghaddam E, Nasiri-Tabrizi B, Basirun WJ, Mehrali M, Sookhakian M, Hamdi M, Alias Y (2015) Characterization of nickel-doped biphasic calcium phosphate/graphene nanoplatelet composites for biomedical application. Mater Sci Eng C Mater Biol Appl 49:656–668

47. Hong CH, Kim MW, Zhang WL, Moon IJ, Choi HJ (2016) Fabrication of smart magnetite/reduced graphene oxide composite nanoparticles and their magnetic stimuli-response. J Colloid Interface Sci 481:194–200
48. Yang H, Bremner DH, Tao L, Li H, Hu J, Zhu L (2016) Carboxymethyl chitosan-mediated synthesis of hyaluronic acid-targeted graphene oxide for cancer drug delivery. Carbohydr Polym 135:72–78
49. Justin R, Tao K, Roman S, Chen D, Xu Y, Geng X, Ross IM, Grant RT, Pearson A, Zhou G, MacNeil S, Sun K, Chen B (2016) Photoluminescent and superparamagnetic reduced graphene oxide–iron oxide quantum dots for dual-modality imaging, drug delivery and photothermal therapy. Carbon 97:54–70
50. Kim H, Namgung R, Singha K, Oh I-K, Kim WJ (2011) Graphene oxide−polyethylenimine nanoconstruct as a gene delivery vector and bioimaging tool. Bioconjug Chem 22:2558–2567
51. Ma X, Tao H, Yang K, Feng L, Cheng L, Shi X, Li Y, Guo L, Liu Z (2012) A functionalized graphene oxide–iron oxide nanocomposite for magnetically targeted drug delivery, photothermal therapy, and magnetic resonance imaging. Nano Res 5(3):199–212
52. Konwar A, Kalita S, Kotoky J, Chowdhury G (2016) Chitosan-iron oxide coated graphene oxide nanocomposite hydrogel: a robust and soft antimicrobial bio-film. ACS Appl Mater Interfaces 8:20625–20634
53. Chen W, Yi P, Zhang Y, Zhang L, Deng Z, Zhang Z (2011) Composites of aminodextran-coated Fe3O4 nanoparticles and graphene oxide for cellular magnetic resonance imaging. ACS Appl Mater Interfaces 3:4085–4091
54. Wang F, Peng E, Zheng B, Li SFY, Xue JM (2015) Synthesis of water-dispersible Gd2O3/GO nanocomposites with enhanced MRI T1 relaxivity. J Phys Chem C 119:23735–23742
55. Wang Y, Chen J-T, Yan X-P (2013) Fabrication of transferrin functionalized gold nanoclusters/graphene oxide nanocomposite for turn-on near-infrared fluorescent bioimaging of cancer cells and small animals. Anal Chem 89:2529–2535
56. Weaver CL, LaRosa JM, Luo X, Cui XT (2014) Electrically controlled drug delivery from graphene oxide nanocomposite films. ACS Nano 8:1834–1843
57. Yang K, Feng L, Shi X, Liu Z (2013) Nano-graphene in biomedicine: theranostic applications. Chem Soc Rev 42:530–547
58. Scherer F, Anton M, Schillinger U, Henke J, Bergemann C, Kruger A, Gansbacher B (2002) Magnetofection: enhancing and targeting gene delivery by magnetic force in vitro and in vivo. Gene Ther 9:102–109
59. Kim H, Kim WJ (2014) Photothermally controlled gene delivery by reduced graphene oxide–polyethylenimine nanocomposite. Small 10:117–126
60. Bai L-Z, Zhao D-L, Xu Y, Zhang J-M, Gao Y-L, Zhao L-Y, Tang J-T (2012) Inductive heating property of graphene oxide–Fe3O4 nanoparticles hybrid in an AC magnetic field for localized hyperthermia. Mater Lett 68:399–401
61. Moroz P, Jones SK, Gray BN (2002) Magnetically mediated hyperthermia: current status and future directions. Int J Hyperthermia 18:267–284
62. Jordan A, Wust P, Fahling H (1993) Inductive heating of ferrimagnetic particles and magnetic fluids: physical evaluation of their potential for hyperthermia. Int J Hyperthermia 9:51–68
63. Yang X, Wang Y, Huang X, Ma Y, Huang Y, Yang R, Duan H, Chen Y (2011) Multi-functionalized graphene oxide based anticancer drug-carrier with dual-targeting function and pH-sensitivity. J Mater Chem 21:3448–3454
64. Abdelhamid HN, Wu H-F (2013) Multifunctional graphene magnetic nanosheet decorated with chitosan for highly sensitive detection of pathogenic bacteria. J Mater Chem B 1:3950–3961
65. Liu Q, Shi J, Cheng M, Li G, Cao D, Jiang G (2012) Preparation of graphene-encapsulated magnetic microspheres for protein/peptide enrichment and MALDI-TOF MS analysis. Chem Commun 48:1874–1876
66. Mannoor MS, Tao H, Clayton JD, Sengupta A, Kaplan DL, Naik RR, Verma N, Omenetto FG, McAlpine MC (2012) Graphene-based wireless bacteria detection on tooth enamel. Nat Commun 3:763.

Chapter 11
Magnetic Nanoparticle-Based Hyperthermia for Cancer Treatment: Factors Affecting Heat Generation Efficiency

Yasir Javed, Khuram Ali, and Yasir Jamil

11.1 Introduction

The importance of nanotechnology-based medicines, i.e., nanomedicines, has been increasing greatly in recent years [1]. Owing to the familiar side effects of anticancer drugs, medicines with high efficacy and selectivity were indispensable [2]. The problem of inconsistent proliferation of drugs at tumor sites while causing comparatively less damage to normal tissues can be resolved with nanoparticles. Nanoparticles can release drugs by the action of an external signal, pH values, or physiological conditions inside tissues or cells [3]. In addition, there are great economic benefits associated with the use of nanotechnology in cancer treatment. In general, nanotechnology is poised to have a ground-breaking impact on cancer diagnosis and therapy [4, 5].

Noninvasive, early-stage cancer detection is a major challenge and a precondition for its treatment. It is also important to secure the greatest therapeutic advantages. In cancer treatment, cell-specific and localized drug delivery is a crucial challenge [6]. A powerful fight against cancer requires efficient attacks on cancer cells while preserving normal cells from unnecessary drug loadings [7]. Conversely, the majority of anticancer drugs are developed with a view to simply killing cancer cells and distributing drugs in healthy organs or tissues, without regard for the concomitant severe side effects in normal tissues [8]. Furthermore, for fast elimination and broad distribution from healthy/nontargeted organs and tissues, high dosage levels are administered. This is not usually economical and also raises toxicity issues. Such large quantities and the related toxicity problems have limited current cancer therapies [9, 10].

Y. Javed (✉) • K. Ali • Y. Jamil
Nano-Optoelectronics Research Laboratory, Department of Physics, University of Agriculture Faisalabad, Faisalabad 38040, Pakistan
e-mail: myasi60@hotmail.com; khuram_uaf@yahoo.com; yasirjamil@yahoo.com

© Springer International Publishing AG 2017

S.K. Sharma (ed.), *Complex Magnetic Nanostructures*,
DOI 10.1007/978-3-319-52087-2_11

The use of heat as a healing source for a variety of diseases has been observed for around 3000 years ago in India. Hippocrates (540–480 BC) used hot sand in the summer to cure diseases. Hyperthermia comes from Greek words *hyper*, meaning "raise," and *therme*, meaning "heat." The first use of *hyperthermia* in connection with cancer treatment was by a Roman doctor, Cornelius Celsus Aulus, who observed high thermal sensitivity to early-stage cancer [11]. In the Middle Ages, hyperthermia was used with respect to several disease treatments such as malaria, and the first proper work on hyperthermia was published in 1886 [12]. Although the idea of using heat to treat cancer has been around for years, results had not evolved according to expectations initially. In 1975, the first international congress on hyperthermia oncology in Washington represented a major step toward hyperthermia research activities in the scientific community. In later years, different groups on hyperthermia had formed in the USA, Europe, and Japan.

In hyperthermia, body tissues are subjected to elevated temperatures by means of external (alternating field) and internal (nanoparticle) devices (Fig. 11.1). Electromagnetic radiation demonstrates active interactions with tissues, which allows for potential applications in thermal therapies. Owing to their limitations for treatment in deep seated tissues, alternating magnetic fields in a frequency range up to 10 MHz offer great potential for treatment in deep tissue areas. Human tissues are usually diamagnetic and show negligible magnetic effects. However, AC magnetic fields induce eddy currents in any conducting Medium. These eddy currents finally subject to losses [14–16]. Clinical studies have been performed to estimate the AC field tolerance level in the human body [17]. The results showed that the acceptable level is confined to the product of the frequency and field strength [18–20],

$$fH_{\mathrm{a}} < 4.85 \times 10^{8}\ \mathrm{A.m/s}. \tag{11.1}$$

It has been reported that cancer cells are more sensitive to temperature (approximately 42–48 °C) compared to normal cells (approximately 50 °C) and tumor development can stop in this temperature range [21, 22]. Temperature ranges for cancer treatment can be split into two parts; one is the hyperthermia range, in which temperatures between 41 to 48 °C are used for cancer treatment, while

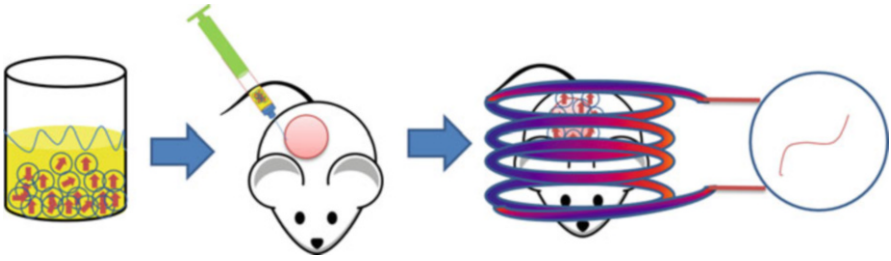

Fig. 11.1 Schematic of magnetic hyperthermia measurement (Reproduced with permission from [13])

the second is the thermoablation range, which uses temperatures above 47–56 °C [23, 24]. Thermoablation causes acute necrosis, coagulation, or carbonization of tissues, which is why it is not required in the majority of clinical hyperthermia treatments [25]. The efficient response of hyperthermia relies on the temperature rise and exposure time. For example, Valdagni and coworkers [26] compared responses in patients subject to 24% radiation therapy alone with the responses of those subject to 69% radiation therapy plus hyperthermia and noted an increase in local control of metastatic lymph nodes without a concomitant increase in toxicity. The researchers followed the two treatments (radiation therapy alone and radiation therapy plus hyperthermia) in random trials on metastatic lymph nodes in stage IV head and neck cancer patients for 5 years.

Hyperthermia treatments can be classified broadly into three groups: whole-body hyperthermia, regional hyperthermia, and local hyperthermia. Whole-body hyperthermia is usually used in cancer that can spread from its primary site (site of origin) to other organs; such cancer is called metastatic cancer [27]. The other two types of hyperthermia are more useful in localized tumors. These two types can be further subdivided into external, interstitial, and endocavity hyperthermia. Moreover, heat generation processes can also modify according to the target region and by other parameters controlling heat generation [28, 29].

For efficient hyperthermia, delivery mechanisms should be noninvasive, be highly tissue specific, and have the ability to produce high-intensity heat confined to a limited area in deep tissues [13]. The dose rate requires a balance between the quantity of magnetic fluid needed for therapeutic efficacy and damaging effects on normal cells [30]. Gilchrist and coworkers [31] were the first to report magnetic nanomaterials for hyperthermia in the 1950s and later years; magnetic nanoparticles had shown promising capabilities to satisfy all the aforementioned requirements [4, 32–37]. Magnetic nanoparticles have been used in diagnosing, imaging, and treating cancer with different techniques [38, 39]. Magnetic fluids can be delivered very efficiently to specific sites inside an organism noninvasively with the help of different drug delivery routes and subsequently heated using alternating magnetic fields at frequencies harmless to healthy tissues [40, 41]. Additionally, alternating magnetic fields can be used to direct magnetic nanoparticles to some extent for nonspecific remote localization [42]. Targeted localization can be attained by functionalizing nanoparticles with appropriate biopolymers. Magnetic nanoparticles have also shown a tendency to aggregate inside certain types of cancer tumors [43]. The majority of nanoparticles for hyperthermia consist of magnetite (Fe_3O_4) and ferrites with cobalt, nickel, and other substitutes. These materials range from nanometers to a few microns in size.

Currently, the focus has shifted toward single-domain nanoparticles, called superparamagnetic particles, owing to their high absorbance of power, at body acceptable magnetic fields and frequencies, as compare to multidomain nanoparticles, [13, 44, 45]. This type of magnetism arises in tiny ferromagnetic or ferrimagnetic nanoparticles where magnetic spins can flip randomly owing to temperature. In this case, when we measure the magnetization for much longer times than their relaxation time, the overall magnetization becomes zero, i.e., a so-called superparamagnetic

state. Nanoparticles can be magnetized by applying an external field that shows higher magnetic susceptibility than usual paramagnetic materials. The anisotropic energy of superparamagnetic nanoparticles corresponds to their volume. When the particle size decreases [46–49], the anisotropic energy also decreases, and at a certain threshold of particle size it can be equal to or less than the thermal energy $k_B T$. This implies that magnetization reversal can happen below this energy barrier. The overall magnetic moment can rotate freely, whereas internal moments stay magnetically intact, i.e., ferromagnetic or antiferromagnetic.

In summary, many research groups have investigated the ability of magnetic nanoparticles to generate heat in vivo using different types of nanoparticles, field parameters (different frequency and amplitude), and thermometry methods [47–49]. However, researchers continue to study the toxicity of nanoparticles [50], different cancer types [51–53], and field optimization and to improve biological targeting by more efficient drug delivery methods. This chapter covers the physical principles and different crucial aspects that can affect the heat efficiency of magnetic nanoparticles.

11.2 Physical Basis of Magnetic Hyperthermia

To understand the physics behind the generation of heat from nanoparticles under an AC magnetic field, a key point is to fine tune the properties of the nanoparticles for efficient hyperthermia treatment. Magnetic nanoparticles show heating effects due to heating losses during their magnetization reversal processes [4, 25, 54]. Although a magnetic field can be established by different methods, inductive coils are an efficient source owing to the uniform magnetic field inside the coils. The intensity of the field can be calculated by

$$H_{\mathrm{a}} = \frac{NI}{L}, \tag{11.2}$$

where N is the number of turns of coils, I is the coil current, and L is the length of the coil. There are three main mechanisms responsible for these losses. First are eddy currents, which arise owing to friction heating; this mechanism is mostly developed in bulk materials (around 1 cm in size) [55]. Second is magnetic heating from hysteresis losses, which occurs in multidomain nanoparticles (at least 100 nm). Third and more relevant to nanoparticles is magnetic heating from relaxation mechanisms, i.e., Néel and Brownian relaxation mechanisms [in the nanometric range, i.e., 20 nm (for iron oxide), also called superparamagnetic nanoparticles] [56]. These mechanisms are discussed in detail in what follows.

11.2.1 Eddy Currents and Hysteresis Losses

The two less effective heat mechanisms are eddy currents and hysteresis losses that were initially considered for hyperthermia heat generation. When a changing magnetic field is applied on a conducting material, a swirling current is produced called an eddy current. By Lenz's law, the current moves so as to produce a magnetic field opposing the change, and for this, in a conductor, electrons move in a plane perpendicular to the applied magnetic field. This opposing tendency of the eddy current causes energy loss. In other words, it transforms the useful form of energy, i.e., kinetic energy, to heat. This heat formation is the main source of hyperthermia treatment in large particles. Eddy current escalates radially, therefore it is expected that maximum losses will be induced in sections with the highest cross-sectional area. If we consider a uniform magnetic field and cross-sectional area as a cylinder (Fig. 11.2a), the power generation can be calculated by integrating the time-averaged current density over the cross-sectional area:

$$P = \sigma(\pi \mu_0 f H_a)^2 r^2, \tag{11.3}$$

where σ is the bulk tissue conductivity, μ_o is the permeability of free space, f is the applied frequency, H_a is the applied field strength, and r is the effective radius.

This equation shows that current losses depend on the square of three factors, frequency, field strength, and radius. Therefore, losses will rise as we increase the frequency or applied field and be higher at the periphery of large cross-sectional tissues.

But eddy currents are not generated entirely from magnetic materials; tissues also have the capability to induce eddy currents owing to their low specific electrical conductivity, but their heating effect is far below the required therapeutic dose [57, 59]. Because eddy currents are induced mostly by bigger particles (a few millimeters in size), their contribution to heat generation is negligible when their size is reduced to the nanometer range.

11.2.2 Hysteresis Losses

As mentioned earlier, hysteresis losses are mainly due to multidomain nanoparticles. Ferromagnetic materials contain different regions in which there is uniform magnetization or all the magnetic spins align in one direction. These regions are called magnetic domains and each domain is separated by domain walls (Fig. 11.2). Domains emerged to reduce the overall magnetostatic energy of materials. When we apply an AC magnetic field to such materials, their magnetization aligns during the positive half cycle along the field and they demagnetize during the negative half cycle. This sequence of magnetization and demagnetization is usually represented in the form of a nonlinear curve called a hysteresis loop. The area

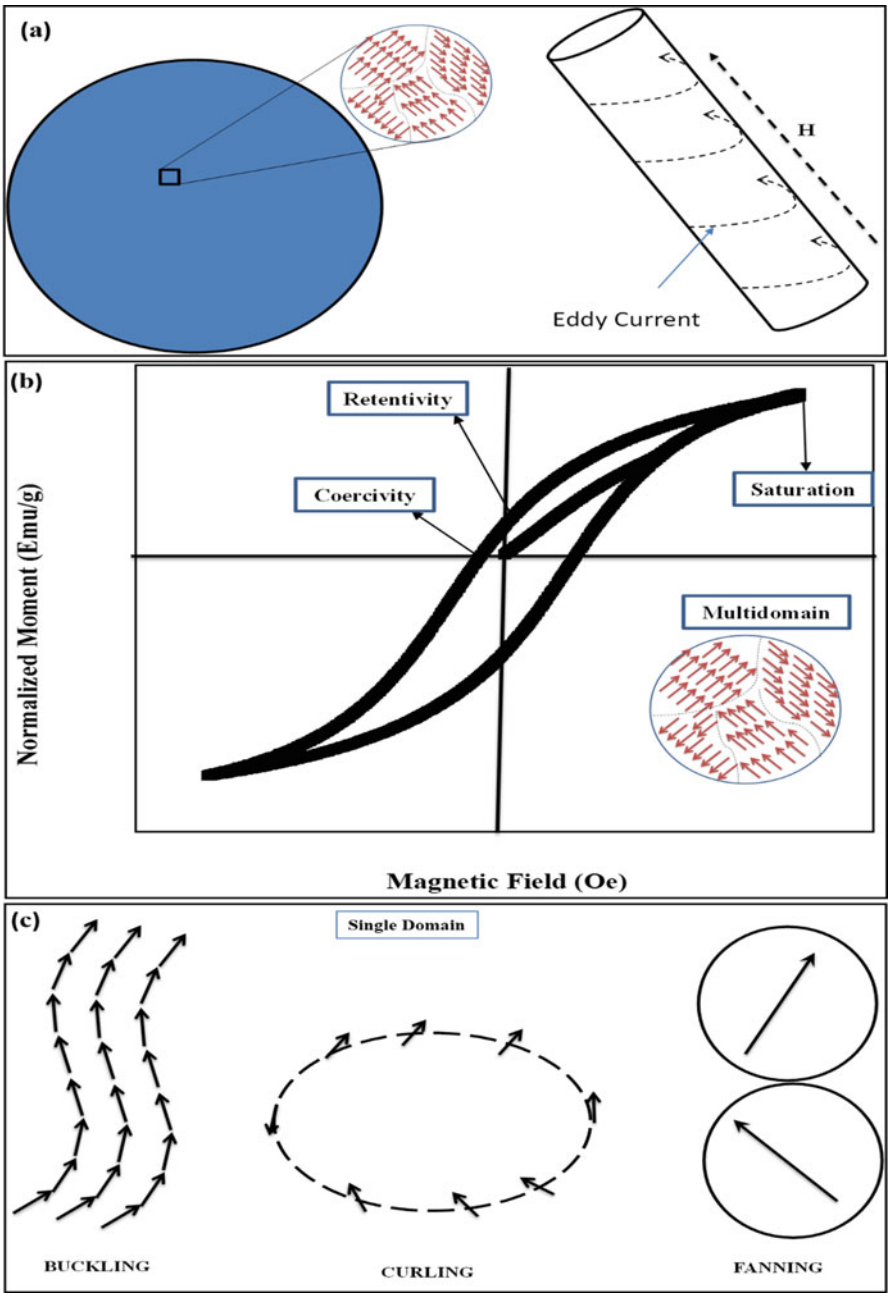

Fig. 11.2 (**a**) Schematic of eddy current. (**b**) Hysteresis of cobalt ferrite nanoparticles injected in mice at 10 K temperature using vibrating sample magnetometer. (**c**) Reversal mechanisms in single-domain ferromagnetic nanoparticles, buckling, curling, fanning. (Reproduced with permission from [57, 58])

under the curve represents both the strength of the magnetic material, i.e., hard magnetic material or soft magnetic materials, and heat loss during the AC cycle [60]. Actually, by the application of an external field, magnetic moments tend to minimize their potential energy by aligning in the direction of the applied field. In multidomain nanomaterials, these domains align and expand at the expense of neighboring domains. This movement of domain walls do not come back to their normal positions, when the field returns to zero and this behavior evolves hysteresis loop [61]. A hysteresis loop of cobalt ferrite nanoparticles injected into mice intravenously at 10 K is shown in Fig. 11.2b. Different points are described in the figure, such as saturation point, retentivity, and the coercive field. In nanomedicines, frequencies in the kilohertz to megahertz range and a field strength between $H = 0$–40 kA/m are commonly used [62].

The lack of retraceability of magnetization curves can also be observed in the absence of domain walls, i.e., in a single domain, where much lower values of coercivity than anticipated by the Stoner–Wohlfarth model were observed. The reversal processes here are very complicated, such as buckling, curling, and fanning. These processes are difficult to explain using classical physical models such as the Stoner–Wohlfarth model, in which uniform magnetization reversal in single-domain particles is observed. In contrast, Hergt and coworkers [63] found a power law for the field dependence of losses for a small-amplitude range. They formulated an expression that anticipated losses on the basis of the applied field parameters and particle size distribution [64]. Their experimental values and theoretical estimations provide specific loss power in the range of superparamagnetic nanoparticles. A schematic of three reversal mechanisms in the case of a single domain is shown in Fig. 11.2c [60].

11.2.3 Néel and Brownian Relaxations

At much smaller dimensions, i.e., a few tens of nanometers, a group of distinctive moments inside a magnetic particle is considered as a single giant spin that represents the total magnetization of the particle. At this size threshold, thermal fluctuations cause the flipping of the magnetization away from its normal state by controlling the magnetic energy. This phenomenon arises when the anisotropic energy barrier scales down to a particular position where thermal motion dominates this barrier. This thermally triggered process is called superparamagnetic [65]. The critical diameter for superparamagnetic behavior can be obtained by considering the spherical shape of a nanoparticle and modifying the relation used to illustrate the probability of relaxation. In the superparamagnetic phenomenon, although remanence and hysteresis mechanisms disappear, appreciable losses can still be observed owing to moment relaxation processes [66, 67].

Two relaxation mechanisms are involved in superparamagnetic nanoparticles: Néel relaxation and Brownian relaxation (Fig. 11.3). Néel relaxation involves the movement of all the spins in the particles and, hence, the magnetization direction,

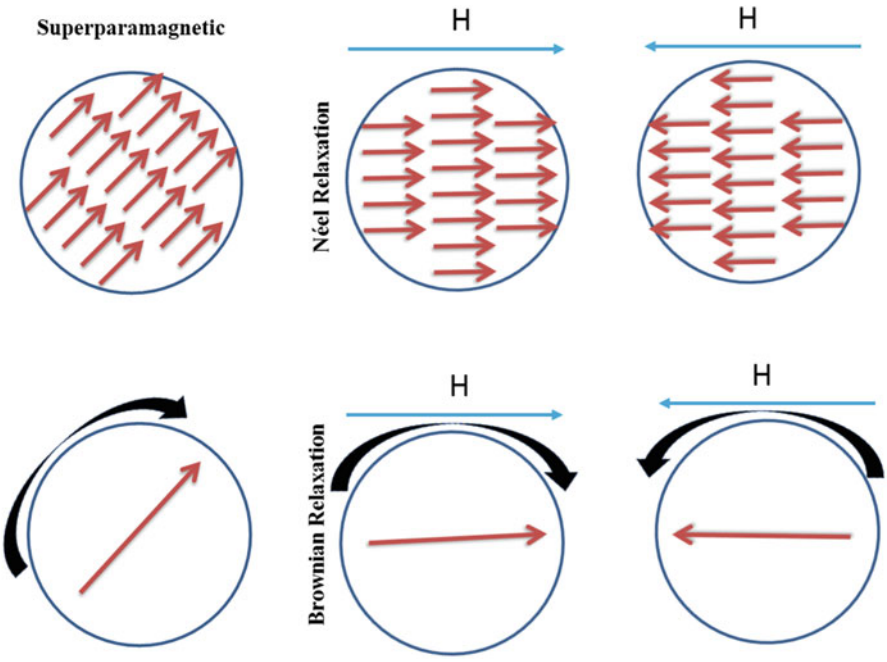

Fig. 11.3 Schematic of Néel and Brownian relaxation mechanisms of heat generation (Reproduced with permission from [4])

but not essentially the physical movement of the particle. These oscillations in the magnetization can occur in a specific time, called the relaxation time. These fluctuations develop above a certain critical temperature T_B. Below T_B, spin blocks are assumed to be fixed. Consequently, T_B is called the blocking temperature and suggests the superparamagnetic limit for steady magnetization. The time period of fluctuations can alter by changing the temperature and volume of a particle. Louis Néel [68, 69] proposed this temperature dependency and gave the following equation:

$$\tau_N = \frac{\sqrt{\pi}}{2}\tau_0 \frac{e^{\Gamma}}{\sqrt{\Gamma}}, \tag{11.4}$$

where

$$\Gamma = \frac{K_\mu V_M}{k_B T}. \tag{11.5}$$

Here, τ_o is the attempt time and $\tau_0 = 10^{-9}$ s, Γ is the ratio of anisotropy to thermal energies, K_μ is the anisotropy energy density, V_M is the volume of the suspension, and k_B is Boltzmann's constant.

Néel relaxation gives the vital relationship between anisotropic energy K and thermal energy kT, which provides the relaxation of the inner magnetic core. Brownian relaxation depends on the viscosity of the fluid and hydrodynamic volume of the nanoparticle [70]. In this relaxation, the particle itself can rotate and align with the external field. This movement depends on the hydrodynamic constraints of nanoparticles and suspended medium. It is also governed by the characteristic time. This characteristic relaxation time can be determined by the rotational mobility of the suspended magnetic nanoparticles and is given by

$$\tau_{\mathrm{B}} = \frac{3\eta V_{\mathrm{H}}}{k_{\mathrm{B}} T}, \tag{11.6}$$

where V_{H} is the hydrodynamic volume, and η is the viscosity of the liquid solvent.

Néel relaxation emerges for smaller particle sizes as a dominant process, whereas above a certain size range, the Brownian relaxation mechanism is more prominent. For close to the critical size limit, both mechanisms can be observed and the total effect can be calculated by taking their geometric mean [71, 72]:

$$\tau = \frac{\tau_{\mathrm{B}} \tau_{\mathrm{N}}}{\tau_{\mathrm{B}} + \tau_{\mathrm{N}}}. \tag{11.7}$$

However, distinguishing the contribution of the two mechanisms is very challenging, and experimental studies have been performed to meet this challenge. Fortin et al. [54] found that cobalt ferrite and maghemite nanoparticles have lower specific absorption rate (SAR) values in intracellular endosomes than when dispersed in water. They observed that Brownian mechanisms were prominent in the case of cobalt ferrite and Néel relaxation for maghemite nanoparticles. Similarly, Zhang and coworkers used magnetite nanoparticles dispersed in polydimethylsiloxane (PMDS) and water to differentiate the two relaxation mechanisms. They concluded that there was higher specific absorption when magnetite nanoparticles were dispersed in water due to both mechanisms. However, an additional contribution arises due to Néel relaxation by increasing the frequency and strength of an alternating magnetic field [73].

11.2.3.1 Calculation of Specific Absorption Rate for Magnetic Hyperthermia

The basic relation between the magnetic field and applied electromagnetic field is

$$B = \mu_0 \left(H_{\mathrm{a}} + M\right). \tag{11.8}$$

The increase in the internal energy for a complete cycle can be determined by integrating the following relation:

$$U = -\mu_0 \oint M \, dH. \tag{11.9}$$

This relation shows that eddy currents and resonance factors can be neglected. Because both the applied field and magnetization are time dependent and the field is sinusoidal, both the applied field and magnetization can be written in terms of field strength and frequency:

$$H(t) = H_a \cos(2\pi ft), \tag{11.10}$$

$$M(t) = H_a\left(\chi' \cos(2\pi ft) + \chi'' \sin(2\pi ft), \right. \tag{11.11}$$

where χ' and χ'' represent the in-phase and out-of-phase components of magnetic susceptibility, respectively. By solving and simplifying these equations, a final relation for the SAR is obtained:

$$\text{SAR} = \mu_0 \pi \chi_0 f H_0^2 \frac{2\pi ft}{1 + (2\pi ft)^2} \sim \left[\frac{w}{m^3}\right]. \tag{11.12}$$

The heat generation of magnetic nanoparticles is generally presented in units of W/g. The heat produced per unit volume can be calculated by the product of the SAR value and the concentration of nanoparticles [58]. When the heat reaches a specific area of infected tissues, the temperature above the therapeutic threshold of 42 °C can be managed for half an hour to kill cancer cells. Nanoparticle size has a significant influence on relaxation mechanisms and maximum heat observed at a particular radius according to the type of magnetic material. Figure 11.4 shows the size-dependent heating curves for Fe_3O_4 and γ-Fe_2O_3. The SAR peak position depends mainly on the anisotropy of the materials; however, the frequency, viscosity, and temperature also have a slight effect [58]. Maghemite nanoparticles have high SAR values at sizes around 11–12 nm. The size dependency suggests that polydispersity ultimately will be an important factor. A narrow size distribution will be more useful for hyperthermia than highly polydisperse fluids. Motoyama et al. [74] studied the SAR generation of magnetite nanoparticles of 13 different sizes under different alternating magnetic field conditions. They considered the nanoparticles according to their surface area. The particle size ranged from 10 to 120 nm. They observed that the two highest values of SAR between 12 and 190 W/g, for different frequencies and values increased by increasing the intensity of the field. Particles with a smaller specific area had a strong influence on the intensity of the field compared to larger particles.

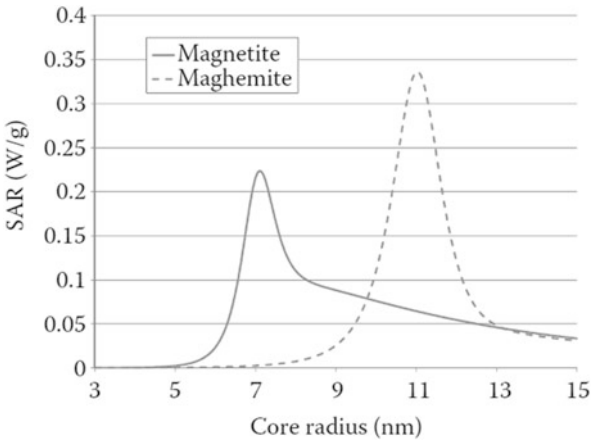

Fig. 11.4 Comparison of size-dependent SAR values for iron oxide (magnetite and maghemite) in water. Field strength, 10 kA/m; frequency 250 kHz [58] (Reproduced with permission from [58])

11.3 Magnetic Fluids for Hyperthermia

Owing to the notable heat loss in an AC magnetic field, a number of heat mediators have been established. Mediators are nanomaterials that have the ability to produce high heating power per particle in unit mass. Therefore, various types and shapes of magnetic nanoparticles have been investigated and used as a source of heat generation. These materials include metals such as Fe, Mn, Co, Ni, Zn, Gd, Mg, and their oxides; in particular, iron oxide–based nanomaterials have been explored extensively for their potential in hyperthermia [60, 75–78]. Superparamagnetic iron oxide nanoparticles have shown excellent properties for heat mediation. In addition, different ferrites, for example, $CoFe_2O_4$, $Li_{0.5}Fe_{2.5}O_4$, $NiFe_2O_4$, $ZnFe_2O_4$, $CuFe_2O_4$, and $MgFe_2O_4$, have also been considered for hyperthermia [79–84]. Zinc-rich ferrite nanoparticles 11 nm in size are capable of self-regulated magnetic heating in local glioma therapy [85]. Ferromagnetic composite nanoparticles, such as iron-doped gold [86], zinc manganese–doped iron oxides ($Zn_xMn_{1-x}Fe_3O_4$) [87], and zinc manganese gadolinium–doped iron oxides [87], have also been investigated as potential candidates for hyperthermia. However, iron oxide nanoparticles are the main priority of researchers owing to their lower toxicity, biocompatibility, and metabolization in the body [88]. Although the aforementioned nanomaterials show an overwhelming response to external AC magnetic fields, their stability under different conditions is also very critical.

11.3.1 Solvent Media

SAR values depend on the viscosity of the medium in which the nanoparticles are suspended. Heirgeist et al. [89] probed the heat generation capability of ferrofluids in molten and solidified gel. There was a considerable power loss in the liquid

phase compared to the solid phase. A more detailed study was performed by Fortin and coworkers [54] to distinguish the contribution from Brownian and Néel relaxation mechanisms. It was observed that with a more viscous medium (glycerol is 500 times more viscous than water), the contribution from Brownian relaxation fizzled out and the main contribution came from Néel relaxation, though Brownian mechanisms were prominent in the case of water for particle sizes above 9 nm (cobalt ferrite) and 17 nm (maghemite). The Néel contribution was frequency dependent. At a frequency of 1 MHz, the Néel contribution was highest for particle sizes of 7 nm (cobalt ferrite) and 14 nm (maghemite). However, there is still a need to explore the influence of viscosity on SAR values.

11.3.2 Anisotropy of Nanoparticles

Another important factor is growing nanoparticles with high anisotropy (controlled shape or monocrystalline). Nanoparticles have been studied in different size distributions as well as in different shapes (spherical [90], cubes [91], flowers [92]). Regular-shaped iron oxide (magnetite or maghemite), i.e., nanocubes, exhibit remarkably improved efficiency over their spherical counterparts [93]. Even iron oxide nanoflowers (20–25 nm) have better SLP values. Nanoflowers are actually multicore nanoparticles oriented in such a way as to produce a monocrystalline structure. This internal collective organization modifies their magnetic properties, which enhances their heating efficiency significantly [92] (Fig. 11.5).

11.3.3 Biological Environment

Usually hyperthermia studies are performed in biological environments (model medium, cell culture, or mice) that nanomaterials encounter when they go in vivo [95]. The high surface-to-volume ratio of nanoparticles increases the possibility of undergoing chemical and physical transformations owing to this biological microenvironment, which can affect the technologically relevant properties of nanomaterials [96, 97]. These transformations can lead to crystal dissolution and generate different ions. Such ions can be very toxic because they can induce hydroxyl radicals by a Fenton reaction that can damage DNA, proteins, and lipids in vivo [98, 99]. Different factors can modulate these transformations such as the functionalization of nanomaterials (organic/inorganic) and the nature of the material [100].

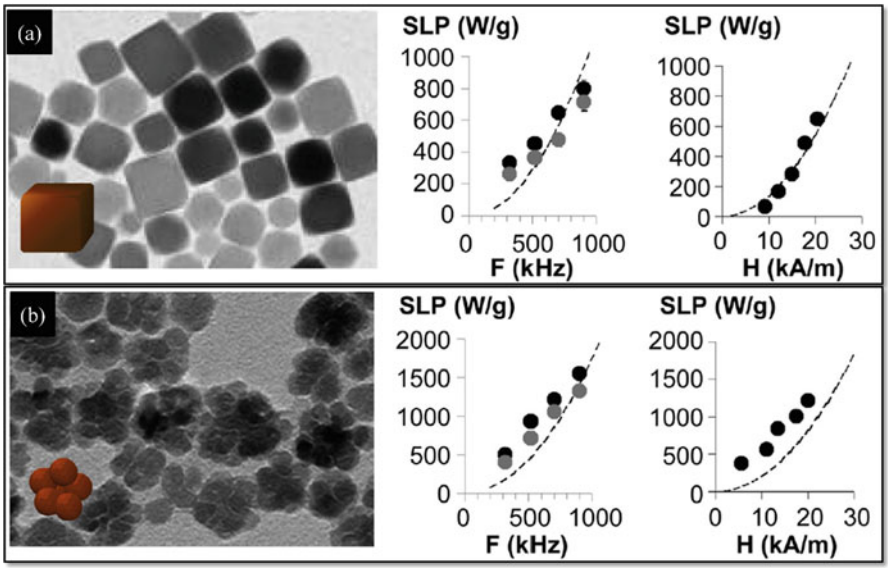

Fig. 11.5 TEM micrograph (*left*) and heating generation abilities [*right*, SLP (w/g) as a function of frequency and strength of applied magnetic field], iron oxide nanocubes with side face of approximately 18 nm. (**a**) Iron oxide nanoflowers approximately 25 nm in size. (**b**) SLPs were measured by making the fluids in water (*black circles*) and in glycerol (*gray circles*). The dotted lines indicate the poor agreement with linear response theory [94] (Reproduced with permission from [94])

11.3.4 Synthesis Protocols

The properties of nanomaterials largely depend on the synthesis protocols because magnetic properties can change with morphology and structure [101]. There is still a need to develop good synthesis methods to produce nanoparticles that have controlled sizes and shapes, have narrow distributions, and are free of crystal defects. The two major issues in the chemical methods are the formation of monodisperse nanostructures and the reproducibility of reactions. For controlled synthesis, nucleation should be separated from growth, and there should be no nucleation during the growth process [102]. By considering these conditions, various physical, chemical, and biological methods have evolved during the different research stages. Physical methods are mostly used in engineering and electronics, whereas chemical and biological protocols are used to produce nanomaterials for biomedical applications. These methods include coprecipitation [103], thermal decomposition [104], microemulsion [105], hydrothermal synthesis [106], polyols [107], sol-gels, combustion, and others. Each method has its own advantages and disadvantages that make it suitable for the synthesis of certain nanomaterials. Every protocol has a certain working solvent. For hyperthermia, we need nanoparticles' suspension in water, so the nanoparticles go through a ligand exchange process before they are made water dispersible [108].

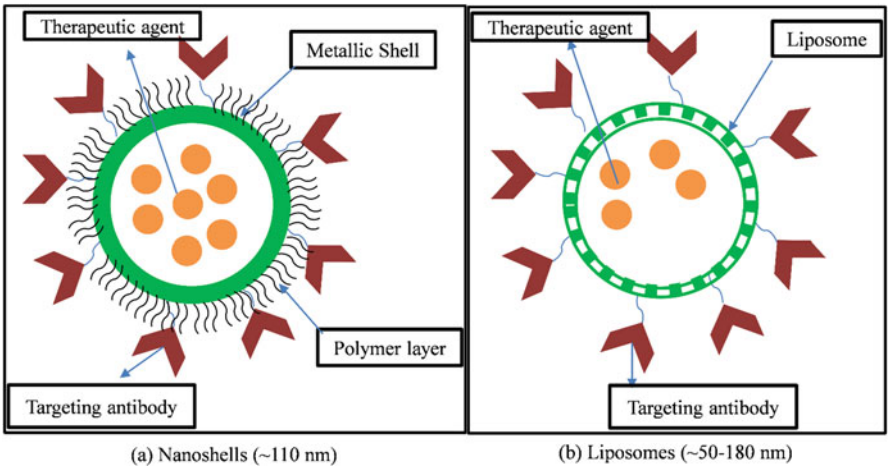

Fig. 11.6 Example of multifunctional nanocarriers for cancer treatment. A metal can be used to encapsulate the therapeutic nanoparticles followed by functionalization of biocompatible polymer and targeted biological antibodies. (**a**) Liposomes can also be used as carrier vehicles since they contain at least one lipid bilayer. (**b**) Reproduced with permission from [110]. Copyright (2009) American Chemical Society

11.3.5 Multifunctionality

The coupling of nanoparticles with other functional species (organic or inorganic materials) can further enhance their efficiency for heating [109]. Multifunctionality provides targeting, imaging, sensing, and therapeutic payloads simultaneously (Fig. 11.6) [110]. These multifunctional nanoparticles have significantly improved the diagnosis and treatment of prostate cancer [111]. Multifunctional nanoparticles for specific targeting as well as for optical tracking using a two-photon fluorescent probe have also been formulated. This type of nanoparticle has been adopted for the magneto-cytolysis of MCF-7 and UCI cancer cells by applying a DC magnetic field with additional optical tracking properties [112].

11.4 Biocompatibility

To develop nanomaterials for in vivo applications, nanoparticles must be acceptable to the body, in other words, nanoparticles should be biocompatible [39]. Because these nanomaterials are not a part of our body, bare nanoparticles can be rejected by macrophages very rapidly from the bloodstream prior to their use for a given application [113]. For example, dextran-coated Fe_3O_4 nanoparticles after IV administration in rats cleared very rapidly (half-life of 10 min) initially, then slowed down after some time (half-life of 92 min). During the initial 2 h, particles

spread throughout the whole body, including the liver and spleen. However, over time, the particles accumulated in the macrophages of the splenic marginal zone. The particles piled up in this region for 48 h, after which there was a decrease till day 25. Iron oxide stores in Kupffer cells of the liver result in slow accumulations, [114]. Iron oxide even persists for a long time in the body, we observed iron oxide–gold dimers in mice even after 1 year of their administration, which confirms their long stay in the body. Figure 11.7a–e shows the iron oxide–gold dimers present after 1 year in the spleen. The nanoparticles were injected intravenously. Although the iron oxide part of the dimers had been degraded, we observed gold particles as large aggregates, small chains, and separate particles (Fig. 11.7b) [115]. In the case of hyperthermia, an AC magnetic field cycle needs to be applied after some specified amount of time, and nanoparticles should stay inside the body at the target site for a longer period of time [45]. All these concerns demand biocompatible nanoparticles. It is usually believed that nanoparticles are eliminated from the body following therapy, which is not necessarily the case. Therefore, the toxicity of nanoparticles and the functionalization of materials are major concerns for developing nanoparticles as heating sources for hyperthermia [116]. In addition, it can use to prevent opsonization and the formation of protein corona on nanoparticle surfaces, when introduced into blood compartments. Therefore, nanoparticles should be characterized for their physicochemical and physiological properties to ensure a longer circulation time [117].

Nanoparticles are made biocompatible by their surface modifications, usually by applying a coat of biocompatible molecule, such as dextran, glucose, polyvinyl alcohol (PVA), or phospholipids [118]. This coating layer provides a channel between the nanoparticle and the target site on cells and it provides colloidal stability. The colloidal stability depends on the particle size, charge, and surface chemistry in order to avoid gravitational forces and steric and coulomb repulsions [119]. There are specific binding sites on the surface of cells that are usually targeted using antibodies such as folic acid. Antibodies have the tendency to bind to their corresponding antigens, which results in highly accurate cell labeling. The attachment of folic acid can increase the cytotoxicity against folate receptors, but it had a mild effect on A549 cells [120, 121]. Nanoparticles are usually coated by organic polymer layers, and inorganic coatings, such as silica and gold, have also been developed [122]. These inorganic coatings protect nanoparticles from the environment and provide additional properties of the coating material such as the plasmonic properties of gold. The thin gold layer it heated up itself under an alternating magnetic field during hyperthermia process [123]. In fact, gold-coated iron oxide produces more heat compared to iron oxide alone [124]. Javed et al. [125] investigated the influence of gold layers with different nominal thickness (3, 5, and 7 nm) on the degradation mechanisms of iron oxide nanoparticles (Fig. 11.8a–c). A layer 3 nm thick that forms 3D clusters of gold on nanoparticles was not as efficient as a later 7 nm thick to control degradation. A continuous layer forms with a nominal thickness of 7 nm and serves as an effective shield against surface corrosion. The loss of the iron contents of single nanoparticles was followed by the use of single-particle EDX analysis in scanning transmission electron microscopy (STEM) mode.

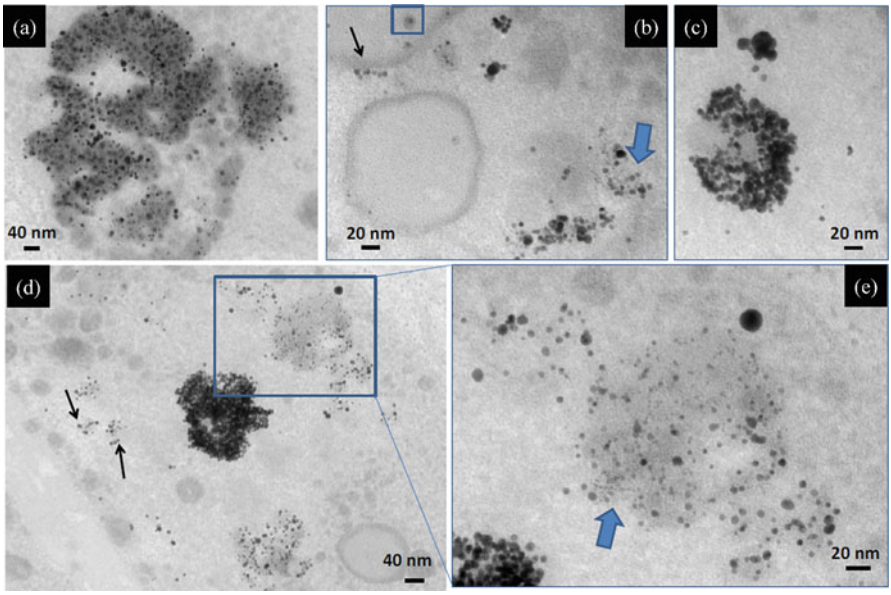

Fig. 11.7 (**a–e**) Amphiphlic polymer–coated iron oxide–gold dimers in spleen after 1 year following intravenous (IV) administration. Isolated heterostructures can still be observed (*blue box*) (**b**), but the majority are a gold moiety of the heterostructure assembled as large aggregates (**c**), or gold chains (*black arrows*); (**d**) degraded gold entities can also be observed in (**e**) [115] (Reproduced with permission from [115]. Copyright (2015) American Chemical Society)

There was a rapid loss of iron with respect to gold in a layer of gold with a nominal thickness of 3 nm, whereas there was almost no loss in the case of the 7 nm gold layer (Fig. 11.8d).

Physicochemical properties of nanoparticles, such as their size, shape, composition, charge, and surface chemistry, can play a significant role in the pharmacokinetics of nanoparticles [126]. These factors administer the flow of nanoparticles in different parts of an organism and also control circulation time, nanoparticle intracellular trafficking, drug release, and toxicity [127]. Nanoparticles less than 100 nm in size have a longer circulation time. But the size of nanoparticles can also influence the surface pressure and adhesion forces [128]. Nanoparticles have extraordinary interfacial chemical and physical reactivity owing to a high surface area. Generally, kidneys can eliminate nanoparticles less than 6 nm in size more rapidly compared to larger ones functionalized by, for example, polymers and lipids [129]. Larger particles are usually stored in the spleen and liver and more specifically in the lysosomes of macrophages cells, where they are processed by the acidic environment, different enzymes, and proteins [116]. The factors related to biocompatibility are discussed briefly in this section.

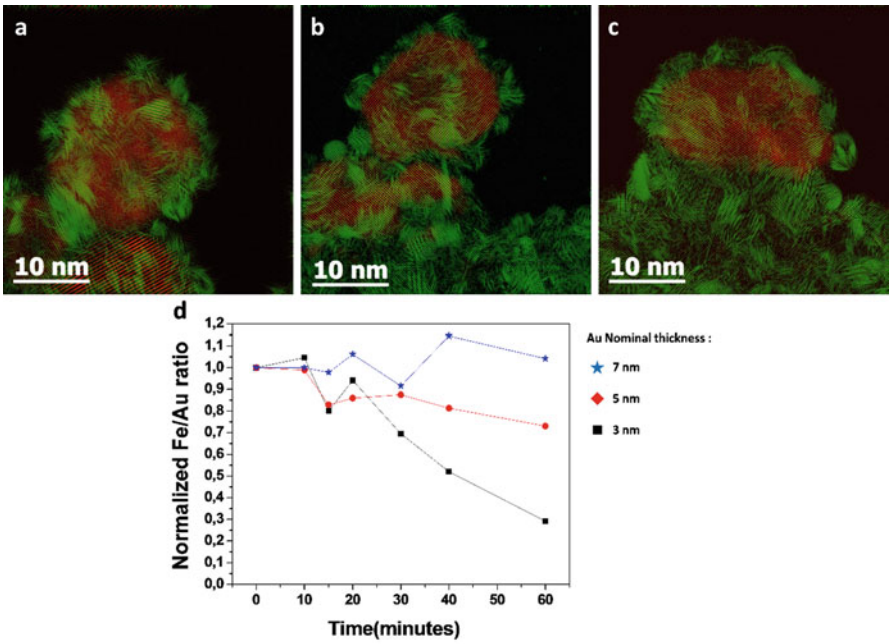

Fig. 11.8 Low-pass-filtered, high-resolution images of nanoparticles covered by layers of gold with nominal thicknesses of (**a**) 3 nm, (**b**) 5 nm, and (**c**) 7 nm. (**d**) Follow up of iron loss by chemical composition analysis in STEM mode [125] (Reproduced with permission from [125])

11.4.1 Opsonization

Interactions of nanoparticles with bound ligands and cellular receptors are governed by the morphology of the nanoparticles and the density of the polymer on the surface. The functionalization of nanoparticles helps to keep them for a longer time in the body and limits their nonspecific distribution [130]. Intravenous administration has a drawback in the form of rapid clearance of nanoparticles from the bloodstream as a result of the opsonization process. This is the process of attaching any blood serum component, which can help to identify phagocytes. Macrophages such as Kupffer cells and others in the liver cannot precisely recognize nanoparticles themselves but instead use opsonized proteins attached to the surface of the nanoparticles. The most common opsonized proteins are C3, C4, C5, and immunoglobuline. The binding and clearance of nanoparticles by nonphagocytic cells can also be influenced by the adsorption of blood plasma proteins. For instance, after binding of proteins such as C3b, C4b, or iC3b, nanoparticles can then interact with platelets and erythrocytes [131].

To overcome this problem, nanoparticles are usually coated with a variety of polymer materials that can produce a hydrophilic steric barrier [132]. This manipulated steric boundary should oppose surface adsorption processes and as

a result reduce the chances of nanoparticles' clearance by macrophages in the blood stream. This also increases the possibility of nanoparticles' targeting specific nonmacrophage elements. The pharmacokinetics of these modified nanoparticles depends on the density of the polymer materials [118]. Al-Hanbali et al. [133] showed that the attachment of at least 11,500 poloxamine molecules was required on the surface of 230 nm polystyrene nanoparticles to overcome opsonization and increase the circulation time compared to bare nanoparticles. Under these circumstances, a layer of polyethylene oxide with the appropriate density can form on the surface of nanoparticles. It was assumed that polymeric chains have a brushlike configuration to reduce prompt complement activation and increase circulation time. A thin polymer layer or low surface density can speed complement activation and, as a result, shorten circulation time. Thus, a higher polymer density on the surface of nanoparticles allows for steric stabilization, limits protein absorption, and increases circulation time.

11.4.2 Surface Charge

The surface charge of nanoparticles also plays a crucial role in subsequent intracellular processing events. Therefore, the realization of interactions between cells and nanoparticles is key to determining the uptake and localization of nanoparticles [134]. There is faster uptake in vivo when nanoparticles have a positive surface charge versus a neutral or negative charge owing to the negative charge on the surface of cell membranes. This is done by the electrostatic attractions between two surfaces. However, positively charged particles clear more quickly from the blood and cause hemolysis and platelet aggregation. Thus a smaller size, neutral or negative zeta potential, and PEG coating of the particle surface are highly influential factors for increased circulation time in the blood after IV administration [135].

11.4.3 Protein Corona

Another important factor is the coating of a protein layer on the nanoparticle in biological matrices, the so-called protein corona. There are 1000 different proteins with different concentrations present in the blood plasma. Consequently, upon injection of nanoparticles into the body, different biological entities try to adsorb onto nanoparticles' surface [136]. However, proteins present in higher concentrations adsorb first, followed by the replacement of high-affinity proteins. They can transform and protect the surface of xenobiotic particles and control their biological properties and, consequently, their behavior in the micro environment. Physicochemical properties, type of physiological environment, and exposure time are critical factors governing the structure and composition of corona formation [137]. The protein corona confers a new biological identity to nanoparticles, which

controls physiological responses such as aggregation, cellular uptake, circulation time, kinetics, transportation, accumulation, and toxicity [138].

The formation of a protein corona depends on the binding affinities between proteins and nanoparticles and protein–protein interactions. Proteins with high affinity are bound more tightly, and a corona so formed is called a hard corona. These proteins cannot desorb easily from the surface of nanoparticles. Proteins that adsorb with low affinity form a soft corona. These are loosely bound proteins. The concern raised by the adsorption of proteins or protein corona formation has been explored very little because it is a very complex situation when nanoparticles are administered directly into a living organism. Additionally, there is no general protein corona for all nanomaterials; in fact, protein corona formation is distinct for the different nanomaterials and there are many dependent factors [139].

11.4.4 Toxicity

The toxicity of nanoparticles and functionalized polymers is usually determined by many factors, such as dose rate, composition, administration method, biodegradability, surface chemistry, shape, and many more. An understanding of animals' and nanomaterials' toxicity profiles is necessary to guarantee their safe use [140]. It is usually believed that nanoparticles are more toxic than larger particles of the same chemical composition and that toxicity is inversely proportional to particle size [141]. Surface modification of nanoparticles is a vital tool in reducing toxicological effects. In addition, during oral or dermal exposure or inhalation, nanoparticles can accumulate in the lungs and may absorb across the gastrointestinal tract. A common method of evaluating in vitro toxicity is by the use of fluorescent dyes to determine cell death by necrosis and apoptosis. Cell death because of injury is called necrosis and is usually identified by membrane breakage and discharging to other cell surroundings, which results in an immune response, whereas apoptosis is systematic cell death where cells retain their membrane intact till the last stage, apoptosis. Then the cell constituents transform into amino acids and nucleotides that can be recycled and used again by nearby cells. Superparamagnetic iron oxide nanoparticles can activate apoptosis itself in cells; consequently, necrosis cannot be used to measure this action in the early stages in vitro and can only be useful in the late stages when the cell membrane disintegrates [142]. Therefore, it is necessary to measure both necrosis and apoptosis simultaneously. More specifically regarding the toxicity of iron oxide nanoparticles in vivo, after infiltrating into cells, these nanoparticles reside in endosomes/lysosomes and then, after processing, are released into the cytoplasm and sequestered in ferritin proteins. It has been observed that after inhalation, they accumulate largely in the liver and spleen and in small quantities in the lungs and brain. Their toxic effects appear in the form of cell lysis, inflammation, and a reduction in cell viability. Naqvi and coworkers [143] observed that a low dose (20–200 μg/mL, exposure time 2 h) of iron oxide (30 nm) caused more cell toxicity than a high dose (300–500 μg/mL, exposure time 6 h).

However, there was 20% less cell death when dextran-functionalized iron oxide nanoparticles (100–150 nm, 1 mg/mL) were incubated for 7 days in human macrophages. It is commonly believed that cell death is caused by the generation of reactive oxygen species as a result of Fenton reactions. These produce oxide and hydroxyl ions that can stimulate DNA damage and the oxidative degradation of lipids by extracting electrons.

In brief, for hyperthermia, nanoparticles should be water dispersible, biocompatible, smaller in size, negatively or neutrally charged, and nontoxic. However, there are still a few limitations on the efficient delivery of nanoparticles at target sites. An embolus can form in the blood vessels owing to the aggregation of nanocarriers. Second, complications can arise as a result of the focus on nanoparticles from animal models because of the larger gap that exists between intended sites and magnets in such models.

11.5 Measurement Systems

Although much work has been done on magnetic hyperthermia based on parameter control (e.g., size, shape, distribution) to improve the heating capabilities of nanoparticles, few sophisticated systems have been made available on the market for measuring specific loss power. Most systems designed for experiments are built by different research groups. They use these homemade systems to measure heat loss in the form of nanoparticle fluid and for experimentation in mice. On the other hand, some commercial devices are the magnetherm by nanoTherics (Newcastle under Lyme, UK), the DM100 series from nB nanoScale Biomagnetics (Zaragoza, Spain), EASYHEAT from Ambrell (Scottsville, NY, USA), or the MGF1000 in vitro magnetic field generator by the European Institute of Science AB (Lund, Sweden). These commercial devices have offered a range of variations in AC magnetic fields, i.e. frequency, amplitude, or flux density. These devices provide reliable and reproducible results for nanoparticle heating.

Regarding the homemade systems for hyperthermia that are being used by different research groups, these devices are usually based on simple resonant RLC circuits to create an AC magnetic field with a copper coil [54, 144–146]. Researchers all over the world are using locally made devices applying the aforementioned idea to make certain modifications, for example, changing the coil diameter, number of turns, or cooling agents. Here we will discuss a few systems that have been reported in the literature.

Fortin et al. [54] tried to distinguish the contributions of Néel and Brownian relaxation mechanisms with respect to specific loss of power. They used a device with a copper coil 16 mm in diameter having a frequency range of 300 kHz to 1.1 MHz and an amplitude up to 27 kA/m. Variations in frequency and amplitude are made using a variable capacitor (10 pF–4 nF) in series and self-inductance of 25 μH. To avoid heat generated by the coil, continuous circulation of nonane was maintained during measurements. A small sample volume of 300 μL was

used so that a homogenous magnetic field could be established on the particles A fluorooptic thermometer was used for temperature measurements. The researchers presented quantitative magnetic hyperthermia data matching with theoretical predictions considering relevant parameters such as size, materials, solvent, and field characteristics. Ma and coworkers [145] investigated the size dependence of iron oxide nanoparticles on heat generation. They used a three-loop copper coil with a frequency of 80 kHz and amplitude of 32.5 kA/m for calorimetric measurements. In addition, they used an asbestos sleeve to avoid excessive heat produced by the copper coil. An alcohol thermometer was used to measure the heat generated by the particles. Magnetic fluids were prepared in water at a concentration of 2 g/L. The maximum SAR value (75.6 W/[g of Fe]) was observed at a particle size of 46 nm. Further increases in the particle size showed a low heat generation efficiency. Sadat et al. [147] used a 10-turn coil that was 84 mm long and had an inner diameter of 39 mm. A sinusoidal 13.56 MHz frequency signal was generated by a radio frequency generator. Cold water circulation was used to cool down the coil from the high AC current. A fiber optic temperature sensor (FOT-L-SD) was connected to detect the temperature signal. The researchers observed high SAR values for uncoated nanoparticles compared to coated or confined nanoparticles in another material such as iron oxide in a Si shell. They attributed the high absorption rate in uncoated nanoparticles to Néel relaxation and hysteresis losses whereas dipole–dipole interactions caused lower SAR values. The schematics of the system are shown in Fig. 11.9a–c.

A safe and effective external magnetic field is required to stimulate implanted nanoparticles. Major issues for designing such a system are field uniformity, patient convenience, and proficiency at working on the entire body. Multiturn inductive coils, discussed earlier, satisfy the requirements for small animal preclinical trails [148].

Clinical trials: Although the European Union (EU) approved several iron oxide nanoparticles, the US Food and Drug Administration (FDA) has endorsed three nanoparticles (Feraheme, polyglucose coated superparamagnetic iron oxide nanoparticles, dextran-coated iron oxide (Feridex), and silicon-coated iron oxide (GastroMark). Feridex and GastroMark were later withdrawn over concerns regarding their long-term toxicity in vivo [149]. Nanoparticle-based induction hyperthermia (thermal ablation) was first investigated by Kida et al. [150] for brain tumor treatment in 1990. Fe-Pt alloy particles were studied in connection with metastatic brain tumor along with radiation therapy. The particles were of millimeter size (15–20 mm long with a diameter of 1.8 mm). The temperature of the tissues raised up to 46 °C during treatment. In two cases, there was complete destruction of tumor (complete response), whereas in one case, a 50% tumor volume reduction occurred (partial response). In another study, 23 patients with brain tumor were treated by the aforementioned method and the response rate was 34.8% on average [151]. However, there are few studies on intracranial tumor therapy, apparently because of complications such as that it required infiltration through

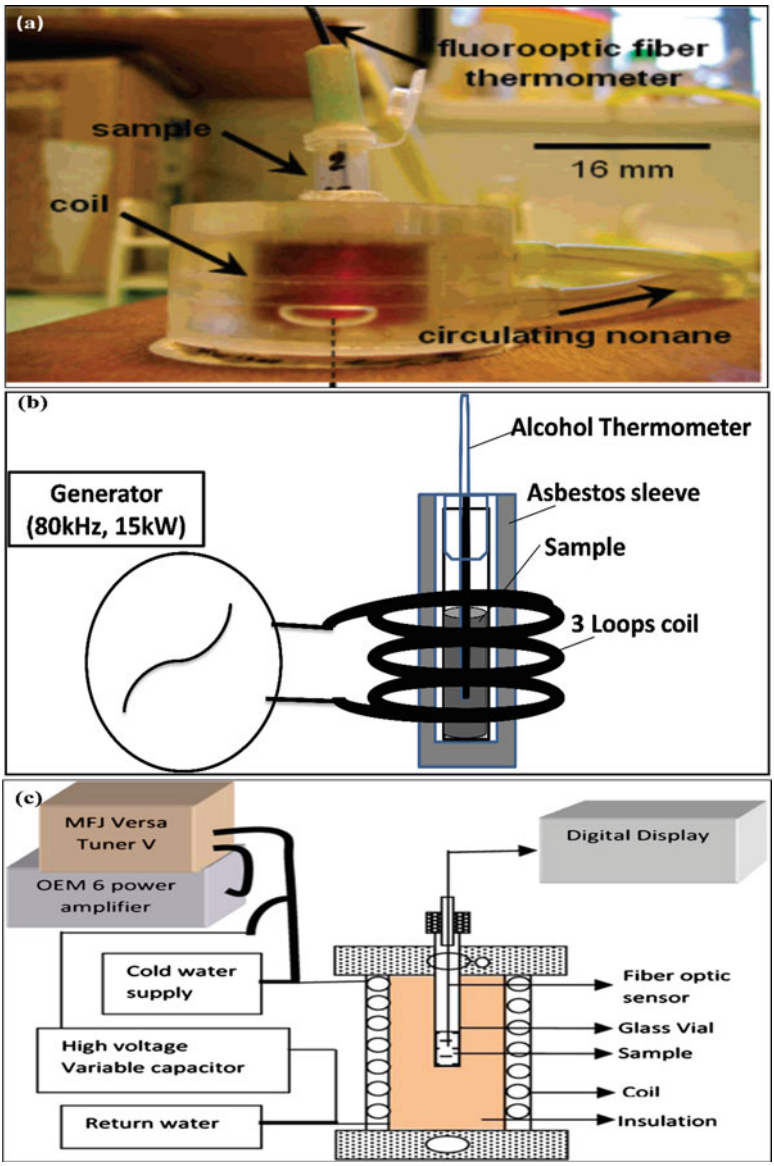

Fig. 11.9 Homemade systems used by different research groups: (**a**) [54]; (**b**) [145]; (**c**) [147] (Reproduced with permission from [54, 145, 147]. Copyright (2007)American Chemical Society)

the skull, which can cause significant trauma. Another implication is the access of nanoparticles to the tumor site by passing through healthy brain tissue, which can also be critical. These limitations hamper the application of induction hyperthermia in other brain tumor applications [152].

Hyperthermia based on superparamagnetic nanoparticles has also been applied in combination with other therapies. Aminosilane-coated iron oxide nanoparticles 12 nm in size were administered intratumorally following tumor resection. Treatment by radiotherapy and 100 kHz variable magnetic field combined was compared with traditional radiotherapy alone. Patient survival was prolonged from 13.4 months to 23.2 months and the tumor revival time was also enhanced [153, 154]. Patient rehabilitation was evaluated by MRI and CT overlay (Fig. 11.10a–f). Phase 1 trails showed no systematic toxicities upon intratumoral administration. However, patients felt some discomfort owing to the rise in temperature around the tumor to 44 °C [156]. Magnetic hyperthermia coupled with chemotherapy generated collective malignant cell death.

Methoterxate-functionalized iron oxide nanoparticles (10 nm) were activated by a 300 kHz, 130 Gs alternating magnetic field. The combined therapy produced greater apoptotic response [157]. A phase II study was performed in recurrent glioblastoma. The study revealed the utility of integrating magnetic nanoparticle–based hyperthermia immediately before or after radiotherapy.

11.6 Conclusions

The generation of localized heat by magnetic nanoparticles and an alternating magnetic field in the area surrounding malignant cells has the potential to kill cancer cells. The method can be employed alone or coupled with radio- or chemotherapy to enhance its efficacy. Despite all the advances, proper technology development remains immature. A few crucial enhancements must be made to improve the clinical viability of magnetic nanoparticle–based hyperthermia:

1. The functionalization of nanoparticles is required for biocompatibility, biological recognition, toxicity reduction, and nanoparticle life cycle regulation.
2. Although iron oxide nanoparticles show reasonably high SAR values, improvements can be made by higher magnetic moment nanoparticles. This includes iron–iron oxide composites, magnetosomes, and iron–cobalt core shell structures.
3. By incorporating magnetic nanoparticles into multifunctional systems, their therapeutic, imaging, and diagnostic capabilities can be improved.
4. An alternating magnetic field should selectively heat the nanoparticles, engulfing the tumors and avoiding the accumulation of nanoparticles in other regions, for example, the liver or kidney. In addition, alternating waves can deliver enhanced power input.
5. Nanoparticles should absorb sufficient power to reach cytolytic tumor temperatures but maintain the surrounding tissue temperature at manageable levels.

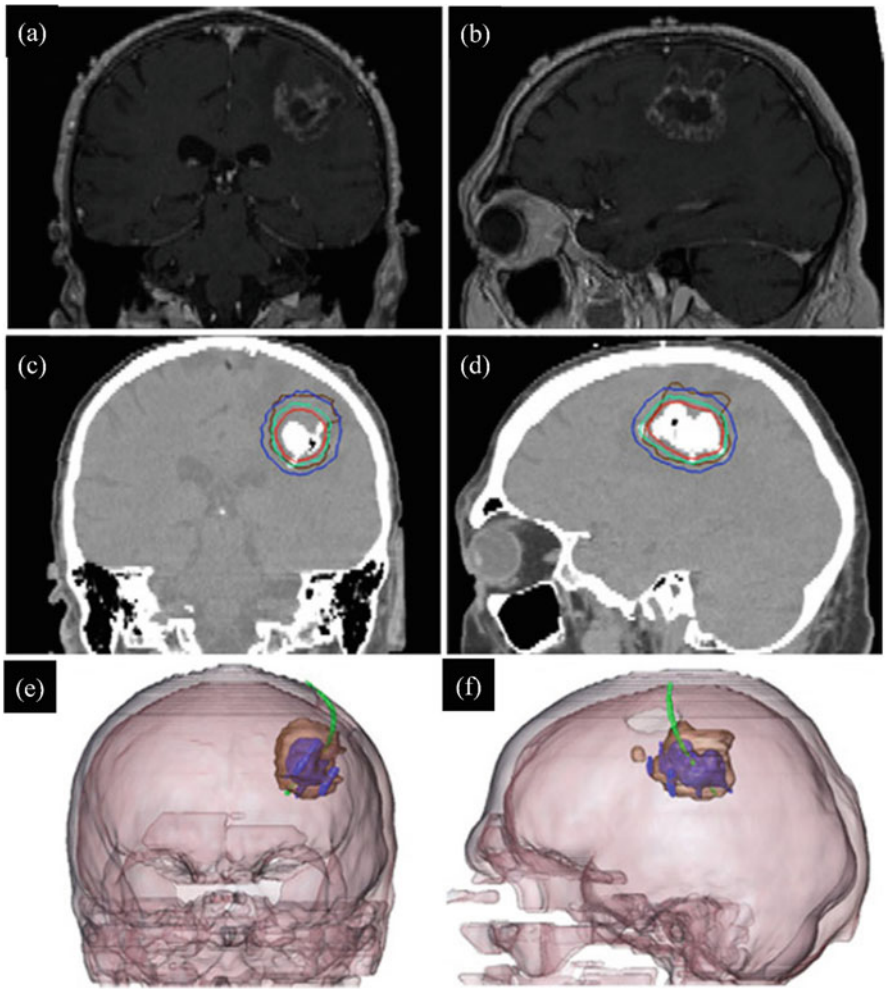

Fig. 11.10 Glioblastoma recurrence. (**a**, **b**) Control brain MRI. (**c**, **d**) Magnetic nanoparticle deposits in brains are shown in the form of hyperdense areas (CT image). Calculated treatment temperatures are represented in the form of isothermal lines, minimum 40 °C (*blue*), maximum 50 °C (*red*). The *brown line* shows the tumor area. (**e**, **f**) 3D reconstruction of merged MRI and CT [155] (Reproduced with permission from [155])

6. Noninvasive in vivo tracking of nanoparticles is necessary to confirm that nanoparticles reside at the target site.
7. The efficacy of the method should be accurately evaluated so that concerns related to dose rate, temperature, exposure time, administration procedure, and repetition of treatments can be addressed.

References

1. Caster JM, Patel AN, Zhang T, Wang A (2016) Investigational nanomedicines in 2016: a review of nanotherapeutics currently undergoing clinical trials. Wiley Interdisciplinary Reviews: Nanomedicine and Nanobiotechnology (In press)
2. Del Burgo LS, Hernãindez RM, Orive G, Pedraz JL (2014) Nanotherapeutic approaches for brain cancer management. Nanomedicine: Nanotechnology, Biology and Medicine 10: e905–e919
3. De Jong WH, Borm PJA (2008) Drug delivery and nanoparticles: applications and hazards. Int J Nanomedicine 3:133
4. Deatsch AE, Evans BA (2014) Heating efficiency in magnetic nanoparticle hyperthermia. J. Magn. Magn. Mater. 354:163–172
5. Deraco M, Kusamura S, Virzì S, Puccio F, Macrì A, Famulari C, Solazzo M, Bonomi S, Iusco DR, Baratti D (2011) Cytoreductive surgery and hyperthermic intraperitoneal chemotherapy as upfront therapy for advanced epithelial ovarian cancer: multi-institutional phase-II trial. Gynecol Oncol 122:215–220
6. Gobbo OL, Sjaastad K, Radomski MW, Volkov Y, Prina-Mello A (2015) Magnetic nanoparticles in cancer theranostics. Theranostics 5:1249
7. Casanovas O (2012) Cancer: Limitations of therapies exposed. Nature 484:44–46
8. Garattini S, Bertele V (2002) Efficacy, safety, and cost of new anticancer drugs. Br Med J 325:269
9. Jain RK (2001) Normalizing tumor vasculature with anti-angiogenic therapy: A new paradigm for combination therapy. Nat Med 7:987–989
10. Van der Seldt AA, Lubberink M, Bahce I, Walraven M, de Boer MP, Greuter HN, Hendrikse NH, Eriksson J, Windhorst AD, Postmus PE, Verheul HM, Serné EH, Lammertsma AA, Smit EF (2012) Rapid decrease in delivery of chemotherapy to tumors after Anti-VEGF therapy: Implications for scheduling of anti-angiogenic drugs. Cancer Cell 21:82–91
11. Sardari D, Verga N (2011) Cancer treatment with hyperthermia. In: Özdemir Ö (ed) Current cancer treatment-novel beyond conventional approaches. InTech, Istanbul, pp 455–475
12. Bush W (1886) Uber den Finfluss wetchen heftigere Eryspelen zuweilen auf organlsierte Neubildungen dusuben. Verh Natruch Preuss Rhein Westphal 23:28–30
13. Jordan A, Scholz R, Wust P, Fähling H, Felix R (1999) Magnetic fluid hyperthermia (MFH): Cancer treatment with AC magnetic field induced excitation of biocompatible superparamagnetic nanoparticles. J. Magn. Magn. Mater. 201:413–419
14. Banobre-López M, Teijeiro A, Rivas J (2013) Magnetic nanoparticle-based hyperthermia for cancer treatment. Rep Practical Oncol Radiother 18:397–400
15. Chichel A, Skowronek J, Kubaszewska M, Kanikowski M (2007) Hyperthermia description of a method and a review of clinical applications. Rep Practical Oncol Radiother 12:267–275
16. Salunkhe AB, Khot VM, Pawar SH (2014) Magnetic hyperthermia with magnetic nanoparticles: a status review. Curr Top Med Chem 14:572–594
17. Wust P, Nadobny J, Fahling H, Riess H, Koch K, John W, Felix R (1991) Determinant factors and disturbances in controlling power distribution patterns by the hyperthermia-ring system BSD-2000. 2. Measuring techniques and analysis. Strahlenther Onkol 167:172–180
18. Andreu I, Natividad E (2013) Accuracy of available methods for quantifying the heat power generation of nanoparticles for magnetic hyperthermia. Int J Hyperthermia 29:739–751
19. Khushrushahi SR (2005) A quantitative design and analysis of magnetic nanoparticle heating systems. Massachusetts Institute of Technology, Cambridge, MA
20. Presman A (2013) Electromagnetic fields and life. Springer, Berlin
21. Cavaliere R, Giogatto BC, Giovanella BC (1967) Selective heat sensitivity of cancer cells. Cancer 20:1351–1381
22. Levine EM, Robbins EB (1970) Differential temperature sensitivity of normal and cancer cells in culture. J Cell Physiol 76:373–379

23. Diederich CJ (2005) Thermal ablation and high-temperature thermal therapy: overview of technology and clinical implementation. Int J Hyperthermia 21:745–753
24. Gneveckow U, Jordan A, Scholz R, Brüss V, Waldöfner N, Ricke J, Feussner A, Hildebrandt B, Rau B, Wust P (2004) Description and characterization of the novel hyperthermia- and thermoablation-system MFH 300F for clinical magnetic fluid hyperthermia. Med Phys 31:1444–1451
25. Dutz S, Hergt R (2013) Magnetic nanoparticle heating and heat transfer on a microscale: basic principles, realities and physical limitations of hyperthermia for tumour therapy. Int J Hyperthermia 29:790–800
26. Valdagni R, Amichetti M (1994) Report of long-term follow-up in a randomized trial comparing radiation therapy and radiation therapy plus hyperthermia to metastatic lymphnodes in stage IV head and neck patients. Int J Radiat Oncol Biol Phys 28:163–169
27. Abdeen S, Praseetha PK (2013) Diagnostics and treatment of metastatic cancers with magnetic nanoparticles. J Nanomedicine Biosci Discov 2013
28. Falk MH, Issels RD (2001) Hyperthermia in oncology. Int J Hyperthermia 17:1–18
29. Jia D, Liu J (2010) Current devices for high-performance whole-body hyperthermia therapy. Expert Rev Med Devices 7:407–423
30. Kim DH, Lee SH, Im KH, Kim KN, Kim KM, Shim IB, Lee MH, Lee YK (2006) Surface-modified magnetite nanoparticles for hyperthermia: Preparation, characterization, and cytotoxicity studies. Curr Appl Phys 6:e242–e246
31. Gilchrist RK, Medal R, Shorey WD, Hanselman RC, Parrott JC, Taylor CB (1957) Selective inductive heating of lymph nodes. Ann Surg 146:596
32. Bai L-Z, Zhao D-L, Xu Y, Zhang J-M, Gao Y-L, Zhao L-Y, Tang J-T (2012) Inductive heating property of graphene oxide-Fe_3O_4 nanoparticles hybrid in an AC magnetic field for localized hyperthermia. Mater Lett 68:399–401
33. Behdadfar B, Kermanpur A, Sadeghi-Aliabadi H, Del Puerto Morales M, Mozaffari M (2012) Synthesis of aqueous ferrofluids of Zn x Fe_3O_4 nanoparticles by citric acid assisted hydrothermal-reduction route for magnetic hyperthermia applications. J. Magn. Magn. Mater. 324:2211–2217
34. Cantillon MP, Wald LL, Zahn M, Adalsteinsson E (2010) Proposing magnetic nanoparticle hyperthermia in low field MRI. Concepts in Magnetic Resonance Part A 36:36–47
35. Fathi Karkan S, Mohammadhosseini M, Panahi Y, Milani M, Zarghami N, Akbarzadeh A, Abasi E, Hosseini A, Davaran S (2016) Magnetic nanoparticles in cancer diagnosis and treatment: a review. Artif Cells Nanomed Biotechnol:1–5
36. Giustini AJ, Petryk AA, Cassim SM, Tate JA, Baker I, Hoopes PI (2010) Magnetic nanoparticle hyperthermia in cancer treatment. Nano Life 1:17–32
37. Goya GF, Grazu V, Ibarra MR (2008) Magnetic nanoparticles for cancer therapy. Current Nanoscience 4:1–16
38. Ito A, Shinkai M, Honda H, Kobayashi T (2005) Medical application of functionalized magnetic nanoparticles. J Biosci Bioeng 100:1–11
39. Pankhurst QA, Connolly J, Jones SK, Dobson JJ (2003) Applications of magnetic nanoparticles in biomedicine. J Phys D Appl Phys 36:R167
40. Choi H, Choi SR, Zhou R, Kung HF, Chen IW (2004) Iron oxide nanoparticles as magnetic resonance contrast agent for tumor imaging via folate receptor-targeted delivery. Acad Radiol 11:996–1004
41. Peng X-H, Qian X, Mao H, Wang AY, Chen ZG, Nie S, Shin DM (2008) Targeted magnetic iron oxide nanoparticles for tumor imaging and therapy. Int J Nanomedicine 3:311–321
42. Jain TK, Richey J, Strand M, Leslie-Pelecky DL, Flask CA, Labhasetwar V (2008) Magnetic nanoparticles with dual functional properties: drug delivery and magnetic resonance imaging. Biomaterials 29:4012–4021
43. Liu X, Chen Y, Li H, Huang N, Jin Q, Ren K, Ji J (2013) Enhanced retention and cellular uptake of nanoparticles in tumors by controlling their aggregation behavior. ACS Nano 7:6244–6257

44. Alonso J, Khurshid H, Devkota J, Nemati Z, Khadka NK, Srikanth H, Pan J, Phan M-H (2016) Superparamagnetic nanoparticles encapsulated in lipid vesicles for advanced magnetic hyperthermia and biodetection. J Appl Phys 119:083904
45. Cervadoro A, Giverso C, Pande R, Sarangi S, Preziosi L, Wosik J, Brazdeikis A, Decuzzi P (2013) Design maps for the hyperthermic treatment of tumors with superparamagnetic nanoparticles. PLoS One 8:e57332
46. Haring M, Schiller J, Mayr J, Grijalvo S, Eritja R, Díaz DD (2015) Magnetic gel composites for hyperthermia cancer therapy. Gels 1:135–161
47. Hoopes PJ, Petryk AA, Gimi B, Giustini AJ, Weaver JB, Bischof J, Chamberlain R, Garwood M (2012) In vivo imaging and quantification of iron oxide nanoparticle uptake and biodistribution. In: SPIE Medical Imaging. International Society for Optics and Photonics, p 83170R-83170R-83179.
48. Stelter L, Pinkernelle JG, Michel R, Schwartlander R, Raschzok N, Morgul MH, Koch M, Denecke T, Ruf J, Baumler H (2010) Modification of aminosilanized superparamagnetic nanoparticles: feasibility of multimodal detection using 3 T MRI, small animal PET, and fluorescence imaging. Mol Imaging Biol 12:25–34
49. Wust P, Gneveckow U, Johannsen M, Böhmer D, Henkel T, Kahmann F, Sehouli J, Felix R (2006) Magnetic nanoparticles for interstitial thermotherapyâ€feasibility, tolerance and achieved temperatures. Int J Hyperthermia 22:673–685
50. Pöttler M, Staicu A, Zaloga J, Unterweger H, Weigel B, Schreiber E, Hofmann S, Wiest I, Jeschke U, Alexiou C (2015) Genotoxicity of superparamagnetic iron oxide nanoparticles in granulosa cells. Int J Mol Sci 16:26280–26290
51. Ahmed M, De Rosales RT, Douek M (2013) Preclinical studies of the role of iron oxide magnetic nanoparticles for nonpalpable lesion localization in breast cancer. J Surg Res 185:27–35
52. Sadhukha T, Wiedmann TS, Panyam J (2013) Inhalable magnetic nanoparticles for targeted hyperthermia in lung cancer therapy. Biomaterials 34:5163–5171
53. Taratula O, Dani RK, Schumann C, Xu H, Wang A, Song H, Dhagat P, Taratula O (2013) Multifunctional nanomedicine platform for concurrent delivery of chemotherapeutic drugs and mild hyperthermia to ovarian cancer cells. Int J Pharm 458:169–180
54. Fortin J-P, Wilhelm C, Servais J, Ménager C, Bacri J-C, Gazeau F (2007) Size-sorted anionic iron oxide nanomagnets as colloidal mediators for magnetic hyperthermia. J Am Chem Soc 129:2628–2635
55. Shreshtha PP, Mohite SS, Jadhav MGK (2015) Review on thermal seeds in magnetic hyperthermia therapy. IJITR 3:2283–2287
56. Hergt R, Andra W, D'ambly CG, Hilger I, Kaiser WA, Richter U, Schmidt HG (1998) Physical limits of hyperthermia using magnetite fine particles. IEEE Trans Magn 34:3745–3754
57. Ramprasad R, Zurcher P, Petras M, Miller M, Renaud P (2004) Magnetic properties of metallic ferromagnetic nanoparticle composites. J Appl Phys 96:519–529
58. Rosensweig RE (2002) Heating magnetic fluid with alternating magnetic field. J. Magn. Magn. Mater. 252:370–374
59. Andra W, Nowak H (2007) Magnetism in medicine: a handbook. Wiley, New York
60. Gubin SP, Koksharov YA, Khomutov GB, Yurkov GVE (2005) Magnetic nanoparticles: preparation, structure and properties. Russ Chem Rev 74:489–520
61. Burrows F, Parker C, Evans RFL, Hancock Y, Hovorka O, Chantrell RW (2010) Energy losses in interacting fine-particle magnetic composites. J Phys D Appl Phys 43:474010
62. Dennis CL, Jackson AJ, Borchers JA, Hoopes PJ, Strawbridge R, Foreman AR, Van Lierop J, Grüttner C, Ivkov R (2009) Nearly complete regression of tumors via collective behavior of magnetic nanoparticles in hyperthermia. Nanotechnology 20:395103
63. Hergt R, Dutz S, Müller R, Zeisberger M (2006) Magnetic particle hyperthermia: nanoparticle magnetism and materials development for cancer therapy. J Phys Condens Matter 18:S2919
64. Hergt R, Dutz S, Röder M (2008) Effects of size distribution on hysteresis losses of magnetic nanoparticles for hyperthermia. J Phys Condens Matter 20:385214

65. Gittleman JI, Abeles B, Bozowski S (1974) Superparamagnetism and relaxation effects in granular Ni-SiO_2 and Ni-Al_2O_3 films. Phys Rev B 9:3891
66. Jordan A, Wust P, Fähling H, John W, Hinz A, Felix R (2009) Inductive heating of ferrimagnetic particles and magnetic fluids: physical evaluation of their potential for hyperthermia. Int J Hyperthermia 25:499–511
67. Lu AH, Salabas EEL, Schüth F (2007) Magnetic nanoparticles: synthesis, protection, functionalization, and application. Angew Chem Int Ed 46:1222–1244
68. Kurti N (1988) Selected works of louis neel. CRC Press, Boca Raton, FL
69. Neel L (1950) Theorie du trainage magnetique des substances massives dans le domaine de Rayleigh. Journal de Physique et le Radium 11:49–61
70. Brown WF Jr (1963) Thermal fluctuations of a single domain particle. J Appl Phys 34: 1319–1320
71. Deissler RJ, Wu Y, Martens MA (2014) Dependence of brownian and neel relaxation times on magnetic field strength. Med Phys 41:012301
72. Lima E Jr, Torres TE, Rossi LM, Rechenberg HR, Berquo TS, Ibarra A, Marquina C, Ibarra MR, Goya GF (2013) Size dependence of the magnetic relaxation and specific power absorption in iron oxide nanoparticles. J Nanopart Res 15:1–11
73. Zhang X, Chen S, Wang H-M, Hsieh S-L, Wu C-H, Chou H-H, Hsieh S (2010) Role of neel and brownian relaxation mechanisms for water-based Fe_3O_4 nanoparticle ferrofluids in hyperthermia. Biomed Eng: Appl Basis Commun 22:393–399
74. Motoyama J, Hakata T, Kato R, Yamashita N, Morino T, Kobayashi T, Honda H (2010) Size dependent heat generation of magnetic nanoparticles under AC magnetic field for cancer therapy. In: Animal cell technology: Basic & applied aspects. Springer, pp 415–421
75. Guibert CM, Dupuis V, Peyre V, Fresnais JRM (2015) Hyperthermia of magnetic nanoparticles: experimental study of the role of aggregation. J Phys Chem C 119:28148–28154
76. Obaidat IM, Issa B, Haik Y (2015) Magnetic properties of magnetic nanoparticles for efficient hyperthermia. Nanomaterials 5:63–89
77. Thanh NTK (2012) Magnetic nanoparticles: from fabrication to clinical applications. CRC press, Boca Raton, FL
78. Yahya N (2011) Carbon and oxide nanostructures: synthesis, characterisation and applications. Springer, Berlin
79. Basti H, Hanini A, Levy M, Tahar LB, Herbst F, Smiri LS, Kacem K, Gavard J, Wilhelm C, Gazeau F (2014) Size tuned polyol-made $Zn_{0.9}M_{0.1}Fe_2O_4$ (M=Mn, Co, Ni) ferrite nanoparticles as potential heating agents for magnetic hyperthermia: from synthesis control to toxicity survey. Mater Res Exp 1:045047
80. Beji Z, Hanini A, Smiri LS, Gavard J, Kacem K, Villain F, Grenèche JM, Chau F, Ammar S (2010) Magnetic properties of Zn-substituted $MnFe_2O_4$ nanoparticles synthesized in polyol as potential heating agents for hyperthermia. Evaluation of their toxicity on Endothelial cells. Chem Mater 22:5420–5429
81. Cespedes E, Byrne JM, Farrow N, Moise S, Coker VS, Bencsik M, Lloyd JR, Telling ND (2014) Bacterially synthesized ferrite nanoparticles for magnetic hyperthermia applications. Nanoscale 6:12958–12970
82. Hanini A, Lartigue L, Gavard J, Schmitt A, Kacem K, Wilhelm C, Gazeau F, Chau F, Ammar S (2016) Thermosensitivity profile of malignant glioma U87-MG cells and human endothelial cells following $\hat{I}^3$-Fe_2O_3 NPs internalization and magnetic field application. RSC Advances 6:15415–15423
83. Lin M, Huang J, Sha M (2014) Recent advances in nanosized Mn-Zn ferrite magnetic fluid hyperthermia for cancer treatment. J Nanosci Nanotechnol 14:792–802
84. Veverka M, Zăväta K, Kaman O, Veverka P, Knížek K, Pollert E, Burian M, Kašpar P (2014) Magnetic heating by silica-coated Co-Zn ferrite particles. J Phys D Appl Phys 47:065503
85. Hanini A, Lartigue L, Gavard J, Kacem K, Wilhelm C, Gazeau F, Chau FO, Ammar S (2016) Zinc substituted ferrite nanoparticles with $Zn_{0.9}Fe_{2.1}O_4$ formula used as heating agents for in vitro hyperthermia assay on glioma cells. J. Magn. Magn. Mater. 416:315–320

86. Wijaya A, Brown KA, Alper JD, Hamad-Schifferli K (2007) Magnetic field heating study of Fe-doped Au nanoparticles. J Magn Magn Mater 309:15–19
87. Hilger I, Kaiser WA (2012) Iron oxide-based nanostructures for MRI and magnetic hyperthermia. Nanomedicine 7:1443–1459
88. Neuberger T, Schöpf B, Hofmann H, Hofmann M, Von Rechenberg B (2005) Superparamagnetic nanoparticles for biomedical applications: possibilities and limitations of a new drug delivery system. J. Magn. Magn. Mater. 293:483–496
89. Hiergeist R, Andrã W, Buske N, Hergt R, Hilger I, Richter U, Kaiser W (1999) Application of magnetite ferrofluids for hyperthermia. J Magn Magn Mater 201:420–422
90. Gonzales-Weimuller M, Zeisberger M, Krishnan KM (2009) Size-dependant heating rates of iron oxide nanoparticles for magnetic fluid hyperthermia. J. Magn. Magn. Mater. 321: 1947–1950
91. Guardia P, Di Corato R, Lartigue L, Wilhelm C, Espinosa A, Garcia-Hernandez M, Gazeau F, Manna L, Pellegrino T (2012) Water-soluble iron oxide nanocubes with high values of specific absorption rate for cancer cell hyperthermia treatment. ACS Nano 6:3080–3091
92. Lartigue LN, Hugounenq P, Alloyeau D, Clarke SP, Lévy M, Bacri J-C, Bazzi R, Brougham DF, Wilhelm C, Gazeau F (2012) Cooperative organization in iron oxide multi-core nanoparticles potentiates their efficiency as heating mediators and MRI contrast agents. ACS Nano 6:10935–10949
93. Kolosnjaj-Tabi J, Di Corato R, Lartigue LN, Marangon I, Guardia P, Silva AKA, Luciani N, Clément O, Flaud P, Singh JV (2014) Heat-generating iron oxide nanocubes: subtle "destructurators" of the tumoral microenvironment. ACS Nano 8:4268–4283
94. Di Corato R, Espinosa A, Lartigue L, Tharaud M, Chat S, Pellegrino T, Ménager C, Gazeau F, Wilhelm C (2014) Magnetic hyperthermia efficiency in the cellular environment for different nanoparticle designs. Biomaterials 35:6400–6411
95. Gandhi S, Arami H, Krishnan KM (2016) Detection of cancer-specific proteases using magnetic relaxation of peptide-conjugated nanoparticles in biological environment. Nano Lett
96. Lowry GV, Gregory KB, Apte SS, Lead JR (2012) Transformations of nanomaterials in the environment. Environ Sci Technol 46:6893–6899
97. Thomas CR, George S, Horst AM, Ji Z, Miller RJ, Peralta-Videa JR, Xia T, Pokhrel S, Maìdler L, Gardea-Torresdey JL (2011) Nanomaterials in the environment: from materials to high-throughput screening to organisms. ACS Nano 5:13–20
98. Levard C, Hotze EM, Lowry GV, Brown GE Jr (2012) Environmental transformations of silver nanoparticles: impact on stability and toxicity. Environ Sci Technol 46:6900–6914
99. Xia T, Zhao Y, Sager T, George S, Pokhrel S, Li N, Schoenfeld D, Meng H, Lin S, Wang X (2011) Decreased dissolution of ZnO by iron doping yields nanoparticles with reduced toxicity in the rodent lung and zebrafish embryos. ACS Nano 5:1223–1235
100. Kolosnjaj-Tabi J, Lartigue LN, Javed Y, Luciani N, Pellegrino T, Wilhelm C, Alloyeau D, Gazeau F (2016) Biotransformations of magnetic nanoparticles in the body. Nano Today 11:280–284
101. Koksharov YA (2009) Magnetism of nanoparticles: Effects of size, shape, and interactions. In: Gubin SP (ed) Magnetic nanoparticles. Wiley-VCH, pp 197–254
102. Alloyeau D, Dachraoui W, Javed Y, Belkahla H, Wang G, Lecoq HLN, Ammar S, Ersen O, Wisnet A, Gazeau F (2015) Unravelling kinetic and thermodynamic effects on the growth of gold nanoplates by liquid transmission electron microscopy. Nano Lett 15:2574–2581
103. Laurent S, Dutz S, Häfeli UO, Mahmoudi M (2011) Magnetic fluid hyperthermia: focus on superparamagnetic iron oxide nanoparticles. Adv Colloid Interface Sci 166:8–23
104. Chen D, Xu R (1998) Hydrothermal synthesis and characterization of nanocrystalline Fe_3O_4 powders. Mater Res Bull 33:1015–1021
105. Lawrence MJ, Rees GD (2000) Microemulsion-based media as novel drug delivery systems. Adv Drug Deliv Rev 45:89–121
106. Titirici M-M, Antonietti M, Thomas A (2006) A generalized synthesis of metal oxide hollow spheres using a hydrothermal approach. Chem Mater 18:3808–3812

107. Cheng C, Xu F, Gu H (2011) Facile synthesis and morphology evolution of magnetic iron oxide nanoparticles in different polyol processes. New J Chem 35:1072–1079
108. Laurent S, Forge D, Port M, Roch A, Robic C, Vander Elst L, Muller RN (2008) Magnetic iron oxide nanoparticles: synthesis, stabilization, vectorization, physicochemical characterizations, and biological applications. Chem Rev 108:2064–2110
109. Hoskins C, Min Y, Gueorguieva M, Mcdougall C, Volovick A, Prentice P, Wang Z, Melzer A, Cuschieri A, Wang L (2012) Hybrid gold-iron oxide nanoparticles as a multifunctional platform for biomedical application. J Nanobiotechnol 10:1
110. Gao J, Gu H, Xu B (2009) Multifunctional magnetic nanoparticles: design, synthesis, and biomedical applications. Acc Chem Res 42:1097–1107
111. Salvador-Morales C, Gao W, Ghatalia P, Murshed F, Aizu W, Langer R, Farokhzad OC (2009) Multifunctional nanoparticles for prostate cancer therapy. Expert Rev Anticancer Ther 9: 211–221
112. Bergey EJ, Levy L, Wang X, Krebs LJ, Lal M, Kim K-S, Pakatchi S, Liebow C, Prasad PN (2002) DC magnetic field induced magnetocytolysis of cancer cells targeted by LH-RH magnetic nanoparticles in vitro. Biomed Microdevices 4:293–299
113. Berry CC, Curtis ASG (2003) Functionalisation of magnetic nanoparticles for applications in biomedicine. J Phys D Appl Phys 36:R198
114. Briley-Saebo KC, Johansson LO, Hustvedt SO, Haldorsen AG, Bjørnerud A, Fayad ZA, Ahlstrom HK (2006) Clearance of iron oxide particles in rat liver: effect of hydrated particle size and coating material on liver metabolism. Invest Radiol 41:560–571
115. Kolosnjaj-Tabi J, Javed Y, Lartigue LN, Volatron J, Elgrabli D, Marangon I, Pugliese G, Caron B, Figuerola A, Luciani N (2015) The one year fate of iron oxide coated gold nanoparticles in mice. ACS Nano 9:7925–7939
116. Levy M, Luciani N, Alloyeau D, Elgrabli D, Deveaux V, Pechoux C, Chat S, Wang G, Vats N, Gendron FO (2011) Long term in vivo biotransformation of iron oxide nanoparticles. Biomaterials 32:3988–3999
117. Mahmoudi M, Lynch I, Ejtehadi MR, Monopoli MP, Bombelli FB, Laurent S (2011) Protein nanoparticle interactions: opportunities and challenges. Chem Rev 111:5610–5637
118. Sperling RA, Parak WJ (2010) Surface modification, functionalization and bioconjugation of colloidal inorganic nanoparticles. Philos Trans R Soc Lond A: Math Phys Eng Sci 368: 1333–1383
119. Lazzari S, Moscatelli D, Codari F, Salmona M, Morbidelli M, Diomede L (2012) Colloidal stability of polymeric nanoparticles in biological fluids. J Nanopart Res 14:1–10
120. Ditto AJ, Shah KN, Robishaw NK, Panzner MJ, Youngs WJ, Yun YH (2012) The Interactions between l-tyrosine based nanoparticles decorated with folic acid and cervical cancer cells under physiological flow. Mol Pharm 9:3089–3098
121. Kumar S, Aaron J, Sokolov K (2008) Directional conjugation of antibodies to nanoparticles for synthesis of multiplexed optical contrast agents with both delivery and targeting moieties. Nat Protoc 3:314–320
122. Gupta AK, Gupta M (2005) Synthesis and surface engineering of iron oxide nanoparticles for biomedical applications. Biomaterials 26:3995–4021
123. Sperling RA, Gil PR, Zhang F, Zanella M, Parak WJ (2008) Biological applications of gold nanoparticles. Chem Soc Rev 37:1896–1908
124. Mohammad F, Balaji G, Weber A, Uppu RM, Kumar CSSR (2010) Influence of gold nanoshell on hyperthermia of superparamagnetic iron oxide nanoparticles. J Phys Chem C 114:19194–19201
125. Javed Y, Lartigue LN, Hugounenq P, Vuong QL, Gossuin Y, Bazzi R, Wilhelm C, Ricolleau C, Gazeau F, Alloyeau D (2014) Biodegradation mechanisms of iron oxide monocrystalline nanoflowers and tunable shield effect of gold coating. Small 10:3325–3337
126. Li S-D, Huang L (2008) Pharmacokinetics and biodistribution of nanoparticles. Mol Pharm 5:496–504
127. Owens DE, Peppas NA (2006) Opsonization, biodistribution, and pharmacokinetics of polymeric nanoparticles. Int J Pharm 307:93–102

128. Shilo M, Sharon A, Baranes K, Motiei M, Lellouche J-PM, Popovtzer R (2015) The effect of nanoparticle size on the probability to cross the blood-brain barrier: an in-vitro endothelial cell model. J Nanobiotechnol 13:1
129. Longmire M, Choyke PL, Kobayashi H (2008) Clearance properties of nano-sized particles and molecules as imaging agents: considerations and caveats.
130. Alexis F, Pridgen E, Molnar LK, Farokhzad OC (2008) Factors affecting the clearance and biodistribution of polymeric nanoparticles. Mol Pharm 5:505–515
131. Czuprynski CJ (2016) Opsonization and Phagocytosis. Encyclopedia of Immunotoxicology: 674–676
132. Salmaso S, Caliceti P (2013) Stealth properties to improve therapeutic efficacy of drug nanocarriers. J Drug Deliv 2013:19
133. Al-Hanbali O, Rutt KJ, Sarker DK, Hunter AC, Moghimi SM (2006) Concentration dependent structural ordering of poloxamine 908 on polystyrene nanoparticles and their modulatory role on complement consumption. J Nanosci Nanotechnol 6:3126–3133
134. Jo DH, Kim JH, Lee TG, Kim JH (2015) Size, surface charge, and shape determine therapeutic effects of nanoparticles on brain and retinal diseases. Nanomed: Nanotechnol, Biol Med 11:1603–1611
135. Frohlich E (2012) The role of surface charge in cellular uptake and cytotoxicity of medical nanoparticles. Int J Nanomedicine 7:5577–5591
136. Rahman M, Laurent S, Tawil N, Yahia LH, Mahmoudi M (2013) Nanoparticle and protein corona. In: Protein-nanoparticle interactions. Springer, pp 21–44
137. Dell'orco D, Lundqvist M, Oslakovic C, Cedervall T, Linse S (2010) Modeling the time evolution of the nanoparticle-protein corona in a body fluid. PLoS One 5:e10949
138. Bargheer D, Nielsen J, Gébel G, Heine M, Salmen SC, Stauber R, Weller H, Heeren J, Nielsen P (2015) The fate of a designed protein corona on nanoparticles in vitro and in vivo. Beilstein J Nanotechnol 6:36–46
139. Foroozandeh P, Aziz AA (2015) Merging worlds of nanomaterials and biological environment: factors governing protein corona formation on nanoparticles and its biological consequences. Nanoscale Res Lett 10:1–12
140. Medina C, Santos-Martinez MJ, Radomski A, Corrigan OI, Radomski MW (2007) Nanoparticles: pharmacological and toxicological significance. Br J Pharmacol 150:552–558
141. Shang L, Nienhaus K, Nienhaus GU (2014) Engineered nanoparticles interacting with cells: size matters. J Nanobiotechnol 12:1
142. Cummings BS, Wills LP, Schnellmann RG (2012) Measurement of cell death in Mammalian cells. Current Protocols in Pharmacology 12.18. 11–12.18. 24.
143. Naqvi S, Samim M, Abdin M, Ahmed FJ, Maitra A, Prashant C, Dinda AK (2009) Concentration-dependent toxicity of iron oxide nanoparticles mediated by increased oxidative stress. Int J Nanomedicine 5:983–989
144. Ghosh R, Pradhan L, Devi YP, Meena SS, Tewari R, Kumar A, Sharma S, Gajbhiye NS, Vatsa RK, Pandey BN (2011) Induction heating studies of Fe_3O_4 magnetic nanoparticles capped with oleic acid and polyethylene glycol for hyperthermia. J Mater Chem 21:13388–13398
145. Ma M, Wu Y, Zhou J, Sun Y, Zhang Y, Gu N (2004) Size dependence of specific power absorption of Fe_3O_4 particles in AC magnetic field. J. Magn. Magn. Mater. 268:33–39
146. Zhao D-L, Wang X-X, Zeng X-W, Xia Q-S, Tang J-T (2009) Preparation and inductive heating property of Fe_3O_4 chitosan composite nanoparticles in an AC magnetic field for localized hyperthermia. J Alloys Compd 477:739–743
147. Sadat ME, Patel R, Sookoor J, Bud'ko SL, Ewing RC, Zhang J, Xu H, Wang Y, Pauletti GM, Mast DB (2014) Effect of spatial confinement on magnetic hyperthermia via dipolar interactions in Fe_3O_4 nanoparticles for biomedical applications. Mater Sci Eng C 42:52–63
148. Kozissnik B, Bohorquez AC, Dobson J, Rinaldi C (2013) Magnetic fluid hyperthermia: Advances, challenges, and opportunity. Int J Hyperthermia 29:706–714
149. Fadeel B, Garcia-Bennett AE (2010) Better safe than sorry: Understanding the toxicological properties of inorganic nanoparticles manufactured for biomedical applications. Adv Drug Deliv Rev 62:362–374

150. Kida Y, Ishiguri H, Ichimi K, Kobayashi T (1990) Hyperthermia of metastatic brain tumor with implant heating system: a preliminary clinical results. No shinkei geka. Neurol Surg 18:521–526
151. Kobayashi T, Kida Y, Matsui M, Amemiya Y (1990) Interstitial hyperthermia of malignant brain tumors using implant heating system (IHS). No shinkei geka. Neurol Surg 18:247–252
152. Luo S, Wang LF, Ding WJ, Wang H, Zhou JM, Jin HK, Su SF, Ouyang WW (2014) Clinical trials of magnetic induction hyperthermia for treatment of tumours. OA Cancer 2:2
153. Hentschel M, Mirtsch S, Jordan A, Wust P, Vogl TH, Semmler W, Wolf KJ, Felix R (1997) Heat response of HT29 cells depends strongly on perfusion–A 31P NMR spectroscopy, HPLC and cell survival analysis. Int J Hyperthermia 13:69–82
154. Maier-Hauff K, Rothe R, Scholz R, Gneveckow U, Wust P, Thiesen B, Feussner A, Von Deimling A, Waldoefner N, Felix R (2007) Intracranial thermotherapy using magnetic nanoparticles combined with external beam radiotherapy: results of a feasibility study on patients with glioblastoma multiforme. J Neurooncol 81:53–60
155. Maier-Hauff K, Ulrich F, Nestler D, Niehoff H, Wust P, Thiesen B, Orawa H, Budach V, Jordan A (2011) Efficacy and safety of intratumoral thermotherapy using magnetic iron-oxide nanoparticles combined with external beam radiotherapy on patients with recurrent glioblastoma multiforme. J Neurooncol 103:317–324
156. Johannsen M, Gneveckow U, Thiesen B, Taymoorian K, Cho CH, Waldöfner N, Scholz R, Jordan A, Loening SA, Wust P (2007) Thermotherapy of prostate cancer using magnetic nanoparticles: Feasibility, imaging, and three-dimensional temperature distribution. Eur Urol 52:1653–1662
157. Gao F, Yan Z, Zhou J, Cai Y, Tang J (2012) Methotrexate-conjugated magnetic nanoparticles for thermochemotherapy and magnetic resonance imaging of tumor. J Nanopart Res 14:1–10

Chapter 12
Magnetic Core-Shell Nanoparticles for Biomedical Applications

Samir Mandal and Keya Chaudhuri

12.1 Introduction

Nanoscale objects are powerful devices in biotechnology medicine and biomedical sciences. They are potential applicants in recent clinical diagnostics and therapeutic techniques. Nanoparticles can be composed of numerous materials such as liposomes, polymeric micelles, block ionomer complexes, dendrimers, carbon, inorganic and polymeric nanoparticles, nanorods, quantum dots, iron oxide, gadolinium oxide, cadmium selenide–based quantum dots, and crystals of gold [1, 2]. Among these, iron oxide nanoparticles (IONPs) have drawn major attention, particularly for biomedical purposes thanks to their properties like biocompatibility, low toxicity, stability, availability for surface modification, and higher relaxation values. All have been tested preclinically or clinically for targeted drug and gene delivery and as agents to enhance diagnostic imaging output like in magnetic resonance imaging (MRI) [3]. Properties present only on the nanoscale level, like the increased intensity of fluorescent light emission of semiconductor crystals (quantum dots) or switchable magnetic properties of superparamagnetic iron oxide nanoparticles (SPIONs), make these materials unique and useful for applications in the biomedical field of medical imaging and cell tracking.

S. Mandal • K. Chaudhuri
Molecular Genetics Division, CSIR-Indian Institute of Chemical Biology, 4, Raja S. C. Mullick Road, Kolkata 700032, India
e-mail: kchaudhuri@iicb.res.in; keya.chaudhuri@gmail.com

© Springer International Publishing AG 2017

S.K. Sharma (ed.), *Complex Magnetic Nanostructures*,
DOI 10.1007/978-3-319-52087-2_12

Without any surface modification, IONPs tend to agglomerate owing to their high surface-area-to-volume ratio, and aggregation results in the fast detection of nanoparticles by the immune system. To provide high colloidal stability and overcome the agglomeration tendency, coating is required on the surface of magnetic core-shell nanoparticles. Limitations associated with the utilization of IONPs in biomedicine are also overcome by coating the surface. For example, an appropriate coating substance can result in the dispersion of nanomaterials in biological surroundings, which may permit further functionalization of the surface, prevent nonspecific adsorption of plasma proteins on nanoparticles, improve compatibility in blood, and can hinder degradation by macrophages [4, 5].

Moreover, uncovered IONPs can be simply oxidized in air, resulting in the loss of magnetic and colloidal strength [6]. Surface coating of IONPs can be attained using various polymeric substances like polyethylene glycol (PEG), dextran, chitosan, polyvinyl alcohol (PVA), or starch [7, 8]. Furthermore, a few inorganic substances like gold or silica have also been used as a coating material [9]. Nowadays nonpolymeric organic substances like oleic acid, carboxylates, and alkyl phosphonates have also been used to coat the surface of IONPs [9].

IONPs smaller than 20 nm are bestowed with superparamagnetic properties and are therefore known as SPIONs. This supermagnetic property is vital for several applications in the biomedical field, and its uniqueness lies in the fact that as soon as the external magnetic field is removed, the magnetism of superparamagnetic materials is switched off. SPIONs are thus regarded as having high potential for a variety of uses in biomedicine, both for diagnosis and for therapy. For example, SPIONs can be used for MRI, early detection of inflammatory cancer and diabetes, hyperthermia, stem cell tracking, tissue repair, gene therapy, and manipulation of cell organelles [10]. Additionally, current studies have revealed the challenging role of surface-functionalized SPIONs in site-specific drug targeting [11]. The targeting potential of magnetic nanoparticles can be strengthened by immobilizing specific ligands on a surface, which is predicted to support the affinity of nanoparticles to the sites of attention. Such lignads are usually peptides, proteins, polysaccharides, antibodies, and aptamers [12]. Moreover, major progress in the internalization of nanoparticles by targeted cells can be achieved by choosing a proper ligand [13]. Intracellular delivery of curative drugs could be accomplished using stimulus-receptive coatings in the outer surface of nanoparticles. These advanced nanomachines are better in comparison to nontargeted ones and are expected to tackle current constraints on cancer treatment like nonspecific delivery of drugs in the body, unwanted health effects due to the necessity of a high dose to achieve the requisite high local drug concentration, cancer cells becoming resistant to drugs, and nonspecific toxic outcomes.

12.2 Types of Magnetic Core-Shell Nanoparticles

A magnetic core-shell nanoparticle, as the name implies, is a type of nanoparticle having a core or inner magnetic material and an outer shell composed of coating material. Varieties of core-shell nanoparticles have been prepared with diverse composition in close interaction and distinct use. The arrangement can be achieved by the interaction of inorganic/inorganic, inorganic/organic, and organic/inorganic materials. Normally, magnetic core-shell nanoparticles can be classified into two different categories as described below.

12.2.1 Magnetic Oxide Core Shell

Being of relatively inert surface composition, maghemite (or magnetite) magnetic nanomaterials generally do not allow for strong covalent bond formation with functional molecules. The use of silica as a shell on the surface of magnetic nanostructures has been reported to enhance the reactivity of magnetic nanomaterials. A variety of surface functional groups are employed to link with the silica shell through covalent bond formation. Functionalized silica-coated core-shell magnetic nanostructures can be utilized as fluorescence sensors through covalent bond formation with some fluorescent dye molecules [14].

Ferrite nanoparticle clusters, which are composed of approximately 80 maghemite superparamagnetic oxide nanocluster per bead with a silica shell, have a lot of advantages in comparison to metal nanoparticles. These are as follows: (1) superior chemical and thermodynamic stability, (2) precise size distribution, (3) higher colloidal stability, (4) dependence of the magnetic moment on the nanoparticle cluster size, (5) preservation of superparamagnetic properties regardless of cluster size of nanostructures, and (6) direct covalent attachment by the silica surface.

12.2.2 Metallic Magnet Core Shell

The material of a magnetic nanocore may be deactivated by gentle oxidation or the use of surfactants or polymers [15]. In an oxidative environment, an antiferromagnetic CoO layer was created on the surface of a Co nanoparticle. Recently, the exchange bias synthetic procedure was used to prepare a Co-core CoO-shell nanostructure coated with a thin gold outermost layer [16]. In addition, much attention has been paid to recently introduced nanoparticles having a magnetic core comprised either of metallic iron or cobalt with an inactive grapheme shell [17]. The benefits in contrast to ferrite or elemental nanoscale objects are (1) superior magnetization and (2) high stability in a wide range of pH and organic solvents.

12.3 Synthesis of Magnetic Core-Shell Nanoparticles

Magnetic core-shell nanoparticle synthesis is a two-step procedure. The first step is the synthesis of magnetic nanomaterials followed by encapsulation of the magnetic core materials with preferred organic or inorganic materials depending on the choice. The synthesis can be affected by a range of combinations such as organic/inorganic, inorganic/organic, and inorganic/inorganic materials in close affinity. The choice of shell materials in core-shell nanostructures is largely determined by the ultimate application and usefulness desired. Normally silica, various metals and nonmetallic oxides, drug molecules, and polymers are used as the coating substances.

The synthesis of magnetic IONPs with requisite characteristics is a challenging task for researchers, who must tackle two main challenges. First is the optimization of experimental conditions for generating monodispersed particles of the appropriate size, and second is reproducibility. Further purification procedures become necessary if the reaction product does not have a homogeneous and narrow size distribution. The aforementioned criteria are essential because the clinical potential of nanoparticles depends on monodispersity, shape, and size [7, 9]. Nowadays, numerous techniques have been adopted where efficient synthesis resulted in monodispersed, stable, and biocompatible nanoparticle populations. These techniques could be used to develop high-quality IONPs with the requisite size and shape. The most general methods for the synthesis of IONPs are coprecipitation techniques, microemulsion formation, hydrothermal synthesis, and thermal decomposition of iron complexes. Other methods, like electrochemical synthesis, sol-gel synthesis, laser pyrolysis, and sonochemical reactions, may be utilized for the synthesis of magnetic nanostructures [18]. In the present chapter, coprecipitation, microemulsion, hydrothermal synthesis, and thermal decomposition methods for the synthesis of IONPs are discussed in detail.

12.3.1 Coprecipitation Method

The slow addition of a base to a mixture of aqueous Fe^{2+}/Fe^{3+} salt solutions under an inert atmosphere at elevated temperature or room temperature could be employed for the synthesis of iron oxide (Fe_3O_4 or γ-Fe_2O_3) nanoparticles. This procedure is called the coprecipitation method since two ions are precipitated simultaneously. The magnetic property, composition, and morphology largely depend on the Fe^{2+}/Fe^{3+} ratio, concentration of sodium hydroxide, stabilizing agent, and temperature. If the synthetic reaction conditions are unaltered, the size, shape, and morphology of the magnetite nanoparticles are totally reproducible. However, in acidic pH, these nanoparticles are readily oxidized to a more stable maghemite form. The transformation of magnetite to maghemite is facilitated by forming acidic dispersion, followed by iron (III) nitrate administration. The maghemite particle is magnetically stable over a wide range of pH.

Though the magnetite particles are converted into maghemite form easily, the controlling narrow particle size distribution in Fe_3O_4, using the coprecipitation technique, is difficult. A broad range of particle size distribution with irregular magnetic activity would result if the blocking temperature fluctuates. The coprecipitation method is popular because of its simplicity and high yield in comparison to other methods of IONP preparation.

Magnetite (Fe_3O_4) or maghemite (Fe_2O_3) is produced in a reduction reaction of iron salts under alkaline conditions. For the synthesis of the magnetite form of iron oxide, aqueous solutions of ferric (Fe^{3+}) and ferrous (Fe^{2+}) ions are mixed in a 2:1 molar ratio and precipitated by the addition of a strong base like sodium hydroxide. The pH range of the solution must lie between 9 and 14 for efficient magnetite production. The magnetite particles are sedimented as a black solid. The stoichiometric chemical reaction for magnetite formation is given by

$$Fe^{2+} + 2Fe^{3+} + 8OH^{-} \rightarrow Fe_3O_4 + 4H_2O.$$

This reaction must be performed in an oxygen-free environment, since magnetite is very much prone to aerial oxidation [9]. Magnetite is transformed into more stable maghemite in the presence of oxygen directed as follows:

$$Fe_3O_4 + 2H^{+} \rightarrow \gamma\text{-}Fe_2O_3 + Fe^{2+} + H_2O.$$

In the presence of oxygen, magnetite (Fe_3O_4) particles can also be transformed into $Fe(OH)_3$ according to the following reaction:

$$Fe_3O_4 + 0.25O_2 + 4.5H_2O \rightarrow 3Fe(OH)_3.$$

The physical and chemical properties of nanostructures are affected by the oxidation/reduction priority of iron ions. Thus, an inert gas environment is required for carrying out the reaction. For example, an N_2/argon gas environment is required during the precipitation process, which can check the deterioration of Fe_3O_4. It is also observed that smaller particle sizes are associated with an oxygen-free environment during synthesis [6]. The size, shape, and morphology of nanoparticles can be regulated by modulating the type of salt (e.g., chlorides, sulfates, nitrates, perchlorates), the Fe^{2+}/Fe^{3+} molar ratio, the reaction temperature, the pH range of the solution, and the ionic strength of the medium [19]. The coprecipitation procedure is simple, fast, and of high yield and it produces nanoparticles with a wide range of sizes. To bypass the polydispersity of size, many efforts have been made. A coprecipitation synthesis method has been reported where the researchers were able to manipulate the size and homogeneity of the nanoparticles produced. Briefly, they controlled the pH of the ferrite solution uniformly using urea. The urea was decomposed by heating prior to the addition of the base to precipitate the iron

salts in the solution. A uniform particle size was associated with a consistent pH distribution of the ferrite solution. The mechanism of the reaction is as follows [20]:

$$CO(NH_2)_2 + H_2O \xrightarrow{\Delta} 2NH_3 + CO_2,$$

$$NH_3 + H_2O \rightarrow NH_4^+ + OH^-.$$

Since the decomposition of urea around 90 °C generates ammonia, and ammonia in water produces hydroxyl ions, increasing the pH of the solution. Thus alteration of the amount of urea might lead to the formation of a monodisperse nanoparticle population, resulting in a controlled IONP size.

12.3.2 Microemulsion Method

The coprecipitation method normally yields polydispersed particles; other techniques have been developed that give more control over nanoparticle dimensions. The microemulsion technique is one such alternative method producing IONPs with a narrow size distribution. The thermodynamically stable isotropic dispersion of two immiscible liquids in the presence of a suitable surfactant is a microemulsion technique. Water-in-oil reverse micelles have generally been employed for the synthesis of IONPs with narrow size distribution and uniform physical properties. Sodium bis(2-ethylhexylsulfosuccinate) (AOT), sodium dodecyl sulfate (SDS), and cetyltrimethyl-ammonium bromide (CTAB) and are the commonly used surfactants for the synthesis of IONPs [20]. Surfactant molecules generate a monolayer at the water and oil interface by the dissolution of hydrophobic parts of surfactant molecules in the oil phase and hydrophilic groups in the aqueous phase [6]. In this microemulsion technique, the aqueous solution is iron salts are dissolved in the core of the reverse micelle and the precipitation reaction is carried out inside the aqueous core. Thus, by manipulating the size of the aqueous core, one can adjust the nanoparticle size.

The synthesis of SPIONs with a narrow particle size distribution has been reported utilizing AOT/n-hexane reverse micelles in an N_2 atmosphere [21]. The size of the reverse micelle core was kept within the nanometer range, and as a result, SPIONs with a size of around 15 nm was obtained. In another study, using a microemulsion of cyclohexane/Brij-97/aqueous phase, the synthesis of SPIONs with a size distribution of 3.5 ± 0.6 nm with high magnetization values was achieved. The microemulsion technique produces a relatively good size distribution and shape control, and the use of potentially toxic surfactants makes this method bioincompatible. However, the aggregation and colloidal instability required further modification.

12.3.3 Hydrothermal Synthesis Method

A wide range of nanostructures can be synthesized by applying hydrothermal conditions. A liquid-solid-solution reaction has been employed for the synthesis of a diverse array of nanocrystals. The system employed for the synthesis consisted of a solid-liquid-solution matrix containing metal linoleate (solid), an ethanol linoleic acid (liquid), and a water-ethanol solution at different reaction temperatures under hydrothermal conditions [22]. This approach is based on phase transfer and a separation mechanism occurring at the liquid-solid-solution interfaces present during the synthesis. Using hydrothermal reduction, monodisperse, hydrophilic, single-crystal ferrite microspheres were synthesized. According to this process, a mixture of $FeCl_3$, sodium acetate, ethylene glycol, and PEG was stirred vigorously till a clear solution was formed, followed by sealing in a Teflon-coated stainless-steel autoclave, and heated to 200 °C for 8–72 h.

The aforementioned four synthetic methods have some advantages and disadvantages. Among the four methods, coprecipitation is the preferred route in terms of the simplicity of the synthesis. The thermal decomposition method can be considered the best in terms of controlling the size and morphology of nanoparticles. As a substitute, microemulsions can also be employed to synthesize monodispersed nanoparticles having various morphologies. However, a large amount of solvent is needed in this method. Hydrothermal synthesis, although it generates superior quality nanoparticles, is a comparatively little investigated method for the synthesis of magnetic nanoparticles. To date, magnetic nanoparticles are synthesized on a large scale by the use of coprecipitation and thermal decomposition procedures.

12.3.4 Thermal Decomposition

The synthesis of magnetic particles with the desired shape and size derived from the idea of quality semiconductor nanocrystals and oxide-nanoparticle synthesis involving a thermal decomposition technique using nonaqueous media [23]. Organometallic compounds upon thermal decomposition in high-boiling-point organic solvents with stabilizing surfactants produce monodisperse magnetic nanocrystals of smaller size [4]. In this process, the frequently used surfactants are fatty acids, oleic acid [24], and hexadecylamine [25]. Metal acetylacetonates [M(acac)n] (M = Fe, Mn, Co, Ni, Cr; n = 2 or 3, acac = acetylacetonate), metal cupferronates (MxCupx) [M = metal ion; Cup = N-nitrosophenylhydroxylamine, $C_6H_5N(NO)O$-], or carbonyls [26] can be used as organometallic precursors. The size and shape of a magnetic nanocomposite can be regulated by varying the ratio of the starting reagents including organometallic compounds, surfactant, and solvent. The reaction temperature, time, and aging period are also vital for the precise control of the size and shape of magnetic nanoparticles. If the metal is in a zero valent state, for example in carbonyls, thermal decomposition primarily tends to

lead to the creation of the metal; however, a two-step procedure is often used to make oxide nanoparticles. For example, at 100 °C, iron pentacarbonyl is capable of decomposing into a mixture of oleic acid and octyl ether, followed by the addition of a mild oxidant like trimethylamine oxide $(CH_3)_3NO$ at a higher temperature, and produces monodisperse γ-Fe_2O_3 nanocrystals approximately 12 nm in size [26]. Upon decomposition a precursor with cationic metal centers produces oxide nanoparticles. For example, Fe_3O_4 is formed upon decomposition of $Fe(acac)_3$ in the presence of oleoylamine, 1,2-hexadecanediol, and oleic acid in phenol ether [26]. The pyrolysis of metal fatty acid salts (such as salts of decanoic acid, lauric acid, myristic acid, palmitic acid, oleic acid, and stearic acid) in a nonaqueous solution (octadecene, n-eicosane, tetracosane, or a mixture of octadecene and tetracosane) generated size- and shape-controlled magnetic oxide nanocrystals [27]. This method provides nearly monodisperse Fe_3O_4 nanocrystals having a wide range of size-adjustable capacity (4–50 nm) with controlled shapes, including dots and cubes. This method has been successfully employed for the synthesis of Cr_2O_3, MnO, Co_3O_4, and NiO magnetic nanocrystals. Variation of the reactivity and concentration of the precursors is the key factor to control the size and shape of nanocrystals. Variation of the concentration and chain length of fatty acids determines the reactivity of the materials. Generally, a faster reaction rate is associated with a shorter chain length. Alcohols or primary amines are often employed to speed up the reaction rate and decrease the reaction temperature.

An analogous thermal decomposition procedure has been proposed for the production of monodisperse iron oxide nanostructures [28]. An iron oleate complex have been synthesized in situ using iron (III) chloride and sodium oleate and then thermally decomposed between 240 and 320 °C in various solvent systems such as 1-hexadecene, 1-octadecene, 1-eicosene, octyl ether, and trioctylamine. In this method, the particle size depends on the decomposition temperature and aging period. In this reaction, aging plays an important and necessary role in the production of IONPs. Nanoparticles synthesized by this method are capable of dispersion in various organic solvents, together with hexane and toluene. Monodisperse iron nanoparticles (6–15 nm) can be synthesized by decomposing iron pentacarbonyl and the iron oleate complex at different temperatures, and these can again be oxidized to magnetite [29]. This procedure is equivalent to seed-mediated growth and therefore can be explained by the classical LaMer mechanism.

In biotechnology applications, water-soluble magnetic nanoparticles are more advantageous. This requirement led to the preparation of water-soluble Fe_3O_4 nanocrystals with $FeCl_3 \cdot 6H_2O$ as an iron source and 2-pyrrolidone as a coordinating solvent under refluxing conditions (245 °C) [30]. In this method, the mean particle size is controlled at 4, 12, and 60 nm, respectively, when the reflux times are 1, 10, and 24 h. With increasing reflux time, a change in the shapes of particles from spherical to cubic morphologies was observed. Recently, water-soluble magnetite nanoparticles were synthesized using one-pot synthesis under analogous reaction

states with the addition of a surface capping agent like α,ω-dicarboxyl-terminated poly (ethylene glycol) [31]. These nanoparticles are used as MRI contrast agents for the diagnosis of cancer.

Metallic nanoparticles can also be prepared by a thermal decomposition method. Metallic nanoparticles have many advantages over other metal oxide nanoparticles owing to their larger magnetization. Thermal breakdown of $[Fe(CO)_5]$ in the presence of polyisobutene in decalin in a nitrogen atmosphere at 170 °C produces metallic iron nanoparticles [32]. Depending on the $[Fe(CO)_5]$/polyisobutene ratio, the size of the particle can be adjusted from 3 to 10 nm, with a polydispersity of approximately 10%. Susceptibility measurements revealed that the iron nanoparticles prepared in this way can be easily oxidized by exposure to air. This oxidation can generate a marginal increase in particle sizes approximately by a factor of 1.3. Iron nanocubes can be synthesized by the breakdown of $Fe[N(Si(CH_3)_3)_2]_2$ with H_2 in the presence of hexadecylammonium chloride or hexadecylamine and oleic acid at 150 °C [33]. The edge-length of the nanocubes varied from 7 to 8.3 nm along with the varying relative concentrations of amine and acid ligand. These nanocubes can accumulate into expanded crystalline superlattices by having their crystallographic axes aligned.

Cobalt nanoparticles can also be prepared by the thermal decomposition method. Their shape and morphology both can be controlled by this method [34]. Cobalt nanodisks can also be prepared by the thermal decomposition of a cobalt carbonyl precursor [35]. The high-temperature reduction of noncarbonyl organometallic complexes produces cobalt nanorods [36] and nickel nanorods [37]. For example, the decomposition of $[Co(H_3\text{-}C_8H_{13})(H_4\text{-}C_8H_{12})]$ with H_2 in anisole at 150 °C in the presence of a combination of hexadecylamine and a fatty acid (lauric, octanoic, or stearic acid) produces monodisperse ferromagnetic cobalt nanorods. The variation of diameter and length of the cobalt nanorods largly depends upon the different acids used [36].

Magnetic alloy nanoparticles have many advantages over other magnetic nanoparticles owing to their enhanced magnetic susceptibility, high magnetic anisotropy, and large coercivities. Besides $CoPt_3$ and FePt, metal phosphides have generated a lot of interest in nanotechnology and chemistry [38]. Hexagonal iron phosphide and related materials have been thoroughly studied for their ferromagnetism, magnetoresistance, and magnetocaloric effects [39]. Recently, iron (III) acetylacetonate and manganese carbonyl with tris(trimethylsilyl) phosphane at elevated temperatures have been exploited to prepare FeP and MnP nanoparticles, respectively [40]. Further, the thermal decomposition of a precursor/surfactant mixture solution was applied to prepare antiferromagnetic FeP nanorods [41]. Using a syringe pump technique and thermal decomposition of iron pentacarbonyl in trioctylphosphane generates distinct iron phosphide (Fe_2P) nanorods.

12.4 Functionalization of Magnetic Nanoparticles by Natural/Synthetic Polymers

For the synthesis, storage, and use of IONPs, their stability is extremely important. Bare nanoparticles generally agglomerate and form clusters, reducing their large surface area. Surface coating imparts colloidal stability and prevents agglomeration. To achieve further functionalization and targeting, the selection of appropriate coating material is essential and nanoparticles can be designed as soluble in biological media. The desirable properties of coating materials include the high chemical affinity of iron oxide core, nonimmunogenicity, nonantigenicity, and protection from opsonization by plasma proteins [42].

According to literature reports, many different polymeric coating materials have been found to be used, among those the present review focuses on coatings with PEG, PVA, chitosan, and dextran, as these polymeric materials have been most commonly used [43].

12.4.1 Polyethylene Glycol

PEG is a synthetic polymer, which is often preferred in nanoparticle functionalization because of its several advantages, especially for biomedical uses. First, it is a biocompatible polymer having a hydrophilic nature and therefore can be dissolved in water. The US Food and Drug Administration (FDA) has approved the biocompatibility of PEG [44]. Second, there are reports that PEG enhances the biocompatibility of iron oxide nanostructures and removes fast blood clearance, increasing the blood circulation time of nanoparticles, ultimately benefitting drug release applications. PEG coating further enhances the internalization competence of nanoparticles into cells [45]. Apart from its excellent solubility and stability in aqueous media, it is also stable in physiological saline [9]. The only disadvantage of a PEG coating is its nonbiodegradability in the human body; the metabolic clearance of PEG is so far not fully known [46].

PEG coating has usually been achieved either during or after the preparation of nanostructures. Nanostructures coated with PEG following a synthesis reaction have been shown to possess better dispersion profiles than those coated with PEG during synthesis reactions [47]. A number of methods are available in the literature for coating IONPs with PEG. A chemical coprecipitation method has been described as a facile route to synthesize PEG-coated Fe_3O_4 nanoparticles [48]. This procedure involves the mixing of PEG with ferric and ferrous sulfate as precursor, which was subsequently precipitated simultaneously by the addition of base. Another two-step approach has been described that is comprised of IONP synthesis by a coprecipitation method, followed by coating with PEG by the addition of PEG solution to an iron oxide suspension and stirring for 24 h [49]. PEG hydrogel–coated IONPs have been prepared by surface-initiated photopolymerization reactions [50].

In this process, a prepolymer solution composed of PEG, accelerator, initiator, and water and then exposed to green light using an argon ion laser to initiate the photopolymerization reaction.

12.4.2 Polyvinyl Alcohol

PVA is another popular coating material used usually for biomedical applications, for several reasons. First, it is biocompatible and hydrophilic in nature. Second, it has low toxicity and resists the aggregation of nanoparticles in a biological environment [45]. In addition, synthesis procedures in the presence of PVA lead to the formation of monodispersed particles. The multihydroxyl structure of PVA results in its enhanced crystallinity, culminating in necessary thermomechanical properties like high elastic modulus, crystallinity, and tensile strength in bioapplications [45]. PVA has the interesting property of retaining its elastic modulus even with high water content in hydrogels. Therefore, it is appropriate for a number of applications ranging from drug delivery to wound healing [51]. It has been shown that PVA-coated IONPs have drawbacks in tissue penetration [52].

12.4.3 Chitosan

Chitosan is a cationic polysaccharide having structural similarities with cellulose. It is made up of 2-amino-2-deoxy-H-D-glucan linked with glycosidic linkages. Owing to the presence of primary amine groups, chitosan has a great importance in pharmaceutical applications. Its mucoadhesive property and positive charge have made it attractive for drug delivery applications. Chitosan is not water-soluble in basic or neutral pH conditions, whereas in acidic pH with amino groups being protonated, chitosan becomes water-soluble. Chitosan does not elicit an allergic reaction and is regarded as biocompatible. It is capable of biodegradation, leading to the formation of nontoxic amino sugars [9]. It has found applications in affinity protein purification and magnetic bioseparation. Owing to these features, chitosan-coated IONPs are regarded as promising candidates for tissue engineering applications [53].

There are a number of studies on chitosan-coated IONPs for biomedical applications. Chitosan-coated nanoparticles synthesized by a controlled coprecipitation method yielding particles 12 nm in size showed superparamagnetic properties and were therefore suitable for biomedical applications. Another study reported the synthesis of IONPs coated with chitosan followed by modification of the surface of the particles with PVA [54]. This hybrid coating system had low protein adsorption because of its surface zeta potential and is regarded as a promising candidate for in vivo drug delivery applications.

12.4.4 Dextran

Dextran is an essential material that has been used for coating IONPs for fundamental applications like MRI, cancer imaging, and cancer treatments [42]. Dextran coating on SPIONs has been clinically approved in the MRI of liver [55]. Dextran, although biocompatible in nature, is not degradable in the human body since dextranase, the enzyme degrading dextran, cannot be synthesized by human cell lines [56]. One of the disadvantages of dextran coating is the formation of weak bonds with IONP surfaces, which affects applications negatively [42]. Another disadvantage of dextran is its unfavorable effect on compound tolerance, which leads to limited infusion in a slow process [57].

Various reports about the dextran coating of IONPs for biomedical applications are available in the literature. Dextran-coated monocrystalline IONPs have been used for the intracellular magnetic labeling of various target cells [58]. IONPs were treated with epichlorohydrin to crosslink dextran preventing dissociation under certain biological conditions. Further functionalization of the surface was also carried out by ammonia. The derivatized particles were found to be internalized into cells over 100-fold more efficiently than nonmodified particles [58]. In another study, the synthesis of dextran-coated IONPs conjugated with bombesin was produced as a targeting contrast agent for breast cancer imaging using MRI. A one-step coprecipitation method was used for the synthesis of 6 nm dextran-coated IONPs where dextran was mixed with iron salts, which were precipitated with ammonia. The system was shown to possess good diagnostic advantage in mice with breast tumors [59].

12.5 Biomedical Applications

Over the past 20 years, IONPs have been used for various biomedical applications, including MRI, tissue repair, detoxification of biological fluids, immunoassays, hyperthermia, drug delivery, gene delivery, cell tracking, bioseparation, cell separation, and manipulation of cellular organelles. In recent years, new techniques have been used to functionally acclimatize nanoparticles for clinical applications. In this chapter, these approaches, their current limitations, and developments have been explained in detail.

12.5.1 Imaging Applications of IONPs

12.5.1.1 Photoacoustic Imaging

In the past few decades, fluorescence and bioluminescence imaging have been used mostly in vivo to envisage biological tissues. The limitation of these systems

is due to their attaining simultaneously high spatial resolution and adequate penetration depth [60]. Photoacoustic imaging (PAI), also called optoacoustic or thermoacoustic imaging, is a potential new area with the prospect of overcoming this limitation.

The photoacoustic effect, which is the basis of PAI, was first reported by Alexander Graham Bell in 1880 by the recognition of sound produced by light [61]. The photoacoustic effect in this context refers to the production of ultrasound (acoustic) waves following the adsorption of electromagnetic radiation by tissue chromophores, and these ultrasound waves in turn generate images of tissues based on the extent of the optical absorption [60]. In this way a depth of a few centimeters with a scalable spatial resolution is possible, which offers elevated contrast and greater spatial resolution at the same time. However, the photoacoustic effect has developed widely in the last decade for biomedical applications like breast, skin, and cardiovascular system imaging [61].

In an ideal PAI, the optical absorption of the preferred object needs to be enhanced for better image contrast, while for deeper signal dissemination, the optical absorption of normal tissues must be low [62]. Many studies have focused on finding contrast agents, and currently contrast agents are considered to be of two types: endogenous and exogenous. The most popular endogenous agents are melanin and hemoglobin [63, 64]. Indocyanine green (ICG), gold nanoparticles, single wall nanotubes (SWNTs), quantum dots (QDs) and fluorescent proteins were reported as the most widespread exogenous contrast agents [62, 65].

The benefits of using endogenous agents for imaging are their safety and ability to demonstrate proper physiological conditions. Endogenous agents cannot be used for visualization of nonvascularized tissues, although they are capable of visualizing vasculature tissues [60]. Furthermore, they are insufficient for the recognition of early-stage tumors [62]. As a result, exogenous contrast agents like gold nanoparticles are essential for improved PAI. Note that most frequently used exogenous agents have limitations in accomplishing efficient and precise targeting [60].

For this purpose, gold-coated IONPs are useful for preparing dual mode nanoparticle having ability for photoacoustic imaging with MRI simultaneously [66]. The shell thickness and surface properties of IONPs must be regulated accurately since they establish magnetic attraction, photon scattering, near-infrared (NIR) absorption, and added biomolecular conjugation [67].

Many studies have proposed the direct coating of gold onto IONPs [68]. For example, hybrid nanoparticles with an iron oxide core and a gold nanoshell have been synthesized and characterized [69]. These nanoparticles showed superparamagnetic properties and a significant absorbance in the NIR region, which is essential for successful PAI. It has been demonstrated that gold coating on IONPs normally produces particles larger than 100–200 nm in diameter with uneven surfaces, which negatively influences the MRI response [67]. These observations led to the recent report of a synthesis of SPIONPs coated with a gold shell by generating a gap between the core and the shell [67]. The results illustrated that these nanoparticles are bestowed with extremely integrated characteristics, including

electronic, magnetic, optical, acoustic, and thermal properties. This strategy created a contrast agent with excellent MRI and PAI capabilities, and the procedure is known as magnetomotive photoacoustic (mmPA) imaging.

12.5.1.2 Magnetic Resonance Imaging

The past decade has seen increased applications of MRI. However, MRI agents need to enhance image contrast among normal and diseased tissue in order to distinguish healthy tissues from pathological ones. A variety of contrast agents have been proposed. So far, paramagnetic contrast drugs, such as paramagnetic gadolinium chelates, have been exploited in MRI experiments [70]. These drugs are known to function by shortening the T1 relaxation time (longitudinal relaxation time) of water in tissues. Alternatively, superparamagnetic nanoparticles enhance diagnostic specificity and sensitivity owing to their finer properties, for instance higher molar relaxivities and ability to reduce both T1 relaxation time and T2 transversal relaxation time [71]. The competence of these particles is determined by their size, charge, and coating material, and they can be improved by the additional alteration of their surface properties using certain biologically active materials such as specific antibodies, receptor ligands, polysaccharides, and proteins [72, 73].

A few SPIONs, such as Feridex, Resovist, Sinerem, and Clariscan, were accepted for clinical applications some time ago [74]. Feridex with dextran coating (hydrodynamic size 120 nm) has been reported to be used for cellular labeling and liver imaging. Resovist, coated with carboxydextran (hydrodynamic size 60 nm), has been utilized for liver imaging. Sinerem has found several applications, such as in the imaging of metastatic lymph nodes, areas of macrophages, and as blood pool material. The size of Sinerem lies between 15 and 30 nm together with its dextran coating. Clariscan has also been used in blood pooling and has a coating of around 20 nm of PEGylated starch [9]. However, these commercial contrast agents cannot be altered further for tissue targeting purposes. At present, several studies have focused on generating novel MRI contrast materials, where a number of approaches have been used to attain the requisite targeting capability [75, 76]. For example, a superparamagnetic MRI contrast agent coated with dextran has been used to target endothelial inflammatory adhesion molecule E-selectin [77]. The use of a synthetic mimetic of sialyl Lewisx, a natural ligand of E-selectin expressed in leukocytes, further functionalized the contrast agent in vitro (on cultured human umbilical vein endothelial cells) and in vivo (on a mouse model of hepatitis).

A new MRI contrast drug for in vivo cancer imaging was reported recently. The contrast agent was designed to contain an antibiofouling polymer that is thermally cross-linked with SPIONs (Fig. 12.1) but holds no targeting ligands on its surface. This agent has been found to accumulate in tumor cells [78]. Surface coating layers on the nanoparticle enhance permeability and retention, providing significant tumor detection. This new contrast material has been demonstrated to deliver anticancer drugs to tumors with high competence. Therefore, it has proven useful as a drug delivery carrier, which may be advantageous equally for cancer imaging and therapy.

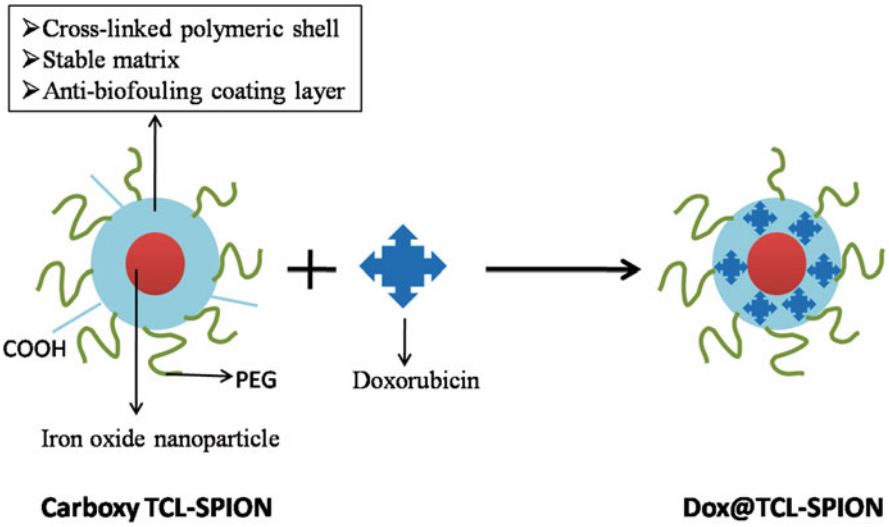

Fig. 12.1 Schematic diagram showing drug-conjugated antibiofouling polymer coated with thermally cross-linked SPIONs

In vivo experiments on animal models established that elevated amounts of SPIONs accumulated in the tumor microenvironment, and drug release kinetics in vitro proved that within 50 min 60% of the drug was released.

The synthesis of multifunctional SPIONs was reported and found use in targeted drug delivery and positron emission tomography (PET)/MRI [79]. Doxorubicin (DOX), cRGD, PET 64Cu chelators, and tumor targeting ligands were linked onto PEGylated SPIONs. The efficacy of this structure as a contrast agent for MRI was examined in an in vitro study using MRI relaxivity. Interestingly, these new contrast agents could assemble in the tumor region in greater amounts compared with free cRGD, the MRI relaxivity being comparable to that of Feridex. These multifunctional SPIONs can be exploited for both cancer therapy and PET/MRI [79]. Moreover, in vivo experiments demonstrated that 64Cu-labeled cRGD-conjugated SPIO nanocarriers gathered in the tumor region but not in normal tissues.

12.5.2 Drug Delivery

The limitations in drug delivery involve the absorption of hydrophobic drugs as well as site-specific targeting of the drug. Targeted delivery depends on the improved efficacy and biocompatibility of the drug. As a result, the design of appropriate delivery vehicles for drug release at specific sites and significant absorption of the drug by specific cells will be crucial advancements in therapeutics. Nanoparticle-based drug delivery is emerging as a growing field due to its remarkable features,

like small size, along with the strong physical properties of the nanomaterials [72, 80]. The superparamagnetic behavior of nanoparticles depends on their size. Another vital aspect of SPIONs is the lack of permanent magnetization, which helps nanoparticles to preserve their colloidal stability [81]. Since a critical level of magnetization is necessary for biomedical applications, there needs to be a tradeoff between the minimum size to prevent aggregation but still have enough magnetization to retain the magnetic application [81]. Nanoparticles, because of their small size, can easily penetrate into peripheral tissue with effective enhanced permeation and retention (EPR), especially in the case of cancer [81]. The penetration power of nanoparticles through leaky vasculatures can be used for the design of drug targeting vehicles. Nanoparticles can be encapsulated with therapeutic molecules through surface attachment or entrapment [82]. Other advantages include the reduction of multidrug resistance (MDR), which occurs especially for hydrophobic drugs. MDR is caused by an ATP binding cassette (ABC), which is a transporter generally overexpressed in cancer cells, that pumps hydrophobic drugs out. SPIONs can be used in conjunction with DOX to overcome MDR as well as to increase the efficacy of drug delivery [83].

For the delivery of magnetic nanoparticles, one must use either magnetic force or passive targeting strategy. Passive targeting is effected using the reticuloendothelial system (RES), a very important clearance system in the body. As bare nanoparticles enter the body, they are exposed to opsonins, which are plasma proteins identifying nonself structures, and nanoparticles, because of their high surface tension, readily attach to opsonins. The extent of attachment depends on the nanoparticle size, shape, and aggregation state and the surface charge. For example, nanoparticles greater than 250 nm are cleared readily by RES clearance and move from the bloodstream into the spleen [81]. Further, nanomaterials 10–100 nm in size are cleared by liver cells, while nanoparticles of less than 10 nm are cleared renally [84]. The optimal size range of nanoparticles for drug delivery applications has been suggested to be 10–100 nm because the bloodstream clearance time for this size range is higher compared to other sizes of nanomaterials [81].

Active targeting means the functionalization of nanoparticles by different targeting agents [85]. The procedure consists of the adhesion of coating/targeting molecules to the structure followed by the loading of drugs. There are different ways of loading, for example, covalent conjugation or physical adsorption [81]. In one of the early clinical trial and release studies, human serum albumin microspheres coated with magnetite-containing doxorubicin were used as anticancer agent [86]. Later, these trials continued with epidoxorubicin-conjugated magnetic nanoparticles [87].

For improved colloidal stability, various nanoparticle stabilizers with adequate biocompatibility have been used. Organosilane molecules with amine groups such as (3-aminopropyltriethoxysilane) APTES and APTMS are some examples [82]. Other compounds, like silica derivatives, which are chemically inert, have not been used in biological applications.

There are various studies on drug conjugation on SPIONs, especially IONPs, involved in both imaging and drug delivery. SPIONs functionalized with reversibly bound drugs have the potential to be delivered to specific sites [46]. The synthesis of IONPs having a dimension of 10 nm and with enormous colloidal stability is by functional polymers capable of attaching DOX through a pH-sensitive imine bond formation [88]. This bond cleaves in acidic pH, making the nanomachine suitable for potential targeting in a tumor environment, which is acidic in nature. Two- and three-dimensional cell models of IONP uptake and intracellular release of DOX demonstrate that this MRI negative contrast drug is suitable for both diagnosis and therapy. The delivery of antibiotics like ofloxacin and ciprofloxacin from APTES-coated IONPs has been demonstrated [82]. Further, starch derivative–covered IONPs functionalized with phosphate groups have been used in chemotherapy that targeted mitoxantrone to the tumor site [89]. In addition, other nanocomposite designs are found in the literature, where SPIONs and quantum dots find application in the targeted delivery of camptomicin, an anticancer agent [90].

In recent times, an insulin-loaded iron oxide–chitosan nanohybrid has been synthesized and the prospective drug delivery potential of the nanomaterial was examined through an oral delivery route for the management of type II diabetes [91]. Interestingly, the insulin-loaded iron oxide–chitosan nanocomposite could lower blood glucose levels by more than 51% in mild diabetic, subdiabetic, and severely diabetic rats. Another report showed promising results for hybrid magnetic nanogels composed of SPIONs modified by chitosan and CdTe quantum dots [92]. Spherical hybrid nanogels smaller than 160 nm were utilized for insulin delivery and found to be promising for insulin delivery as well as for cell imaging purposes.

The molecular markers overexpressed in cancer cells can be utilized for specific targeting strategies. For example, in breast cancer cells, HER2 receptors are overexpressed, and conjugation of anti-HER2 antibody onto nanoparticle surfaces was used for selective targeting [93]. Similarly, folic acid has been used for targeting HeLa and MCF7 cells [94]. Tumor endothelial cells are known to express cell surface receptors for angiogenesis [46]. One such target, avb3 integrin, plays a key role in endothelial cell survival during angiogenesis. Ligands like Arg-Gly-Asp (RGD) peptide for targeting avb3 integrin on cell surface have been utilized for SPION attachment [46]. CREKA also targets fibrin and is found mostly around tumor areas in the case of selected tumor types [95].

12.5.3 Cell Tracking

Specific cell tracking could be another possible application of IONPs. To label and track cells under in vivo conditions, adequate quantities of magnetic nanoparticles must be introduced into the cultured cells. Under these conditions, cell tracking can be obtained at a resolution close to the size of the cell. This requires the conjugation of cell-permeable peptides or transfection agents onto the negatively charged surface of the nanoparticles [9]. To enhance SPION uptake by cells, nanoparticles can be

additionally functionalized with some specific peptides, or peptides coated with dendrimers, which increase cellular internalization [96, 97]. Stem cell tracking and tracking of immune cells and (T) lymphocytes have been demonstrated by this technology [98].

IONPs having a diameter of around 50 nm have been synthesized with silica coating. For proper labeling and tracking of human mesenchymal stem cells (hMSCs), fluorescein isothiocyanate (FITC)-conjugated IONPs were prepared. The labeling was performed by clathrin- and actin-dependent endocytosis followed by intracellular localization in late endosomes/lysosomes [99]. These bifunctionalized nanoparticles can generate adequate MRI contrast, while the viability and proliferation of the labeled stem cells are unaltered. Another report suggests labeling and tracking mesenchymal stem cells (MSCs) and hematopoietic (CD34+) stem cells through ferumoxide–protamine sulfate complexes. The authors demonstrated that labeled cells showed no short- or long-term toxicity and showed comparable cell proliferation with unlabeled cells [100].

MRI cell tracking of rat T-cells under in vivo conditions was carried out by labeling them with superparamagnetic dextran-coated iron oxide particles [101]. Tissue inflammation was induced, which attracted labeled T-cells by adding calcium ionophore. This study provided the first of its kind of a successful cell tracking in vivo by MRI. The experiments of immune cell tracking is comprised of additional targeted strategies with additional functionalization through transfection agents. In this way, T-cells were tracked in vivo by introducing SPIONs derivatized with a peptide sequence from transactivator protein (Tat) of HIV-1 into cells [102]. MRI, fluorescence-activated cell sorting, and biodistribution analysis demonstrated that T-cells were proficiently labeled and tracked with these superparamagnetic agents with no alteration of their normal activation.

12.5.4 Magnetic Fluid Hyperthermia

Magnetic fluid hyperthermia (MFH), where an alternating magnetic field is used to release a drug to the proper site, has often been used for cancer therapy. This alternating field generates heat, which effectively releases the drug inside tissue or cells and sometimes the heat affects the cellular mechanism, resulting in the destruction of the solid tumor. A hyperthermia agent serves as energy absorber to convert into cytotoxic heat energy and specifically destroy tumor cells since tumor cells are more vulnerable to heat compared to healthy cells [103]. Hence, for the treatment of tumor cells, magnetic nanoparticles have great importance. The magnetic induction of magnetic nanoparticles can be done by irradiation with microwaves, sound waves, and radio frequency waves [104]. The magnetic moments of superparamagnetic nanoparticles are free to fluctuate in response to thermal energy owing to their single-domain low energy state, and this makes them suitable for hyperthermia applications. Their small size and unique magnetic properties make SPIONs promising candidates. The Curie temperature, the temperature at

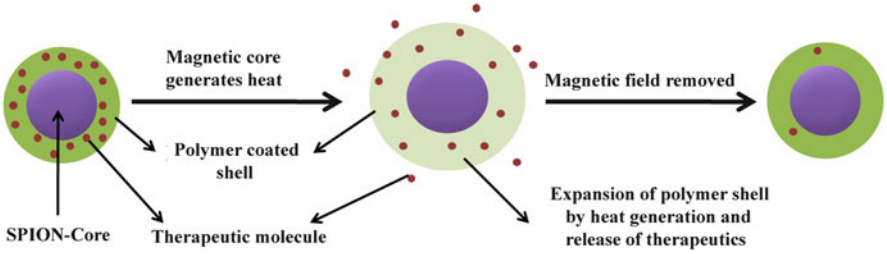

Fig. 12.2 Schematic diagram of drug release mechanism during hyperthermia treatment

which magnetic materials lose their permanent magnetic properties and convert to diamagnetic materials, is almost 100 °C for SPIONs [89]. However, SPIONs are essentially coated with PEG/PVA/chitosan/dextran/aminosilane to cope with biocompatibility issues [45, 105].

The first hyperthermia experiment exploiting paramagnetic materials dates back to 1957. In that early experiment, a 1.2 MHz magnetic field was utilized for IONPs to achieve a size of up to 100 nm [106]. A regional hyperthermia application was run clinically on prostate cancer and considered to be a first trial [107]. Later on, microparticles of iron oxide doped with yttrium were used for MRI combined with hyperthermia to treat liver cancer [108].

Hyperthermia management combined with drug release was performed using folic acid and beta cyclodextrin–functionalized IONPs [109]. The drug was fit into the system (Fig. 12.2) using beta cyclodextrin through hydrophobic interactions. The release of the drug was affected by applying high-frequency magnetic fields that heated the system up to 42–45 °C. This helped to depress the hydrophobic interaction between the drug and beta cyclodextrin, thereby releasing the drug. Therefore, in this temperature range, both drug and hyperthermia treatments occur concurrently [109].

Further, hyperthermia has some restrictions. First, hyperthermia is more successful as a local application instead of a regional one. Second, the application is only promising at a fixed temperature range of 42–45 °C for local hyperthermia [110]. Also, the released heat should be such as to target a specific site rather than healthy cells. Thus, optimizations of the size and colloidal stability of nanoparticles are critical for clinical application of magnetic fluid hyperthermia therapy [110, 111].

12.5.5 Gene Delivery

Gene delivery can be done using viral or nonviral vectors. Viral vectors, owing to their toxicity and severe immune response, are not favored in general. Nonviral gene delivery strategies, like needle and jet inoculation, hydrodynamic gene transfer, gene gun, electroporation, and sonoporation, are not competent enough for transfer of

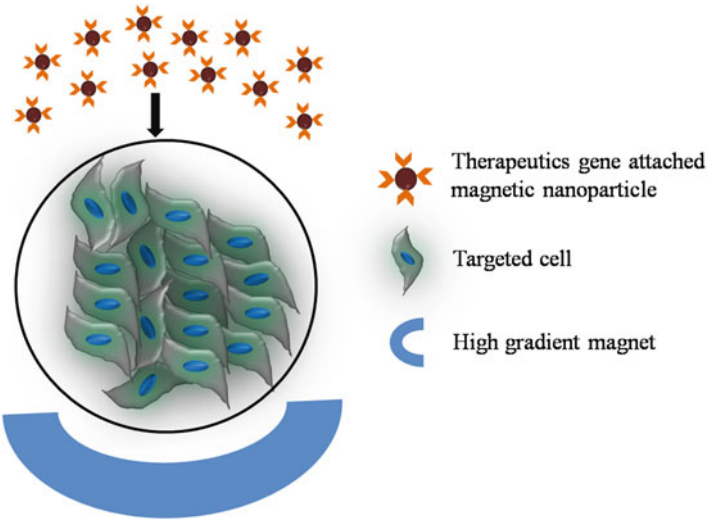

Fig. 12.3 Schematic representation of external magnetic field–directed gene delivery in vitro using magnetic nanoparticles

genes [112]. Gene therapy has been applied primarily for genetic disorder–related diseases, especially for immune system–linked diseases, for example, chronic granulomatus disorder and severe combined immune deficiency, for neurodegenerative disorders like Parkinson's disease and Huntington disease, and in a range of cancers [113]. The aim of gene delivery is to replace or silence the defective gene causing the disease. The constraints are on the delivery of genes to the specific target, and there is difficulty in examining the subsequent target response [114].

Recently, magnetic nanoparticles have emerged as a promising candidate for gene delivery, both in vitro and in vivo. The strategy, known as magnetofection, has been employed by linking therapeutic genes onto magnetic nanoparticles, which are then targeted to specific sites through high gradient external magnetic fields (Fig. 12.3) [115]. This specific system has two benefits in vivo, first by facilitating external magnetic field–induced sedimentation, and second, by external magnetic field–directed targeting of tumor sites for gene delivery. Magnetic nanoparticles release genes either by enzymatic degradation or by hydrolysis of the polymer coating around the nanocore [115]. IONPs are capable of gene transfection at targeted sites by external magnetic induction [116]. For the binding of negatively charged plasmids, positively charged coating materials, such as PVA, polyethylenimine (PEI), and chitosan, have been used [117]. For example, for targeted delivery of DNA from magnetic nanoparticles, adeno-associated virus (AVV), encoding green fluorescent protein (GFP), and a cleavable heparin sulfate linker have been used [118].

12.5.6 Bioseparation

Magnetic separation is widely utilized in biotechnology, and in recent times it has been the most useful application of magnetic nanoparticles. Quite a few magnetic nanoparticle types have been synthesized for this purpose, but novel and advanced techniques, which can be used in the case of dilute solutions of targeted molecules, must be explored [119]. SPIONs have been used in a magnetic separation technique for the separation of proteins and cells. Traditional separation techniques, for example, various chromatography techniques and ultrafiltration, are more complex and costly in comparison to magnetic separation processes. Additionally, a purification process in the magnetic separation technique with SPIONs can be achieved with only one test tube, resulting in great simplicity in comparison to other procedures [9].

In the magnetic separation procedure, affinity ligands to attract specific targets are immobilized on the surface of nanoparticles. Then, the addition of target molecules to the sample will lead to purification or separation. Following an incubation period, magnetic nanoparticles attach to the specific target molecule and subsequently be simply extracted from the sample with an external magnetic field (Fig. 12.4) [119]. The beauty of this technique lies in its direct application to crude materials and its efficient separation of small particles. For protein isolation,

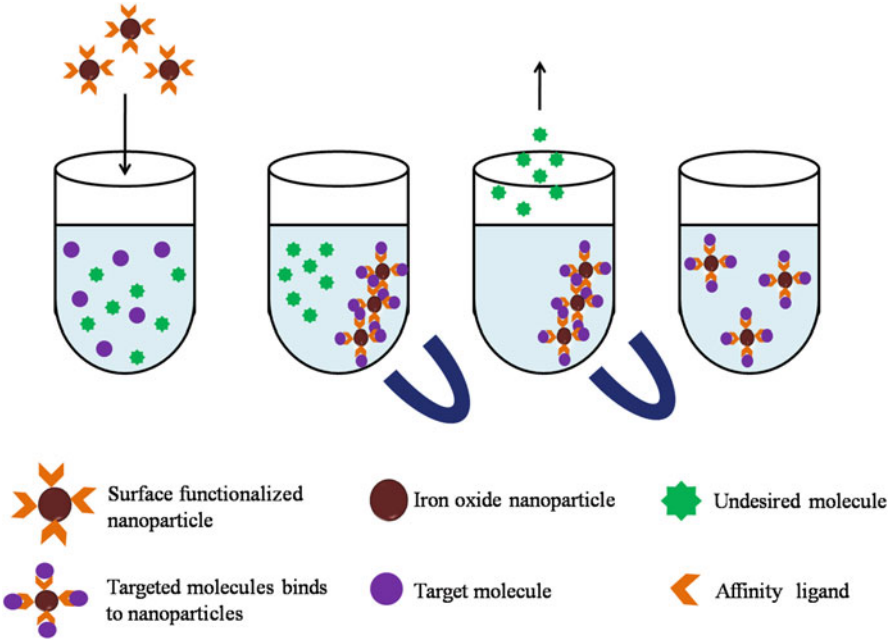

Fig. 12.4 Schematic representation showing external magnetic field directed separation

the affinity ligands are streptavidin, nitrilotriacetic acid, antibodies, proteins A and G, trypsin, and trypsin inhibitor [120]. A small permanent magnet can be enough, though stronger rare-earth magnets are also commercially available [119].

For the isolation of avidin protein, superparamagnetic γ-Fe_2O_3 nanoparticles have been synthesized via a site-exchange reaction [121]. Oleic acid–protected nanoparticles were further functionalized with charged bipyridinium carboxylic acids and biotin. Bipyridinium significantly improved the water solubility of nanoparticles, while biotin, which has high affinity for avidin, was utilized for surface localization. A new method for the transformation of cells followed by the selection of transformed cells using a magnetite cationic liposome (MCL)/DNA complex has been reported. Here, MCLs were associated with a plasmid vector, and the transformants were detached with an external magnetic field [122].

12.5.7 Tissue Repair

Wound healing in the body involves the joining of tissues at the damaged site, and the generation of tissue rejoining is facilitated by temperatures greater than 55 °C [123]. Laser systems are currently being used to induce heat inside tissues, which, however, leads to tissue necrosis in the applied region [124]. To minimize tissue damage, less harmful wavelengths and low-power lasers must be employed [56]. In this connection emerged the use of IONPs for tissue repair, and this procedure is known as soldering or welding. In this technology, two tissue surfaces are brought near, and then the merging of the tissues is increased by placing IONPs in between, and finally the requisite amount of heat is supplied to the tissue-nanoparticle system. It is desirable to use gold or silica coatings because there is strong absorbance of light. In this way, wavelengths causing minimum harm to tissues and higher-wavelength lasers have been used.

12.5.8 Manipulation of Cellular Organelles

The magnetic manipulation of cellular organelles finds application in management from a distance without making contact. Nanoparticles are functionalized with particular targeting agents for precise recognition by an organelle. It is essentially an attractive approach because it provides information on cell function and inherent signaling pathways. The manipulation of cytoskeleton, lysosomes, and mitochondria through IONPs has been discussed in this chapter because these organelles were commonly considered for targeting purposes in previous studies.

The first example of organelle manipulation via IONPs is cytoskeleton manipulation. The structure of a cell is maintained by microtubules, the primary component of cytoskeleton, which is again regulated by a signaling pathway called Ran/RCC1. This was shown by conjugating IONPs with a regulatory protein,

RanGTP. Experiments were done with *Xenopus laevis* egg extracts, and it was shown that in the presence of a magnetic field, the direction of the microtubule fibers was determined by the direction of the external magnetic lines of force.

Lysosome is another organelle that can be manipulated by IONPs. When lysosome membrane permeability exceeds a critical value, cell death occurs. This phenomenon can be effectively utilized for killing cancer cells. IONPs 14 nm in size have been synthesized and coated with proteins recognizing the epidermal growth factor receptor (EGFR) [125]. EGFR is overexpressed in cancer cells, making it a suitable target. IONPs coated with target proteins were fast internalized in the lysosomes of cancer cells. When an alternating magnetic field is applied externally, IONPs cause heating of the lysosomes, eventually damaging the lysosomal membranes, which increased permeability and, finally, bring about cell death [125].

Another important organelle manipulated by IONPs is mitochondria. Mitochondria play significant roles in signaling, cellular differentiation, cell death, and growth. Therefore, the manipulation of mitochondria may lead to treatment for many diseases, including cancer. IONPs 50 nm in diameter coated with cytochrome c-specific binding aptamers have been synthesized for this purpose [126]. When these particles were inoculated in HeLa cells, they were all found to be targeted specifically to mitochondria and internalized rapidly. In the presence of an external static magnetic field, the viability of cancer cells diminished significantly [126].

12.6 Conclusion

In this chapter, we have summed up the functions of IONPs in biomedical applications. The exploitation of IONPs in PAI, MRI, drug delivery, cell tracking, magnetic fluid hyperthermia, gene delivery, bioseparation, tissue repair, and the manipulation of cellular organelles has been discussed in depth. Although remarkable progress has been made with the exploitation of IONPs, wide-ranging investigations are needed for long-term toxicity studies and clinical trials. The destinies of IONPs following in vivo treatment, like the exclusion route and retention time in specific organs, are a field of interest.

References

1. Mandal S, Hossain M, Devi PS, Kumar GS, Chaudhuri K (2013) Interaction of carbon nanoparticles to serum albumin: elucidation of the extent of perturbation of serum albumin conformations and thermodynamical parameters. J Hazard Mater 15:238–245
2. Mandal S, Hossain M, Muruganandan T, Kumar GS, Chaudhuri K (2013) Gold nanoparticles alter Taq DNA polymerase activity during polymerase chain reaction. RSC Adv 3:20793–20799

3. Bridot J-L, Faure A-C, Laurent S, Riviere C, Billotey C, Hiba B et al (2007) Hybrid gadolinium oxide nanoparticles: multimodal contrast agents for in vivo imaging. J Am Chem Soc 129(16):5076–5084
4. Sun S, Zeng H, Robinson DB, Raoux S, Rice PM, Wang SX et al (2004) Monodisperse MFe_2O_4 (M=Fe, Co, Mn) nanoparticles. J Am Chem Soc 126(1):273–279
5. Mandal S, Chaudhuri K (2012) A Simple method for the synthesis of ultrafine carbon nanoparticles and its interaction with bovine serum albumin. Adv Sci Lett 5(1):139–143
6. Gupta AK, Curtis ASG (2004) Lactoferrin and ceruloplasmin derivatized superparamagnetic iron oxide nanoparticles for targeting cell surface receptors. Biomaterials 25(15):3029–3040
7. Mahmoudi M, Simchi A, Imani M (2010) Recent advances in surface engineering of superparamagnetic iron oxide nanoparticles for biomedical applications. J Iran Chem Soc 7(2):S1–S27
8. Lin C-W, Tseng SJ, Kempson IM, Yang S-C, Hong T-M, Yang P-C (2013) Extracellular delivery of modified oligonucleotide and superparamagnetic iron oxide nanoparticles from a degradable hydrogel triggered by tumor acidosis. Biomaterials 34(17):4387–4393
9. Laurent S, Forge D, Port M, Roch A, Robic C, Vander Elst L et al (2008) Magnetic iron oxide nanoparticles: synthesis, stabilization, vectorization, physicochemical characterizations, and biological applications. Chem Rev 108(6):2064–2110
10. Sonvico F, Mornet SP, Vasseur SB, Dubernet C, Jaillard D, Degrouard J et al (2005) Folate-conjugated iron oxide nanoparticles for solid tumor targeting as potential specific magnetic hyperthermia mediators: synthesis, physicochemical characterization, and in vitro experiments. Bioconjug Chem 16(5):1181–1188
11. Nasongkla N, Shuai X, Ai H, Weinberg BD, Pink J, Boothman DA et al (2004) cRGD-functionalized polymer micelles for targeted doxorubicin delivery. Angew Chem Int Ed Engl 43(46):6483–6487
12. Dias A, Hussain A, Marcos AS, Roque ACA (2011) A biotechnological perspective on the application of iron oxide magnetic colloids modified with polysaccharides. Biotechnol Adv 29(1):142–155
13. Basuki JS, Esser L, Duong HTT, Zhang Q, Wilson P, Whittaker MR et al (2014) Magnetic nanoparticles with diblock glycopolymer shells give lectin concentration-dependent MRI signals and selective cell uptake. Chem Sci 5:715–726
14. Kralj S, Rojnik M, Jagodič M, Kos J, Makovec D (2012) Effect of surface charge on the cellular uptake of fluorescent magnetic nanoparticles. J Nanopart Res 14:1–14
15. Lu AH, Salabas EL, Schüth F (2007) Magnetic nanoparticles: synthesis, protection, functionalization, and application. Angew Chem Int Ed Engl 46(8):1222–1244
16. Johnson SH, Johnson CL, May SJ, Hirsch S, Cole MW, Spanier JE (2009) Co@ CoO@ Au core-multi-shell nanocrystals. J Mater Chem 20:439–443
17. Grass RN, Stark WJ (2006) Gas phase synthesis of fcc-cobalt nanoparticles. J Mater Chem 16:1825–1830
18. Shafi KVPM, Ulman A, Yan X, Yang N-L, Estournes C, White H et al (2001) Sonochemical synthesis of functionalized amorphous iron oxide nanoparticles. Langmuir 17(16):5093–5097
19. Sjøgren CE, Briley-Saebø K, Hanson M, Johansson C (1994) Magnetic characterization of iron oxides for magnetic resonance imaging. Magn Reson Med 31(3):268–272
20. Jiang W, Yang H-C, Yang S-Y, Horng H-E, Hung JC, Chen YC et al (2004) Preparation and properties of superparamagnetic nanoparticles with narrow size distribution and biocompatible. J Magn Magn Mater 283(2–3):210–214
21. Gupta AK, Wells S (2004) Surface-modified superparamagnetic nanoparticles for drug delivery: preparation, characterization, and cytotoxicity studies. IEEE Trans Nanobioscience 3(1):66–73
22. Wang X, Zhuang J, Peng Q, Li Y (2005) A general strategy for nanocrystal synthesis. Nature 437:121–124
23. Peng X, Wickham J, Alivisatos AP (1998) Kinetics of II–VI and III–V colloidal semiconductor nanocrystal growth: "Focusing" of size distributions. J Am Chem Soc 120(21):5343–5344

24. Samia ACS, Hyzer K, Schlueter JA, Qin C-J, Jiang JS, Bader SD et al (2005) Ligand effect on the growth and the digestion of Co nanocrystals. Am Chem Soc 127(12):4126–4127
25. Li Y, Afzaal M, O'Brien P (2006) The synthesis of amine-capped magnetic (Fe, Mn, Co, Ni) oxide nanocrystals and their surface modification for aqueous dispersibility. J Mater Chem 16:2175–2180
26. Farrell D, Majetich SA, Wilcoxon JP (2003) Preparation and characterization of monodisperse Fe nanoparticles. Phys Chem B 107(40):11022–11030
27. Sun S, Zeng H (2002) Size-controlled synthesis of magnetite nanoparticles. J Am Chem Soc 124(28):8204–8205
28. Li Z, Kawashita M, Araki N, Mitsumori M, Hiraoka M, Doi M (2011) Preparation of magnetic iron oxide nanoparticles for hyperthermia of cancer in a $FeCl_2$-$NaNO_3$-NaOH aqueous system. J Biomater Appl 25(7):643–661
29. Park J, Lee E, Hwang NM, Kang M, Kim SC, Hwang Y et al (2005) One-nanometer-scale size-controlled synthesis of monodisperse magnetic Iron oxide nanoparticles. Angew Chem Int Ed Engl 44(19):2932–2937
30. Li Z, Sun Q, Gao M (2004) Preparation of water-soluble magnetite nanocrystals from hydrated ferric salts in 2-pyrrolidone: mechanism leading to Fe_3O_4. Angew Chem Int Ed Engl 44(1):123–126
31. Hu FQ, Wei L, Zhou Z, Ran YL, Li Z, Gao MY (2006) Preparation of biocompatible magnetite nanocrystals for in vivo magnetic resonance detection of cancer. Adv Mater 18(19):2553–2556
32. Rosensweig RE (2002) Heating magnetic fluid with alternating magnetic field. J Magn Magn Mater 252:370–374
33. Dumestre F, Chaudret B, Amiens C, Renaud P, Fejes P (2004) Superlattices of iron nanocubes synthesized from Fe $[N(SiMe_3)_2]_2$. Science 303(5659):821–823
34. Song Q, Zhang ZJ (2004) Shape control and associated magnetic properties of spinel cobalt ferrite nanocrystals. J Am Chem Soc 126(19):6164–6168
35. Puntes VF, Krishnan KM, Alivisatos AP (2001) Colloidal nanocrystal shape and size control: the case of cobalt. Science 291(5511):2115–2117
36. Dumestre F, Chaudret B, Amiens C, Respaud M, Fejes P, Renaud P et al (2003) Unprecedented Crystalline Super-Lattices of Monodisperse Cobalt Nanorods. Angew Chem Int Ed Engl 42(42):5213–5216
37. Cordente N, Respaud M, Fo S, Casanove M-J, Amiens C, Chaudret B (2001) Synthesis and magnetic properties of nickel nanorods. Nano Lett 1(10):565–568
38. Sun S, Murray CB, Weller D, Folks L, Moser A (2000) Monodisperse FePt nanoparticles and ferromagnetic FePt nanocrystal superlattices. Science 287(5460):1989–1992
39. Tegus O, Brük E, Buschow KHJ, De Boer FR (2002) Transition-metal-based magnetic refrigerants for room-temperature applications. Nature 415:150–152
40. Perera SC, Tsoi G, Wenger LE, Brock SL (2003) Synthesis of MnP nanocrystals by treatment of metal carbonyl complexes with phosphines: a new, versatile route to nanoscale transition metal phosphides. J Am Chem Soc 125(46):13960–13961
41. Qian C, Kim F, Ma L, Tsui F, Yang P, Liu J (2004) Solution-phase synthesis of single-crystalline iron phosphide nanorods/nanowires. J Am Chem Soc 126(4):1195–1198
42. McCarthy JR, Weissleder R (2008) Multifunctional magnetic nanoparticles for targeted imaging and therapy. Adv Drug Deliv Rev 60(11):1241–1251
43. Ling D, Hyeon T (2013) Chemical design of biocompatible iron oxide nanoparticles for medical applications. Small 9(9–10):1450–1466
44. Nazli C, Ergenc TI, Yar Y, Acar HY, Kizilel S (2012) RGDS-functionalized polyethylene glycol hydrogel-coated magnetic iron oxide nanoparticles enhance specific intracellular uptake by HeLa cells. Int J Nanomedicine 7:1903–1920
45. Mahmoudi M, Sant S, Wang B, Laurent S, Sen T (2011) Superparamagnetic iron oxide nanoparticles (SPIONs): development, surface modification and applications in chemotherapy. Adv Drug Deliv Rev 63(1–2):24–46

46. Neuberger T, Schöpf B, Hofmann H, Hofmann M, Von Rechenberg B (2005) Superparamagnetic nanoparticles for biomedical applications: possibilities and limitations of a new drug delivery system. J Magn Magn Mater 293(1):483–496
47. Kataby G, Ulman A, Prozorov R, Gedanken A (1998) Coating of amorphous iron nanoparticles by long-chain alcohols. Langmuir 14(7):1512–1515
48. Anbarasu M, Anandan M, Chinnasamy E, Gopinath V, Balamurugan K (2015) Synthesis and characterization of polyethylene glycol (PEG) coated Fe_3O_4 nanoparticles by chemical co-precipitation method for biomedical applications. Spectrochim Acta A Mol Biomol Spectrosc 135:536–539
49. Masoudi A, Hosseini HRM, Shokrgozar MA, Ahmadi R, Oghabian MA (2012) The effect of poly (ethylene glycol) coating on colloidal stability of superparamagnetic iron oxide nanoparticles as potential MRI contrast agent. Int J Pharm 433(1–2):129–141
50. Demirer GS, Okur AC, Kizilel S (2015) Synthesis and design of biologically inspired biocompatible iron oxide nanoparticles for biomedical applications. J Mater Chem B 3:7831–7849
51. Rahman MM, Afrin S, Haque P (2014) Characterization of crystalline cellulose of jute reinforced poly (vinyl alcohol)(PVA) biocomposite film for potential biomedical applications. Progress Biomater 3:1–9
52. Zhang Y, Kohler N, Zhang M (2002) Surface modification of superparamagnetic magnetite nanoparticles and their intracellular uptake. Biomaterials 23(7):1553–1561
53. Shubayev VI, Pisanic TR, Jin S (2009) Magnetic nanoparticles for theragnostics. Adv Drug Deliv Rev 61(6):467–477
54. Shagholani H, Ghoreishi SM, Mousazadeh M (2015) Improvement of interaction between PVA and chitosan via magnetite nanoparticles for drug delivery application. Int J Biol Macromol 78:130–136
55. Zhu X-M, Wang YX, Leung KC, Lee S-F, Zhao F, Wang D-W et al (2012) Enhanced cellular uptake of aminosilane-coated superparamagnetic iron oxide nanoparticles in mammalian cell lines. Int J Nanomedicine 7:953–964
56. Gupta AK, Gupta M (2005) Synthesis and surface engineering of iron oxide nanoparticles for biomedical applications. Biomaterials 26(18):3995–4021
57. Du L, Chen J, Qi Y, Li D, Yuan C, Lin MC et al (2007) Preparation and biomedical application of a non-polymer coated superparamagnetic nanoparticle. Int J Nanomedicine 2(4):805–812. http://www.dovepress.com/articles.php?journal_id=5
58. Josephson L, Tung C-H, Moore A, Weissleder R (1999) High-efficiency intracellular magnetic labeling with novel superparamagnetic-Tat peptide conjugates. Bioconjug Chem 10(2):186–191
59. Jafari A, Salouti M, Shayesteh SF, Heidari Z, Rajabi AB, Boustani K et al (2015) Synthesis and characterization of Bombesin-superparamagnetic iron oxide nanoparticles as a targeted contrast agent for imaging of breast cancer using MRI. Nanotechnology 26(7):075101
60. Zeng L, Piao Z, Huang S, Jia W, Chen Z (2015) Label-free optical-resolution photoacoustic microscopy of superficial microvasculature using a compact visible laser diode excitation. Opt Express 23(24):31026–31033
61. Xu M, Wang LV (2006) Photoacoustic imaging in biomedicine. Rev Sci Instrum 77:041101
62. Zhang Y, Hong H, Cai W. Photoacoustic imaging. Cold Spring Harbor Laboratory Press. p. pdb. top065508.
63. Wang X, Pang Y, Ku G, Stoica G, Wang LV (2003) Three-dimensional laser-induced photoacoustic tomography of mouse brain with the skin and skull intact. Opt Lett 28(19):1739–1741
64. Oh J-T, Li M-L, Zhang HF, Maslov K, Stoica G, Wang LV (2006) Three-dimensional imaging of skin melanoma in vivo by dual-wavelength photoacoustic microscopy. J Biomed Opt 11(3):034032–034034
65. Shashkov EV, Everts M, Galanzha EI, Zharov VP (2008) Quantum dots as multimodal photoacoustic and photothermal contrast agents. Nano Lett 8(11):3953–3958
66. Luke GP, Yeager D, Emelianov SY (2012) Biomedical applications of photoacoustic imaging with exogenous contrast agents. Ann Biomed Eng 40(2):422–437

67. Jin Y, Jia C, Huang S-W, O'Donnell M, Gao X (2010) Multifunctional nanoparticles as coupled contrast agents. Nat Commun 1:41
68. Xu Z, Hou Y, Sun S (2007) Magnetic core/shell Fe_3O_4/Au and Fe_3O_4/Au/Ag nanoparticles with tunable plasmonic properties. J Am Chem Soc 129(28):8698–8699
69. Ji X, Shao R, Elliott AM, Stafford RJ, Esparza-Coss E, Bankson JA et al (2007) Bifunctional gold nanoshells with a superparamagnetic iron oxide-silica core suitable for both MR imaging and photothermal therapy. J Phys Chem C 111(17):6245–6251
70. Tartaj P, del Puerto MM, Veintemillas-Verdaguer S, González-Carreño T, Serna CJ (2003) The preparation of magnetic nanoparticles for applications in biomedicine. J Phys D Appl Phys 42(22):R182
71. Basuki JS, Esser L, Zetterlund PB, Whittaker MR, Boyer C, Davis TP (2013) Grafting of P (OEGA) onto magnetic nanoparticles using Cu (0) mediated polymerization: comparing grafting "from" and "to" approaches in the search for the optimal material design of nanoparticle MRI contrast agents. Macromolecules 46(15):6038–6047
72. Mandal S, Chatterjee N, Das S, Saha KD, Chaudhuri K (2014) Magnetic core–shell nanoprobe for sensitive killing of cancer cells via induction with a strong external magnetic field. RSC Adv 4:20077–20085
73. Basuki JS, Jacquemin A, Esser L, Li Y, Boyer C, Davis TP (2014) A block copolymer-stabilized co-precipitation approach to magnetic iron oxide nanoparticles for potential use as MRI contrast agents. Polym Chem 5:2611–2620
74. Bremerich J, Bilecen D, Reimer P (2007) MR angiography with blood pool contrast agents. Eur Radiol 17(12):3017–3024
75. Ito A, Shinkai M, Honda H, Kobayashi T (2005) Medical application of functionalized magnetic nanoparticles. J Biosci Bioeng 100(1):1–11
76. Mandal S, Chaudhuri K (2016) Engineered magnetic core shell nanoprobes: synthesis and applications to cancer imaging and therapeutics. World J Biol Chem 7(1):158–167
77. Sb B, Laurent S, Elst LV, Muller RN (2006) Specific E-selectin targeting with a superparamagnetic MRI contrast agent. Contrast Media Mol Imaging 1(1):15–22
78. Yu MK, Jeong YY, Park J, Park S, Kim JW, Min JJ et al (2008) Drug-loaded superparamagnetic iron oxide nanoparticles for combined cancer imaging and therapy in vivo. Angew Chem Int Ed Engl 47(29):5362–5365
79. Yang X, Hong H, Grailer JJ, Rowland IJ, Javadi A, Hurley SA et al (2011) cRGD-functionalized, DOX-conjugated, and 64 Cu-labeled superparamagnetic iron oxide nanoparticles for targeted anticancer drug delivery and PET/MR imaging. Biomaterials 32(17):4151–4160
80. Orive G, Hernandez RM, Rodríguez Gascón A, Domínguez-Gil A, Pedraz JL (2003) Drug delivery in biotechnology: present and future. Curr Opin Biotechnol 14(6):659–664
81. Colombo M, Carregal-Romero S, Casula MF, Gutierrez L, Morales MP, Boehm IB et al (2012) Biological applications of magnetic nanoparticles. Chem Soc Rev 41:4306–4334
82. Mashhadizadeh MH, Amoli-Diva M (2013) Atomic absorption spectrometric determination of Al^{3+} and Cr^{3+} after preconcentration and separation on 3-mercaptopropionic acid modified silica coated-Fe_3O_4 nanoparticles. J Anal At Spectrom 28:251–258
83. Kievit FM, Wang FY, Fang C, Mok H, Wang K, Silber JR et al (2011) Doxorubicin loaded iron oxide nanoparticles overcome multidrug resistance in cancer in vitro. J Control Release 152(1):76–83
84. Chomoucka J, Drbohlavova J, Huska D, Adam V, Kizek R, Hubalek J (2010) Magnetic nanoparticles and targeted drug delivering. Pharmacol Res 62(2):144–149
85. N'Guyen TTT, Duong HTT, Basuki J, Vr M, Pascual S, Cm G et al (2013) Functional iron oxide magnetic nanoparticles with hyperthermia-induced drug release ability by using a combination of orthogonal click reactions. Angew Chem Int Ed Engl 52(52):14152–14156
86. McBain SC, Yiu HHP, Dobson J (2008) Magnetic nanoparticles for gene and drug delivery. Int J Nanomedicine 3(2):169–180

87. Wilson MW, Kerlan RK Jr, Fidelman NA, Venook AP, LaBerge JM, Koda J et al (2004) Hepatocellular carcinoma: regional therapy with a magnetic targeted carrier bound to doxorubicin in a dual MR imaging/conventional angiography suite–initial experience with four patients. Radiology 230(1):287–293
88. Basuki JS, Duong HTT, Macmillan A, Erlich RB, Esser L, Akerfeldt MC et al (2013) Using fluorescence lifetime imaging microscopy to monitor theranostic nanoparticle uptake and intracellular doxorubicin release. ACS Nano 7(11):10175–10189
89. Laurent S, Dutz S, Häfeli UO, Mahmoudi M (2011) Magnetic fluid hyperthermia: focus on superparamagnetic iron oxide nanoparticles. Adv Colloid Interface Sci 166(1–2):8–23
90. Shen J-M, Guan X-M, Liu X-Y, Lan J-F, Cheng T, Zhang H-X (2012) Luminescent/magnetic hybrid nanoparticles with folate-conjugated peptide composites for tumor-targeted drug delivery. Bioconjug Chem 23(5):1010–1021
91. Kebede A, Singh AK, Rai PK, Giri NK, Rai AK, Watal G et al (2013) Controlled synthesis, characterization, and application of iron oxide nanoparticles for oral delivery of insulin. Lasers Med Sci 28(2):579–587
92. Shen J-M, Xu L, Lu Y, Cao H-M, Xu Z-G, Chen T et al (2012) Chitosan-based luminescent/magnetic hybrid nanogels for insulin delivery, cell imaging, and antidiabetic research of dietary supplements. Int J Pharm 427(2):400–409
93. Yu MK, Kim D, Lee IH, So JS, Jeong YY (2011) Jon S. Image-guided prostate cancer therapy using aptamer-functionalized thermally cross-linked superparamagnetic iron oxide nanoparticles. Small 7(15):2241–2249
94. Chen F-H, Zhang L-M, Chen Q-T, Zhang Y, Zhang Z-J (2010) Synthesis of a novel magnetic drug delivery system composed of doxorubicin-conjugated Fe_3O_4 nanoparticle cores and a PEG-functionalized porous silica shell. Chem Commun (Camb) 46(45):8633–8635
95. Kruse AM, Meenach SA, Anderson KW, Hilt JZ (2014) Synthesis and characterization of CREKA-conjugated iron oxide nanoparticles for hyperthermia applications. Acta Biomater 10(6):2622–2629
96. Zhao M, Kircher MF, Josephson L, Weissleder R (2002) Differential conjugation of tat peptide to superparamagnetic nanoparticles and its effect on cellular uptake. Bioconjug Chem 13(4):840–844
97. Strable E, Bulte JWM, Moskowitz B, Vivekanandan K, Allen M, Douglas T (2001) Synthesis and characterization of soluble iron oxide-dendrimer composites. Chem Mater 13(6):2201–2209
98. Bulte JWM, Kraitchman DL (2004) Iron oxide MR contrast agents for molecular and cellular imaging. NMR Biomed 17(7):484–499
99. Lu C-W, Hung Y, Hsiao J-K, Yao M, Chung T-H, Lin Y-S et al (2007) Bifunctional magnetic silica nanoparticles for highly efficient human stem cell labeling. Nano Lett 7(1):149–154
100. Arbab AS, Yocum GT, Kalish H, Jordan EK, Anderson SA, Khakoo AY et al (2004) Efficient magnetic cell labeling with protamine sulfate complexed to ferumoxides for cellular MRI. Blood 104(4):1217–1223
101. Yeh TC, Zhang W, Ildstad ST, Ho C (1995) In vivo dynamic MRI tracking of rat T-cells labeled with superparamagnetic iron-oxide particles. Magn Reson Med 33(2):200–208
102. Dodd CH, Hsu H-C, Chu W-J, Yang P, Zhang H-G, Mountz JD et al (2001) Normal T-cell response and in vivo magnetic resonance imaging of T cells loaded with HIV transactivator-peptide-derived superparamagnetic nanoparticles. J Immunol Methods 256(1–2):89–105
103. Cherukuri P, Glazer ES, Curley SA (2010) Targeted hyperthermia using metal nanoparticles. Adv Drug Deliv Rev 62(3):339–345
104. Chatterjee DK, Diagaradjane P, Krishnan S (2011) Nanoparticle-mediated hyperthermia in cancer therapy. Ther Deliv 2(8):1001–1014
105. Silva AC, Oliveira TR, Mamani JB, Malheiros SMF, Malavolta L, Pavon LF et al (2011) Application of hyperthermia induced by superparamagnetic iron oxide nanoparticles in glioma treatment. Int J Nanomedicine 6:591–603
106. Johannsen M, Thiesen B, Wust P, Jordan A (2010) Magnetic nanoparticle hyperthermia for prostate cancer. Int J Hyperthermia 26(8):790–795

107. Johannsen M, Gneveckow U, Eckelt L, Feussner A, Waldöfner N, Scholz R et al (2005) Clinical hyperthermia of prostate cancer using magnetic nanoparticles: presentation of a new interstitial technique. Int J Hyperthermia 21(7):637–647
108. Gordon AC, Lewandowski RJ, Salem R, Day DE, Omary RA, Larson AC (2014) Localized hyperthermia with iron oxide-doped yttrium microparticles: steps toward image-guided thermoradiotherapy in liver cancer. J Vasc Interv Radiol 25(3):397–404
109. Hayashi K, Ono K, Suzuki H, Sawada M, Moriya M, Sakamoto W et al (2010) High-frequency, magnetic-field-responsive drug release from magnetic nanoparticle/organic hybrid based on hyperthermic effect. ACS Appl Mater Interfaces 2(7):1903–1911
110. Dobbrow C, Schmidt AM (2012) Improvement of the oxidation stability of cobalt nanoparticles. Beilstein J Nanotechnol 3:75–81
111. Hergt R, Dutz S (2007) Magnetic particle hyperthermia—biophysical limitations of a visionary tumour therapy. J Magn Magn Mater 311(1):187–192
112. Walther W, Siegel R, Kobelt D, Knösel T, Dietel M, Bembenek A et al (2008) Novel jet-injection technology for nonviral intratumoral gene transfer in patients with melanoma and breast cancer. Clin Cancer Res 14(22):7545–7553
113. Cederfjäll E, Sahin G, Kirik D (2012) Key factors determining the efficacy of gene therapy for continuous DOPA delivery in the Parkinsonian brain. Neurobiol Dis 48(2):222–227
114. Huschka R, Barhoumi A, Liu Q, Roth JA, Ji L, Halas NJ (2012) Gene silencing by gold nanoshell-mediated delivery and laser-triggered release of antisense oligonucleotide and siRNA. ACS Nano 6(9):7681–7691
115. Dobson J (2006) Gene therapy progress and prospects: magnetic nanoparticle-based gene delivery. Gene Ther 13(4):283–287
116. Boyer C, Priyanto P, Davis TP, Pissuwan D, Bulmus V, Kavallaris M et al (2010) Anti-fouling magnetic nanoparticles for siRNA delivery. J Mater Chem 20:255–265
117. Yu-Feng T, Shu-Jun H, Shi-Shen Y, Liang-Mo M (2013) Oxide magnetic semiconductors: materials, properties, and devices. Chinese Physics B 22(8):088505
118. Mah C, Fraites TJ Jr, Zolotukhin I, Song S, Flotte TR, Dobson J et al (2002) Improved method of recombinant AAV2 delivery for systemic targeted gene therapy. Mol Ther 6(1):106–112
119. Safarik I, Safarikova M (2004) Magnetic techniques for the isolation and purification of proteins and peptides. Biomagn Res Technol 2:1
120. Widjojoatmodjo MN, Fluit AC, Torensma R, Verhoef J (1993) Comparison of immunomagnetic beads coated with protein A, protein G, or goat anti-mouse immunoglobulins Applications in enzyme immunoassays and immunomagnetic separations. J Immunol Methods 165(1):11–19
121. Fan J, Lu J, Xu R, Jiang R, Gao Y (2003) Use of water-dispersible Fe_2O_3 nanoparticles with narrow size distributions in isolating avidin. J Colloid Interface Sci 266(1):215–218
122. Nagatani N, Shinkai M, Honda H, Kobayashi T (1998) Development of a new transformation method using magnetite cationic liposomes and magnetic selection of transformed cells. Biotech Techn 12(7):525–528
123. Lobel B, Eyal O, Kariv N, Katzir A (2000) Temperature controlled CO_2 laser welding of soft tissues: urinary bladder welding in different animal models (rats, rabbits, and cats). Lasers Surg Med 26(1):4–12
124. Dew DK, Supik L, Darrow CR, Price GF (1993) Tissue repair using lasers: a review. Orthopedics 16(5):581–587
125. Domenech M, Marrero-Berrios I, Torres-Lugo M, Rinaldi C (2013) Lysosomal membrane permeabilization by targeted magnetic nanoparticles in alternating magnetic fields. ACS Nano 7(6):5091–5101
126. Choi J, Shin J, Lee J, Cha M (2012) Magnetic response of mitochondria-targeted cancer cells with bacterial magnetic nanoparticles. Chem Commun 48:7474–7476

Index

© Springer International Publishing AG 2017

S.K. Sharma (ed.), *Complex Magnetic Nanostructures*,
DOI 10.1007/978-3-319-52087-2